AGH University of Science and Technology
Faculty of Physics and Applied Computer Science

Doctoral thesis

Rafał Sikora

Measurement of the diffractive central exclusive production in the STAR experiment at RHIC and the ATLAS experiment at LHC

Supervisors: **prof. dr hab. inż. Mariusz Przybycień**
dr inż. Leszek Adamczyk

Cracow, September 2020

Declaration of the author of this dissertation:

Aware of legal responsibility for making untrue statements I hereby declare that I have written this dissertation myself and all the contents of the dissertation have been obtained by legal means.

date, author signature

Declaration of the thesis Supervisor:

This dissertation is ready to be reviewed.

date, supervisor signature

Executive summary

We live in the era of the most powerful particle colliders ever built, reaching unprecedented centre-of-mass system energies ($\sqrt{s}$) and luminosities. The attention of the high-energy physics community is focused on searches of the New Physics phenomena and measurements related to the rare processes within the Standard Model, including production of the Higgs boson, discovered in 2012. However, there are numerous physics processes of significant contribution to the total cross section, which are not well measured nor described theoretically, still being a subject to studies. Such processes are often recognised as a background in the analyses of rare process and thus their mismodelling leads to large uncertainties of the results of such analyses.

Among the aforementioned class of physics processes are diffractive interactions, occurring in the high-energy limit via exchange of the colourless object called the Pomeron. Diffraction is experimentally revealed by presence of the rapidity gap, or gaps, in the topology of the final state. It contributes about 30% to the total proton-proton cross section at the centre-of-mass system energies achievable at the two proton-proton colliders currently in operation: the Relativistic Heavy Ion Collider (RHIC) and the Large Hadron Collider (LHC).

The inelastic diffractive processes can further be divided into single, double and central diffraction. The last one proceeds via the Double Pomeron Exchange (DPE), which occurs when each of the interacting beam particles emits a Pomeron and scatters at small angle. The Pomerons form a neutral state X, while the beam particles get excited, dissociate or stay intact. If all particles of the state X are well separated from the beam particles or their remnants, we talk about the central exclusive production (CEP), written as $B_1 + B_2 \to B_1^{(*)} + X + B_2^{(*)}$. CEP in high-energy proton-proton collisions is dominated by the DPE, with additional contributions from photon-Pomeron and photon-photon interactions, the last one being non-diffractive CEP.

In this dissertation the study of diffractive CEP in proton-proton collisions with the measurement of the forward-scattered protons is presented. The process is measured in the STAR experiment at RHIC and the ATLAS experiment at the LHC, at $\sqrt{s} = 200$ GeV and 13 TeV, respectively. It is the first time when CEP is measured at such high centre-of-mass system energies with the detection of forward-scattered beam particles. This is enabled by dedicated devices housed inside the Roman Pot vessels, which are mounted at the accelerator beam pipe and which allow detectors to closely approach the beamline and to tag particles scattered at low angles. As a result, the exclusivity can be confirmed by the momentum balance of all detected particles, rather then inferred from the double rapidity gap topology, as is done in the experiments without these special forward detectors.

The thesis starts with the introductory part providing theoretical basis required to understand and follow the flow thereof. Phenomenological description of diffractive CEP developed in the language of the Regge theory is described and the Monte Carlo (MC) event generators implementing various models of the process are introduced. The following two parts contain details of analyses performed respectively at STAR and ATLAS, including description of the hardware and experimental techniques used during the data taking, in an event reconstruction and in the physics analysis. These techniques are conceptually similar but, despite of the same physics process being analysed, required adjustment for the two independent measurements. It is a direct consequence of completely different experimental conditions at STAR and ATLAS. In the last part, the results obtained in the two experiments are discussed and conclusions are presented.

The primary results of the physics analyses are the cross sections for the diffractive CEP of identified

charged hadron systems, $p + p \to p + X + p$, where $X = \pi^+\pi^-, K^+K^-, p\bar{p}$ (STAR), and $X = \pi^+\pi^-$, $2\pi^+2\pi^-, 3\pi^+3\pi^-, 4\pi^+4\pi^-$ (ATLAS), measured within the fiducial kinematic region corresponding to the geometrical coverage of detection systems used at STAR and ATLAS experiments. The reached experimental precision is several times better than the precision of the measurement of CEP with the forward proton tagging at the highest-so-far $\sqrt{s}$, performed by the AFS and the SFM experiments at the ISR. Measurement of $4\pi^+4\pi^-$ central systems in ATLAS is probably the only measurement of such high central state multiplicity in the CEP process.

These fiducial cross sections are compared with the available models of the continuum production, of which none is able to describe the data in all studied production channels. It indicates a significant contribution from resonance production, as well as interference effects between different production mechanisms.

Single differential cross sections as a function of the invariant mass of the centrally produced $\pi^+\pi^-$ pairs are extrapolated to the Lorentz-invariant phase space region which allows decomposition into continuum and resonant part, together with an identification of the observed resonances. These are $f_0(980)$ and $f_0(1500)$ (scalar mesons), and $f_2(1270)$ (tensor meson). There is no clear evidence for the production of the vector mesons such as $\rho(770)$. It confirms the dominance of the DIPE mechanism in CEP at studied energies and in the available kinematic range. On the other hand, there are strong pieces of evidence for the production of the $f_0(500)$, a resonance around the mass of 1370 MeV - presumably $f_0(1370)$, and a resonance around the mass of 2.3 GeV.

Parameters of resonances extracted with the fit to extrapolated invariant mass cross section are the integrated resonance production cross section and the relative phases between the amplitudes, in a few cases also the resonance mass and the width. The production cross sections are found to strongly change with the azimuthal separation of the forward-scattered protons, hence on the incident angle of the IPomerons in the laboratory in the plane transverse to the incoming beams. It is observed that the scalar mesons are preferentially produced at low such angles. In this configuration, the relative momentum of interacting IPomerons is reduced. In connection with the fact, that the simplest chromodynamical representation of the IPomeron is a colour-neutral pair of gluons, enhancement of the production in this configuration may suggest some gluon content in the resonant state, or even the gluon bound state ("glueball"). One of the observed scalar mesons, which resembles the described production enhancement, $f_0(1500)$, is generally considered as a potential lowest-mass glueball.

The contributions from the non-resonant production to CEP cross sections were extracted from the data and confronted with the dedicated continuum models. Comparisons provided limits on the range of parameters of these models describing the meson form factors and absorption effects related to the rapidity gap survival probability.

In the single differential cross sections as a function of the invariant mass of the centrally produced $2\pi^+2\pi^-$ system, the axial-vector resonance, $f_1(1285)$, was identified and the integrated cross sections were determined for two ranges of azimuthal angle between forward-scattered protons. Within the fiducial phase-space, the $f_1(1285)$ production is found independent from that angle.

Detection of the forward-scattered protons enabled reconstruction of the squared four-momentum transfer t and later the exponential fit to double differential cross section in t_1 and t_2 in the $\pi^+\pi^-$ and $2\pi^+2\pi^-$ channels. The extracted slope parameters, in the case of CEP of $\pi^+\pi^-$ pairs, vary significantly along with the studied range of the invariant mass of the central system, and the azimuthal angle between the scattered beam protons.

The results from the presented study are expected to provide strong constraints to parameters of the models of DIPE in high-energy particle interactions.

Streszczenie

Żyjemy w erze najpotężniejszych zderzaczy cząstek jakie kiedykolwiek zbudowano, osiągających niespotykane wcześniej energie zderzeń w układzie środka masy oraz świetlności. Uwaga środowiska fizyków wysokich energii jest skoncentrowana na poszukiwaniach zjawisk Nowej Fizyki oraz pomiarach związanych z rzadkimi procesami przewidywanymi przez Model Standardowy, takimi jak produkcja odkrytego w 2012 roku bozonu Higgsa. Obok tych niezwykle ciekawych zagadnień można wyodrębnić liczną grupę procesów fizycznych o istotnym wkładzie do całkowitego przekroju czynnego, które nie zostały dotychczas precyzyjnie zmierzone ani opisane teoretycznie i wciąż wymagają badań w celu lepszego ich zrozumienia. Często bywają one istotnym tłem w analizach dedykowanych rzadkim procesom, przez co niepewności w ich modelowaniu zmniejszają precyzję pomiarów w owych analizach.

Pośród wspomnianej klasy procesów fizycznych można wyróżnić oddziaływania dyfrakcyjne, które przy dostatecznie dużych energiach zachodzą wyłącznie poprzez wymianę bezbarwnego obiektu zwanwgo IPomeronem. W eksperymentach zjawisko dyfrakcji rozpoznaje się poprzez występowanie w konfiguracji stanu końcowego przerwy (lub przerw) w przestrzeni pospieszności. Dyfrakcja ma około trzydziestoprocentowy wkład do całkowitego przekroju czynnego na oddziaływanie proton-proton przy energiach zderzeń w układzie środka masy osiągalnych w dwóch działających obecnie zderzaczach protonów: Zderzacza Relatywistycznych Ciężkich Jonów (ang. RHIC) oraz Wielkiego Zderzacza Hadronów (ang. LHC).

Nieelastyczne procesy dyfrakcyjne dzieli się na pojedynczą, podwójną oraz centralną dyfrakcję. Ta ostatnia zachodzi poprzez podwójną wymianę IPomeronu (ang. DIPE), mającą miejsce, gdy obie z oddziałujących cząstek ze zderzanych wiązek emitują IPomeron i rozpraszają się pod niewielkimi kątami. Obiektem uformowanym przez oddziałujące IPomerony jest neutralny stan X, zaś cząstki wiązek zostają wzbudzone, dysocjują lub zachowują swój stan. W przypadku, gdy wszystkie cząstki stanu X są wyraźnie odseparowane od cząstek wiązek lub produktów ich fragmentacji, mówi się o centralnej produkcji ekskluzywnej (ang. CEP), co zapisuje się jako $B_1 + B_2 \rightarrow B_1^{(*)} + X + B_2^{(*)}$. CEP w wysokoenergetycznych zderzeniach proton-proton zachodzi głównie poprzez DIPE. Dodatkowo obserwuje się przyczynek pochodzący od oddziaływań foton-IPomeron i foton-foton, z których ten drugi można określić jako niedyfrakcyjną CEP.

Niniejsza rozprawa zawiera opis badań dyfrakcyjnej centralnej produkcji ekskluzywnej opracowanych na podstawie danych ze zderzeń proton-proton z jednoczesnym pomiarem protonów rozproszonych "do przodu". Proces zmierzono w ramach eksperymentu STAR na zderzaczu RHIC oraz eksperymentu ATLAS na zderzaczu LHC przy energiach zderzeń proton-proton w układzie środka masy równych odpowiednio 200 GeV i 13 TeV. Jest to pierwszy pomiar procesu CEP przy tak wysokich energiach zderzeń z jednoczesną detekcją cząstek wiązek rozproszonych w kierunku "do przodu". Było to możliwe dzięki wyspecjalizowanym detektorom umieszczonym we wnękach zintegrowanych z elementami zderzacza, nazywanych rzymskimi garnkami (ang. Roman Pot), które umożliwiają znaczne zbliżenie detektorów do wiązek, a dzięki temu detekcję cząstek rozproszonych pod niewielkimi kątami. Pozwala to wykazać ekskluzywność mierzonego procesu poprzez balans całkowitego pędu układu mierzonych cząstek, inaczej niż w przypadku eksperymentów nieposiadających omawianych detektorów, które wnioskują o ekskluzywności na podstawie dwóch przerw w pospieszności.

Praca rozpoczyna się od wstępu zawierającego teoretyczne podstawy wymagane do prześledzenia toku opisywanych badań. Przedstawiony został tu opis dyfrakcyjnej CEP rozwinięty w języku teorii

Regge, a także generatory przypadków implementujące różne modele procesu, wykorzystujące do tego metody Monte Carlo (MC). Kolejne dwie części zawierają dokładny opis analiz przeprowadzonych w ramach eksperymentu STAR i ATLAS. Składa się na nie przedstawienie układu detekcyjnego oraz technik eksperymentalnych wykorzystanych przy zbieraniu danych, rekonstrukcji przypadków i analizie fizycznej. Techniki te są koncepcyjnie podobne, lecz pomimo analizy tego samego procesu fizycznego w dwóch eksperymentach, niezbędna była ich adaptacja do tych dwóch niezależnych pomiarów. Wynika to bezpośrednio z odmiennych warunków eksperymentalnych występujących przy detektorze STAR i ATLAS. W ostatniej części pracy dyskutowane są wyniki obu analiz oraz przedstawione zostają płynące z nich konkluzje.

Zasadniczym wynikiem przeprowadzonych analiz fizycznych są przekroje czynne na proces dyfrakcyjnej CEP układów zidentyfikowanych hadronów, $p + p \to p + X + p$, gdzie $X = \pi^+\pi^-, K^+K^-, p\bar{p}$ (eksperyment STAR), oraz $X = \pi^+\pi^-, 2\pi^+2\pi^-, 3\pi^+3\pi^-, 4\pi^+4\pi^-$ (eksperyment ATLAS), zmierzone w ograniczonym obszarze przestrzeni fazowej (ang. fiducial cross sections) określonym na kinematycznych wielkościach opisujących stan centralny i protony rozproszone "do przodu", odpowiadającym geometrycznemu pokryciu systemów pomiarowych w eksperymencie STAR i ATLAS. Uzyskana precyzja pomiaru jest kilkukrotnie wyższa od tej osiągniętej w pomiarze CEP z detekcją rozproszonych cząstek wiązki przy dotychczasowej najwyższej energii zderzeń, wykonanej przez eksperymenty AFS oraz SFM przy zderzaczu ISR. Pomiar centralnego stanu $4\pi^+4\pi^-$ w eksperymencie ATLAS jest prawdopodobnie jedynym pomiarem stanu centralnego o tak dużej krotności w procesie CEP.

Przekroje czynne fiducial zostały porównane z dostępnymi modelami kontinuum (nierezonansowej CEP), spośród których żaden nie opisuje poprawnie otrzymanych punktów pomiarowych w każdym z badanych kanałów reakcji. Wskazuje to na znaczący wkład składowej rezonansowej, implikując również niepomijalny wpływ kwantowych efektów interferencyjnych pomiędzy różnymi mechanizmami produkcji.

Różniczkowe przekroje czynne w funkcji masy niezmienniczej centralnie wyprodukowanej pary $\pi^+\pi^-$ są ekstrapolowane do lorentzowsko-niezmienniczego obszaru przestrzeni fazowej umożliwiając dekompozycję na część nierezonansową i rezonansową, jak również identyfikację zaobserwowanych stanów rezonansowych. Są nimi mezony skalarne $f_0(980)$ i $f_0(1500)$, a także mezon tensorowy $f_2(1270)$. Brak jest świadectwa produkcji mezonów wektorowych jak np. $\rho(770)$, co potwierdza dominację podwójnej wymiany IPomeronu w CEP przy badanych energiach zderzeń i w dostępnym obszarze kinematycznym. Istnieje z kolei znaczące wskazanie na produkcję stanu $f_0(500)$, rezonansu w okolicach masy 1370 MeV - potencjalnie mezonu $f_0(1370)$, oraz rezonansu o masie około 2.3 GeV.

Z przeprowadzonego dopasowania założonego modelu do ekstrapolowanego przekroju czynnego w funkcji masy niezmienniczej pary $\pi^+\pi^-$ otrzymano parametry rezonansów: całkowity przekrój czynny na produkcję rezonansu w badanym kanale oraz przesunięcie fazowe amplitudy na produkcję rezonansu, jak również w kilku przypadkach masę i szerokość rezonansu. Obserwuje się silną zależność przekroju czynnego na produkcję rezonansów od separacji azymutalnej protonów rozproszonych "do przodu", co odpowiada kątowi zderzenia dwóch oddziałujących IPomeronów w układzie laboratoryjnym w płaszczyźnie prostopadłej do zderzających się wiązek. W takiej konfiguracji względny pęd IPomeronów jest zredukowany, co w połączeniu z podstawową reprezentacją chromodynamiczną IPomeronu w postaci kolorowo-neutralnej kombinacji dwóch gluonów, może wskazywać - w przypadku wzmocnienia produkcji w takiej konfiguracji - na istnienie komponenty gluonowej w stanie rezonansowym, a nawet całkowicie gluonowej naturze takiego stanu (stan związany gluonów, ang. glueball). Jednym z rezonansów w przypadku którego zaobserwowano opisaną zależność jest $f_0(1500)$, powszechnie wskazywany jako potencjalny glueball o najniższej masie.

Wyodrębniony wkład do przekroju czynnego na proces CEP od produkcji nierezonansowej został porównany z dedykowanymi modelami kontinuum. Z porównania wynikają ograniczenia na pewne parametry tych modeli związane z czynnikami postaci mezonów (ang. form factors) i efektami absorpcyjnymi, powiązanymi z prawdopodobieństwem zachowania przerwy w pospieszności (ang. rapidity gap survival probability) w stanie końcowym.

W przypadku różniczkowego przekroju czynnego w funkcji masy niezmienniczej centralnie wyprodukowanego stanu $2\pi^+2\pi^-$ zidentyfikowano osiowo-wektorowy mezon $f_1(1285)$. Wyznaczono wycałkowane przekroje czynne na produkcję tego rezonansu w dostępnym obszarze przestrzeni fazowej, osobno dla dwóch zakresów kąta azymutalnego pomiędzy rozproszonymi protonami wiązki. Przekrój czynny fiducial na produkcję rezonansu okazał się nie zależeć od wspomnianego kąta.

Detekcja protonów rozproszonych "do przodu" umożliwiła rekonstrukcję wielkości t będącej kwadratem przekazu czteropędu w wierzchołku protonowym, a w konsekwencji, w przypadku produkcji stanów $\pi^+\pi^-$ i $2\pi^+2\pi^-$, dopasowanie funkcji wykładniczej do podwójnie-różniczkowego przekroju czynnego w funkcji t_1 i t_2. W przypadku CEP par $\pi^+\pi^-$ wartość parametru nachylenia rozkładu wykładniczego zmienia się istotnie w zakresie badanych mas niezmienniczych stanu centralnego, jak również zależy od kąta azymutalnego pomiędzy rozproszonymi protonami wiązki.

Oczekuje się, że otrzymane wyniki nałożą silne ograniczenia na parametry modeli DIPE w wysokoenergetycznych oddziaływaniach cząstek.

Acknowledgements

Over the last six years everything in my life revolved around the PhD studies. It was a difficult time full of work on one side, and satisfaction on the other. There are many people who have helped me during this period (and long before), and to whom I am very grateful and committed.

At the beginning I would like to thank my supervisors, Prof. Mariusz Przybycień and Dr. Leszek Adamczyk. I am indebted to Prof. Przybycień, as he is the person who introduced me to the scientific projects during the B.Sc. studies, first to the European Student Moon Orbiter (ESMO) project, later to the STAR experiment at RHIC. Since then he has guided me and took care of my progress, and I would probably not have entered the high energy physics without his efforts. I would like to express my deepest gratitude to Dr. Adamczyk, with whom I have closely worked since my B.Sc. studies. He was supervising my analysis of the elastic proton-proton scattering at STAR for the B.Sc. and M.Sc. degrees, and the CEP analysis at STAR and ATLAS for the PhD degree. He was always helpful and available for discussions. I really learned a lot from him and I appreciate highly his competences. I am thankful to both of my supervisors for introducing me to the "forward physics" and providing the possibility to analyse the CEP process at STAR and ATLAS.

Since the first experience with the STAR experiment an important person in my scientific career is Dr. Włodzimierz Guryn, the father of the Roman Pot program at STAR. I am very grateful to him for teaching me to look at problems from different perspectives, and for hospitality during my visits to BNL. I always appreciate and respect his opinion.

I wish to thank Dr. Iwona Grabowska-Bołd who has enabled me to join the ATLAS group at the AGH UST and to participate in the ATLAS experiment.

For the years of doctoral studies I have closely worked with my office mate, (since July - Dr.) Łukasz Fulek. I want to thank him for many discussions and cooperation in STAR and ATLAS activities.

I express my gratitude to my high school physics teacher, M.Sc. Romuald Kondys, who developed my interest in physics and helped prepare for scientific competitions.

I thank my Parents for their care, efforts and support of my education through nearly 30 years. I am very grateful to them, and my Grandparents, for all I have got.

This work was partly supported by the National Science Centre of Poland under grants UMO-2015/19/B/ST2/00989 and UMO-2015/18/M/ST2/00162. The author has been also supported by the Smoluchowski scholarship from the KNOW funding.

Podziękowania

Ostatnie sześć lat mojego życia w głównej mierze toczyło się wokół tematu studiów doktoranckich. Był to czas trudny, pełen pracy, z którego jednocześnie czerpałem wiele satysfakcji. W tym miejscu chciałbym wyrazić swoją wdzięczność i zobowiązanie wobec tak wielu osób, które w tym (a także wcześniejszym) okresie były mi pomocne.

Pragnę przede wszystkim podziękować moim promotorom, prof. dr. hab. inż. Mariuszowi Przybycieniowi oraz dr. inż. Leszkowi Adamczykowi. Jestem wdzięczny prof. Przybycieniowi, gdyż wprowadził mnie w projekty naukowe w czasie studiów inżynierskich, najpierw w projekt budowy studenckiego orbitera księżycowego (ang. European Student Moon Orbiter, ESMO), a później w eksperyment STAR na zderzaczu RHIC. Od tamtego czasu prowadzi i wspiera mój rozwój. Bez jego udziału pewnie nie zająłbym się tematyką fizyki wysokich energii. Chciałbym wyrazić głębokie podziękowanie dr. Adamczykowi z którym blisko współpracowałem od czasu studiów inżynierskich. Nadzorował prowadzoną przez mnie analizę elastycznego rozpraszania proton-proton w eksperymencie STAR, która była tematem mojej pracy inżynierskiej oraz magisterskiej, jak również analizy CEP w eksperymentach STAR i ATLAS, będące tematem tej pracy. Zawsze mogłem oczekiwać pomocy z jego strony i nigdy nie zabrakło mu dla mnie czasu. Bardzo wiele się od niego nauczyłem i doceniam jego wysokie kompetencje. Obu promotorom dziękuję za wprowadzenie mnie w tematykę "fizyki do przodu" i umożliwienie prowadzenia analizy CEP w eksperymentach STAR oraz ATLAS.

Od pierwszego kontaktu z eksperymentem STAR ważną osobą w mojej naukowej karierze jest dr Włodzimierz Guryn, ojciec programu detektorów Roman Pot w STAR. Jestem mu bardzo wdzięczny za naukę spojrzenia z różnej perspektywy na pojawiające się w analizie problemy, jak również za niezwykłą gościnność w czasie pobytów w BNL. Zawsze wysoko cenię i szanuję jego opinię.

Chcę podziękować dr hab. inż. Iwonie Grabowskiej-Bołd za włączenie do grupy ATLAS w AGH i umożliwienie współpracy w ramach eksperymentu ATLAS.

Przez lata studiów doktoranckich blisko współpracowałem z kolegą (od lipca - dr. inż.) Łukaszem Fulkiem. Chcę mu podziękować za niezliczone dyskusje i współpracę w aktywnościach w eksperymentach STAR i ATLAS.

Wyrażam wdzięczność mojemu nauczycielowi fizyki w liceum, mgr. Romualdowi Kondysowi, który wzbudził moje zainteresowanie fizyką i pomagał w przygotowaniach do olimipiad naukowych.

Dziękuję moim Rodzicom za troskę, wysiłek i wsparcie mojej edukacji przez blisko 30 lat. Jestem im, jak również Dziadkom, bardzo wdzięczny za wszystko, co otrzymałem.

Praca powstała w wyniku realizacji projektów badawczych nr UMO-2015/19/B/ST2/00989 oraz UMO-2015/18/M/ST2/00162 finansowanych ze środków Narodowego Centrum Nauki. Autor otrzymał również wsparcie w ramach stypendium Smoluchowskiego z funduszu KNOW.

Author's contribution

As a doctoral student, I have been involved in several activities, in addition to the physics analyses presented in the thesis. They were mainly related to the STAR experiment, which I joined as a bachelor student in summer 2012. My work related to the ATLAS experiment started in fall 2015. Regarding the results presented in the thesis, they were obtained solely by myself, except for some analyses ingredients, which are common to the whole experiment and obligatory to be applied in all data analyses. In all such cases this is appropriately referenced in the text.

I actively participated in the commissioning of the STAR Roman Pot (RP) system for the data-taking campaign of 2015, when the data set used in the analysis presented in Part II of this thesis, was collected. It was the first time when the RPs at STAR where operating in regular runs and in this configuration. On the hardware side, I tested the RP trigger counters before the data-taking and maintained the detectors in the collider tunnel. I have also contributed to development of the logic of triggers involving proton tagging in RPs and participated in the synchronisation of the timing of the RP system and the STAR central detector at the very beginning of data-taking. During the data-taking, I have been monitoring the data quality by performing fast online and offline analyses. I have also prepared and maintained RP data summary web page and electronic logbook.

With the data being already 'on tape', my efforts were focused on software-related tasks. I developed, implemented and validated the RP track reconstruction code, which is, since then, integrated into the official STAR software. I co-developed Geant4 simulation of the RP system at STAR, implementing e.g. geometry of the Roman Pot vessels, SSD detectors and trigger counters, data digitisation and embedding of the simulated data into the real data. This detector model enables systematic studies of the reconstruction efficiency, beam-induced and geometrical acceptance effects, which are the crucial elements in physics analyses of processes with forward-scattered protons.

Experience gained during 2015 data-taking campaign and through the process of analysis of these data, helped to improve the CEP trigger for 2017 data-taking campaign at larger proton-proton centre-of-mass system energy of 510 GeV. I also participated in the preparation of the RP detectors to this data-taking campaign. Overall, I took part in a number of the STAR experiment shifts, starting from the regular shift crew, through the role of detector operator, finally taking responsibility for a several weeks as a STAR shift leader.

During the years of doctoral studies there was a number of internal STAR and ATLAS experiment meetings, where I presented the analyses updates and often successfully proposed innovative analysis methods in front of collaborators. Most of the meetings were informal (e.g. physics working group meetings), but there were some more formal, e.g. ATLAS Standard Model Meeting in Madrid (2016) or annual STAR Collaboration meetings where results were presented to a significant number of ATLAS or STAR collaborators.

I had an opportunity to practice my organisational skills, playing an active role as a co-organizer of the STAR Collaboration Meeting in Kraków in August 2019, which gathered dozens of scientists from all over the world.

In total, as a doctoral student I spent 6 months at BNL and 2 months at CERN. I presented results of physics analyses described in this dissertation in form of oral presentations at 4 recognised international workshops. I also participated in 3 physics schools. At these schools, I presented posters 2 times, each

time winning the prize for the best poster. The list of main conferences, workshops and schools in which I participated, as well conference proceedings and posters, is provided below.

All scientific papers and conference presentations of my (co-)authorship can be found at INSPIRE (ID: 1342374) and ORCID (ID: 0000-0001-5185-2367). For the published article of my principal authorship, Ref. [1], I have personally prepared the HEPdata record and the Rivet analysis routine.

Published articles of my leading (•) or significant (∘) contributions

[•] STAR Collaboration, J. Adam et al. (R. Sikora), *Measurement of the central exclusive production of charged particle pairs in proton-proton collisions at* $\sqrt{s} = 200$ *GeV with the STAR detector at RHIC*, JHEP **07** (2020) 178, arXiv: 2004.11078 [hep-ex]. (identical to Ref. [1])

[∘] STAR Collaboration, J. Adam et al. (R. Sikora), *Results on Total and Elastic Cross Sections in Proton-Proton Collisions at* $\sqrt{s} = 200$ *GeV*, Phys. Lett. B **808** (2020) 135663, arXiv: 2003.12136 [hep-ex]. (identical to Ref. [2])

[∘] J. Chwastowski et al. (R. Sikora), *Feasibility Studies of Exclusive Diffractive Bremsstrahlung Measurement at RHIC Energies*, Acta Phys. Polon. B **26** (2015) 10, arXiv: 1501.06264 [hep-ex].

Conference presentations and proceedings

[Pres. 1] R.Sikora (for the STAR Collaboration), *Measurement of the central exclusive production of charged particle pairs in proton-proton collisions at* $\sqrt{s} = 200$ *GeV with the STAR detector at RHIC* [video record], 40$^{\text{th}}$ International Conference on High Energy Physics, 28 July - 6 August 2020, Prague, Czech Republic (online).

[Pres. 2] R.Sikora (for the STAR Collaboration), *Recent results on Central Exclusive Production with the STAR detector at RHIC*, Diffraction and Low-x 2018, 26 August - 1 September 2018, Reggio di Calabria, Italy. Proceedings: *Recent results on Central Exclusive Production with the STAR detector at RHIC*, Acta Phys. Polon. Proc. Supp. **12** (2019) 811, arXiv: 1811.03315 [hep-ex].

[Pres. 3] R.Sikora (for the STAR Collaboration), *Recent results on Central Exclusive Production with the STAR detector at RHIC*, Diffraction 2016, 2-8 September 2016, Acireale, Italy. Proceedings: *Central Exclusive Production in the STAR Experiment at RHIC*, AIP Conf. Proc. **1819** (2017) 40012, arXiv: 1611.07823 [nucl-ex].

[Pres. 4] R.Sikora (for the STAR Collaboration), *Central Exclusive Production of meson pairs in proton-proton collisions at* $\sqrt{s} = 200$ *GeV in the STAR experiment at RHIC*, Low-x Meeting 2015, 1-5 September 2015, Sandomierz, Poland.

[Pres. 5] R.Sikora, *Study of elastic proton-proton scattering with the STAR detector at RHIC*, XXXVI-th IEEE-SPIE Joint Symposium Wilga 2015, 24-31 May 2015, Wilga, Poland. Proceedings: *Study of elastic proton-proton scattering with the STAR detector at RHIC*, Proc. SPIE Int. Soc. Opt. Eng. **9662** (2015) 96622F.

Participation in physics schools and presented posters

[Sch. 1] *XIV ICFA School on Instrumentation in Elementary Particle Physics*, 27 November - 8 December 2017, La Habana, Cuba. Presented poster: *Central Exclusive Production with forward proton measurement in ATLAS* (Best poster award).

[Sch. 2] *WE-Heraeus Physics School "QCD - Old Challenges and New Opportunities"*, 24-30 September 2017, Bad Honnef, Germany. Presented poster: *Central Exclusive Production with forward proton measurement in ATLAS* (Best poster award).

[Sch. 3] *2016 European School of High-Energy Physics*, 15-28 June 2016, Skeikampen, Norway.

Contents

Part I

Introduction

This dissertation reports the measurement of the diffractive central exclusive production in the STAR experiment at RHIC and in the ATLAS experiment at the LHC.

In the following introductory part, a compact review of the theory topics directly connected with the conducted measurements is presented. The introduction has been limited to those elements of theory of particle physics, which are crucial to understanding the goals of the experimental parts of the thesis (II, III) and to follow the discussion of results (part IV), presented thereafter. At the end of this part, the main objectives of the research are presented.

Throughout the thesis the convention $c = \hbar = 1$ is used. The list of frequently used acronyms is provided in App. A.

1. Theoretical introduction

1.1 The Standard Model

The Standard Model (SM) of particle physics is the current, widely accepted, theory of elementary particles and their interactions. It describes three out of four fundamental forces in nature: the electromagnetic force - responsible e.g. for repulsion (attraction) of the same-sign (opposite-sign) electric charges, the strong force - binding e.g. the nuclei in atomic nucleus together despite of the Coulomb repulsion, and the weak force - manifesting itself e.g. through the beta decays of radioactive isotopes. The remaining force, irrelevant at the particle level and hence not discussed - gravity - is described by the general theory of relativity and is not currently included in the SM.

Several classes of elementary particles, introduced in Tab. 1.1, can be distinguished. The first type are quarks, q, undergoing all fundamental interactions. The second are leptons, ℓ, which interact electromagnetically (charged) and weakly (all). The two aforementioned kinds of SM particles form a group of elementary fermions. The third group of elementary particles are gauge bosons, which mediate the interactions: gluons - strong, photon - electromagnetic, Z and $W^{\pm}$ - weak. The last piece of the SM is the Higgs boson, responsible for a mass hierarchy of other elementary particles. The Higgs boson was discovered in 2012 by ATLAS [3] and CMS [4] experiments at the LHC, after extensive searches conducted in numerous experiments for past several decades.

Quarks and leptons are accompanied by their anti-particles, which have the same mass but the opposite electric charge. They are grouped in three generations. Measurement of the production cross section of the Z boson in the e^+e^- collisions at LEP [6, 7] has proven existence of exactly three quark-lepton families within the SM. Complex objects, like hadrons, are made of three quarks (baryons,

1st generation		2nd generation		3rd generation					
2.3 MeV 2/3 1/2	UP u	1.28 GeV 2/3 1/2	CHARM c	173 GeV 2/3 1/2	TOP t	0 0 1	GLUON g	0 0 1	PHOTON γ
4.8 MeV −1/3 1/2	DOWN d	95 MeV −1/3 1/2	STRANGE s	4.18 GeV −1/3 1/2	BOTTOM b	91.2 GeV 0 1	Z BOSON Z	80.4 GeV ±1 1	W BOSON W
511 keV −1 1/2	ELECTRON e	105.7 MeV −1 1/2	MUON μ	1.777 GeV −1 1/2	TAU τ				
< 2 eV 0 1/2	ELECTRON NEUTRINO ν_e	< 2 eV 0 1/2	MUON NEUTRINO ν_μ	< 2 eV 0 1/2	TAU NEUTRINO ν_τ				
						125 GeV 0 0	HIGGS BOSON H		

Table 1.1: The elementary particles in the Standard Model. In each cell, the name and symbol of a particle, its experimentally determined (asymptotic) mass, electric charge and spin are provided. Quarks, leptons and gauge bosons are represented by cells filled with light orange, green and blue colour, respectively. The Higgs boson is in violet. Values provided in the table were taken from [5].

e.g. *uud* - proton) or quark-anti-quark pair (mesons, e.g. $u\bar{d}$ - π^+). Hadrons are formed of only such combinations of (anti-)quarks, which lead to integer total electric charge.

To this day the SM provides precise theoretical predictions for a variety of processes, successfully validated in experiments. There are no measurements of SM processes, whose results would be in tension with the predictions at the statistically significant level. However, it is well known that the SM is not complete, and will be in the future replaced by a deeper theory.

1.2 Strong interactions

1.2.1 The quantum chromodynamics

Part of the SM which describes the strong force is the quantum chromodynamics (QCD). In this quantum field theory, an interaction between quarks is carried by gluons. Analogously to electrodynamics, in which an attribute required for the electromagnetic interaction to take place is an electric charge, strong force occurs between objects carrying the so-called colour charge. However, there is not just one, but three colours in QCD: red, green and blue, accompanied by their anti-colours: anti-red, anti-green and anti-blue. Quarks (anti-quarks) carry a single colour (anti-colour), while gluons contain a pair of colour and anti-colour. There are eight linearly independent combinations of colours and anti-colours, which determine existence of eight gluons in QCD. Since gluons carry the colour charge they can themselves be a subject to the strong force. The self-interaction of gluons makes the QCD a very different theory from the electromagnetism (QED) and is a consequence of non-abelianity of the theory.

A simplified form of the QCD potential V_{QCD}, which describes the strong field generated by a (anti-)quark and perceived by another (anti-)quark at distance r, can be written as

$$V_{\mathrm{QCD}}(r) \approx C\frac{\alpha_s}{r} + \lambda r, \qquad \lambda > 0,\ \alpha_s > 0, \tag{1.1}$$

(see, for example, Ref. [8]). The Coulomb-like term in Eq. (1.1) is dominant at short distances, typically below ~ 0.2 fm. Factor C, taking a discrete values spanning between $-4/3$ to $1/6$, depends on the colours of interacting (anti-)quarks. For some combinations of colours, C takes the positive values and the strong force becomes repulsive as r approaches zero. The linear term, relevant at larger distances, defines the maximum spatial separation of quarks. With $\lambda \sim 1$ GeV/fm the energy contained in a gluon "string" extending between quarks separated by only a fraction of femtometer is large enough to produce a $q\bar{q}$ state, following the mass-energy equivalence. It is one of the main properties of QCD, called the colour confinement, explaining non-existence of free quarks and any non-colour-neutral objects in nature.

The strong coupling constant α_s, defining the strength of gluon-mediated force, depends on the energy scale Q involved in an interaction. It runs with increasing Q^2 as an inverse logarithm, as written in Eq. (1.2):

$$\alpha_s(Q^2) \propto \frac{1}{\ln Q^2/\Lambda^2_{\mathrm{QCD}}}. \tag{1.2}$$

The scale parameter $\Lambda_{\mathrm{QCD}} \approx 0.2$ GeV (mass scale of light hadrons) determines the applicability of the perturbation theorem. The predicted behaviour of α_s as a function of Q, together with experimental

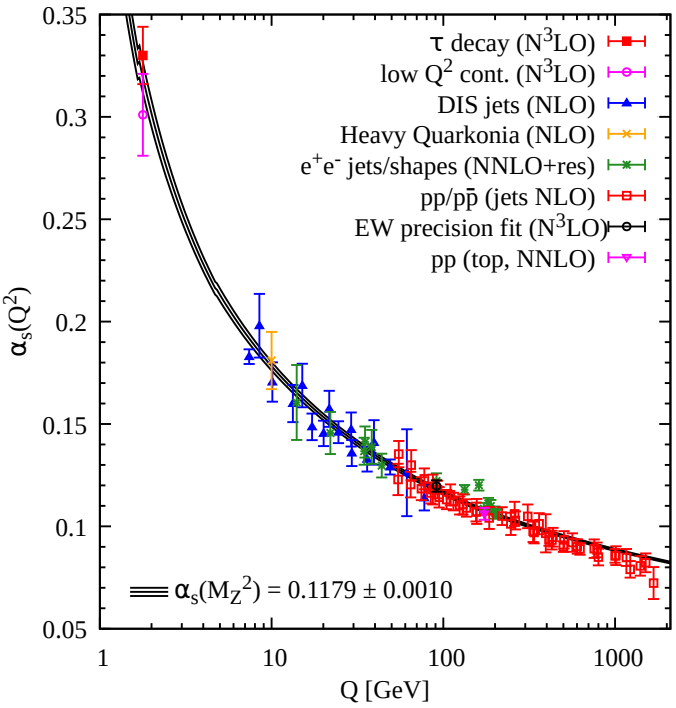

Figure 1.1: Dependence of the strong coupling constant α_s on the energy scale Q (from [5]). The solid lines show the predicted trend and its theoretical uncertainty, while colour points represent values of α_s extracted from the data using specific observables/processes provided in the legend, and using QCD predictions at given order of perturbation calculus.

values of α_s at given energy scale (colour points), are shown in Fig. 1.1. A decreasing value of α_s with an increasing energy scale is another characteristic property of the QCD, called the asymptotic freedom. In the limit of small length scale (distance) and large energy scale (momentum) the quarks act as they were unbinded, nearly free.

The value of α_s much below unity, $\alpha_s \ll 1$, enables application of the perturbation calculations of amplitudes, and thus cross sections, for processes occurring with large energy scale - so-called hard processes.

1.2.2 The Regge theory

In the regime of soft processes, without presence of a scale significantly larger than Λ_{QCD}, the perturbative QCD (pQCD) calculations cannot be applied. However, complementary approaches exist. An example is the lattice QCD, using extensive numerical calculations to propagate the quantum states following the QCD rules in a discrete space-time. Another possibility is the Regge theory, originally used to describe the strong interactions in 1960s, before the QCD was formulated.

In order to introduce the basics of the Regge theory, it is educative to consider a simple 2-body scattering process (see Fig. 1.2)

$$1 + 2 \rightarrow 3 + 4. \tag{1.3}$$

It is also useful to define the set of three Lorentz-invariant quantities, often referred to as the Mandelstam variables:

$$s \equiv (p_1 + p_2)^2 = (p_3 + p_4)^2, \tag{1.4}$$

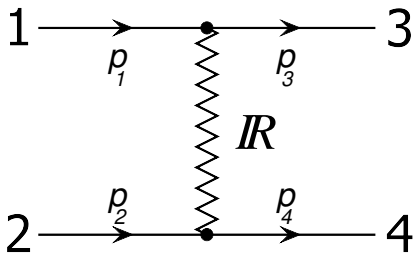

Figure 1.2: Generic diagram of the IReggeon exchange.

$$t \equiv (p_1 - p_3)^2 = (p_2 - p_4)^2, \tag{1.5}$$

$$u \equiv (p_1 - p_4)^2 = (p_2 - p_3)^2, \tag{1.6}$$

with p_1 and p_2 denoting the four-momenta of the initial state particles, and p_3 and p_4 - the four-momenta of the final state particles. The quantities s and t are, respectively, the squares of the total energy of 1 and 2 in their centre-of-mass reference frame, and the four-momentum transferred in the scattering. Only two Mandelstam variables are independent, as they follow the identity:

$$s + t + u = \sum_{i=1}^{4} m_i^2. \tag{1.7}$$

Typically s and t are used to describe the kinematics of the process.

An important concept incorporated in the Regge theory is the idea of complex angular momentum. According to the theory, an interaction occurs via exchange of an object of spin α which might not be necessarily integer nor even real. This object is referred to as the Regge trajectory, $\alpha(t)$. Regge trajectories, also called IReggeons and denoted by IR (Fig. 1.2), for positive integer values of spin, $\alpha \equiv$ J, represent the resonances of the mass equal to $\sqrt{t}$ [9]. A sample Regge trajectory is shown in Fig. 1.3, with the set of resonances lying on (sharing) this trajectory. Typically the linear form of Regge trajectories is assumed,

$$\alpha(t) = \alpha(0) + \alpha' t, \tag{1.8}$$

which is dictated by the leading components in a Taylor series expansion. Intriguingly, such form typically well describes sets of resonances spanning along a wide range of t, like in Fig 1.3.

It can be demonstrated (see [9, 10]), that in this framework, in the limit of large s ($s \gg |t|$), the amplitude for the single IReggeon exchange process can be formulated as

$$A(s,t) = \beta(t)\,\zeta(t)\,s^{\alpha(t)}, \tag{1.9}$$

with $\beta(t)$ being the residue of the amplitude in the complex angular momentum plane (of the so-called Regge pole), and $\zeta(t)$ is a signature factor of the form

$$\zeta(t) = -\frac{1 \pm \exp\left[-i\pi\alpha(t)\right]}{\sin\left[\pi\alpha(t)\right]}. \tag{1.10}$$

The residue function $\beta(t)$ can be understood, in terms of Feynman rules of QCD, as a product of couplings in vertices 1IR3 and 2IR4, while the term $\zeta(t)s^{\alpha(t)}$ as a IReggeon propagator. The differential cross section, $d\sigma/dt$, at given s is related to the amplitude via Eq. (1.11):

$$\frac{d\sigma}{dt} = \frac{1}{16\pi s^2}\left|A^2(s,t)\right|. \tag{1.11}$$

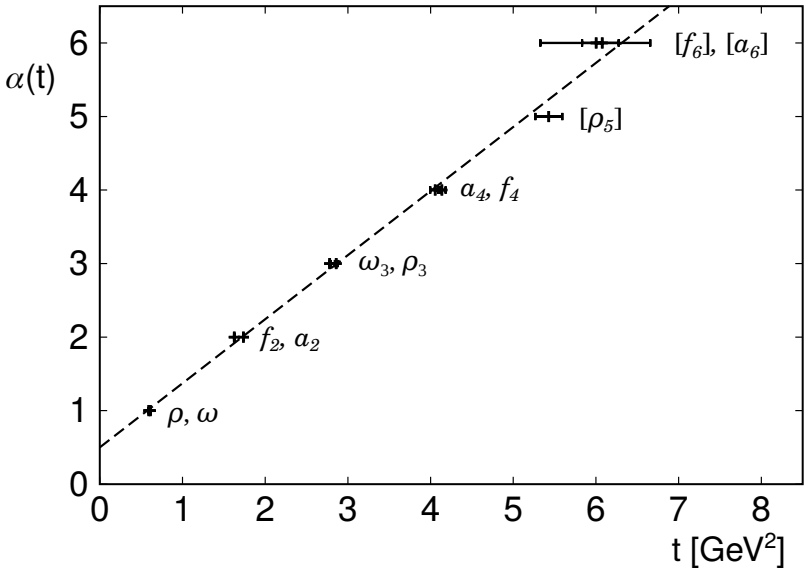

Figure 1.3: The Chew-Frautschi plot [11] with the real part of spin α (y-axis) plotted against the squared four-momentum transfer t (squared mass of an object exchanged in the t-channel, x-axis). The dashed line represents a sample Regge trajectory. The bound states (of integer spin) lying on this particular trajectory are marked with crosses, accompanied by the horizontal bars spanning along the uncertainty range of the squared resonance mass. Not definitely-established states are labelled inside the square brackets. The figure was adopted from Ref. [10].

1.3 Diffraction in high energy particle interactions

The term "diffraction" was introduced to high energy physics due to similarity between the angular distribution of particles scattered at small polar angles (θ)[1] and the intensity of light diffractively scattered on an obstacle [9, 12]. In both cases, the multi-peak structure in the radial intensity of scattered particles/light is observed, with the most pronounced forward[2] peak separated from the secondary maxima with "dips".

1.3.1 The eikonal picture

Particle diffraction can be examined from the geometrical perspective, in the very similar way to the diffraction of light. The incident particle can be considered as a plane wave, while the target particle as an opaque obstacle. Then, the (azimuthally symmetric) scattering amplitude for the ℝReggeon exchange, $A(s,t)$, can be connected with the so-called profile function $\Gamma(s,b)$ in the impact parameter (b) space, through the Fourier-Bessel (Hankel) transformation [9]

$$A(s,t) = i\,4\pi s \int_0^{+\infty} db\, b\, \mathcal{J}_0(qb)\,\Gamma(s,b). \tag{1.12}$$

In Eq. (1.12) $\mathcal{J}_n$ denotes the Bessel function of the first kind of order n (here $n = 0$), and q - in the limit of small scattering angles, which we consider here - is the transverse momentum transfer $q \approx \sqrt{-t}$.

[1] In collider experiments z-axis is typically coinciding with the direction of one of the incoming beams, hence zero polar angle corresponds to the beam axis.

[2] The term "forward" is used as a synonym for scattering at the very small polar angle θ.

$\Gamma(s,b)$ is connected with the target opacity and governs information about the spatial extension of the interaction region. For the demonstration purposes we can insert some particular profile function to Eq. (1.12), for example a simple step function $\theta(R-b)$ representing a "black disk" of radius R. The obtained amplitude,

$$A(s,t) \overset{q\approx\sqrt{-t}}{=} i\,4\pi s\,\frac{R}{\sqrt{-t}}\,\mathcal{J}_1\left(\sqrt{-t}\,R\right), \tag{1.13}$$

can be inserted to Eq. (1.11), leading to

$$\frac{d\sigma}{dt} = \frac{\pi R^2}{|t|}\,\mathcal{J}_1^2(\sqrt{-t}\,R) = \left|\mathcal{J}_1^2(x) \overset{x\to 0}{\approx} \frac{x^2}{4} - \frac{x^4}{16}\right| = \frac{\pi R^2}{4}\left(1 - \frac{|t|R^2}{4}\right) \approx \frac{\pi R^2}{4}\exp\left[-\frac{R^2}{4}|t|\right]. \tag{1.14}$$

In Eq. (1.14) we see form of the differential cross section in the limit of $t \to 0$, proportional to the exponent:

$$\frac{d\sigma}{d|t|} \propto \exp\left[-B|t|\right], \tag{1.15}$$

which typically well describes the shape of the forward scattering peak. The the slope parameter B in Eq. (1.15) incorporates radius R of the target ($B \propto R^2$). Above (simplified) example shows the connection between the shape of $d\sigma/dt$ and the size of the hadron, which is qualitatively independent of the assumed form of the profile function [12]. The slope parameter can vary with t, hence its general definition is

$$B(s,t) = \frac{\partial}{\partial t}\left[\ln\frac{\partial\sigma}{\partial t}\right]. \tag{1.16}$$

From above one concludes, that measurement of the t variable in the diffractive scattering is particularly valuable, as it allows the study of the size of interaction region. It typically requires detection of the forward-going particles, although exceptions are possible (e.g. [13]).

1.3.2 The ℙomeron

It has been generally established, that, in the language of the Regge theory, high energy physics diffraction occurs via exchange of the specific Regge trajectory(ies), called the ℙomeron, denoted by ℙ. It was introduced phenomenologically in early 1960s [14, 15] in order to explain nearly constant (in fact, slowly rising) total hadron-hadron cross section as a functions of the centre-of-mass energy (Fig. 1.4).

An explanation was delivered by the property of the S-matrix [9, 10], used in the Regge framework, called the unitarity. This property reflects that the total probability for all possible scattering processes must be equal to one. It leads to simple relation between the total hadron-hadron cross section, σ_{tot}, with the elastic hadron-hadron scattering amplitude, A_{el}, at forward direction ($t = 0$). This relation is the so-called optical theorem, written as

$$\sigma_{\text{tot}}(s) = s^{-1}\,\text{Im}\left\{A_{\text{el}}(s, t=0)\right\}. \tag{1.17}$$

Connecting representation of the Regge amplitude from Eq. (1.9) and the optical theorem in Eq. (1.17) makes it evident, that s-independent total cross section is achieved only if the intercept $\alpha(0)$ of the trajectory responsible for the elastic scattering is equal to one. This "phenomenological" ℙomeron trajectory is often represented in the linear form

$$\alpha_{\mathbb{P}}(t) = \alpha_{\mathbb{P}}(0) + \alpha'_{\mathbb{P}}\,t \tag{1.18}$$

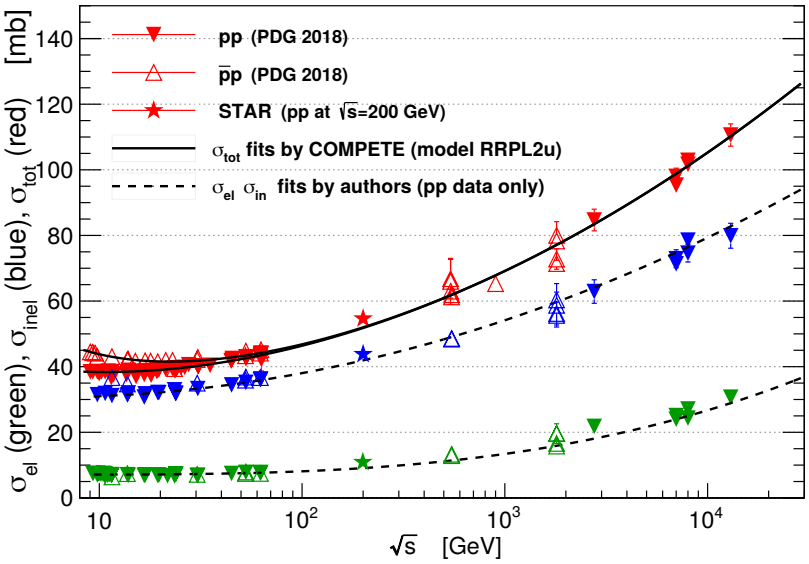

Figure 1.4: The evolution of the total pp (closed red triangles) and $p\bar{p}$ (open red triangles) cross section (y-axis) with $\sqrt{s}$ (x-axis, logarithmic scale). In addition to the total cross section, also elastic and inelastic cross sections are shown as, respectively, green and blue markers. Fits represented with lines do not include the recent measurement from the STAR experiment at $\sqrt{s} = 200$ GeV. Figure taken from from Ref. [2].

with the parameters equal to [16]:

$$\alpha_{\mathbb{P}}(0) \approx 1.08, \qquad \alpha'_{\mathbb{P}} \approx 0.25 \text{ GeV}^{-2}. \tag{1.19}$$

The value of the ℙomeron intercept $\alpha_{\mathbb{P}}(0)$ slightly greater than one enables the experimentally observed slow rise of the total cross section with increasing centre-of-mass energy. In the geometrical picture, the target hadron size (hence B) grows as the $\sqrt{s}$ increases, leading to the rise of the total cross section (larger interaction area) and steeper slope of the $d\sigma/dt$, which is also observed in experiments.

Since the ℙomeron is exchanged in elastic scattering of hadrons, in which the initial and final state particles are identical, it must be a colour singlet object and carry the vacuum quantum numbers [9, 10]: positive parity P = 1, positive charge conjugation C = 1, and isospin I = 0, from which positive G-parity $\mathrm{G} \equiv \mathrm{C} \cdot (-1)^{\mathrm{I}} = 1$ follows.

From the QCD perspective, the simplest representation of the ℙomeron, which satisfies the above quantum numbers criteria, is a pair of oppositely coloured gluons. However, higher order combinations of gluons and quarks can also contribute to this particular ℙeggeon. The helicity structure of the ℙomeron is not fully established. Experimental results [17] seem to rule out the spin-zero (scalar) ℙomeron [18]. For a long time ℙomeron was treated as a non-conserved vector current (spin-one, e.g. [19–22]), but currently the models assuming an effective spin-two (tensor) model for the ℙomeron helicity are developed [23, 24].

A characteristic feature of the ℙomeron exchange is spatial configuration of the final state particles with a distinctive region void of particles ("gap"), a consequence of the vacuum properties of the ℙomeron. It is different from non-diffractive hadronic processes, in which coloured gluons or quarks are exchanged between two interacting hadrons. Usually, the former interact with the QCD fluctuations of the vacuum spreading out particles which fill the space. The gap is typically described in the space

of rapidity, y, defined as

$$y = \frac{1}{2} \ln \frac{E + p_z}{E - p_z}, \tag{1.20}$$

and called the rapidity gap. In the laboratory frame it is often convenient to use the so-called pseudorapidity (η), defined geometrically as

$$\eta = -\ln\left(\tan\frac{\theta}{2}\right). \tag{1.21}$$

For massless particles, rapidity is identical to pseudorapidity.

The diffraction taking place in the regime of large momentum transfers, studied e.g. in electron-proton (ep) collisions at HERA [25–27], can be considered as an exchange of the "hard" $\mathbb{P}$omeron, and the process can be then treated perturbatively. It is the so-called BFKL [28, 29] approach, with the $\mathbb{P}$omeron approximated with two gluons with intermediate gluons between them (gluon ladder). Representation of the BFKL $\mathbb{P}$omeron in the form of trajectory gives an intercept $\alpha_{\mathbb{P}}(0) \sim 1.4$ (assuming $\alpha_S \approx 0.2$) [9], larger than value quoted in Eq. (1.19). It yields continuous discussions on the multiplicity of $\mathbb{P}$omeron trajectories and the scale-dependence of the $\mathbb{P}$omeron intercept $\alpha_{\mathbb{P}}(0; Q^2)$ [9].

It is worth mentioning the potential P- and C-odd (P = −1, C = −1) counterpart of the $\mathbb{P}$omeron, the $\mathbb{O}$dderon, with the leading order QCD representation by three gluons in a colour singlet. If such trajectory contributes to the high energy hadron scattering, it would reveal itself in the shape of $d\sigma/dt$ at large values of $-t \gtrsim 1$ GeV^2 differently for elastic pp and $p\bar{p}$ scattering [9, 10]. Another effect would be a non-vanishing difference between the total pp and $p\bar{p}$ cross section at high centre-of-mass energies [9, 10]. The former case was studied at ISR, with some non-definite hints of presence of the $\mathbb{O}$dderon exchange [30]. The latter is not examined, lacking the precision measurements at $p + \bar{p}$ collider with forward (anti-)proton tagging at sufficiently large $\sqrt{s}$. At HERA the search for photon-$\mathbb{O}$dderon was conducted in π^0 production [31], giving results consistent with non-existence of the $\mathbb{O}$dderon. Recently, some effects in the elastic proton-proton scattering at $\sqrt{s} = 13$ TeV at the LHC have been reported [32], which can be attributed to the presence of the $\mathbb{O}$dderon exchange. Summing up, the question of whether the $\mathbb{O}$dderon contributes to high energy scattering, or not, still remains open.

1.3.3 Classification of diffractive processes

The diffractive processes - those involving exchange of $\mathbb{P}$omeron(s) between the interacting hadrons - are generally divided into a few classes, as described below. They are graphically presented in Fig. 1.5 with the corresponding leading order (Regge picture) Feynman diagram and sketch of the event topology in the laboratory frame (in the azimuthal angle φ and pseudorapidity plane). Processes are discussed in the limit of high centre-of-mass energies of two interacting hadron beams, B_1 and B_2, neglecting possible contributions from the secondary $\mathbb{R}$eggeons.

The most basic diffractive process, already mentioned in Sec. 1.3.2, is the elastic scattering[3] (Fig. 1.5a). It is characterised by only two back-to-back hadrons in the final state, which are the initial state hadrons that stay intact after the interaction. The rapidity gap in elastic scattering is the most evident (the widest) among all diffractive processes. The process contributes about 25% − 30% to the total cross section at the highest centre-of-mass energies achievable at the colliders (Fig. 1.4).

[3] Sometimes in the literature only inelastic processes are included to diffraction.

The second class of diffractive process, is single diffractive dissociation, or single diffraction (SD), shown in Fig. 1.5b. In this type of interaction also a single IPomeron exchange occurs. One of the hadrons stays intact, while the other dissociates or gets excited. The mass of the dissociated system

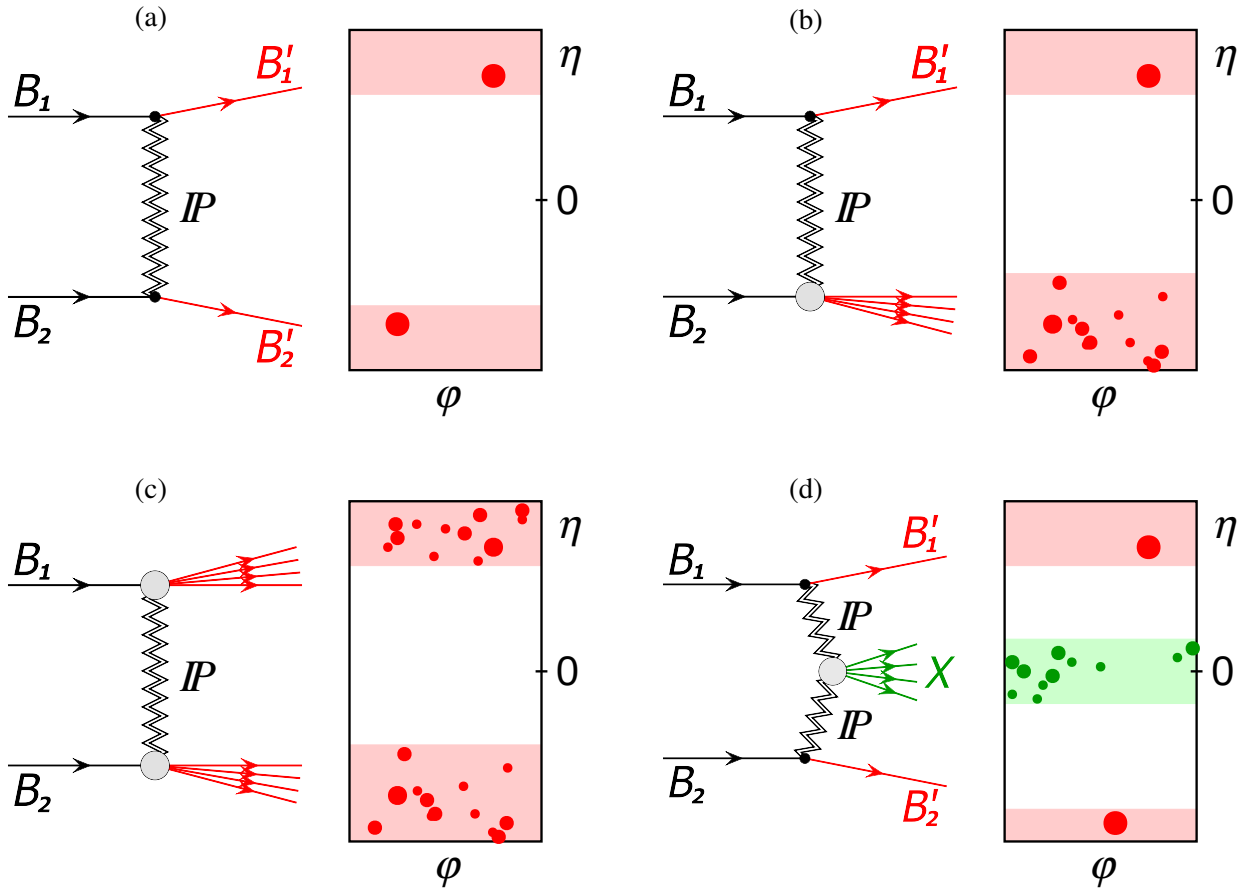

Figure 1.5: Diagrams representing the main types of diffractive processes, together with schematic representation of the event topology in (φ, η) space: (a) elastic scattering, (b) single diffractive dissociation, (c) double diffractive dissociation, central diffraction (d) without and (e) with dissociation of the forward-scattered beam particle(s). Forward-scattered/dissociated beam particles are marked with single/multiple red lines. In applicable cases, the centrally produced particles are marked with green colour. The white area in each (φ, η) space represents the rapidity gap(s), characteristic for the IPomeron exchange.

M_{SD} is connected with the (fractional) energy loss of the intact hadron ξ[4],

$$\xi \equiv \frac{E_0 - E}{E_0}, \tag{1.22}$$

by $M_{\mathrm{SD}} = \sqrt{\xi s}$. An example of the (very low mass) SD can be diffractive excitation of the proton, $p + p \to p + p^* \to p + p + \pi^+ + \pi^-$, with a Lorentz-boosted pair of opposite-charge pions moving alongside the proton in the forward direction. A recent study of the SD process in pp collisions at $\sqrt{s} = 200$ GeV and 13 TeV can be found in Ref. [33].

The third class of diffractive processes is the double diffractive dissociation, or double diffraction (DD), with both beams dissociating (or getting excited and relaxing) after the IPomeron exchange. An example of the DD process can be the case with both of the protons dissociating to $p\pi^+\pi^-$, i.e. $p + p \to p^* + p^* \to p + p + 2\pi^+ + 2\pi^-$.

The last type, the central diffraction (CD) depicted in Figs. 1.5d and 1.5e, occurs through the Double IPomeron Exchange, which is separately described in the following section (Sec. 1.3.4).

1.3.4 The Double IPomeron Exchange

The Double IPomeron Exchange [34–38], abbreviated DIPE, is characteristic among diffractive interactions due to the two rapidity gaps, separating each of the forward-going beam particles (or remnants) from the central, neutral system, formed in the fusion of two IPomerons. The interaction between IPomerons is marked in Figs. 1.5d and 1.5e with grey circle, and may involve resonant or non-resonant production. The beam hadrons may both stay intact (Fig. 1.5d), or one/both of the incoming particles may dissociate (Fig. 1.5e, diagram with both beams dissociated is not drawn). The former case is sometimes, a little misleadingly, called the elastic CD, while the latter case - inelastic CD.

From the isospin and the C-parity of the IPomeron, and conservation of the quantum numbers in strong interactions, we get possible I^{G} properties of the state X produced in DIPE:

$$\mathrm{I}^{\mathrm{G}} = 0^+. \tag{1.23}$$

Possible J^{PC} combinations [39, 40] are

$$\mathrm{J}^{\mathrm{PC}} = N^{\pm+}, \quad N = 0, 1, 2, \ldots . \tag{1.24}$$

The selection rules are more restrictive for the central systems consisting of two identical particles (modulo the electric charge, e.g. $X = \pi^0\pi^0, K^+K^-$):

$$\mathrm{J}^{\mathrm{PC}} = N^{++}, \quad N = 0, 2, 4, \ldots , \tag{1.25}$$

what is often found in the literature as a general rule for all states produced in DIPE. Equations (1.23) and (1.25) make the DIPE typically referred to as the spin-parity filter process.

The simplest and most numerous states produced through the DIPE are pairs of hadrons whose total charge equals zero (Fig. 1.6 shows production of oppositely-charged hadrons). The pairs of the lowest mass, which can be produced, are $\pi^0\pi^0$ and $\pi^+\pi^-$. From the experimental perspective more encouraging is the latter case, since, in general, it is easier to reconstruct tracks of charged particles.

[4] If $E \gg m^2$, then $E \simeq p$ and ξ can be called the fractional momentum loss.

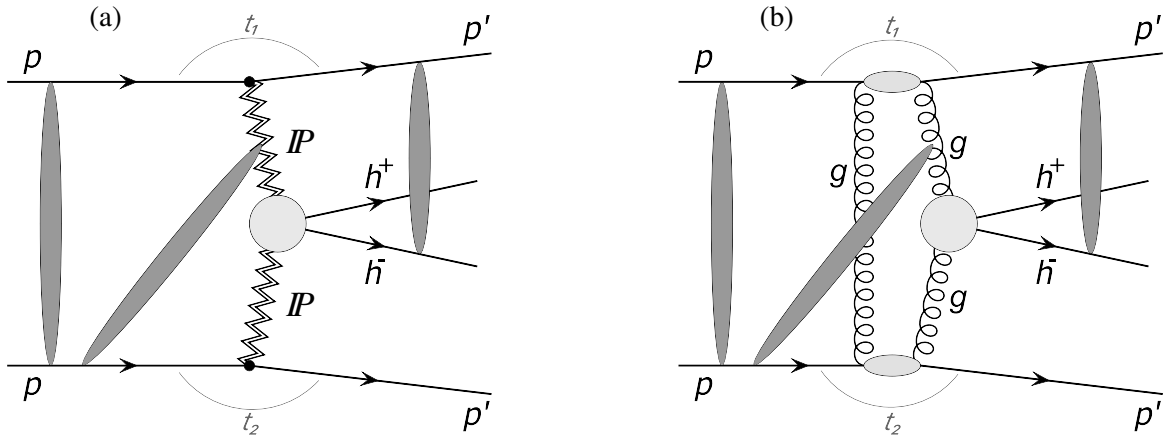

Figure 1.6: Diagrams of DIPE of two opposite-charge hadrons in proton-proton collision, with both protons staying intact. Figure a shows the Regge representation, whereas Fig. b depicts the same process in the leading order pQCD. The light grey circle denotes the non-resonant or resonant mechanism of production of h^+h^-. Dark grey ovals illustrate some possible absorption effects, described in some more detail in Sec. 1.4.2.

Systems dedicated to reconstructing low momentum charged particles tracks belong typically to the basic equipment of the high energy physics experiments, together with low energy calorimeters needed for reconstruction of neutral particles.

Aforementioned production of the lightest states proceeds in the vast majority in the fully non-perturbative regime (Fig. 1.6a), with the low four-momentum transfers ($-t_1$ and $-t_2$) and low invariant masses of the central state (up to a few GeV). It is described with the Regge-based phenomenological models, introduced in Sec. 2.1. For large invariant masses of the central state, sizeably larger than Λ_{QCD}, the perturbative picture is used to describe the DIPE [41]. In this approach, the central state emerges from the fusion of two gluons, while the third gluon connects the lines of the beam particles to compensate the flow of the colour (Fig. 1.6b). Such hard DIPE can lead to production of, for instance, pair of high transverse momentum photons (e.g. [42]), pair of jets (e.g. [43]), χ_{c0} meson (e.g. [44]), or potentially even the Higgs boson (postulated in e.g. [45]).

1.4 Central Exclusive Production

1.4.1 Definition and properties

The Central Exclusive Production (CEP) is a general name for the class of processes with all particles of the centrally produced final state being measured. The adjective "central" serves to distinguish between the particles produced in the central rapidity region from the two forward-scattered intact or dissociated beam particles. "Exclusive" emphasises the sole production of the studied particles. The CEP of state X can be written as

$$B_1 + B_2 \rightarrow B_1^{\prime(*)} + X + B_2^{\prime(*)}. \tag{1.26}$$

Here, the apostrophe "'" is used to denote the scattered intact beam particle, while the asterisk "*" marks the excited or dissociated beam particle. In the latter case, the process is sometimes described in the literature as a semi-exclusive central production. Schematic drawing of the CEP process within a detector is presented in Fig. 1.7.

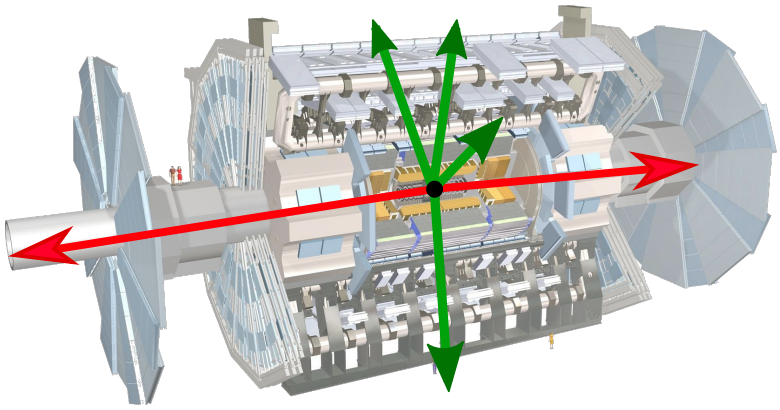

Figure 1.7: Graphical illustration of the Central Production event, drawn on top of the main detector in the high energy physics collider experiment (here - the ATLAS experiment [46]). Depicted event corresponds to that drawn in Fig. 1.5d, with the same colour code used for the forward-scattered and mid-rapidity particles. The arrows represent momenta of particles right after the interaction (hence not influenced by e.g. magnetic field).

The above definition includes the situation with the forward-going system being undetected. In such case, the exclusivity is inferred from the event topology, typically from the rapidity gaps in mid-forward region of the detector. As a result, sample of CEP events can be contaminated with a non-negligible fraction of non-exclusive events. The efficient and nearly unambiguous recognition of the CEP events is possible provided the forward detectors, which enable reconstruction of the scattered intact beam particles and, as a result, verification of the exclusivity assumption via momentum balance of all final state particles.

Following the momentum and energy conservation, in all CEP processes, the mass m_X and rapidity y_X of the central state can be expressed in terms of the fractional momentum losses at proton vertices:

$$m_X = \sqrt{s\left(\xi_1\xi_2 \sin^2(\Delta\alpha/2) - (1-\xi_1-\xi_2)\cos^2(\Delta\alpha/2)\right)} \overset{\Delta\alpha=\pi}{=} \sqrt{s\,\xi_1\xi_2}, \tag{1.27}$$

$$y_X = \frac{1}{2}\ln\frac{\xi_1}{\xi_2}, \tag{1.28}$$

where $\Delta\alpha$ is the angle between the two forward-scattered beams particles or their remnants. Equations (1.27) and (1.28) are true for masses of the beam particles negligible compared to their momenta in the centre-of-mass reference frame.

Several kinds of CEP processes can be distinguished. First, the central state can be produced in the fully photon-induced interaction, $\gamma\gamma$, also called double photon exchange. Because of the electromagnetic coupling α_{EM} being roughly two orders of magnitude smaller than α_S, this CEP mechanism is suitable for studies in e^+e^- or in ultra peripheral heavy-ion collisions. The photon flux factor, proportional to the product of squared atomic numbers of interacting nuclei, can then enhance the $\gamma\gamma$ cross section to the measurable level.

The second possibility is the photoproduction process. In this process, one of the beam particles is a source of a photon, typically of low virtuality, while the other a source of a Reggeon, typically the IPomeron. As a result a vector meson is produced, e.g. ρ or J/ψ.

The third possibility is an interaction of the fully strong nature, in the high energy limit - the DIPE. At $\sqrt{s}$ values below these achievable at the LHC, the exchanges of secondary Reggeons can also

contribute [39]. This class, in a domain of low invariant masses of the centrally produced states, is referred to as the diffractive CEP. An overview of the related measurements is the subject of Chap. 3.

1.4.2 Absorption effects

All CEP processes involving colliding hadrons (ions) are sensitive to the absorption effects, also called survival or rescattering effects. They arise from the non-zero probability for production of particles additional to those from the primary interaction. Thus, the exclusivity of the primary event is spoiled and the rapidity gaps become populated. The major ingredient to this dumping[5] of the cross section in CEP processes comes from interaction between the spectator partons of the colliding hadrons. It is shown symbolically in Figs. 1.6a,b with the leftmost dark grey oval. Additional rescatterings can also contribute (other ellipses in Fig. 1.6, not all possibilities depicted), but are less significant.

The rapidity gap survival probability is represented by the ratio of the exclusive cross section with the absorption effects taken into account, and the bare exclusive cross section:

$$\langle S \rangle^2 = \frac{\iint d^2\vec{b}_1 \iint d^2\vec{b}_2 \left|\mathcal{M}\left(s, \vec{b}_1, \vec{b}_2\right)\right|^2 \exp\left[-\Omega(s,b)\right]}{\iint d^2\vec{b}_1 \iint d^2\vec{b}_2 \left|\mathcal{M}\left(s, \vec{b}_1, \vec{b}_2\right)\right|^2} \tag{1.29}$$

In the eikonal model, the former can be obtained through convolution of the bare squared amplitude for the exclusive process and probability for lack of inelastic interaction between the beams [47]. In Eq. (1.29) $\vec{b}_1$ and $\vec{b}_2$ denote two-vectors of the impact parameters of particles 1 and 2 (the impact parameter $b = |\vec{b}_1 - \vec{b}_2|$), $\mathcal{M}$ is the matrix element for the process under study, and Ω is the so-called opacity connected with the profile function $\Gamma(s,b)$, defined in Sec. 1.3.1, through the relation

$$\exp\left[-\Omega(s,b)\right] = 1 - \Gamma(s,b). \tag{1.30}$$

Absorption may generally differ between various phase space configurations of the particles. It may be especially sensitive to the four momenta transferred between the colliding particles.

1.5 Gluon bound states

As mentioned in Sec. 1.2.1, gluons, the gauge bosons of QCD, can directly couple. It introduces possibility to form the real, colourless states solely from gluons. The simplest possible gluon bound state, also called glueball, satisfying the requirement of colour neutrality is a pair of oppositely-coloured gluons, gg. More complex combinations are also possible (e.g. ggg), yielding, however, larger masses due to increase of the binding energy.

Glueballs do not fall within the definition of baryons, as they do not contain valence quarks and thus their baryon number is zero. Therefore, glueballs are categorised as exotic mesons (an example of other exotic state could be the $q\bar{q}g$ hybrid). Same as a regular mesons, glueballs are bosons - the superposition of a spin-one gluons can yield only an integer spin.

Glueballs have not yet been unequivocally and undeniably observed in experiment. Confirmation of existence of these hadrons, which are predicted by the QCD theory - verified and proofed in

[5] Or, potentially, redistribution (change of the shape).

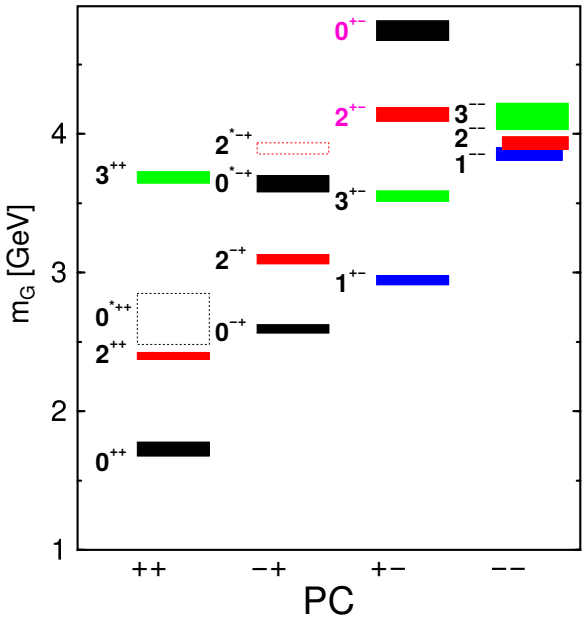

Figure 1.8: Spectrum of glueballs from quenched lattice QCD calculations (from [54]). Predicted masses m_G of glueballs of different parity P and charge conjugation C, indicated on the horizontal axis, are represented by the vertical position of boxes whose height marks the theoretical uncertainty of m_G (excluding uncertainty of the hadronic scale). Colours of boxes are connected with the spin of the glueball, e.g. black - scalar, blue - vector, red - tensor. An independent approaches of determining the glueball spectrum also exist, see e.g. Ref. [55] for a result involving anti-de Sitter supergravity (in that case the final scale of glueball masses is adjusted to match the mass of the lightest $J^{PC} = 2^{++}$ meson from the lattice calculations).

multiple areas - is one of the most important quests of modern experimental physics. Indirect hints of glueballs were observed in an excess of the neutral clusters in the three-jet events at the LEP collider experiments [48–50]. The main path of searches, however, leads through the spectroscopy of the plenteous family of hadronic resonances produced in the gluon-rich reactions, such as DIPE or radiative decays of J/ψ. Such efforts were done, for example, by the experiments at the ISR collider [51, 52], or by the fixed-target experiments at SPS (see [53] and references therein). The entire difficulty to definitely establish a non-$q\bar{q}$ meson arises from the possible mixing with $q\bar{q}$, represented by Eq. (1.31):

$$|M\rangle = \sin\phi_G \cdot |q\bar{q}\rangle + \cos\phi_G \cdot |gg\rangle\,. \tag{1.31}$$

When the intrinsic properties of the quark-anti-quark pair (spin, parity) are identical to these of the glueball, and their masses are similar, the observable meson M is a superposition of a regular meson $q\bar{q}$ and the gluon bound state gg. The mixing angle, ϕ_G, determines the amount of the gluonic content in the meson.

Calculations on the lattice provide expectations for the masses of glueballs. Figure 1.8 shows predicted spectrum of glueballs of different quantum numbers. As we read from it, the lightest scalar glueball is predicted around $m_G \approx 1.7$ GeV, and the lightest tensor glueball is predicted around $m_G \approx 2.4$ GeV. However, these numbers are burdened with an uncertainty of the hadronic scale and typically a few-hundred MeV mass range is quoted. Therefore, scalar and tensor glueballs are expected between 1.5 – 1.8 GeV and 2.0 – 2.5 GeV, respectively, with the caveat that lighter states are not definitely excluded. Within the above mass ranges there are a few resonances considered as potential glueballs or mixed $q\bar{q} - gg$ states. For the scalar glueball, the most promising candidates are: $f_0(1370)$,

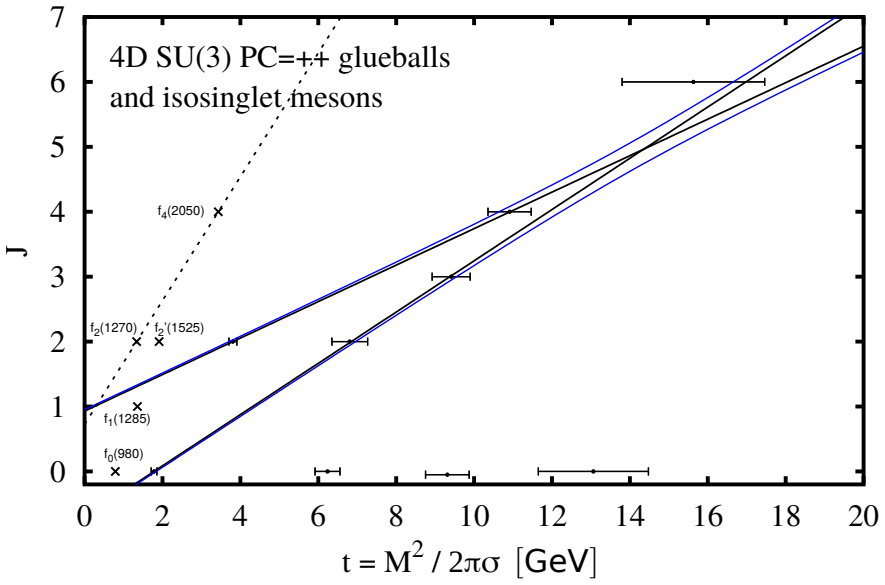

Figure 1.9: Trajectories of glueballs obtained from the lattice calculations (adopted from [58]). Two glueball trajectories are shown with straight solid lines. Since it is forbidden for leading and sub-leading trajectories to cross each other (resulting in a double-pole), the blue hyperbolae indicating potential behaviour at large t are also drawn. The dotted line shows exactly the same leading mesonic trajectory(ies) as in Fig. 1.3. In addition, coordinates of some isosinglet mesons observed experimentally are plotted.

$f_0(1500)$, $f_0(1710)$ [56, 57], but also states such as $f_0(500)$ and $f_0(980)$ are not definitely recognised as $q\bar{q}$. In the tensor sector also a wealthy of candidates appears, starting with the $f_2(1950)$, through $f_2(2010)$, $f_2(2300)$, $f_2(2340)$, and others.

Property of single gluons - lack of flavour, is expected to be also inherited by glueballs. This should reveal as a flavour-blindness, resulting in a similar branching ratio to mesons independently of their flavours. Hence, in order to define the state as a glueball, multiple decay channels should be measured and their branching fractions compared. Large asymmetry in a decay rate to e.g. $\pi^+\pi^-$ and K^+K^- would disfavour a state from being a glueball.

It is worth reminding that the leading order QCD representation of the $\mathbb{P}$omeron is a pair of gluons, therefore PC = ++ glueballs can be considered as the mass eigenstates of the $\mathbb{P}$omeron. Consequently, in the Regge picture such glueballs should lie on the $\mathbb{P}$omeron trajectory. In Fig. 1.9 the glueball trajectories are shown, obtained from the extrapolation of the glueball masses from the lattice calculations to the continuum space of angular momentum [58, 59]. It is noteworthy, that the lower-slope trajectory coincides with the $\mathbb{P}$omeron trajectory from Eq. (1.18). However, a difference is present in the intercepts, which is above unity in case of phenomenological $\mathbb{P}$omeron, and below unity in the pure glueball trajectory from Fig. 1.9. This might be explained by a possible mixture of the gg with $q\bar{q}$ in the $\mathbb{P}$omeron. The $\mathbb{P}$omeron trajectory from Eq. (1.18), crossing through the J = 2 at positive mass domain and thus containing possible $J^{PC} = 2^{++}$ glueball, can be considered as a leading glueball trajectory. The sub-leading trajectory has significantly larger slope and negative intercept, hence contains the lightest $J^{PC} = 0^{++}$ glueball.

Analogously to the $\mathbb{P}$omeron case, ggg glueball (sometimes called oddball) instance is called the $\mathbb{O}$dderon. For a detailed review on the topic of meson spectroscopy and glueballs, see e.g. [5] and [57].

2. Models of diffractive CEP

2.1 Phenomenological description of low-mass DIPE

Description of diffractive CEP of the low-mass states, which is here of the particular focus, is generally performed in the Regge framework. The models of exclusive production involve phenomenological elements, which, at the current state of knowledge, cannot be avoided. In order to introduce the basic elements of the models we will stick to the CEP in proton-proton collisions, assuming no dissociation of the beam particles:

$$p + p \to p' + X + p'. \tag{2.1}$$

We will also focus on the exclusive production of the simple state $X = \pi^+\pi^-$, which is experimentally the easiest to measure. The models for exclusive production of other channels are conceptually very similar. We will omit the absorption effects, whose introduction is not straightforward and goes beyond the scope of this introduction.

The exclusive production of central $\pi^+\pi^-$ pair can proceed twofold. The pair can be produced directly (continuum production, Fig. 2.1a) or through an intermediate resonance f (resonant production, Fig. 2.1b). Therefore, the matrix element for the exclusive $\pi^+\pi^-$ production, $\mathcal{M}$, is a sum of the continuum term ($\mathcal{M}_{\text{cont}}$) and the resonant term ($\mathcal{M}_{\text{res}}$),

$$\mathcal{M} = \mathcal{M}_{\text{cont}} + \mathcal{M}_{\text{res}}. \tag{2.2}$$

Contributions to the continuum production might be from the DIPE (IPIP), from IPomeron-IReggeon exchanges (IPIR), from IReggeon-IReggeon exchanges (IPIR),

$$\mathcal{M}_{\text{cont}} = \mathcal{M}_{\text{cont}}^{\mathbb{P}\mathbb{P}} + \mathcal{M}_{\text{cont}}^{\mathbb{P}\mathbb{R}} + \mathcal{M}_{\text{cont}}^{\mathbb{R}\mathbb{R}}, \tag{2.3}$$

as well as from additional exchanges involving the Odderon and photon. The two last cases are not included in Eq. (2.3) because, firstly, not experimentally confirmed contributions to diffraction from

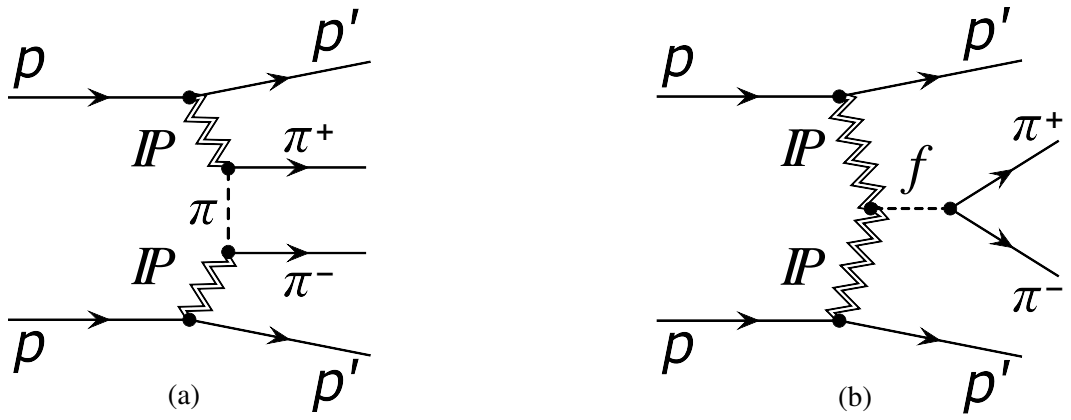

Figure 2.1: Diagrams of exclusive $\pi^+\pi^-$ production through DIPE in proton-proton collision, with both protons surviving the interaction. Plot (a) shows the continuum production through the exchange of the off-shell pion between the IPomerons, whereas plot (b) shows the resonant production mechanism, with the IPomerons directly coupling to a resonance f, which later decays to the $\pi^+\pi^-$ pair. The Figure is an expanded version of Fig. 1.6a (without visualised rescatterings).

the Odderon, and, secondly, low $|t|$ in the proton vertices with photon being exchanged, yielding low visible cross section.

The situation is similar for the resonant $\pi^+\pi^-$ production. Here also contributions from all combinations of exchanged objects have to be considered, with appropriate treatment of the selection rules (quantum numbers). We can shortly write it as

$$\mathcal{M}_{\text{res}} = \sum_f \mathcal{M}_{\text{res},f} \tag{2.4}$$

with $\mathcal{M}_{\text{res},f}$ representing sum of the amplitudes corresponding to various exchanges that lead to production of the resonance f, and the sum runs over different resonant states f.

In the end, the cross section is obtained though integration of the matrix element

$$\sigma = \frac{1}{16\pi s^2\,(4\pi)^4}\int dt_1 dt_2 dy_1 dy_2 dp_{\text{T}}^2\,|\mathcal{M}|^2 = \frac{1}{16\pi s^2\,(4\pi)^4}\int dt_1 dt_2 dy_1 dy_2 dp_{\text{T}}^2\,\left|\mathcal{M}_{\text{cont}} + \mathcal{M}_{\text{res}}\right|^2, \tag{2.5}$$

where s is the squared centre-of-mass energy of the colliding protons, t_1 and t_2 are the squared four-momenta carried by Pomerons, y_1 and y_2 are the rapidities of the final state pions and p_{T} is the transverse momentum of the $\pi^+\pi^-$ pair. The relation between the matrix element and the cross section is explicitly written in Eq. (2.5) to emphasize the well known feature of quantum mechanical physics, namely the quantum interference. All amplitudes representing the same initial and final states must be added coherently, which results in the enhancement or suppression of the cross section in various regions of the phase space, depending on the relative phases between contributing amplitudes. Decomposition of the experimental cross section to independent contributions always requires dedicated analysis.

Over past decade several groups have published theoretical developments on the CEP, in particular on the production of $\pi^+\pi^-$ pairs. The continuum production has been studied in e.g. Ref. [24, 41, 47, 60, 61] and the models for the resonant production in e.g. [24, 62][1]. The commonly used representation [47, 60] of the matrix element for the continuum production of $\pi^+\pi^-$, with only the DPE mechanism considered, is

$$\mathcal{M}_{\text{cont}} = F_p(t_1)\,\underbrace{\sigma_0\left(\frac{s_1}{s_0}\right)^{\alpha_{\mathbb{P}}(t_1)}}_{p\text{-}\mathbb{P}\text{-}\pi^+}\,F_\pi(\hat{t})\,\underbrace{\frac{1}{\hat{t}-m_\pi^2}}_{\text{off-shell }\pi}\,F_\pi(\hat{t})\,\underbrace{\sigma_0\left(\frac{s_2}{s_0}\right)^{\alpha_{\mathbb{P}}(t_2)}}_{\pi^-\text{-}\mathbb{P}\text{-}p}\,F_p(t_2) \quad + \quad u\text{-channel} \tag{2.6}$$

In this complicated, at first sight, equation, the t_1 and t_2 are the squared four-momenta transfers in proton vertices, the s_1 and s_2 are the squared centre-of-mass energies of the proton and real pion connected by the Pomeron in Fig. 2.1a, $\hat{t}$ is the squared four-momentum carried by the intermediate pion of mass m_π, F_p and F_π are respectively the proton and the virtual pion form factors, and σ_0 is the proton-pion elastic scattering cross section at the squared proton-pion centre-of-mass energy s_0. Only the t-channel pion exchange is explicitly written in Eq. (2.6), but also u-channel exchange should be accounted, obtained through interchange of π^+ with π^-. The proton form factor is typically assumed to be $\propto \exp\left[B_{p\pi}\,t/2\right]$, with $B_{p\pi}$ representing the slope of $d\sigma/dt$ in elastic proton-pion scattering, but some authors postulate other forms (e.g. two-channel model [47]). σ_0 is obtained

[1] Other phenomenological papers on CEP of various particle species, which should not be overlooked are: [39, 63–69].

from a fit to low-energy scattering data [70]. The intermediate pion form factor is generally not known. A few parameterisations, normalised to unity at $\hat{t} = m_\pi$, can be found in the literature:

$$F_\pi^{\mathrm{exp}}(\hat{t}) = \exp \frac{\hat{t} - m_\pi^2}{\Lambda_{\mathrm{exp}}^2} \tag{2.7}$$

$$F_\pi^{\mathrm{or}}(\hat{t}) = \exp \frac{a_{\mathrm{or}} - \sqrt{-\hat{t} + m_\pi^2 + a_{\mathrm{or}}^2}}{\Lambda_{\mathrm{or}}} \tag{2.8}$$

$$F_\pi^{\mathrm{pow}}(\hat{t}) = \left(1 - \frac{\hat{t} - m_\pi^2}{\Lambda_{\mathrm{pow}}^2}\right)^{-1} \tag{2.9}$$

$$F_\pi^{\mathrm{mon}}(\hat{t}) = \frac{\Lambda_{\mathrm{mon}}^2 - m_\pi^2}{\Lambda_{\mathrm{mon}}^2 - \hat{t}} \tag{2.10}$$

Equations (2.7-2.10) represent, respectively, the exponential, the Orear-like, the power-like and the monopole pion form factor. Determination of the proper form factor and values of the parameters is a subject of the experimental study, as it requires measurement of the cross-section and comparisons between data and models. A serious difficulty comes from the aforementioned interference effects with resonant production and secondary $\mathbb{R}$eggeon exchanges, as well as from the rescattering.

The calculations for the resonant production are more complicated than for the continuum and hence will not be introduced. The $\mathbb{P}$omeron-$\mathbb{P}$omeron-f form factors are not well known, similarly to precise values of the $\mathbb{P}$omeron-$\mathbb{P}$omeron-f couplings. Depending on the assumed helicity structure of the $\mathbb{P}$omeron (vector vs. tensor) and the spin of the resonance, the couplings may also differ in forms, being not a simple scalar but a tensor. As in case of the continuum, measurements of the resonance production cross sections are needed to limit the model uncertainties, which at the moment are large [24].

2.2 Monte Carlo generators

Comparisons of the data with model predictions are best done through dedicated Monte Carlo generators. With such tools one is able to obtain predictions for the phase space accessible in the measurement, which typically differs between experiments, and even within a single experiment may change during data analysis. In this section a few event generators of exclusive processes are presented. The selection below is based on the processes which can contribute to the events observed in the measurement of diffractive CEP, the topic of this study. Generators below give information on the entire kinematics of the reaction per event (provide four-momenta of all particles in the final state).

The GenEx [71] event generator is based on the phenomenological model introduced in Refs. [60, 64]. It allows generation of exclusive continuum production of $\pi^+\pi^-$ or K^+K^- pairs. The absorption corrections are not included in this generator. One can vary the Λ_{exp} parameter of the only available meson form factor (exponential). In the near future GenEx should be extended to allow generation of the CEP of resonances and other exclusive processes, e.g. diffractive Bremsstrahlung [72].

The DiMe [47] event generator is based on the phenomenological model introduced in Ref. [41]. Similarly to GenEx, it also provides generation of exclusive $\pi^+\pi^-$ and K^+K^- pairs produced via the continuum mechanism. However, other channels are also implemented, e.g. exclusive $\rho\rho$ or $\phi\phi$. Contrary to GenEx, it includes modelling of the absorption effects with four different models for absorption available. Three different parameterisations of meson form factor are implemented (exponential, Orear-like and powe-like), with a possibility to set values of their parameters.

The widely used Pythia 8 [73] event generator also includes a few models of diffraction. However,

only the MBR model [74] was tuned to describe the CD - inclusive DIPE measurement by CDF [75]. In this model, the exclusive final state occurs from fragmentation and hadronisation of the central state based on the Lund string model. The MBR model implemented in the latest Pythia 8.244 allows generation of the central state starting from the mass threshold of 0.5 GeV. It has to be stressed, that the generator is not intended to provide trustworthy results for exclusive processes, especially in diffraction with large overall cross section uncertainties.

Another event generator is the SuperChic3 [76]. It is a wide-scope generator, with the processes of the largest importance to this study being the exclusive production of χ_{c0}, as well as, potentially present (but expected at low level) $\rho(770)$ meson. The latter meson is also generated in STARlight [77], but without information on the kinematics of the forward system.

There are ongoing developments of the EPOS event generator [78] to include modelling of the CD, which in the current version EPOS-LHC is not available [79]. This should come in the near future with the EPOS 3 [80].

Very recently a powerful event generator called GRANIITTI has been released [81]. From the description of the generator it follows, that all major exclusive channels are possible to generate using various models, with a freedom in choice of their parameters. This generator, however, was not used in comparisons with data due to too late release.

3. Experimental overview of diffractive CEP

An interest of the experimental physicists in the study of the diffractive CEP dates back to 1970s. At that time, multiple efforts were done to measure the theoretically-postulated DIPE process with the $\pi^+\pi^-$ in the final state, accompanied with the "fast" proton from the incident beam and the "slow" proton of the target [82–84]. The biggest experimental difficulty was in reduction of the low-mass SD background, and also in low statistical precision.

The measurement of DIPE became more feasible with the ISR collider in operation. Indications for the DIPE were getting more significant [85, 86] until the measurement of DIPE at $\sqrt{s} = 63$ GeV was finally reported by the AFS Collaboration [87] in 1983. This observation was followed by more detailed study [51], from which the Fig. 3.1a originates. The AFS analysis involved Partial Wave Analysis (PWA) of the exclusive $\pi^+\pi^-$ channel, as well as observation of exclusive production of K^+K^-, $p\bar{p}$ and $2\pi^+2\pi^-$. In addition to this, some small data sample from $\alpha + \alpha$ collisions at $\sqrt{s} = 126$ GeV was analysed and exclusive $\pi^+\pi^-$ was observed. The measurement was performed with the forward-scattered protons (or α particles) only in the "up-up" or "down-down" configuration (also called anti-diagonal, or anti-elastic configuration), hence limiting the probed phase space to the region with the azimuthal separation between the forward scattered protons, $\Delta\varphi$, close to 0°.

In the following years results from the SFM experiment were published [52, 89–91]. The PWA was done for exclusive $\pi^+\pi^-$ [52] and $2\pi^+2\pi^-$ [91], and the cross sections were measured, also for other channels [90]. These results had an advantage of probing both elastic (also called diagonal) and anti-elastic configuration of the forward-scattered protons. Thus comparisons between $\Delta\varphi < 90°$ and $\Delta\varphi > 90°$ were enabled, demonstrating asymmetries of $d\sigma/dm$ between these two cases.

Results from ISR revealed characteristic features of the DIPE: broad spectrum extending from the production threshold up to a few GeV, with several structures; in case of $\pi^+\pi^-$, a sharp drop of $d\sigma/dm$ around 1 GeV was observed, due to $f_0(980)$, and a peak around 1.25 GeV due to (dominantly) $f_2(1270)$

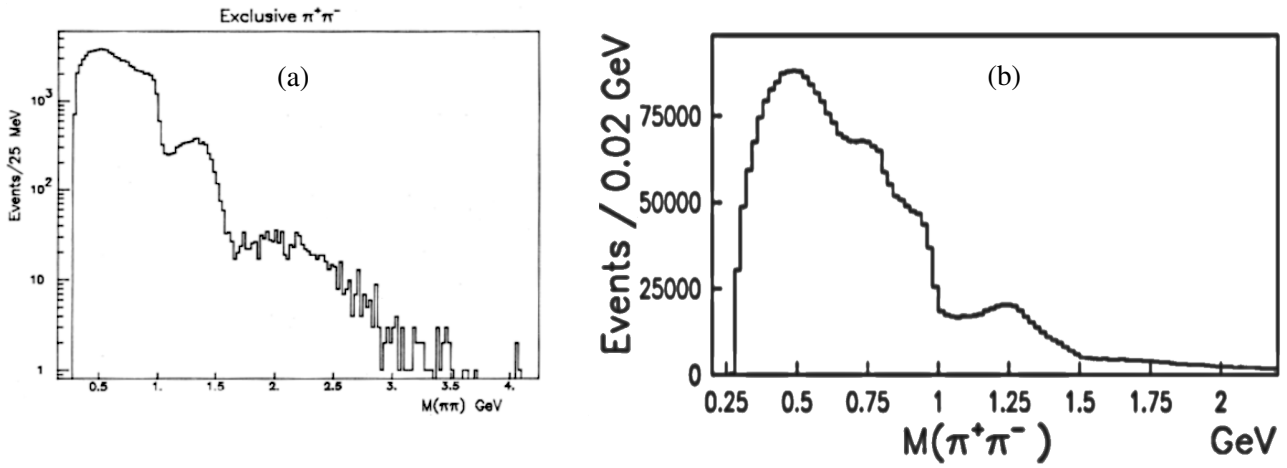

Figure 3.1: Selected results from the measurements of diffractive CEP with detection of intact beam/target particles. Invariant mass of exclusive $\pi^+\pi^-$ from (a) the AFS experiment at the ISR collider (pp at $\sqrt{s} =$ 63 GeV, logarithmic y-scale, from [51]) and (b) from the fixed-target experiment WA102 in pp collisions at $\sqrt{s} = 29.1$ GeV (from [88]).

(Fig. 3.1a, the same features are observed by later experiments, see Fig. 3.2). Although analysis by both AFS and SFM were profound and comprehensive, the published cross sections had a large scale factor uncertainty of the order of 50%.

In 1990s the family of fixed-target WA experiments at SPS provided measurements from $p + p$ collisions, with the highest centre-of-mass energy achieved in WA102, $\sqrt{s} = 29.1$ GeV. The wealthy of spectroscopic results on multiple exclusive channels were published [22, 88, 92–100]. The experiment had an advantage of full azimuthal coverage for the fast and slow protons. In connection with the PWA being conducted for multiple exclusive channels, $\Delta\varphi$-dependence of production of many resonances was studied. Figure 3.1b shows an exclusive $\pi^+\pi^-$ mass spectrum recorded by WA102 [88]. A small peak around 0.8 GeV is the evidence of presence of the $\rho(770)$. From this observation one concludes, that WA102 results could not be interpreted as solely DPE-induced, but there was a non-negligible contribution from $\mathbb{P}$omeron-$\mathbb{R}$eggeon and $\mathbb{R}$eggeon-$\mathbb{R}$eggeon exchanges.

Next measurements of diffractive CEP were provided by the CDF Collaboration at the Tevatron. Exclusive reactions in $p\bar{p}$ collisions were first measured for the hard-scale DPE mechanism [42–44]. In 2015 the results on exclusive $\pi^+\pi^-$ pair production at $\sqrt{s} = 0.9$ TeV and 1.96 TeV were published [101] (Fig. 3.2b). At such high centre-of-mass energies contributions from exchanges of the secondary $\mathbb{R}$eggeons are expected to be negligible, nevertheless the measurement was based on the double-gap event topology, without tagging intact (anti)proton. This naturally implied admixture of events with dissociation of the beam particles, and some contribution from photoproduction (reduced by the cut on transverse momentum of $\pi^+\pi^-$ pairs).

In the meantime (2014), the preliminary (proof-of-principle) results on CEP of $\pi^+\pi^-$ from the STAR experiment were made public [102] (Fig. 3.2a). This way STAR became the first collider experiment, after more than a decade, that demonstrated capability of tagging forward-scattered beam particles and correlating them with the tracks measured in the central detector. The normalisation (cross section) uncertainty was much lower than in results from the ISR experiments, but the statistics was poor. Due to the expected significant increase in data statistics at the same c.m.s. energy after the detector upgrade, a decision was made not to publish those data. Also the fixed-target COMPASS experiment at SPS showed progress on measurement of the CEP of $\pi^+\pi^-$ [103], but this low-$\sqrt{s}$ measurement with large contributions from $\mathbb{P} - \mathbb{R}$ and $\mathbb{R} - \mathbb{R}$ has not turned into publication.

Since the start of operations, the LHC experiments were also making efforts to conduct measurements of the diffractive CEP. The ALICE experiment has been long ago reporting performance of the double-gap trigger in proton-proton collisions at $\sqrt{s} = 7$ TeV [104] (Fig. 3.2c). Recently, performance plots from large dataset recorded at $\sqrt{s} = 13$ TeV were also made available [105]. Unfortunately, ALICE does not have capability of detection of forward-scattered protons. The same is true for the CMS experiment (alone), which has posted preprint of article reporting measurement of (semi-)CEP of $\pi^+\pi^-$ at $\sqrt{s} = 7$ TeV [106] and very recently published the results of the measurement at 13 TeV [107]. In both ALICE and CMS, similarly to CDF, contributions from DPE, photoproduction and dissociation of beam protons cannot be separated. The situation is more optimistic for CMS+TOTEM, which reported performance of common detection of the central diffractive system and forward-scattered protons at $\sqrt{s} = 13$ TeV [108]. However, any physics results has not yet been released. One should also mention the LHCb Collaboration, which has potential to deliver results on exclusive $\pi^+\pi^-$ in pp and p+Pb [109], but again, is limited to the measurement of solely the central system (of the significantly non-central rapidity).

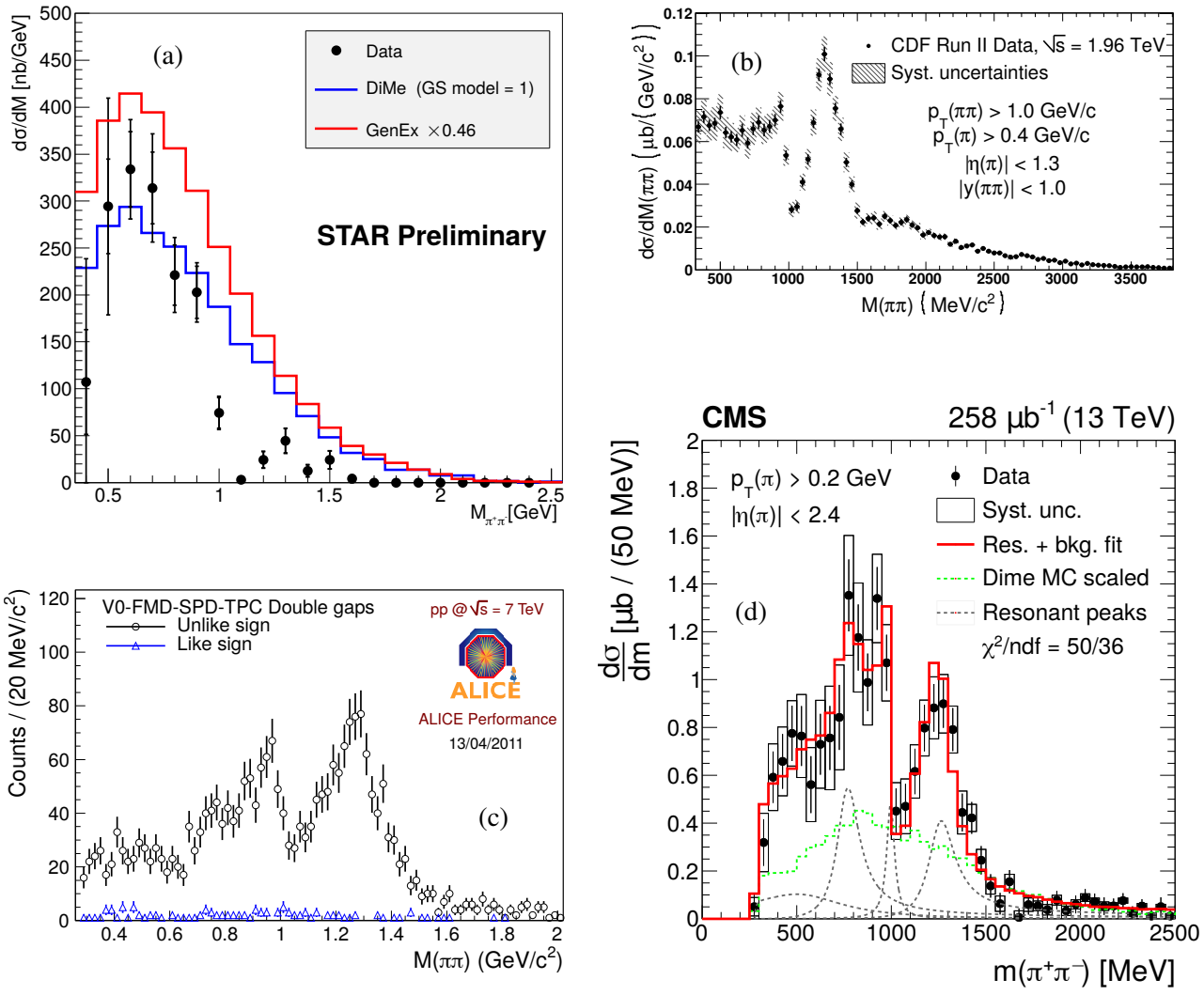

Figure 3.2: Selected results from the recent measurements of diffractive CEP. Invariant mass of exclusive $\pi^+\pi^-$ pairs measured by (a) STAR in pp collisions at $\sqrt{s} = 200$ GeV (preliminary result, from [102]), (b) CDF in $p\bar{p}$ collisions at $\sqrt{s} = 1.96$ TeV (from [101]), (c) ALICE in pp at $\sqrt{s} = 7$ TeV (performance plot, from [104]), and (d) CMS in pp at $\sqrt{s} = 13$ TeV (from [107])..

Summing up, the measurements from AFS and SFM at ISR were, until recently[1], the highest-$\sqrt{s}$ published results on diffractive CEP with the forward-scattered hadrons detected. These data, however, had significant systematic uncertainties on the cross section normalisation of about 50%. For this reason, among others, many ongoing experiments have been competing to deliver precise measurements of the diffractive CEP processes, with exclusive $\pi^+\pi^-$ at the first place. High precision results of data analyses from STAR ($\sqrt{s} = 200$ GeV) and ATLAS ($\sqrt{s} = 13$ TeV), not mentioned earlier in this chapter and presented in this dissertation, should potentially have a large impact on understanding of diffractive CEP, given their advantage of detection of all final state particles.

[1] Before the results described in this dissertation were published.

4. Objectives of the research

Introductory sections have, hopefully, indicated, that diffractive processes in high energy physics are not satisfactorily understood nor explored. The $\mathbb{P}$omeron physics, especially in the low-t domain, is described by the phenomenological models without a chance of the fully-perturbative treatment in the QCD framework. Particularly interesting and natural way to uncover the characteristic of the $\mathbb{P}$omeron seems to lead through investigation of exclusive diffractive processes, which provide full information about the reaction. This suggests the D$\mathbb{P}$E as the most suitable object of studies in the hadron-hadron collider experiments equipped with the forward detectors. The process is, in itself, interesting, and gives a chance to explore intriguing QCD phenomena. Having this in mind, the following plan of the experimental work follows.

The general objective of presented study is selection, reconstruction and systematic analysis of the low-mass CEP of neutral combinations of identified charged hadrons in pp collisions, with detection of the forward-scattered protons. Analysis shall be performed at two centre-of-mass energies, $\sqrt{s}$ = 200 GeV (the STAR experiment) and 13 TeV (the ATLAS experiment), which enables study of the $\sqrt{s}$-dependence of the process. Aforementioned high energies of pp collisions, and tagging of the intact protons, should naturally select the D$\mathbb{P}$E as the main production mechanism contributing to CEP events.

It involves measurement of differential fiducial cross sections of identified states as function of multiple observables, related to the central system (e.g. invariant mass, rapidity) and to diffractively-scattered protons (e.g. squared four-momentum transfer, azimuthal angle). Large attention should put on minimisation of the systematic uncertainties of the cross sections, which have dominated overall uncertainties in previous measurements of the process.

As a next step, the differential fiducial cross sections should be compared with available models of measured reaction channels. Currently, only models of the continuum production are implemented in the generators. The comparisons are expected to provide limits on the parameters of these models. They should, for example, indicate the mesons' form factors which would provide the best agreement between models and data in the shape and normalisation of differential cross sections. The comparisons should also help to revise models of absorption.

If possible, recognition of resonances produced in the CEP process should be performed, simultaneously with determination of their production cross sections, possibly multi-differentially. Such measurement may constrain values (and forms) of couplings of the $\mathbb{P}$omeron to various f-resonance states. Angular distributions of the central state particles may indicate the spin content in the mass spectrum. Also, as always in D$\mathbb{P}$E process, observation of resonances considered as glueball candidates may bring another piece to the long lasting puzzle of existence of these peculiar QCD objects.

Last but not least, a forward-scattered proton tagging should be fully exploited by, for example, extraction of the exponential slope parameter from the double differential cross section in t_1 and t_2. Again, its variation with the invariant mass of the central state, together with establishing the resonances in the mass spectrum, can provide a discrimination between the $\mathbb{P}\mathbb{P}f$ couplings predicted theoretically.

Part II

The STAR experiment

In this part the STAR experiment at RHIC and the physics analysis of the data from proton-proton collisions at $\sqrt{s} = 200$ GeV collected by the experiment in 2015 are described. Majority of the physics results obtained in this analysis were published in Ref. [1].

5. Experimental setup

5.1 The Relativistic Heavy Ion Collider

The Relativistic Heavy Ion Collider (RHIC) [111] (Fig. 5.1) is located at Brookhaven National Laboratory [112] in New York State (USA). Circumference of the collider amounts 3.8 km, which makes it the second-largest particle collider in the world currently in operation. RHIC provides collisions of protons or several heavy ion species (i.e. *d*, Au, Cu, Ru, Zr, and U nuclei) at the centre-of-mass energies reaching up to 510 GeV (in proton-proton) or up to 200 GeV per nucleon pair (in other configurations). The unique capability of RHIC among other machines of this kind is possibility to collide polarised protons [113, 114], with their spins aligned longitudinally or transversely. This feature enables study of the spin effects in particle interactions (e.g. [17]).

The collider consists of two rings, with beams circulating clockwise (the so-called blue ring) and counter-clockwise (yellow ring). There are a few interaction regions (IRs) where the beams cross and collision take place. Their location is typically described using the time convention, with the northmost and southmost IRs denoted as 12 o'clock and 6 o'clock IR, respectively.

First collisions at RHIC took place in year 2000, with four independent experiments installed at the collider ring: PHOBOS [115, 116], BRAHMS [117, 118], PHENIX [119, 120] and STAR [121, 122]. In 2002 the PP2PP experiment [123, 124] was installed at the same IR as the BRAHMS experiment. Currently the two largest experiments remain active - PHENIX and STAR. The latter is equipped with the set of forward detectors incorporated from the PP2PP experiment in 2009, aimed at tagging protons scattered at very small angles. The description of the STAR detector is presented in the following section.

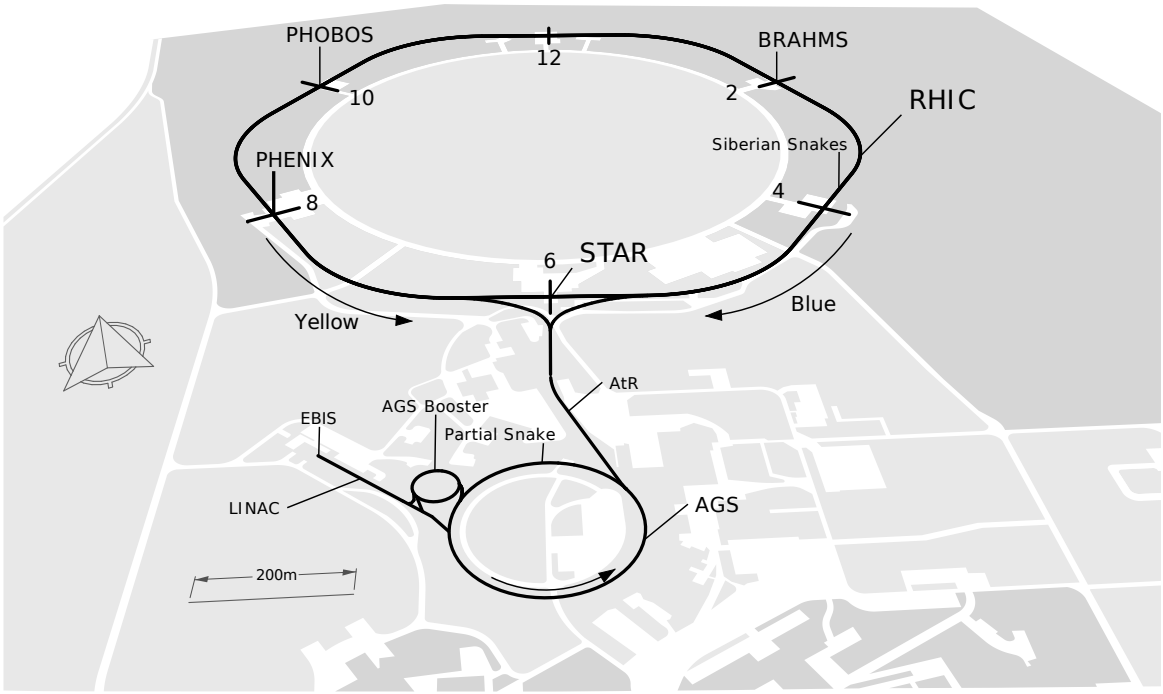

Figure 5.1: Schematic view of the RHIC complex. Figure adopted from [110].

5.2 The STAR detector

The Solenoidal Tracker at RHIC (STAR) [122] (Fig. 5.2) is a general-purpose detector installed at 6 o'clock IR at RHIC (Fig. 5.1). It was primarily designed to study the characteristics of the heavy-ion collisions, especially the properties of the quark-gluon plasma (QGP) [125] - a state of matter which is believed to fill the Universe up to a few microseconds after the Big Bang. Nevertheless, continuous upgrades of the detection systems provide capability to conduct variety of measurements also in proton-proton collisions, or even enable the experiment to run in the fixed-target mode [126].

The central detector is mounted with its z-axis (the main axis, coincides with the nominal beamline trajectory) positioned nearly parallel to the east-west direction, therefore detector is often divided into its West ($z > 0$) and East ($z < 0$) part. The x-axis is pointing radially outside of the ring. The y-axis is pointing upwards. In this way the right-handed STAR coordinate system is defined.

The STAR detector is enclosed in 0.5 Tesla solenoidal magnetic field and has a full azimuthal coverage for the charged particle tracking and for electromagnetic (EM) calorimetry within $|\eta| < 1$. The former is provided by the Time Projection Chamber (TPC) [128], the latter by the barrel EM calorimeter (BEMC) [129] which is supported by the endcap EM calorimeter (EEMC) [130] on one side, extending the calorimeter acceptance up to $\eta \approx 2$.

An important component of the STAR detector is the Time of Flight (TOF) [131] system, a precise timing detector covering also full azimuthal angle although in slightly narrower η range, $|\eta| < 0.9$. Other sub-detectors particularly important for the CEP analysis are the Beam-Beam Counters (BBCs) [132], Zero-Degree Calorimeter (ZDC) system [133] and, most importantly, the Roman Pot (RP) system in Phase II* configuration. Also the Heavy Flavour Tracker (HFT) [134] has been used in the analysis to study some detector effects. The following sections introduce the major subsystems used in the measurement.

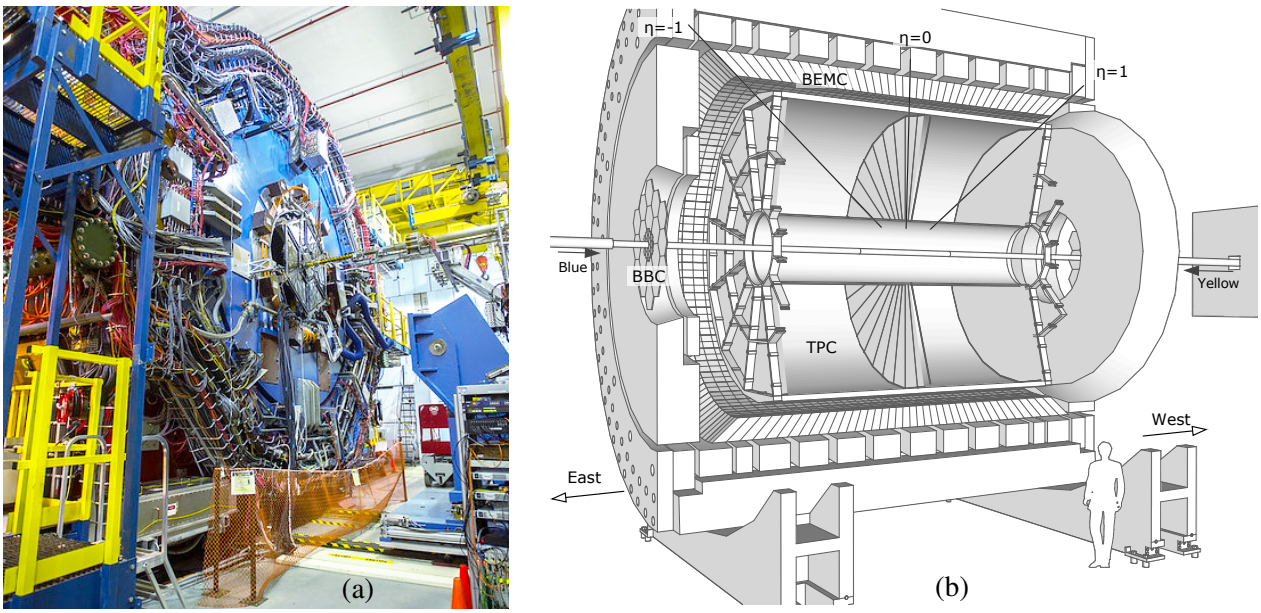

Figure 5.2: (a) Photograph [127] and (b) longitudinal section of the model of the STAR central detector [110].

5.2.1 Time Projection Chamber

Detection of charged particles' tracks is provided by the TPC [128] (Fig. 5.3), the core of the STAR detector. It is a 4.2 m long cylinder of the inner and outer radius equal to 0.5 m and 2 m, respectively. Such geometry results in pseudorapidity coverage for central tracking of about $\Delta\eta \approx 3$ units, but region of high reconstruction efficiency typically used in analyses is narrower, extending symmetrically from -1 to 1. Within this η range the minimum transverse momentum (p_T) of reconstructed particles is approximately 150 MeV, while the p_T resolution is about 2-3% at $p_T \lesssim 1$ GeV and rises linearly to several percent for particles with p_T of a few GeV.

The high negative voltage (-28 kV) is applied to the inner membrane (Fig. 5.3) to form the electric field directed along the main TPC axis. The chamber is filled with the P-10 gas mixture [135]. As a result, charged particles traversing the TPC volume ionise the gas, and created ions travel through the TPC to the inner membrane (positive charges) or endcap anodes (negative charges). At the endcaps the Multi Wire Proportional Chambers (MWPC) [128] are installed, each with 45 pad rows which allow to determine (x, y)-position of the ion clusters. The known drift velocity of the ions inside the TPC of approximately 5.5 cm/µs and time of signal detection in MWPC provides the z-position of the cluster.

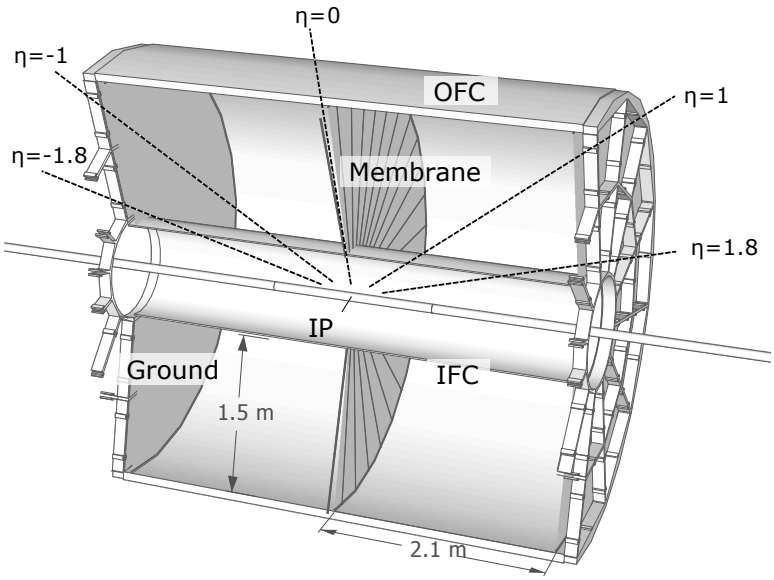

Figure 5.3: Schematic view of the Time Projection Chamber at STAR. Figure taken from [110].

5.2.2 Beam Beam Counters

The BBCs are plastic scintillator detectors (Fig. 5.4a) placed in the endcap regions of the STAR detector at $z \pm 3.7$ m (marked violet in Fig. 5.2b). They cover pseudorapidity ranges of $2.1 < |\eta| < 3.3$ (large BBC tiles, also BBC-large or BBC-L) and $3.3 < |\eta| < 5$ (small BBC tiles, also BBC-small or BBC-S). All tiles have hexagonal shape (Fig. 5.4b). On each side of the central detector there are eighteen small tiles read by sixteen photomultiplier tubes (PMTs) and eighteen large tiles read by eight PMTs. It gives in total twenty four read-out channels per side. In the experiment BBCs are typically used to provide a minimum-bias (MB) trigger and monitor the collision rate.

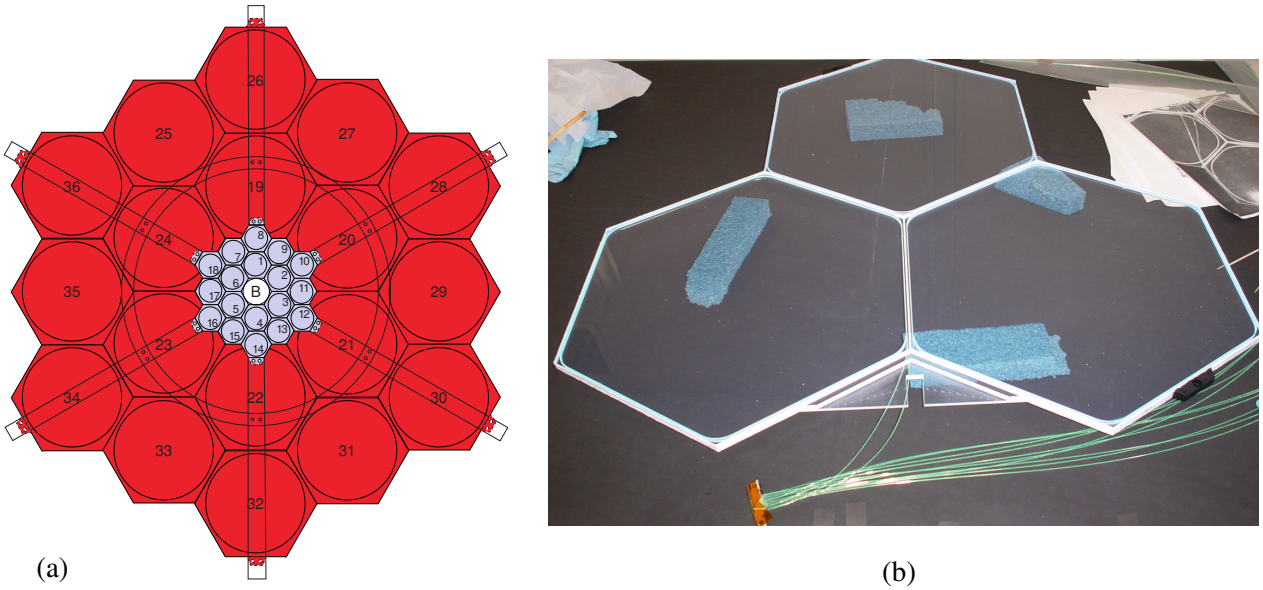

(a) (b)

Figure 5.4: (a) Schematic drawing of the BBC detector with small and large tiles marked with grey and red colour, respectively, and (b) photograph of three adjacent hexagonal scintillator tiles with wavelength shifters attached at the edges. Figures taken from [136] (left) and from [137] (right).

5.2.3 Zero-Degree Calorimiters

The ZDCs [133, 138] (Fig. 5.5a) are built of three calorimeter modules (Fig. 5.5b), each composed of alternating layers of tungsten plates and scintillating fibres read by a common PMT. ZDCs are designed to tag neutral particles (mostly neutrons) which leave the interaction region close to the beam direction. They are installed on both sides of the IR at $z = \pm 18$ m and $x = y = 0$. Their general application is monitoring of the instantaneous luminosity delivered to the experiment, as well as providing the trigger information about the ion dissociation on either side.

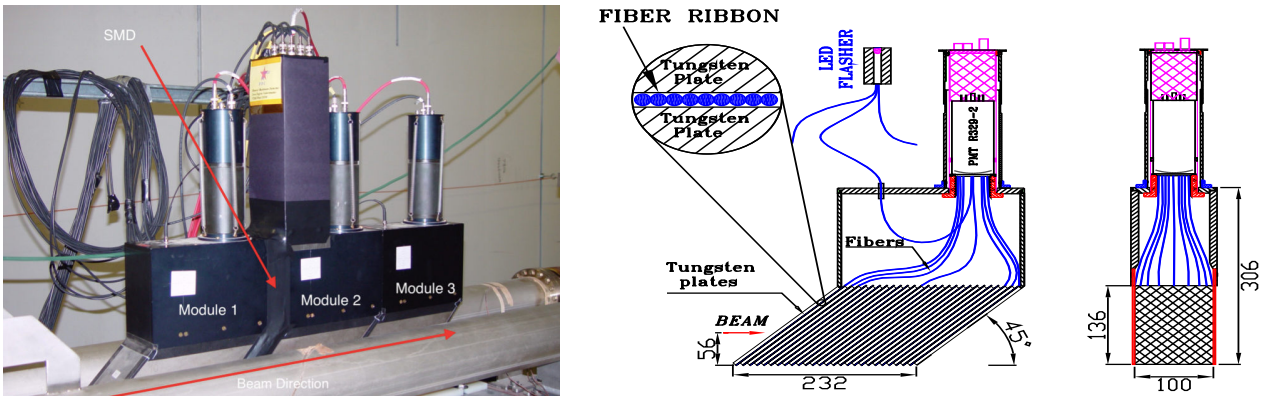

(a) (b)

Figure 5.5: (a) Photograph of the ZDC detector and (b) schematic side (left) and front (right) view of a single module (length unit is mm). Figures taken from [139] (left) and from [133] (right).

5.2.4 Time of Flight

The TOF detector [131, 140, 141] is a system of adjacent Multi-gap Resistive Plate Chambers (MRPCs, Fig. 5.6a). A high voltage (> 10 kV) is applied to the plates separated by the alternating layers of glass and gas (mixture of freon and isobutane). Charged particle traversing the module eject the electrons from the electrode which ignites the avalanche. Signal results from charge collected on the other electrode.

The MRPCs are installed on trays, which are half of the length of the TPC (see Fig. 5.6b). The trays fully surround the TPC on its east and west half. There are 120 trays in total, 60 per one TPC half, with 32 MRPC modules in each tray. The resulting geometrical coverage is about $|\eta| < 0.9$.

At the trigger level TOF is often used to measure the event multiplicity. What is crucial for the CEP measurement, TOF helps to discriminate TPC tracks arrived in preceding/posterior bunch crossings (out-of-time pile-up) from the in-time tracks. But over all, TOF is a precise timing detector, with a time resolution ranging between 60-100 ps. In connection with the TPC track information, it provides significant enhancement of the PID capabilities at large tracks' momenta (~1 GeV).

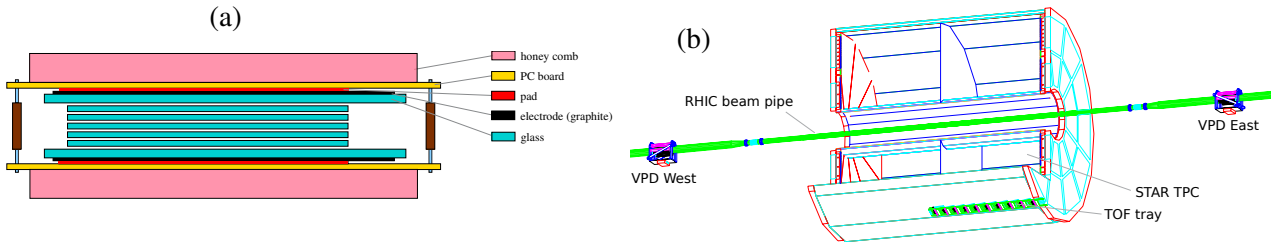

Figure 5.6: (a) Schematic illustration of the MRPC module and (b) visualisation of the placement of a single TOF tray around the STAR TPC. Figures taken from [142] (left) and from [137] (right).

5.2.5 Heavy Flavour Tracker

Improvement of the tracking resolution for collisions taking place within $|z| \lesssim 10$ cm is provided by the HFT detector [134, 145]. It is a system of multi-layer silicon pixel (PXL) and strip detectors (IST

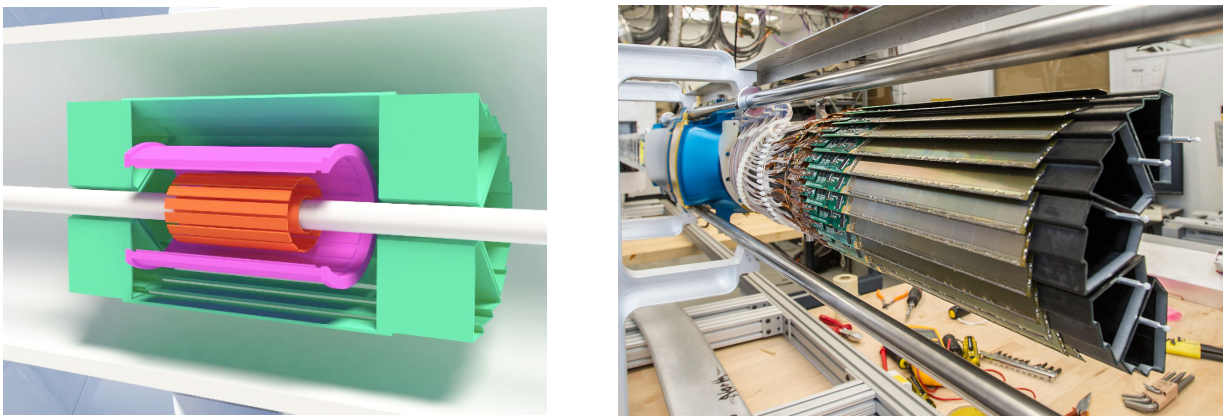

(a) (b)

Figure 5.7: (a) Model with a cut-away view and (b) photograph of a half module of the HFT detector. In Fig. a the innermost PXL component is shown in orange, the IST in magenta, and the SST in green. Figures taken from [143] (left) and from [144] (right).

and SST) tightly surrounding the nominal interaction point (IP). The elements, marked in Fig. 5.7a with orange (PXL), magenta (IST) and green (SST), are placed at radii of 2.5 and 8 cm (PXL), 14 cm (IST) and 22 cm (SST). The detector enables reconstruction of secondary decay vertices of open heavy flavour hadrons. Figure 5.7b shows the half module of the outermost HFT part, the SST.

5.2.6 Roman Pot system

One of the major detection systems used in this analysis is the Roman Pot setup in Phase II* configuration (Roman Pots in Phase I took data with STAR during special runs in last days of *pp* collisions in 2009, see e.g. [17, 146]). It allows to trigger on forward-scattered protons and reconstruct their momenta with high efficiency and precision.

As presented in Figure 5.8 (top) the Roman Pot setup consists of detectors located in two stations on each side of the IP in a distance of 15.8 m and 17.6 m from the IP. Each station has two RPs positioned vertically, one above and the other below the beamline (Figs. 5.8 (bottom) and 5.9). Detectors are situated downstream the DX dipole magnets responsible for head-on targeting of the incoming beams and bending outgoing beams back into the accelerator pipeline.

A single RP vessel (Fig. 5.10a) houses a package of four silicon strip detector (SSD) planes (Fig. 5.10b) - one pair of SSDs with vertical and one with horizontal orientation of the strips, and hence measurement of the position of a proton hit is possible in both transverse spatial coordinates. The pitch (distance between neighbouring strips) in a single detector is 100 µm, therefore intrinsic spatial resolution is at the level of $100\ \mu m/\sqrt{12} \approx 30\ \mu m$. In addition to the silicon detectors, each package contains a plate made of the plastic scintillator, that covers whole active area of a SSD, attached at the back. Two lightguides are glued at the top edge of scintillator which direct the light generated when ionizing particle passes through it to the PMTs connected at the very end of each. This counter is used to trigger on forward protons and also provides the timing information.

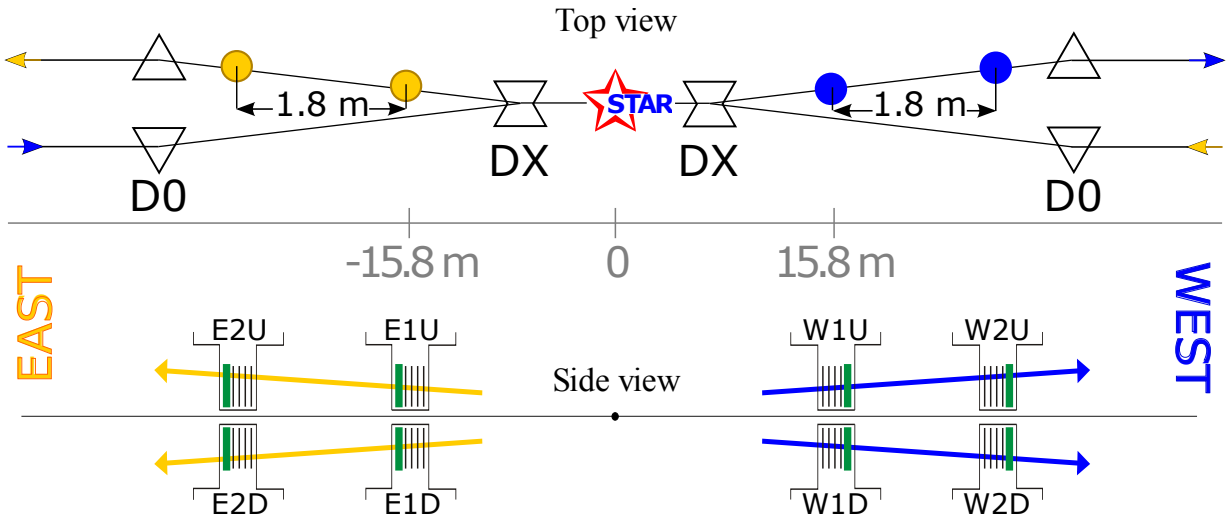

Figure 5.8: Schematic representation of the Roman Pot Phase II* at STAR (not to scale). DX and D0 are the dipole magnets. East RPs are installed at the "yellow" RHIC ring, while west RPs at "blue" ring. Each RP is named with three characters denoting the STAR side (E(ast) or W(est)), the number of station in terms of distance from IP (1 or 2), and position w.r.t. beamline (U(p) or D(own)). Arrows in the bottom part of the Figure demonstrate combinations of RPs forming four branches, in which proton tracks can be reconstructed (see Sec. 6.2).

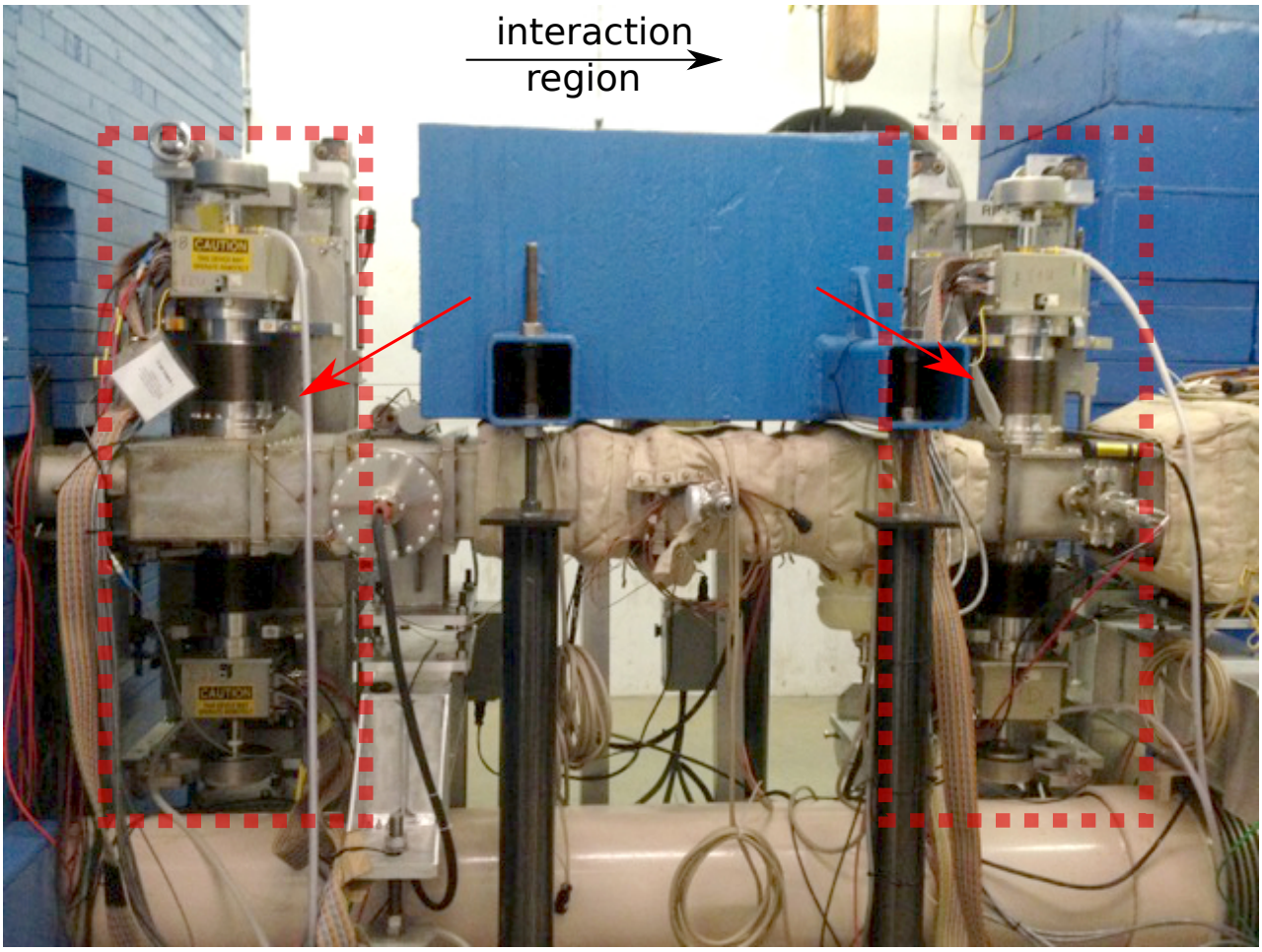

Figure 5.9: Photograph of the RP system at east side of the STAR IR. Two RP stations are marked with dashed red rectangles and red arrows.

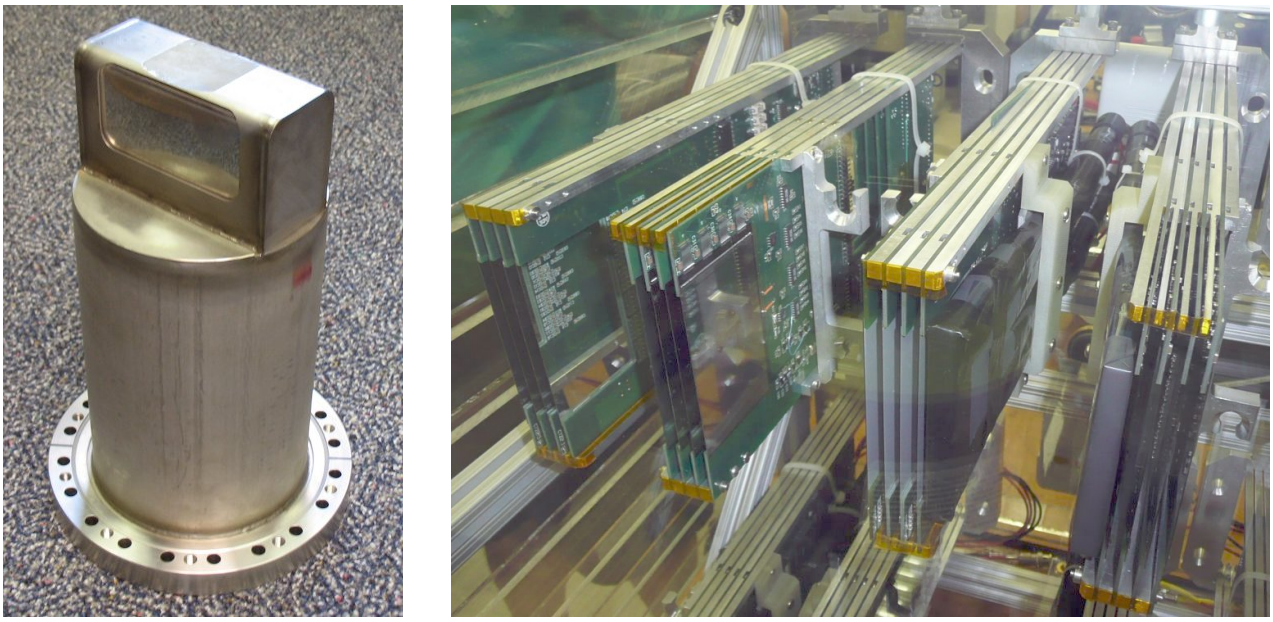

(a) (b)

Figure 5.10: Photograph of (a) Roman Pot vessel and (b) SSD packages stored in the protective atmosphere.

5.2.7 Trigger system

Selection of events interesting from the perspective of physics studies is performed by the STAR trigger system [147]. The trigger system is built from three levels: level 0 (L0), level 1 (L2) and level 2 (L2), which reduce the event rate resulting from the $\approx$ 10 MHz collision frequency (100 ns bunch spacing in RHIC). Currently STAR makes use of primarily the L0 trigger information (hit/no-hit data from the trigger detectors) and, in case the rate exceeds the capabilities of the Data Acquisition (DAQ) system, the triggers are prescaled. At the end the DAQ rate amount approximately 1.5 kHz.

6. Event reconstruction

6.1 Central detector data reconstruction

Track reconstruction in the TPC starts with an attempt to form in each pad of MWPC a cluster which centre is assumed to correspond to the (x, y, z) position of the hit. Clusters are used as input objects to the track finding algorithm [148]. First, a few-hit seeds of tracks are formed. Next, the algorithm using a Kalman filter [148, 149] iteratively extends the tracks with hits which match the expected helical path of the original particle, taking into account EM field, material budget and the multiple Coulomb scattering. Each time a hit is attached to the track being reconstructed, the associated helix is recalculated. The algorithm does not allow the hits to be shared between different tracks. The procedure ends if there are no more hits left matching any of tracks[1]. The tracks reconstructed according to the above procedure are called the "global tracks", as they are not assigned to any interaction vertex.

Independently from the track reconstruction in TPC, signals in TOF detector are processed and those detected within predefined time window and of strength exceeding the threshold are recognised as valid hits. Each hit contains information about detection time. Every global track in an event is extrapolated to the TOF barrel and verified if it points to a TOF cell with reconstructed hit within the extrapolation uncertainties. If yes, the track is matched with that TOF hit.

Global tracks matched with TOF hits are used in the primary vertex reconstruction. The vertex finding algorithm [150, 151] is subject to the beamline constraint, which forces vertex to be reconstructed at (x, y) position equal to that of the beamline trajectory at given z. For each track, the distance of the closest approach (DCA) of its helical extension to the beamline (d_0) is calculated. The z-coordinate of the DCA point, z_0, determines potential longitudinal position of the vertex. Tracks whose d_0 is small enough and whose z_0's are close to each other, form a common vertex. The z-coordinate of the vertex, z_{vtx}, is determined as the average z_0 of the corresponding tracks weighted with the track's quality. Global tracks not matched with hits in TOF are then attached to reconstructed vertices if their DCA to the vertex (radial - DCA(R), and longitudinal - DCA(z)) is small enough, i.e. consistent with the vertex within track extrapolation uncertainties. All tracks assigned to the primary vertex are refitted with an additional hit point, the vertex, and called the primary tracks.

In addition to the momentum vector or the number of hit points used in the fit, $N_{\text{hits}}^{\text{fit}}$, information assigned to each track is supplemented with the specific energy loss, dE/dx. It is reconstructed from the energy of clusters (hits) that form the track. The value of dE/dx in a single hit follows the Landau distribution, whose MPV (most probable value) depends on the known properties of the TPC gas and on the ratio of particle's momentum and mass, p/m. Therefore, using the measured momentum and dE/dx, it is possible to identify the particle. Given that there are at least several hits in a track, dE/dx is reconstructed as the MPV of the Landau distribution obtained by the likelihood fit to dE/dx of clusters forming the track. Usually in analysis the quantity $n\sigma_X$ is used which reflects compatibility of track's dE/dx with that expected from particle of type X. Is is defined as

$$n\sigma_X = \left(\ln \frac{dE/dx}{dE/dx_X^{\text{exp.}}} \right) \Big/ \sigma_{dE/dx} \tag{6.1}$$

[1] Some triggers include also data from HFT. In such case HFT hits are also used in the track reconstruction.

where dE/dx is the ionization energy loss of the TPC track, $dE/dx_X^{\text{exp.}}$ is the Bichsel [152] expectation for given particle type ($X = \pi$, K, p) at reconstructed track momentum, and $\sigma_{dE/dx}$ is the relative statistical uncertainty of reconstructed dE/dx (obtained from the likelihood fit). Quantity $n\sigma_X$ for particle X is, in ideal case, the Gaussian pull with mean at zero and width of one.

Data from the BBC detector (as well as from the ZDC detector) does not require any software reconstruction. For each channel (PMT) the information about the signal strength (ADC counts) and the time (TDC counts) are available, the same as at the trigger level.

6.2 RP data reconstruction

6.2.1 RP track points and tracks

Raw RP data are provided as ADC counts in each SSD channel representing the energy deposited in the silicon layer. These data are subject to the clustering procedure (described in Refs. [2, 146, 153]), which reconstructs the low-level data objects, the clusters, from the series of adjacent channels with the signal strength significantly exceeding the pedestal. Cluster is characterised by its length (number of adjacent strips with signal above the threshold), equivalent of energy (sum of ADC counts in each constituent strip), and position (average coordinate of strips weighted with the ADC counts in corresponding channels). Another low-level data are information about time (TAC counts) and signal strength (ADC) for each PMT. These data are corrected to improve resolution of timing (with the method described in [146]), which can later be used in physics analyses (Sec. 9.2.4).

Physics analysis uses mainly the high-level objects which are the track points and tracks. These objects represent real particles in the same way as the TPC tracks represent particles traversing TPC. Concept of track point and track is depicted in Fig. 6.1. Track point represents reconstructed (x, y, z) position of the hit in single RP detector, while track represents reconstructed forward-scattered proton with all associated observables, such as momentum at the IP, $\vec{p} = (p_x, p_y, p_z)$.

The algorithm for RP track reconstruction is a multi-track algorithm. First, independently in each RP detector, matching cluster pairs in SSDs with the same strip orientation are found based on local position in the detector. The two matched clusters form hit, and its position is determined as the average position of two clusters. If there are no matching clusters in corresponding planes, a single cluster forms a hit. All possible combinations of x- and y-hits are used to form (x, y) track points (z is given by the RP location along the beamline). Therefore, it is possible to have many track points reconstructed in a single RP detector. Finally the tracks are reconstructed from all possible combinations of pairs of

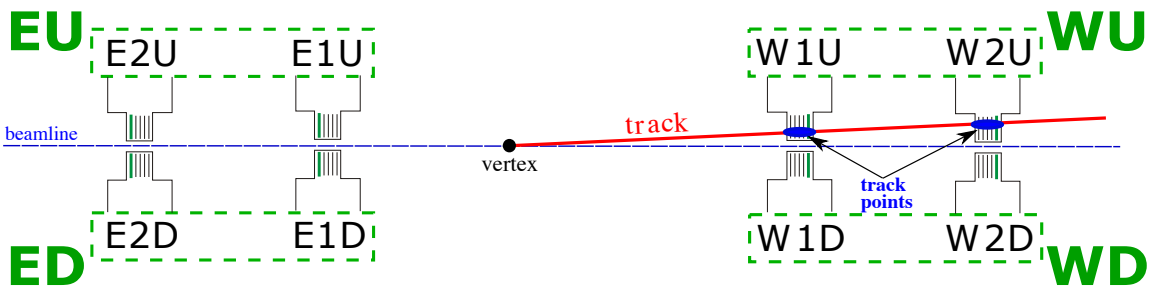

Figure 6.1: Side view of the RP system setup (not to scale) with an illustration of RP track point and track. RP detectors belonging to the same RP branches are marked in green, with the name of a branch provided next to it.

track points in near and far RP stations in the same branch. These RP tracks are called the global tracks. Reconstruction of momentum of forward-scattered proton represented by the global track is described in App. B. If track points are reconstructed only in one RP detector in a branch, then tracks are formed from a single track point assuming in the reconstruction that $\xi = 0$ (beam-momentum proton). Such tracks are called local tracks.

6.2.2 RP alignment

Reconstruction of proton momentum requires precise knowledge of positions of the detectors in space. Detector alignment is done for this purpose, which involves a few steps. At first, dedicated RP survey is performed which provides initial calibration of the linear variable differential transformers (LVDTs) installed in RP movement system. Next, the alignment analysis using elastic scattering events [2] is done which employs collinearity of the elastically scattered protons to tune the initial RP position estimates.

The above steps are sufficient to conduct the elastic scattering analysis. This is because one can use momentum balance constraint of elastically scattered protons (collinearity constraint) and calculate scattering angle from the straight line fit to all track points of East and West proton tracks, without knowledge of position of the interaction vertex. However, kinematics of forward protons scattered in inelastic interaction ($\xi > 0$, e.g. in CD or SD) can be fully reconstructed only if the information about the vertex is available (App. B).

To determine average vertex position needed to reconstruct off-beam-momentum proton tracks a method was developed using the elastic scattering data. Event selection similar to that presented in Sec. 12.4 is performed. Selected clean sample of elastic scattering events is used to prepare plots of the position of the track point in near RP station (x^{RP} or y^{RP}) vs. the local angle of the track with respect to the z-axis (θ_x^{RP} or θ_y^{RP}, Fig. 6.2). The least squares fit of a straight line (with perpendicular offsets) to all data points in the scatterplot is performed. As a result four lines are obtained, two for each pair of elastic branches (arms), one per each transverse spatial coordinate. The slope of the line has interpretation of the distance from the nominal IP ($z = 0$) to the near RP station at 15.8 m. One can see that the slopes are well consistent with this value. The intercept of the line equals to the average position of the vertex in given coordinate. One finds that $\langle x \rangle_{\mathrm{IP}}$ obtained from the fits to data points in two independent elastic arms are perfectly consistent, while in $\langle y \rangle_{\mathrm{IP}}$ parameters differ by 1.5 standard deviations, considered to be in acceptable agreement. Extracted values of average positions of the vertex are averaged, leading to $\langle x \rangle_{\mathrm{IP}} = 0.42$ mm and $\langle y \rangle_{\mathrm{IP}} = 0.45$ mm. These numbers are used in the reconstruction of proton tracks and in generation of MC events. An earlier study showed that $\langle z \rangle_{\mathrm{IP}} = 3$ cm, which is much smaller than the distance between nominal IP and the Roman Pots. Such small offset does not bias proton momentum reconstruction, therefore it is neglected. The above values were validated with a dedicated MC simulation (introduced in Sec. 8.1.1) as well as were checked for stability throughout the entire data-taking period.

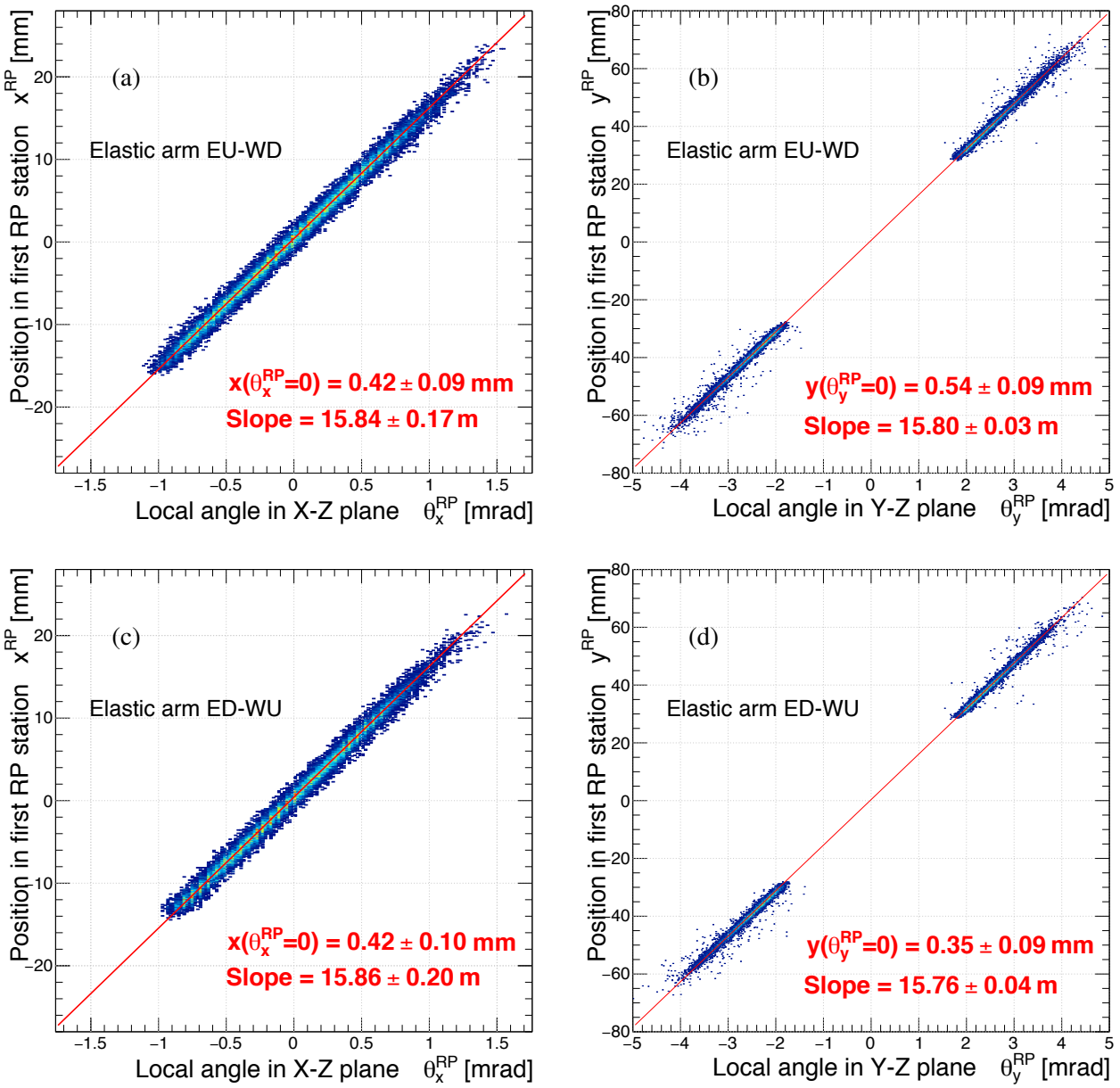

Figure 6.2: Correlation between the hit position of constituent track point in the first RP station (y-axis) and the local angle of track (x-axis) in elastic scattering events measured in (a,b) arm EU-WD and (c,d) arm ED-WU. The intercepts can be interpreted as the average positions of the interaction vertex in the transversal plane.

7. Data

Presented analysis makes use of data from pp collisions at $\sqrt{s} = 200$ GeV collected during 10 week period between February and April 2015. Data were taken during regular STAR runs with normal beam conditions (betatron function at STAR IR $\beta^* = 0.85$ m, peak luminosity $L^{\text{peak}} \approx 1.2{\cdot}10^{32}$ cm^{-2}s^{-1}) [154], with an average number of inelastic interactions per bunch crossing close to $\mu = 1$. The RP detectors were included in the data-taking only after first 30-60 minutes of the RHIC fill, when the collision rate and beam-induced backgrounds dropped to acceptable level.

Logic of all triggers dedicated to measurements of diffractive processes involved the trigger bits defined below. The trigger bits use the naming convention (EU, ED, WU, WD) introduced in Fig. 6.1 for the RP branches, for the basic logical components. These trigger components are assigned the "true" value if there is a signal in at least one of four channels (PMTs) in the given branch.

- **ET = (EU && WD) || (ED && WU)** ≡ signal in RP branches on two sides of IP, opposite to each other w.r.t. IP (in elastic or diagonal configuration).
- **IT = (EU && WU) || (ED && WD)** ≡ signal in RP branches on two sides of IP, both above or below the beamline (in anti-elastic or anti-diagonal configuration).

The main trigger designed for studies of CD, and CEP in particular, RP_CPT2, was defined as

$$\begin{aligned} \text{RP\_CPT2} \;=\; & \big(\text{(ET \&\& !IT)} \;\|\; \text{(!ET \&\& IT)}\big) \\ & \text{\&\& !BBC-E \&\& !BBC-W \&\& !ZDC-E \&\& !ZDC-W} \\ & \text{\&\& TOF} \geq 2. \end{aligned} \tag{7.1}$$

Components of the RP_CPT2 trigger are schematically shown in Fig. 7.1. Definition from Eq. (7.1) is explained in the list below:

1. **(ET && !IT) || (!ET && IT)** ≡ signal in at least one RP on each side of the STAR central detector - to ensure presence of two forward-scattered protons; a veto was imposed on simultaneous signal in RPs above and below the beamline to suppress events involving proton dissociation or pile-up interaction,
2. **!BBC-E && !BBC-W && !ZDC-E && !ZDC-W** ≡ veto on any signal in small BBC tiles or ZDCs on any side of STAR central detector - such requirement is in accordance with the double-gap topology of CEP events, it mostly filtered out CEP events with proton(s) dissociation or parallel pile-up event(s),

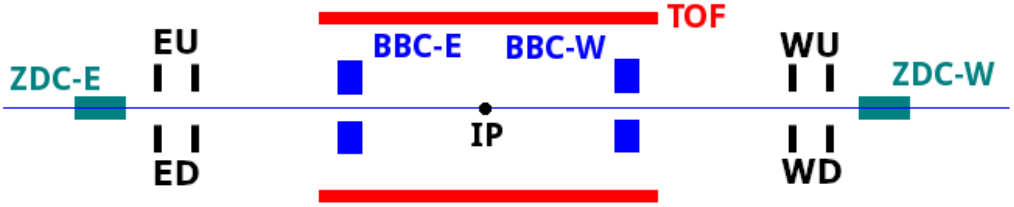

Figure 7.1: Schematic view of the trigger components used in definitions of triggers dedicated to measurements of diffractive processes.

3. **TOF≥2** ≡ at least 2 trigger-level hits in TOF - aim of this condition was to ensure activity in the mid-rapidity; since the lowest multiplicity allowed in CEP is 2, that was the lower threshold of L0 TOF multiplicity.

This trigger was running with an average prescale of 5 and average DAQ rate of 250 Hz, which allowed to collect in total about 560 M events corresponding to 14.2 pb^{-1} of integrated luminosity. These data are spread over more than 1000 runs, which are the basic data units at STAR. Each run, on average, corresponds to 30 minutes of data-taking.

In some parts of the analysis also elastic proton-proton scattering data were used. These data were collected with RP_ET trigger defined as

$$\text{RP\_ET} \quad = \quad \text{ET}, \tag{7.2}$$

hence requiring only back-to-back topology of trigger signals in RPs, as expected in elastic scattering process. Integrated number of collected RP_ET triggers amounts to 136 M.

Last but not least, the zero-bias data were also used in some parts of analysis. These data were collected with a fully random trigger, prescaled to run with approximate DAQ rate of 1-2 Hz. About 2 M zero-bias triggers were collected in total. An important feature of zero-bias data is its randomness, providing data also from the so-called abort gaps, when there were no colliding bunches in the STAR IR, hence enriched with information on e.g. detector noise.

8. Monte Carlo simulation

This chapter contains description of the MC tools developed for the analysis (Sec. 8.1), MC samples used for determination of reconstruction and selection efficiencies, for modelling of background contribution and for comparison of hadron level cross sections with model predictions (Sec. 8.2), and some improvements of existing MC simulation necessary to perform the measurement with reduced systematic uncertainties (Sec. 8.3).

8.1 Development of new Monte Carlo tools

8.1.1 Simulation of the RP system

Original simulation tool of the STAR detector, called STARsim, is implemented in Geant3 [155] framework and does not include the RP detectors. For this reason a dedicated tool was prepared to enable a precise simulation of the RP subsystem. Development of this software started as two independent projects, one devoted to modelling of the RPs and SSDs package [146, 156], and the other aimed to implement in the simulation the collider elements including magnets and the spatial distribution of their fields [157, 158]. The projects were finally merged and developed to match the needs of analyses of forward processes at STAR [2, 33].

The simulation program is a standalone Geant4 [159] application that allows for simulation of the passage of any type of particle from the IP to the RPs, and store both the true and detector level information in the standard STAR data format. For the reconstruction, the original STAR software is used, the same which is also used for the real data reconstruction. The program allows for choosing of multiple options, e.g. customise the beam conditions, magnet settings (beam energy), RPs positions, and many others.

The geometry of the collider elements (beam pipe, magnets) and RP detectors (vessel, SSD packages) is implemented in accordance to the technical drawings and has been consulted with the designers thereof. In case of RP vessels and detector packages not only technical drawings were used, but appropriate dimensions were also determined with a dedicated survey. Fig. 8.1 shows a few renderings of the RP housing and the SSD package implemented in Geant4. They can be confronted with the photographs of the RP and SSD package in Fig. 5.10. In Fig. 8.2 we show the general view of the "world" volume in Geant4 simulation with the most significant elements of the geometry marked

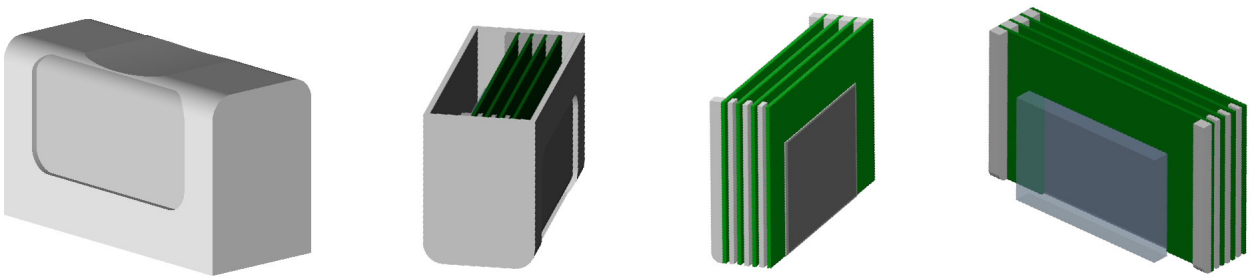

Figure 8.1: Geant4 implementations of the RP vessel and SSD package with trigger counter.

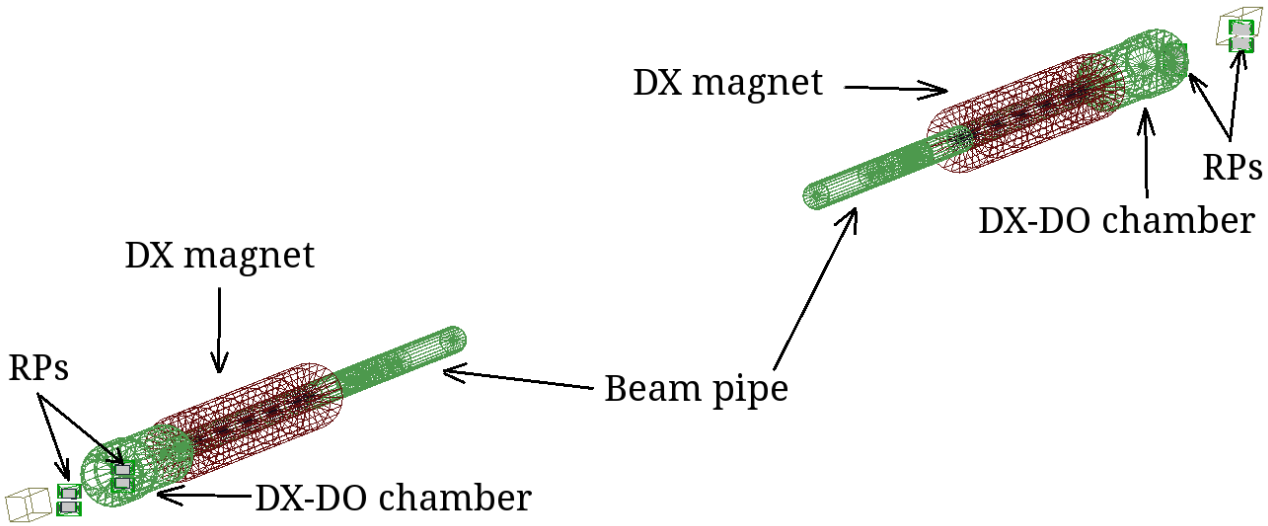

Figure 8.2: A general view of the Geant4 implementation of STAR RP system and the elements of the RHIC accelerator.

with arrows and appropriately labelled.

It turned out during initial validations of the Geant4 simulation with elastic proton-proton scattering events that the distribution of the (x, y) position of the proton in RPs does not agree between the data and MC at a satisfactory level. It was understood that the perfect positioning of the elements of the collider assumed in the geometry model may need some tuning, especially precise positioning of the DX magnet, which particularly limits acceptance of the RP detectors. The DX magnets are moved each time the switch between symmetric (e.g. pp) and asymmetric (e.g. p+Au) collisions occurs to accommodate for the non-zero tilt of the beams in asymmetric collisions required to close beam orbits and provide collisions in the STAR IR. Therefore lateral offset of this element was expected to be the most significant ingredient needed to correctly describe forward proton acceptance in the RP location.

In order to quantitatively determine the agreement between the true DX position and the position implemented in Geant4, a dedicated analysis of the DX "shadow" in the two-dimensional histogram of proton hit was performed. The prepared algorithm looked for a sharp drop of event counts along the x-coordinate in the histogram of y- vs. x-position of the track points in collinear elastic scattering events with single proton tracks on both sides of the IP. The result (for a single RP station) is presented in Fig. 8.3a and 8.3b for the data and MC, respectively. The envelope of the DX shadow found by the algorithm is marked with black points. The points were transformed by swapping x and y axis and fitted with a circle, as shown in Fig. 8.3c. The parameters of the circle (radius R and centre point (x_0, y_0)) do not reflect directly the position of the DX, but they were used to find the best shift of the DX on the east and west side in the iterative method. The satisfactory agreement of the DX aperture envelopes between the data and MC was finally found with the shifts of the DX magnets with respect to their nominal positions equal to $\Delta x_{\mathrm{DX}}^{\mathrm{East}} = -3.1$ mm, $\Delta y_{\mathrm{DX}}^{\mathrm{East}} = 4.0$ mm, $\Delta x_{\mathrm{DX}}^{\mathrm{West}} = -2.4$ mm, $\Delta y_{\mathrm{DX}}^{\mathrm{West}} = 0.4$ mm. The comparison of the DX shadow envelope after the tune is shown in Fig. 8.3d.

The general STAR practice is to perform the embedding of the output of a MC simulation into the real data, which helps to reproduce all collision environment effects in the reconstruction of the simulated signal. The most common practice is to embed simulated signal into the zero bias triggers,

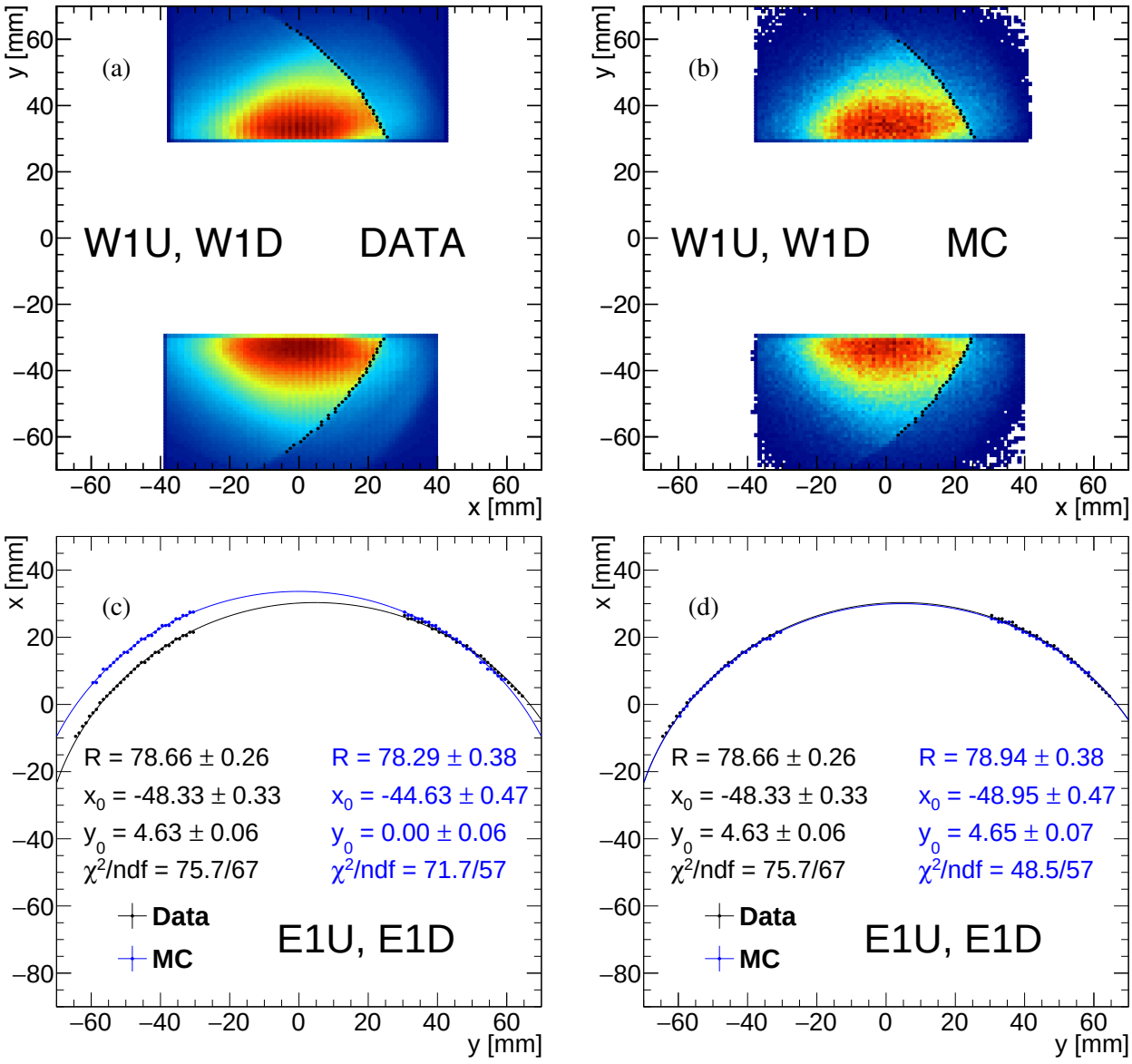

Figure 8.3: Sample hit map of track points of proton tracks in events selected as elastic scattering in (a) the data and (b) Geant4 simulation. The DX magnet aperture "shadow" is marked with black points. The DX aperture envelopes were fitted with circles (c) which helped to establish the offsets of DX magnet positions in x and y with respect to the ideal (nominal) geometry, leading to nearly perfect agreement between the data and MC after introducing the offsets in Geant4 geometry (d).

which by definition provide unbiased information about the real environment in which data were collected. Such feasibility is also implemented in the Geant4 simulation, which has an option that allows overlaying the real data with the simulated RP detectors response.

Merging of the simulated signal with the data is done for the SSD data, as well as the PMT data. In the case of the PMT data for each channel the ADC is set to the sum of values in the data and simulation, while the TAC is set to the larger (earlier signal) of the two values. In case of the SSD data, the merging is done at the level of reconstructed clusters. At the end of the simulation of an event, a dedicated algorithm is run for every SSD plane which adds vectors of clusters from the data and from the simulation and merges overlapping clusters (recalculates their length, sums energy, updates cluster

position). This new collection of clusters is provided to the track reconstruction algorithm, which returns a new set of track points and tracks.

8.1.2 Fast MC generator

Proper estimation of the particle identification efficiency requires a good modelling of the detector response in terms of the dE/dx and TOF time measurements. Also a large number of simulated events is necessary to reduce the statistical uncertainties of the efficiency. The former was provided by adjusting dE/dx spectra from embedded MC to match the data, as explained in Sec. 8.3.1. The latter, however, is not easy to achieve using the standard STAR simulation framework for exclusive K^+K^- and $p\bar{p}$ whose identification is most challenging and information about identification efficiency is the most needed among studied species. Specially for the study of particle (exclusive pair) identification a dedicated MC simulation was prepared.

This dedicated MC simulation was designed to work as follows (simulation of a single event of the CEP of a pair of particles of a certain type is described):

1. The vertex position z_{vtx} is generated from a predefined distribution.
2. Kinematics of central state particles is set: momentum (magnitude) p, pseudorapidity η and azimuthal angle ϕ of positive and negative charge particles are generated from predefined distributions.
3. Both particles are tested if doubled radius of curvature $2R$ of associated track in the magnetic field of the TPC ($B = 0.5$ T, $R \propto p_{\text{T}}/B$) is smaller than the radius of TOF detector barell (assumed 212 cm). If not then event is skipped and procedure is restarted (back to 1.).
4. The particles are propagated from the vertex at $(0, 0, z_{\text{vtx}})$ through the magnetic field of TPC using Newton's method with the time step (in the laboratory) equal 100 ps, corresponding to space step < 3 cm.
5. After step 4. the position of the TOF cell is known, allowing to calculate the TOF path length L between the vertex and position of the TOF hit. Also the TOF hit time t is then known, further smeared by adding random number from the normal distribution with the mean at 0 and the standard deviation $\sigma_{\text{TOF}} = 60$ ps to account for the finite TOF time measurement resolution. In addition to this, reconstructed tracks' (transverse) momenta are defined as the true momenta smeared by 6 MeV if $p_{\text{T}} < 0.3$ GeV or by 2.4 MeV + 1.2% $\times\, p_{\text{T}}$ if $p_{\text{T}} > 0.3$ GeV, to account for finite TPC momentum resolution. At this stage it is possible to calculate m^2_{TOF} using Eq. (C.6).
6. The dE/dx measurement is also simulated. For each particle a dE/dx is generated from the distribution of the form given in Eq. (8.6) with parameters (for given particle ID and momentum) which are extracted from the data, as elaborated in Sec. 8.3.1. This assures that the simulated dE/dx exactly matches the data. Once dE/dx for both particles (tracks) is obtained, value of the dE/dx error (more strictly: the relative uncertainty of dE/dx) is also set up. This quantity depends on the number of TPC hit points used in the reconstruction of dE/dx (the more hits in tracks, the better resolution of dE/dx), which obviously is not accessible without full STAR simulation in Geant3. This problem is solved by extracting the dependence of $\sigma_{dE/dx}/(dE/dx)$ on the TOF path length from the data (from CEP events, Fig. 8.4). Since the length of the TOF

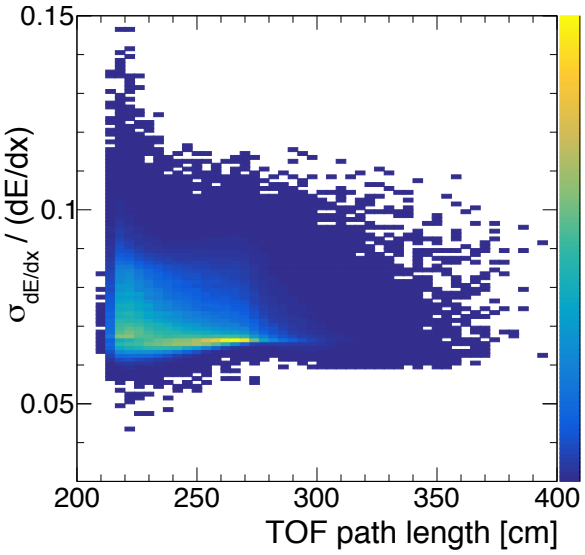

Figure 8.4: Correlation between the relative uncertainty of dE/dx and the track TOF path length. The distribution was obtained for the exclusive event candidates after full selection.

path is very strongly correlated with the number of hits forming the track and thus the number of hits used to reconstruct dE/dx, one is allowed to generate $\sigma_{dE/dx}/(dE/dx)$ from the distributions for particular TOF path lengths calculated in the step 5 and use it as a measured ones. In this way the simulation preserves relevant correlations between dE/dx-related quantities. After these steps are taken the $n\sigma_X$ ($X = \pi, K, p$) variables are calculated for each track using the definition (Eq. (6.1)), in exactly the same way as it is done during standard data reconstruction.

8.2 Monte Carlo samples

Below all MC samples prepared for the CEP analysis are described. All samples were generated with the parameters (such as e.g. vertex distribution) set to best match the data. If possible, the same runs were simulated as the data used in the physics analysis. Because of limited computing resources only selected samples were subject to the full event embedding. All MC samples embedded to data ("pile-up MC") were also available in a version without embedding (pure simulation, "no pile-up MC").

8.2.1 Exclusive signal

Signal sample with exclusive $\pi^+\pi^-$ was prepared with GenEx event generator. Each event has been passed independently through STARsim and Geant4 simulation of the RP detectors, then merged, and fully embedded into a zero-bias event. Before passing through the STAR detector model, events were filtered in order to gain production efficiency. At the particle level pions were required to have $p_T > 0.15$ GeV and $|\eta| < 1$, while forward scattered protons (after added beam divergence) were required to fit within fiducial region envelope (Eq. (9.2)) extended by three standard deviations of the angular beam divergence.

Also a sample of signal events for PID efficiency studies was generated using the fast MC generator introduced in Sec. 8.1.2. In this sample, distributions of several kinematic quantities were defined

based on the data.

For determination of e.g. the geometrical acceptance of the RP stations, (a phase space) MC samples were generated using the uniform distribution for invariant mass, rapidity and forward-scattered protons' azimuthal angle, and exponential t-distribution.

8.2.2 Background modelling

Two samples (Central Diffractive and Minimum Bias) of Pythia 8 events have been generated for background studies. In both cases the MBR model was used for the Pomeron flux. The generated events were passed through the Geant3 simulation of the STAR detector (STARsim) and the Geant4 simulation of the RP detectors. In order to increase the generation efficiency of the useful events, the events were filtered at the generation levels to ensure later lack of signal in the BBC-large detectors. This was done by analytical propagation of all charged particles through the magnetic field of TPC with the helical paths resulting from their momenta. Both samples were finally partially (only the simulated RP response) embedded into zero-bias and elastic trigger (RP_ET) data, respectfully. Full embedding would require a large amount of CPU time and it was found unnecessary to embed the TPC tracks into zero-bias data to obtain reliable agreement between distributions of desired quantities as is shown in the following.

8.2.3 Model predictions

The following MC samples were produced for comparisons of the measured fiducial cross sections with the model predictions.

- Exclusive $\pi^+\pi^-$ and K^+K^- from GenEx using the exponential form factor with $\Lambda^2_{\text{exp}} = 1.0$ GeV^2.
- Exclusive $\pi^+\pi^-$ and K^+K^- from DiMe using the exponential form factor with $\Lambda^2_{\text{exp}} = 1.0$ GeV^2 and "model 1" of absorption effects.
- Exclusive $\pi^+\pi^-$, K^+K^- and $p\bar{p}$ from Pythia 8.244 using the MBR model of the Pomeron flux, with the minimum generated mass of the central system equal to 0.5 GeV (the lowest limit allowed in Pythia).

8.2.4 Other

Some other MC samples were also used, mainly targeted to deliver estimates of the reconstruction efficiency of the objects used in physics analysis. These are:

- Sample of single particle (π^+, π^-, K^+, K^-, p, $\bar{p}$) MC embedded into zero-bias data. The particles' kinematics were generated with a uniform p_{T} and η to populate all regions of measured phase space. The sample was dedicated for determination of the TPC track reconstruction and TOF matching efficiency.
- Sample of forward scattered protons from GenEx simulated in Geant4 and embedded into zero-bias data. This independent embedded MC sample was prepared especially for determination of the RP track reconstruction and selection efficiency.

- Elastic proton-proton scattering events simulated in Geant4 and embedded into zero-bias data. The sample was mainly prepared for determination of the systematic uncertainties related to the RP system.
- Sample of Minimum Bias Pythia 8 MC embedded into zero-bias data. The sample was prepared for determination of the systematic uncertainties related to dead material in front of the TPC and its influence on the TPC track reconstruction efficiency.

8.3 Improvements of the Monte Carlo simulation

8.3.1 Adjustment of the simulated dE/dx

Particle identification in CEP analysis is done using merged information from the TPC (dE/dx) and from the TOF (time of hit macthed to TPC track). It was found that the dE/dx information from the MC events simulated with STARsim poorly matches the data. It was found that the origin of the data-MC inconsistency lies in the (unmodifiable) model of energy loss used in the STARsim. Therefore, in order to tune simulated response of the TPC in terms of dE/dx, hence also make all other comparisons between data and MC more reliable, a correction method was developed based on proper transformation (recalculation) of simulated dE/dx to obtain new dE/dx whose distribution matches the data.

We know that the $n\sigma_X$ (where $X = \pi, K, p, ...$) variable for particle X follows the standardised normal distribution

$$f(n\sigma_X) = \mathcal{N}(n\sigma_X; \mu = 0, \sigma = 1), \tag{8.1}$$

therefore dE/dx itself follows, by definition, the log-normal distribution[1]:

$$f(dE/dx) = \mathcal{LogN}(dE/dx; \mu = \langle dE/dx\rangle, \sigma = \sigma_{dE/dx}) = \frac{1}{\sqrt{2\pi}\cdot\sigma\cdot dE/dx}\exp\left[-\frac{\ln^2\frac{dE/dx}{\mu}}{2\sigma^2}\right]. \tag{8.2}$$

The desired transformation should preserve the shape of dE/dx distribution so that it is still described by $\mathcal{LogN}$, however it should change μ and σ so that these values are compatible with the data. The transformation that satisfies above postulate is

$$dE'/dx = c\cdot(dE/dx)^a. \tag{8.3}$$

Parameters of the distribution $\mathcal{LogN}(dE'/dx)$ are then

$$\mu' = c\cdot\mu^a, \quad \sigma' = a\cdot\sigma. \tag{8.4}$$

From above we get formulae for parameters of the transformation:

$$a = \sigma'/\sigma, \quad c = \mu'/\mu^a. \tag{8.5}$$

To sum up, one has to find the MPV ($\langle dE/dx\rangle$) and width parameter of the dE/dx spectrum ($\sigma_{dE/dx}$) for each particle in the data and MC, and use relations (8.5) in order to find parameters of the transformation introduced in Eq. (8.3).

[1] In this analysis a modified parameterisation of the log-normal distribution is used. In the original definition the numerator inside the exponent has the form $[\ln(dE/dx) - \mu]^2$. In the modified definition the form $\ln^2[(dE/dx)/\mu]$ is used (μ is substituted with $\ln\mu$), which matches the definition of $n\sigma_X$ from Eq. (6.1).

The most challenging part of the task was extraction of the $\langle dE/dx \rangle$ and $\sigma_{dE/dx}$ from the data. In case of MC one can select tracks matched to true-level particles of the given ID and thus separate dE/dx of different particle species, which makes extraction of the distribution shape straightforward. Unfortunately, it is not possible to apply the same method to the data - here one has to deal with overlap of the reconstructed dE/dx from different particles. Therefore fits of sum of $f(dE/dx)$ corresponding to different particles were performed to reconstructed track dE/dx in narrow momentum bins. The width of momentum bins (20 MeV) was chosen to compromise statistics and validity of assumption of constant parameters of dE/dx distribution over bin range.

It was found during the fit attempts that log-normal distribution is not a perfect model of the reconstructed dE/dx. The problems with description of the data were mainly in the high-value tail part of the distribution from a single particle. Precise model was necessary to obtain satisfactory quality of fits and trustworthy values of parameters. After some research the best model of dE/dx distribution from single particle was found to be

$$f(dE/dx) = \begin{cases} \frac{A}{\sqrt{2\pi}\cdot\sigma\cdot dE/dx} \exp\left(-\frac{1}{2}\left(\frac{\ln \frac{dE/dx}{\langle dE/dx\rangle}}{\sigma}\right)^2 \right) & \text{for } \frac{\ln \frac{dE/dx}{\langle dE/dx\rangle}}{\sigma} \leq k \\ \frac{A}{\sqrt{2\pi}\cdot\sigma\cdot dE/dx} \exp\left(-k\cdot\frac{\ln \frac{dE/dx}{\langle dE/dx\rangle}}{\sigma} + \frac{1}{2}k^2 \right) & \text{for } \frac{\ln \frac{dE/dx}{\langle dE/dx\rangle}}{\sigma} > k. \end{cases} \tag{8.6}$$

Such form was motivated by the function discussed in Ref. [160], and here adopted for the log-normal instead of normal distribution. Because the modification of the log-normal distribution is introduced only at high-value tail, the validity of the transformation discussed above still holds. To reduce the complexity of the fit, the parameter k was fixed to the same value equal to 2.2, for all particle species. It was checked that this value worked well for both data and the embedded MC. Particles and their anti-particles were assumed to have the same dE/dx distributions at a given momentum and were analysed together. The same track selection was used both for data and MC, with the quality criteria described in Sec. 9.2.2. The sample fit in a single momentum bin is shown in Fig. 8.5.

Results of the fits for all considered particle species (pions, kaons, protons, electrons and deuterons) are presented in Fig. 8.6 with colour markers. Figures 8.6a and 8.6b show the offset of the MPV of reconstructed dE/dx relative to the Bichsel parameterisation in the data and embedded MC, respectively,

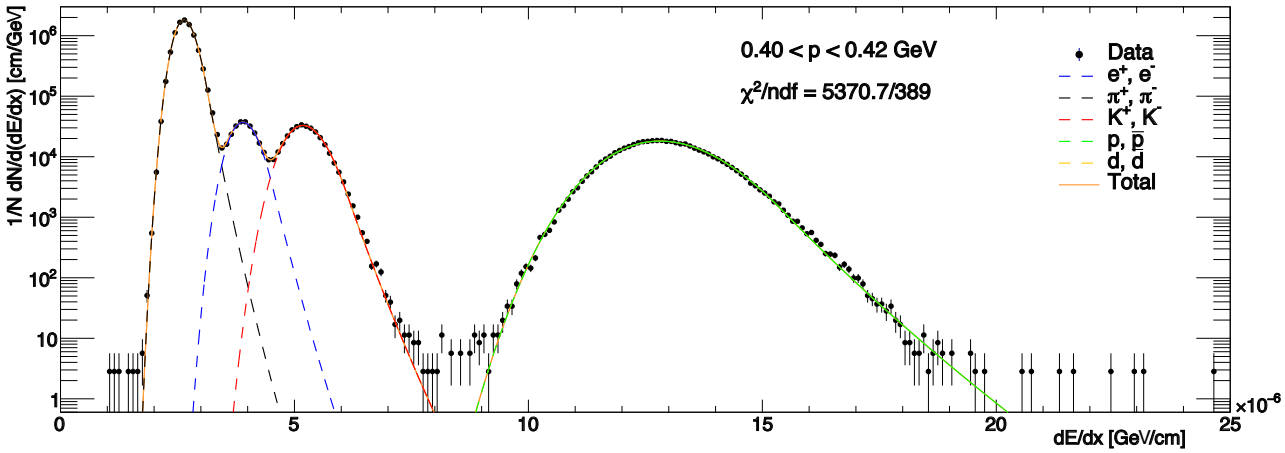

Figure 8.5: Sample fit of sum of functions from Eq. (8.6) to the dE/dx spectra in the data in a single momentum bin. Contributions from particular species are marked with different colours, as explained in the legend.

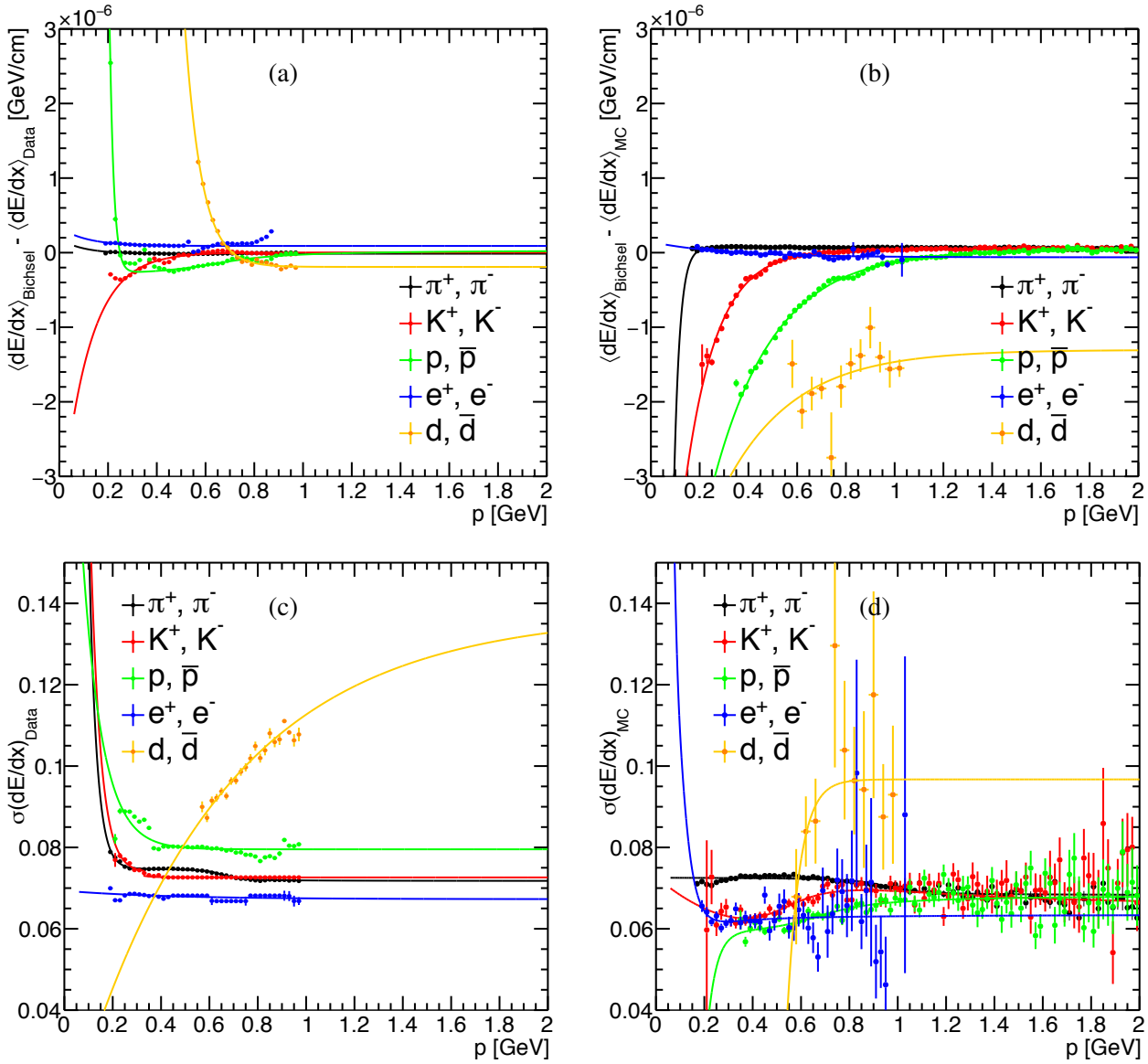

Figure 8.6: Difference between MPV of dE/dx predicted by the Bichsel parameterisation and obtained from the fit of Eq. (8.6) to the dE/dx distribution in (a) the data and (b) MC sample and dE/dx width parameter in (c) data and (d) MC as a function of reconstructed particle momentum for a few particle species. Solid lines represent fits to points of corresponding colour. Only statistical errors are shown.

and Fig. 8.6c and 8.6d show the width of reconstructed dE/dx (in the same order). It was empirically found that the function

$$g(p) = P_1 + P_2 \cdot \exp(-P_3 \cdot p) + P_4 \cdot \arctan(P_5 \cdot (p - P_6)) \tag{8.7}$$

is able to describe well the dependence of the points shown in Fig. 8.6 on the track momentum. This function was fitted to points corresponding to each particle type and fit result is shown in Fig. 8.6.

The correctness of the entire procedure described in this section was verified by comparing the reconstructed track dE/dx between the data and embedded MC before and after the dE/dx transformation given by Eq. (8.3). Some difficulty arose in this comparison due to inconsistent relative content of different particle species in the data and embedded MC sample. Problem was solved by

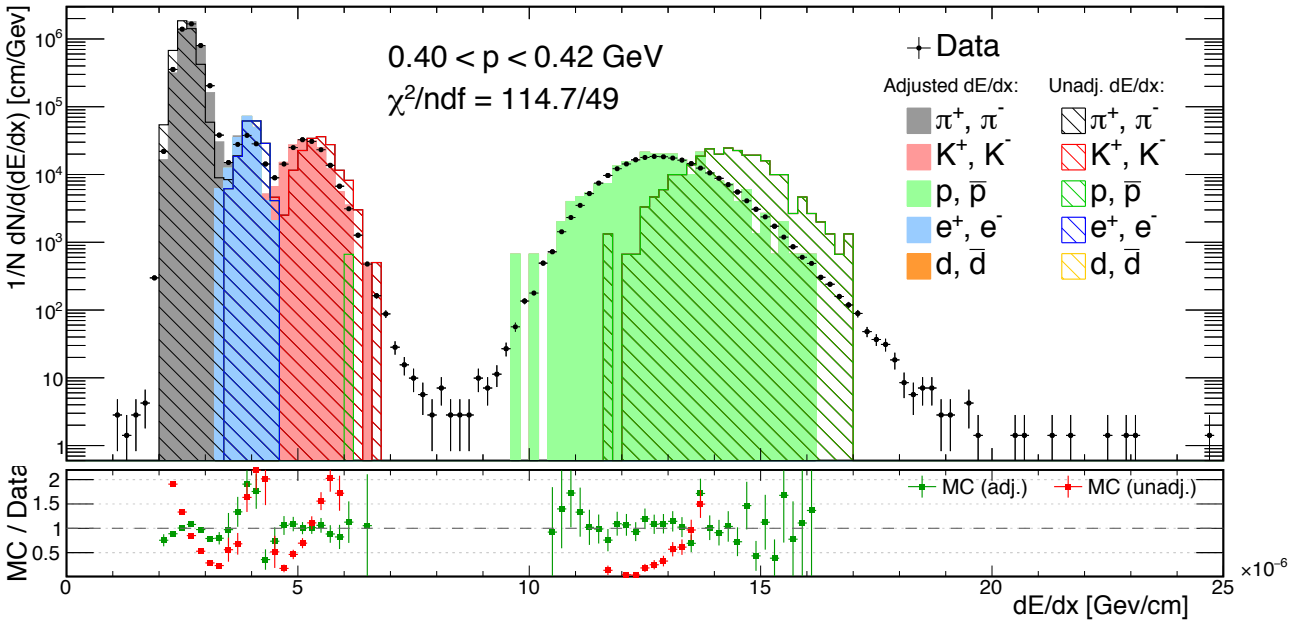

Figure 8.7: Sample comparison of dE/dx spectrum between data and embedded MC (before and after dE/dx adjustment) in a single momentum bin. Lower pad shows the ratio between embedded MC and data before and after dE/dx adjustment. In both upper and lower pads the same colour code is used. Only statistical errors are shown. Due to limited statistics of embedded MC some data points do not have corresponding entries in MC.

separating dE/dx histograms of different particle species in MC (in the same way as it was done for extraction of dE/dx MPV and σ for each particle ID) and fitting the sum of histograms from different particle types to the data histogram (in momentum bins). The only free parameters in the fit were relative contents of histogram from single particle type in the data histogram. A sample comparison between the dE/dx in data and embedded MC is presented in Fig. 8.7. Fits were done for adjusted dE/dx (filled green). Histograms for unadjusted dE/dx (hashed red) were composed using the same relative content of particles as obtained from the fit of adjusted dE/dx. The ratio of the MC to the data shown in the lower panel of Fig. 8.7 clearly demonstrates better agreement of the MC and the data in terms of position and width of peaks in dE/dx spectrum after the adjustment.

Exactly the same cross-check was done for $n\sigma_X$ variables, which are directly used to identify particles in physics analysis. They carry information about the distance (in width units) of reconstructed dE/dx from the MPV of dE/dx according to Bichsel parametrization - they are kind of a pull variables. For every track $n\sigma_X$ was recalculated using its definition:

$$n\sigma_X = \left(\ln \frac{dE'/dx}{dE/dx_X^{\text{exp.}}} \right) \Big/ \sigma_{dE/dx} \,, \tag{8.8}$$

where instead of original dE/dx the adjusted one (dE'/dx) was used. Uncertainty of reconstructed dE/dx was left unchanged. The sample comparison of $n\sigma_{\text{pion}}$, $n\sigma_{\text{kaon}}$ and $n\sigma_{\text{proton}}$ variables can be found in Fig. 8.8. As in the case of dE/dx comparison, in the lower panels of Fig. 8.8 the ratios of the MC to the data also demonstrate better agreement of the MC and the data, which was the goal of the adjustment.

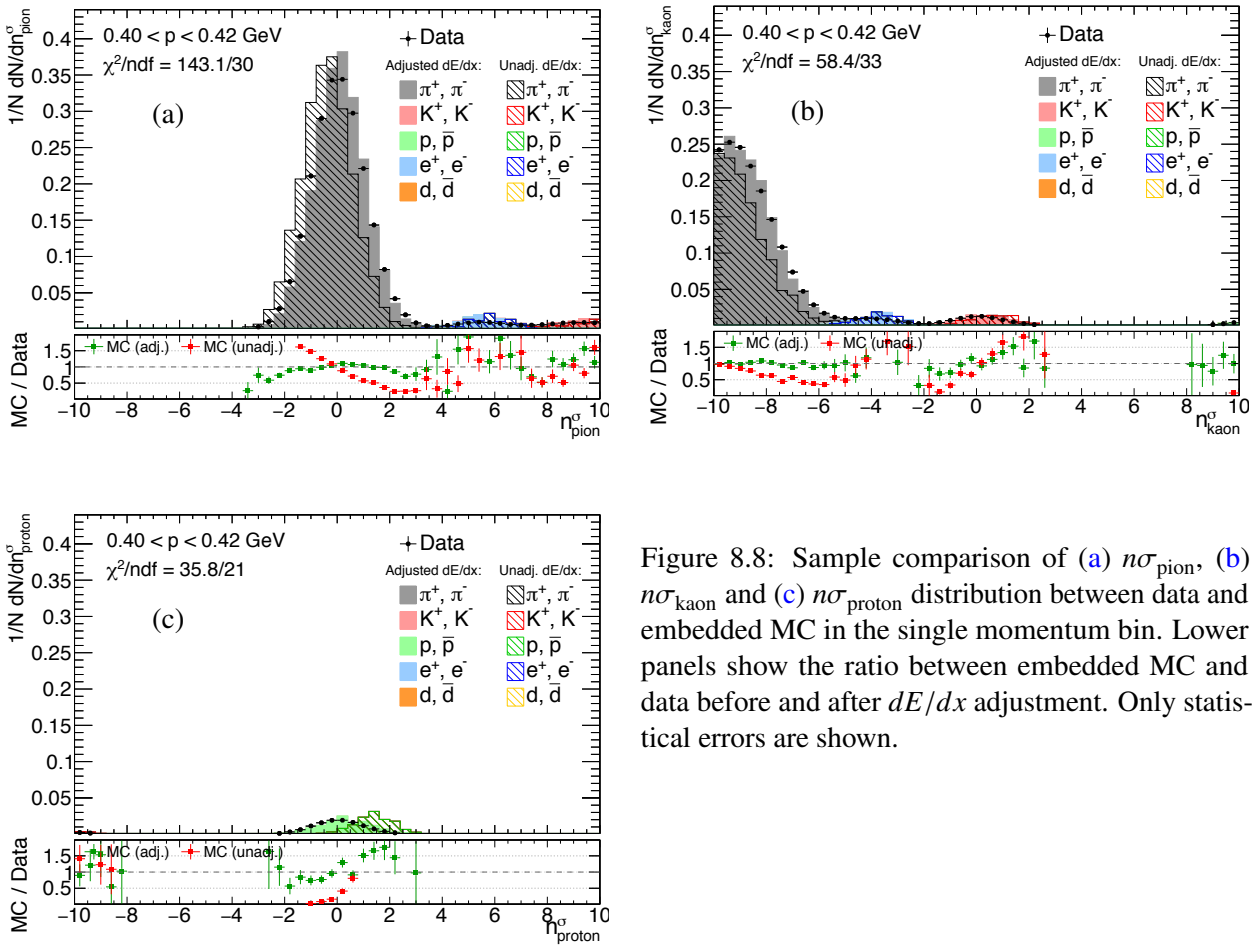

Figure 8.8: Sample comparison of (a) $n\sigma_{\text{pion}}$, (b) $n\sigma_{\text{kaon}}$ and (c) $n\sigma_{\text{proton}}$ distribution between data and embedded MC in the single momentum bin. Lower panels show the ratio between embedded MC and data before and after dE/dx adjustment. Only statistical errors are shown.

8.3.2 Adjustment of the simulated TPC track pointing resolution

It was found during the analysis that distributions of quantities which describe the pointing resolution of the TPC tracks do not agree well between the data and embedded MC. Namely, the resolutions of the global helices associated with the tracks were found to be significantly better in the STAR simulation than in the data, what manifests as narrower DCA and d_0 distribution in the embedded MC, comparing to corresponding distribution in the data. The plausible reason for this is lack of modelling of the TPC distortions, which are present in the real experiment.

This problem affected the momentum resolution and could potentially introduce bias to e.g. TPC track reconstruction efficiency calculated from MC. Therefore, the resolution adjustment procedure was applied to find appropriate parameters of the "artificial" helix deterioration to obtain an agreement between DCA and d_0 distributions (and all related resolutions) in the data and embedded MC.

In order to worsen pointing resolution in the MC a smearing of the helix radius $\sigma(R)$ was introduced (Fig. 8.9). It was decided to account also for possible systematic bias of the helix radius $\Delta\mu(R)$[2], which may be present e.g. due to differences in the material budget used in the simulation and reconstruction. Both smearing and bias of the helix radius were introduced only for MC tracks which were matched with the true-level particles since only simulated tracks require adjustment (tracks from zero-bias event

[2]Transverse impact parameter d_0 takes positive value if the beamline is contained inside the helix (in the yz-plane projection), otherwise it is negative. Any asymmetry in the d_0 distribution in the MC with respect to the data indicates presence of systematic difference in reconstructed d_0, hence also in reconstructed R.

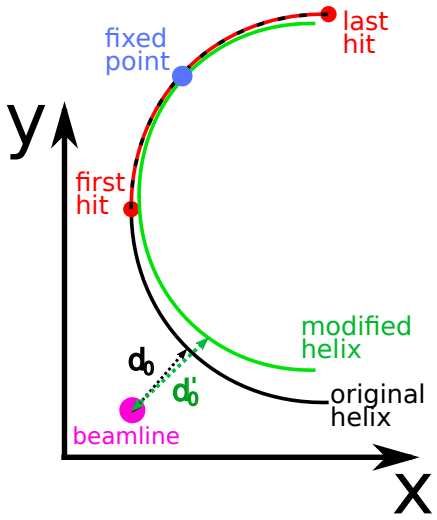

Figure 8.9: Sketch of helix modification procedure and d_0 calculation.

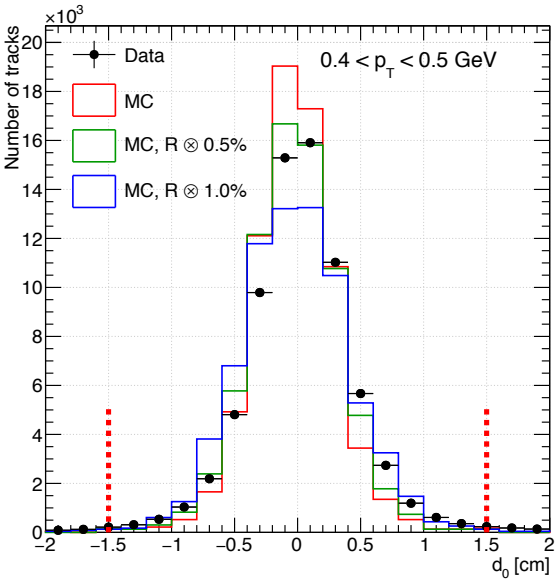

Figure 8.10: Example of comparison of d_0 histograms in single p_T bin in the data (black points) and embedded MC (coloured lines) in the procedure of TPC pointing resolution adjustment. Only a few MC histograms were shown for explanatory purposes.

used in embedding already contain all detector effects).

Extraction of the $\Delta\mu(R)$ and $\sigma(R)$ parameters required to achieve agreement of the pointing resolution between embedded MC and the data involved following steps:

1. Series of d_0 histograms in bins of p_T (100 MeV wide) was prepared, each for different size of distortion (different $\Delta\mu(R)$ and $\sigma(R)$) of global helix of the TPC tracks matched with true-level particles (example plot in single p_T bin is shown in Fig. 8.10):

   (a) for each set of parameters $\Delta\mu(R)$ and $\sigma(R)$ the helix radius R was recalculated independently for each track following the relation:

   $$R' = R \cdot \mathcal{N}\Big(1 + \Delta\mu(R),\ \sigma(R)\Big), \tag{8.9}$$

   (b) a new helix of the radius R' was assigned to the track and used to recalculate d_0. The modified helix was obtained by changing the radius of the original helix from R to R' with a fixed middle point between the first and last TPC hit of the global track represented by the helix (Fig. 8.9). The momentum of the track was also recalculated:

   $$p_T' = p_T \cdot \frac{R'}{R}, \qquad \eta' = \eta \cdot \frac{R'}{R}. \tag{8.10}$$

2. In each p_T bin the χ^2/NDF was calculated between the data and MC for d_0 histogram in a range -1.5 cm < d_0 < 1.5 cm (corresponding to d_0 cut used in the physics analysis), for every point in parameter space of radius distortion (for every set of $\Delta\mu(R)$ and $\sigma(R)$). An example (single p_T bin) of map of $-\chi^2$/NDF in a parameter space is presented in Fig 8.11.

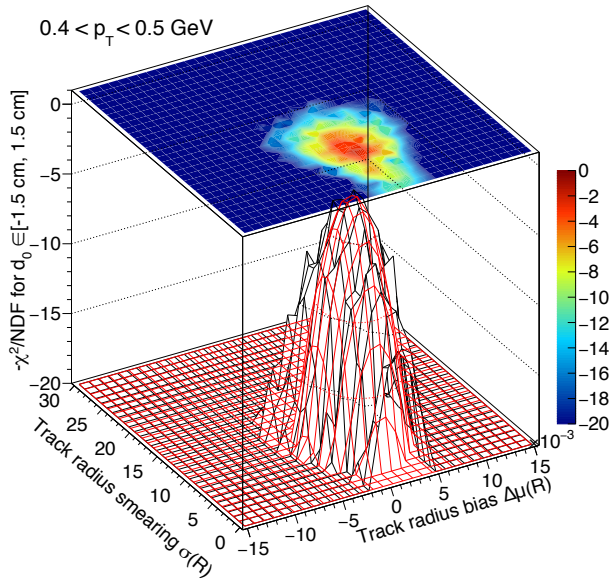

Figure 8.11: Example of $-\chi^2/\mathrm{NDF}$ map in a parameter space in the procedure of TPC pointing resolution adjustment. The red surface represents parabola fitted in the vicinity of the global minimum.

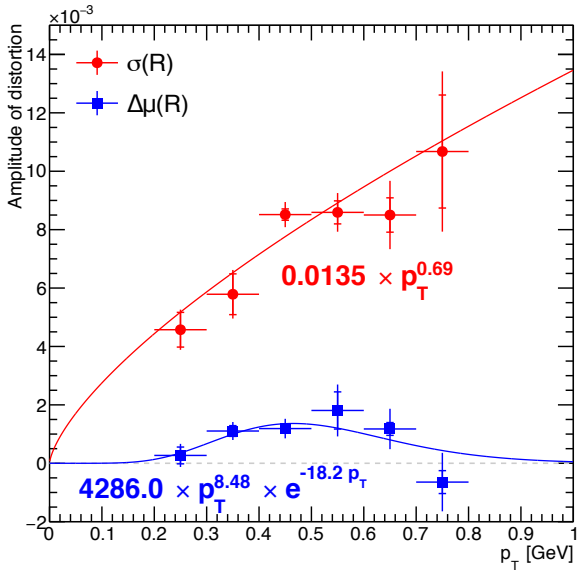

Figure 8.12: Best-fit parameters from the described adjustment procedure. Uncertainties resulting solely from the fit of Eq. (8.11) to $-\chi^2/\mathrm{NDF}$ are represented by the lines with perpendicular endings. Total uncertainties (Eq. (8.12)) extend beyond. The empirical functions fitted to points are drawn with corresponding colours, and formula of each is written aside.

3. In each bin of recalculated p_T the paraboloid $z(x, y;\ a, b, x_0, y_0, z_0)$ given in Eq. (8.11) ($z = \chi^2/\mathrm{NDF},\ x = \Delta\mu(R),\ y = \sigma(R)$) was fitted to $-\chi^2/\mathrm{NDF}$ in the global minimum region to obtain the best-fit distortion parameters.

$$z = z_0 - a(x - x_0)^2 - b(y - y_0)^2. \tag{8.11}$$

4. The best-fit smearing $\sigma(R)$ (corresponding to the paraboloid parameter y_0) and best-fit bias $\Delta\mu(R)$ (corresponding to x_0) from individual p_T bins was plotted as a function of global track p_T (Fig. 8.12). Each point was assigned with an error being a quadratic sum of two components: the error on x_0 (y_0) resulting from the paraboloid fit to $-\chi^2/\mathrm{NDF}$, and length of corresponding semi-axis of ellipsis formed by the intersection of fitted paraboloid with the xy-plane at $z = z_0 - 1/\mathrm{NDF}$ (from definition of the parameter uncertainty given by the change of overall χ^2 by 1 unit). Resultant formulae for the error of each individual point in Fig. 8.12 are

$$\delta\left(\Delta\mu(R)\right) = \sqrt{\delta^2_{\mathrm{fit}}(x_0) + \frac{1}{2a \cdot \mathrm{NDF}}}, \qquad \delta\left(\sigma(R)\right) = \sqrt{\delta^2_{\mathrm{fit}}(y_0) + \frac{1}{2b \cdot \mathrm{NDF}}}. \tag{8.12}$$

From Fig. 8.10 one can read that $\mathrm{NDF} = 14$. In calculation of the uncertainties, a possible correlation between $\Delta\mu(R)$ and $\sigma(R)$ has not been taken into account.

5. The empirically determined functions were fitted to points representing $\Delta\mu(R)$ and $\sigma(R)$ dependence on the global track p_T. Their forms and values of the parameters are given in Fig. 8.12.

Helices of global TPC tracks were deteriorated according to Eq. (8.9) and using the parameterisations of global track p_T-dependence of $\Delta\mu(R)$ and $\sigma(R)$ from Fig. 8.12, to verify if better agreement

between the data and embedded MC is found after the adjustment. Filled histograms in Fig. 8.13 show d_0 and DCA distributions after the described adjustment, and filled circles in the bottom panel show their ratio to the data points. Clearly, there is much better agreement in the transverse pointing resolution between embedded MC and the data after the adjustment (Figs. 8.13a and 8.13b). The longitudinal resolution remains nearly unchanged (Fig. 8.13c). The remaining differences may arise from incomplete theoretical model of the CEP process implemented in GenEx leading to different p_T spectra of the data and the model (e.g. model does not contain resonant $\pi^+\pi^-$ production).

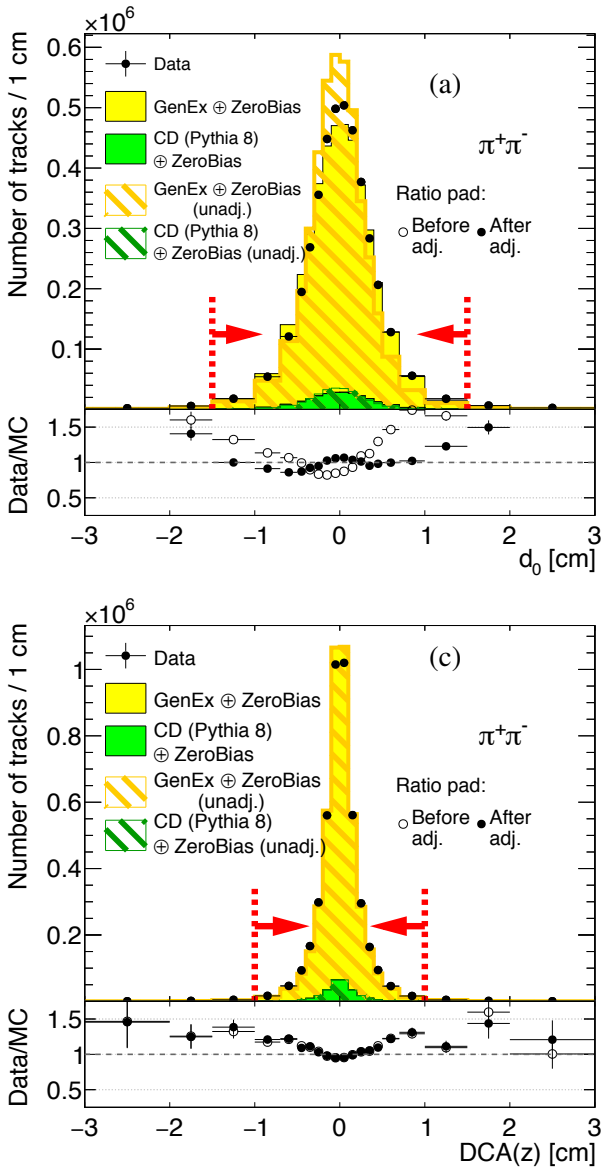

Figure 8.13: Comparisons of distributions of pion (a) transverse impact parameter d_0, and (b) transverse and (c) z-component of the DCA between the global helix and primary vertex in the data (CEP) and embedded MC (GenEx). Distributions for unadjusted helices are drawn as hashed histograms, while filled histograms are for adjusted helices. Normalisations of the signal and backgrounds were established as explained in Sec. 10.3 (MB background was omitted). Red dashed lines and red arrows indicate the range of each quantity which is accepted in analysis.

9. Event selection

In this chapter, the selection cuts used for signal extraction are presented. In Sec. 9.1 a condensed list of cuts is introduced. Detailed description[1] of each cut can be found in Sec. 9.2.

9.1 List of cuts[2]

SC1. Exactly one primary vertex with TPC track(s) matched with hits in TOF is found.

SC2. TPC vertex from SC1 is placed within $|z_{\text{vtx}}| < 80$ cm.

SC3. Exactly two opposite-sign primary TPC tracks (SC3.2) of good quality (SC3.4) matched with hits in TOF (SC3.1) and reconstructed within kinematic region of high TPC acceptance (SC3.3), with associated global tracks characterised by small distance of closest approach to the primary vertex (SC3.5) and high proximity to each other at the beamline (SC3.6).

- **SC3.1**. Exactly two TOF-matched primary tracks.
- **SC3.2**. Tracks are of opposite signs.
- **SC3.3**. Both tracks are contained within the kinematic range: $|\eta| < 0.7, \quad p_{\text{T}} > 0.2$ GeV.
- **SC3.4**. Associated global tracks satisfy quality criteria: $N_{\text{hits}}^{\text{fit}} \geq 25, \quad N_{\text{hits}}^{\text{dE/dx}} \geq 15,$ $|d_0| < 1.5$ cm.
- **SC3.5**. Associated global tracks match well to the prim. vertex: $\text{DCA}(R) < 1.5$ cm, $|\text{DCA}(z)| < 1$ cm.
- **SC3.6**. Associated global tracks are close at the beamline: $|\Delta z_0| < 2$ cm.

SC4. Exactly one RP track on each side of STAR central detector (SC4.3) of good quality (SC4.1), with local angles consistent with the IP being the track origin (SC4.2), lying within fiducial region of high geometrical acceptance (SC4.4).

- **SC4.1**. RP tracks contain only track-points with at least three (out of four) planes used in reconstruction.
- **SC4.2**. Local angles $(\theta_x^{\text{RP}}, \theta_y^{\text{RP}})$ consistent with expectation for protons originating from the IP

$$-2 \text{ mrad} < \theta_x^{\text{RP}} - x^{\text{RP}}/|z^{\text{RP}}| < 4 \text{ mrad}, \qquad -2 \text{ mrad} < \theta_y^{\text{RP}} - y^{\text{RP}}/|z^{\text{RP}}| < 2 \text{ mrad}.$$

- **SC4.3**. Exactly one track passing the cuts SC4.1-SC4.2 on each side side.
- **SC4.4**. Tracks passing cut SC4.3 lie within the fiducial (p_x, p_y) region defined as:

$$0.2 < |p_y| < 0.4, \quad -0.2 < p_x, \quad (p_x + 0.3)^2 + p_y^2 < 0.5^2 \quad \text{(all in GeV)}.$$

[1] For electronic version readers: you can directly move to description of a given cut by clicking on corresponding bold cut number **SCX** at the start of line in the list of cuts.

[2] Some cuts (e.g. SC3) are decomposed to constituent sub-cuts. A cut is formed by the logical AND of all its sub-cuts. Events must pass all cuts to be identified as a signal.

SC5. Vertex z-positions measured in the TPC and reconstructed from the difference of proton detection time in the West and in the East RP stations are consistent with each other within the resolution (at $3.5\sigma(z_{\text{vtx}}^{\text{RP}})$ level):

$$|\Delta z_{\text{vtx}}| = |z_{\text{vtx}}^{\text{RP}} - z_{\text{vtx}}^{\text{TPC}}| < 36 \text{ cm}.$$

SC6. No signal in any tile of BBC-large (East or West) with ADC > ADC_{thr} and 100 < TDC < 2400, where ADC_{thr} is specific for each channel (see Tab. 9.1).

SC7. Maximally three reconstructed TOF clusters $N_{\text{cltrs}}^{\text{TOF}} \leq 3$.

SC8. Particle (pair) identification:

SC8.1. Identification of particle pairs based on dE/dx ($\chi^2 \equiv \chi^2_{dE/dx}$) and m^2_{TOF}:

if $\chi^2(\pi\pi) > 9$ **and** $\chi^2(KK) > 9$ **and** $\chi^2(pp) < 9$ **and** $m^2_{\text{TOF}} > 0.6$ GeV $\rightarrow$ $p\bar{p}$,

elif $\chi^2(\pi\pi) > 9$ **and** $\chi^2(KK) < 9$ **and** $\chi^2(pp) > 9$ **and** $m^2_{\text{TOF}} > 0.15$ GeV $\rightarrow$ K^+K^-,

elif $\chi^2(\pi\pi) < 12$ $\rightarrow$ $\pi^+\pi^-$.

SC8.2. Restricting fiducial cuts on K^+K^- and $p\bar{p}$ (to reduce misidentifications and assure high PID efficiency):

if K^+K^-: $p_{\text{T}} > 0.3$ GeV, $\min(p_{\text{T}}^+, p_{\text{T}}^-) < 0.7$ GeV,

if $p\bar{p}$: $p_{\text{T}} > 0.4$ GeV, $\min(p_{\text{T}}^+, p_{\text{T}}^-) < 1.1$ GeV.

SC9. Missing (total) momentum of TPC tracks and RP tracks $p_{\text{T}}^{\text{miss}} < 75$ MeV.

9.2 Description of cuts

9.2.1 (SC1, SC2) Primary vertex and its z-position

Following the trigger logic introduced in Chap. 7, CEP analysis was aimed to be carried in a clean, pile-up-free environment, therefore cut on primary vertices multiplicity was introduced to reject events with more than one interaction per bunch crossing. Exactly one primary vertex containing TPC tracks matched with hits in TOF was required. Later in the text such events are referred to as a "single TOF vertex" events. Figure 9.1 shows the comparison of the primary vertices multiplicity in all RP_CPT2 triggers and in the embedded MC. The MC is normalised to agree with the data in the number of events in the analysed multiplicity-one bin. The data are not described by the MC, which is expected. All MC events represent the signal, while the data have many background events included before any signal selection cuts are applied. One can notice significant excess of the multiplicity-zero events in the data over the MC predictions, potentially from the triggers initiated by the noise signals in the TOF system in coincidence with the elastic scattering events.

A single TOF vertex was required to be placed within the range (−80 cm, 80 cm) along the z-axis (Fig. 9.2). Events with vertices away from the nominal IP have low acceptance both for the central tracks and for the forward-scattered protons (comparing to events with vertices close to the nominal IP). Their inclusion to analysis would naturally introduce large systematic uncertainties.

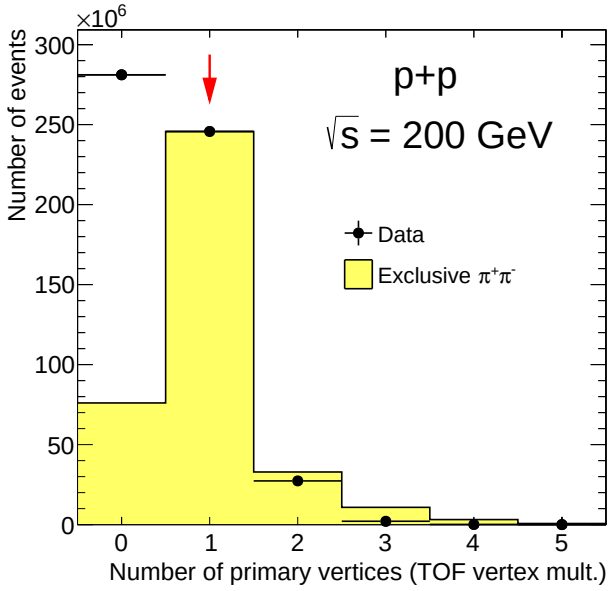

Figure 9.1: Primary vertex multiplicity. Red arrow marks bin with events with exactly one primary vertex (with track(s) matched with hit(s) in TOF), which are used in the analysis. Expectations from embedded $\pi^+\pi^-$ signal MC (normalised to the content of the single TOF vertex bin) has also been shown.

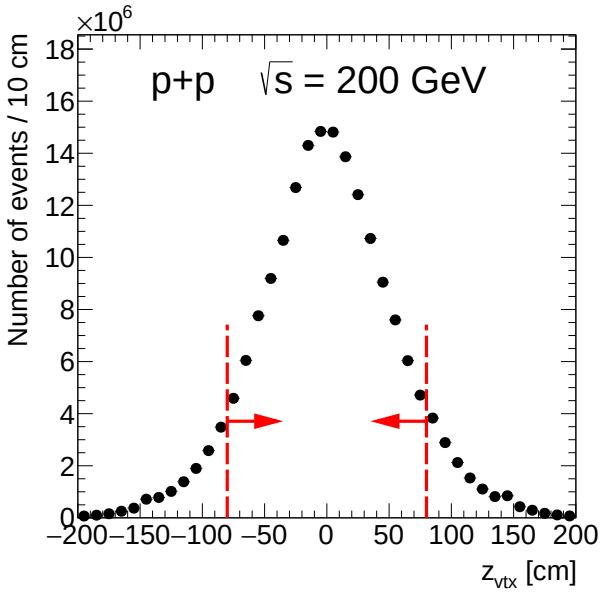

Figure 9.2: z-position of the primary vertex in single TOF vertex events (passing cut SC1). Red dashed line indicate range of longitudinal vertex position accepted in analysis.

In Fig 9.3, comparison between data and MC distributions for the z-position of the single TOF vertex is shown. The ratio of the distributions which is compatible with unity indicates proper position, width and shape of the vertex distribution assumed in the MC generation (a Gaussian distribution with mean at zero and width $\sigma(z_{\text{vtx}}) = 52$ cm).

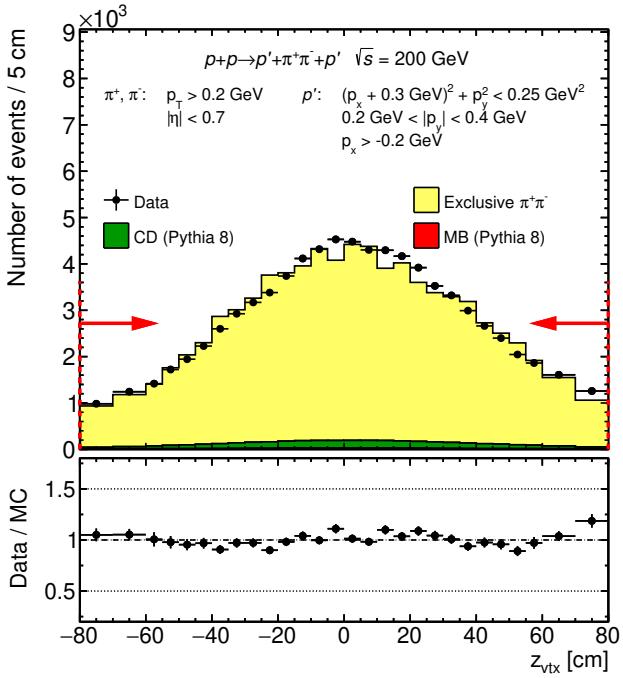

Figure 9.3: Comparison of z_{vtx} distribution between data and embedded MC after full selection. Data are represented by black points, while stacked MC predictions are drawn as histograms of different colours. Histogram from each MC process has been normalised according to prescription in Sec. 10.3. Vertical error bars represent statistical uncertainties, horizontal bars represent bin sizes. Comparison is shown only for the z-vertex range corresponding to offline selection cut SC2 due to limited vertex range used in MC generation to increase a generation efficiency.

9.2.2 (SC3) TPC tracks

To reconstruct the central state, exactly two opposite-sign primary TPC tracks matched with hit in TOF were required. Matching with TOF guaranteed that analysed tracks originate from the triggered bunch crossing (ensured that tracks were ”in-time“). It is in accordance with the trigger logic which required at least two L0 TOF hits, as well as it enables more accurate particle identification with merged time-of-flight and dE/dx method, comparing to sole usage of dE/dx. Primary tracks not matched with a hit in TOF, whose average multiplicity in single TOF vertex is ∼8, are hardly distinguished between real and fake (off-time) tracks, which is an additional reason for not analysing events with only one TOF-matched primary TPC track (the other track might be unmatched due to TOF inefficiency).

Figure 9.4 shows the multiplicity of primary tracks matched with a hit in TOF in the single TOF vertex events. In addition to data, also the embedded signal MC is shown, scaled to agree in the number of events with exactly two TOF-matched TPC tracks in data. An excess of events with more than two TOF tracks in data compared to embedded signal MC is a direct consequence of the significant contribution from the background processes with only cuts SC1 and SC2 applied.

Cuts on the quantities reflecting quality of reconstructed TPC tracks were also applied. Limits were imposed on the number of hits used in TPC track reconstruction ($N_{\text{hits}}^{\text{fit}} \geq 25$) and the number of hits used in specific energy loss reconstruction ($N_{\text{hits}}^{\text{dE/dx}} \geq 15$), in order to achieve good momentum and dE/dx resolution. Distributions of aforementioned quantities together with spectrum of fraction of number of hits potentially generated by the track and finally used in the reconstruction, $N_{\text{hits}}^{\text{fit}}/N_{\text{hits}}^{\text{poss}}$, are shown in Fig. 9.5. One can see, that embedded MC simulation describes the data well.

In addition to this, helices of global tracks associated with selected primary TOF tracks were required to point well to the primary vertex (DCA(R) < 1.5 cm and |DCA(z)| < 1 cm). Longitudinal separation of helices at the beamline, Δz_0, was restricted to $|\Delta z_0| < 2$ cm, which coincides with the cut

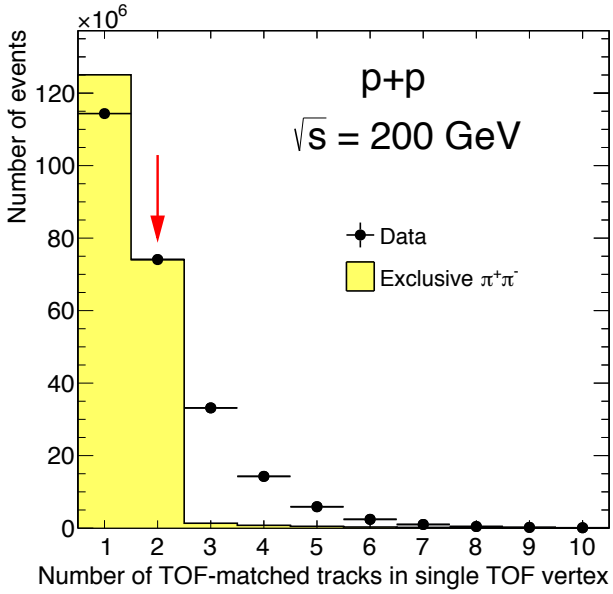

Figure 9.4: Multiplicity of primary TPC tracks matched with a hit in TOF for the single TOF vertex events. Red arrow marks bin with events with exactly two primary tracks matched with a hit in TOF, which are used in the analysis. Expectation from embedded $\pi^+\pi^-$ signal MC (normalised to the content of the bin representing two TOF tracks) has also been shown.

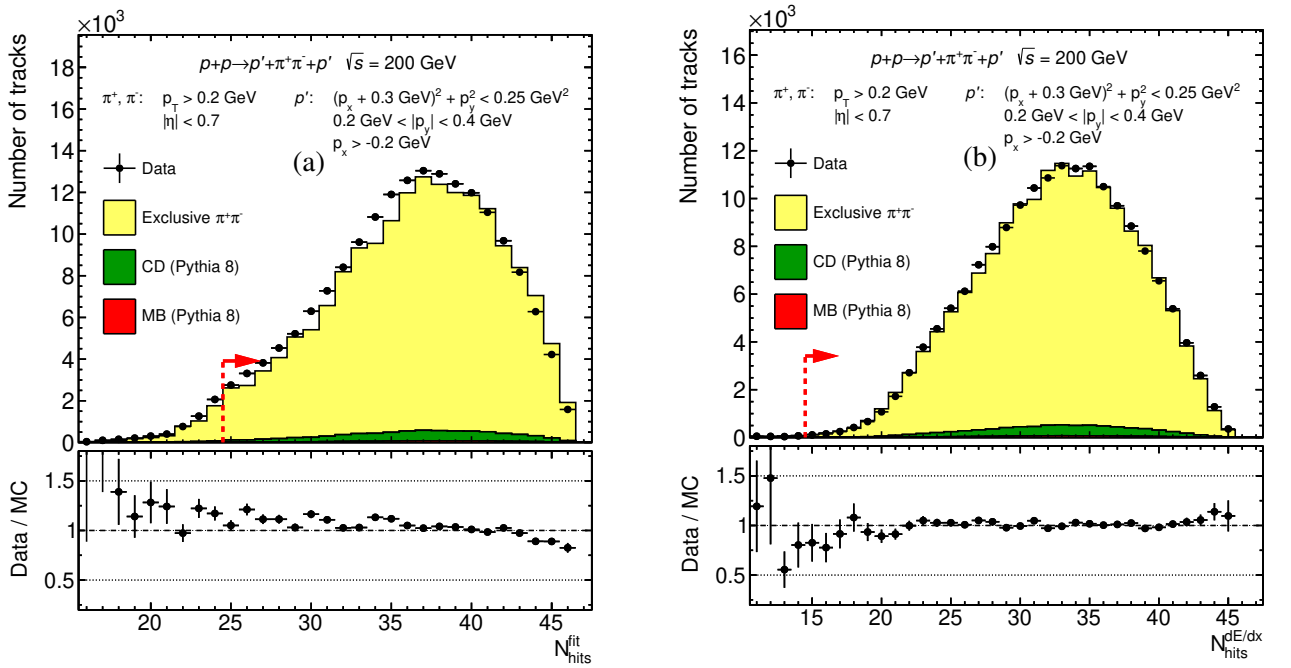

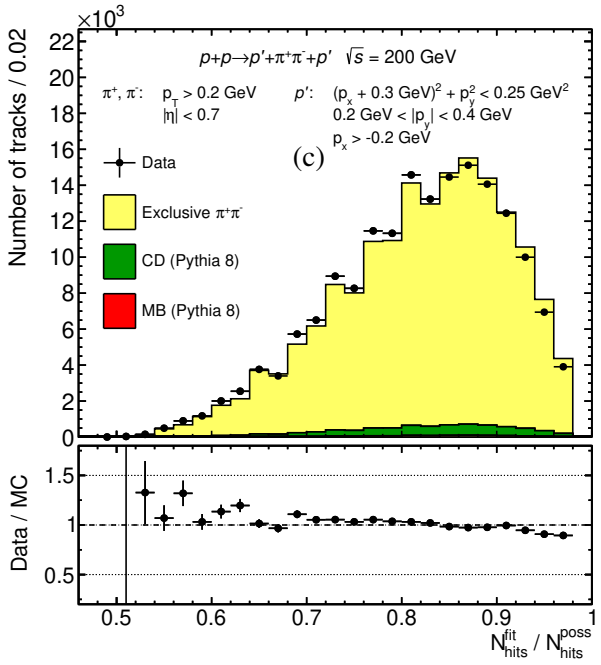

Figure 9.5: Comparison of (a) the number of hits used in TPC track reconstruction $N_{\text{hits}}^{\text{fit}}$, (b) the number of hits used in specific energy loss reconstruction $N_{\text{hits}}^{\text{dE/dx}}$ and (c) the fraction of the number of hits potentially generated by a track and finally used in the reconstruction $N_{\text{hits}}^{\text{fit}}/N_{\text{hits}}^{\text{poss}}$ in the data (black points) and embedded MC (stacked colour histograms). Normalisations of the signal and backgrounds were established according to description in Sec. 10.3. Predictions for MCs other than GenEx (yellow) were replaced by predictions for GenEx scaled to have the same integrals as replaced histograms - this was driven by the fact that only GenEx was embedded into zero-bias TPC data, which is required to describe the shape of distributions of presented quantities. Vertical error bars represent statistical uncertainties, horizontal bars represent bin sizes. Red dashed lines and red arrows indicate the range of each quantity, which is accepted in the analysis.

on |DCA(z)|. Distributions of these quantities together with comparison to embedded MC are shown in Fig. 8.13.

Tracks were finally required to have p_{T} and η within the fiducial range of high geometrical acceptance and efficiency, $p_{\text{T}} > 0.2$ GeV and $|\eta| < 0.7$. Figure 9.6 shows the comparison of the track pseudorapidity and azimuthal angle between data and embedded MC. These distributions are quite well described by MC. Large modulation in the ϕ distribution (enhancement at $\phi = \pm\pi/2$) is related to the geometrical acceptance of RPs mounted above and below the beamline - central particles' pair is always back-to-back in azimuth with respect to pair of forward-scattered protons, therefore pairs produced in "up" or "down" direction are preferred.

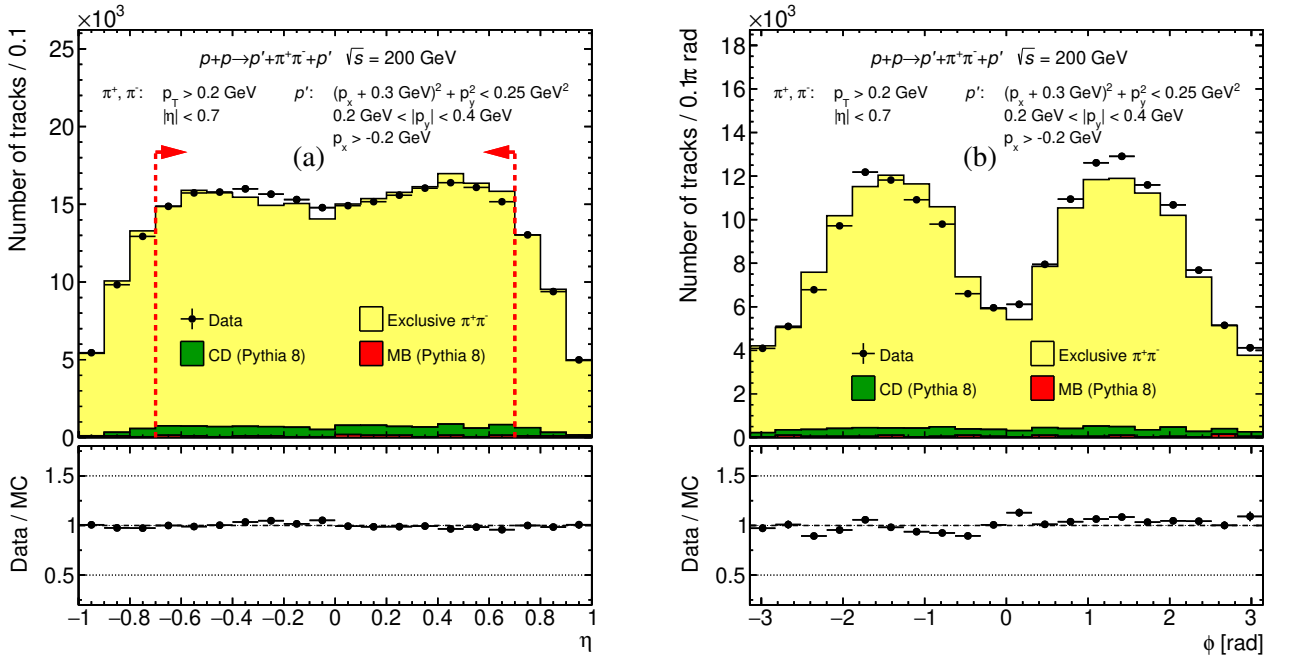

Figure 9.6: Comparison of (a) the track pseudorapidity and (b) the track azimuthal angle between the data (black points) and embedded MC (stacked colour histograms). Normalisations of the signal and backgrounds were established according to description in Sec. 10.3. Vertical error bars represent statistical uncertainties, horizontal bars represent bin sizes. Red dashed lines and red arrows indicate the range of the pseudorapidity interval accepted in the analysis.

9.2.3 (SC4) RP tracks

Forward proton tracks were selected in the following way. First, all RP tracks which contained track points that had been formed of less than three hits out of maximally four possible (one hit per silicon plane), were rejected. This is natural consequence of the very high single plane efficiency > 99.5%, and prevents including in the analysis tracks with track points formed from unmatched pairs of clusters in both x- and y-coordinate (e.g. from electronics noise).

Next, preselected tracks were verified for consistency of their local angles with the hypothesis on their origin from the STAR IP. Using Geant4 simulation of the RP system, the impact of the apertures limiting RP acceptance for the forward-scattered protons generated at the STAR IR, was tested. The result is shown in Fig. 9.7, where density maps of reconstructed RP track local angle θ^{RP} and corresponding track coordinate in RP station are drawn (only branch WU is shown as the picture is similar in the case of other branches). Only RP tracks matched with generated primary forward protons were used to fill the histograms. Clear bands of primary proton tracks can be distinguished in the top plots (Figs. 9.7a and 9.7b), with some very small number of tracks significantly scattered on the beam pipe, DX magnet and the detector dead material. One-dimensional representation of the correlation between local angle and position can be obtained by constructing quantities

$$\widetilde{\Delta}\theta_x^{RP} = \theta_x^{\mathrm{RP}} - x^{\mathrm{RP}}/|z^{\mathrm{RP}}|, \qquad \widetilde{\Delta}\theta_y^{RP} = \theta_y^{\mathrm{RP}} - y^{\mathrm{RP}}/|z^{\mathrm{RP}}|, \tag{9.1}$$

which reflect deviations of reconstructed local angle from expectation for forward proton with the beam momentum, and whose distributions are presented in Fig. 9.7c and Fig. 9.7d, respectively. On these one-dimensional histograms one can clearly see peaks from the true primary tracks. The optimal

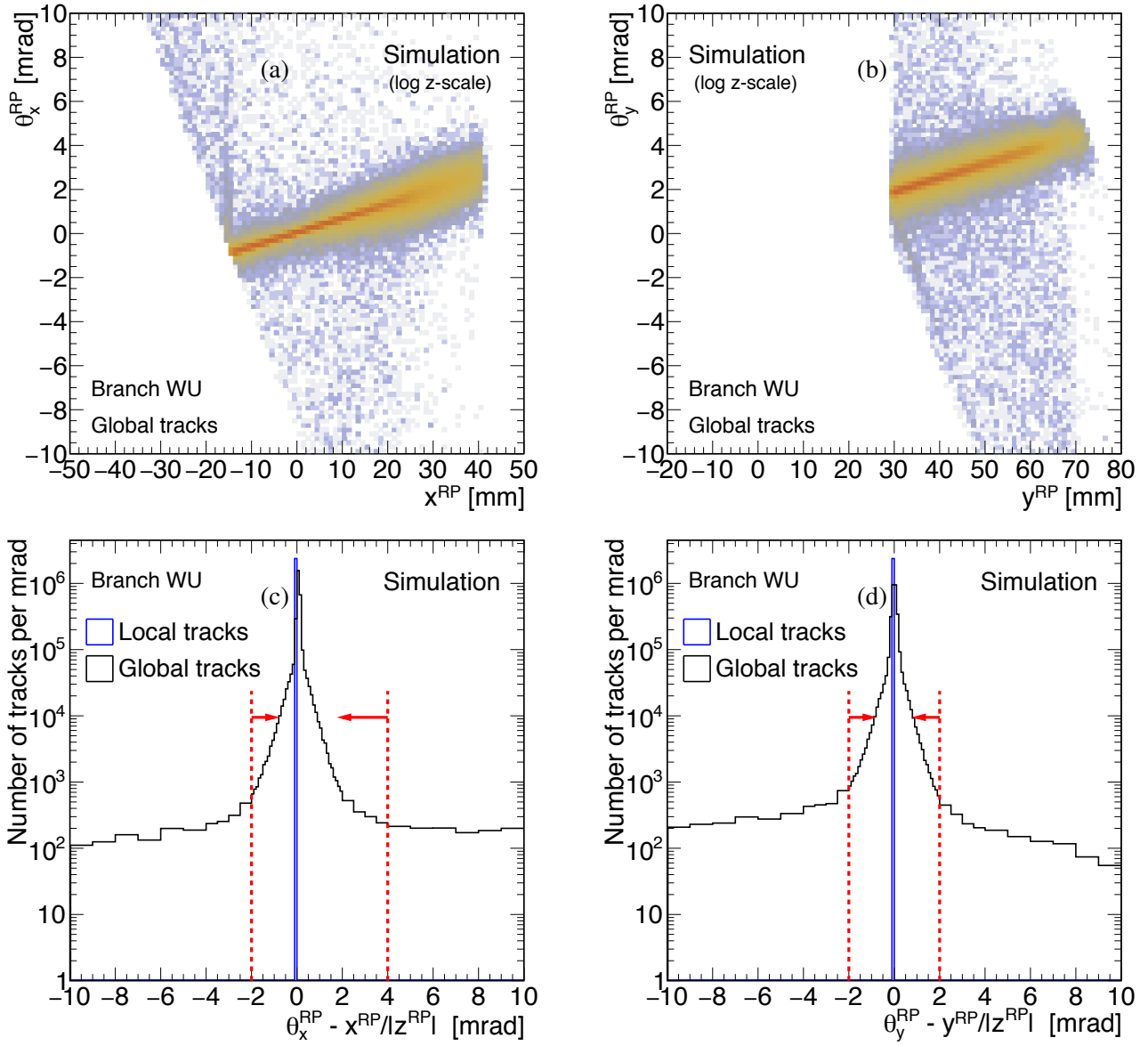

Figure 9.7: Typical correlation between local angle (vertical axis) and position (horizontal axis) of RP tracks matched with true level primary protons for (a) x- and (b) y-coordinate, here shown for branch WU. The same events are contained in plots (c) and (d) for x- and y-coordinate respectively, where difference between reconstructed local angle and local angle expected from the elastic track is histogrammed. Red lines and arrows visualise cuts imposed on RP tracks for final selection (cuts SC4.2).

restriction for $\widetilde{\Delta}\theta_x^{RP}$ was defined from -2 mrad to 4 mrad, and for $\widetilde{\Delta}\theta_y^{RP}$ from -2 mrad to 2 mrad. The intention of more inclusive upper cut on $\widetilde{\Delta}\theta_x^{RP}$ equal to 4 mrad was to preserve tracks of protons with very large ξ, whose local angle highly deviates from that of elastically scattered protons (DX magnets bends more protons with lower momentum) and which might have been underpopulated in MC (GenEx predictions were used). The blue spikes at zero in Figs. 9.7c and 9.7d represent local tracks (formed of single track points). These tracks were reconstructed assuming their momentum being equal to the beam momentum (angle at vertex equal to angle at RP station), therefore $\widetilde{\Delta}\theta_x^{RP}$ and $\widetilde{\Delta}\theta_y^{RP}$ is zero by definition. Once the above selection was applied, exactly one RP track on each side of STAR passing the selection, was required. In addition to this, only events with the RP tracks contained within the

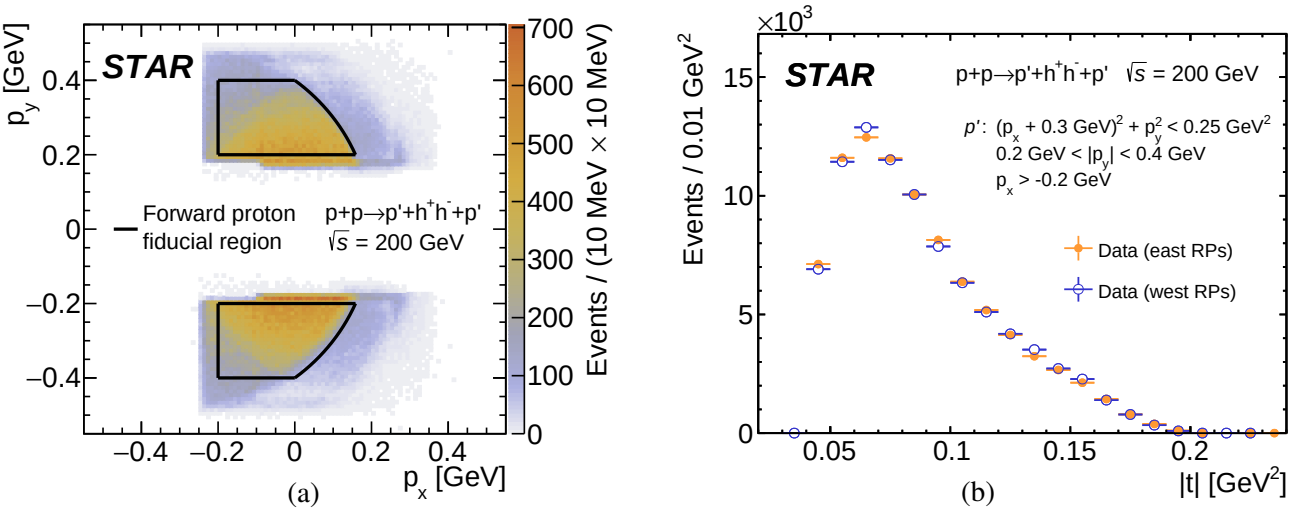

Figure 9.8: (a) Merged distributions of diffractively scattered protons momenta p_y vs. p_x in exclusive h^+h^- events reconstructed with the East and West RP stations, are shown together with the kinematic region used in the measurement marked with the black line. (b) Distributions of measured squared four momenta transfers at the proton vertices for exclusive h^+h^- events with all particles in the fiducial phase space are shown for East and West stations with yellow and blue colour, respectively.

(p_x, p_y) envelope, defined as

$$0.2 < |p_y| < 0.4, \quad -0.2 < p_x, \quad (p_x + 0.3)^2 + p_y^2 < 0.5^2 \quad \text{(all in GeV)}, \tag{9.2}$$

were accepted. This fiducial area is drawn with black solid line on top of the (p_x, p_y) distribution of all measured CEP candidates (Fig. 9.8a). It was chosen to compromise signal statistics and systematic uncertainties of the RP-related efficiencies. The distribution of t variable for tracks enclosed with the envelope given by Eq. (9.2), is shown in Fig. 9.8b.

In the remaining part of the section, comparisons of the track points position distributions between the data and embedded MC are shown. In Fig. 9.9 side-by-side comparisons of two-dimensional hit maps from the data and embedded MC are presented. Figures 9.10 and 9.11 show the same comparisons, but between their x- and y-projections for each RP separately. One can see, that simulation generally describes data well, both in terms of shapes (which is mainly sensitive to detector alignment and geometry/apertures) and track points normalisations in various RPs (which is mainly sensitive to reconstruction efficiency).

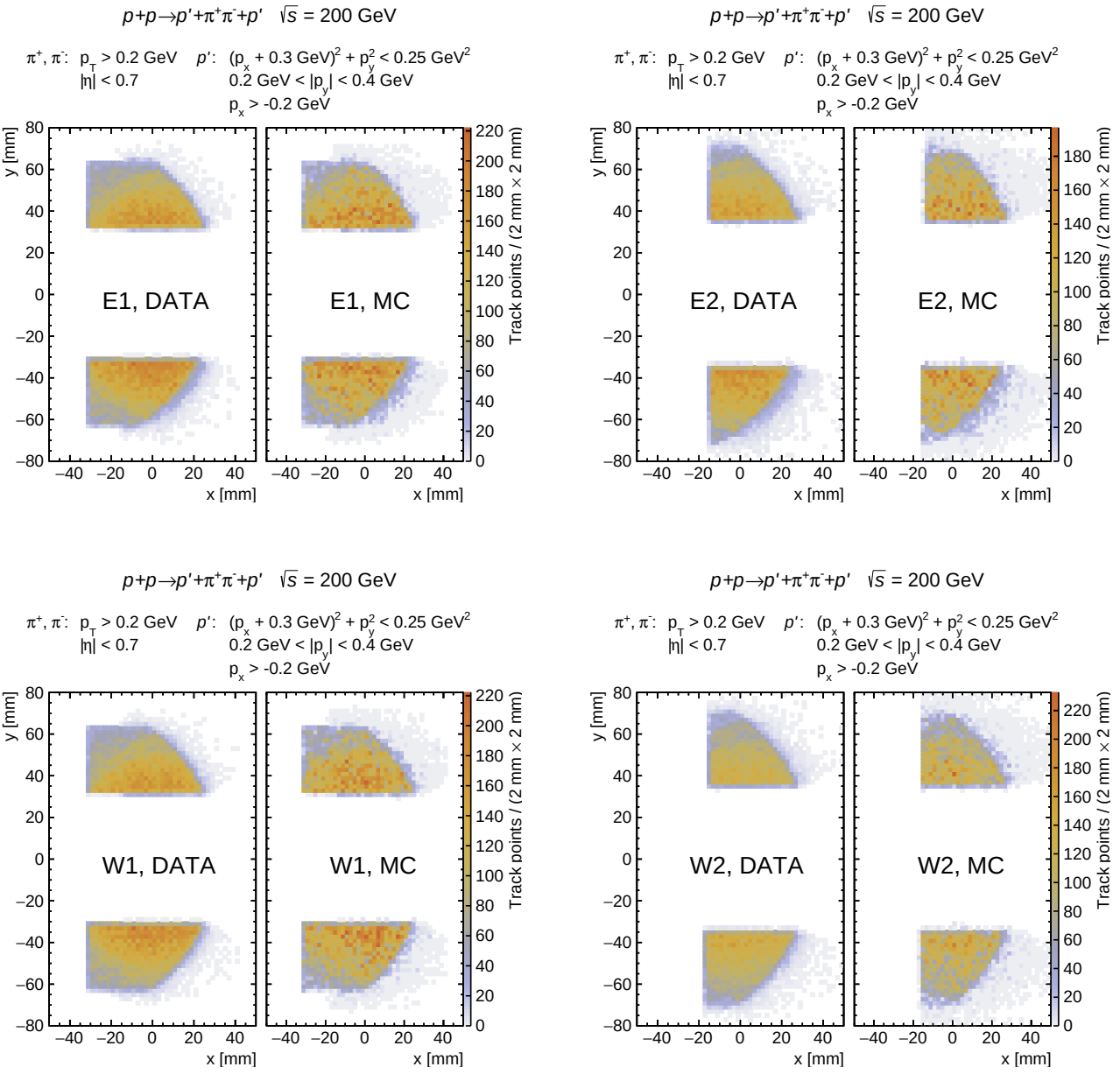

Figure 9.9: Comparison of two-dimensional track points' density maps in the data (left panels) and stacked embedded MC (right panels). Each subfigure corresponds to a single RP station with positions of the track points measured in the upper and in the lower RP detectors, respectively. Normalisations of the signal and backgrounds were established according to description in Sec. 10.3.

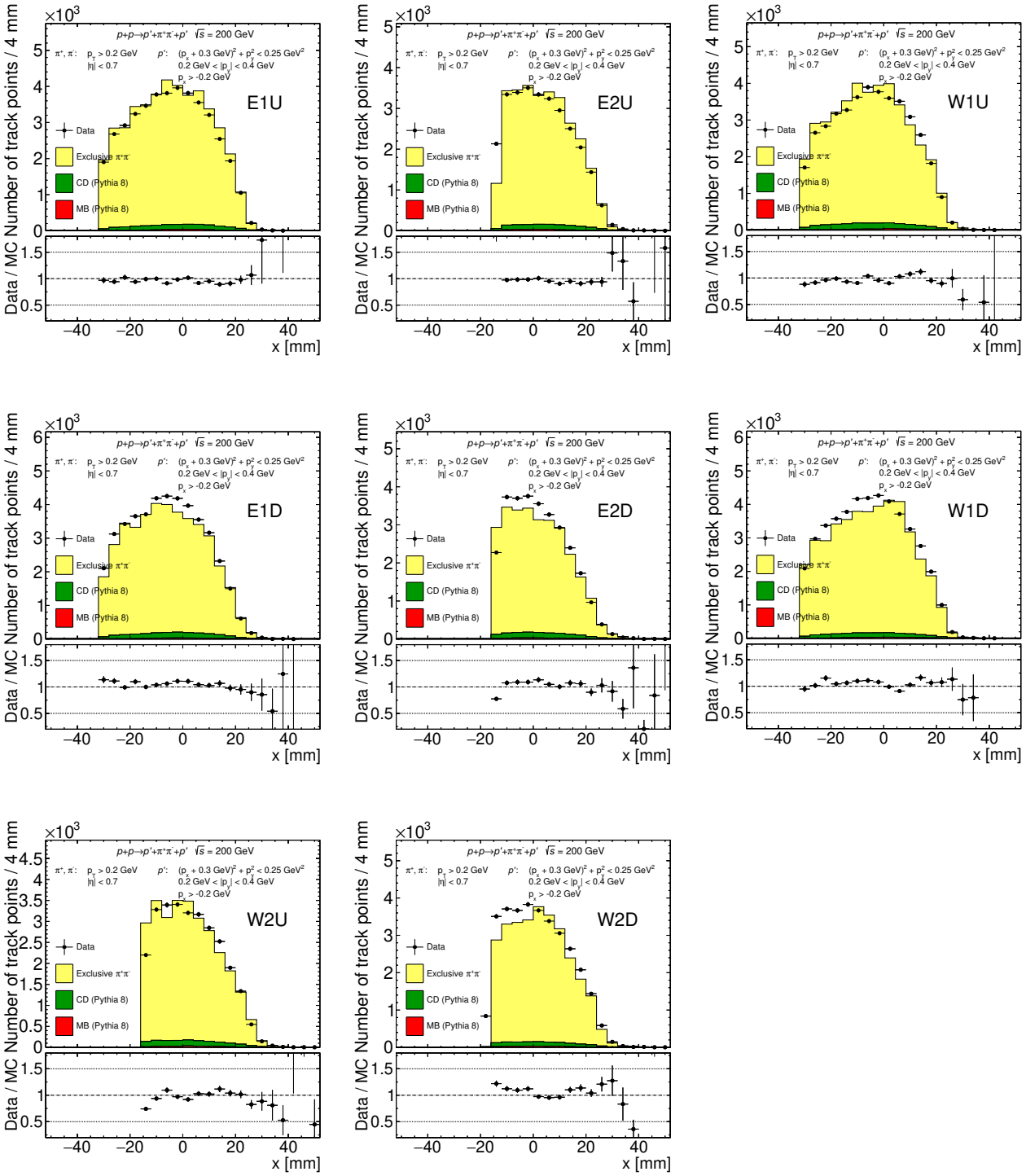

Figure 9.10: Comparison of x-position of track points between the data (black points) and embedded MC (stacked colour histograms). Each subfigure corresponds to the single RP station, whose name is printed in the plots. Vertical error bars represent statistical uncertainties, horizontal bars represent bin sizes. Normalisations of the signal and backgrounds were established according to description in Sec. 10.3.

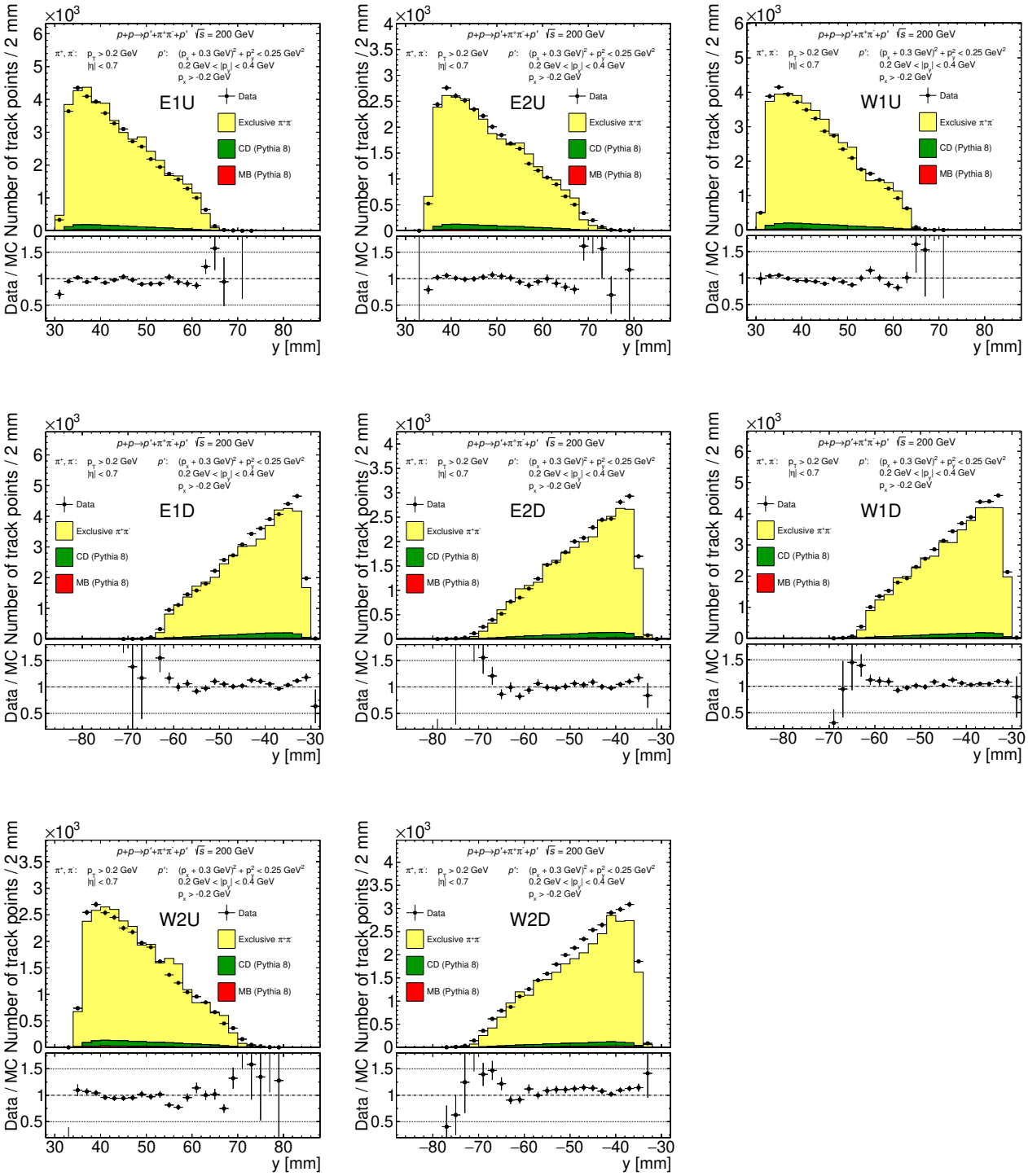

Figure 9.11: Comparison of y-position of track points between the data (black points) and embedded MC (stacked colour histograms). Each subfigure corresponds to the single RP station, whose name is printed in the plots. Vertical error bars represent statistical uncertainties, horizontal bars represent bin sizes. Normalisations of the signal and backgrounds were established according to description in Sec. 10.3.

9.2.4 (SC5) TPC-RP z-vertex matching

In CEP, tracks in the central detector and tracks in Roman Pots originate from the same interaction vertex. Measurement of the time of detection of the forward-scattered protons in RPs gives access to reconstruction of the position of the vertex

$$z_{\mathrm{vtx}}^{\mathrm{RP}} = c \cdot \frac{t_{\mathrm{W}}^{\mathrm{RP}} - t_{\mathrm{E}}^{\mathrm{RP}}}{2} \tag{9.3}$$

independently from using TPC tracks, which allows their comparison and additional rejection of the background if the two values disagree. Time of detection of proton in RP is an average of all TAC values from PMTs in RPs used to form a track, corrected for the slewing effect [146] and transformed to unit of time (all these steps are done at the level of raw data reconstruction). In Fig. 9.12 the comparisons of the $z_{\mathrm{vtx}}^{\mathrm{RP}}$ and $z_{\mathrm{vtx}}^{\mathrm{TPC}}$ are shown with some preselection cuts applied. A clear signal from the CD events (hence also CEP events) is manifesting in high correlation of the two values (diagonal in Fig. 9.12a) or a relatively narrow peak centred at zero for the difference of the two values (Fig. 9.12b).

The sum of two Gaussian distributions was fitted to data in Fig. 9.12b yielding good description of the distribution of $\Delta z_{\mathrm{vtx}} = z_{\mathrm{vtx}}^{\mathrm{RP}} - z_{\mathrm{vtx}}^{\mathrm{TPC}}$ with the width parameters $\sigma_1 = 10.3$ cm (CD signal) and $\sigma_2 = 73.9$ cm (pile-up). The first parameter reflects the time resolution of RPs (resolution of the $z_{\mathrm{vtx}}^{\mathrm{RP}}$ measurement, $\sigma(z_{\mathrm{vtx}}^{\mathrm{RP}})$), as the TPC resolution is much better (~ 1 cm). Value of the second parameter, consistent with $\sqrt{2}\sigma(z_{\mathrm{vtx}}) \approx \sqrt{2} \cdot 52$ cm ≈ 73.5 cm, confirms that the wide distribution under the narrow signal peak is uncorrelated background, in other words forward protons originating from a different vertex than the central tracks. To reject this background without significant loss of the signal, the $3.5\sigma(z_{\mathrm{vtx}}^{\mathrm{RP}})$ cut was introduced on Δz_{vtx} ($|\Delta z_{\mathrm{vtx}}| < 36$ cm).

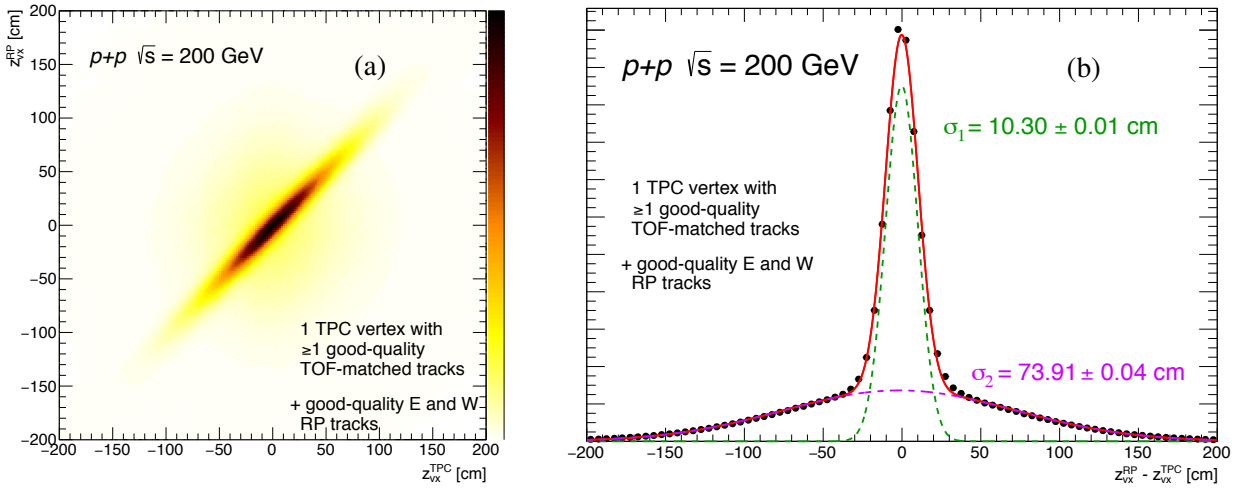

Figure 9.12: (a) Correlation and (b) difference of z-vertex positions measured in Roman Pots and TPC in RP_CPT2 triggers, after preselection described in the plots.

9.2.5 (SC6) BBC-large signal veto

At the trigger level a veto on signal in BBC-small detectors is used. During offline analysis it was found that the non-exclusive background can be reduced if an additional veto on signal in BBC-large detectors is added. It is connected with the fact, that vast majority of selected RP_CPT2 triggers were

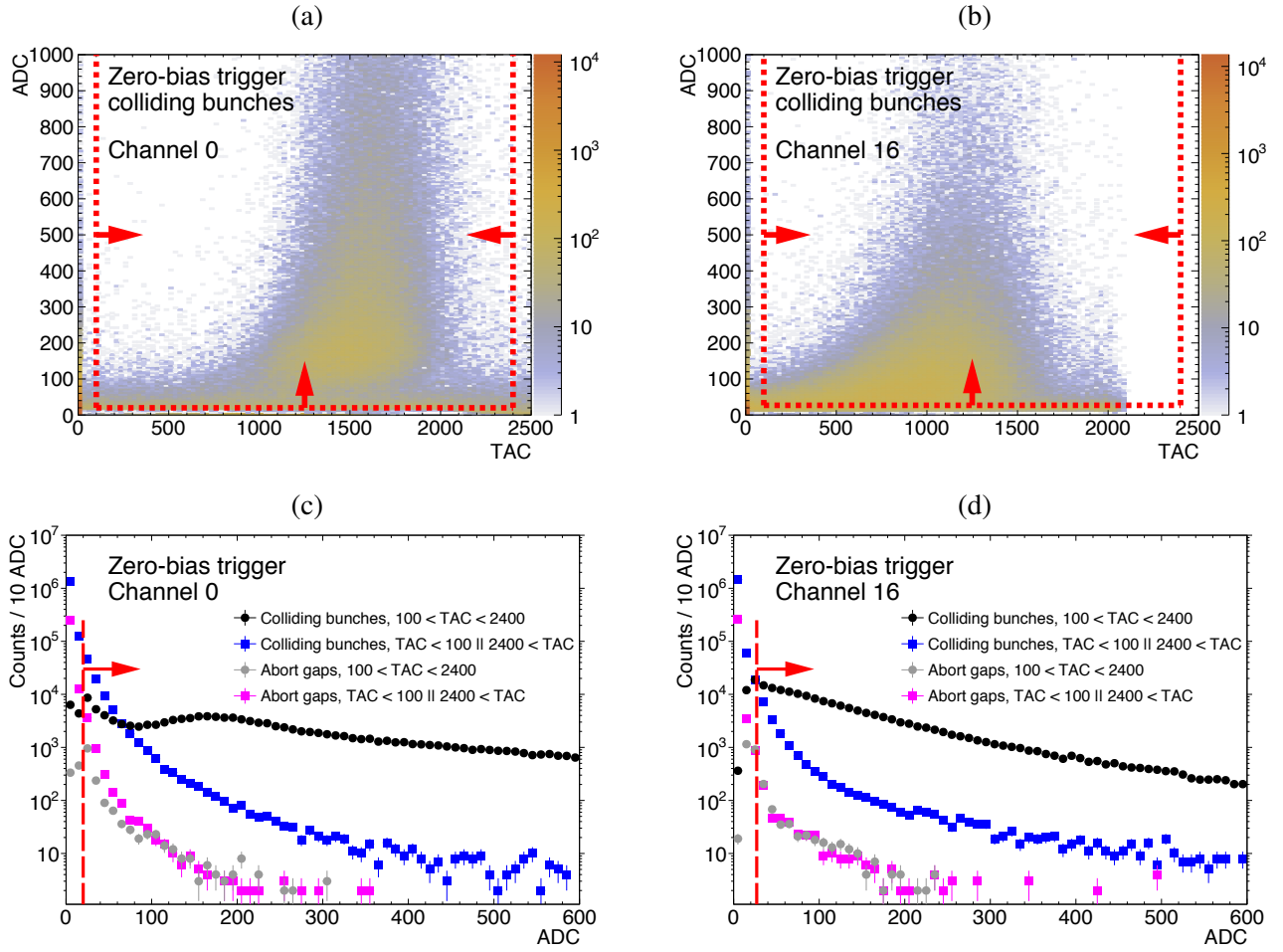

Figure 9.13: Sample BBC-small (left column) and BBC-large (right column) response in zero-bias data. Top row shows ADC vs. TAC distributions, while bottom row shows projection of the corresponding two-dimensional distribution on the y-axis (ADC) in the TAC range quoted in the legend, for both abort gaps and colliding bunches. Red lines and arrows indicate thresholds for a signal in presented channels.

from the CD process, into which the CEP belongs. Many of CD events have particles produced in the rapidity region outside of the TPC and TOF acceptance, some hitting the BBC-large tiles. Presence of signal in BBC-large is therefore a signature of non-exclusive background or a pile-up interaction.

The response of BBC-large tiles is different from that of BBC-small tiles, as shown in sample plots in Fig. 9.13. Typically, in BBC-small tiles, a peak is visible in ADC distribution around 150 – 200 (Figs. 9.13a and 9.13c), which is a signature of a good separation of the electronics noise and signal from the ionising particle. No such feature is observed in corresponding distributions for the BBC-large tiles (Figs. 9.13b and 9.13d), which can be explained by the difference in geometry (in size) of small and large tiles. In BBC-large tiles the path that scintillation light must travel to reach PMT is much longer in comparison to BBC-small tiles (multiple reflections on the main tile surface due to small thickness of the tile) therefore light signal is highly attenuated and extended in time. This is a possible reason for the lack of signal peak in the ADC distribution in BBC-large tile spectrum (Fig. 9.13d), as well as the late-TAC (TAC$\lesssim$ 600, ADC$<$ 100) tail in the ADC vs. TAC spectrum (slewing effect, Fig. 9.13b). Nevertheless, the above features of BBC-large response do not disqualify this detector from being used to veto, as in such case lower detection efficiency only reduces the background

rejection power.

Each channel of the BBC-large has different response to signal from ionising particle, as well as different level of noise. It was decided to set up a signal threshold for each channel based on the study of the noise in abort gaps (in zero-bias data). This noise, in principle, should be solely the electronics noise, but possible is also some signal from the off-time pile-up (from preceding bunch crossings). For each channel, the probability to detect a signal with ADC above certain threshold and with TAC contained within 100 to 2400 interval (the same window is default for BBC-small) was calculated. The result is shown in Fig. 9.14. Final ADC thresholds in each BBC-large channel were established by requiring that the noise in BBC-large would cause a veto in maximally 3.5% of events. This value was chosen, because it was consistent with an average ADC threshold of 40, which was found to be optimal in terms of efficiency and sample purity in the preliminary studies, as well as it was acceptably low. To transform it to $\mathrm{ADC}_{\mathrm{thr}}$ it was first assumed that the noise is uncorrelated between the channels. With this assumption one can relate the probability of the veto in whole BBC-large detector (East and West) caused by noise, $\mathcal{P}^{\mathrm{noise}}_{\mathrm{veto}}$, to the probability of the signal induced by noise in single BBC-large channel, $\mathcal{P}^{\mathrm{noise}}_{i,\mathrm{sig}}$, as:

$$\mathcal{P}^{\mathrm{noise}}_{\mathrm{veto}} = 1 - \mathcal{P}^{\mathrm{noise}}_{!\mathrm{veto}} = 1 - \left(1 - \mathcal{P}^{\mathrm{noise}}_{i,\mathrm{sig}}\right)^{N^{\mathrm{BBC}}_{\mathrm{ch}}} . \tag{9.4}$$

In the equation above $N^{\mathrm{BBC}}_{\mathrm{ch}}$ denotes the number of active channels in BBC-large. There were 14 active channels in BBC-large (2 dead channels were found on the West side). Transformation of Eq. 9.4 to the form presented below gives the threshold probability for a single BBC-large channel:

$$\mathcal{P}^{\mathrm{noise}}_{i,\mathrm{sig}} = 1 - \sqrt[N^{\mathrm{BBC}}_{\mathrm{ch}}]{1 - \mathcal{P}^{\mathrm{noise}}_{\mathrm{veto}}} = 1 - \sqrt[14]{1 - 0.035} \approx 0.0025. \tag{9.5}$$

In the last step, this number was translated to the ADC threshold for each channel of BBC-large. For

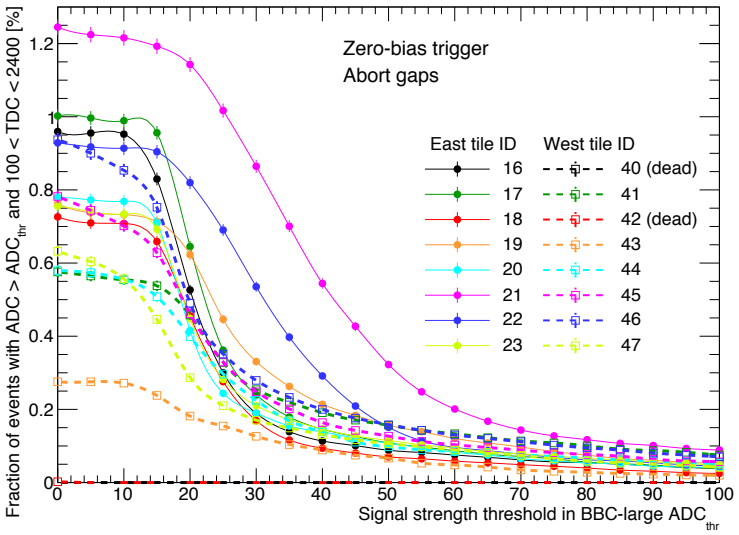

Figure 9.14: Percentage of events in abort gaps from zero-bias triggers with the ADC counts larger than the ADC threshold given in the x-axis, for each BBC-large channel. Measured points with statistical uncertainties are connected with a line of corresponding colour for better visualisation.

East		West	
i	$\mathrm{ADC}_{\mathrm{thr}}$	i	$\mathrm{ADC}_{\mathrm{thr}}$
16	27	40	(dead)
17	30	41	31
18	26	42	(dead)
19	37	43	14
20	25	44	29
21	55	45	30
22	43	46	33
23	27	47	22

Table 9.1: Offline ADC thresholds in BBC-large.

this purpose Fig. 9.14 was used. The x-axis projection of the crossing point of each colour line with the y-axis value of 0.0025 defines $\mathrm{ADC}_{\mathrm{thr}}$ for each particular channel. These numbers are listed in Tab. 9.1. An event was rejected from analysis if any of the BBC-large channels registered signal above threshold, $\mathrm{ADC}_i > \mathrm{ADC}_{i,\mathrm{thr}}$, and $100 < \mathrm{TAC}_i < 2400$.

9.2.6 (SC7) TOF clusters limit

The TOF system in CEP analysis was mainly used to distinguish real TPC tracks from the off-time fake tracks, as well as to help with the PID. However, it was also used to reject non-CEP events in which the TPC tracks were not reconstructed or were not successfully matched with a TOF hit. For this purpose, a concept of a TOF cluster is defined as the group of TOF hits, which are close in space and time:

$$R < 0.1 \quad \text{and} \quad \Delta t < 1.5 \text{ ns}. \tag{9.6}$$

The distance R in (ϕ, η) space between two TOF cells with detected hits is defined as

$$R = \sqrt{(\eta_{\mathrm{hit},1} - \eta_{\mathrm{hit},2})^2 + (\phi_{\mathrm{hit},1} - \phi_{\mathrm{hit},2})^2}, \tag{9.7}$$

and the time difference is given by

$$\Delta t = |t_{\mathrm{hit},1} - t_{\mathrm{hit},2}|. \tag{9.8}$$

Single TOF cluster was formed from the group of hits among which there was at least one pair of hits satisfying Ineqs. (9.6). Such clusters of TOF hits are expected to be induced by a single primary particles, possibly associated with the secondary particles (e.g. delta rays). The most important assumption is that a single particle does not produce two or more clusters.

Distributions of R and Δt are presented in Fig. 9.15. From these pictures one can find justification for the limits used in Ineqs. (9.6). Clear enhancement is visible at $R < 0.1$ and $\Delta t < 1.5$ ns, which

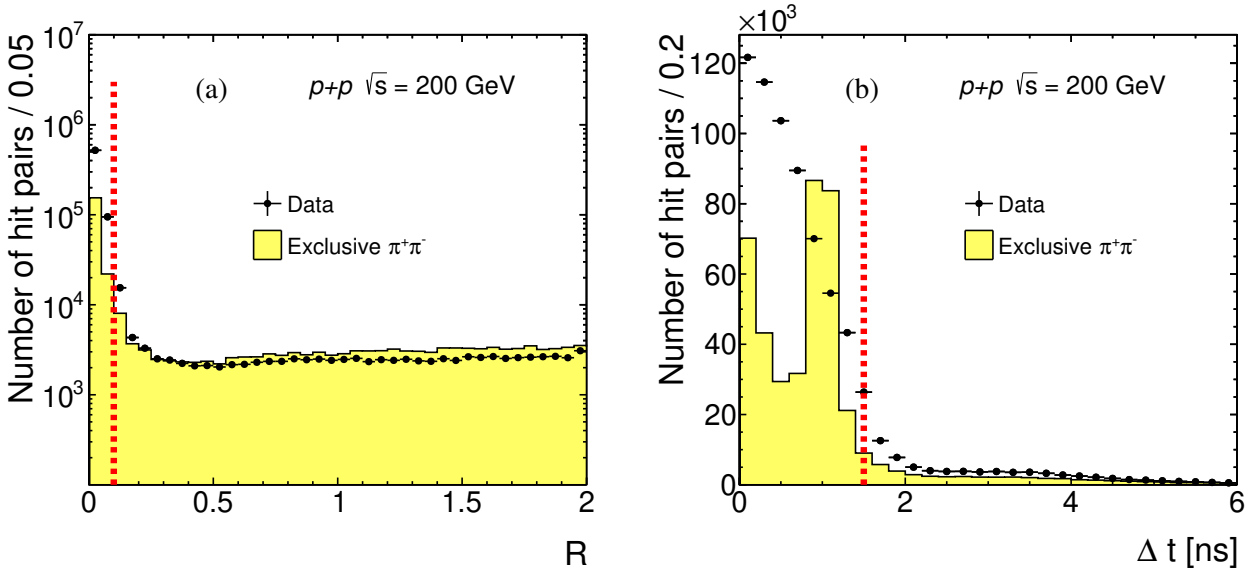

Figure 9.15: Distributions of (a) space and (b) time distance between TOF hits in the clustering procedure. Each of distributions contains entries from hit pairs satisfying matching requirement imposed on the other quantity (the overflow bins are not shown). Data are shown as black points with vertical error bars representing statistical uncertainties and horizontal bars representing bin sizes. Expectations from embedded $\pi^+\pi^-$ signal MC, normalised to the same integrals at $R > 0.5$ (a) or at $\Delta t > 2$ ns (b), has also been shown. Dashed red lines mark limits used in the TOF clustering.

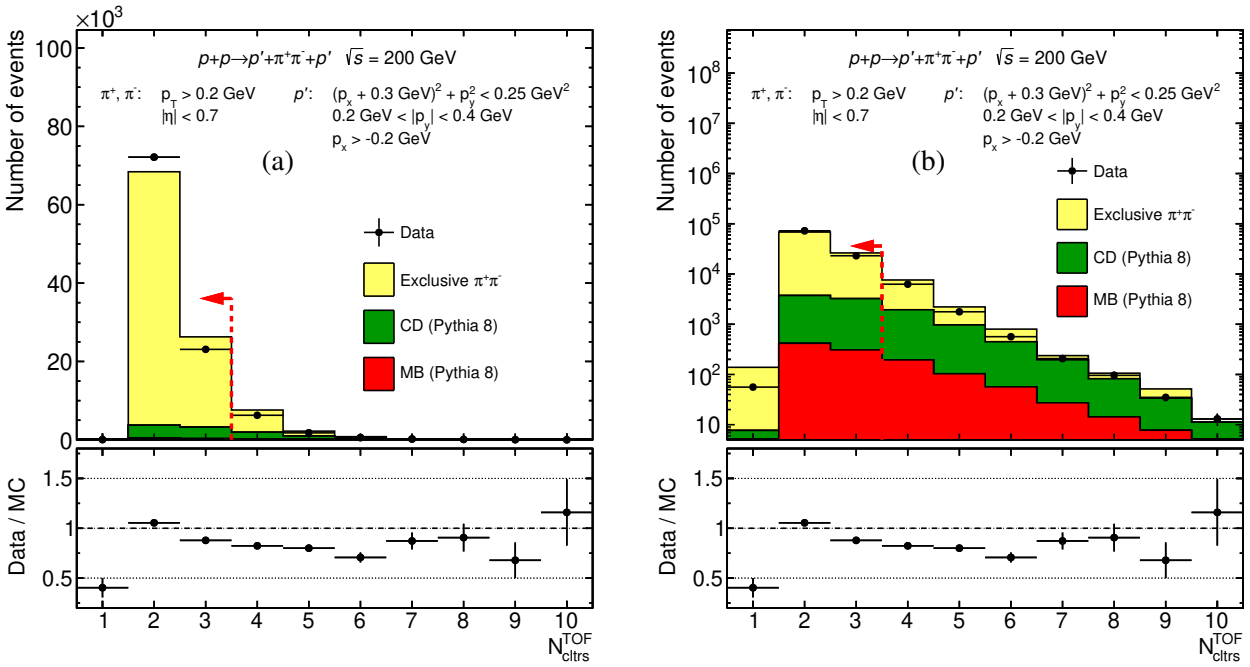

Figure 9.16: Distribution of TOF cluster multiplicity $N_{\text{cltr}}^{\text{TOF}}$ after all selection cuts except cut SC7. Two plots differ only in the y-axis ((a) linear and (b) logarithmic). Data are represented by black points, while stacked MC predictions are drawn as histograms of different colours. Histogram from each MC process has been normalised according to prescription in Sec. 10.3. Vertical error bars represent statistical uncertainties, horizontal bars represent bin sizes.

arises from the TOF hits originating from the same particle. Distribution of Δt significantly differs from the zero-bias-embedded signal MC. The observed mismatch between data and MC can be assigned to imperfect TOF simulation. However, data and MC are in qualitative agreement, in the sense, that the main parts of the time signal are in both cases contained at $\Delta t < 1.5$ ns. This level of description of data by MC is considered sufficient, given that efficiency correction related to cut on $N_{\text{cltrs}}^{\text{TOF}}$ is extracted from the data themselves.

Comparison of data and MC in terms of multiplicity of TOF clusters is presented in Fig. 9.16. The agreement between the two is acceptable. From the comparisons one can see that higher multiplicities are features of backgrounds (e.g. TOF hits reconstructed but TPC tracks not, or matching between TPC track and TOF hit unsuccessful), hence no more than one additional TOF cluster was allowed per event - in total the number of reconstructed TOF clusters $N_{\text{cltrs}}^{\text{TOF}}$ could not exceed three.

9.2.7 (SC8) Particle identification

Particles were identified using combined information from the TPC (dE/dx) and TOF (time of hit detection in the TOF subsystem). Merging informations from two sources led to reduction of misidentifications, as well as gave access to higher kaon and proton momentum range where dE/dx of different species overlap. From $n\sigma_X$ of the two tracks the χ^2 statistic for a XX pair hypothesis was calculated:

$$\chi^2_{dE/dx}(XX) = \left(n\sigma_X^{\text{trk1}}\right)^2 + \left(n\sigma_X^{\text{trk2}}\right)^2 . \tag{9.9}$$

Sometimes also $n\sigma_X^{\text{pair}}$ quantity is quoted (which is not a Gaussian pull like $n\sigma_X$), which is defined as $\sqrt{\chi^2_{dE/dx}(XX)}$. The time of detection of a particle in the TOF system was used to reconstruct its squared mass m^2_{TOF}. For this purpose the time of primary interaction is typically used ("start time"), reconstructed by detecting fragments of dissociated beam particles in VPD detectors on both sides of the interaction point[3]. However, it is not accessible in the CEP events, because the initial protons survive the interaction intact. The problem was overcame by assuming that both central tracks are of the same type, which is natural expectation for CEP events in this analysis. With this assumption, the measured tracks' momenta and lengths of helical paths between the primary vertex and TOF, and the difference between times of TOF hits matched with the tracks, allowed calculating m^2_{TOF}. The derivation of the formula used to obtain m^2_{TOF} is presented in App. C. Because of the resolution effects, the reconstructed m^2_{TOF} may take an unphysical, negative value. If that was the case, the $m^2_{\text{TOF}} = 0$ was assumed.

Particle identification involved a few steps. First, the pp hypothesis was verified:

$$\overbrace{\chi^2_{dE/dx}(pp) < 9 \quad \& \quad \underbrace{m^2_{\text{TOF}} > 0.6\ \text{GeV}^2}_{\text{unlikely } \pi\pi \text{ or } KK} \quad \& \quad \chi^2_{dE/dx}(\pi\pi) > 9 \quad \& \quad \chi^2_{dE/dx}(KK) > 9}^{\text{likely } pp}. \tag{9.10}$$

If any of above was not satisfied, the pair was checked for compatibility with KK hypothesis:

$$\overbrace{\chi^2_{dE/dx}(KK) < 9 \quad \& \quad \underbrace{m^2_{\text{TOF}} > 0.15\ \text{GeV}^2}_{\text{unlikely } \pi\pi} \quad \& \quad \chi^2_{dE/dx}(\pi\pi) > 9}^{\text{likely } KK} \quad \& \quad \underbrace{\chi^2_{dE/dx}(pp) > 9}_{\text{unlikely } pp}. \tag{9.11}$$

In the case, that the pair was neither recognised as $p\bar{p}$ nor K^+K^-, it was assumed to be a $\pi^+\pi^-$ pair if the dE/dx of positive and negative charge tracks were consistent with the pion hypothesis:

$$\chi^2_{dE/dx}(\pi\pi) < 12. \tag{9.12}$$

In Fig. 9.17, two-dimensional distributions of $n\sigma^{\text{pair}}$ variables are presented, what helps better understand the behaviour and aim of the χ^2 cuts in Eqs. (9.10), (9.11). Regions of enriched population of specific pair species are appropriately labelled in each plot. Similar connections between $n\sigma^{\text{pair}}$ and m^2_{TOF} are also shown in Fig. 9.17. Distributions of $\chi^2_{dE/dx}$ and m^2_{TOF} for CEP event candidates before PID cuts are shown in Fig. 9.18.

[3]Time measured from protons in the RP detectors cannot be used because RP readout runs on an independent clock from that used by VPD and TOF.

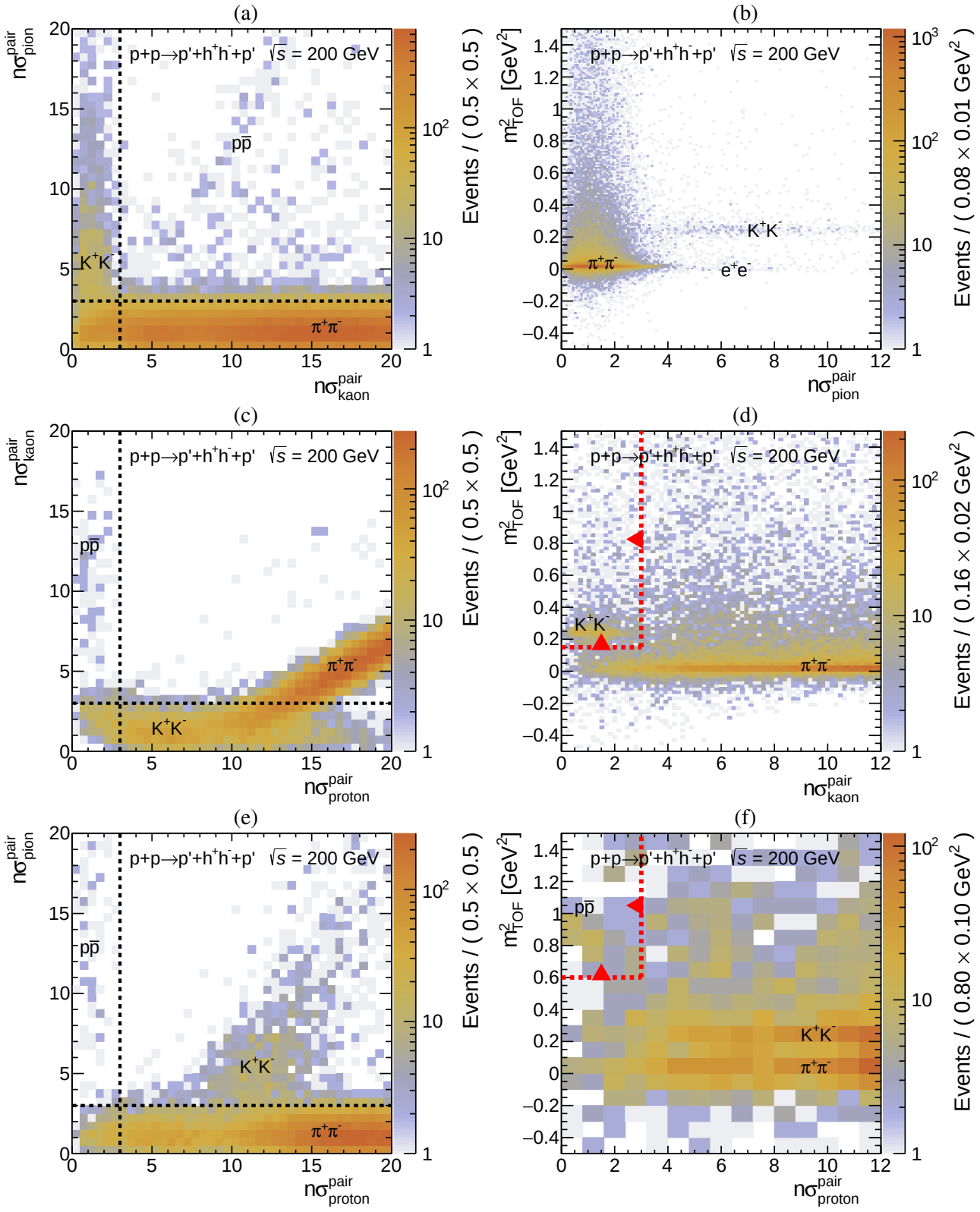

Figure 9.17: Two-dimensional distributions of (a) $n\sigma_{\pi}^{\text{pair}}$ vs. $n\sigma_{K}^{\text{pair}}$, (b) m^2_{TOF} vs. $n\sigma_{\pi}^{\text{pair}}$, (c) $n\sigma_{K}^{\text{pair}}$ vs. $n\sigma_{p}^{\text{pair}}$, (d) m^2_{TOF} vs. $n\sigma_{K}^{\text{pair}}$, (e) $n\sigma_{\pi}^{\text{pair}}$ vs. $n\sigma_{p}^{\text{pair}}$ and (f) m^2_{TOF} vs. $n\sigma_{p}^{\text{pair}}$, for exclusive event candidates after full event selection except PID cuts SC8. In the left column, dashed lines indicate the values of $n\sigma^{\text{pair}}$ which are used in pair identification ($n\sigma_{X}^{\text{pair}} = 3$ which is equivalent to $\chi^2(XX) = 9$). In the right column, dashed red lines and arrows indicate the PID cuts imposed on plotted quantities to select exclusive pairs of given particle species.

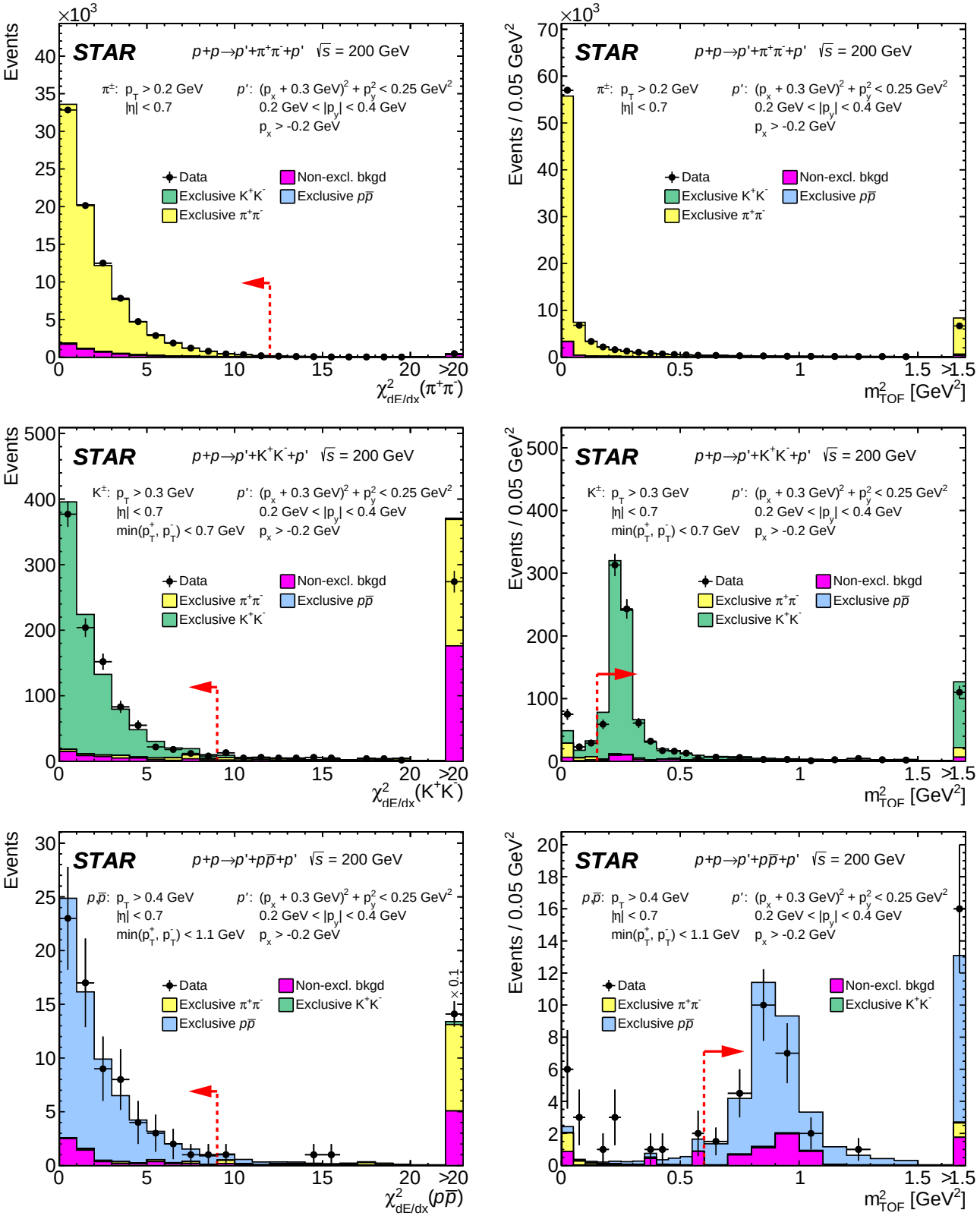

Figure 9.18: Raw distributions of $\chi^2_{dE/dx}$ (left column) and m^2_{TOF} (right column) for exclusive $\pi^+\pi^-$ (top row), K^+K^- (middle row) and $p\bar{p}$ (bottom row) candidates after full event selection. Data are shown as black points, while stacked MC predictions for signal and backgrounds are shown as colour histograms. Dashed red lines and arrows indicate the value of the cut imposed on the plotted quantity to select exclusive pairs of given particle species. Last bins in each subfigure are overflows representing an integral of the tail of distribution. Presented distributions were obtained after all the cuts were applied, except the cut on presented quantity in the last step in PID algorithm used to select pairs of given species. Non-exclusive background was determined with a method described in Sec. 10.2.1, while predictions for exclusive contributions were obtained as described in Sec. 10.2.2.

9.2.8 (SC9) Exclusivity cut (missing p_{T} cut)

The most important cut used in this analysis to select events of exclusively produced pairs of particles was the missing transverse momentum, or the total transverse momentum cut. It benefits from detection and reconstruction of the forward-scattered protons in RP detectors. The observable $p_{\mathrm{T}}^{\mathrm{miss}}$ used to select exclusive event is defined as:

$$p_{\mathrm{T}}^{\mathrm{miss}} = \left(\vec{p}_{p'}^{\,\mathrm{E}} + \vec{p}_{h^+} + \vec{p}_{h^-} + \vec{p}_{p'}^{\,\mathrm{W}}\right)_{\mathrm{T}} = \sqrt{\left(p_x^{\mathrm{miss}}\right)^2 + \left(p_y^{\mathrm{miss}}\right)^2}. \tag{9.13}$$

Figure 9.19 shows the (anti-)correlation between the momentum components of the forward system (sum of two forward-scattered protons' momenta) and the central system (sum of two central tracks' momenta). The enhanced band at anti-diagonal, restricted by the dashed lines, contains events balanced in momentum within measurement uncertainties, a signature of exclusivity. Events outside this band are the non exclusive backgrounds, in most cases CD events with some particles undetected. Slight horizontal enhancement in all distributions around $[\vec{p}_{p'}^{\,\mathrm{W}} + \vec{p}_{p'}^{\,\mathrm{E}}]_x = [\vec{p}_{p'}^{\,\mathrm{W}} + \vec{p}_{p'}^{\,\mathrm{E}}]_y = 0$ is the signature of the elastic proton-proton scattering background with some non-elastic pile-up interaction which mimics the CEP event. All these backgrounds are reasonably low after the exclusivity cut, as described in Sec. 10.1.1.

The momentum balance is shown one-dimensionally in Fig. 9.20, with the sums of x- and y-components of the momenta shown respectively in the left and right column for each analysed particle species. The sum of signal and background (both assumed to be described by a Gaussian) was fitted to the p_x^{miss} and p_y^{miss} distributions. Results of the fits are given in each plot. One can notice, that the widths of Gaussian functions representing the exclusive signal are consistent among species and amount $\sigma(p_x^{\mathrm{miss}}) = 27.4$ MeV for the x-component of the total momentum, and $\sigma(p_y^{\mathrm{miss}}) = 28.1$ MeV for the y-component of the total momentum, taking the values of the lowest statistical uncertainty - for $\pi^+\pi^-$. These values are measures of the total momentum resolution respectively for p_x^{miss} and p_y^{miss}. Having these numbers, it is possible to form an elliptical cut on the missing momentum:

$$\left(\frac{p_x^{\mathrm{miss}}}{\sigma(p_x^{\mathrm{miss}})}\right)^2 + \left(\frac{p_y^{\mathrm{miss}}}{\sigma(p_y^{\mathrm{miss}})}\right)^2 < n_{\mathrm{cut}}^2 \tag{9.14}$$

where n_{cut} is the parameter denoting radius of limiting ellipsis in units of standard deviations of the distributions of total momentum components (resolutions). Since these resolutions are nearly identical ($\sigma(p_x^{\mathrm{miss}}) \approx \sigma(p_y^{\mathrm{miss}}) \approx \sigma(p_{x,y}^{\mathrm{miss}})$) such cut can be reduced to one-dimensional cut on a single quantity:

$$\left(p_x^{\mathrm{miss}}\right)^2 + \left(p_y^{\mathrm{miss}}\right)^2 < \left(n_{\mathrm{cut}} \cdot \sigma(p_{x,y}^{\mathrm{miss}})\right)^2 \quad \xrightarrow{\sqrt{\ }} \quad p_{\mathrm{T}}^{\mathrm{miss}} < n_{\mathrm{cut}} \cdot \sigma(p_{x,y}^{\mathrm{miss}}) \tag{9.15}$$

In current analysis the n_{cut} was set to 2.5, which translates to threshold value $2.5 \cdot 30$ MeV $= 75$ MeV. Such value was found to optimally balance the final sample purity and signal selection efficiency.

In Fig. 9.21, the missing transverse momentum distributions are presented for the three studied CEP channels. The peaks at $p_{\mathrm{T}}^{\mathrm{miss}} < 75$ MeV represent the signal events, which are finally selected with the exclusivity cut marked with dashed red lines, while parts of the $p_{\mathrm{T}}^{\mathrm{miss}}$ distributions extending above the cut values represent the background events. The same-sign events are also shown, obtained with exactly the same event selection cuts as the nominal sample except for the requirement that the

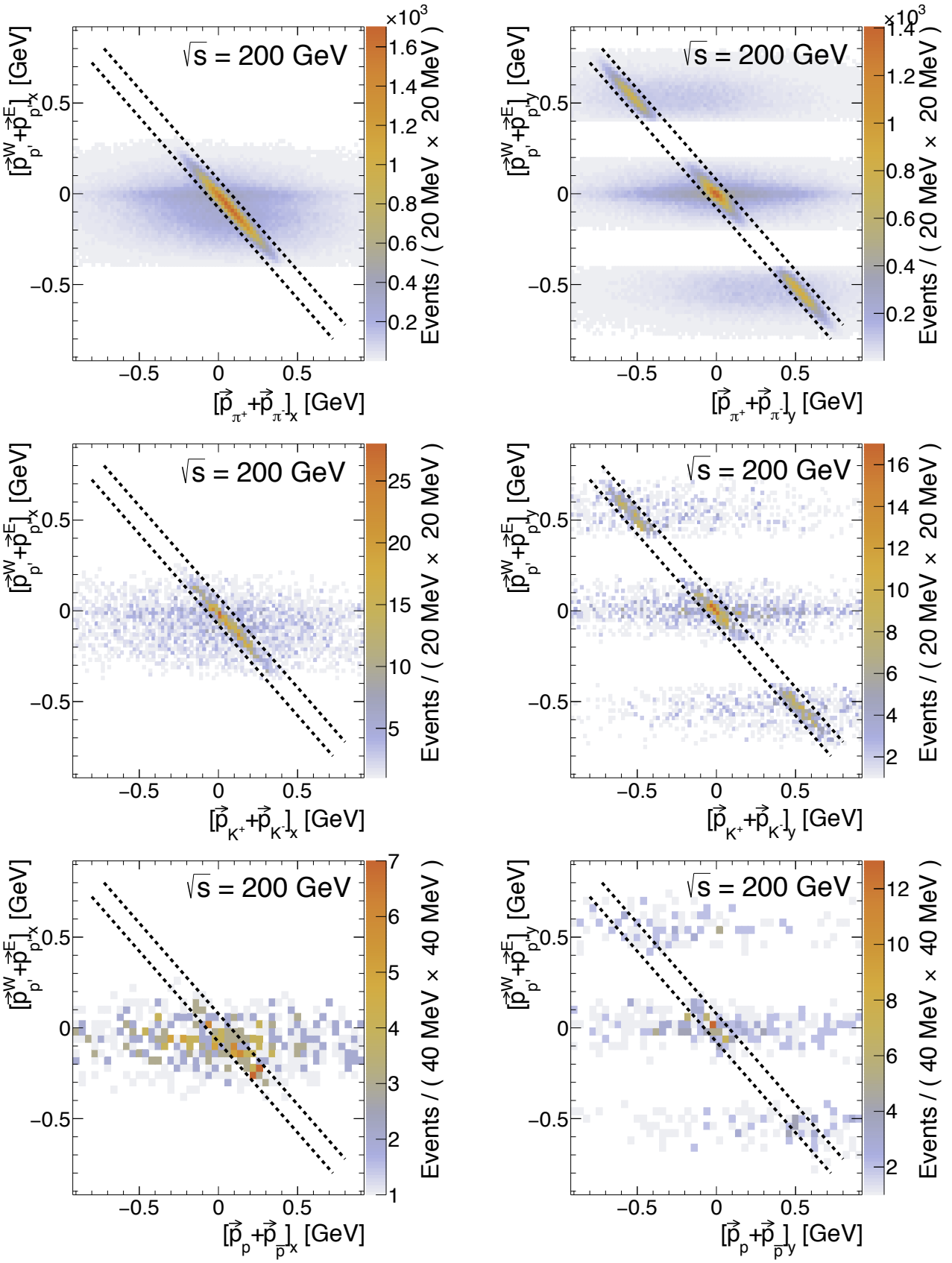

Figure 9.19: Two-dimensional distributions of sum of forward protons momenta (x-axis) and sum of central tracks momenta (y-axis) for exclusive $\pi^+\pi^-$ (top row), K^+K^- (middle row) and $p\bar{p}$ (bottom row) event candidates after full event selection, except the exclusivity cut SC9. Left and right column shows correlation of respectively x- and y-component of tracks' momenta. Anti-diagonal representing perfect momentum balance of the central and forward system is limited with dashed lines extending by $\pm 2.5\sigma$ ($\sigma \approx 30$ MeV) around the anti-diagonal. Three distinct horizontal regions in plots on the right hand side correspond to different forward proton configurations: elastic-like (protons in branches EU&WD or ED&WU, $\left|[\vec{p}^{\,\mathrm{W}}_{p'} + \vec{p}^{\,\mathrm{E}}_{p'}]_y\right| < 0.2$ GeV) and anti-elastic configuration (protons in branches ED&WD or EU&WU, $\left|[\vec{p}^{\,\mathrm{W}}_{p'} + \vec{p}^{\,\mathrm{E}}_{p'}]_y\right| > 0.4$ GeV).

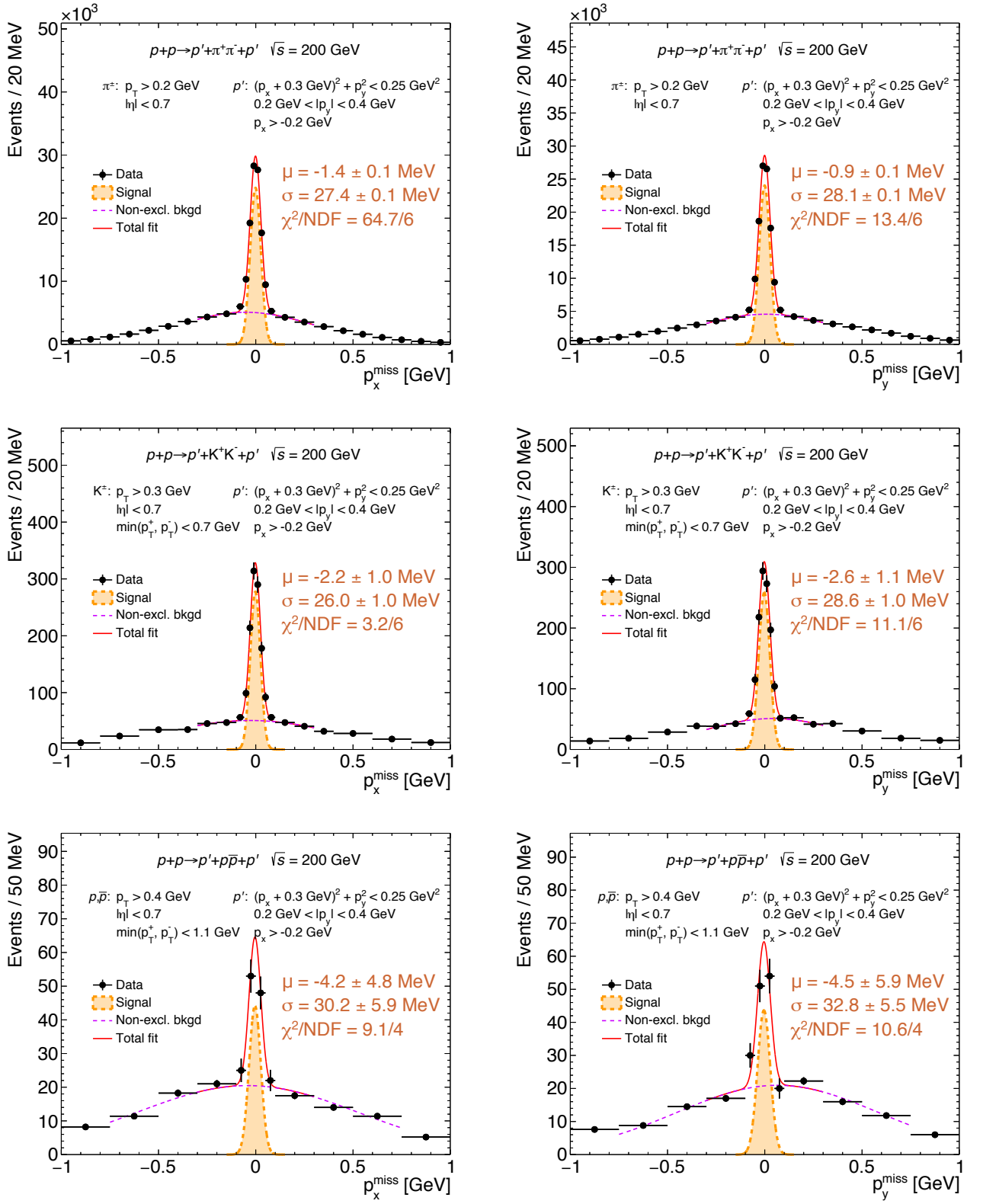

Figure 9.20: Distributions of p_x^{miss} (left column) and p_y^{miss} (right column) for exclusive $\pi^+\pi^-$ (top row), K^+K^- (middle row) and $p\bar{p}$ (bottom row) candidates after full event selection, except exclusivity cut SC9. Solid red line represents the fit of sum of two Gaussian functions representing the exclusive event signal (orange) and non-exclusive background (violet). Parameters of the total momentum resolution for signal events obtained from the fit (given in the plots) roughly agree between all species.

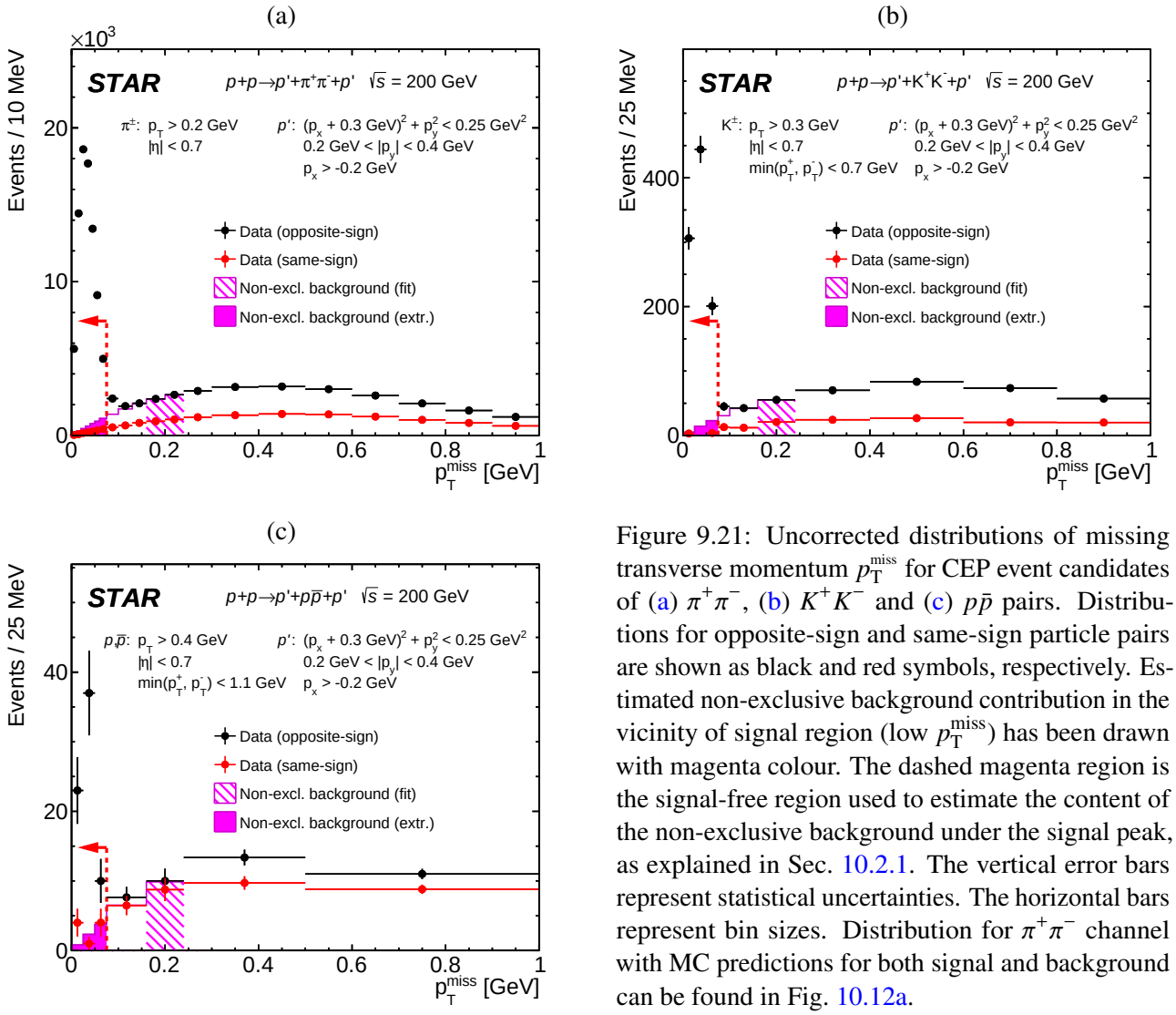

Figure 9.21: Uncorrected distributions of missing transverse momentum $p_{\mathrm{T}}^{\mathrm{miss}}$ for CEP event candidates of (a) $\pi^+\pi^-$, (b) K^+K^- and (c) $p\bar{p}$ pairs. Distributions for opposite-sign and same-sign particle pairs are shown as black and red symbols, respectively. Estimated non-exclusive background contribution in the vicinity of signal region (low $p_{\mathrm{T}}^{\mathrm{miss}}$) has been drawn with magenta colour. The dashed magenta region is the signal-free region used to estimate the content of the non-exclusive background under the signal peak, as explained in Sec. 10.2.1. The vertical error bars represent statistical uncertainties. The horizontal bars represent bin sizes. Distribution for $\pi^+\pi^-$ channel with MC predictions for both signal and background can be found in Fig. 10.12a.

two centrally produced tracks should have opposite electric charges. Instead it is required that the charges of the tracks are the same. The shape of $p_{\mathrm{T}}^{\mathrm{miss}}$ distributions above the signal region is very similar in the case of opposite-sign and same-sign events. Based on the behaviour of $p_{\mathrm{T}}^{\mathrm{miss}}$ distributions for the same-sign events in the region of $p_{\mathrm{T}}^{\mathrm{miss}} < 75$ MeV, the opposite-sign background under the signal peak was estimated through extrapolation from the background-dominated region, marked with hatched magenta histogram, to $p_{\mathrm{T}}^{\mathrm{miss}} = 0$ assuming vanishing of the background at this value. The estimated backgrounds in all CEP samples are shown with filled magenta histograms. In Sec. 10.3, a demonstration of various background contributions is provided for exclusive $\pi^+\pi^-$ pairs, explaining all features of the distribution.

10. Backgrounds

In this section, sources of backgrounds present in the CEP data sample and methods of their determination are discussed. Studies are presented, which provide quantitative information on relative content of various background types. Also, the role of cuts discussed in Chap. 9, in the reduction of the backgrounds to a few percent level, is explained.

10.1 Sources of background

10.1.1 Non-exclusive background

The main background present in the final exclusive $\pi^+\pi^-/K^+K^-/p\bar{p}$ sample is the non-exclusive background, i.e. the background from events, which mimic the topology of the CEP of h^+h^- pair. The topology of the signal event is shown in Fig. 10.1a. The event consists of two forward-scattered protons, two opposite-charge central tracks and the rapidity gaps between the forward protons and the central state. There are two general classes of events, which can easily mimic the signal:

- Regular events with some final state particles escaping detection:
  - CD process (Fig. 10.1b) - this process differs from CEP of h^+h^- only by the number of produced particles; protons originate from the same vertex as the central tracks, hence e.g. the correlation of the reconstructed vertex positions from the RP stations and the TPC is still observed.
- Accidental coincidences (pile-up):
  - inelastic (MB) + elastic interaction (Fig. 10.1c) - there may be an overlap between the forward-scattered protons from an elastic scattering and an activity in the central detector from another (inelastic) interaction; it is partially suppressed by the rapidity gap veto in BBC-small (online) and BBC-large (offline); easy to identify through protons collinearity and lack of correlation of z-vertex from RPs and TPC.

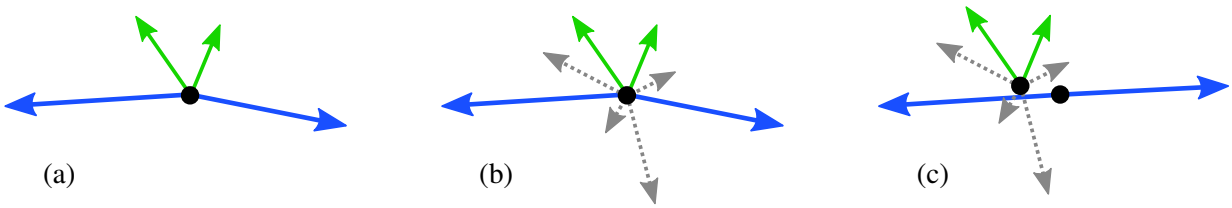

Figure 10.1: Sketches of main processes exhibiting h^+h^- CEP event topology: (a) the CEP of h^+h^- pair (signal), (b) CD event with some particles not detected, and (c) elastic proton-proton scattering event with a pile-up event of an inelastic interaction in the central region. Particles represented by arrows are: forward-scattered protons (blue), detected mid-rapidity particles (green) and undetected particles (dashed grey). Black dots mark primary interaction vertices.

– SD process + beam halo - there may be an overlap between a proton from the SD process on one side and a beam halo proton on the opposite side, and an activity in the central detector from diffractive state; it is supressed by the rapidity gap vetos and rather low beam halo rate;

– two beam halo protons on opposite sides + an inelastic interaction.

} negligibly low

The above backgrounds are further discussed in the following sections.

10.1.2 Exclusive background (particle misidentification)

Another source of background which is connected with the particle identification capabilities, is the exclusive background from the particle species other than the one under study. This effect is schematically shown in Fig. 10.2, and written in the form of a set of Eqs. (10.1), where N_R^{XX} is the number of reconstructed events identified as XX ($X = \pi, K$ or p), N_T^{XX} is the true number of XX events, $N_{bkgd}^{\pi\pi}$ is the number of non-exclusive events among the number of reconstructed events N_R^{XX}, ϵ^{XX} is the identification efficiency for the pair XX, and $\lambda^{XX\to YY}$ is the misidentification probability of the pair XX as YY:

$$N_R^{\pi\pi} = \underbrace{\epsilon^{\pi\pi}\cdot N_T^{\pi\pi}}_{\text{correctly identified pion pairs}} + \underbrace{\lambda^{KK\to\pi\pi}\cdot N_T^{KK}}_{\text{kaon pairs reconstructed as pion pairs}} + \underbrace{\lambda^{p\bar{p}\to\pi\pi}\cdot N_T^{p\bar{p}}}_{\text{proton pairs reconstructed as pion pairs}} + N_{bkgd}^{\pi\pi} \tag{10.1a}$$

$$N_R^{KK} = \underbrace{\lambda^{\pi\pi\to KK}\cdot N_T^{\pi\pi}}_{\text{pion pairs reconstructed as kaon pairs}} + \underbrace{\epsilon^{KK}\cdot N_T^{KK}}_{\text{correctly identified kaon pairs}} + \underbrace{\lambda^{p\bar{p}\to KK}\cdot N_T^{p\bar{p}}}_{\text{proton pairs reconstructed as kaon pairs}} + N_{bkgd}^{KK} \tag{10.1b}$$

$$N_R^{p\bar{p}} = \underbrace{\lambda^{\pi\pi\to p\bar{p}}\cdot N_T^{\pi\pi}}_{\text{pion pairs reconstructed as proton pairs}} + \underbrace{\lambda^{KK\to p\bar{p}}\cdot N_T^{KK}}_{\text{kaon pairs reconstructed as proton pairs}} + \underbrace{\epsilon^{p\bar{p}}\cdot N_T^{p\bar{p}}}_{\text{correctly identified proton pairs}} + N_{bkgd}^{p\bar{p}} \tag{10.1c}$$

Only the three most significant sources of misidentification are considered in Eqs. (10.1). The Eqs. (10.1) treated as a set of simultaneous equations, can be conventionally written in the matrix form and solved for the number of true events of the XX type:

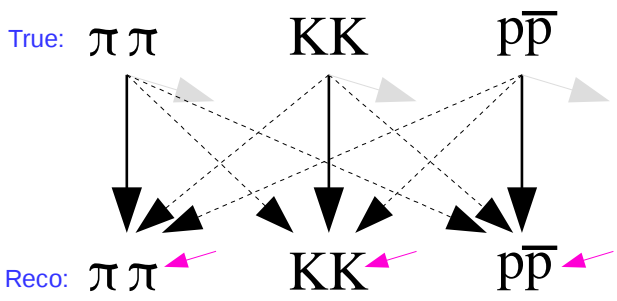

Figure 10.2: Graph illustrating the misidentification problem - the origin of the exclusive background in the selected samples. Gray arrows represent event rejection due to failed PID selection (SC8). Magenta arrows indicate the non-exclusive backgrounds described in Sec. 10.1.1. Solid black arrows represent successful identification, whereas dashed black arrows show possible misidentifications.

$$\begin{bmatrix} N_R^{\pi\pi} - N_{bkgd}^{\pi\pi} \\ N_R^{KK} - N_{bkgd}^{KK} \\ N_R^{p\bar{p}} - N_{bkgd}^{p\bar{p}} \end{bmatrix} = \underbrace{\begin{bmatrix} \epsilon^{\pi\pi} & \lambda^{KK\to\pi\pi} & \lambda^{p\bar{p}\to\pi\pi} \\ \lambda^{\pi\pi\to KK} & \epsilon^{KK} & \lambda^{p\bar{p}\to KK} \\ \lambda^{\pi\pi\to p\bar{p}} & \lambda^{KK\to p\bar{p}} & \epsilon^{p\bar{p}} \end{bmatrix}}_{\text{“mixing matrix” } \Lambda} \begin{bmatrix} N_T^{\pi\pi} \\ N_T^{KK} \\ N_T^{p\bar{p}} \end{bmatrix} \quad \to \quad \begin{bmatrix} N_T^{\pi\pi} \\ N_T^{KK} \\ N_T^{p\bar{p}} \end{bmatrix} = \Lambda^{-1} \begin{bmatrix} N_R^{\pi\pi} - N_{bkgd}^{\pi\pi} \\ N_R^{KK} - N_{bkgd}^{KK} \\ N_R^{p\bar{p}} - N_{bkgd}^{p\bar{p}} \end{bmatrix} \tag{10.2}$$

A semi-data-driven method of estimation of the exclusive background is given in Sec. 10.2.2.

10.2 Background determination

10.2.1 Non-exclusive background

Determination of the non-exclusive background utilises the missing transverse momentum, which is distributed differently for the signal and for the background. High statistics of the data allows to apply a data-driven method, which is desired as it significantly reduces an impact of model-dependence on the results, especially when models of diffraction poorly describe shapes and normalisations of physics observables.

It has already been demonstrated in Sec. 9.2.8 that $p_{\mathrm{T}}^{\mathrm{miss}}$ from exclusive events is much narrower compared to background. Additional feature of $p_{\mathrm{T}}^{\mathrm{miss}}$ - probability density approaching to zero with $p_{\mathrm{T}}^{\mathrm{miss}}$ moving towards zero, helps performing a polynomial fit without constant component to the $p_{\mathrm{T}}^{\mathrm{miss}}$ distribution in the background-dominated range and extrapolation of this polynomial down to $p_{\mathrm{T}}^{\mathrm{miss}} = 0$ under the peak of the CEP signal. The procedure used to determine non-exclusive background content in the signal region is described below. The description assumes determination of non-exclusive background differentially in a single observable X (in 1 dimension), but the procedure naturally applies also to more dimensions.

The following steps need to be done to estimate the background:

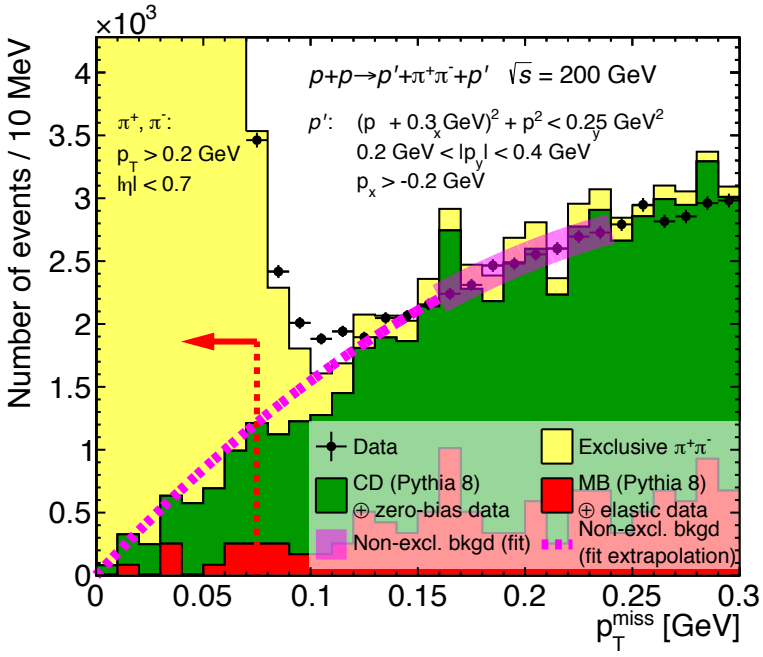

Figure 10.3: Demonstration of non-exclusive background determination method using the $p_{\mathrm{T}}^{\mathrm{miss}}$ distribution. The data are shown with black points, stacked MC predictions are shown with filled histograms, and the fit of the 2nd order polynomial representing the non-exclusive background, together with its extrapolation to $p_{\mathrm{T}}^{\mathrm{miss}} = 0$ is drawn with solid and dashed magenta line, respectively.

1. The two-dimensional distribution of $p_{\mathrm{T}}^{\mathrm{miss}}$ vs. X (without the cut SC9 applied) is looped over all bins in X. Projections onto $p_{\mathrm{T}}^{\mathrm{miss}}$ axis in single (i) bins, $dN_{X,i}/dp_{\mathrm{T}}^{\mathrm{miss}}$, are done for only those bins of X, in which there are signal candidates (more than zero counts in the region $p_{\mathrm{T}}^{\mathrm{miss}} < 75$ MeV).

2. Projections of $p_{\mathrm{T}}^{\mathrm{miss}}$ from bins with signal candidates are summed to a single histogram (like data points in Fig. 10.3):
$$\frac{dN_X}{dp_{\mathrm{T}}^{\mathrm{miss}}} = \sum_i \frac{dN_{X,i}}{dp_{\mathrm{T}}^{\mathrm{miss}}} \tag{10.3}$$

3. A fit of the second-order polynomial, $b\left(p_{\mathrm{T}}^{\mathrm{miss}}\right) = c_1 \cdot p_{\mathrm{T}}^{\mathrm{miss}} + c_2 \cdot \left(p_{\mathrm{T}}^{\mathrm{miss}}\right)^2$, is performed to the $dN_X/dp_{\mathrm{T}}^{\mathrm{miss}}$ in the range 160 MeV $< p_{\mathrm{T}}^{\mathrm{miss}} <$ 240 MeV, which is dominated by the non-exclusive background, and the signal is expected to be negligible in this range. The left edge of the fitting range was chosen to be close to $p_{\mathrm{T}}^{\mathrm{miss}} = 0$, but far enough from the signal peak which could bias the fitted background shape. The right edge of the fitting range was set to provide reasonable width of that range, but on the other hand to be close enough to $p_{\mathrm{T}}^{\mathrm{miss}} = 0$, so that the 2nd order polynomial approximation would still be valid for the background shape. The result of the fit is shown in Fig. 10.3 with semi-transparent magenta line.

4. The ratio, r_{bkgd}, of the integral of the function $b\left(p_{\mathrm{T}}^{\mathrm{miss}}\right)$ in the signal region ($p_{\mathrm{T}}^{\mathrm{miss}} < 75$ MeV))

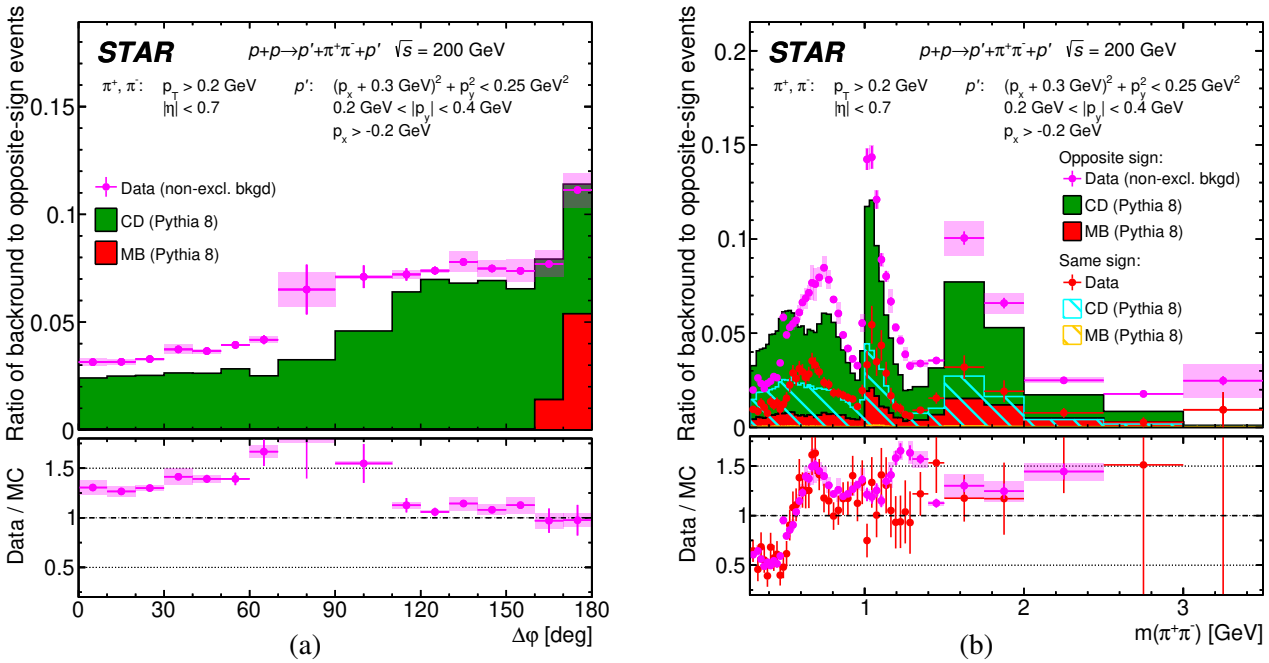

Figure 10.4: Comparison of the non-exclusive background estimation using the data-driven method and the MC predictions for (a) $\Delta\varphi$ and (b) $m(\pi\pi)$. Normalisation of MC components is explained in Sec. 10.3. Opposite-sign non-exclusive background extracted from data is shown with magenta points, while stacked opposite-sign MC predictions are shown with filled histograms. Control same-sign background events are shown with red points for the data, and stacked hatched histograms for MC predictions. Magenta boxes represent systematic uncertainty of the background determination method, estimated as explained in Sec. 12.5.

and in the background dominated (fitted) region 160 MeV $< p_{\mathrm{T}}^{\mathrm{miss}} <$ 240 MeV is obtained:

$$r_{\mathrm{bkgd}} = \int_{0}^{75\ \mathrm{MeV}} b\left(p_{\mathrm{T}}^{\mathrm{miss}}\right) dp_{\mathrm{T}}^{\mathrm{miss}} \Big/ \int_{160\ \mathrm{MeV}}^{240\ \mathrm{MeV}} b\left(p_{\mathrm{T}}^{\mathrm{miss}}\right) dp_{\mathrm{T}}^{\mathrm{miss}} \,. \tag{10.4}$$

5. The non-exclusive background contribution in the i-th bin of X is determined as

$$N_{X,i}^{\text{non-excl}} = r_{\mathrm{bkgd}} \cdot \int_{0}^{75\ \mathrm{MeV}} \frac{dN_{X,i}}{dp_{\mathrm{T}}^{\mathrm{miss}}} dp_{\mathrm{T}}^{\mathrm{miss}}. \tag{10.5}$$

One can see in Fig. 10.3 that fitted polynomial extrapolated to $p_{\mathrm{T}}^{\mathrm{miss}} = 0$ matches well predictions from MC. Figure 10.4 demonstrates, that data-driven method differs from MC predictions by up to 50% in both directions. As one can see, the estimated shapes of the non-exclusive backgrounds in the case of the same-sign and opposite-sign $\pi\pi$ samples, differ significantly. This disqualifies direct usage of the same-sign events as an estimate of the non-exclusive background for the opposite-sign data sample.

10.2.2 Exclusive background

The exclusive background, arising from the wrong particle identification, has been estimated using semi-data-driven method. This method uses the fast MC generator introduced in Sec. 8.1.2, with all quantities relevant for particle identification (dE/dx and its resolution, TOF time measurement resolution, etc.) set in the generator according to their distributions in the data. In order to determine absolute size of migrations between the three measured particle pair's species, it is necessary to know the full distribution of particles' (transverse) momenta - especially in the regions of momentum space where the migrations are significant (regions of non-zero $\lambda^{X\to Y}$ in Fig. 11.24). There are no models of CEP of $\pi^+\pi^-$, K^+K^- and $p\bar{p}$ which describe measured data, therefore it was decided to use measured distributions as an input models of the distribution of p_{T} of negatively and positively charged TPC tracks, $(p_{\mathrm{T}}^-, p_{\mathrm{T}}^+)$[1]. Selected CEP pairs were assumed to have low contamination from the exclusive background. Such an assumption is motivated by the restrictive particle identification algorithm, which based on study from Sec. 11.3.6, provides a high level of identification efficiency and low level of misidentification probability. It is supported by the distributions of $\chi^2_{dE/dx}$ and m^2_{TOF} presented in Fig. 9.18, in which clear features expected for given pair types are seen, without signs of excessful exclusive background.

The following steps were applied to prepare $N_X(p_{\mathrm{T}}^-, p_{\mathrm{T}}^+)$ distributions, where $X = \pi, K, p$, to be used for determination of the exclusive background in the all three CEP samples:

1. The shapes of the p_{T}^- and p_{T}^+ distributions are expected to be identical, so it is justified to average the two-dimensional distributions of $N_X(p_{\mathrm{T}}^-, p_{\mathrm{T}}^+)$ with respect to their diagonals:

$$N_{X,avg}(p_{\mathrm{T}}^-, p_{\mathrm{T}}^+) = N_{X,avg}(p_{\mathrm{T}}^+, p_{\mathrm{T}}^-) = \frac{N_X(p_{\mathrm{T}}^-, p_{\mathrm{T}}^+) + N_X(p_{\mathrm{T}}^+, p_{\mathrm{T}}^-)}{2}. \tag{10.6}$$

The averaged distributions are shown in Figs. 10.5b, 10.6b and 10.7b, respectively.

[1] $(p_{\mathrm{T}}^{\max}, p_{\mathrm{T}}^{\min})$ could be used as well.

2. The averaged distributions are corrected for particle identification efficiency (see Fig. 11.24):

$$N_{X,corr}(p_{\mathrm{T}}^{-}, p_{\mathrm{T}}^{+}) = \frac{N_{X,avg}(p_{\mathrm{T}}^{-}, p_{\mathrm{T}}^{+})}{\epsilon^{X}\left(\max(p_{\mathrm{T}}^{-}, p_{\mathrm{T}}^{+}), \min(p_{\mathrm{T}}^{-}, p_{\mathrm{T}}^{+})\right)}. \tag{10.7}$$

   The corrected distributions are shown in Figs. 10.5c, 10.6c and 10.7c, respectively.

3. Because of the cut SC8.2, in the case of $K^{+}K^{-}$ and $p\bar{p}$ pairs, there is no access to the region where both tracks carry high p_{T}. To overcome this drawback an extrapolation of the distributions is performed into the unmeasured region, using an iterative approach:

$$N_{X,extr}(p_{T,i}^{-}, p_{T,j}^{+}) = f_{extr} \cdot \frac{N_{X,extr}(p_{T,i-1}^{-}, p_{T,j-1}^{+}) + N_{X,extr}(p_{T,i-2}^{-}, p_{T,j-2}^{+})}{2}. \tag{10.8}$$

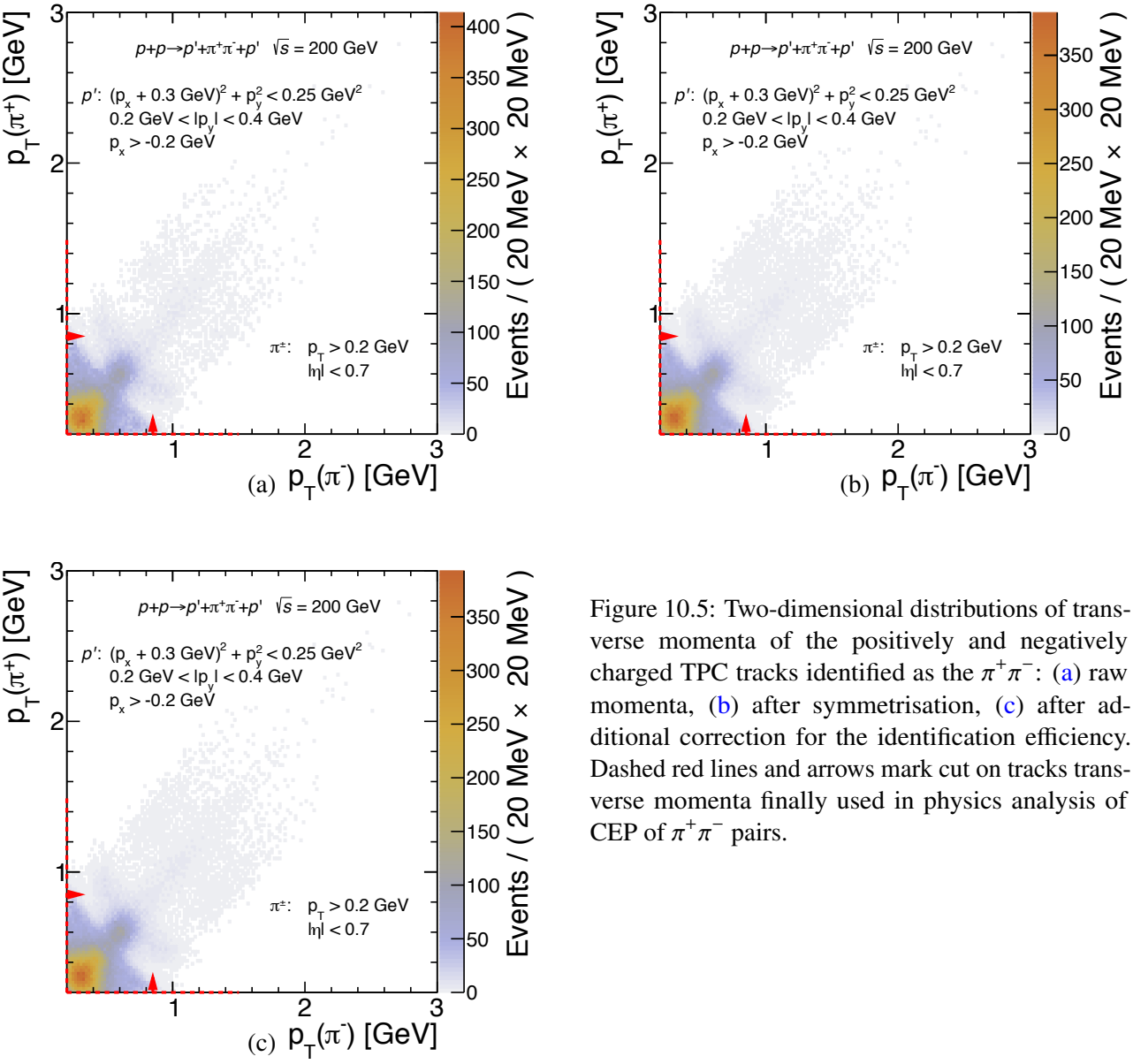

Figure 10.5: Two-dimensional distributions of transverse momenta of the positively and negatively charged TPC tracks identified as the $\pi^{+}\pi^{-}$: (a) raw momenta, (b) after symmetrisation, (c) after additional correction for the identification efficiency. Dashed red lines and arrows mark cut on tracks transverse momenta finally used in physics analysis of CEP of $\pi^{+}\pi^{-}$ pairs.

In the above formula, the factor f_{extr} determines the "steepness" of the distribution with growing track's p_T. As we observe in $\pi^+\pi^-$ channel the high-p_T tail in the distribution tends to diminish and disappears around (2 GeV, 2 GeV). It was found that $f_{extr} = 0.8$ is a reasonable value, to provide similar dependence in the K^+K^- and $p\bar{p}$ channels as in the $\pi^+\pi^-$ case. Final distributions for K^+K^- and $p\bar{p}$ are shown in Figs. 10.6d and 10.7d, respectively.

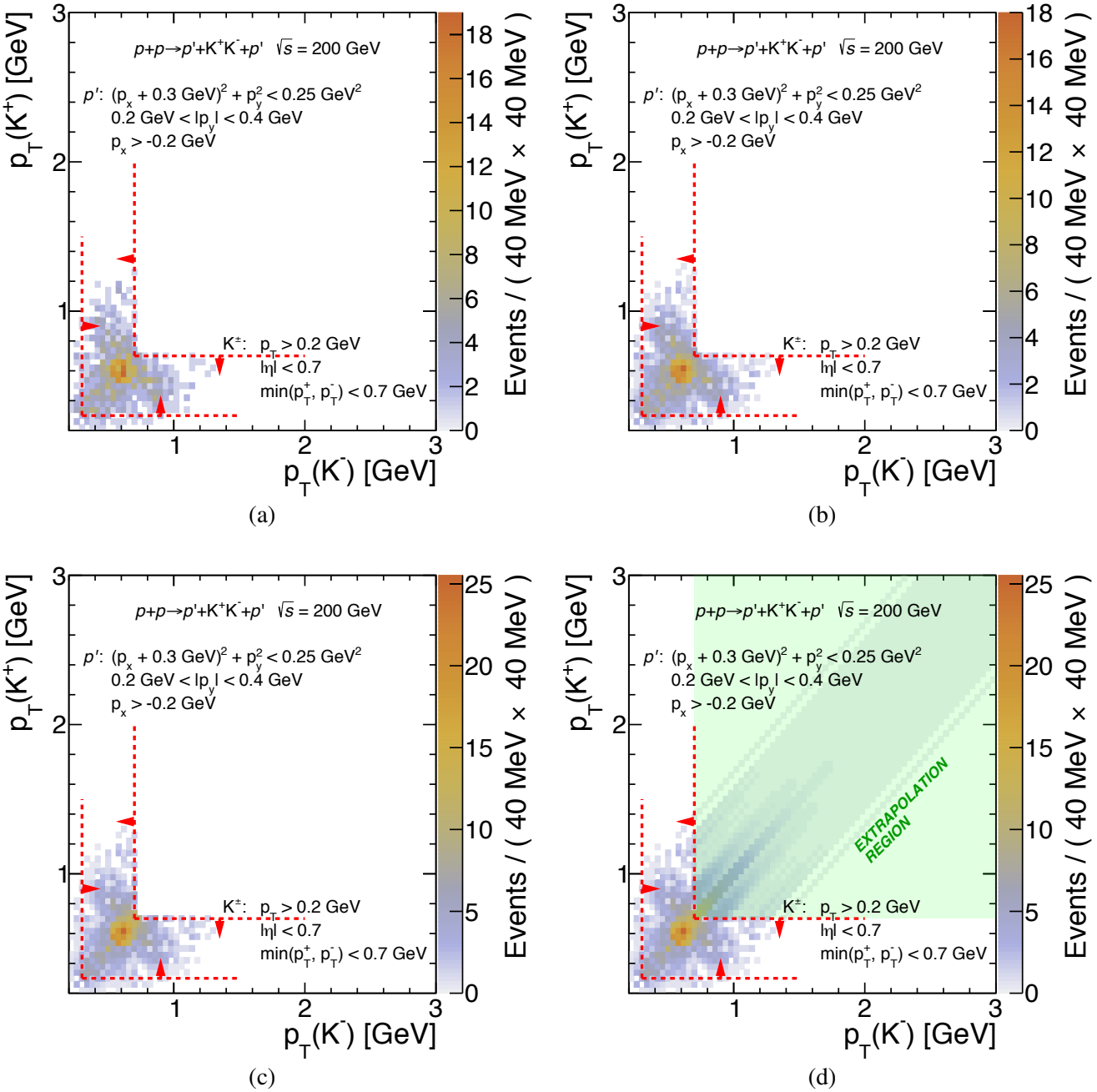

Figure 10.6: Two-dimensional distributions of transverse momenta of the positively and negatively charged TPC tracks identified as the K^+K^-: (a) raw momenta, (b) after symmetrisation, (c) after additional correction for the identification efficiency, (d) after further extrapolation to the unmeasured transverse momentum region (transparent green). Dashed red lines and arrows mark cut on tracks transverse momenta finally used in physics analysis of CEP of K^+K^- pairs.

Distributions from the Figs. 10.5c, 10.6d and 10.7d were used to obtain an estimation of the backgrounds due to misidentification. Samples of exclusive $\pi^+\pi^-$, K^+K^- and $p\bar{p}$ simulated with fast MC, with uniformly distributed (p_T^+, p_T^-) over the range 0.2 GeV $< p_T^-, p_T^+ <$ 3 GeV, were subjected to the PID algorithm from the selection cut SC8. Each event was assigned a weight equal to the data-extracted event density for the given (p_T^-, p_T^+) bin, such that the relative numbers of $\pi^+\pi^-$, K^+K^- and $p\bar{p}$ pairs, were exactly the same as in Figs. 10.5c, 10.6d and 10.7d. Three histograms of $\chi^2_{dE/dx}$

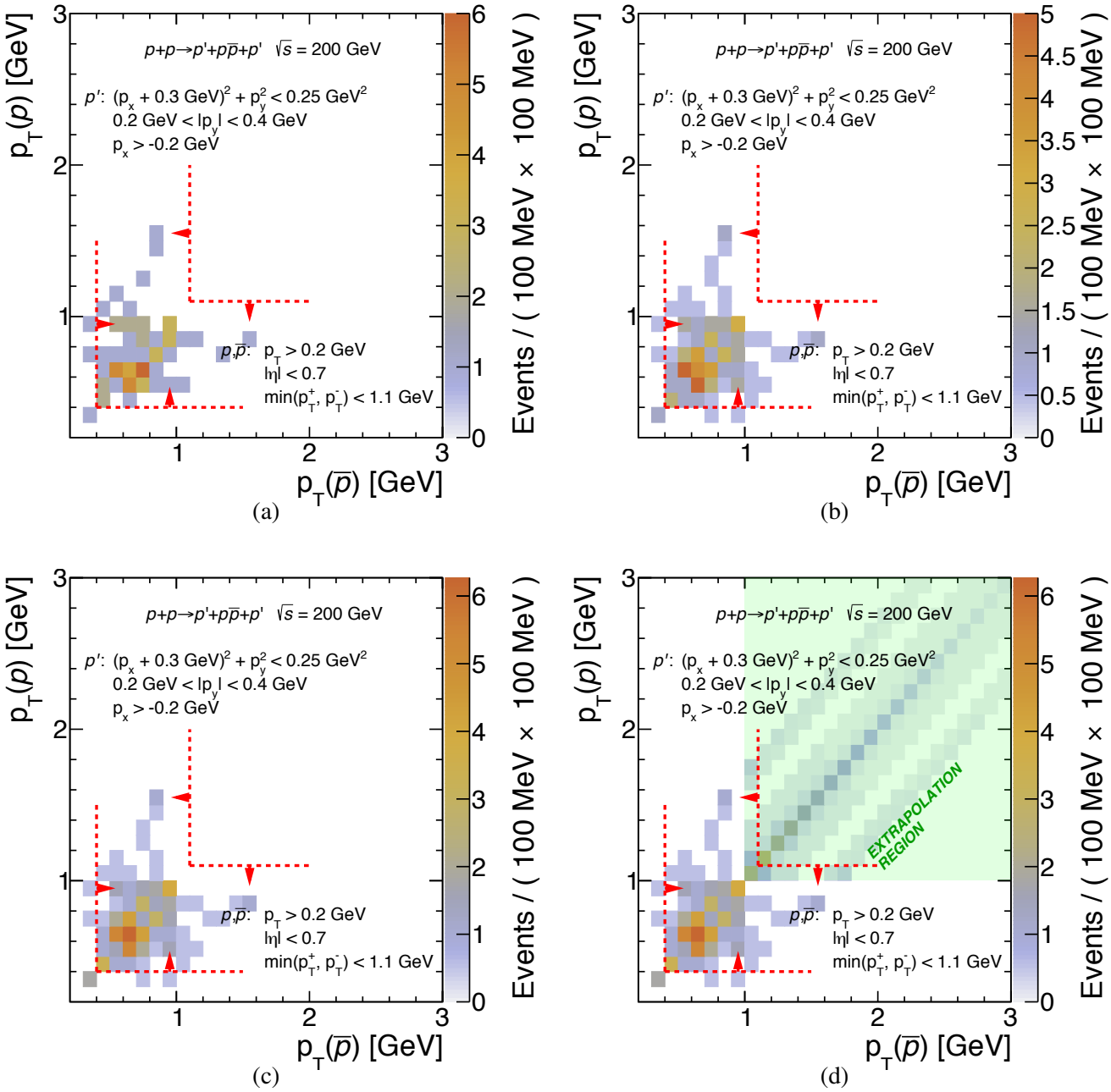

Figure 10.7: Two-dimensional distributions of transverse momenta of the positively and negatively charged TPC tracks identified as the $p\bar{p}$: (a) raw momenta, (b) after symmetrisation, (c) after additional correction for the identification efficiency, (d) after further extrapolation to the unmeasured transverse momentum region (transparent green). Dashed red lines and arrows mark cut on tracks transverse momenta finally used in physics analysis of CEP of $p\bar{p}$ pairs.

and m^2_{TOF} (separately for events identified as the $\pi^+\pi^-$, K^+K^- and $p\bar{p}$) were prepared for each of three types of generated h^+h^- pairs. Those histograms were filled in each event (using the weight mentioned earlier), which corresponded to given reconstructed PID.

The last step involved proper normalisation of the $\chi^2_{dE/dx}$ and m^2_{TOF} histograms. Predictions for each true-level pair type were normalised independently, but the same normalisation was preserved for all quantities and for all reconstructed pair types. Normalisation factors F^{MC}_X of the $\chi^2_{dE/dx}$ and m^2_{TOF} histograms representing prediction for exclusive XX was established such that the number of predicted XX events in the XX signal-dominating region (fiducial region of $\chi^2_{dE/dx}(XX) < 6$), $N^{\mathrm{MC}}_{X\to X,\mathrm{fid}}$, was equal to the number of measured XX events in that region ($N^{\mathrm{data}}_{X,\mathrm{fid}}$) less a number of non-exclusive background events in the same region ($N^{\mathrm{non\text{-}excl}}_{X,\mathrm{fid}}$) extracted with a method introduced in Sec. 10.2.1. It is expressed with the formula:

$$F^{\mathrm{MC}}_X = \frac{N^{\mathrm{data}}_{X,\mathrm{fid}} - N^{\mathrm{non\text{-}excl}}_{X,\mathrm{fid}}}{N^{\mathrm{MC}}_{X\to X,\mathrm{fid}}}, \tag{10.9}$$

where all components are explicitly given by:

$$N^{\mathrm{data}}_{X,\mathrm{fid}} = \int_0^6 \frac{dN^{\mathrm{data}}_X}{d\chi^2_{dE/dx}} d\chi^2_{dE/dx}, \quad N^{\mathrm{non\text{-}excl}}_{X,\mathrm{fid}} = \int_0^6 \frac{dN^{\mathrm{non\text{-}excl}}_{X,\mathrm{fid}}}{d\chi^2_{dE/dx}} d\chi^2_{dE/dx}, \quad N^{\mathrm{MC}}_{X\to X,\mathrm{fid}} = \int_0^6 \frac{dN^{\mathrm{MC}}_{X\to X}}{d\chi^2_{dE/dx}} d\chi^2_{dE/dx}. \tag{10.10}$$

The relative values of the normalisation factors, $F^{\mathrm{MC}}_{\pi\pi}/F^{\mathrm{MC}}_{KK}/F^{\mathrm{MC}}_{pp}$, remain in the following relation 1/1.01/0.88. Comparisons of the data with the fast MC predictions normalised according to the above prescription are shown in Fig. 9.18. Fast MC well reproduces measured spectra of $\chi^2_{dE/dx}$ and m^2_{TOF} for all selected particle pair species.

10.2.3 Estimated non-exclusive and exclusive background contributions

The non-exclusive and exclusive background contributions to each of the studied CEP processes are given in Tab. 10.1. One can see that the dominant source of background is non-exclusive background, which was suppressed down to 5% ($\pi^+\pi^-$, K^+K^-) and 8% ($p\bar{p}$), respectively. The exclusive background is typically not larger than 1%, except in the case of misidentification of $\pi^+\pi^-$ pairs as K^+K^- pairs or $p\bar{p}$ pairs.

	Selected events	**Non-exclusive background**	**Exclusive background**		
			$\boldsymbol{\pi^+\pi^-}$	$\boldsymbol{K^+K^-}$	$\boldsymbol{p\bar{p}}$
$\boldsymbol{\pi^+\pi^-}$	85619	4543 (5.3%)	-	653 (0.8%)	18 (0.0%)
$\boldsymbol{K^+K^-}$	931	50 (5.4%)	28 (3.1%)	-	0 (0.0%)
$\boldsymbol{p\bar{p}}$	68	8 (12.0%)	1 (1.5%)	0 (0.0%)	-

Table 10.1: Summary of non-exclusive and exclusive background contributions to the CEP of $\pi^+\pi^-$, K^+K^- and $p\bar{p}$ pairs. Values in brackets are fractions calculated with respect to number of selected events.

10.3 Normalisation of signal and background models

In order to demonstrate a good understanding of the backgrounds, it is desirable to compare data and MC predictions. The checks have been done for the exclusive $\pi^+\pi^-$ channel only[2] and taking into account the non-exclusive background contribution as the contribution from the particle misidentification is negligible.

Normalisations of the backgrounds have been done separately for two ranges of $\Delta\varphi$. First, MB+elastic background was normalised. By definition this was done only for $\Delta\varphi$ bin representing elastic-like configuration of forward-scattered protons ($\Delta\varphi > 90^\circ$). The MB+elastic MC was scaled to have the same integral as the data in range $|\Delta z_{\text{vtx}}| > 100$ cm. In this range, a sole presence of this type of background was assumed, which is characterised by very wide distribution of Δz_{vtx} because of TPC and RP vertices being uncorrelated. Comparison plots are contained in Figs. 10.8 (Δz_{vtx} separately for two ranges of $\Delta\varphi$) and 10.9 (Δz_{vtx} from two ranges of $\Delta\varphi$ merged together). An important cross-check for the correctness of this assumption is shown in Fig. 10.10, in which the collinearity, defined as:

$$\Delta\theta = \sqrt{(\Delta\theta_x)^2 + \left(\Delta\theta_y\right)^2} = \sqrt{\left(\theta_x^W + \theta_x^E\right)^2 + \left(\theta_y^W + \theta_y^E\right)^2}. \tag{10.11}$$

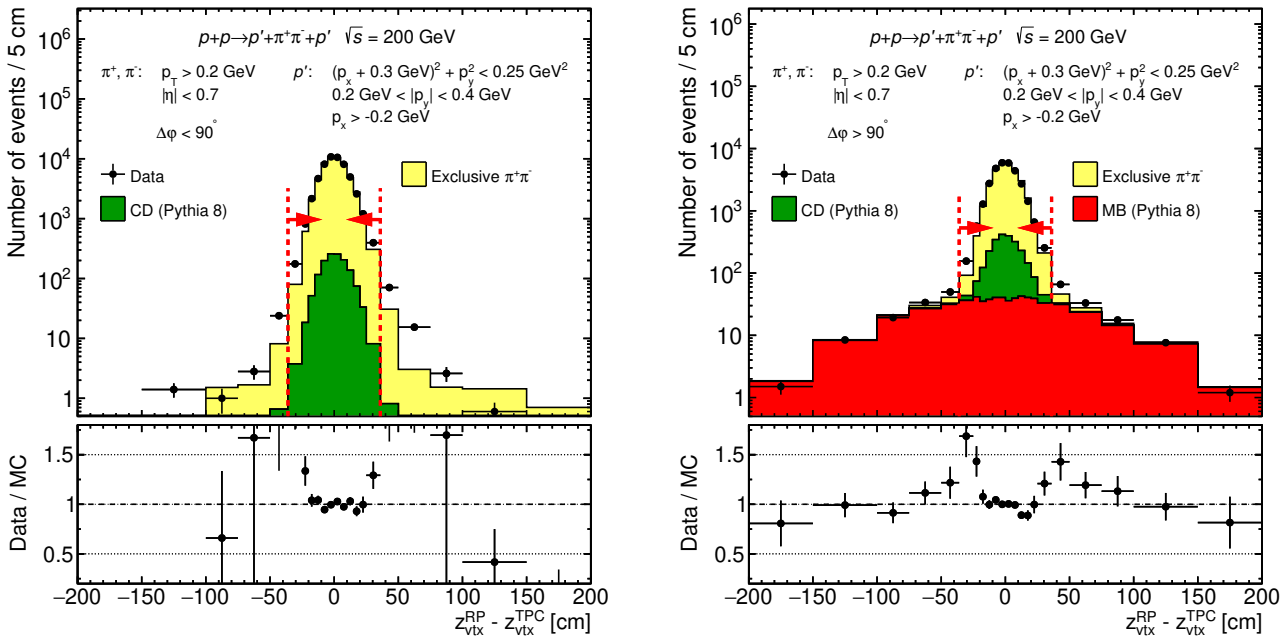

(a) (b)

Figure 10.8: Comparison of Δz_{vtx} for CEP $\pi^+\pi^-$ events in two ranges of $\Delta\varphi$ (left: $\Delta\varphi < 90^\circ$, right: $\Delta\varphi > 90^\circ$) between data and embedded MC after full selection (except cut on the presented quantity). Data are represented by black points, while stacked MC predictions are drawn as histograms of different colors. Histogram from each MC process has been normalised according to prescription in the text. Vertical error bars represent statistical uncertainties, horizontal bars represent bin sizes. Signal selection cut SC5 is marked with dashed red lines and arrows.

[2]The other channels - K^+K^- and $p\bar{p}$ - were not subjected to similar study because of unavailable embedded MC for exclusive K^+K^- and $p\bar{p}$ pairs. However, structure of backgrounds and the level of agreement with MC is expected to be similar to that presented for $\pi^+\pi^-$ pairs.

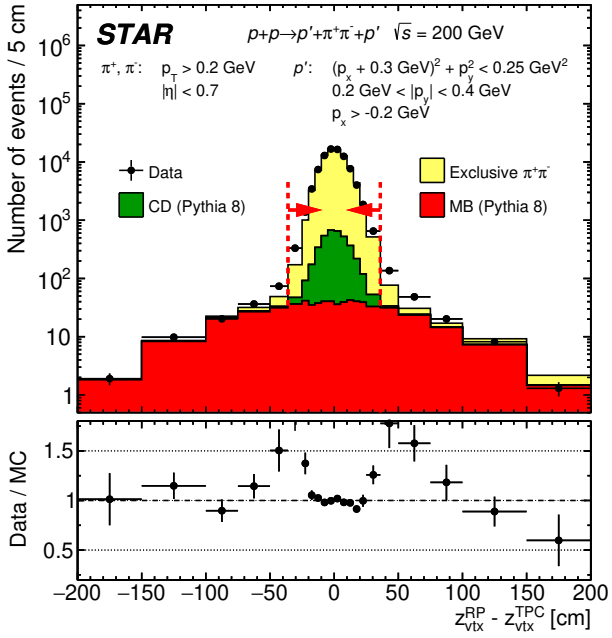

Figure 10.9: Comparison of Δz_{vtx} for CEP $\pi^+\pi^-$ events between data and embedded MC after full selection (except cut on the presented quantity). Data are represented by black points, while stacked MC predictions are drawn as histograms of different colors. Histogram from each MC process has been normalised according to prescription in the text. Vertical error bars represent statistical uncertainties, horizontal bars represent bin sizes. Signal selection cut SC5 is marked with dashed red lines and arrows.

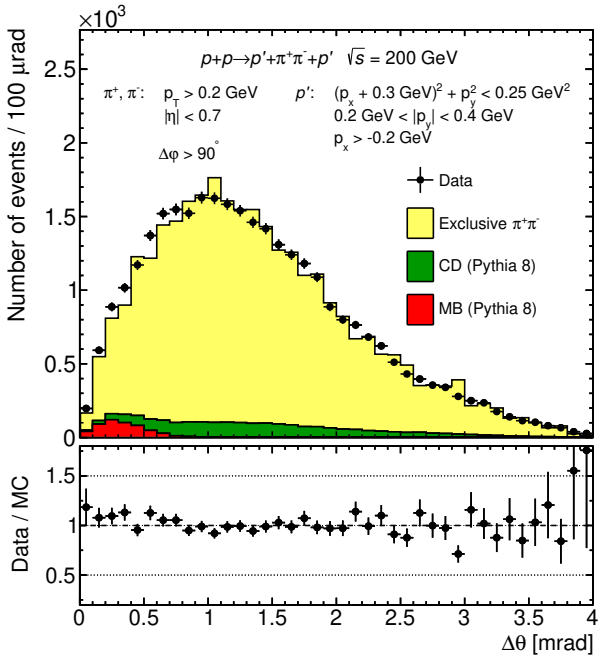

Figure 10.10: Comparison of coliinearity $\Delta\theta$ for CEP $\pi^+\pi^-$ events with $\Delta\varphi > 90^\circ$ between data and embedded MC after full selection. Data are represented by black points, while stacked MC predictions are drawn as histograms of different colors. Histogram from each MC process has been normalised according to prescription in the text. Vertical error bars represent statistical uncertainties, horizontal bars represent bin sizes.

is compared between the data and MC prediction. The angles θ^S_w in Eq. (10.11) denote the scattering angle components along the coordinate w for forward-scattered proton on side S. One can notice the part of distribution close to zero, with nearly perfectly collinear protons. The data is well described by MC, which would unlikely be the case without the contribution from the red histogram representing MB+elastic background. An interesting observation related to this background contribution is that almost all MB+elastic events in the final plots originate from the Central Diffraction process, with the forward protons outside of RP acceptance - non-diffractive events do not pass tight CEP event selection.

In the second step the CD MC was normalised. It was scaled to have the same integral as the data (minus MB+elastic MC in $\Delta\varphi > 90^\circ$ sub-sample) in the range of $p_{\mathrm{T}}^{\mathrm{miss}} > 150$ MeV, where no exclusive signal is expected.

In the last step the exclusive $\pi^+\pi^-$ MC was normalised. It was scaled to have the same integral as the data (minus all considered non-exclusive backgrounds) in the range of $p_{\mathrm{T}}^{\mathrm{miss}} < 75$ MeV, where exclusive signal is dominant. The results of this procedure for the distribution of $p_{\mathrm{T}}^{\mathrm{miss}}$ are given in Figs.10.11 and 10.12. Joint distribution for each quantity - without differentiation with respect to $\Delta\varphi$ - was obtained by adding corresponding event counts from the two $\Delta\varphi$ ranges.

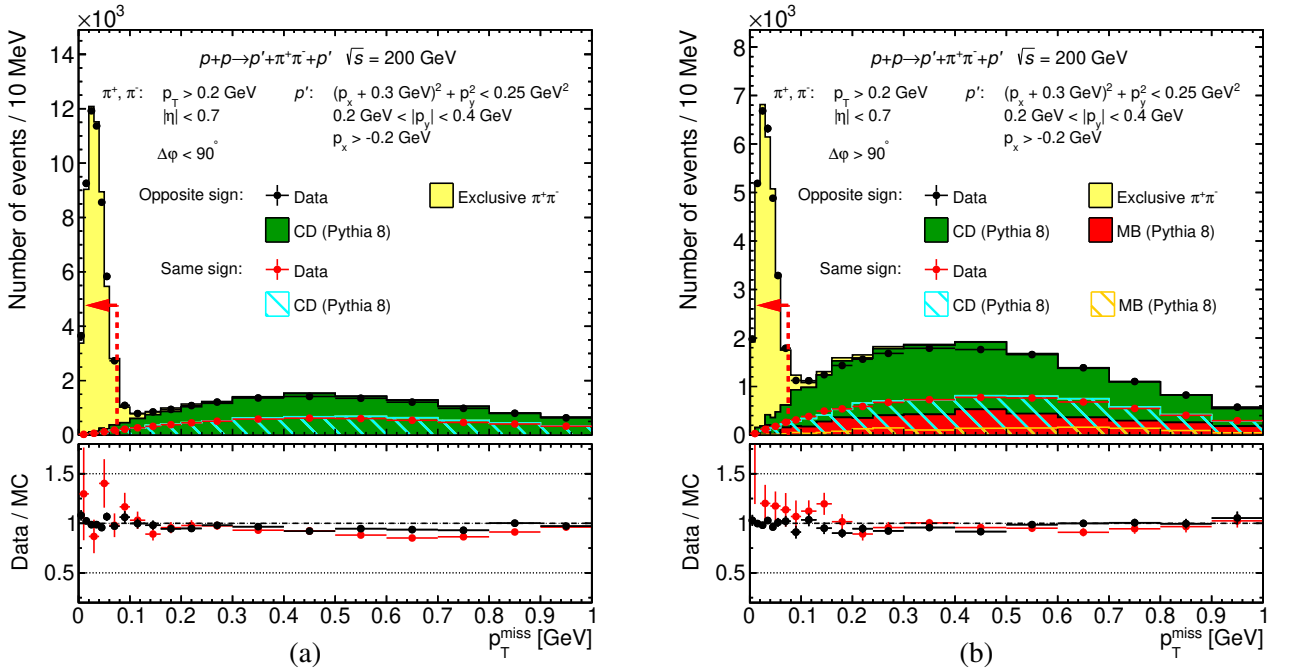

Figure 10.11: Comparison of $p_{\mathrm{T}}^{\mathrm{miss}}$ distributions for CEP of $\pi^+\pi^-$ pairs in two ranges of $\Delta\varphi$: (a) $\Delta\varphi < 90^\circ$ and (b) $\Delta\varphi > 90^\circ$, between data and MC after applying all selection cuts, but the cut on the plotted quantity. In addition to the signal channel (opposite-sign particles) also the backgrounds from the same-sign pairs are shown. Data are represented by black (opposite-sign) or red (same-sign) points, while stacked MC predictions are drawn as filled (opposite-sign) or hatched (same-sign) histograms of different colors. Histogram from each MC process has been normalised according to prescription in the text. Vertical error bars represent statistical uncertainties, horizontal bars represent bin sizes. Signal selection cut SC9 is marked with dashed red lines and arrows.

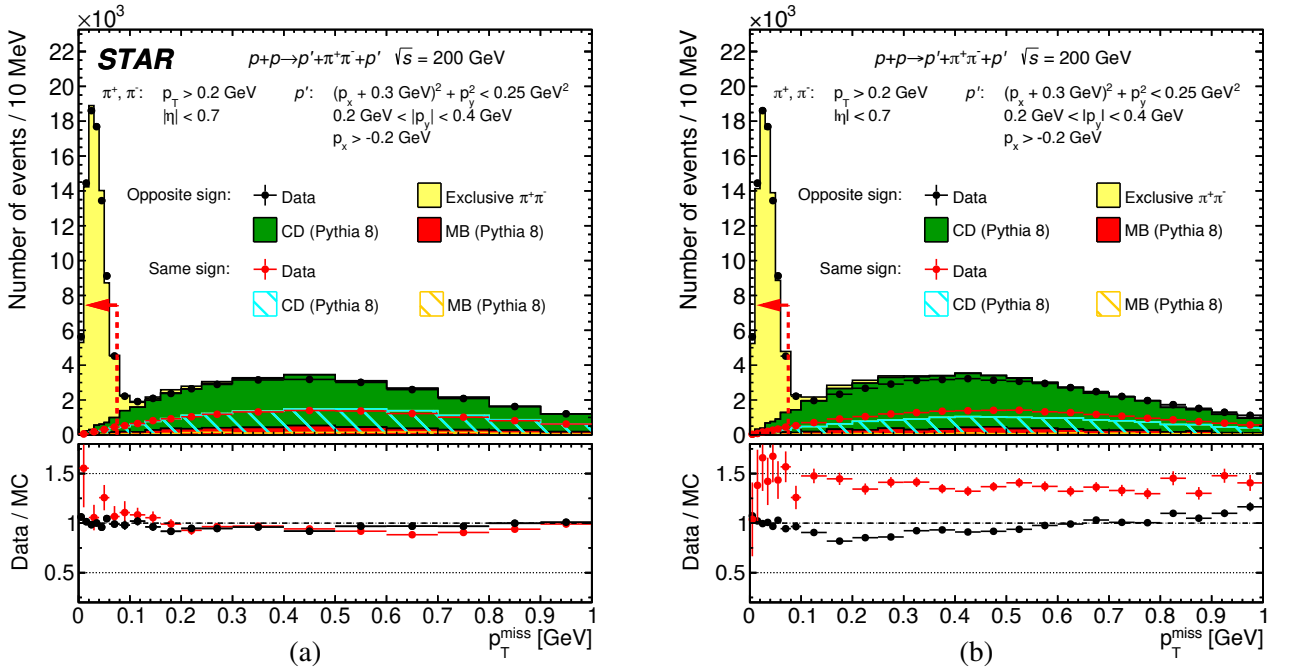

Figure 10.12: Comparison of $p_{\mathrm{T}}^{\mathrm{miss}}$ distributions for CEP of $\pi^+\pi^-$ pairs for the merged $\Delta\varphi$ intervals, and for Pythia MC (a) without and (b) with the events containing only the $\pi^+\pi^-$ pair and a neutral particle(s). Significant inconsistency between data and MC in the ratio of opposite-sign to same-sign events is demonstrated if such events are not rejected from MC predictions.

As can be observed in the comparison plots, presented data are generally well described by MC. In the case of Δz_{vtx}, some small disagreements in the position and width of the simulated signal peak can be noticed, most probably arising from slightly underestimated timing resolution of the RP trigger counters in the simulation. Distribution of $p_{\mathrm{T}}^{\mathrm{miss}}$ is very well described, for both signal and control range. The ratio of the number of the opposite-sign pairs to the number of the same-sign pairs is compatible between data and MC, which was possible to achieve by rejecting in Pythia contributions from events with the central state consisting from two opposite-sign pions and at least one neutral particle. Such events by definition can constitute only to the non-exclusive opposite-sign background. We demonstrate in Fig. 10.12b that if these events are preserved, Pythia MC cannot describe data in the background-dominating region (large $p_{\mathrm{T}}^{\mathrm{miss}}$).

11. Corrections

In this chapter the methodology of extracting hadron-level cross sections from the data is described. Derivations of the relevant acceptances and efficiencies are presented, together with the technical details of the correction procedure. Closure tests performed on MC samples are presented at the end of the chapter, aimed to validate the whole correction procedure.

Wherever possible, a data-driven corrections were derived and applied. For the calculation of many efficiencies, the single particle MC was used instead of the CEP signal MC. It was motivated by, firstly, low (about 10%) overall efficiency of reconstruction of the full CEP event and, secondly, lack of MC generator which would describe the data, hence introducing a need for event re-weighting. In such case enormous number of MC events would be needed to reduce statistical uncertainties of the efficiencies to an acceptably low level.

11.1 Trigger efficiency

11.1.1 TOF trigger

The efficiency of the trigger part related to the TOF subsystem, $\varepsilon^{\text{trig}}_{\text{TOF}}$, was obtained from the zero-bias data. Events with exactly one TOF vertex (cut SC1), two primary, good quality, TOF-matched TPC tracks (cuts SC3.1, SC3.4) and maximally three TOF clusters (cut SC7) were used to calculate the efficiency, defined as the probability of having at least two TOF hits at the trigger level in the selected events (as it was required in the trigger logic):

$$\varepsilon^{\text{trig}}_{\text{TOF}} = \frac{\#\text{events with} \geq 2 \text{ L0 TOF multiplicity and 1 TOF vtx and 2 TOF trks and} \leq 3 \text{ TOF cltrs}}{\#\text{events with 1 TOF vtx and 2 TOF trks and} \leq 3 \text{ TOF cltrs}} \tag{11.1}$$

It has been verified, that the efficiency does not depend on the transverse momenta of the two tracks. In Fig. 11.1, the TOF trigger efficiency as a function of the lower p_{T} of the two TOF-matched tracks is

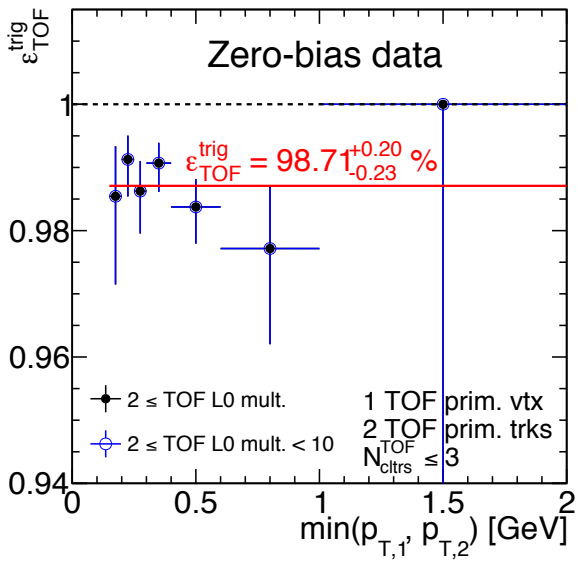

Figure 11.1: The trigger efficiency of the TOF subsystem, as a function of the lower p_{T} of the two TOF-matched tracks. Black points denote efficiency of requirement of at least 2 online TOF hits, while open blue circles represent efficiency with added upper multiplicity limit (< 10). These efficiencies are identical therefore the same efficiency (98.7%, solid red line) is used as a correction factor for all analysed events.

shown. Data points are consistent with a constant value, therefore a single number for this efficiency is used, equal to 98.7%. It is important to account for the fact, that at some point during the data-taking period an upper limit (< 10) on L0 TOF multiplicity was imposed. As one case see from the Fig. 11.1, this upper limit does not influence the TOF trigger efficiency, in the data sample used in this analysis (due to offline cut SC7. Therefore, the same value of the efficiency is used for the entire dataset.

11.1.2 BBC-small and ZDC veto

In the logic of the RP_CPT2 trigger bit, a veto on the signals in BBC-small and ZDC detectors on both sides of STAR was implemented. Common efficiency of the online and offline vetoes, which is used in the final correction procedure, is presented in. Sec. 11.3.4. However, to illustrate the effect of just the online vetoes in BBC-small and ZDCs, the efficiency of joint BBC-small and ZDC veto as a function of the instantaneous luminosity calculated from the zero-bias data is shown in Fig. 11.2. Efficiency calculation method is analogous to that explained in Sec. 11.3.4.

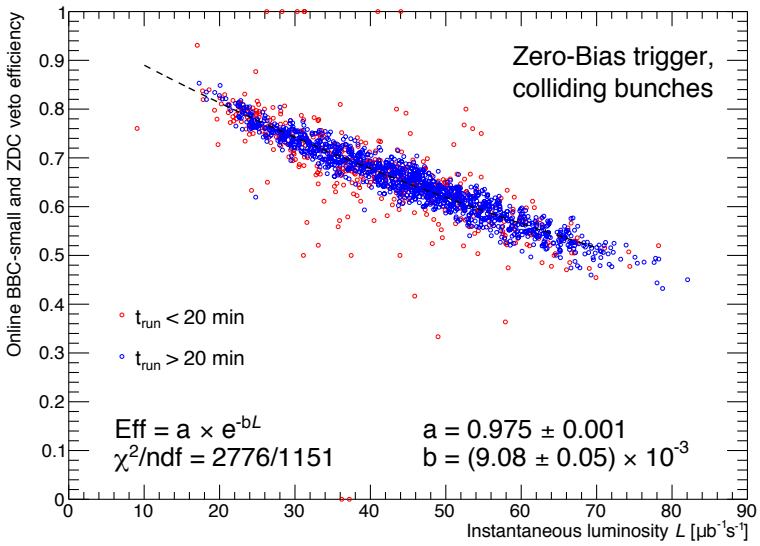

Figure 11.2: Overall efficiency of the online BBC-small and ZDC veto as a function of instantaneous luminosity. Red and blue points represent runs lasting for less and more than 20 minutes, respectively. Black dotted line represents the result of the fit of an exponential function to blue points, with best-fit parameters provided in the plot.

11.1.3 RP trigger

It was verified earlier [146], that the trigger efficiency of a single RP station is close to 100%. However, logic of the RP_CPT2 trigger includes a veto on the simultaneous trigger signal in RP detectors above and below the beamline on the same side of the IP. Probability that secondaries produced due to interaction with dead material (DM), by the forward-scattered proton, which was successfully triggered and reconstructed, trigger a signal in the other RP branch on the same side, $\mathcal{P}^{\text{side}}_{\text{DM veto}}$, can be obtained from the forward-scattered protons (signal) MC embedded into zero-bias data. It was calculated as a probability that a MC-trigger signal is present in the branch on given side other than East and West branches where primary forward-scattered protons are expected from their initial momenta, under condition that these East and West branches detect a MC-trigger signal and there is no veto due to

simultaneous ET&IT trigger bits in the overlayed data (no pile-up veto). The MC-trigger is understood as the MC signal event triggered solely based on the information from the simulated event, with no use of any information from the real data event used for embedding.

The probability $\mathcal{P}^{\text{side}}_{\text{DM veto}}$ was obtained using the following procedure:

1. No simultaneous ET&IT trigger bits were allowed in the data of an event that simulated signal was embedded into.
2. It was verified, if the (true) forward-scattered protons from the signal MC, which were expected to reach any of the RP stations (based on their p_y momentum component) gave the MC-trigger signal in that RP branch. In the following, these events are referred to as *set A*.
3. Events with the MC-trigger signal in a RP branch on the same side but other than the branch with MC-trigger signal expected based on the true forward-scattered proton constitute *set B*.
4. The ratio of the number of events in the *set B* to that in the *set A* is equal to the probability sought:

$$\mathcal{P}^{\text{side}}_{\text{DM veto}}(p_x, p_y, z_{\text{vtx}}) = \frac{N_B(p_x, p_y, z_{\text{vtx}})}{N_A(p_x, p_y, z_{\text{vtx}})}. \tag{11.2}$$

Sample probability $\mathcal{P}^{\text{side}}_{\text{DM veto}}$ obtained using the above procedure is shown in Fig. 11.3.

The efficiency of the discussed trigger veto, which is finally used to correct the data, is equal to the complementary probability:

$$\epsilon^{\text{side}}_{\text{DM veto}} = 1 - \mathcal{P}^{\text{side}}_{\text{DM veto}}. \tag{11.3}$$

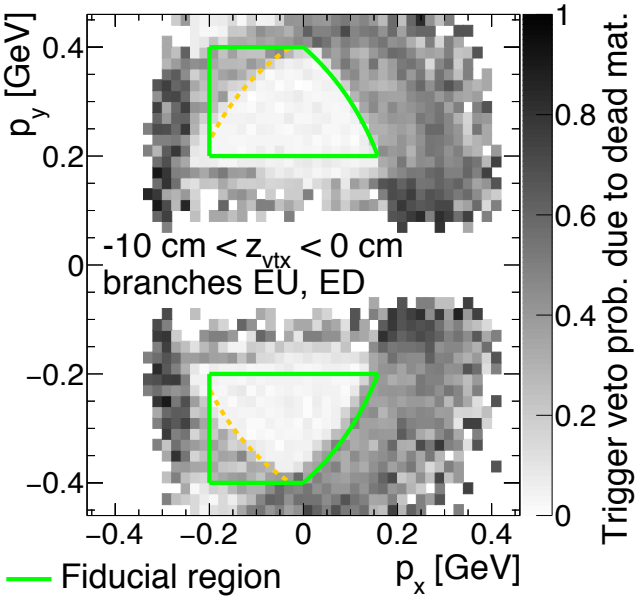

Figure 11.3: Sample probability of ET&IT trigger veto due to forward-scattered proton interaction with dead material. Results were obtained from forward proton MC simulation embedded into zero-bias data.

11.2 Tracks' reconstruction and selection efficiencies

11.2.1 TPC track acceptance, reconstruction and selection efficiency

Joint acceptance and efficiency of reconstruction of a track in the TPC, ϵ_{TPC}, is defined as the probability, that a charged particle from the primary interaction generates a signal in the TPC, which is reconstructed

as a global track, that satisfies all quality criteria (cuts SC3.4). To derive this efficiency the single particle STARsim MC embedded into zero-bias trigger data taken simultaneously with physics triggers was used. Technically, the common method used by STAR to obtain ϵ_{TPC} is the following [33]:

1. True-level primary particles of a given ID and charge are selected and are referred as *set A*.

2. For each particle in the *set A*, it is checked if there exists a global TPC track matched to this particle. All particles from the *set A*, which are associated with a global TPC track satisfying quality criteria (cut SC3.4) form *set B*.

3. The combined information on the TPC geometrical acceptance and the reconstruction efficiency is then calculated as the ratio of the number of particles in the *set B*, N_B, and the number of particles in the *set A*, N_A. The efficiency is obtained in bins of the true level quantities, p_{T}, η and z_{vtx}:

$$\epsilon_{\text{TPC}}\left(p_{\text{T}}, \eta, z_{\text{vtx}};\ \text{sign, ID}\right) = \frac{N_B(p_{\text{T}}, \eta, z_{\text{vtx}};\ \text{sign, ID})}{N_A(p_{\text{T}}, \eta, z_{\text{vtx}};\ \text{sign, ID})}. \tag{11.4}$$

Sample plots of the TPC efficiency for π^- are shown in Fig. 11.4.

According to the nominal matching definition used at STAR, a track is matched to a true-level particle if more than half of the hits used in the reconstruction of the track has been created by this

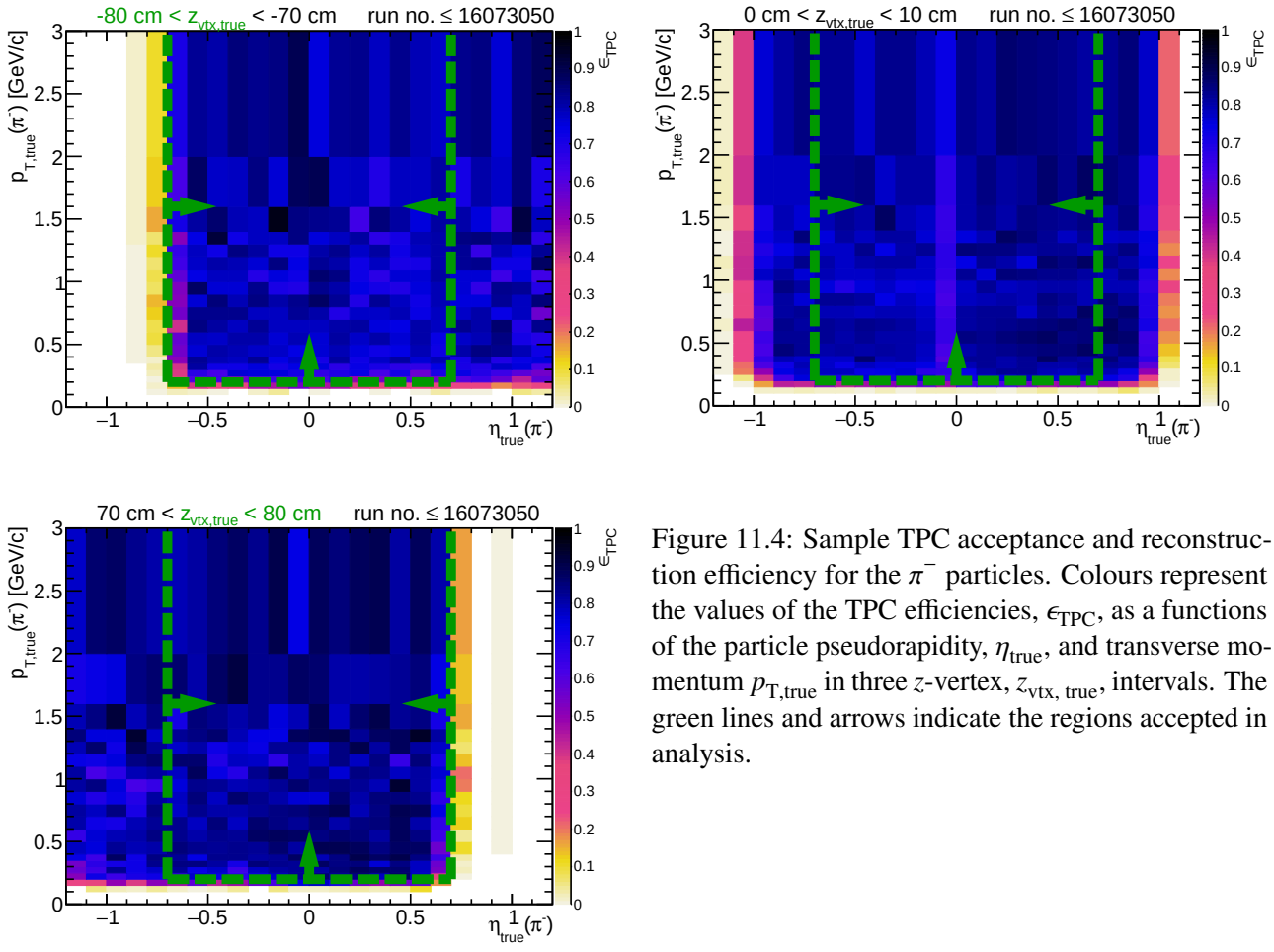

Figure 11.4: Sample TPC acceptance and reconstruction efficiency for the π^- particles. Colours represent the values of the TPC efficiencies, ϵ_{TPC}, as a functions of the particle pseudorapidity, η_{true}, and transverse momentum $p_{\text{T,true}}$ in three z-vertex, $z_{\text{vtx, true}}$, intervals. The green lines and arrows indicate the regions accepted in analysis.

particle. In the earlier analysis of diffractive events in Ref. [33], it was found, that this nominal matching definition results sometimes in matching two tracks to the same particle. Therefore, an additional requirement on the angular distance in the (η, ϕ) plane, between the track and the particle, $\delta(\eta, \phi)$, was introduced. It was defined through relation

$$\delta^2(\eta, \phi) = \left(\eta^{\text{true}} - \eta^{\text{reco}}\right)^2 + \left(\phi^{\text{true}} - \phi^{\text{reco}}\right)^2. \tag{11.5}$$

Distribution of $\delta^2(\eta, \phi)$ for pions is shown in Fig. 11.5a. Based on the distribution, a cut on $\delta^2(\eta, \phi) < 0.15^2$ was applied in the matching procedure in addition to the nominal STAR requirement on the number of hits. It has been checked that this cut value is also appropriate for kaons and (anti-)protons. The influence of making the matching requirement more rigorous on the TPC efficiency is shown in Figs. 11.5b, 11.5c and 11.5d, for different particle species, as a function of p_{T}. Differences between the two approaches are not very significant, except for the efficiency for $\bar{p}$ at very low p_{T}. The extended matching definition helped to reduce an artificial effect of large TPC reconstruction efficiency for anti-protons of low transverse momentum, resulting from the high sensitivity of $\bar{p}$ to the interactions with the inactive material (annihilation on the beam pipe).

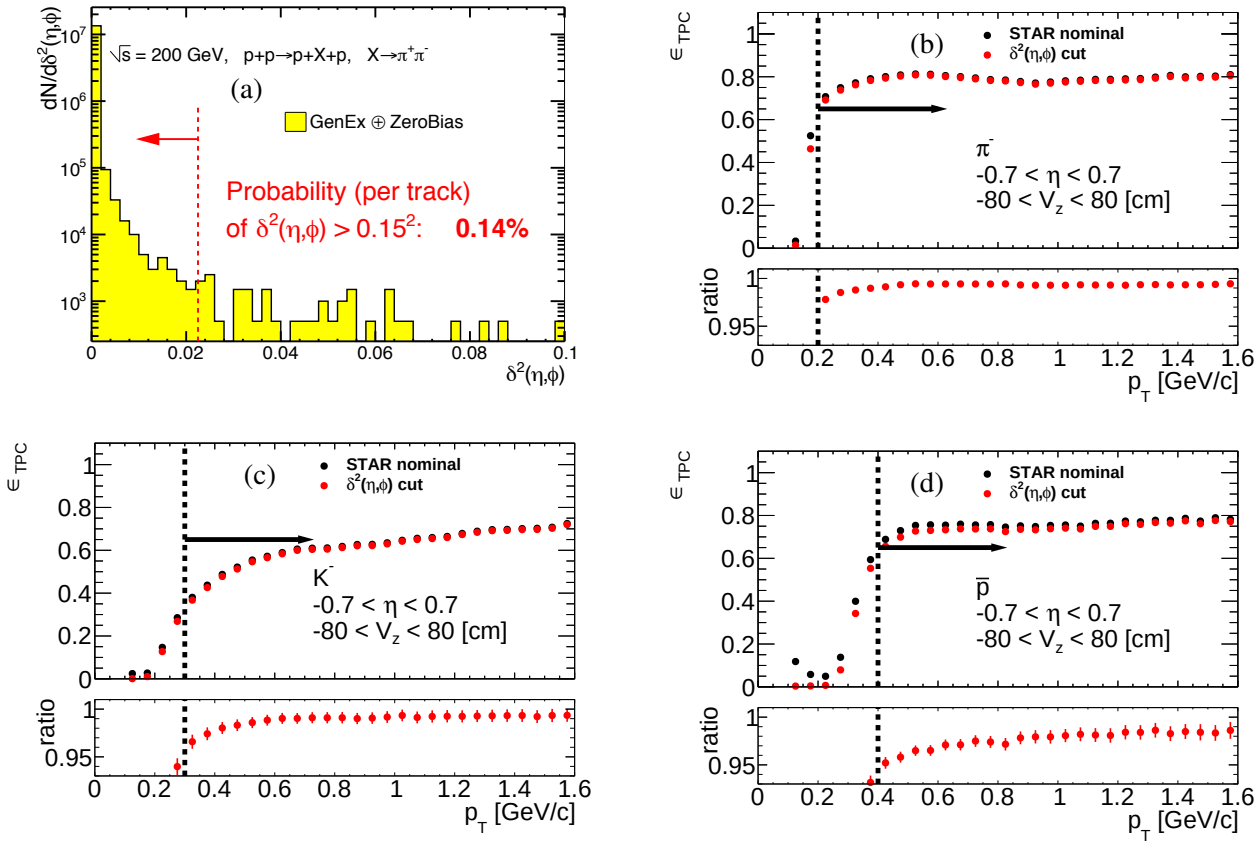

Figure 11.5: a Distribution of $\delta^2(\eta, \phi)$ for tracks matched with true-level pions (using standard matching) in CEP MC embedded into zero-bias triggers. Tracks were taken from events passing full CEP event selection, recognised as exclusive $\pi^+\pi^-$. The vertical red dashed line indicates the cut value of $0.15^2 \approx 0.023$, above which less than 0.14% of tracks is contained. (b,c,d) One-dimensional TPC acceptance and reconstruction efficiency as a function of p_T for π^-, K^- and $\bar{p}$ (courtesy of L. Fulek).

11.2.2 TOF acceptance, hit reconstruction and TPC track matching efficiency

Combined TOF acceptance, hit reconstruction efficiency and matching efficiency with TPC tracks, ϵ_{TOF}, is defined as the probability, that a global TPC track, which satisfies quality criteria (SC3.4) is matched with a hit in the TOF. This quantity is generally referred to as "TOF efficiency".

The efficiency is obtained in a very similar way to the TPC efficiency, also using the single particle STARsim MC embedded into the zero-bias data. From the sample denoted as *set B* in Sec. 11.2.1, a sub-sample of the TOF-matched tracks was extracted, constituting to the *set C* with N_C elements. The TOF efficiency is calculated as

$$\epsilon_{\text{TOF}}\left(p_{\text{T}}, \eta, z_{\text{vtx}};\ \text{sign, ID}\right) = \frac{N_C(p_{\text{T}}, \eta, z_{\text{vtx}};\ \text{sign, ID})}{N_B(p_{\text{T}}, \eta, z_{\text{vtx}};\ \text{sign, ID})}. \tag{11.6}$$

Sample plots of the TOF efficiency for π^- are shown in Fig. 11.6.

The efficiency plots, like the ones shown in Figs. 11.4 and 11.6, have been used to choose some of the selection criteria. The main idea was to maximise both the statistics available for the measurement and the phase-space accessible for the measured processes, keeping at the same time possibly large acceptance and reconstruction efficiencies of TPC and TOF in order to minimise systematic uncertainties. An obvious approach is to accept possibly wide range of longitudinal vertex positions. It was decided to set the cut on $|z_{\text{vtx}}| < 80$ cm (SC2). This cut selects 89% of the normal

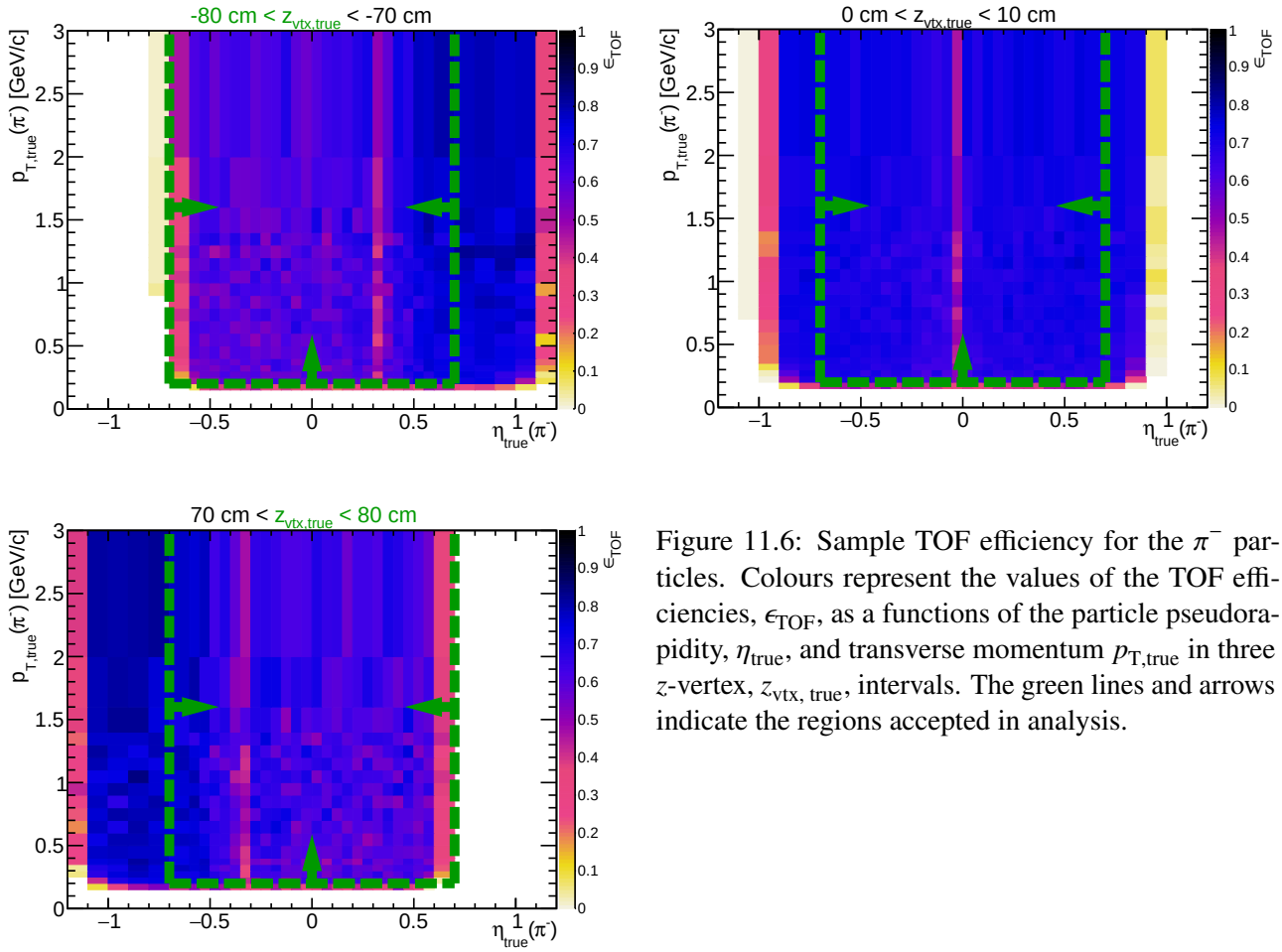

Figure 11.6: Sample TOF efficiency for the π^- particles. Colours represent the values of the TOF efficiencies, ϵ_{TOF}, as a functions of the particle pseudorapidity, η_{true}, and transverse momentum $p_{\text{T,true}}$ in three z-vertex, $z_{\text{vtx, true}}$, intervals. The green lines and arrows indicate the regions accepted in analysis.

distribution with mean at zero and the standard deviation of 50 cm, corresponding to the parameters of z_{vtx} observed in data. In order to maximise the phase-space of the measurements, the cuts on $p_{\text{T}} > 0.2$ GeV and $|\eta| < 0.7$ (SC3.3) were chosen. These cuts (SC2 and SC3.3) are shown in Figs. 11.4 and 11.6 as dashed green lines and arrows. The goal was to have high acceptance and efficiency for a rectangular (p_{T}, η) phase-space with limits independent from z_{vtx}.

To reduce potential bias of the TOF efficiency calculated from the MC simulation, originating from e.g. imperfect description of the real detector geometry and its response, it was decided to derive a correction to the MC-based TOF efficiency. For this purpose, a variation of the tag&probe method was developed and used. This method uses some specific feature of the distribution of a quantity describing two objects (whose trigger/reconstruction/identification/etc. efficiency is studied) which allows to quantify amount of these objects with satisfied/unsatisfied efficiency condition. The TOF efficiency was extracted using tag&probe method from the data and embedded MC, and the difference between the two results was used as the correction.

In the variation of the tag&probe method implemented in this study, a sample of event candidates for the process of CEP of $\pi^+\pi^-$ pairs, with both forward-scattered protons measured in the RP detectors and a TOF-matched TPC track (tag), were used. The missing transverse momentum, $p_{\text{T}}^{\text{miss}}$, was used to determine the signal event yield. In short, events with forward proton track on each side of STAR and with a TOF-matched primary TPC track (tag) were selected. The value of $p_{\text{T}}^{\text{miss}}$ was calculated for all remaining primary TPC tracks of opposite sign but coming from the same vertex as the tag. As the probe, the TPC track was chosen, for which the $p_{\text{T}}^{\text{miss}}$ was minimal. The probe was then checked whether it was matched to a TOF hit or not. The method is illustrated in Fig. 11.7. The TOF efficiency is defined as the ratio of the number of TOF-matched probes, $N_{\text{matched}}^{\text{probes}}$, to the number of all probes,

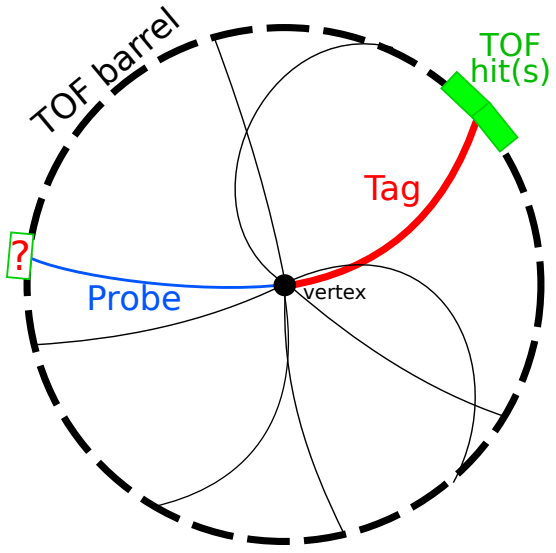

Figure 11.7: Sketch of the cross-sectional view of the central detector together with a CEP event with h^+h^- pair (tag and probe tracks shown in red and blue, respectively) and with off-time pile-up tracks (shown in grey).

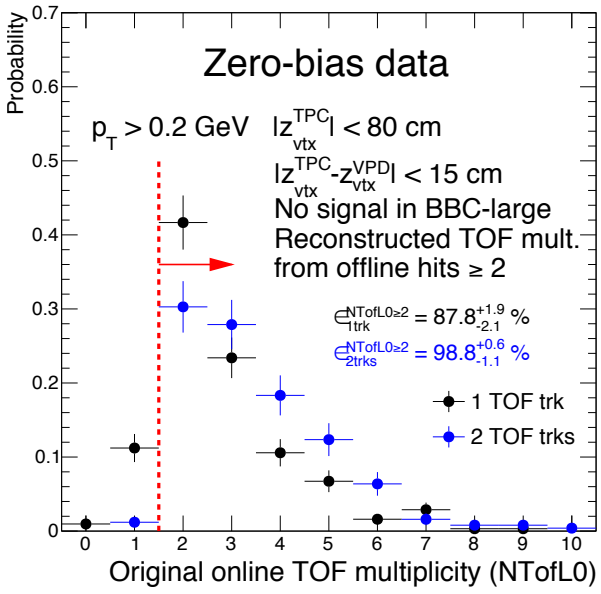

Figure 11.8: Trigger L0 TOF multiplicity, scaled by the total number of events, in events with exactly one (black) or exactly two (blue) primary TPC tracks matched offline with TOF hits, under condition of online TOF mult. reconstructed from offline hits ≥ 2.

$N_{\text{all}}^{\text{probes}}$:

$$\varepsilon^{\text{TOF}} = \frac{N_{\text{matched}}^{\text{probes}}}{N_{\text{all}}^{\text{probes}}} = \frac{N_{\text{matched}}^{\text{probes}}}{N_{\text{matched}}^{\text{probes}} + N_{\text{unmatched}}^{\text{probes}}} = \frac{2N_{\text{TT}}^{\text{events}} + N_{\text{TP}_m}^{\text{events}}}{2N_{\text{TT}}^{\text{events}} + N_{\text{TP}_m}^{\text{events}} + N_{\text{TP}_u}^{\text{events}}} \tag{11.7}$$

The efficiency in Eq. (11.7) is also expressed in terms of numbers of events fulfilling specific tag/probe relations, as explained below:

- $N_{\text{TT}}^{\text{events}}$ - both tracks satisfy the tag criterium - in such events there are also two probes, so the weight two in Eq. (11.7),
- $N_{\text{TP}_m}^{\text{events}}$ - one tag and one probe matched to a TOF hit,
- $N_{\text{TP}_u}^{\text{events}}$ - one tag and one probe not matched to a TOF hit.

The tag&probe procedure used to extract the TOF efficiency from the data and from the MC, is executed in the following steps:

1. Data which passed the trigger RP_CPT2, requiring at least 2 L0 TOF hits, are used in the following. Requirement of at least two TOF hits in the trigger, to ensure presence of at least two TPC tracks, does not in principle comply with the basic idea of the tag&probe method, but as explained in step 4, the tight selection of tags as tracks providing online multiplicity two and firing the TOF trigger allowed to use this method. In the case of MC, the GenEx $\pi^+\pi^-$ sample, embedded into zero-bias data from the runs corresponding to RP_CPT2 triggers, as well as Pythia CD sample for non-exclusive background, were used. The MC events were required to pass the same trigger conditions as the data, except for the online TOF multiplicity requirement, in order to avoid the trigger bias. The trigger bias present in the data was removed by applying the correction described below and shown in Fig. 11.8.
2. Events for this study were selected with nominal cuts used in CEP analysis, except cuts SC3, SC7, SC8 and SC9, which were either removed or modified as explained below.
3. For each event passing the selection criteria, primary TOF-matched TPC tracks of good quality (SC3.4, SC3.5), contained within the kinematic region of the measurement (SC3.3 with the p_{T} threshold lowered to 0.18 GeV to obtain efficiency also for p_{T} where it rapidly changes, and hence allow for more precise fit of the efficiency p_{T}-dependence) and compatible with the pion hypothesis based on dE/dx ($|n\sigma_{\text{pion}}| < 3$) were selected. If any TOF-matched track incompatible with the pion hypothesis was found, the event was removed from the analysis. Also, events with more than two TOF-matched tracks (not two-prong CEP events) were removed from the study.
4. Primary TOF-matched TPC tracks preselected in step 3 were set as tag candidates. In the data they were additionally required to be matched with the TOF hit belonging to a TOF cluster that is expected to provide multiplicity two at the trigger level L0 (to reduce the trigger bias). The following two steps, 5 and 6, were repeated for each track set as a tag.
5. From all primary TPC tracks of opposite sign to the tag preselected in step 3, the one which provides the lowest value of $p_{\text{T}}^{\text{miss}}$ is selected as the probe. In the case when no such primary TPC tracks are found, an event is not analysed further.

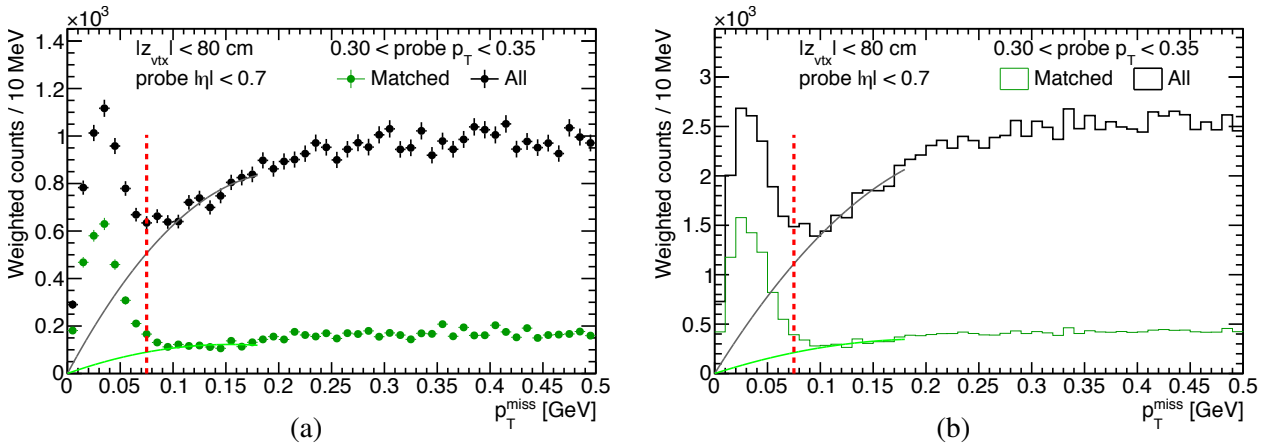

Figure 11.9: Sample distributions of missing transverse momentum, $p_{\mathrm{T}}^{\mathrm{miss}}$, of the p+tag+probe+p system in (a) data and (b) signal+background embedded MC for a selected probe's p_{T} bin. TOF-matched and all probes are shown as green and black histograms, respectively. The red dashed line represents the exclusivity cut ($p_{\mathrm{T}}^{\mathrm{miss}} < 75$ MeV). Background contributions were determined by fits of the 2nd order polynomials to the $p_{\mathrm{T}}^{\mathrm{miss}}$ distributions, performed in the background-dominated interval and extrapolated to the signal region.

6. Two-dimensional histograms of probe's η, p_{T} and z_{vtx} vs. $p_{\mathrm{T}}^{\mathrm{miss}}$ are filled, separately for all probes and for the probes matched with TOF hits. Each entry in the histogram is associated with a weight, taking into account the trigger and vertexing efficiency, obtained from Eq. (11.9) below.
7. In each bin of the quantity q ($\equiv \eta$, p_{T}, z_{vtx}), the distribution of $p_{\mathrm{T}}^{\mathrm{miss}}$ was fitted in the signal-free region and extrapolated to $p_{\mathrm{T}}^{\mathrm{miss}} < 75$ MeV in order to estimate the non-exclusive background as explained in Sec. 10.2.1. The final TOF efficiency, for each bin of the quantity q, was obtained as the ratio of the background-subtracted number of probes matched to TOF hits and the number of all probes in the signal region of $p_{\mathrm{T}}^{\mathrm{miss}} < 75$ MeV (as explained in the sample plots in Fig. 11.9):

$$\varepsilon^{\mathrm{TOF}}(q) = \frac{N_{\mathrm{matched}} - N_{\mathrm{matched}}^{\mathrm{bkgd}}}{N_{\mathrm{all}} - N_{\mathrm{all}}^{\mathrm{bkgd}}}. \tag{11.8}$$

The logic of the RP_CPT2 triggers, which were used in the tag&probe method, requires at least two TOF hits online. Since the system whose efficiency was studied, is also a part of the trigger, the tag should, in principle, be chosen as the track which was linked to two online TOF hits - to make sure that the tag satisfies the trigger condition and thus the probe is not biased by the trigger. Unfortunately, the TOF system works independently for the trigger and for the offline data stream (the readout electronics are independent), therefore there is no information about the connection between the TOF hits at trigger L0 and offline.

The above limitation has been overcome, using the concept of the TOF clusters (see Sec. 9.2.6) and a procedure to unfold/emulate the online TOF multiplicity from the offline hits[1]. Using this tool, the tags were defined as the tracks that were matched to a TOF hit associated with a TOF cluster that provided at least two emulated online TOF hits. It was verified using the zero-bias data, that by requiring the unfolded online number of TOF hits to be at least two, one can efficiently select events in which the true online (L0) number of TOF hits was also at least two. For this purpose, the

[1] According to properties the TOF trigger system provided by the TOF experts in the STAR experiment.

zero-bias data events with single primary TOF vertex and only one(two) TOF-matched TPC track(s), were selected. Also, lack of signal in large BBC tiles was required, similarly as in the physics analysis of CEP. To make sure that the single TOF-matched track comes from beam-beam interaction, signal in VPD detectors was required on both sides of the IP. The z-positions of the primary vertex reconstructed in TPC and reconstructed from the time difference in West and East VPDs were required to be closer than 15 cm. In Fig. 11.8, the distribution of the L0 TOF multiplicity is shown for such selected events. One can see, that the probability of the L0 TOF multiplicity to be greater than one, for a single TOF-matched track, $\epsilon_{1\text{trk}}^{\text{NTofL0}\geq 2}$, is high, about 88%. For events with two reconstructed TOF-matched tracks, the probability of L0 TOF multiplicity to be greater than one, $\epsilon_{2\text{trks}}^{\text{NTofL0}\geq 2}$, is about 99%. These efficiencies were used to obtain the event weights in Eq. (11.9).

The vertexing efficiency was an additional efficiency factor, which has had to be taken into account in this study. This efficiency for a single track depends on matching with the TOF hits, because tracks matched with TOF hits and tracks not matched with TOF hits were used differently in the vertex reconstruction procedure (see Sec. 6.1). Situation is different when both exclusive pion tracks are matched with TOF hits, comparing to the case when only one track is matched with TOF and the other is not. The vertexing efficiency is defined as the probability, that two global TPC tracks satisfying criteria SC3.4, matched with TOF and with true-level primary particles, form a common primary vertex. The vertexing efficiency will be discussed in more detail in Sec. 11.3.1, and here it is used for the case, when both tag and probe are matched with TOF hits, as a function of $|\Delta z_0|$ - the distance in z between DCA points of the tracks projected onto the beamline.

For events with only one of the two exclusively produced pions being matched with TOF, a different vertexing efficiency has to be used. In this case only the TOF-matched track was used in the vertex finding algorithm, while the other was added to the primary vertex later, if it satisfied certain

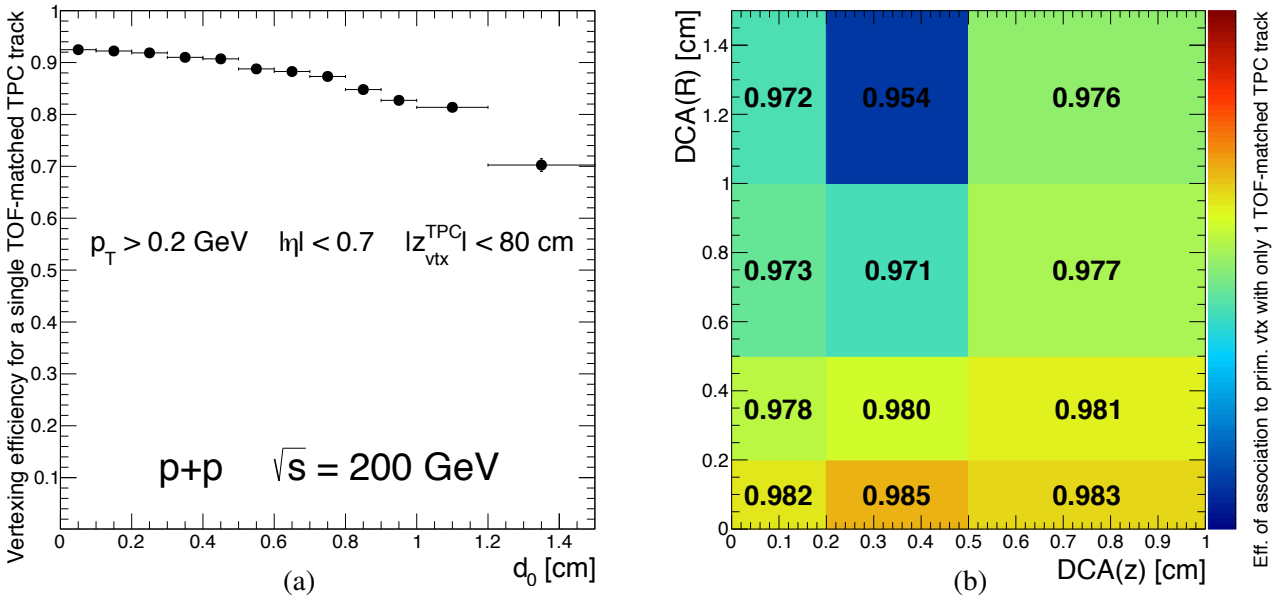

Figure 11.10: (a) Vertex finding efficiency, $\varepsilon_{\text{vtx}}^{\text{nTOF=1}}$, when using only a single TOF-matched TPC track, as a function of the d_0. (b) Efficiency of association of a TPC track not matched with TOF, with the vertex formed from single TOF-matched track, $\varepsilon_{\text{vtx}}^{\text{no-TOF}}$, as a function of radial and longitudinal DCA to the vertex. The tracks were required to be matched with true-level primary particles (pions) as well as to fulfil the cuts SC3.3, SC3.4 and SC3.5).

criteria [151]. Therefore, first the vertexing efficiency was calculated for the single TOF-matched track as a function of the transverse distance to the beamline $|d_0|$ (Fig. 11.10a), and next the efficiency of association of the TPC track not matched with TOF with the primary vertex made of single TOF-matched track was derived (Fig. 11.10b). The final weights of the probes entering the q vs. $p_{\mathrm{T}}^{\mathrm{miss}}$ histograms discussed above, were obtained as:

$$w = \begin{cases} \left[\epsilon_{\mathrm{1trk}}^{\mathrm{NTofL0\geq 2}} \times \varepsilon_{\mathrm{vtx}}^{\mathrm{nTOF=2}}\Big(|\Delta z_0|\Big)\right]^{-1} & \text{for TT, TP}_m \\ \left[\epsilon_{\mathrm{2trks}}^{\mathrm{NTofL0\geq 2}} \times \varepsilon_{\mathrm{vtx}}^{\mathrm{nTOF=1}}\Big(|d_0|\Big) \times \varepsilon_{\mathrm{vtx}}^{\mathrm{no\text{-}TOF}}\Big(\mathrm{DCA}(z), \mathrm{DCA}(R)\Big)\right]^{-1} & \text{for TP}_u \end{cases} . \tag{11.9}$$

The factors related to trigger efficiencies in Eq. (11.9) were applied only in case of real data; for the embedded MC simulations they were set to one. A sample histograms of the $p_{\mathrm{T}}^{\mathrm{miss}}$ distribution in the data and embedded MC filled with entries of weight w are shown in Fig. 11.9.

The dependence of the TOF efficiency on the track p_{T} was assumed to have the form:

$$\varepsilon^{\mathrm{TOF}}(p_{\mathrm{T}}) = \frac{1}{2} \cdot P_1 \cdot \left[\mathrm{Erf}\Big(\frac{p_{\mathrm{T}} - P_2}{P_3}\Big) + 1\right] \tag{11.10}$$

In Fig. 11.11 the final TOF efficiencies obtained with the tag&probe method are shown. From the figure one can see that for some bins of the considered variables, the data and MC differ significantly The comparison of the p_{T}-dependence of TOF efficiency in Fig. 11.11a suggests that the flattening of the efficiency is slower than MC predicts, and that maximum (high-p_{T}) efficiency is generally higher by 3-4% in the data compared to MC. In the η-dependence (Fig. 11.11b), one can see that there are some bins of η in which the agreement between MC and data is satisfactory, while in others the difference is large. The z_{vtx}-dependence (Fig. 11.11c) is in acceptable agreement between the data and MC.

The above observations led to perform the analysis of p_{T}-dependence of TOF efficiency in 4 bins of track pseudorapidity. The results are presented in Fig. 11.12. An additive correction to the TOF efficiency presented above (Fig. 11.6) is introduced:

$$\delta\varepsilon^{\mathrm{TOF}}(p_{\mathrm{T}}) = \varepsilon_{\mathrm{DATA}}^{\mathrm{TOF}}(p_{\mathrm{T}}) - \varepsilon_{\mathrm{MC}}^{\mathrm{TOF}}(p_{\mathrm{T}}), \tag{11.11}$$

where $\varepsilon_{\mathrm{DATA}}^{\mathrm{TOF}}(p_{\mathrm{T}})$ and $\varepsilon_{\mathrm{MC}}^{\mathrm{TOF}}(p_{\mathrm{T}})$ are of the form given by Eq. (11.10) for the data and MC, respectively. The same correction was used for positively and negatively charged particles.

Due to much lower data statistics and unavailable signal MC, a similar study could not have been performed for kaons and protons. We therefore applied the same correction $\delta\varepsilon^{\mathrm{TOF}}(p_{\mathrm{T}})$ to the TOF efficiency for $K^{\pm}$ and $p(\bar{p})$. The related systematic uncertainties are discussed in Sec. 12.3.

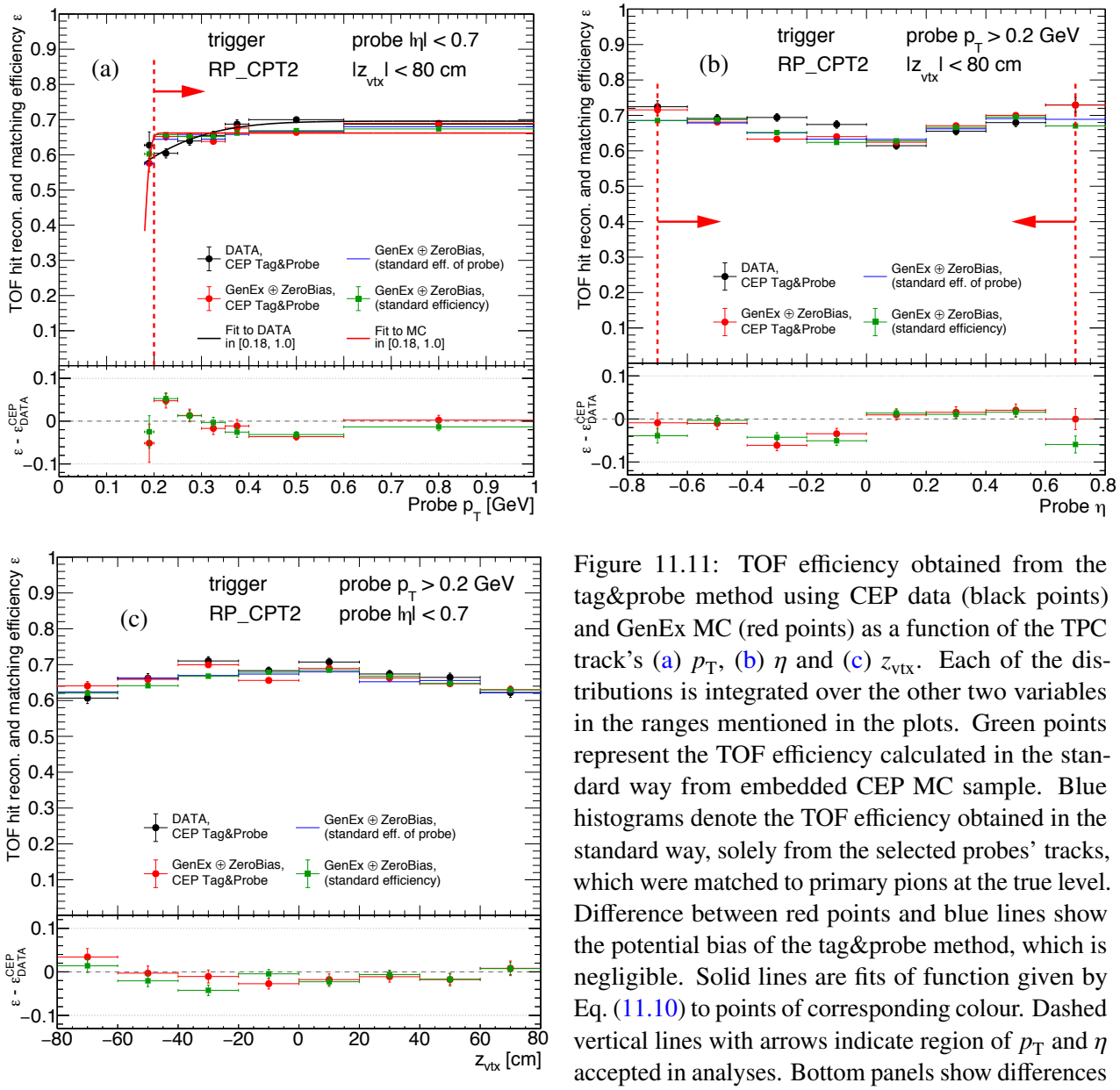

Figure 11.11: TOF efficiency obtained from the tag&probe method using CEP data (black points) and GenEx MC (red points) as a function of the TPC track's (a) p_{T}, (b) η and (c) z_{vtx}. Each of the distributions is integrated over the other two variables in the ranges mentioned in the plots. Green points represent the TOF efficiency calculated in the standard way from embedded CEP MC sample. Blue histograms denote the TOF efficiency obtained in the standard way, solely from the selected probes' tracks, which were matched to primary pions at the true level. Difference between red points and blue lines show the potential bias of the tag&probe method, which is negligible. Solid lines are fits of function given by Eq. (11.10) to points of corresponding colour. Dashed vertical lines with arrows indicate region of p_{T} and η accepted in analyses. Bottom panels show differences of the efficiencies in MC and data.

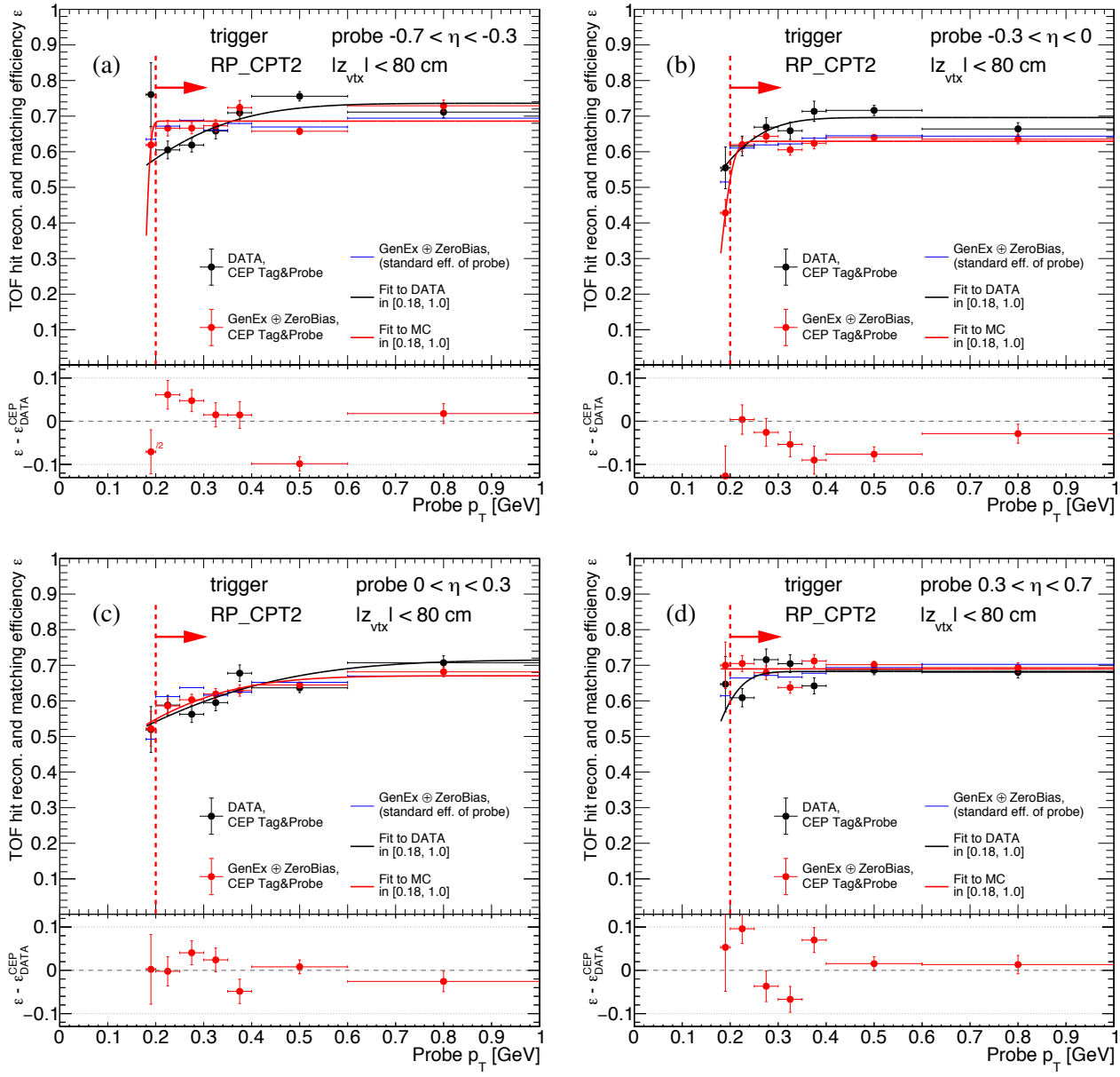

Figure 11.12: TOF efficiency obtained from the tag&probe method using CEP data (black points) and GenEx MC (red points) as a function of the probe p_{T} in four intervals of the probe's pseudorapidity. Blue histograms denote the TOF efficiency obtained in the standard way, solely from the selected probes' tracks, which were matched to primary pions at the true level. Difference between red points and blue lines show the potential bias of tag and probe method. Solid lines are fits of function given by Eq. (11.10) to points of corresponding colour. Dashed vertical lines with arrows indicate region of p_{T} and η accepted in analyses. Bottom panels show differences of the efficiencies in MC and data.

11.2.3 RP track acceptance, reconstruction and selection efficiency

The RPs acceptance and proton track's reconstruction efficiency was obtained by using the same embedded MC sample and technique, as discussed in Sec. 11.1.3 for obtaining the dead material related trigger veto.

The joint RP acceptance and track reconstruction efficiency for a given STAR side (West or East), $\epsilon_{\mathrm{RP}}^{\mathrm{side}}$, was calculated as the probability that a single good quality RP track (SC4.1, SC4.2), matched with true-level primary forward-scattered proton, is reconstructed on the given side in the branch expected based on sign of p_y of the proton, under condition that there is a trigger signal in that branch and there is no trigger signal in the other branch on the same side. Technically the $\epsilon_{\mathrm{RP}}^{\mathrm{side}}$ was obtained in the following procedure:

1. It was verified, if the (true) forward-scattered protons from the signal MC, which were expected to reach any of the RP detectors (based on their p_y momentum component) gave the MC-trigger signal in that RP branch. Additionally it was required, that there is no trigger signal in the other branch on the same side. In the following, these events are referred to as *set A*.

2. The nominal RP track selection algorithm was used to find a single good quality track (SC4.1, SC4.2) on the given side. If found, it was additionally required to be matched with the true primary proton. These events are referred to as *set B*.

3. The efficiency was then determined as the ratio of the numbers of events in the *set B* (N_B) to that in the *set A* (N_A):

$$\epsilon_{\mathrm{RP}}^{\mathrm{side}}(p_x, p_y, z_{\mathrm{vtx}}) = \varepsilon\left(\mathrm{RP}^{\mathrm{side}} \,\middle|\, \mathrm{TR}^{\mathrm{side}} \wedge\ !\mathrm{TR}_{\mathrm{other}}^{\mathrm{side}}\right) = \frac{N_B(p_x, p_y, z_{\mathrm{vtx}})}{N_A(p_x, p_y, z_{\mathrm{vtx}})} \tag{11.12}$$

Sample result of such of the RP track reconstruction efficiency is shown in Fig. 11.13.

The efficiency calculated above, by construction, includes the acceptance and the reconstruction and selection efficiencies, for a single proton. In a CEP event, there are two independent forward-scattered protons, which may be simultaneously not reconstructed or rejected by the selection algorithm due to e.g. elastic pile-up interaction providing additional good quality proton tracks on both sides of IP. One could, in principle, calculate five-dimensional efficiency for both forward protons (in variables $p_x^{\mathrm{E}}, p_y^{\mathrm{E}}, p_x^{\mathrm{W}}, p_y^{\mathrm{W}}$ and z_{vtx}) which would ultimately account for the simultaneous East and West RP detectors inefficiency, however this would require orders of magnitude larger statistics of MC to provide reasonably low statistical uncertainty of the efficiency. Instead, on top of the three-dimensional reconstruction and selection efficiencies for East and West RPs, a correlation between these efficiencies was calculated from embedded MC (Fig. 11.14), as defined in Eq. (D.2) of App. D. A need to account for this correlation was found based on the closure tests performed on the MC sample.

Study of systematic uncertainty of the RP track reconstruction efficiency revealed, that in some part of the fiducial area of RP detectors, marked with dashed yellow lines in Fig. 11.13, a correction needs to be applied to the efficiency obtained from the MC simulation. The details are described in Sec. 12.4.1.

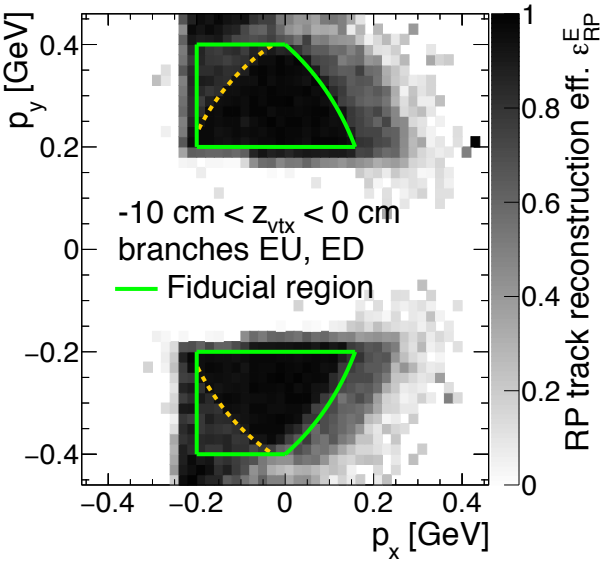

Figure 11.13: Sample RP track reconstruction efficiency in the single z-vertex bin on the East side. The efficiency was calculated using forward proton MC simulation embedded into the zero-bias data sample. Areas surrounded by green lines correspond to the fiducial region used in the measurement, while the dashed yellow lines mark the corner parts of the fiducial region where applying as additional data-driven efficiency correction was necessary needed.

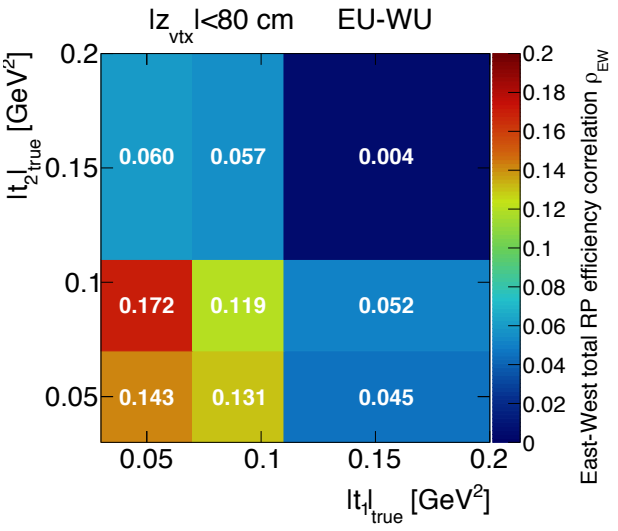

Figure 11.14: Sample correlation of joint RP track reconstruction and trigger efficiency (no dead material veto) between East and West RP detectors calculated from the CEP MC embedded into the zero-bias data. The result for protons reconstructed within the fiducial region marked with green lines on Fig. 11.13 and with $|z_{\text{vtx}}| < 80$ cm for the combination of the East and West upper branches is presented as functions of the squared four-momenta transferred in proton vertices.

11.3 Other reconstruction and selection efficiencies

11.3.1 TPC vertex reconstruction

The vertex reconstruction efficiency is defined as the probability that two global TPC tracks matched with TOF hits, both associated with true-level particles and both satisfying kinematic and quality selection criteria (SC3.3, SC3.4), form a common vertex, such that the DCA(R) and DCA(z) of the both tracks, calculated w.r.t. this vertex, fulfil the cut SC3.5.

This efficiency was calculated as a function of the longitudinal separation between two tracks (global helices) Δz_0. Illustration of this quantity is given in Fig. 11.15. It was considered a natural quantity to present the vertexing efficiency, since the closer to each other the helices are on the beamline, the more probable it is, that the two tracks will form a common primary vertex. It is in accordance with the way the vertexing algorithm works. The vertexing efficiency was calculated from the data in the following way:

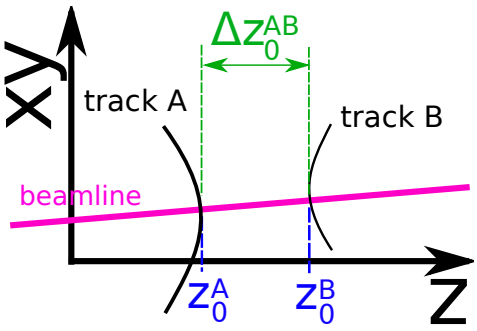

Figure 11.15: Sketch illustrating the definition of the longitudinal separation of two tracks (helices) Δz_0.

1. Data from RP_CPT2 trigger were used. Events were selected with nearly the same cuts as in

nominal CEP analysis (Sec. 9.1). The requirement of exactly one primary vertex with exactly two primary TOF tracks was dropped. Instead, analysis utilised only global TOF tracks - exactly two global TOF tracks were required (cut SC3.1 without primary track requirement), passing also cuts SC3.2-SC3.4. In this case the position of the vertex was reconstructed as

$$z_{\text{vtx}} = (z_0^+ + z_0^-)/2, \tag{11.13}$$

where z_0^+ and z_0^- are longitudinal impact parameters (z-coordinates of points of closest approach to the beamline) of positive and negative charge particle tracks, respectively. The vertex position was normally required to satisfy cut SC2. Events after full selection, classified as exclusive $\pi^+\pi^-$ candidates, formed *set A*.

2. The two global TOF tracks were checked if they have associated primary tracks, and if the the two tracks were assigned to the same primary vertex. If yes, the tracks were additionally subjected to cut SC3.5. Events passing described selection formed *set B*.

3. The efficiency was determined by the ratio of number of events in *set B* (N_B) and *set A* (N_A):

$$\epsilon_{\text{vtx}}(|\Delta z_0|) = \frac{N_B(|\Delta z_0|)}{N_A(|\Delta z_0|)}. \tag{11.14}$$

Distribution of $|\Delta z_0|$ between two CEP global track candidates after full selection is presented in Fig. 11.16. The vertexing efficiency obtained with described method is shown in Fig. 11.17. Solid green points represent efficiency calculated with the non-exclusive background preserved, while open black points represent efficiency with this background subtracted. Since the vertexing efficiency does

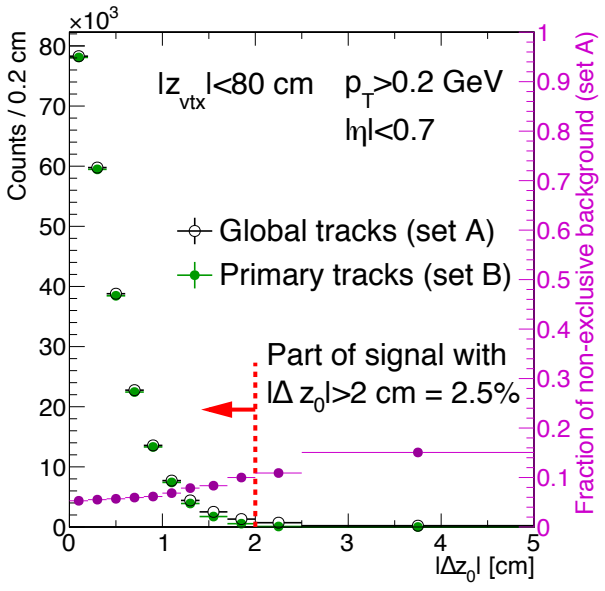

Figure 11.16: Distribution of Δz_0 between the two CEP-candidate global tracks, all (black) and forming a common vertex (green), together with fraction of non-exclusive background in black distribution as a function of $|\Delta z_0|$ (violet points). Dashed red line and arrow marks the cut $|\Delta z_0| < 2$ cm.

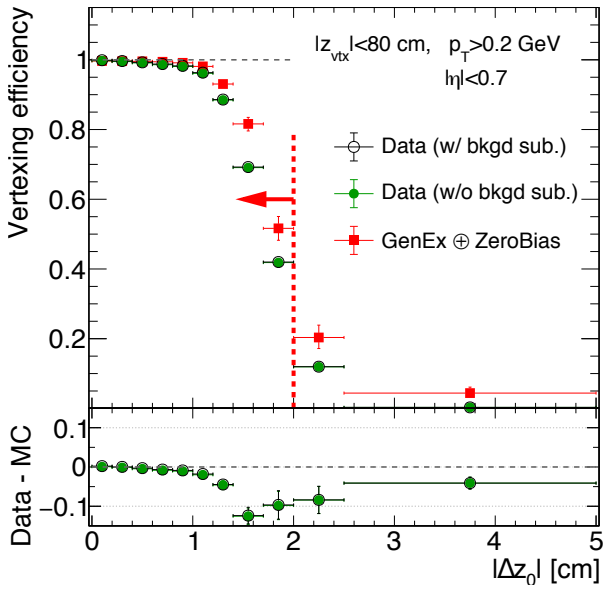

Figure 11.17: Vertexing efficiency calculated from data, with (black circles) and without (green points) the non-exclusive background subtraction, and from embedded MC (red points) as a function of $|\Delta z_0|$ between the two CEP-candidate global tracks.

not depend on the physics process and background is purely of physics origin, the black and green points should overlap. Such picture emerges from the presented comparison. The same efficiency was calculated using CEP MC embedded into zero-bias data and the result is shown in Fig. 11.17 with red points. There is very good agreement between vertexing efficiency in the data and embedded MC for $|\Delta z_0| < 1$ cm, where most ($\sim 80\%$) of the signal is present. The differences in high-$|\Delta z_0|$ tail are understood as a result of the imperfect description of the pointing resolution (here: the transverse resolution) of TPC tracks in STARsim. Although the pointing resolution was adjusted to gain more accurate description of the data by MC simulation as described in Sec. 8.3.2, this has not helped with the vertexing performed already at the level of event reconstruction from raw data (MC). Another reason could be different p_T (thus also d_0) spectrum of CEP tracks in the data and MC (GenEx).

Based on the width of the $|\Delta z_0|$, the background content as a function of $|\Delta z_0|$, and the value of ϵ_{vtx} as a function of $|\Delta z_0|$, it was decided to accept in analysis only tracks, which satisfy the cut $|\Delta z_0| < 2$ cm. This assures, that the vertexing efficiency does not drop below $\sim 30\%$, as well as it coincides with the primary tracks requirement of $|\text{DCA}(z)| < 1$ cm. In the correction procedure, the vertexing efficiency represented by the open black circles in Fig. 11.17 was used for data. To correct the MC distributions e.g. in the closure tests, the red points in Fig. 11.17 were used instead.

The cut on the maximum $|\Delta z_0| < 2$ *cm*, rejected also some small fraction of the signal events. To take into account this inefficiency, an additional efficiency correction was obtained from the data as a function of the lower p_T of two the tracks in the pair. This quantity was chosen because the distribution of Δz_0 gets narrower with increasing p_T of the tracks (with increasing invariant mass of the pair), and the largest contribution to the width of Δz_0 comes from the track with the lower p_T. The efficiency of cut $|\Delta z_0| < 2$ *cm* was calculated in the similar way to the vertexing efficiency, with a modification of the *set B* to include now only those global tracks from *set A*, which satisfy the requirement $|\Delta z_0| < 2$ cm (now called *set B′*):

$$\epsilon_{|\Delta z_0|} = \frac{N_{B'}(\min(p_T))}{N_A(\min(p_T))}. \tag{11.15}$$

Figure 11.18 presents the efficiency for $|\Delta z_0| < 2$ cm as a function of the lower p_T of the central tracks. One can see that the MC simulation (with helices adjusted to match the pointing resolution in data) reasonably well describe the data-driven efficiency.

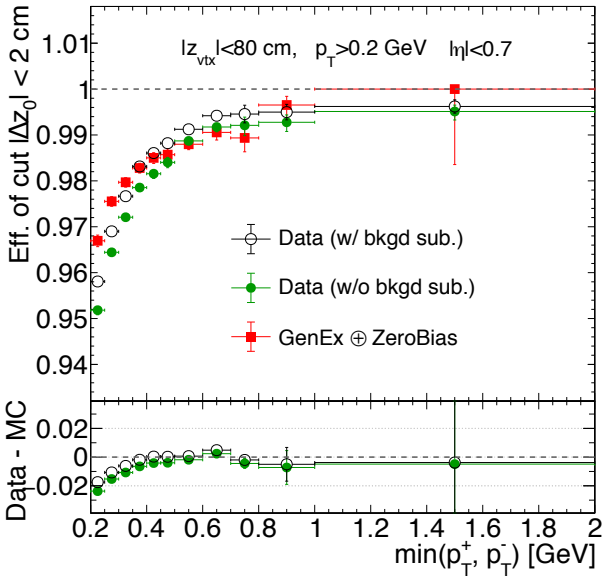

Figure 11.18: Efficiency of the cut on $|\Delta z_0|$ calculated from data, with (black circles) and without (green points) the non-exclusive background subtraction, and from embedded MC (red points) as a function of the lower p_T of the two global tracks in CEP event candidates.

11.3.2 TPC z-vertex cut (SC2)

Removing from analysis specific range of z-positions of primary vertices effectively reduced accepted luminosity with respect to that delivered by the collider. This loss of luminosity must be accounted for when calculating the cross sections. Assuming that the distribution of z_{vtx} is normal ($\mathcal{N}$), then the efficiency of the cut SC2 is equal to:

$$\epsilon_{z_{\text{vtx}}} = \frac{1}{N}\int_{z_{\text{vtx}}^{\text{min}}}^{z_{\text{vtx}}^{\text{max}}} \mathcal{N}(z_{\text{vtx}};\mu,\sigma)\,\mathrm{d}z_{\text{vtx}} = \frac{1}{2}\left[\text{Erf}\left(\frac{z_{\text{vtx}}^{\text{max}}-\mu}{\sqrt{2}\sigma}\right) - \text{Erf}\left(\frac{z_{\text{vtx}}^{\text{min}}-\mu}{\sqrt{2}\sigma}\right)\right], \tag{11.16}$$

where N is the number of all events, $z_{\text{vtx}}^{\text{min}}$ and $z_{\text{vtx}}^{\text{max}}$ are respectively minimum and maximum value of the longitudinal position of the vertex accepted in analysis (here: -80 cm and 80 cm), and the parameters μ and σ are, respectively, the average position and width of the z_{vtx} distribution in data: $\mu = \langle z_{\text{vtx}}\rangle$ and $\sigma = \sigma(z_{\text{vtx}})$.

As the parameters vary significantly between RHIC fills (see Fig. 11.20), they were obtained for each fill separately from Gaussian fits, see Fig. 11.19. The efficiency used in the correction procedure was calculated independently for each fill using presented values of $\langle z_{\text{vtx}}\rangle$ and $\sigma(z_{\text{vtx}})$. Typical value of this efficiency equals $(88 \pm 2)\%$.

11.3.3 TPC-RP z-vertex matching (SC5)

This cut was safely set to $3.5\sigma_{\Delta z_{\text{vtx}}}$, therefore its inefficiency is negligible.

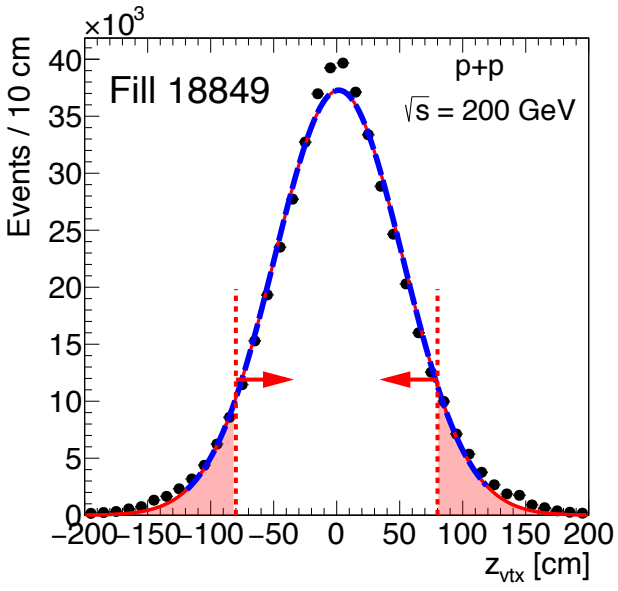

Figure 11.19: Sample distribution of z_{vtx} of single TOF vertices together with the fit of normal distribution (dashed blue) extended outside the range of the fit (solid red). The red area represents part of the distribution rejected by cut SC2 with the cut value marked with dashed red vertical lines and arrows.

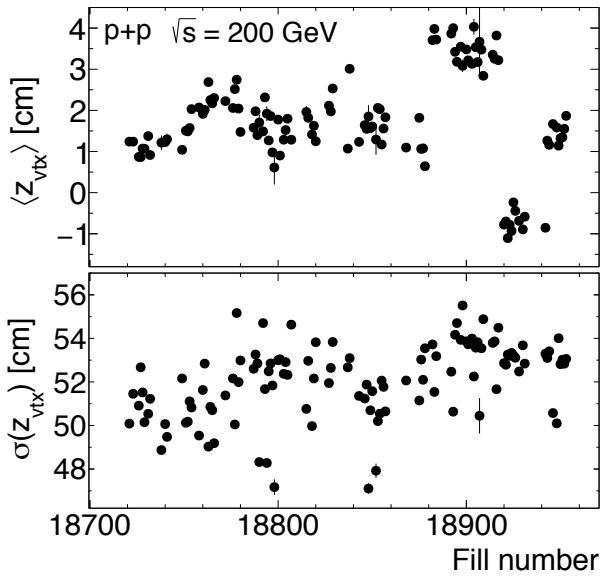

Figure 11.20: Mean (top panel) and width (bottom panel) parameters of the normal distribution, obtained from a fit of normal distribution to z_{vtx} distribution in a range $[-120\text{ cm}, 120\text{ cm}]$ for each RHIC fill, as a function of the fill number.

11.3.4 Primary vertex multiplicity limit (SC1), BBC-large veto (SC6), TOF clusters limit (SC7) and RP system veto due to pile-up

Combined efficiency of the online veto in BBC-small and ZDC (Sec. 11.1.2) and offline cuts (vetoes) on extra TPC-TOF vertices, extra TOF clusters, signal in BBC-large and simultaneous signal in upper and lower RP branches, was calculated using the zero-bias data. For each run, the efficiency was calculated as a fraction of events in which all above mentioned cuts were satisfied and also would be satisfied with the CEP event in given zero-bias event. One can transform this prescription to formula below:

$$\epsilon^{\text{veto}}_{b_E b_W} = \frac{\begin{array}{c}\text{\#events in the run without TOF vertices and without signal in BBC-S, BBC-L, ZDC,} \\ \text{RP branches other than } b_E,\ b_W, \text{ and with no more than 1 reconstructed TOF cluster}\end{array}}{\text{\#events in the run}} \tag{11.17}$$

In Fig. 11.21 this efficiency is presented as a function of the instantaneous luminosity delivered by the machine, for one of four combinations of East and West RP branches. Results for all remaining combinations are basically identical because the effect of ET&IT trigger veto in RPs is not dominant, as well as the trigger in all branches had similar acceptance. The data points were fitted with an exponential function (of the form contained in the plot) which reflects the fact that this efficiency should behave similar to the probability of lack of any interaction in the bunch crossing given by the Poisson distribution:

$$\text{Pois}(0;\mu) = \frac{\mu^0}{0!} \times e^{-\mu} = e^{-\mu}. \tag{11.18}$$

Comparison of the μ parameter in Eq. (11.18) with the fit parameters in Fig. 11.21 leads to approximate determination of the average inelastic interaction probability per bunch crossing equal 0.2 – 0.9. The

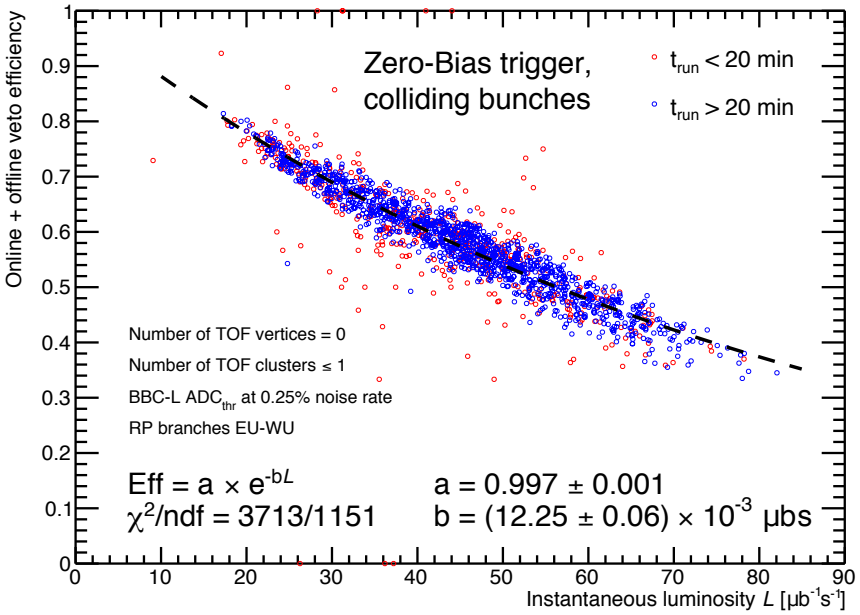

Figure 11.21: Combined efficiency for the online BBC-small, ZDC and ET&IT trigger veto, primary vertices limit (SC1), BBC-large veto (SC6) and TOF clusters limit (SC7) as a function of instantaneous luminosity for all possible combinations of East and West RP branches. Red and blue points represent runs lasting for less and more than 20 minutes, respectively. Black dotted line represents the fit of an exponential function to blue points.

result of the fit, $\epsilon^{\text{veto}}_{b_E b_W}(\mathcal{L})$, is finally used to correct measured data as described in Sec. 11.7.

Comparison of efficiencies in Fig. 11.21 with similar efficiency in Fig. 11.2 demonstrates that offline selection has much smaller impact on the loss of signal events than online selection. It has to be stressed, that the online vetoes were necessary, to set the trigger purity at a satisfactory level, as well as reduce prescale of the trigger.

11.3.5 Maximum number of TOF clusters (SC7)

Correction described in the previous section covers only the inefficiency related to the pile-up interactions. However, it is also possible, that a higher multiplicity of TOF clusters is generated in the exclusive h^+h^- signal event. Therefore, the upper limit on the number of TOF clusters equal to three introduces some inefficiency. To study this effect, a signal MC sample with no-pile-up (only STARsim simulation without embedding in the zero-bias data) was analysed.

In Fig. 11.22 the multiplicity of TOF clusters is shown for the signal MC. One can clearly see, that with cut on $N^{\text{TOF}}_{\text{cltrs}} \leq 3$ some part of the signal is rejected. The signal acceptance level of this cut as a function of the invariant of the $\pi^+\pi^-$ pair is shown on Fig. 11.23. No significant mass dependence is observed, and the value of the acceptance level obtained from the fit of a constant equals to 95.7%.

11.3.6 Particle identification (SC8)

Particle identification efficiency and the misidentification probability for the h^+h^- pairs in the final state were studied as functions of both particles' momenta. To provide small statistical uncertainties over the full p_{T} range accessible for the analysis in the data, a MC sample with a uniform distribution of particles over the momentum interval between 0.2 GeV and 3 GeV was used for this study. Particles'

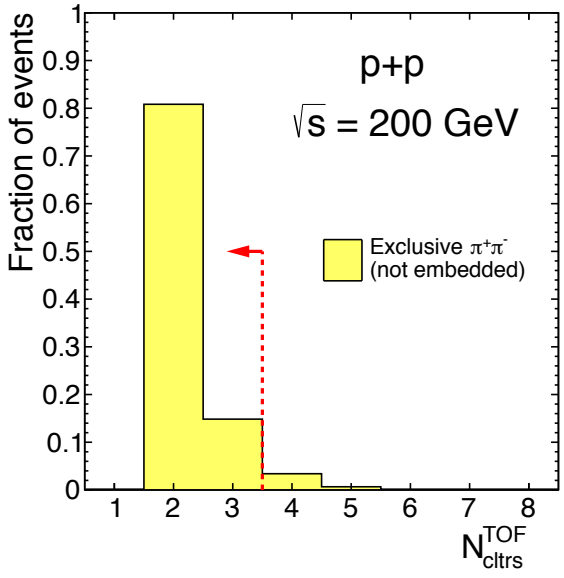

Figure 11.22: TOF clusters multiplicity, $N^{\text{TOF}}_{\text{cltrs}}$, in CEP $\pi^+\pi^-$ MS sample (without embedding). Red dashed line and arrow mark the limit on number of TOF clusters accepted in analysis.

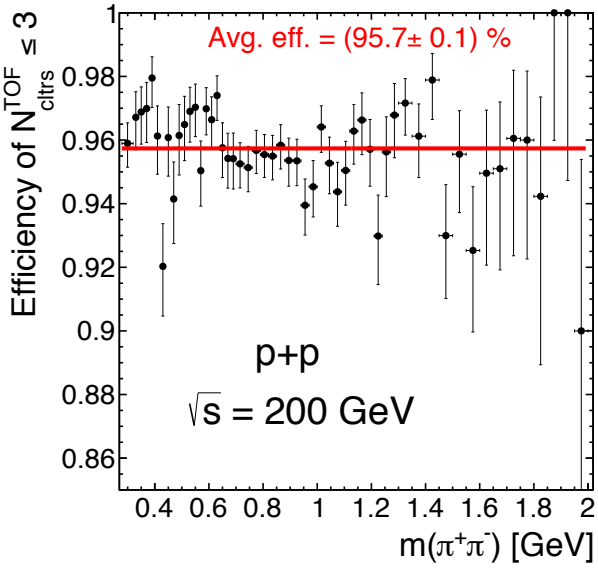

Figure 11.23: Efficiency of the cut $N^{\text{TOF}}_{\text{cltrs}} \leq 3$ as a function of the invariant mass of the $\pi^+\pi^-$, obtained from the MC of CEP of $\pi^+\pi^-$ pairs without embedding into zero-bias data. Red line shows the fit of a constant to all efficiency points.

momenta were considered as the best quantities to study pair identification because $n\sigma_X$ and m^2_{TOF} and their resolutions depend nearly solely on magnitude of momentum.

The identification efficiency ϵ^X and misidentification probability $\lambda^{X\to Y}$ were calculated for each particle species using the pair selection cuts SC8.1 and the following definitions:

$$\epsilon^X(p_{\mathrm{T}}^{\max}, p_{\mathrm{T}}^{\min}) = \frac{N^{\mathrm{reco}X}_{\mathrm{true}X}(p_{\mathrm{T}}^{\max}, p_{\mathrm{T}}^{\min})}{N_{\mathrm{true}X}(p_{\mathrm{T}}^{\max}, p_{\mathrm{T}}^{\min})}, \qquad \lambda^{X\to Y}(p_{\mathrm{T}}^{\max}, p_{\mathrm{T}}^{\min}) = \frac{N^{\mathrm{reco}Y}_{\mathrm{true}X}(p_{\mathrm{T}}^{\max}, p_{\mathrm{T}}^{\min})}{N_{\mathrm{true}X}(p_{\mathrm{T}}^{\max}, p_{\mathrm{T}}^{\min})}, \tag{11.19}$$

where the $N_{\mathrm{true}X}$ is the number of XX pairs at the true level, $N^{\mathrm{reco}X}_{\mathrm{true}X}$ is the number of XX pairs correctly reconstructed as the XX pairs, $N^{\mathrm{reco}Y}_{\mathrm{true}X}$ is the number of XX pairs misidentified as the YY pairs, and $p_{\mathrm{T}}^{\max}$ and $p_{\mathrm{T}}^{\min}$ are the higher and the lower transverse momenta of the particles in a pair, respectively. The results, shown in Fig. 11.24, clearly indicated necessity of adding a cut on the lower transverse

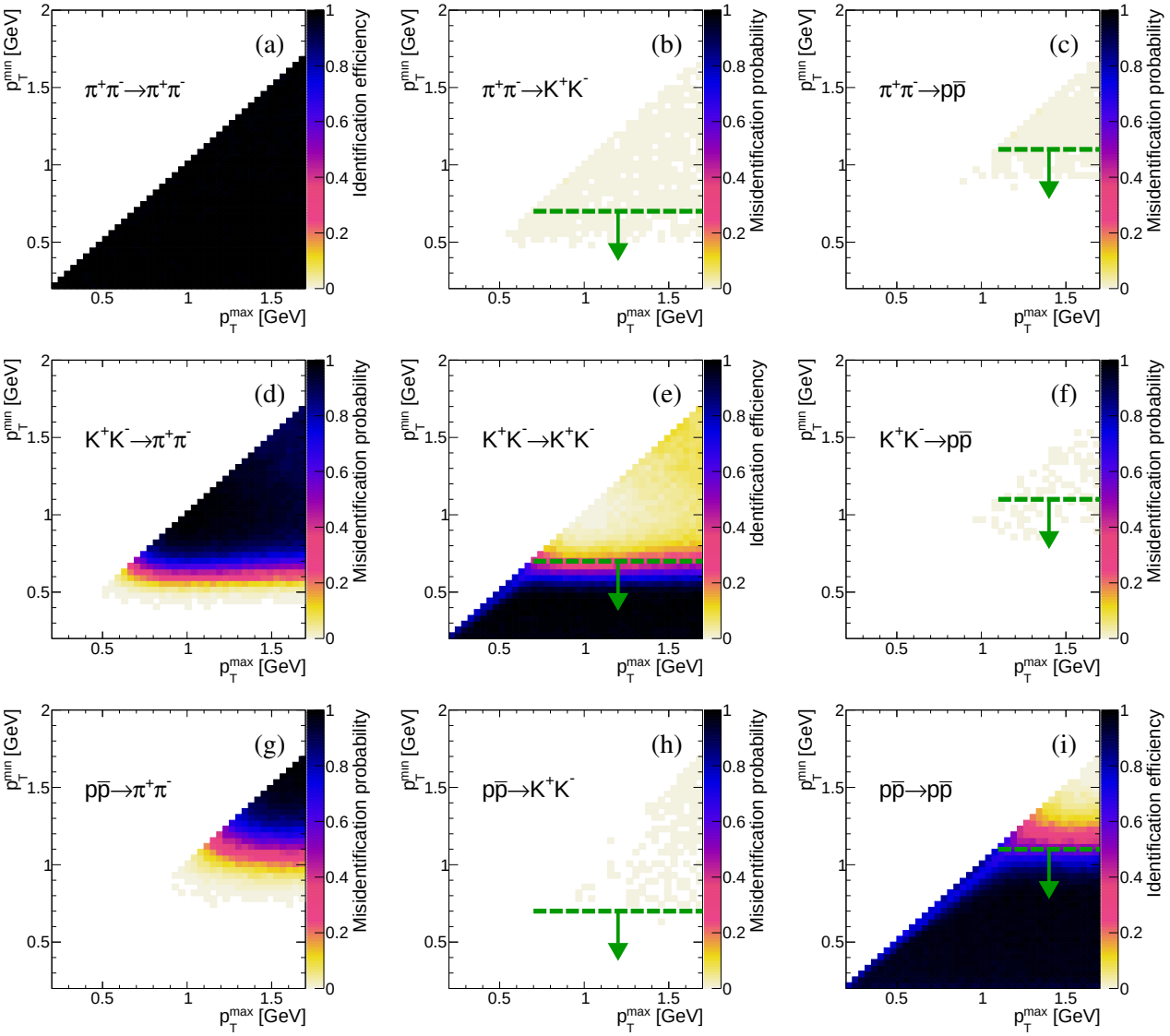

Figure 11.24: PID efficiency (a, e, i) and misidentification probability (b, c, d, f, g, h) as a function of tracks' transverse momenta for CEP of $\pi^+\pi^-$, K^+K^- and $p\bar{p}$ pairs. The results were obtained from the dedicated MC simulation described in Sec. 8.1.2. The green lines and arrows represent the cut value on the lower of the track's p_{T}'s for kaons and protons.

momentum of particle in the pair for K^+K^- and $p\bar{p}$ pairs, as above certain $p_{\mathrm{T}}^{\mathrm{min}}$ the identification efficiency drops to a very low level (< 10%). The cuts (SC8.2) are $p_{\mathrm{T}}^{\mathrm{min}} > 0.7$ GeV for kaons and $p_{\mathrm{T}}^{\mathrm{min}} > 1.1$ GeV for protons, indicated with dashed green lines and arrows.

11.3.7 Exclusivity cut on $p_{\mathrm{T}}^{\mathrm{miss}}$ (SC9)

The resolution of the total transverse momentum in the event is in general determined by the angular divergences of the proton beams. Based on known parameters of the beams (see Ref. [161]) expected divergence for a single beam amounts 180 µrad. In forward proton track reconstruction the direction of the incoming proton is assumed to be the same in each event (aligned with nominal z-axis), hence effectively the transverse components of reconstructed forward protons momenta are smeared by this amount. One can check the comparison of the collinearities of elastically scattered protons in the data and embedded MC (Fig. 12.26) to see a satisfactory agreement between the two with assumed MC angular divergence equal to 180 µrad. For 100 GeV beam such divergence results in a smearing of the transverse momentum components for (elastically) scattered protons equal to $100\ \mathrm{GeV} \times 180 \cdot 10^{-6} = 18$ MeV. Using this value to calculate the resolution of total $p_x(p_y)$ momentum of two forward protons one gets $\sqrt{2} \times 18$ MeV = 25.5 MeV. One can compare it with the output of fits to distributions of $p_x^{\mathrm{miss}}(p_y^{\mathrm{miss}})$ (Fig. 9.20) and find that indeed the angular beam divergence dominates the resolution of the total transverse momentum in CEP events.

There is, however, another ingredient to the total transverse momentum resolution, namely the momentum resolution of the central tracks, whose significance rises with increasing track's p_{T}. Most of CEP events are characterised by low invariant mass of the central tracks pair ($\lesssim 1.5$ GeV) which is inextricably linked with the low momentum of tracks ($\lesssim 0.7$ GeV), therefore an effect of $p_{\mathrm{T}}^{\mathrm{miss}}$ widening is barely visible in the missing momentum distribution integrated over mass (e.g. Fig. 9.20). Nevertheless, one can calculate the efficiency of the exclusivity cut as a function of the central tracks momenta to directly see this effect.

Physics model of the CEP process from GenEx was used in embedded signal MC, therefore there was no sufficient statistics (too low population of high-p_{T} tracks) to calculate the efficiency of $p_{\mathrm{T}}^{\mathrm{miss}}$ cut as a function of central tracks' momenta. In such case the efficiency of this cut was calculated using simplified MC method described below.

This study was performed using the phase space MC, in which momenta of the two central particles were generated from a uniform distribution. They were smeared with a Gaussian distribution, $\mathcal{N}(0, \sigma)$, where $\sigma = 6$ MeV if $p_{\mathrm{T}} < 0.3$ GeV or 2.4 MeV + 1.2% $\times\ p_{\mathrm{T}}$ if $p_{\mathrm{T}} > 0.3$ GeV, was obtained from the embedded MC sample. Next, the components p_x^{miss} and p_y^{miss} of the missing transverse momentum of an event were calculated using these smeared pions' momenta and the hadron level forward-scattered protons' momenta. Finally, both p_x^{miss} and p_y^{miss} were additionally modified using a Gaussian distribution with the parameters taken from Fig. 9.20 (top). The aim of this last step was effectively to apply the detector-like modifications to the forward-scattered protons. The efficiency of the exclusivity cut was obtained as:

$$\epsilon_{p_{\mathrm{T}}^{\mathrm{miss}}}(p^{\mathrm{max}}, p^{\mathrm{min}}) = \frac{N_{p_{\mathrm{T}}^{\mathrm{miss}}}(p^{\mathrm{max}}, p^{\mathrm{min}})}{N_{\mathrm{all}}(p^{\mathrm{max}}, p^{\mathrm{min}})}, \tag{11.20}$$

where N_{all} is the number of all generated CEP events and $N_{p_{\mathrm{T}}^{\mathrm{miss}}}$ is the number of events passing exclusivity cut SC9. The result is shown in Fig. 11.25a.

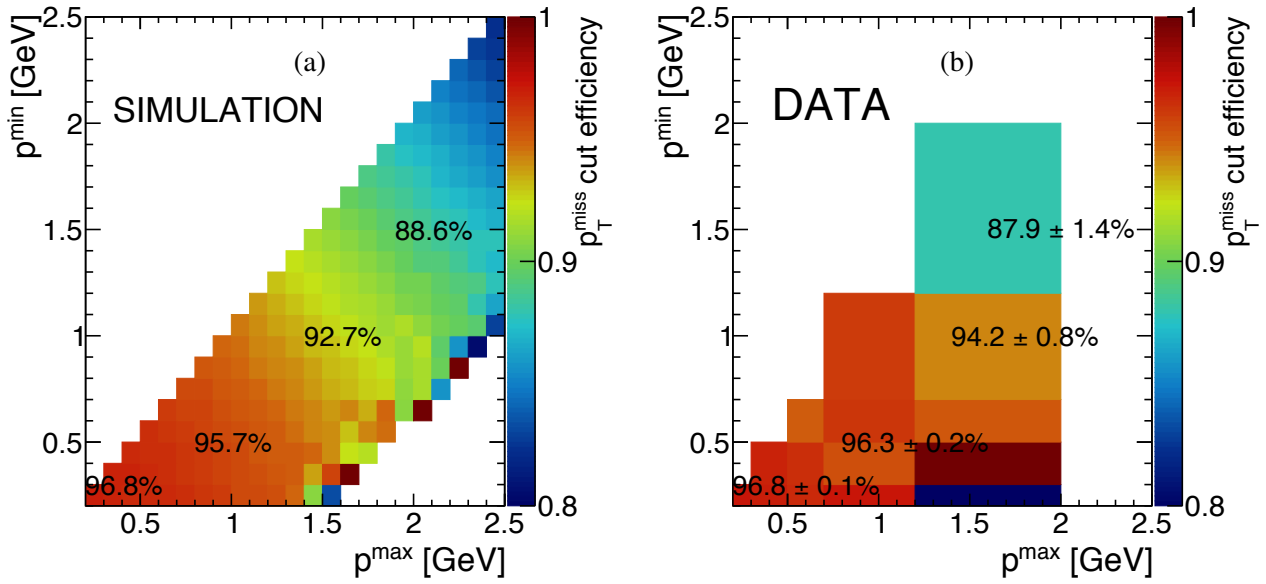

Figure 11.25: Efficiency of the $p_{\mathrm{T}}^{\mathrm{miss}}$ cut as a function of higher (x-axis) and lower (y-axis) momentum of the central tracks, calculated with (a) the MC method described in the text, and (b) the data-driven method. Efficiency in a few points of (p^{max}, p^{min}) space is printed on top of each of the plots. Lower right corners have no entries/low statistics due to kinematic constraints in the fiducial phase space (this region is not populated with events in the data). Binning for the data is significantly wider than for the MC simulation due to limited data statistics.

The exclusivity cut efficiency for the very low momentum tracks (low pair invariant mass) obtained from the above method (96.8%) agrees with the same efficiency obtained from the embedded MC sample (96.4%) for the same momenta range p^{max}, $p^{min} < 0.4$ GeV, what validates the above method. Another validation comes from the comparisons with the efficiency estimated using data-driven method. The same definition of efficiency was used (Eq. (11.20)), but $N_{p_{\mathrm{T}}^{\mathrm{miss}}}$ and N_{all} were estimated from the $p_{\mathrm{T}}^{\mathrm{miss}}$ distributions after all selection cuts except SC9, in bins of (p^{max}, p^{min}). The result for the data is shown in Fig. 11.25b. The efficiency for p^{max}, $p^{min} < 0.4$ GeV ((96.8 ± 0.1)%) perfectly agrees with the efficiency from the method using the phase space MC. Efficiencies for other selected bins also agree between data and simulation.

Clearly, the deterioration of the central track momentum resolution starts to play significant role in efficiency of $p_{\mathrm{T}}^{\mathrm{miss}}$ cut at about 1 GeV track momentum.

11.4 Particle energy loss

A need for the energy loss correction is a result of an assumption made at the level of TPC track reconstruction, that all tracks in the TPC represent charged pions. Therefore, for other particle species the reconstructed momentum is overestimated or underestimated, depending on the true particle identity (its mass). The correction was calculated [33] from single-particle MC sample as a function of reconstructed particle p_{T} in bins of z_{vtx} for all analysed particle species and both positive and negative charges. It was applied independently for each particle in the following procedure:

1. After central particles were identified (cut SC8) an absolute value of the particle transverse momentum correction ($\Delta p_{\mathrm{T}} = |p_{\mathrm{T}}^{\mathrm{meas}} - p_{\mathrm{T}}^{\mathrm{true}}|$) was read from the histogram corresponding to

reconstructed z_{vtx} and to assigned particle ID (example is shown in Fig. 11.26).

2. The momentum correction factor f_p^{corr} was calculated:

$$f_p^{\text{corr}} = \frac{p_{\text{T}}^{\text{meas}} + \Delta p_{\text{T}}}{p_{\text{T}}^{\text{meas}}}. \tag{11.21}$$

3. A new, corrected momentum, $\vec{p}^{\,corr}$, was assigned to the particle:

$$\vec{p}^{\,\text{corr}} = f_p^{\text{corr}} \cdot \vec{p}^{\,\text{meas}}. \tag{11.22}$$

In this way all three components of particle momentum are corrected so that the pseudorapidity of the particle remains unchanged.

This new momentum was further used in analysis, e.g. to determine $p_{\text{T}}^{\text{miss}}$ and calculate cross sections.

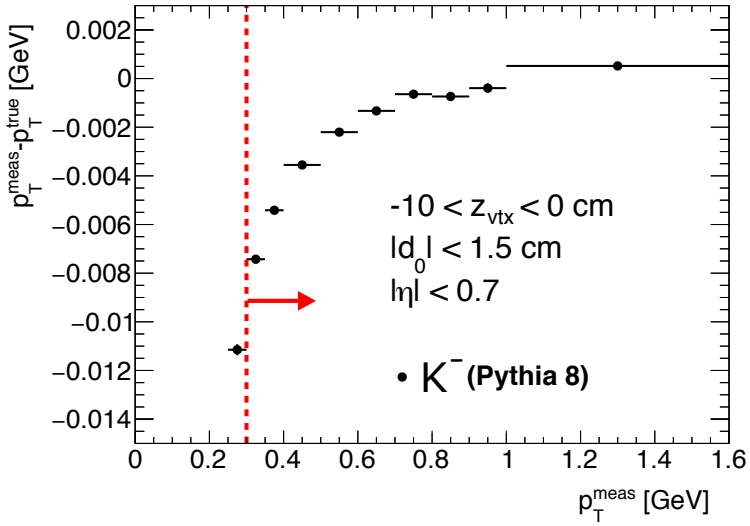

Figure 11.26: Sample energy loss correction $p_{\text{T}}^{\text{meas}} - p_{\text{T}}^{\text{true}}$ for K^- as a function of reconstructed transverse momentum $p_{\text{T}}^{\text{meas}}$ ($|\eta| < 0.7$) in the single z-vertex bin, $-10 < z_{\text{vtx}} < 0$ cm. Red line and arrow indicate region accepted in analyses. Figure courtesy of L. Fulek [33].

11.5 Fake tracks and migrations into/out of the fiducial region

Finite resolutions play a non-negligible role in the presented analysis. Smearing of reconstructed quantities with respect to their true value at the hadron level makes some tracks from outside of the fiducial phase space migrating/leaking into it, as well as some tracks from inside the fiducial region escaping from it.

The discussion below applies to both TPC and RP tracks. Corrections related to migrations and fake tracks were calculated using the following quantities:

- $\boldsymbol{N_{\text{reco}}}$ - number of tracks reconstructed in the fiducial region and matched to the true level particles,
- $\boldsymbol{N^{\text{in}}_{\text{migr.}}}$ - number of tracks reconstructed in the fiducial region and matched to the true level particles from outside of the fiducial region (at the hadron level),
- $\boldsymbol{N^{\text{out}}_{\text{migr.}}}$ - number of tracks reconstructed outside of the fiducial region and matched to the true level particles from the fiducial region (at the hadron level),

- N_{fakes} - number of tracks reconstructed inside the fiducial region and of momentum consistent with the momentum of one of the true level particles, but not matched with it.

All of the above numbers are obtained as functions of reconstructed quantities (TPC tracks: p_{T} and η, RP tracks: p_x and p_y), except $N^{\text{out}}_{\text{migr.}}$ for which true (hadron) level quantities are used. The migration and fake reconstruction probabilities are defined as:

$$f^{\text{in}}_{\text{migr.}} = \frac{N^{\text{in}}_{\text{migr.}}}{N_{\text{reco}}}, \qquad f^{\text{out}}_{\text{migr.}} = \frac{N^{\text{out}}_{\text{migr.}}}{N_{\text{reco}}}, \qquad f_{\text{fakes}} = \frac{N_{\text{fakes}}}{N_{\text{reco}}}. \tag{11.23}$$

The fraction of fake tracks, f_{fakes}, requires some more explanation. The necessary condition to claim a track being fake is that it is not matched with a true level primary particle. However, such tracks should typically have momentum significantly different from that of unmatched primary, therefore total momentum cut SC9 would not be satisfied and thus these tracks should not be subtracted. For this reason, an additional condition to assign a track as fake is that its reconstructed momentum is consistent with that of primary particle. In case of TPC tracks a cut on the angular distance between the track and the primary particle candidate $\delta(\eta, \phi) < 0.15$ was used (see Sec. 11.2.1). For the RP tracks a cut on the difference between true and reconstructed transverse momentum not greater than 100 MeV was used. Such value, somewhat arbitrary, was driven by the width of the distribution of the difference between the true and reconstructed transverse momentum components for matched tracks. In Figs. 11.27 and 11.28 distributions of quantities for matched and not matched tracks are presented, with magenta circles drawn on top marking the conditions used in fake track definitions. Systematic effects connected with the fake track definitions were not considered, as this effect is believed to be much smaller than most of the other systematic uncertainties.

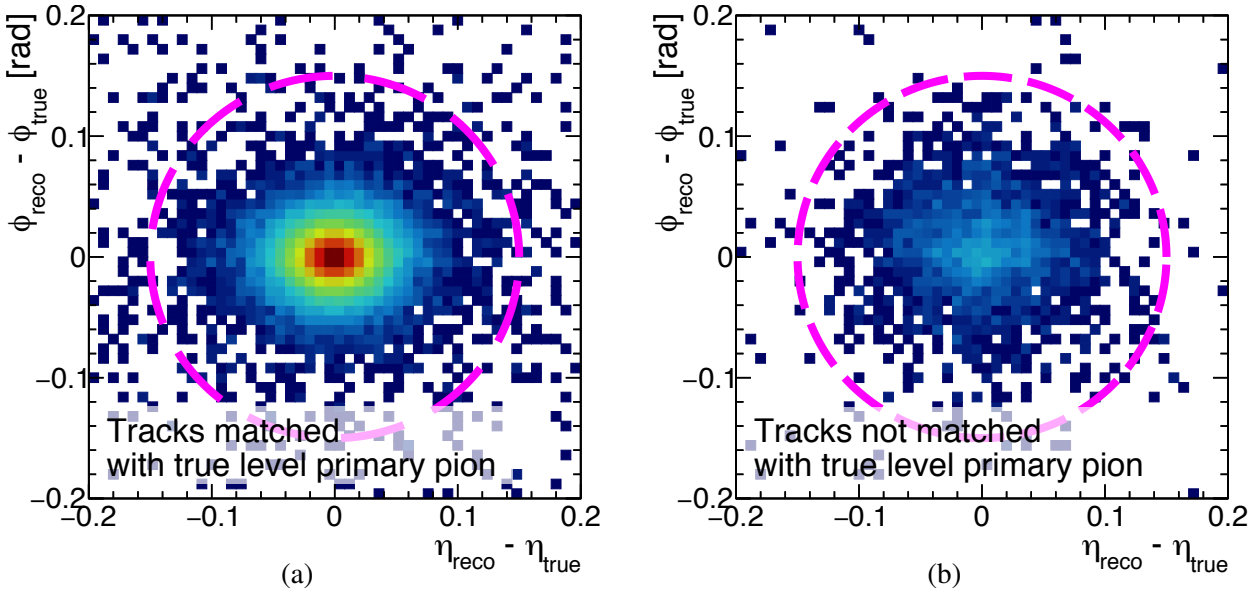

Figure 11.27: Difference between reconstructed and true azimuthal angle vs. pseudorapidity of the TPC tracks and true level primary particle candidates for (a) matched, and (b) not matched pions. Magenta circle of radius 0.15 represents the cut on the maximum distance between the tracks and a corresponding true level primary particle. The same (logarithmic) colour scale has been set up for both plots to better visualize relative content of true and fake tracks.

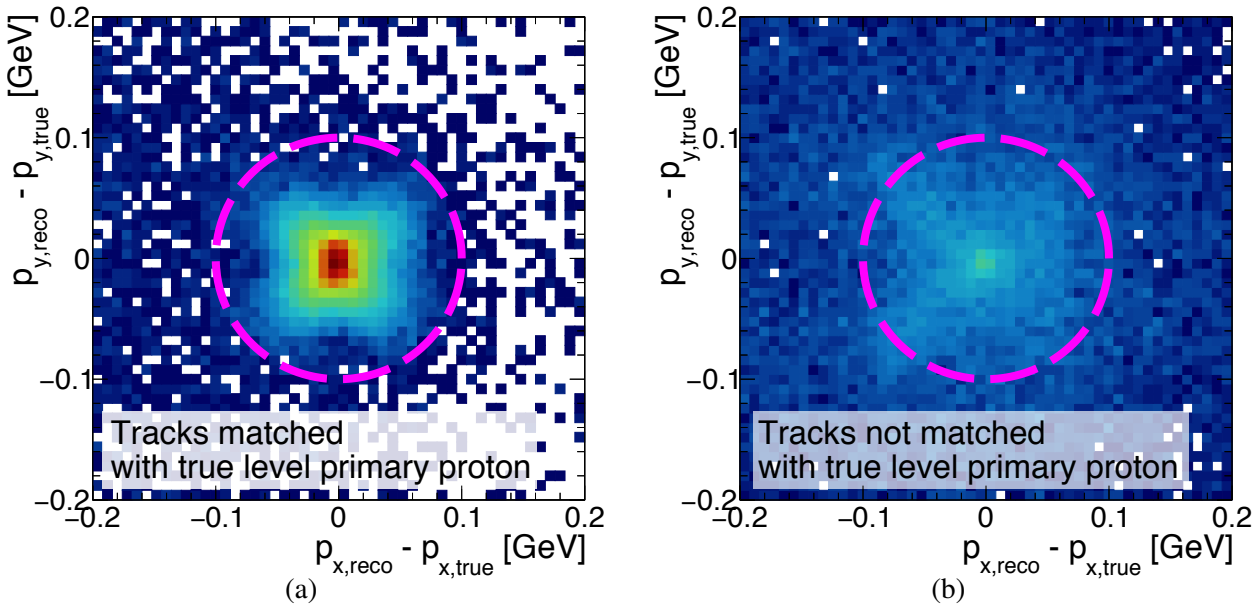

Figure 11.28: Difference between reconstructed and true momentum components of RP tracks (a) matched and (b) not matched with true level primary forward protons. Magenta circle of radius 100 MeV drawn on top of distributions represent cut on the maximum difference between the true and the reconstructed transverse momentum used for determination of fake tracks fraction, as explained in the text. The same (logarithmic) colour scale has been set up for both plots to better visualize relative content of true and fake tracks.

Fraction of tracks, for both TPC and RP detectors, migrating from/to fiducial region or being fake, is shown in Figs. 11.29 and 11.30. Clearly, all mentioned effects are dominant for RP tracks.

A multiplicative correction factor (per track), which takes into account all migrations and fakes, reads:

$$C_{\mathrm{m,f}} = \frac{N_{\mathrm{reco}} + N^{\mathrm{out}}_{\mathrm{migr.}} - N^{\mathrm{in}}_{\mathrm{migr.}} - N_{\mathrm{fakes}}}{N_{\mathrm{reco}}} = 1 + f^{\mathrm{out}}_{\mathrm{migr.}} - f^{\mathrm{in}}_{\mathrm{migr.}} - f_{\mathrm{fakes}}. \tag{11.24}$$

This correction factor is shown in Fig. 11.31a for TPC and in Fig. 11.31b, c) for RP tracks. One can notice, that the most significant contribution to the correction is related to the migrations at the edge of

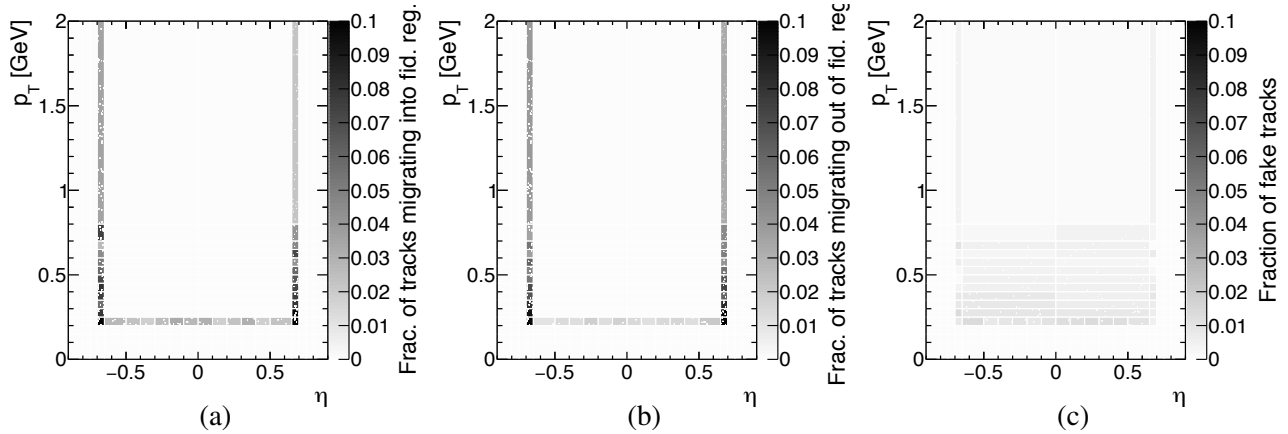

Figure 11.29: Fraction of TOF-matched TPC tracks migrating (a) into, or (b) out of, the fiducial phase space region of acceptance for central tracks. In the case of plot (a) the reconstructed values of p_{T} and η are shown, whereas for (b) the true values of p_{T} and η are shown in the plot. (c) Fraction of fake TOF-matched TPC tracks reconstructed in the fiducial phase space region.

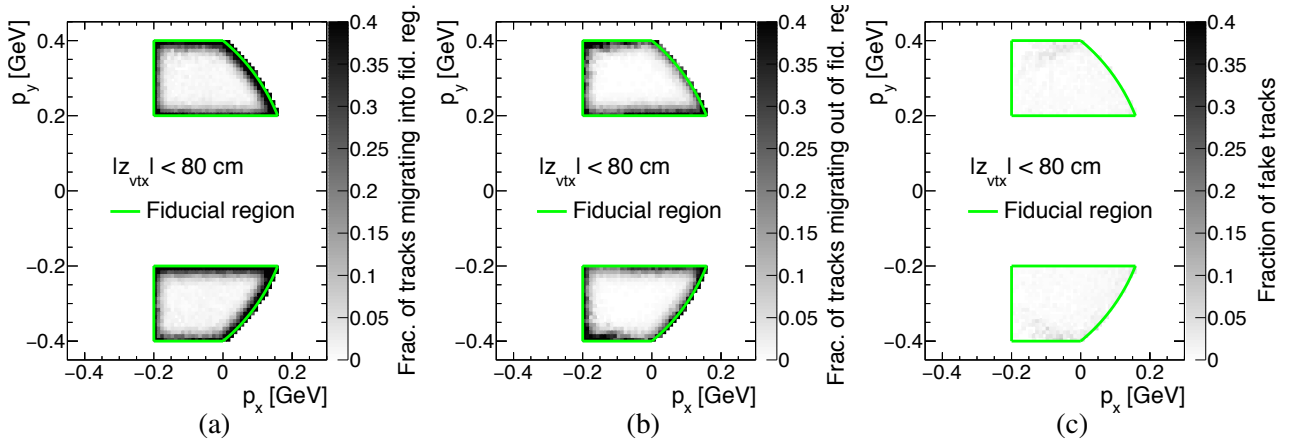

Figure 11.30: Fraction of RP tracks migrating (a) into, or (b) out of the accepted fiducial region of forward-scattered protons' momenta. In the case of (a) the reconstructed values of p_x and p_y are shown, whereas for (b) the true values of p_x and p_y are shown in the plot. (c) Fraction of fake RP tracks reconstructed in the fiducial area.

the fiducial region of the accepted forward-scattered protons. This is a direct consequence of sizeable angular divergence of proton beams. The correction for the RP tracks is different for the two sides of the IP due to changes in alignment and in the reconstruction efficiency of the detectors.

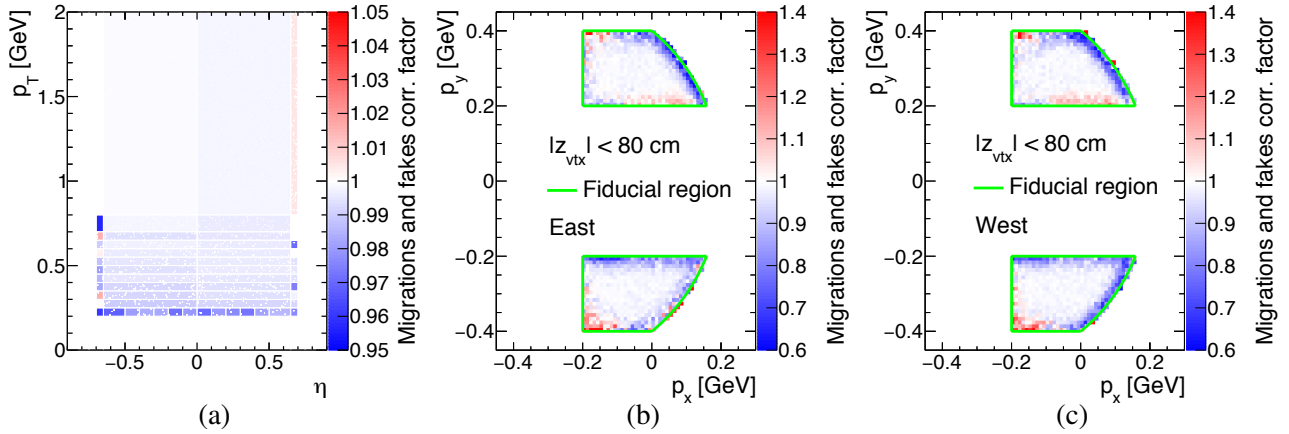

Figure 11.31: Joint correction factors for migrations and fake tracks for (a) TOF-matched TPC tracks, and (b) the East, (c) the West, RP tracks.

11.6 Detector resolutions

In this section studies of detector resolutions with embedded exclusive $\pi^+\pi^-$ signal MC are presented. Fig. 11.32 shows correlation plots between the true-level and the reconstructed-level for several observables used as an independent variables in the differential fiducial cross section measurements, presented in Part IV. These are the invariant mass (Fig. 11.32a) and rapidity (Fig. 11.32b) of the $\pi^+\pi^-$ pairs, azimuthal separation of the forward-scattered protons (Fig. 11.32c), total squared four-momentum transferred in proton vertices (Fig. 11.32d), and cosine of polar angle and azimuthal angle of positive charge pion in the Collins-Soper frame [162] (Figs. 11.32e and 11.32f, respectively).

The resolutions obtained from these studies were used to choose proper binning of the measured differential cross sections. The bin sizes for each quantity were chosen in such a way that they were not

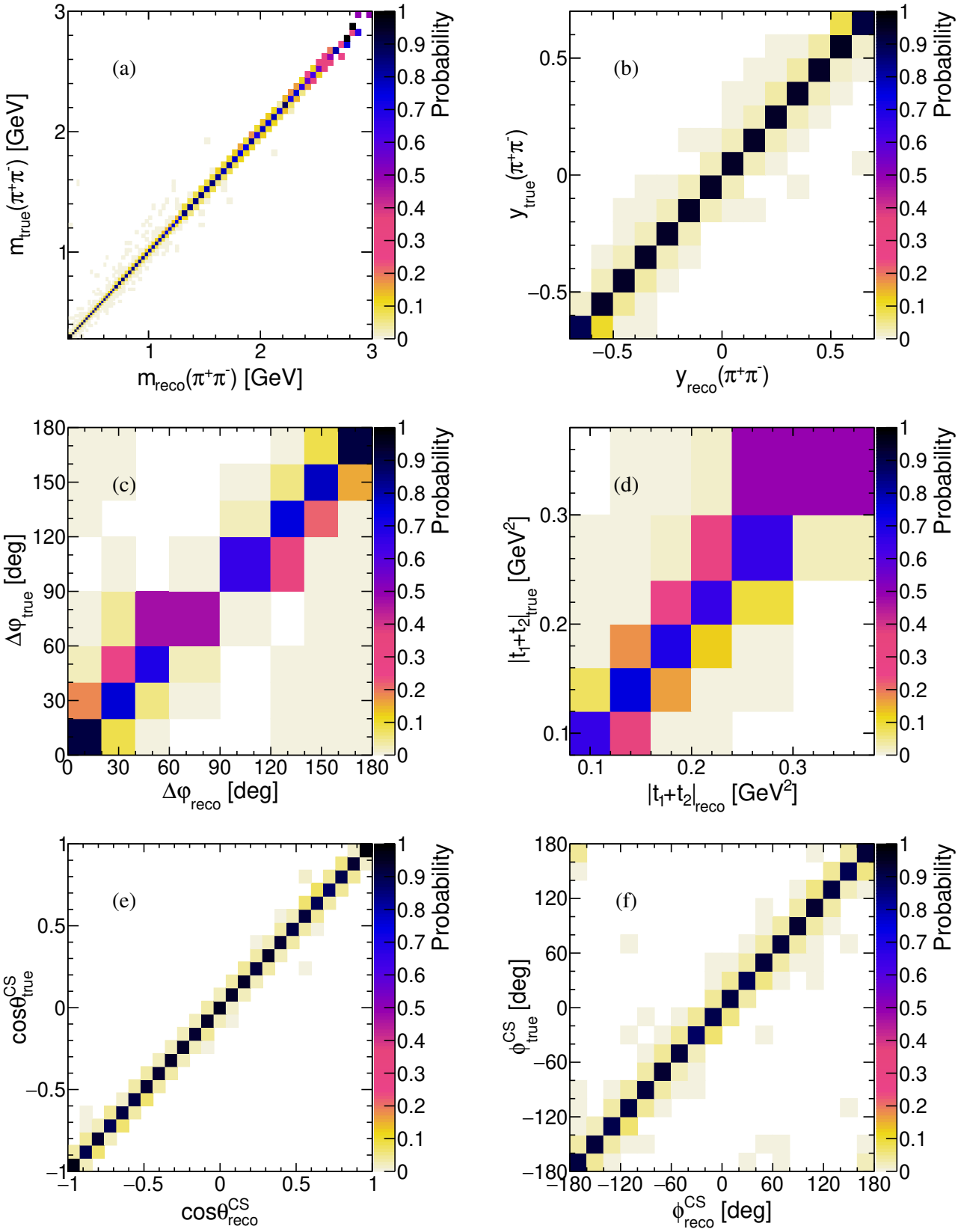

Figure 11.32: Correlation plots between hadron-level and reconstructed quantities for CEP of $\pi^+\pi^-$ pairs from MC embedded in zero-bias data. Shown are (a) invariant mass, $m(\pi^+\pi^-)$, (b) rapidity, $y(\pi^+\pi^-)$, (c) azimuthal angle between the forward-scattered protons, $\Delta\varphi$, (d) sum of four-momenta transfers at the proton vertices, $|t_1 + t_2|$, (e) $\cos\theta^{CS}$, and (f) ϕ^{CS}. On each plot, probabilities in each bin of the true-level quantity are normalised to sum up to one.

narrower than the width of the distribution of the difference between the true- and reconstructed-level quantities.

In the described analysis not only CEP of exclusive $\pi^+\pi^-$ pairs was studied, but also K^+K^- and $p\bar{p}$ channels were analysed. In the two latter cases the binning was typically defined wider with respect to $\pi^+\pi^-$ channel to accommodate for possible worsen of resolutions related to higher particles' masses, and due to lager statistical fluctuations.

11.7 Method of application of the corrections

Differential cross section of a measured quantity q is calculated as:

$$\frac{d\sigma}{dq} = \frac{1}{\Delta q} \cdot \frac{1}{\varepsilon} \cdot \frac{N^w - N^w_{\text{bkgd}}}{L^{\text{eff}}_{\text{int}}}, \tag{11.25}$$

where N^w and N^w_{bkgd} are the weighted numbers of all measured events and the background events, respectively, Δq is the bin width, ε is the joint efficiency of cuts/effects, which do not change on the event-by-event basis, and $L^{\text{eff}}_{\text{int}}$ is the effective integrated luminosity defined as:

$$L^{\text{eff}}_{\text{int}} = \sum_{\text{run}} L^{\text{run}}_{\text{int}} \cdot \epsilon^{\text{veto}}(L^{\text{run}}), \tag{11.26}$$

with the sum running over all analysed runs, and $L^{\text{run}}_{\text{int}}$ and L^{run} being integrated and average instantaneous luminosity for a run, respectively.

The weight assigned to each event, whose distribution is shown in Fig. 11.33 for all three types of analysed particle pairs, was equal to

$$w = w_{\text{TOF\&TPC}} \cdot w_{\text{RP}} \cdot w_{\text{other}}, \tag{11.27}$$

where

$$w_{\text{TOF\&TPC}} = \left[\prod_{\text{sign}} \epsilon_{\text{TOF}}(\text{sign}, \text{ID}) \cdot \prod_{\text{sign}} \epsilon_{\text{TPC}}(\text{sign}, \text{ID}) \right]^{-1}, \tag{11.28}$$

$$w_{\text{RP}} = \left[\epsilon^{\text{E}}_{\text{RP}} \cdot \epsilon^{\text{W}}_{\text{RP}} + \rho_{\text{EW}} \cdot \sqrt{\epsilon^{\text{E}}_{\text{RP}} \cdot \left(1 - \epsilon^{\text{W}}_{\text{RP}}\right) \cdot \epsilon^{\text{W}}_{\text{RP}} \cdot \left(1 - \epsilon^{\text{E}}_{\text{RP}}\right)} \right]^{-1}, \tag{11.29}$$

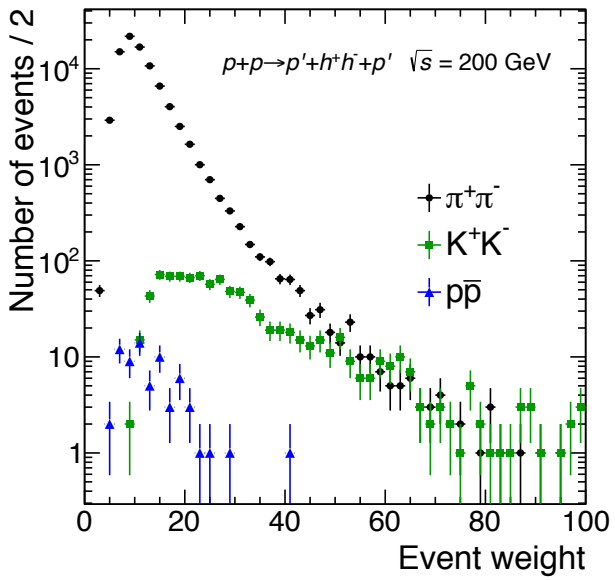

Figure 11.33: Distribution of weights assigned to selected CEP events in $\pi^+\pi^-$ (black circles), K^+K^- (red squares) and $p\bar{p}$ (blue triangles) channel.

and w_{other} is equal to product of all the remaining correction factors and inverse efficiencies discussed in Chap. 11. The weights are large, however they are products of many factors which are in general close to one.

11.8 Closure tests

11.8.1 Data pull

Sanity of the data after applied corrections was verified by preparing a pull histogram of the number of reconstructed and selected CEP events per unit of integrated luminosity (in other words - an integrated cross section). The pull quantity was calculated per run, and is defined as

$$\text{Pull}_i = \begin{cases} \dfrac{\sigma_i - \overline{\sigma}}{u^-(\sigma_i)}, & \text{if } \sigma_i - \overline{\sigma} \geq 0, \\ \dfrac{\sigma_i - \overline{\sigma}}{u^+(\sigma_i)}, & \text{if } \sigma_i - \overline{\sigma} < 0, \end{cases} \tag{11.30}$$

where σ_i is an integrated cross section calculated for i-th run with statistical uncertainty equal to $u^-(\sigma_i)$ or $u^+(\sigma_i)$ (lower or upper 68% confidence level interval), and $\overline{\sigma}$ is the estimator of the expectation value of an integrated cross section. For each run the integrated cross section was calculated as

$$\sigma_i = N_i / L_i, \tag{11.31}$$

where N_i is a number of CEP events in i-th run and L_i is the luminosity collected during i-th run. The estimator $\overline{\sigma}$ was obtained as the weighted average cross section:

$$\overline{\sigma} = \frac{\sum\limits_i \sigma_i \times u^{-2}(\sigma_i)}{\sum\limits_i u^{-2}(\sigma_i)}. \tag{11.32}$$

Final pull distribution is shown in Fig. 11.34 for raw event counts (open circles) and the efficiency-corrected events weighted according to prescription from Eq. (11.27) (filled circles). Parameters of

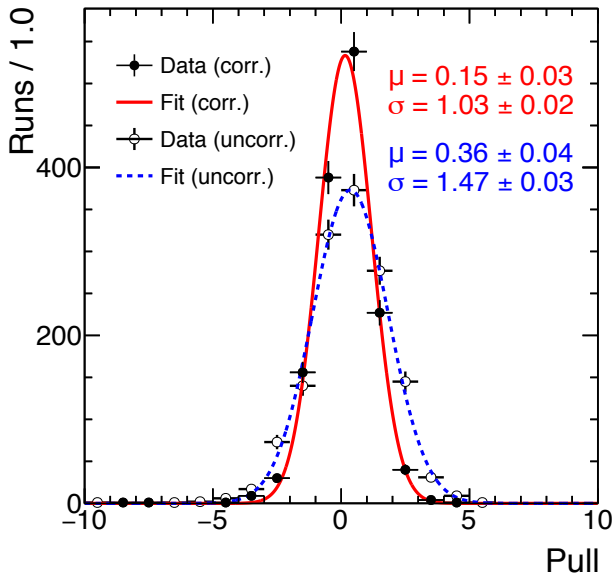

Figure 11.34: Pull histogram of number of events per unit of integrated luminosity. Open circles fitted with dashed blue Gaussian mark uncorrected data, whereas black dots fitted with the red Gaussian denote corrected (weighted) data. Parameters obtained from the fit are provided in the plot.

the Gaussian fits to data points show small deviation of the mean value from zero, and a significant improvement of the width of the distribution after applying of the corrections, which is now consistent with one as it should be.

11.8.2 Monte Carlo closure tests

To verify validity of calculated efficiencies and of the correction method, the closure tests were performed. Signal MC events were subjected to the same analysis flow as the data. Distributions of reconstructed quantities were corrected for inefficiencies as described in Sec. 11.7 and checked if they reproduce corresponding distributions at the true level. The efficiencies used to correct MC events did not include modification of the MC-based efficiencies from the data-driven methods.

In the closure tests presented below, distributions at the true level were assumed to be known with infinite statistical precision (uncertainties are assumed to be equal to 0). This enables statistical comparison of the reconstructed and corrected distributions with those at the true level.

Figure 11.35 shows the closure test for the corrections related to the TPC track reconstruction, TOF matching and TPC vertex reconstruction. The agreement between the generated and corrected events is demonstrated.

The joint RP track reconstruction and selection, and dead material-induced veto efficiency is tested in Fig. 11.36. The agreement between corrected and true-level distributions is evident.

Results of the closure tests including all corrections discussed above are shown in Fig. 11.37 for the $\pi^+\pi^-$ pair invariant mass and rapidity of the pair, and in Fig. 11.38 for the $|t_1 + t_2|$ and $\Delta\varphi$ of the forward-scattered protons. Limited statistics of reconstructed MC events after full event selection

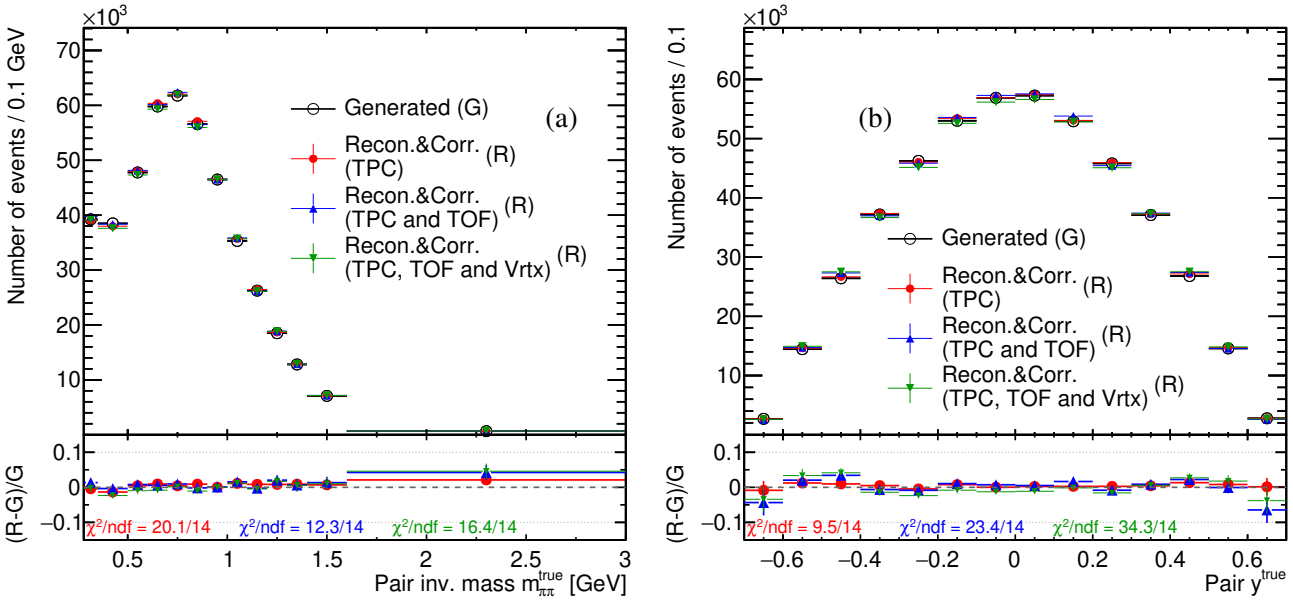

Figure 11.35: Closure tests for (a) invariant mass, and (b) rapidity of the $\pi^+\pi^-$ pairs based on the embedded MC sample. True distributions are compared to the corrected detector level distributions after applying corrections for TPC only (red points), TPC and TOF (blue points) and full correction including additional vertex correction (green points). In the bottom panels, relative differences of the corrected distributions with respect to the true one are shown, together with corresponding χ^2/ndf values for the pairs under consideration.

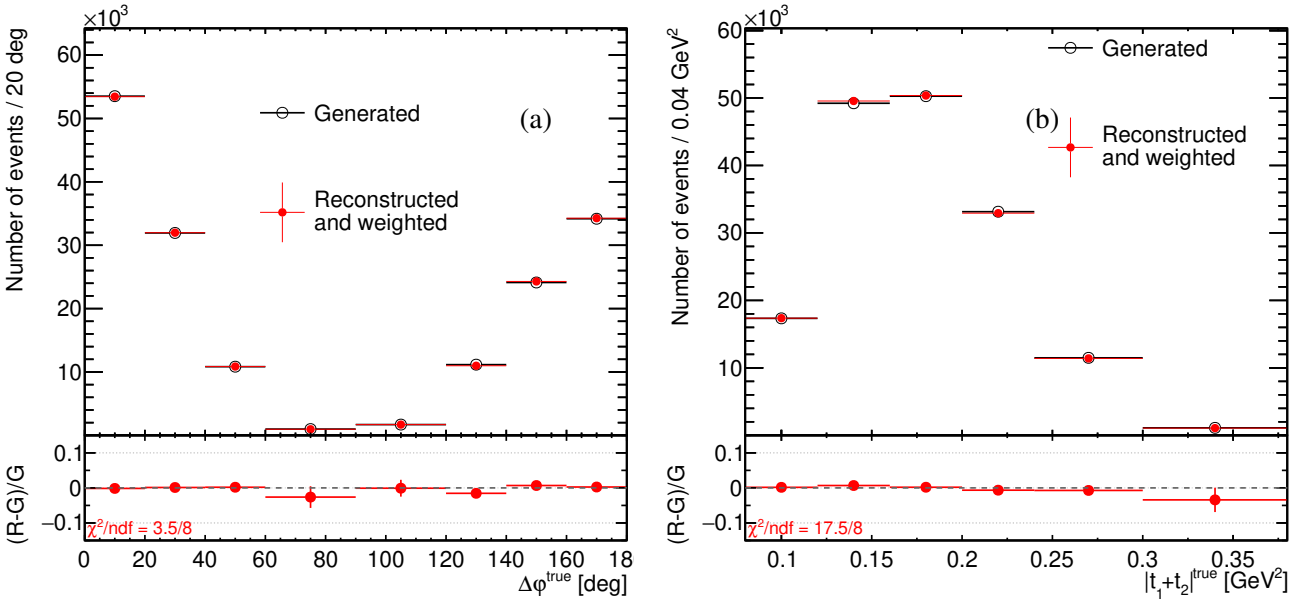

Figure 11.36: Closure tests for distributions of (a) $\Delta\varphi$, and (b) $|t_1 + t_2|$ for the forward-scattered protons based on the embedded MC sample. True distributions are compared to the corrected detector level distributions after applying corrections for the full two forward protons efficiency. In the bottom panels, relative differences of the corrected distributions with respect to the true one are shown, together with corresponding χ^2/ndf values for the pairs under consideration.

makes drawing clear conclusions of the comparisons difficult. However, the agreement between reconstructed and generated level was considered satisfactory and the correction method was thus validated.

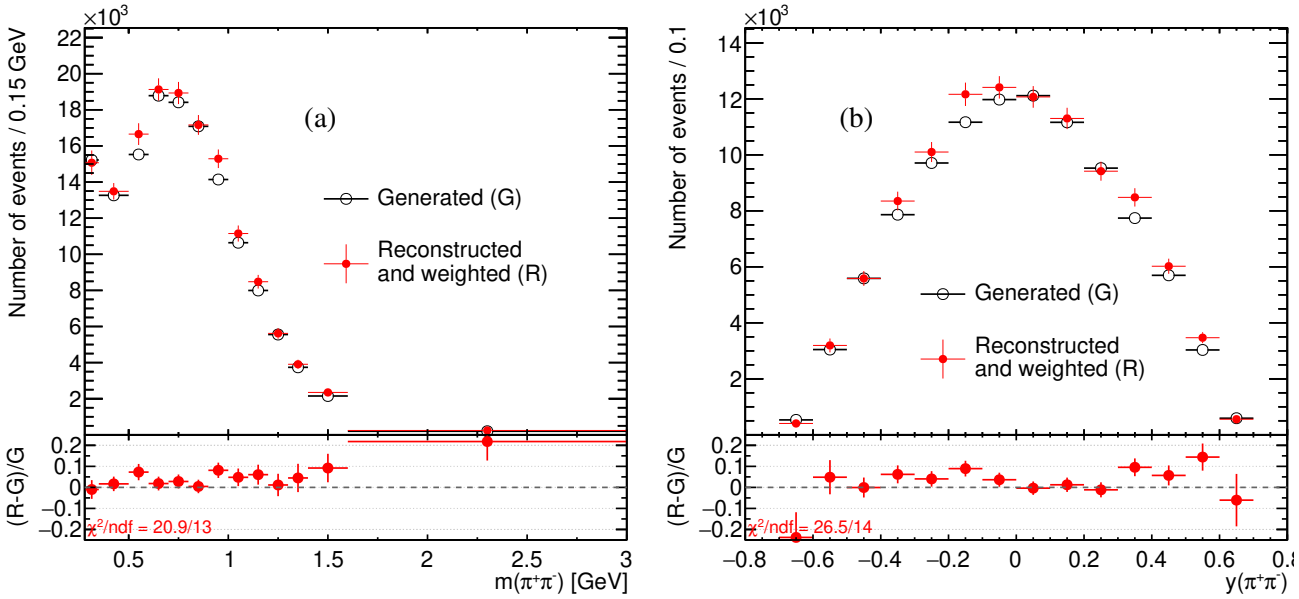

Figure 11.37: Closure tests for (a) invariant mass, and (b) rapidity of the $\pi^+\pi^-$ pairs based on the embedded MC sample. True distributions are compared to the fully corrected (all corrections included) detector level distributions. In the bottom panels, relative differences of the corrected distributions with respect to the true one are shown, together with corresponding χ^2/ndf values for the pairs under consideration.

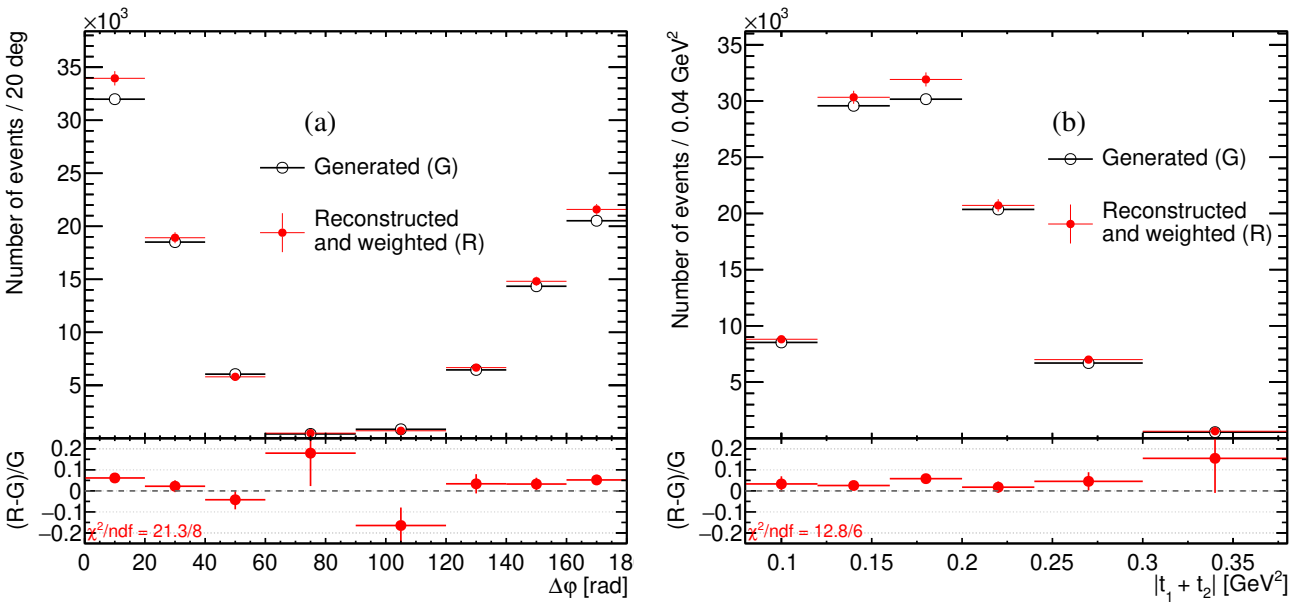

Figure 11.38: Closure tests for distributions of (a) $\Delta\varphi$, and (b) $|t_1 + t_2|$ for the forward-scattered protons based on the embedded MC sample. True distributions are compared to the fully corrected (all corrections included) detector level distributions. In the bottom panels, relative differences of the corrected distributions with respect to the true one are shown, together with corresponding χ^2/ndf values for the pairs under consideration.

11.9 Correction for the geometrical acceptance

One of the goals of this analysis was to obtain information about the production of resonances in the CEP process. Invariant mass distributions in the fiducial region of the measurement could not be directly used to extract and quantitatively describe possible resonances without extrapolation to the full kinematic region of the central pions pair, given by $p_T \to 0$ and $|\eta| \to \infty$ (full solid angle in the central system rest frame). Extrapolation to unmeasured region is always model dependent. Here corrections to the full phase-space are presented, obtained with various assumptions. In calculation of these corrections the factorisation of the central system and the forward-scattered protons phase space was assumed. A phase-space MC generator was used. For the forward-scattered protons a uniform distributions of the azimuthal angles were used, while the exponential shape with the slope parameter of 6 GeV^{-2} was used for t-dependence. The acceptance correction was estimated a the hadron level.

To limit the size of the correction, also the cuts on $|y(\pi^+\pi^-)| < 0.4$ and on $0.05 < -t_1, -t_2 < 0.16$ GeV^2 were added. The measurement was further separated to two regions of $\Delta\varphi < 45^\circ$ and $\Delta\varphi > 135^\circ$, which reduced size of acceptance corrections and related systematic uncertainties. These additional cuts reduce the size of the acceptance corrections and related systematic uncertainties.

Figure 11.39 shows the geometrical acceptance for a central state $\pi^+\pi^-$ in two ranges of $\Delta\varphi$ angle, for the phase-space MC as well as for MC events from DiMe and GenEx generator. One can see a significant differences between the acceptances, depending on the model. Nominally, the acceptance correction for S-wave (spin-zero) central state is used. The remaining points serve as a systematic (model) uncertainties.

Figure 11.40 shows the geometrical acceptance from phase-space MC for the two forward-scattered protons, in two ranges of $\Delta\varphi$: $\Delta\varphi < 45^\circ$ and $\Delta\varphi > 135^\circ$. Comparison with the geometrical acceptances

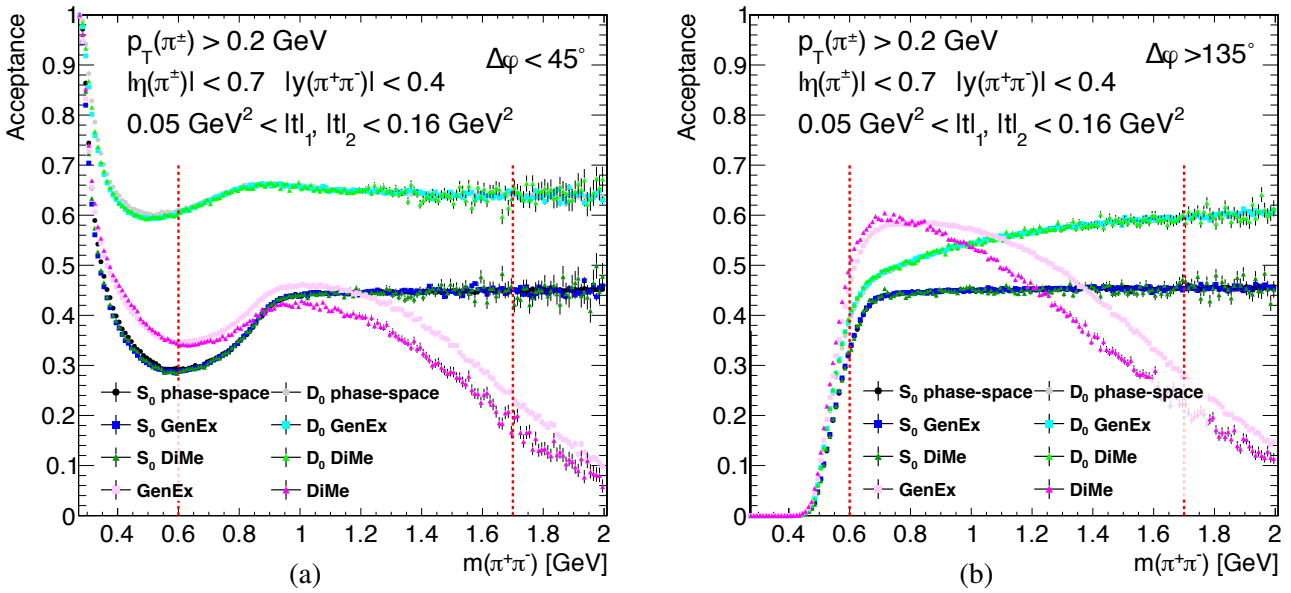

Figure 11.39: Geometrical acceptance for the CEP of $\pi^+\pi^-$ pairs in the fiducial region related to the extrapolation to the Lorentz invariant phase space region defined by $|y(\pi^+\pi^-)| < 0.4$ and $0.05 < -t_1, -t_2 < 0.16$ GeV^2, separately for two intervals of $\Delta\varphi$: (a) $\Delta\varphi < 45^\circ$, and (b) $\Delta\varphi > 135^\circ$. Dashed red lines mark the region, in which the fits to corrected data were performed.

obtained from GenEx and DiMe is presented in Fig. 11.41, where the ratios of acceptances are drawn. As can be seen, the differences between models are low, generally below 5%.

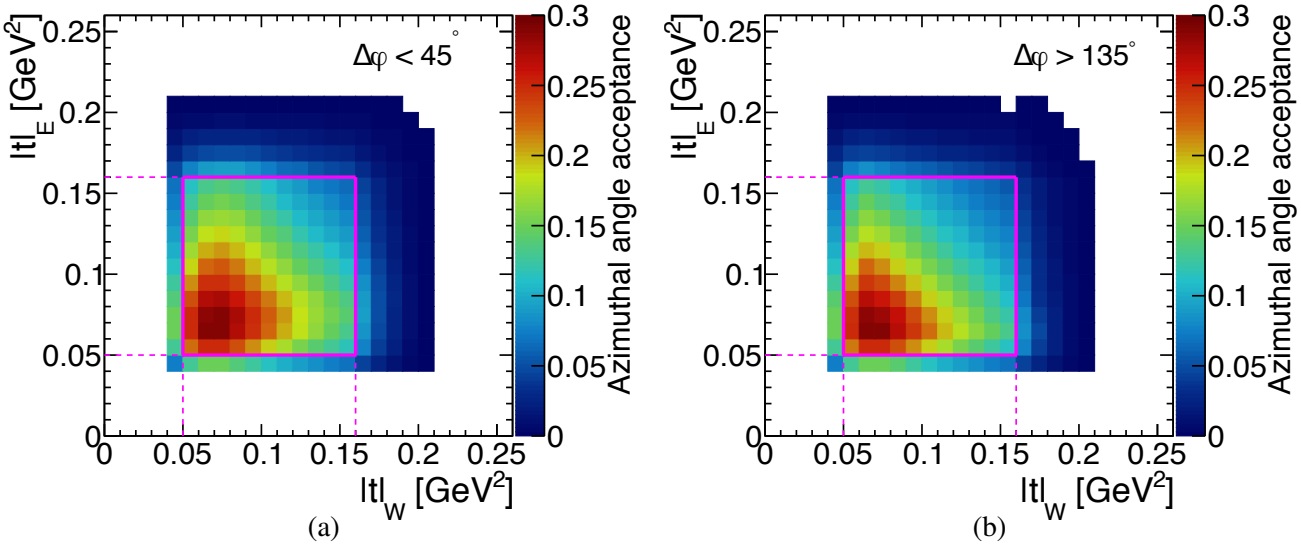

Figure 11.40: Geometrical acceptance for the forward-scattered protons measured in the fiducial region related to the extrapolation to the Lorentz invariant phase space region defined by $|y(\pi^+\pi^-)| < 0.4$ and $0.05 < -t_1, -t_2 < 0.16$ GeV^2, separately for two intervals of $\Delta\varphi$: (a) $\Delta\varphi < 45^\circ$, and (b) $\Delta\varphi > 135^\circ$. Dashed red lines mark the region, in which the fits to corrected data were performed.

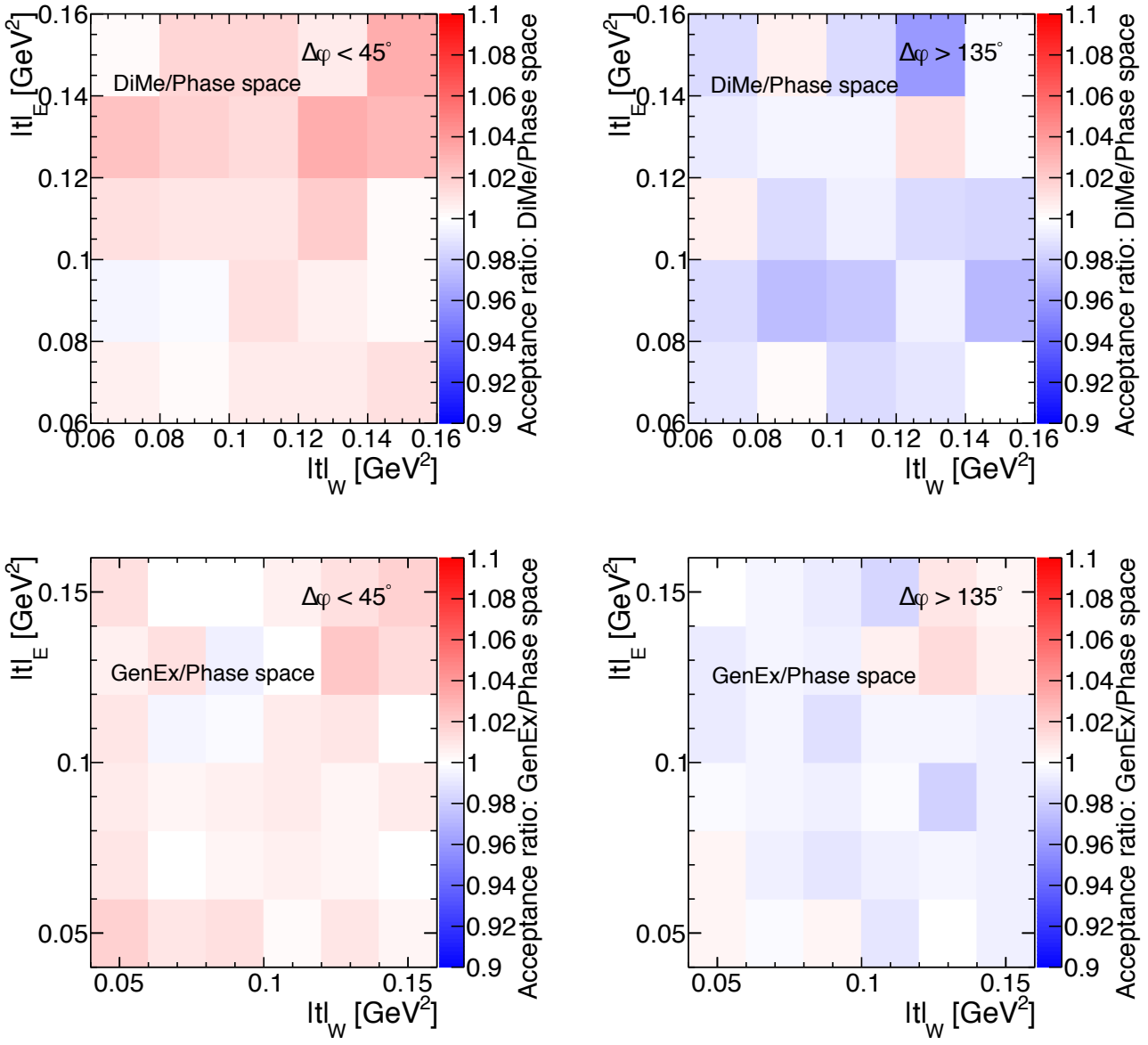

Figure 11.41: Comparison of the geometrical acceptance between (top) DiMe and the phase-space MC, and (bottom) GenEx and the phase-space MC for (left) $\Delta\varphi < 45^\circ$ and (right) $\Delta\varphi > 135^\circ$.

12. Systematic uncertainties

Various sources of systematic uncertainties have been considered in the physics analysis performed in this thesis. Detailed studies, which lead to estimation of their sizes are discussed below. In Sec. 12.5 a summary of sources of systematic uncertainties considered in physics analysis is provided.

12.1 Luminosity

The relative luminosity in the experiment STAR is determined using the coincidence rate in East and West ZDC detectors. An absolute luminosity is provided by special runs, the Van der Meer (VdM) scans [163], which are taken few times during a data taking period. For determination of the systematic uncertainty of the integrated luminosity, a dedicated study of the VdM scans [164] performed during RHIC fill devoted to the measurement of the total and elastic cross sections, was used. In this study, the visible cross section in the ZDC detectors was determined to be equal to 0.294 mb with 4% systematic uncertainty. The number is different from the effective ZDC cross-section used in the initial calculation of the luminosity at STAR, equal to 0.264 mb. The ratio of these numbers, equal to 1.114, was used to correct the nominal luminosity obtained at STAR from the coincidence rate of the East and West ZDC detectors, and an uncertainty of the new value was assumed to be 4% instead of the nominal luminosity uncertainty of 10% used in STAR.

To account for possible fill-by-fill dependence of the luminosity measurement, an additional 4% uncertainty was assigned to the luminosity. It was determined by comparing variations of the effective cross-sections for elastic scattering process relative to the measurement done solely based on data collected during the fill devoted to elastic scattering measurement (#18915, Fig. 12.1). This

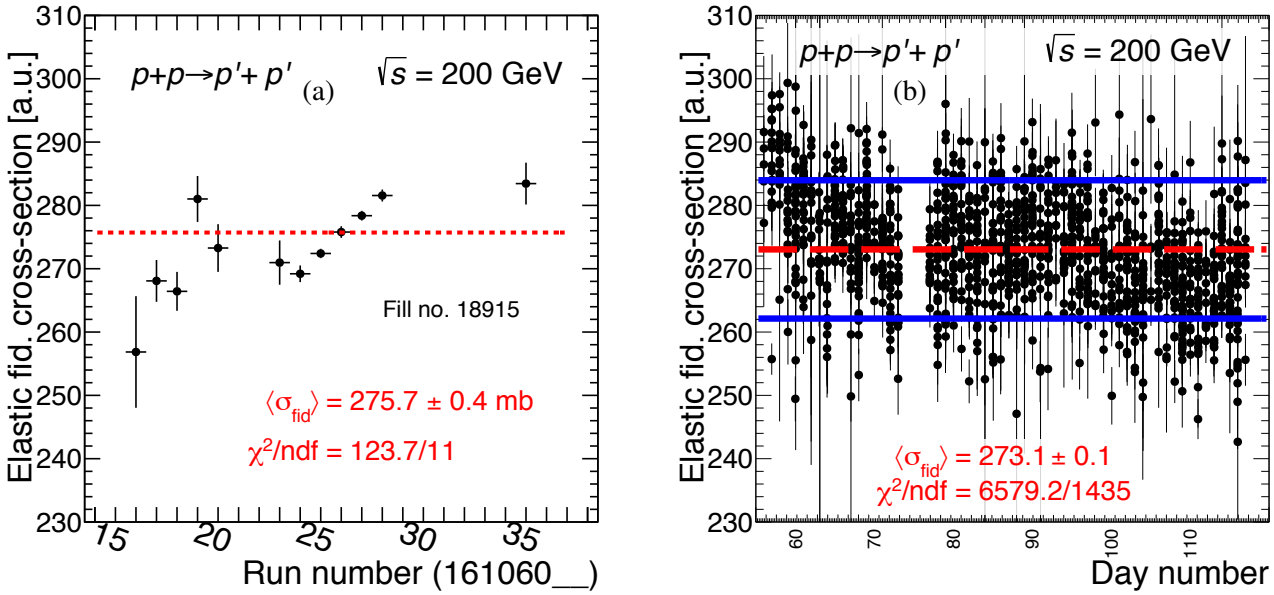

Figure 12.1: Integrated fiducial elastic proton-proton scattering cross-section (a) for runs from the fill #18915, and (b) for all runs. Dashed red lines mark an average fiducial cross-section within displayed run range. Each point corresponds to a single run. Solid blue lines mark ±4% uncertainty bands assigned to the luminosity to account for fill-by-fill variations of luminosity estimates.

effective cross-section was determined from the elastic proton-proton scattering events reconstructed with the same proton track selection as in the CEP analysis. For this purpose, a fiducial region for elastically-scattered proton tracks was chosen as a rectangular (t, φ) window, $0.04 < |t| < 0.1$ GeV^2 and $1.3 < |\varphi| < 1.9$, in which the geometrical acceptance was 100%. The overall luminosity uncertainty of 6% was estimated by the quadratic sum of the two uncertainty sources described above.

12.2 TPC track reconstruction efficiency

The inefficiency of the TPC track reconstruction has multiple sources. First source is related to the geometry of the TPC detector, with some spaces inactive (detector support, wires, etc.). There is also dead material in front of the TPC (beam pipe, the HFT detector), which increases probability of inelastic interactions of primary particles. Next source of inefficiencies are dead read-out channels in the electronics and off-time pile-up hits in the TPC, which are characteristic for this type of detector. TPC is a relatively slow detector and aggregates signals from a long time interval (corresponding to a few hundreds of bunch crossings), defined by the velocity of charge drift. These off-time hits mix with in-time hits yielding deteriorations and inefficiencies in the track reconstruction. Last but not least, particles such as pion or kaons may decay within the TPC volume, hence the fit of a helix to the hit points in TPC may be impossible if decay occurs too early.

In the following sections, systematic uncertainties related to the pile-up effect and to the amount of the dead material in front of the TPC, are estimated. Other sources are not considered here as they are rather well taken into account in the MC simulation.

12.2.1 Pile-up effect

The off-time pile-up significantly reduces TPC track reconstruction efficiency due to high density of hits from preceding or posterior bunch crossings. To take this effect into account, a technique of embedding of generated MC events into zero-bias data is used. Systematic uncertainty related to this approach was studied by comparison of relative changes of the track selection efficiencies with different density of pile-up TPC hits [33]. The embedded MC samples and data were divided into three sub-samples based on mean BBC-small coincidence rate: ⟨BBC_AND⟩ = 700 kHz (low rate), ⟨BBC_AND⟩ = 1100 kHz (moderate rate) and ⟨BBC_AND⟩ = 1400 kHz (high rate), as shown in Fig. 12.2. The higher BBC coincidence rates (which means higher instantaneous luminosity), the more off-time hits are present in the TPC. In Fig. 12.3, distributions of the numbers of hits used in the fits of helices, $N_{\text{hits}}^{\text{fit}}$, are shown for the three sub-samples. A clear shift towards higher values of $N_{\text{hits}}^{\text{fit}}$ is observed for increasing TPC occupancy, as a result of more hits from the pile-up events which are accidentally assigned to a track during reconstruction.

To determine systematic uncertainty related to the embedding procedure, first the effect of variation of the TPC track reconstruction efficiency with changing number of hit points in a track, must be removed. For this purpose, the cut applied on the $N_{\text{hits}}^{\text{fit}}$ (SC3.4) was customised depending on ⟨BBC_AND⟩, such that the selection efficiencies for in-time TPC tracks were roughly the same in all ranges of ⟨BBC_AND⟩. The actual values of the cut were obtained with a data-driven tag&probe method and using the CEP $\pi^+\pi^-$ data sample.

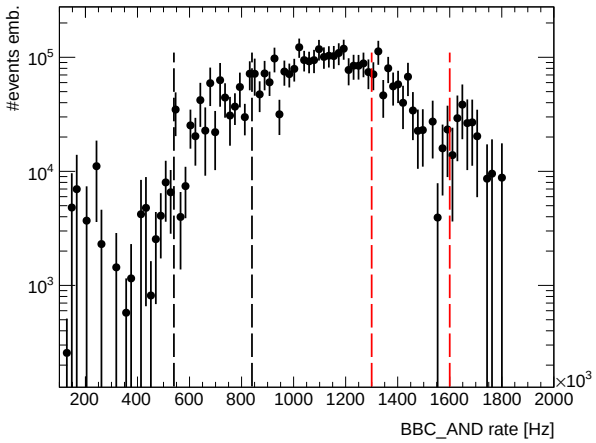

Figure 12.2: Distribution of the number of events in the embedded single particle MC sample as a function of the BBC coincidence rate BBC_AND. The subsequent vertical lines mark the ranges of low, moderate and high BBC-small coincidence rates, respectively. Figure taken from [33].

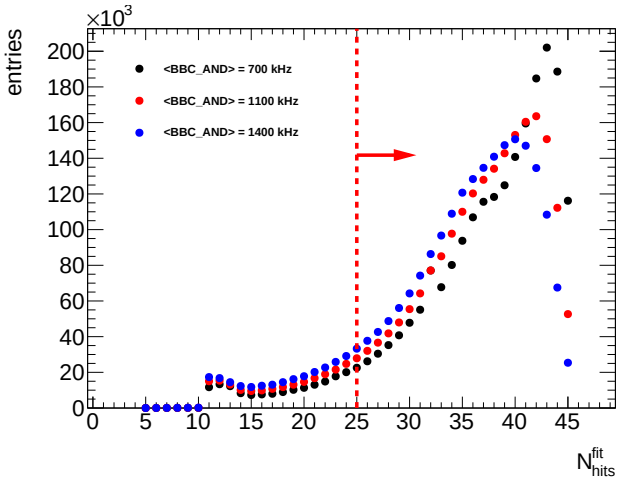

Figure 12.3: Distributions of the number of hits, $N_{\text{hits}}^{\text{fit}}$, used in the TPC track reconstruction in the embedded single particle MC sample. Points of different colours correspond to three disjoint ranges of average BBC coincidence rate provided in the legend. Red line and arrow indicate the region accepted in the analysis with nominal $N_{\text{hits}}^{\text{fit}}$ cut value (SC3.4). Figure taken from [33].

The efficiency of TPC quality cuts, $\varepsilon_{\text{TPC}}^{\text{cuts}}$, was calculated according to Eq. (11.7) with modified definitions of the tag track and probe track, as explained in the following algorithm:

1. Data from RP_CPT2 trigger were used. Events were selected with nominal CEP analysis cuts (Sec. 9.1), except cuts SC3, SC7, SC8 and SC9, which were removed or modified as given below.

2. For each event passing the above selection, global TPC tracks matched with TOF hits were selected. Exactly 2 such tracks, one of positive and one of negative charge, were required. Both tracks were required to be compatible with the pion hypothesis based on dE/dx ($|n\sigma_{\text{pion}}| < 3$). If any of the tracks was found incompatible with the pion hypothesis, the event was removed from the analysis. Also, the tracks were required to be likely a product of the same primary interaction, therefore cut on longitudinal separation along the beamline, $|\Delta z_0| < 3$ cm, was imposed. Also, the z-position of the vertex was required to be contained within nominal margins, $\frac{1}{2}|z_0^+ + z_0^-| < 80$ cm. Primary tracks were not used because some quality cuts are already applied at the level of vertexing, which could introduce a bias in the resultant efficiency.

3. Global TOF-matched TPC tracks preselected in step 2, were checked if they satisfy track quality cuts (SC3.4) with removed cut on $N_{\text{hits}}^{\text{dE/dx}}$ and a modified cut value of $N_{\text{hits}}^{\text{fit}}$ denoted as $\mathbb{N}_{\text{thr}}$ ($N_{\text{hits}}^{\text{fit}} \geq \mathbb{N}_{\text{thr}}$). Tracks which pass the quality cuts were set as tag candidates. In the case, that only one tag candidate was found, step 4 was executed only with this single track. Otherwise, step 4 was repeated for each of the two tracks used as tags.

4. The TPC track of the sign opposite to the tag (preselected in step 2) was checked if it also fulfils the good quality track requirements (cuts SC3.4 with removed $N_{\text{hits}}^{\text{dE/dx}}$ cut and modified $\mathbb{N}_{\text{thr}}$ cut). Two-dimensional histograms of quantities of interest q (probe η if probe $p_{\text{T}} > 0.2$ GeV, probe

p_T if probe $|\eta| < 0.7$) vs. p_T^{miss} were filled, separately for all probes and only for probes satisfying quality cuts.

5. In each bin of the quantity of interest q, the distribution of p_T^{miss} was fitted in the signal-free region with the polynomial describing the background shape, which was then extrapolated to $p_T^{miss} = 0$. The signal yield in a given bin of q was calculated as the integral of the histogram with subtracted integral of the background function, both in the range $p_T^{miss} < 75$ MeV. The final efficiency in a given bin of q was calculated according to Eq. (11.8), with superscript "matched" understood as "passing quality cuts".

A few efficiency curves obtained with the above method using the nominal cut on N_{hits}^{fit} (≥ 25) are plotted in Fig. 12.4. A notable decrease of selection efficiency at negative pseudorapidities is visible in the figure for a run period with dead TPC sector #19. This acceptance loss is accounted for in the TPC efficiency calculated in Sec 11.2.1. Also, a sizeable differences are present for the same run periods with different average rates in BBC. Values of $\mathbb{N}_{thr}$ which equalise the TPC track selection efficiency for different average BBC coincidence rates (marked with green lines in Fig. 12.5), were determined with the procedure described below.

Although number of hit points used in helical TPC track fit is an integer, the value of $\mathbb{N}_{thr}$ which provides the same track selection efficiency at low, moderate and high BBC coincidence rates may lie in between two integers differing by one hit point and thus be a floating point number. To account for this possibility, for the purpose of this study each global TPC track was assigned a new number

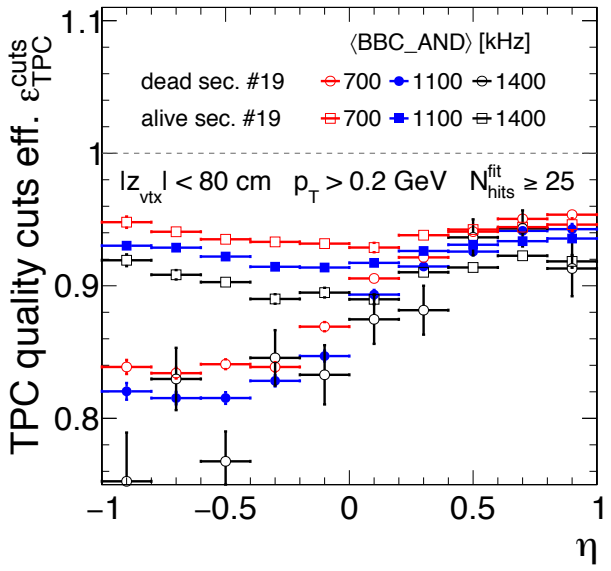

Figure 12.4: Sample comparison of TPC track quality cuts efficiency as a function of track's pseudorapidity, η, obtained with tag&probe method on CEP $\pi^+\pi^-$ events, for a few data samples selected with respect to average rate in BBC and run period. Efficiencies obtained with nominal minimum N_{hits}^{fit} value of 25 are drawn to emphasize effect of the BBC rate (TPC occupancy) on the TPC track reconstruction efficiency.

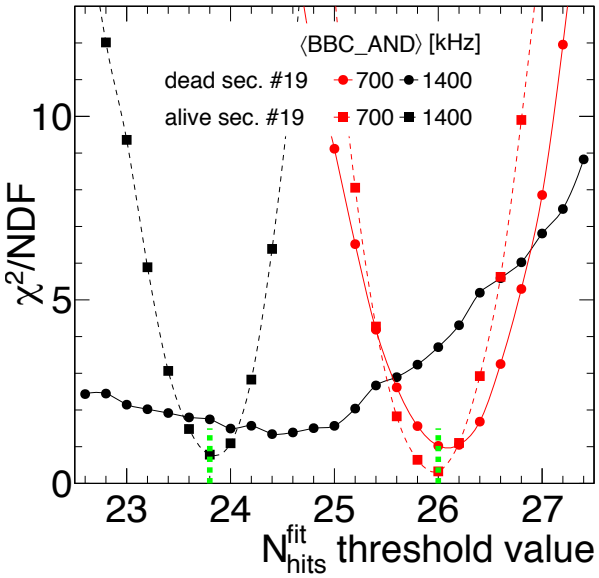

Figure 12.5: χ^2/NDF between the TPC track quality cuts efficiencies obtained with the tag&probe method as a function of the N_{hits}^{fit} cut value. Dashed green vertical lines show approximate N_{hits}^{fit} values for which χ^2/NDF reaches minimum, separately for runs with low- and high-BBC coincidence rate. The black and red lines simply connect the points for a better visibility.

of hit points used in a fit ($N'^{\text{fit}}_{\text{hits}}$), being a sum of an original number of hit points (integer $N^{\text{fit}}_{\text{hits}}$) and a random floating point number between zero and one drawn from the uniform distribution defined over a range [0, 1). With this modification introduced, a scan of the TPC track selection efficiency with the tag&probe method was performed for a set of $\mathbb{N}_{\text{thr}}$ values, starting from 22.6 with a step of 0.2, up to 27.4. For each value of parameter $\mathbb{N}_{\text{thr}}$ a quantity χ^2/NDF was calculated between the η-dependent efficiency obtained for a modified $N^{\text{fit}}_{\text{hits}}$ cut value ($\geq \mathbb{N}_{\text{thr}}$) and for given BBC coincidence rate sample (low/high), and the one obtained with nominal cut value (≥ 25) for a medium BBC rate sample. The result of the scan is shown in Fig. 12.5, where the χ^2/NDF is drawn as a function of the $N^{\text{fit}}_{\text{hits}}$ threshold value in quality cuts SC3.4. For both run periods (with and without malfunctioning part of TPC) we found similar values of $\mathbb{N}_{\text{thr}}$ which provide the same track selection efficiency: 23.8 for high BBC coincidence rate runs, and 26 for low BBC coincidence rate runs, as marked with dashed green lines. Significantly different width of χ^2/NDF for one data sub-sample is an effect of lower event statistics in this subsample (higher statistical uncertainties of efficiency).

Figure 12.6 shows an example of the TPC track selection (SC3.4) efficiency with nominal (for ⟨BBC_AND⟩ = 1100 kHz sample) and modified (for ⟨BBC_AND⟩ = 700 kHz and 1400 kHz samples) quality cut on $N^{\text{fit}}_{\text{hits}}$. The offset between medium and low/high pile-up runs is defined as

$$\Delta\epsilon^{1100,X}_{\text{TPC}} = \epsilon^{1100}_{\text{TPC}} - \epsilon^{X}_{\text{TPC}} \tag{12.1}$$

with $\epsilon^{1100}_{\text{TPC}}$ denoting TPC track selection efficiency calculated from sample with ⟨BBC_AND⟩ = 1100 kHz using nominal $N^{\text{fit}}_{\text{hits}}$ quality cut, and $\epsilon^{X}_{\text{TPC}}$ denoting modified TPC track selection efficiency calculated from samples with ⟨BBC_AND⟩=X kHz and accordingly modified $N^{\text{fit}}_{\text{hits}}$ quality cut.

$\Delta\epsilon^{1100,X}_{\text{TPC}}$ compatible with zero would indicate full agreement of the TPC track selection efficiency from the embedded MC and from the data-driven tag&probe method. Bottom panels in Fig. 12.6 indicate, that the agreement is at the level of 1%, which is assigned as the systematic uncertainty of the single TPC track reconstruction efficiency related to the MC embedding procedure. The same systematic uncertainty is also assigned to the TPC track reconstruction efficiency for positively and negatively charged kaons and protons.

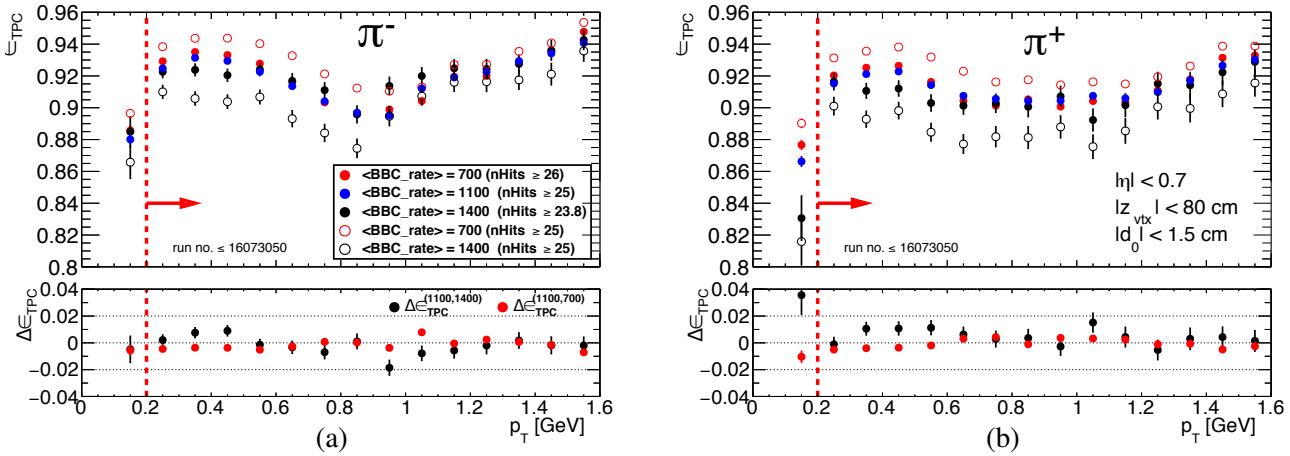

Figure 12.6: TPC track selection efficiency for (a) π^- and (b) π^+, as a function of track's p_T for embedded MC samples with ⟨BBC_AND⟩ = 700 kHz and ⟨BBC_AND⟩ = 1400 kHz. In the bottom panels the quantity $\Delta\epsilon_{\text{TPC}}$ given by Eq. 12.1 is drawn, serving as an indication of the systematic uncertainty of the embedding procedure. Red lines and arrows indicate p_{T} range accepted in the physics analysis. Figures adopted from [33].

12.2.2 Dead material effect

Particle detected and reconstructed in the TPC must first pass through the detector material standing in between the accelerator vacuum and TPC gas. This affects track reconstruction efficiency, as the particle may interact with that material - in worst case inelastically, and induce secondary particles, thus lower reconstruction efficiency. Accuracy of modelling of the detector material in the STAR simulation, especially with the HFT installed, influences systematic error e.g. on the TPC track reconstruction efficiency. In this section the density of secondary vertices is compared between the data and zero-bias-embedded MC. The density of secondary vertices is directly proportional to the amount of the material in a given volume, hence any discrepancy between secondary vertex distribution in the data and MC can be a hint for inaccuracies of the STAR simulation, which should be accordingly covered by the systematic uncertainties. The aim of the study presented below was to obtain a reasonable estimate of the component of systematic error of the TPC track reconstruction efficiency related to the uncertainty on the amount and distribution of inactive material.

Analysis of the distribution of secondary vertices was performed using both zero-bias data and MB Pythia MC embedded into zero-bias triggers. Analysis started with the following selection of events:

1. Exactly one reconstructed primary vertex (with tracks matched to hits in TOF; beamline constraint was used in reconstruction therefore primary vertices lie on the beamline and tracks associated with them have global DCA (d_0) not larger than $\sim$ 1.5 cm).
2. $|z_{\mathrm{vtx}}| < 80$ cm.
3. At least two primary TOF tracks with: $\mathrm{DCA(R)} < 1$ cm, $|\eta| < 1$, $p_{\mathrm{T}} > 0.2$ GeV, $N_{\mathrm{hits}}^{\mathrm{fit}} \geq 25$, $N_{\mathrm{hits}}^{\mathrm{dE/dx}} \geq 15$.

The aim of above criteria was to select pile-up-free events with well defined vertex. The cut on z-vertex is identical to the one used in the nominal analysis (SC2). Figure 12.7 shows comparison of quantities characterising an event. In general a moderate agreement between MC and data can be observed, considered sufficient for trustworthy result of described analysis.

In the next step, the TPC tracks were selected for the search and reconstruction of secondary vertices. The requirements were as follows:

1. Global TPC tracks should be matched with TOF and not associated with any primary TPC track.
2. $|\eta| < 0.7$, $p_{\mathrm{T}} > 0.2$ GeV, $N_{\mathrm{hits}}^{\mathrm{fit}} \geq 25$, $N_{\mathrm{hits}}^{\mathrm{dE/dx}} \geq 15$.
3. Distance of the closest approach to the z-axis at $(x, y) = (0, 0)$, denoted as $d_0^{(0,0)}$, should be larger than the inner radius of the beam pipe: $d_0^{(0,0)} > 2$ cm.

These cuts were intended to select in-time TPC tracks, being with a high probability, products of secondary interactions of primary particle with the detector dead material. The higher limit of accepted $d_0^{(0,0)}$ was set in this analysis, the less background (fake secondary vertices) was found in the secondary vertex distribution, however for a price of limited access to secondary vertices with low radial distance from the z-axis. The cut value of 2 cm was found as a good compromise. In Fig. 12.8, the $d_0^{(0,0)}$ distributions of selected global TOF-matched TPC tracks in the data and embedded MC (without cut on $d_0^{(0,0)}$) are compared. Number of secondary vertices is proportional to both material density and flux of primary particles. To remove bias due to the different fluxes of primary particles in data and

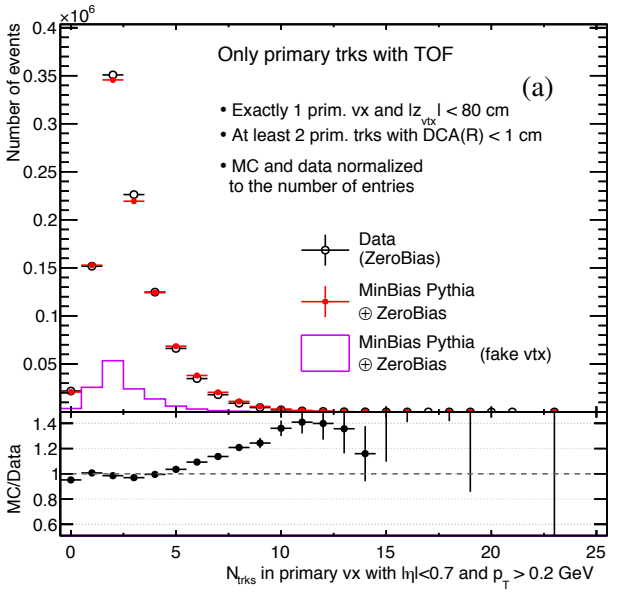

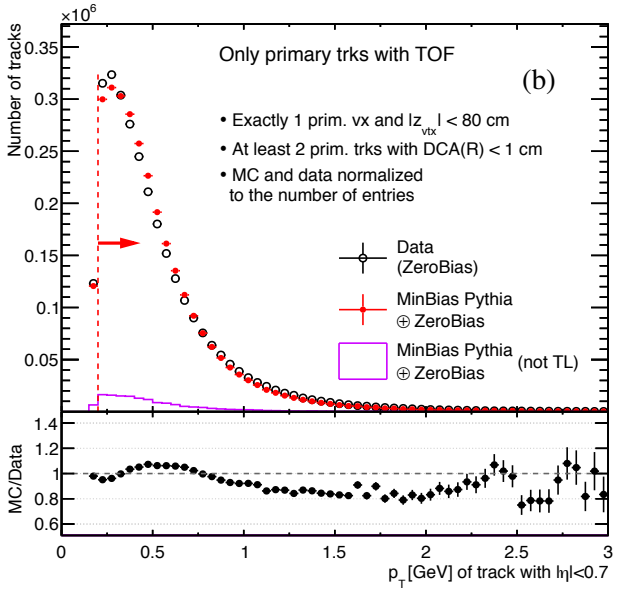

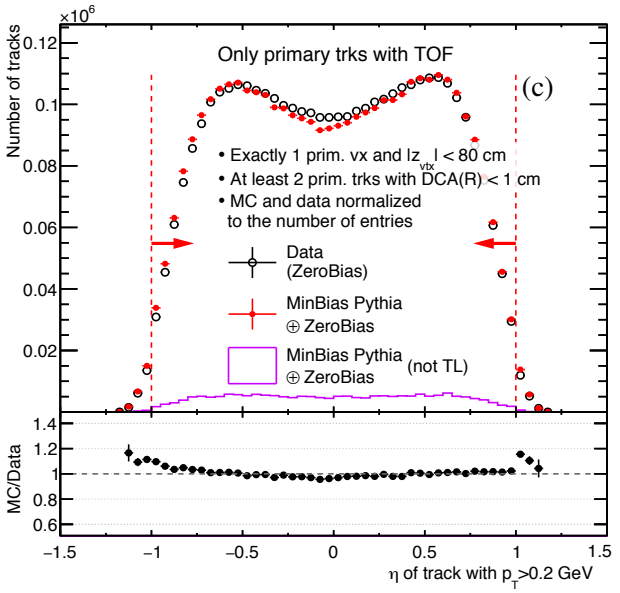

Figure 12.7: Comparison of primary track (a) multiplicity, (b) p_{T} and (c) η distributions in zero-bias data and MB MC embedded into zero-bias triggers. In all subfigures MC histogram is normalised to have the same integral as the data histogram. Violet histogram in (a) represents the fake vertices, defined as vertices with less than a half of constituent tracks being matched with true-level particles. Violet histograms in (b) and (c) represent tracks not matched to true-level particles. Bottom panels show the ratios between MC and data. Red dashed lines and arrows indicate ranges of tracks' p_{T} and η used in the secondary vertices study.

simulation, the latter was scaled by the ratio of the numbers of selected TOF-matched primary TPC tracks in the data and in embedded MC:

$$\text{MC normalisation factor} = \frac{N_{\mathrm{trks}}^{\mathrm{DATA}}}{N_{\mathrm{trks}}^{\mathrm{MC}}}. \tag{12.2}$$

Especially in Fig. 12.8c one can find structures/peaks that might be attributed to subdetectors (PXL, IST, SST) of the HFT. Notable is different yield of histograms, which potentially indicates different amount of simulated dead material with respect to real conditions. Another reason for a difference in yields was found in imperfect simulation of the pointing resolution of the TPC tracks. As shown in Sec. 8.3.2, the track pointing resolution is better in the STAR simulation comparing to data, therefore in MC more true primary particles are reconstructed as primary tracks (are forming/attached to the primary vertices), hence less such tracks is available in the selection of global tracks for secondary vertex reconstruction (comparing to data). However, the adjustment of the pointing resolution, which

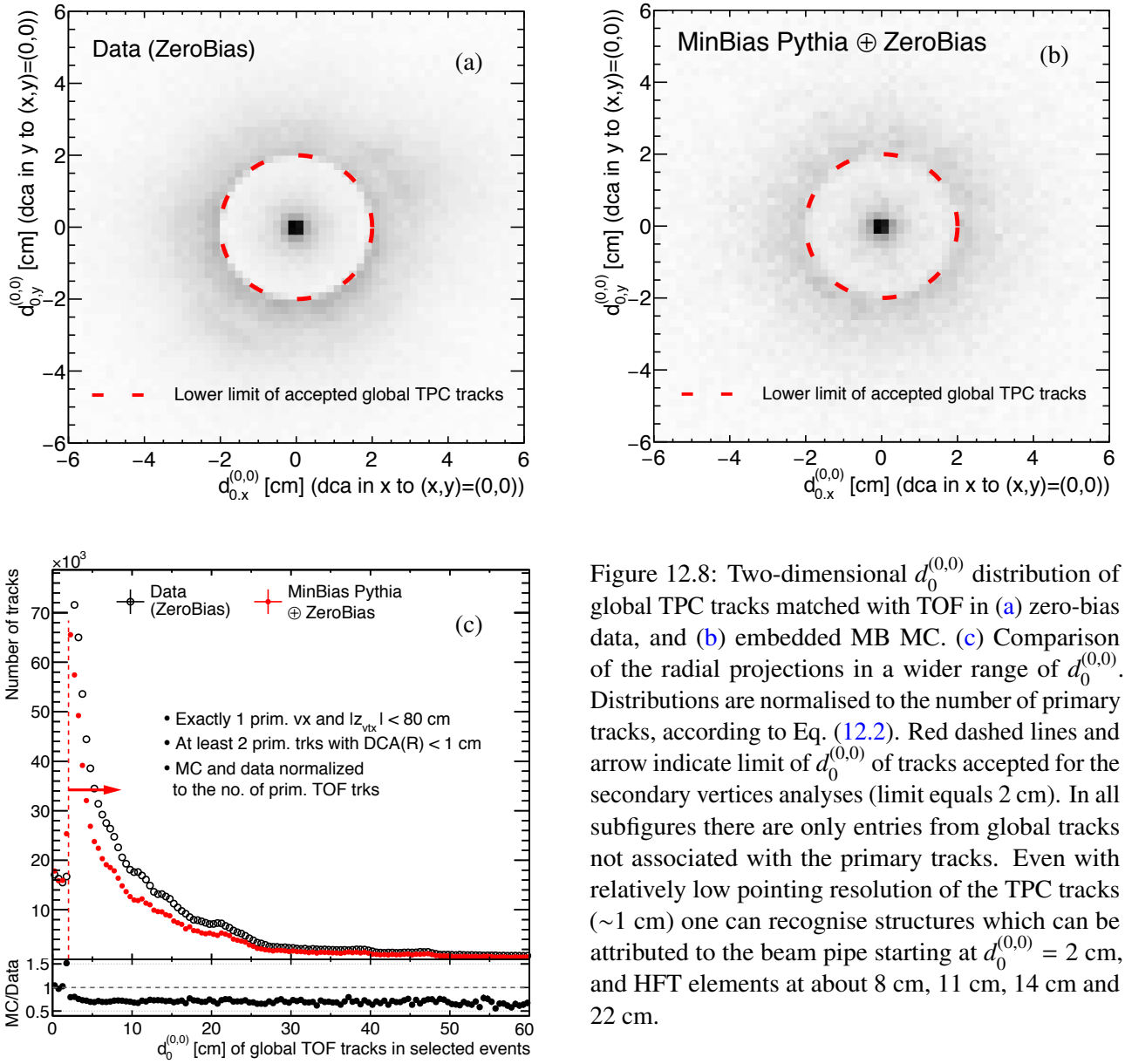

Figure 12.8: Two-dimensional $d_0^{(0,0)}$ distribution of global TPC tracks matched with TOF in (a) zero-bias data, and (b) embedded MB MC. (c) Comparison of the radial projections in a wider range of $d_0^{(0,0)}$. Distributions are normalised to the number of primary tracks, according to Eq. (12.2). Red dashed lines and arrow indicate limit of $d_0^{(0,0)}$ of tracks accepted for the secondary vertices analyses (limit equals 2 cm). In all subfigures there are only entries from global tracks not associated with the primary tracks. Even with relatively low pointing resolution of the TPC tracks (~1 cm) one can recognise structures which can be attributed to the beam pipe starting at $d_0^{(0,0)} = 2$ cm, and HFT elements at about 8 cm, 11 cm, 14 cm and 22 cm.

is applied to the MC tracks (see Sec. 8.3.2) does not help in this case, because the tracks' smearing is applied when the primary vertices have already been reconstructed. This effect is accounted later in the background subtraction procedure to reveal the studied difference in the amount of existing and simulated dead material.

After selection of the secondary track candidates, the following algorithm for secondary vertex reconstruction was used:

1. A loop was executed over all pairs of secondary track candidates. Pairs whose DCA was less than 0.5 cm (nearby tracks passing a proximity cut) were stored.
2. Pairs of nearby tracks from step 1, which shared a common track, were used to form larger sets of tracks.
3. A loop was executed over all sets defined in step 2. For each set, a loop over all pairs from a given set was executed and the worst-matching tracks (these with largest DCA to others) were

rejected until all combinations of tracks' pairs had DCA less than 0.5 cm.

4. Based on a number of tracks in secondary vertex, total charge, specific energy loss, dE/dx, cosine of the opening angle of two tracks, $\cos(\Delta\theta)$, and invariant mass of the two tracks, m_{inv}, the vertex is classified as originating from resonance decay, photoconversion or being of nuclear/hadronic nature (the following *if* statements were performed subsequently):

   (a) if there are at least two tracks pointing to the vertex, or exactly two tracks of the same sign, or exactly two tracks of the opposite sign and the tracks are back-to-back ($\cos(\Delta\theta) < -0.99$), the vertex was recognised as hadronic;

   (b) if $|n\sigma_{\text{pion}}| < 3$ for both tracks and invariant mass (assuming pion masses for the tracks) was in the range 0.470 GeV to 0.515 GeV (Fig. 12.9a) the vertex was recognised as originating from the decay of K^0_S;

   (c) if $|n\sigma_{\text{pion}}| < 3$ for one track and $|n^{\sigma}_{\text{proton}}| < 3$ for the other, and invariant mass (assuming pion and proton masses, respectively) was in the range 1.107 GeV to 1.123 GeV (Fig. 12.9b) the vertex was recognised as originating from the $\Lambda/\bar{\Lambda}$ decay;

   (d) if $|n\sigma_{\text{electron}}| < 3$ for both tracks and invariant mass (assuming electron mass) was less than 0.09 GeV and cosine of the opening angle between two tracks $\cos(\Delta\theta) > 0.95$ (Fig. 12.9c) the vertex was recognised as originating from photoconversion;

   (e) if none of the above was true, the vertex was recognised as hadronic.

5. Vertex position was calculated as the average DCA point of all track pairs in the vertex.

As a result secondary vertices were reconstructed, whose track multiplicity distribution is depicted in Fig. 12.10. Analysis was continued only with vertices of track multiplicity equal to two. The first reason was that most of vertices consist of just a pair of tracks. Another reason was the background subtraction method developed only for vertices made of two tracks. In addition to this, only vertices representing primary particles in the pseudorapidity range $-0.7 < \eta < 0.7$ were analysed. To enable such a selection, a new variable, η_{vtx}, is defined, as the pseudorapidity of the secondary vertex' parent

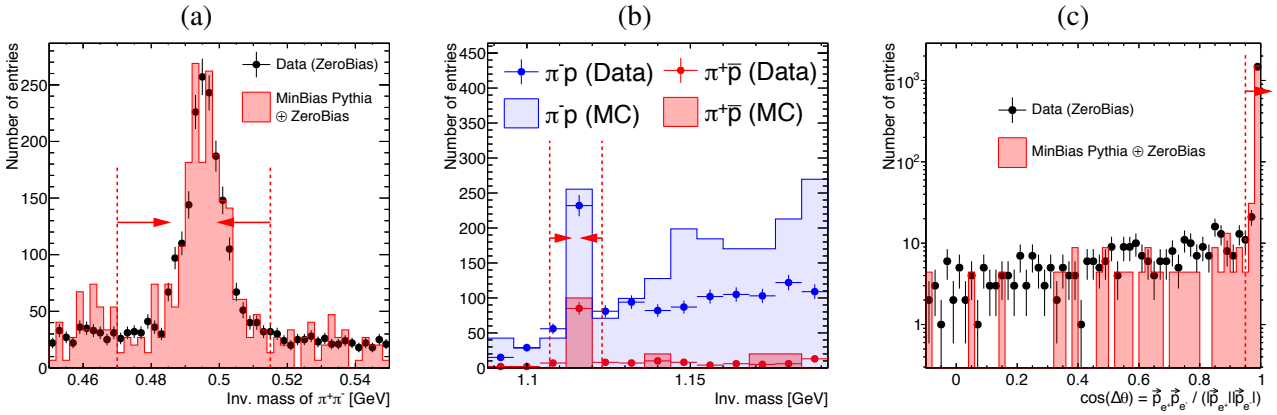

Figure 12.9: Invariant mass of two opposite-sign tracks forming a secondary vertex, recognised as (a) $\pi^+\pi^-$, or (b) $\pi^+\bar{p}/\pi^- p$ pairs, and (c) cosine of the opening angle between two opposite-sign tracks recognised as e^+e^- pair. Dashed red lines and red arrows indicate ranges of quantities which define particular nature of the secondary vertex (photoconversion/resonance decay/hadronic). Zero-bias data are shown as points, while embedded MB MC as filled histograms.

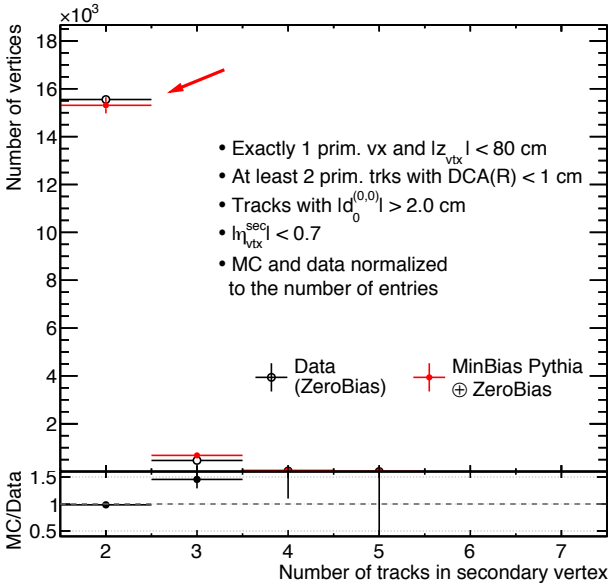

Figure 12.10: Multiplicity of tracks in the secondary vertices. Only vertices with two tracks (indicated with red arrow) were used in the final analysis.

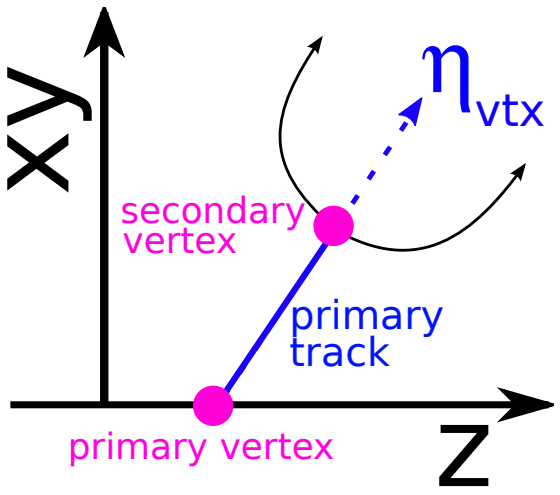

Figure 12.11: Sketch explaining the meaning of the variable η_{vtx}.

primary track (see Fig. 12.11). Only the secondary vertices characterised by $|\eta_{\mathrm{vtx}}| < 0.7$ were included to final analysis.

Raw distributions of the radial, $R_{\mathrm{vtx}}^{\mathrm{secondary}}$, and along the z-axis, $z_{\mathrm{vtx}}^{\mathrm{secondary}}$, positions of the secondary vertices are shown in Fig. 12.12. In the $R_{\mathrm{vtx}}^{\mathrm{secondary}}$ spectrum, one can observe peaks in the regions where the HFT subdetectors are placed. Peaks seem to lie on top of a tail whose origin has been traced to the

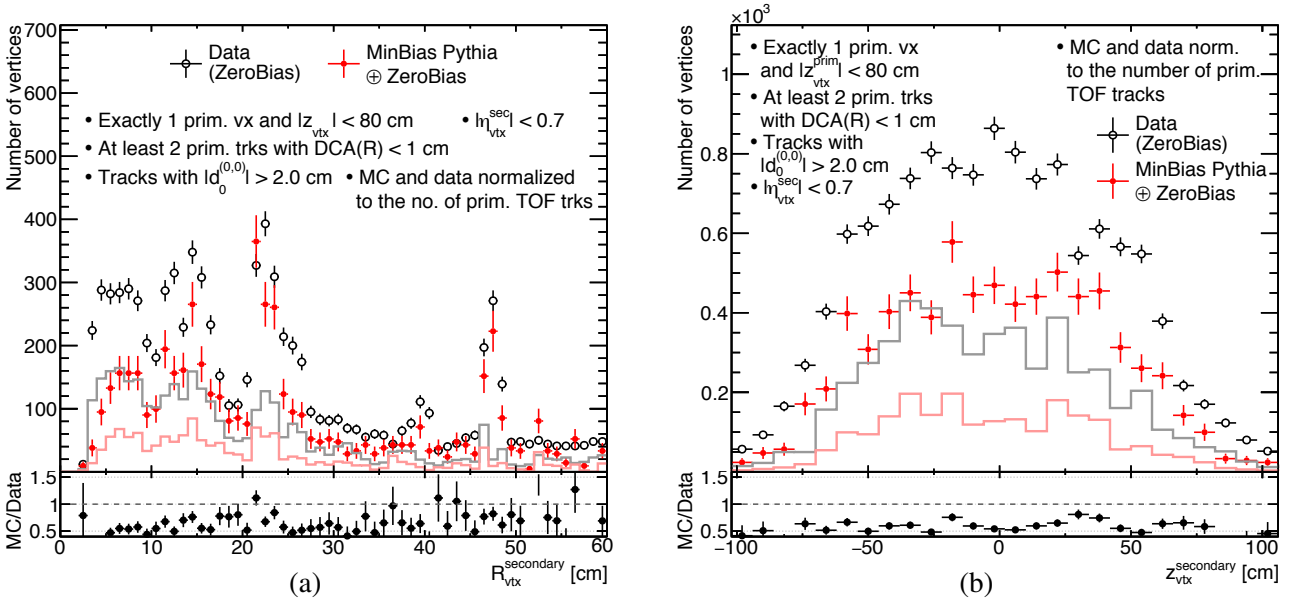

Figure 12.12: Comparison of raw (a) $R_{\mathrm{vtx}}^{\mathrm{secondary}}$ and (b) $z_{\mathrm{vtx}}^{\mathrm{secondary}}$ distribution in the data (open black circles) and embedded MC (filled red circles). The histograms represent background contents to the distributions of the same colour, and estimated as explained in the text. The bottom panels show the ratios of MC to data without the backgrounds subtraction. Only positions of vertices recognised as products of hadronic interactions are shown in the plots.

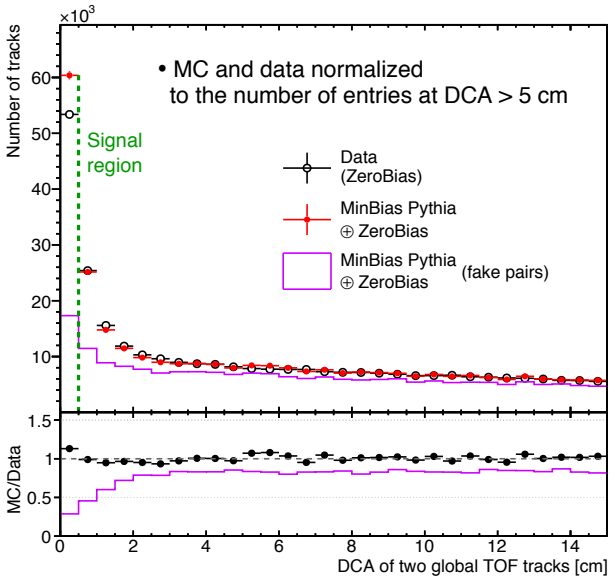

Figure 12.13: Comparison of DCA between all pairs of secondary track candidates selected for the secondary vertex reconstruction in the data and embedded MC. MC histogram is normalised to the data at DCA > 5 cm. Violet histogram depicts pairs contained in MC histogram and not originating from the same vertex. In the bottom panel, the full dots represent the ratio of MC to data, and the violet line represents the ratio of the violet histogram and the red points.

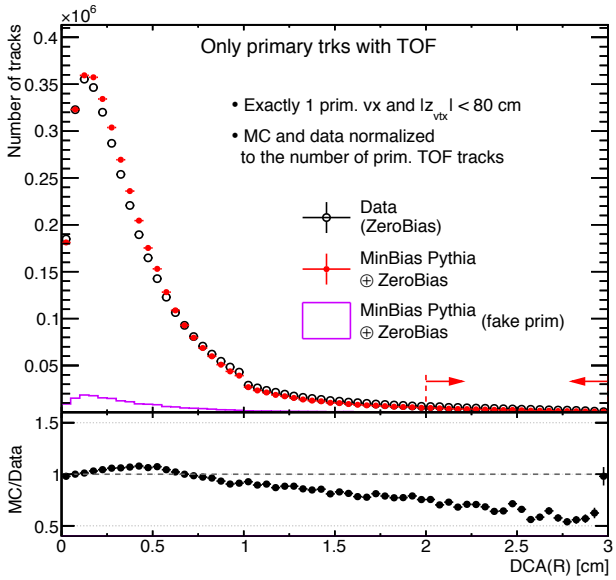

Figure 12.14: Comparison of radial DCA of all primary tracks matched with TOF and passing quality criteria in events selected for secondary vertex analysis, between the data and embedded MC. Violet histogram represents tracks not matched to true-level particles. The bottom panel shows the ratio of MC to data. Red dashed lines and arrows limit region used to find normalisation that compensates different background yield in reconstructed secondary vertex distributions in data and embedded MC. Discontinuity at 1 cm is due to selection of events with at least two tracks of DCA(R) < 1 cm.

secondary vertices made of pair of tracks, one of which was a true primary track that was not associated with any primary vertex and, unfortunately, passed selection of global tracks for the secondary vertex reconstruction. For this reason a method of estimation of the background was invented, as described in the next paragraph. Without this background subtracted, the ratio of MC to data varies mostly between 0.5 and 0.7.

Based on Fig. 12.13 one can find that the most optimal cut to select pairs of tracks from the secondary vertices is as low as about 0.5 cm. The fraction of background vertices extracted from embedded MC (violet line in the bottom panel of Fig. 12.13) was used to determine shape of the background as a function of $R_{\mathrm{vtx}}^{\mathrm{secondary}}$ and $z_{\mathrm{vtx}}^{\mathrm{secondary}}$ (solid lines in Fig. 12.12). This background was calculated as a product of each bin content and the fraction of background vertices extracted from the distribution of DCA between tracks forming a vertex in that bin.

The background fraction extracted from the ratio of the violet and the red histograms in Fig. 12.13 could be used directly only for MC. In the case of data, an additional correction factor, κ, which can be extracted from the ratio of the radial DCA of the primary TPC tracks in events selected for the secondary vertex study (Fig. 12.14), is needed. This ratio at large DCA(R) provides estimate of how many more true primary TPC tracks in the data are not recognised as primary tracks (comparing to MC) and hence overpopulate/enrich sample of global tracks which are selected for the reconstruction of secondary vertices, by definition increasing number of fake background secondary vertices. The value

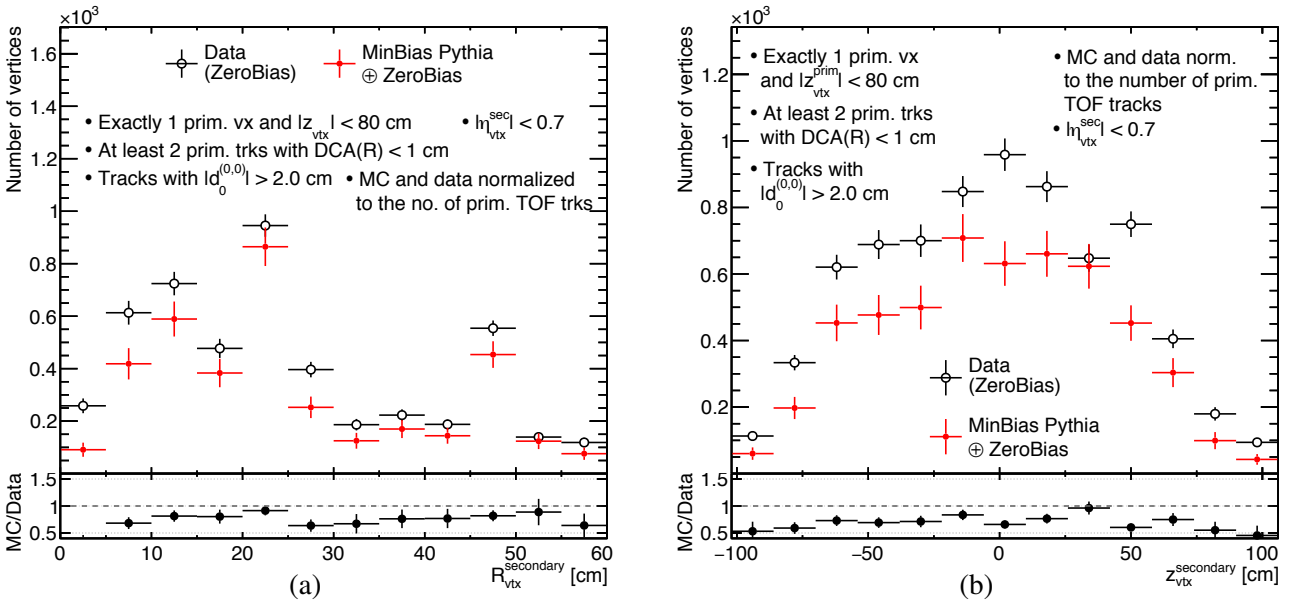

Figure 12.15: Comparison of background-subtracted (a) $R_{\mathrm{vtx}}^{\mathrm{secondary}}$, and (b) $z_{\mathrm{vtx}}^{\mathrm{secondary}}$ distribution in the data (open black circles) and embedded MC (full red dots).

of κ read from Fig. 12.14 is ≈ 1.8. This value is used to recalculate the background fraction in each data bin, so that the ratio of background to true secondary vertices increases by factor κ, comparing to MC.

Background determined with the described method is shown in Fig. 12.12 with the solid lines coloured according to corresponding markers. This background was subtracted and resulting distributions of the secondary vertex positions in the transverse and longitudinal direction are presented in Fig. 12.15. In general, a systematic difference is observed between the dead material amount in the data and STAR simulation of the order of 25%, which is considered as a systematic uncertainty on the amount of the dead material in front of TPC.

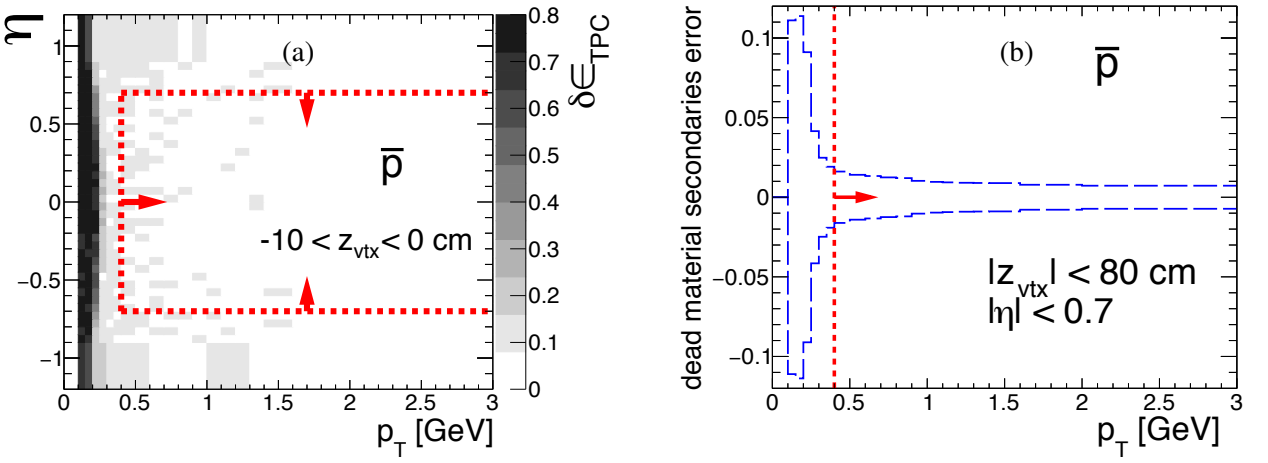

Figure 12.16: (a) Sample distribution of fraction of primary antiprotons dissociated before reaching the inner TPC radius as a function of p_{T} (x-axis) and η (y-axis) in a single z-vertex bin. (b) Estimated systematic uncertainty of the TPC reconstruction efficiency for antiprotons as a function of antiproton transverse momentum. Red lines and arrows indicate region accepted in the analysis. Figures courtesy of L. Fulek.

The systematic uncertainty related to the dead material in front of TPC was translated to uncertainty of the TPC track reconstruction efficiency using no-pile-up MC samples. First, fraction of particles dissociated due to interaction with dead material before the inner TPC radius, $\delta\epsilon_{\mathrm{TPC}}$, was determined. The sample result for $\bar{p}$, which is most sensitive to this effect, is shown in Fig. 12.16a. Next, the systematic uncertainty of the TPC track reconstruction efficiency was calculated as $\pm 0.25 \cdot \delta\epsilon_{\mathrm{TPC}}$, and is shown in Fig. 12.16b.

12.2.3 TPC track quality cuts variation

Sensitivity of the measured fiducial cross sections on the variation of the quality cuts used in the TPC tracks selection, was also tested. Any change of these cuts required re-calculation of the TPC track reconstruction and TOF matching efficiencies (the latter is conditional w.r.t. the former). Two types of working points were evaluated, "loose" and "tight", with different sets of cuts on d_0, $N_{\mathrm{fit}}^{\mathrm{hits}}$ and $N_{\mathrm{dE/dx}}^{\mathrm{hits}}$ (cuts SC3.4) compared to the nominal working point. The loose and tight cuts are defined as follows:

- loose cuts on the numbers of hit points: $N_{\mathrm{hits}}^{\mathrm{fit}} \geq 20$, $N_{\mathrm{hits}}^{\mathrm{dE/dx}} \geq 12$,
- tight cuts on the numbers of hit points: $N_{\mathrm{hits}}^{\mathrm{fit}} \geq 28$, $N_{\mathrm{hits}}^{\mathrm{dE/dx}} \geq 17$,
- loose d_0 cut: $|d_0| < 3$ cm,
- tight d_0 cut: $|d_0| < 1$ cm.

Observed ratios of the cross-sections obtained with modified cuts and accordingly redefined TPC and TOF efficiencies, to the nominal cross-section, are shown in Fig. 12.17 as a function of the $\pi^+\pi^-$ pair invariant mass. The upward and downward relative changes of the cross-sections were added in quadrature. The resulting systematic uncertainty of the cross-section related to the TPC track quality cuts was estimated to be $\pm 1.5\%$.

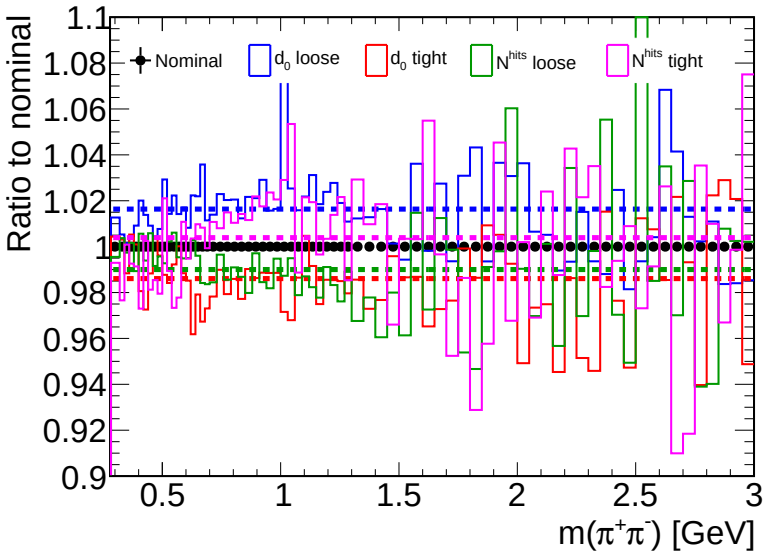

Figure 12.17: Result of variation of the TPC track quality cuts on the fiducial differential exclusive $\pi^+\pi^-$ production cross-section as a function of the invariant mass of $\pi^+\pi^-$. Dashed horizontal lines represent an average ratio for a modified cut shown in the same colour.

12.3 TOF matching efficiency

Systematic uncertainty of the TOF efficiency related to the accuracy of the TOF system simulation in STARsim and the data driven TOF efficiency correction derived in Sec. 11.2.2 was estimated by comparing the nominal TOF efficiency (from the simulation and with added the aforementioned data-driven correction to TOF efficiency) with the one obtained using an independent method described below. Systematic uncertainty of the TOF efficiency related to the pile-up has been estimated in Ref. [33] and found to be negligible, hence it is not further discussed.

In some STAR analyses, the TOF hit reconstruction and matching efficiency is determined from the data with the use of BEMC. Real (in-time) tracks are selected based on the fact that they match to BEMC cluster. If they do, the TOF efficiency is calculated as a ratio of the number of TOF-matched tracks to the number of all tracks. This solution may provide slightly biased efficiency, because the signal in the detector placed behind TOF, such as BEMC, ensures that particle still followed the original helical path past the last hit of the track in TPC (Fig. 12.18). Also, BEMC clusters require significant energy deposits to be reconstructed, which may favour tracks which generated secondaries in front of the BEMC, hence possibly also in front of TOF thus increasing a chance to reconstruct hit in TOF.

To estimate systematic error of the TOF efficiency it was decided to determine this efficiency using the TPC tracks containing hits in HFT. Since the HFT is a fast (silicon) detector, the TPC track which contains hits in the HFT is very probably a real track of particle produced in the proton-proton interaction. Using these HFT-tagged tracks, the potential bias related to matching with BEMC cluster is omitted.

The HFT-tagged tracks were selected as the primary tracks passing the quality cuts SC3.4 (only the TPC hits were counted). These tracks were required to contain hits in two HFT layers: IST ans SST, which vastly reduced probability to select an off-time track in TPC (PXL was not used in reconstruction

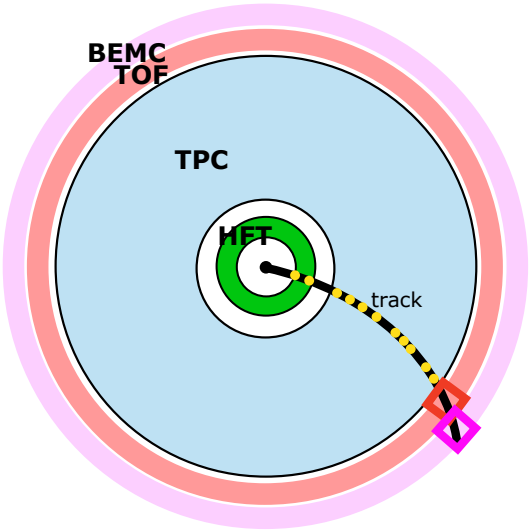

Figure 12.18: Sketch of the cross section of the central detector and the track reconstructed with hits in HFT. Presence of the HFT hits in a reconstructed track can be used as a tagger of the in-time tracks.

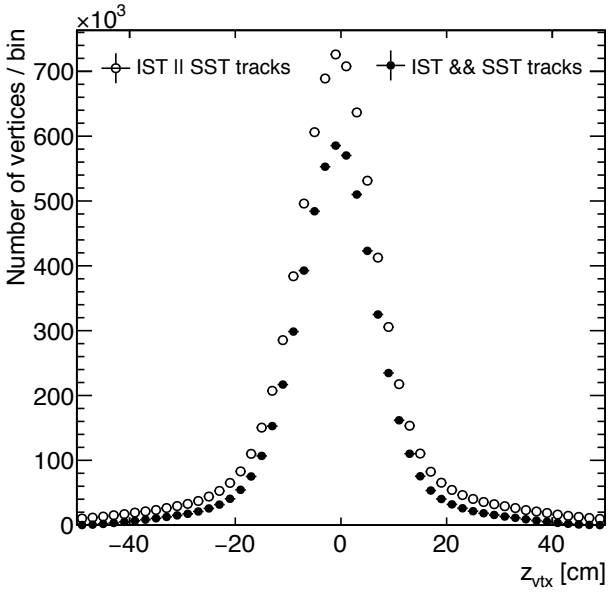

Figure 12.19: Distribution of z-position of vertices containing TPC tracks with HFT hits (st_ssd stream). Open circles represent vertices with tracks with hits in IST or SST, full circles - IST and SST.

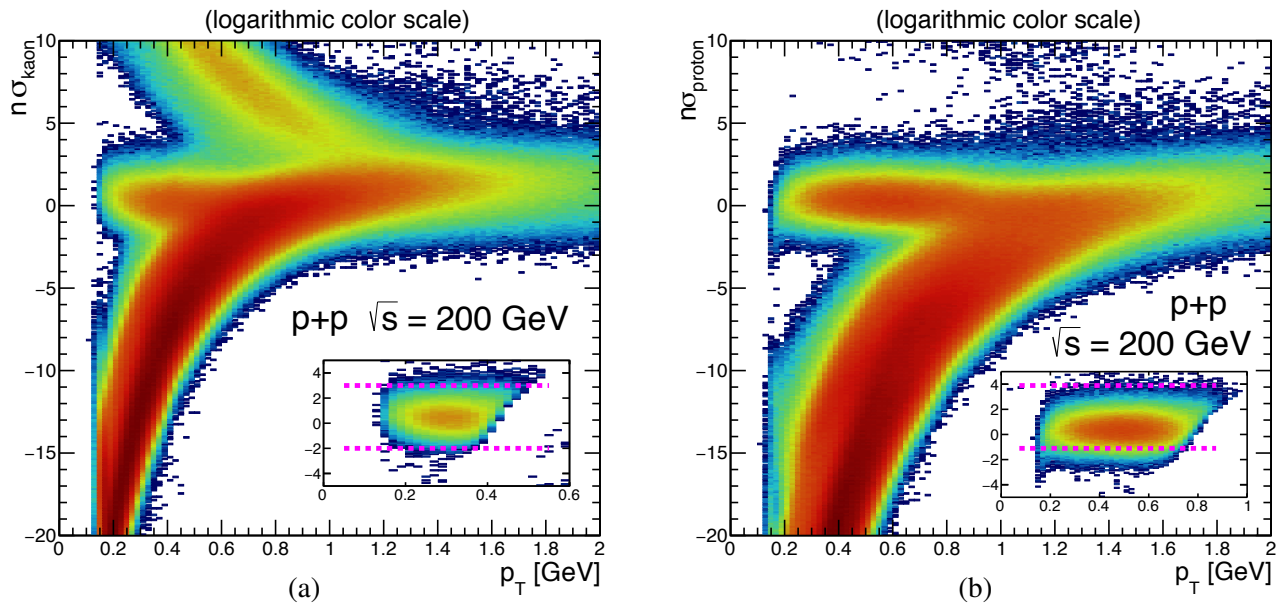

Figure 12.20: Distribution of (a) $n\sigma_{\text{kaon}}$ and (b) $n\sigma_{\text{proton}}$ vs. track p_{T} for tracks containing HFT hits. The insert in each subfigure shows the corresponding $n\sigma$ vs. p_{T} distribution after preselection of tracks of given species (without cut on variable in y-axis). Dashed magenta lines represent final cuts on corresponding $n\sigma$ quantity used to select tracks of given species.

due to problems in firmware). As shown in Fig. 12.19, the z_{vtx} coverage of the HFT-tagged tracks is limited to about ±20 cm. Such cut on the z-position of the vertex, $|z_{\text{vtx}}| < 20$ cm, was imposed to remove tracks from the tails of the distribution, which generally have large $|\eta|$.

Identification of particles was done using the specific energy loss measured in the TPC. The following requirements were imposed on $n\sigma$ in order to select three species of particles, which tracks were used for the TOF efficiency analysis:

- pions: $|n\sigma_{\text{pion}}| < 2$,
- kaons: $-2 < n\sigma_{\text{proton}} < 2.5$ && $|n\sigma_{\text{pion}}| > 3.5$ && $|n\sigma_{\text{electron}}| > 3.5$ && $|n\sigma_{\text{proton}}| > 3.5$,
- protons: $-2 < n\sigma_{\text{proton}} < 3$ && $|n\sigma_{\text{pion}}| > 3.5$ && $|n\sigma_{\text{electron}}| > 3.5$ && $|n\sigma_{\text{kaon}}| > 3.5$.

Selection of pions by cut solely on $n\sigma_{\text{pion}}$ (without additional cuts on $n\sigma$ for kaon, proton and electron hypothesis) was driven by the dominance of pion production over other species and by the fact that the dE/dx of pions overlap with kaons and protons at momenta which are relatively large, hence the TOF efficiency is saturated and similar for all particle species. More sophisticated selection was used for kaons and protons. Figure 12.20 shows the $n\sigma$ versus track's p_{T} distributions, before and after selection of kaons and protons. One can see that clean samples of these particles were selected, for the price of limited coverage in track's p_{T}.

From selected sample of pion, kaon and proton tracks, the TOF hit reconstruction and matching efficiency was obtained as the ratio of the number of tracks matched with TOF to the number of all selected tracks. This efficiency was compared with the efficiency extracted from the zero-bias-embedded single particle MC, calculated for $|z_{\text{vtx}}| < 20$ cm and averaged between positive- and negative-charge particles. The result of comparison - the difference between efficiency calculated with HFT-tagged tracks and efficiency from single particle MC, is presented in Fig. 12.21 (subfigures

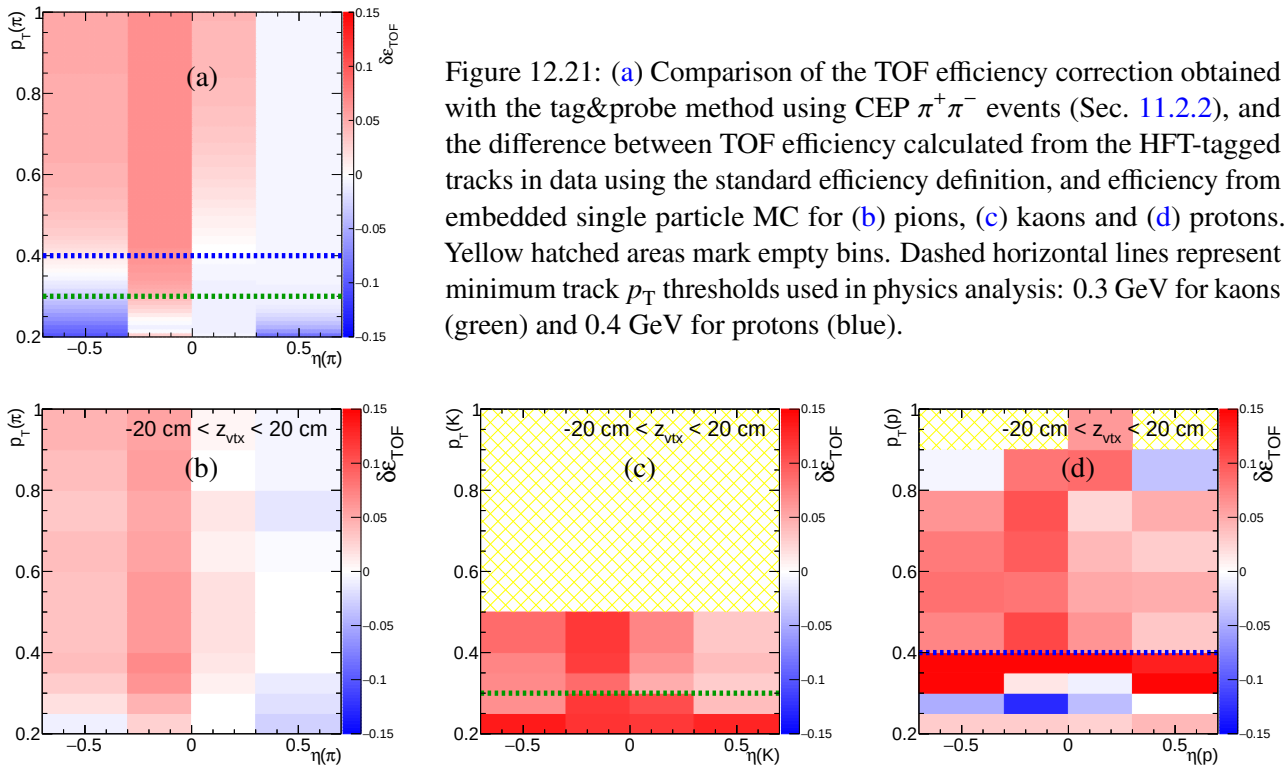

Figure 12.21: (a) Comparison of the TOF efficiency correction obtained with the tag&probe method using CEP $\pi^+\pi^-$ events (Sec. 11.2.2), and the difference between TOF efficiency calculated from the HFT-tagged tracks in data using the standard efficiency definition, and efficiency from embedded single particle MC for (b) pions, (c) kaons and (d) protons. Yellow hatched areas mark empty bins. Dashed horizontal lines represent minimum track p_T thresholds used in physics analysis: 0.3 GeV for kaons (green) and 0.4 GeV for protons (blue).

12.21b-12.21d). This difference could be interpreted as a data-driven correction to the TOF efficiency calculated from single particle MC, alternative to correction derived with tag&probe method on CEP events, described in Sec. 11.2.2.

Differences between the alternative corrections in Figs. 12.21b-d and the correction from tag&probe method (Fig.12.21a), $\Delta\delta\varepsilon_{\mathrm{TOF}}$, could be used as a measure of the uncertainty of the overall TOF efficiency. These differences are shown in Fig. 12.22. It was decided to symmetrise the systematic uncertainty of the TOF efficiency. For this purpose, on top of the correction to TOF efficiency from the tag&probe method, half of the difference from Fig. 12.22 to the TOF efficiency of corresponding

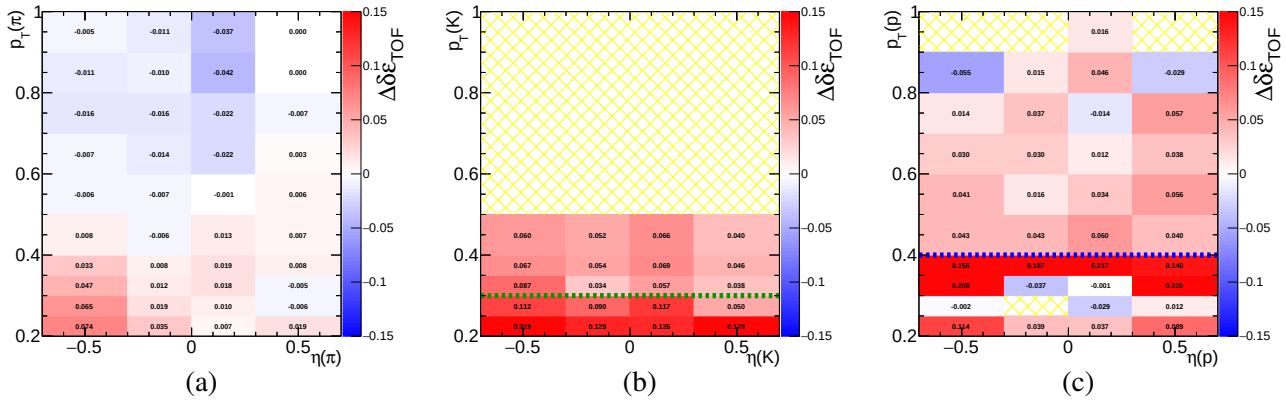

Figure 12.22: Difference between the TOF efficiency correction estimated with the HFT-tagged tracks for (a) pions, (b) kaons and (c) protons, and the correction obtained from the tag&probe method applied to the CEP $\pi^+\pi^-$ events. The subsequent plots in the figure are obtained as differences between plots Fig. 12.21b,c,d and the plot in Fig. 12.21a, respectively. Yellow hatched areas mark bins which are empty in Fig. 12.21. Dashed horizontal lines represent minimum track p_T thresholds used in the analysis: 0.3 GeV for kaons (green) and 0.4 GeV for protons (blue).

particle type was added. The systematic uncertainty of the TOF efficiency in each (η, p_T) bin was set to the absolute value of the half of that difference, $\frac{1}{2}|\Delta\delta\varepsilon_{TOF}|$. In the following, it is assumed that the systematic uncertainty for tracks with $|z_{vtx}| > 20$ cm is the same as for the HFT tracks studied here ($|z_{vtx}| < 20$ cm). For high-p_T tracks, with no direct estimates of $\Delta\delta\varepsilon_{TOF}$, the average value from two closest, but non-empty lower-p_T bins (in a given η bin) was used as a correction, and the maximum absolute value among the three closest, but non-empty p_T bins (in given η bin) was used as a systematic uncertainty.

The effective systematic uncertainties, represented one-dimensionally as a function of track's p_T and η, are shown in Fig. 12.23. From the figure one can read out, that the uncertainties for pion, kaon and proton tracks, are of the order of 1%, 3% and 2%, respectively.

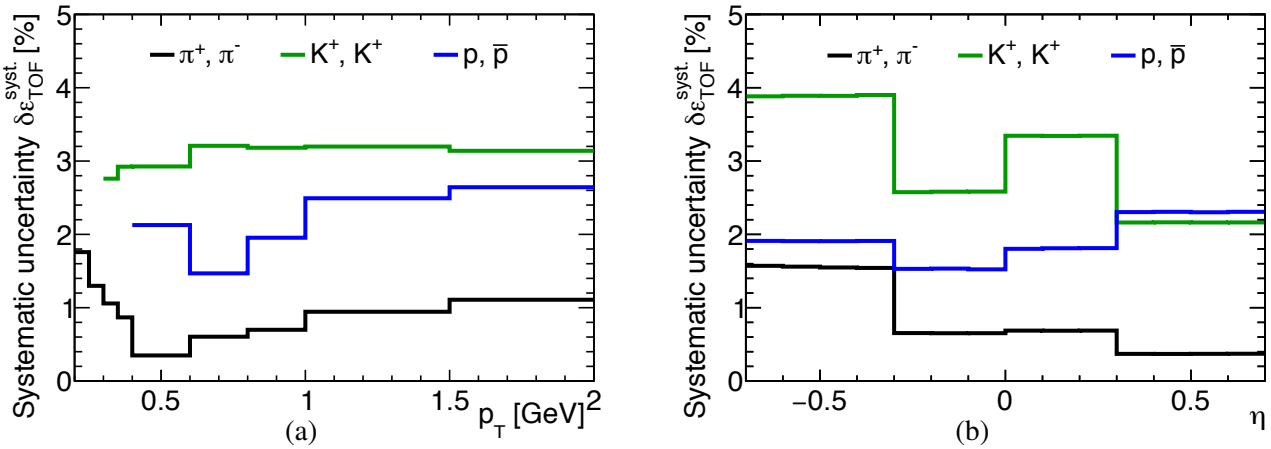

Figure 12.23: Effective systematic uncertainty of the TOF efficiency related to the simulation accuracy, shown as functions of the track's (a) p_T and (b) η. The p_T-dependence was calculated for tracks within $|\eta| < 0.7$, while η-dependence was calculated for tracks with p_T greater than the threshold set for a given particle species (SC8.2).

12.4 RP track reconstruction and trigger efficiency

12.4.1 Track (absolute) reconstruction efficiency

Nominally, the RP track reconstruction efficiency was obtained from the zero-bias-embedded MC events, as a probability, that a forward-scattered proton, when transported from the IP to the RP stations, produces hits in SSDs, that are reconstructed as a track point(s), which form a track passing the selection cuts (SC4.1). The systematic uncertainty of this efficiency, which reflects the accuracy of the simulation (modelling of the dead material, signal digitisation, etc.), has been estimated using elastic scattering events. The same analysis scheme was used for the data and for embedded elastic scattering MC events. The difference between efficiency estimates extracted from the data and simulation, was used as a measure of the systematic uncertainty of the nominal RP track reconstruction efficiency.

Although in the thesis, a different processes is studied, the difference between the measured and simulated elastic proton-proton scattering events, should be a good measure of the systematic uncertainty. Elastic scattering was chosen for this study as it is the cleanest process involving forward-scattered protons - backgrounds can be suppressed relatively easy with the collinearity constraint. In addition to this, parameters of the proton track (its momentum, position in the detector) can be

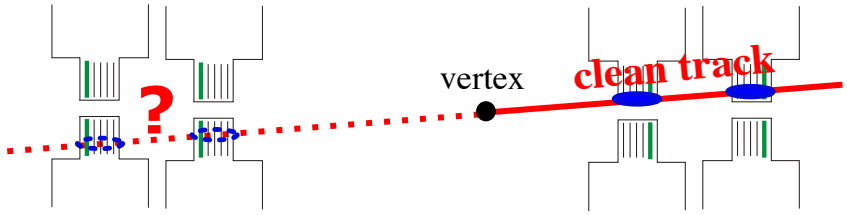

Figure 12.24: Sketch of an elastic scattering event with forward-scattered protons within the acceptance of the RP stations, illustrating the method used for estimation of the RP track reconstruction efficiency.

reconstructed even in the case of lack of signal in one or both detectors in a branch. An additional argument to use elastic scattering is that in CEP of states with low invariant masses ($\lesssim 3$ GeV), the forward-scattered protons have $\xi \approx 0$, rarely exceeding 0.05 in studied rapidity range of the central state.

The idea behind this study, was to select elastic proton-proton scattering events using the elastic trigger data (RP_ET, see Chap. 7), with a clean RP track with ξ consistent with zero within $3.5\sigma(\xi)$ in one of branches with the trigger, and counting how often there was reconstructed and successfully selected collinear RP track in the opposite branch with the trigger signal. The method is illustrated in Fig. 12.24. Detailed description of the algorithm is provided below:

1. Elastic proton-proton scattering MC events (generated with the slope of the t-distribution $B = 14.3$ GeV^{-2}, according to the measurement from Ref. [2]) passed through the magnetic field and RP detectors simulation in Geant4 and embedded into zero-bias data, were subjected to the same trigger conditions as data (signals in trigger counters in opposite RP branches were required). The zero-bias data used in embedding were taken from the same runs for which RP_ET triggers were analysed. Also, number of simulated events for each run was proportional to the number of elastic scattering events in that run.

2. Since RP_ET triggers can be fired not only by elastic interactions but also, for instance, by central diffraction events, minimum bias events with forward remnants of protons, overlaps of single diffraction events with beam halo protons, etc., several vetoes were applied to suppress non-elastic interaction/pile-up:

   - TOF L0 multiplicity = 0,
   - empty BBC-S and BBC-L,
   - empty ZDC,
   - empty VPD,
   - no. of reconstructed TOF hits = 0,
   - false state of RP_IT trigger bit (trigger signal only in RP branches forming an elastic trigger bit RP_ET).

   Distributions of ξ in data and MC simulation, before and after applying the above vetoes, are shown in Fig. 12.25. Before the vetoes are applied, a significant contribution of non-elastic forward protons in the data sample is clearly visible (excess over MC for $\xi > 0.01$). A satisfactory agreement between the data and MC is obtained after applying the vetoes, which indicates a successful purification of the data sample.

3. From the difference between average time of the trigger signal in West and East RP stations, the z-position of the vertex was reconstructed and required to satisfy condition $|z_{\rm vtx}| < 80$ cm, which is the same as the range of $z_{\rm vtx}$ accepted in physics analysis.

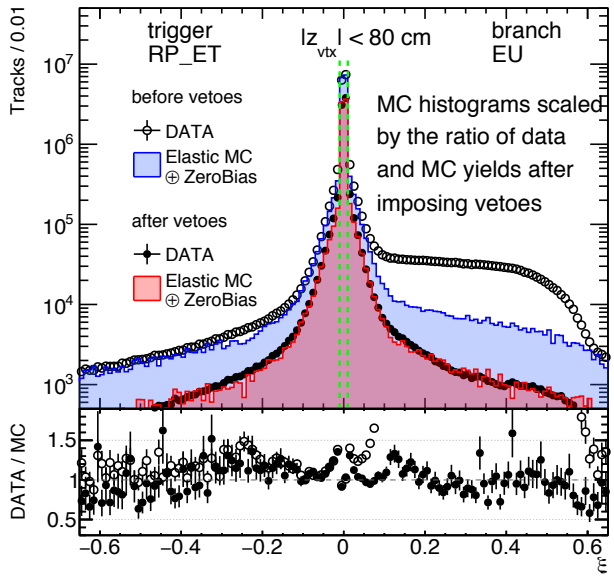

Figure 12.25: Fractional momentum loss ,ξ, of clean proton tracks in the EU branch before and after imply-ing the vetoes discussed in the text. Data are shown by opened and filled circles, while the elastic MC events embedded into zero-bias data are shown as filled histograms. MC histograms are scaled by the ratio of data and MC yields after applying the vetoes. The bottom panel shows the ratio of corresponding distributions in the data and MC. Dashed green ver-tical lines show the ξ range of tracks accepted for the RP track (and also track point) efficiency studies, $|\xi| < 0.01$.

4. A clean set of track points was required on one side of the IP (tagging side or reference side) in the branch with the trigger signal. The "clean set of track points" is defined as one of the following combinations of the numbers of reconstructed track points in the 1st and in the 2nd RP station in the given branch: 1 and 0, 0 and 1, or 1 and 1. From the clean set of track points, an RP track was reconstructed using in addition the z-position of the vertex obtained in step 3. Only tracks with $|\xi| < 0.01$ were used as a reference tracks (tags) in this study.

5. It was checked if there was an RP track passing the track selection cuts used in the CEP analysis (SC4.1 and SC4.2) in the 'probed' branch (opposite to the reference branch and with the trigger signal). If the probe track was found, the collinearity between the tag and the probe tracks was checked. The differences between the x- and y-components of the polar angles (calculated with respect to the original beam directions) of the two tracks are shown in Fig. 12.26. The two tracks were claimed to be collinear, and the event was tagged as elastic, if the both differences were within 3.5 standard deviations ($\approx$ 180 µrad).

6. The RP track reconstruction efficiency, ε, is defined as a probability, that exactly one probe RP track was reconstructed and selected in the studied branch.

7. Steps 4-6 were performed for each side separately.

The efficiencies obtained using the above method were calculated as a function of the expected transverse momentum components of the proton in the branch under study. These components were assumed to be equal to the (p_x, p_y) of the track in the tagging branch taken with the "-" sign to reflect the fact that elastically scattered protons have opposite momentum, $(p_x^{\mathrm{E}}, p_y^{\mathrm{E}}, p_z^{\mathrm{E}}) = (-p_x^{\mathrm{W}}, -p_y^{\mathrm{W}}, -p_z^{\mathrm{W}})$ (in the centre-of-mass reference frame, which here is identical with the laboratory frame, modulo beam divergence).

A sample result for a single branch is presented in Fig. 12.27. One can see, that the difference between RP track reconstruction efficiency estimated from the data and from embedded MC do not differ by more than $\sim 5\%$. In the central part of the fiducial region used in CEP analysis (Eq. (9.2)), where sensitivity to the edge effects (uncertainty on aperture positions), to dead material effects and to inaccuracies in simulated angular beam divergence is suppressed, the difference is not larger than

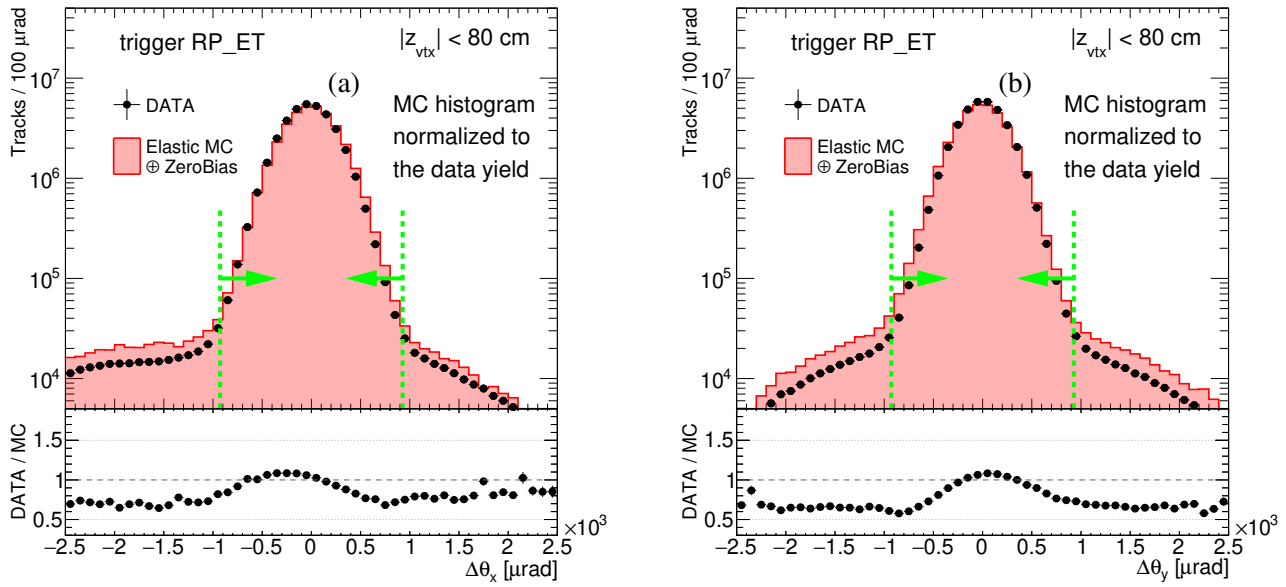

Figure 12.26: Collinearity between the reference and the probe tracks in terms of the differences between x- and y-components of the polar angles (a) $\Delta\theta_x$, and (b) $\Delta\theta_y$. An elastic track is claimed as reconstructed if the collinearity of two tracks does not exceed 3.5 standard deviations, as marked with dashed green vertical lines and arrows.

$\sim 1\%$. This value was used as the systematic uncertainty on the track reconstruction efficiency related to the signal digitisation, embedding and the track reconstruction algorithm. The largest difference between the data and simulation is observed in the corner of the fiducial region roughly described by:

$$(p_x - 0.2)^2 + p_y^2 > 0.46^2 \quad \text{(all in GeV)}, \tag{12.3}$$

where the RF shield between the 1st and the 2nd RP stations, and possibly also the front part of the DX-D0 chamber partially interfere with the RP detectors. This may indicate that the thickness/density of these elements is not accurately modelled (too thick/dense pieces of material implemented in the simulation). Therefore, a correction to the RP track reconstruction efficiency in the corner of the fiducial region (Ineq. 12.3), equal to the difference between data and MC track reconstruction efficiency estimates presented in Fig.12.27a (and corresponding plots for other branches), was introduced. A conservative systematic uncertainty was assigned to the efficiency in this corner region equal to the absolute value of the correction. Also, for the remaining part of the fiducial (p_x, p_y) region, a systematic uncertainty of the RP track reconstruction efficiency was assigned equal to the absolute value of the difference between data and MC track reconstruction efficiency estimates shown in Fig. 12.27a (similar for other branches). These differences should also cover uncertainties related to the angular beam divergence effects and error on positions of limiting apertures in the simulation.

12.4.2 Track point (relative) reconstruction efficiency

A single track point reconstruction efficiency can be studied in a way similar to the track reconstruction efficiency. In contrast to the latter, to estimate track point reconstruction efficiency one can fully reconstruct elastic scattering event independently from the studied detector, which provides even higher purity of the sample in comparison to the track reconstruction efficiency.

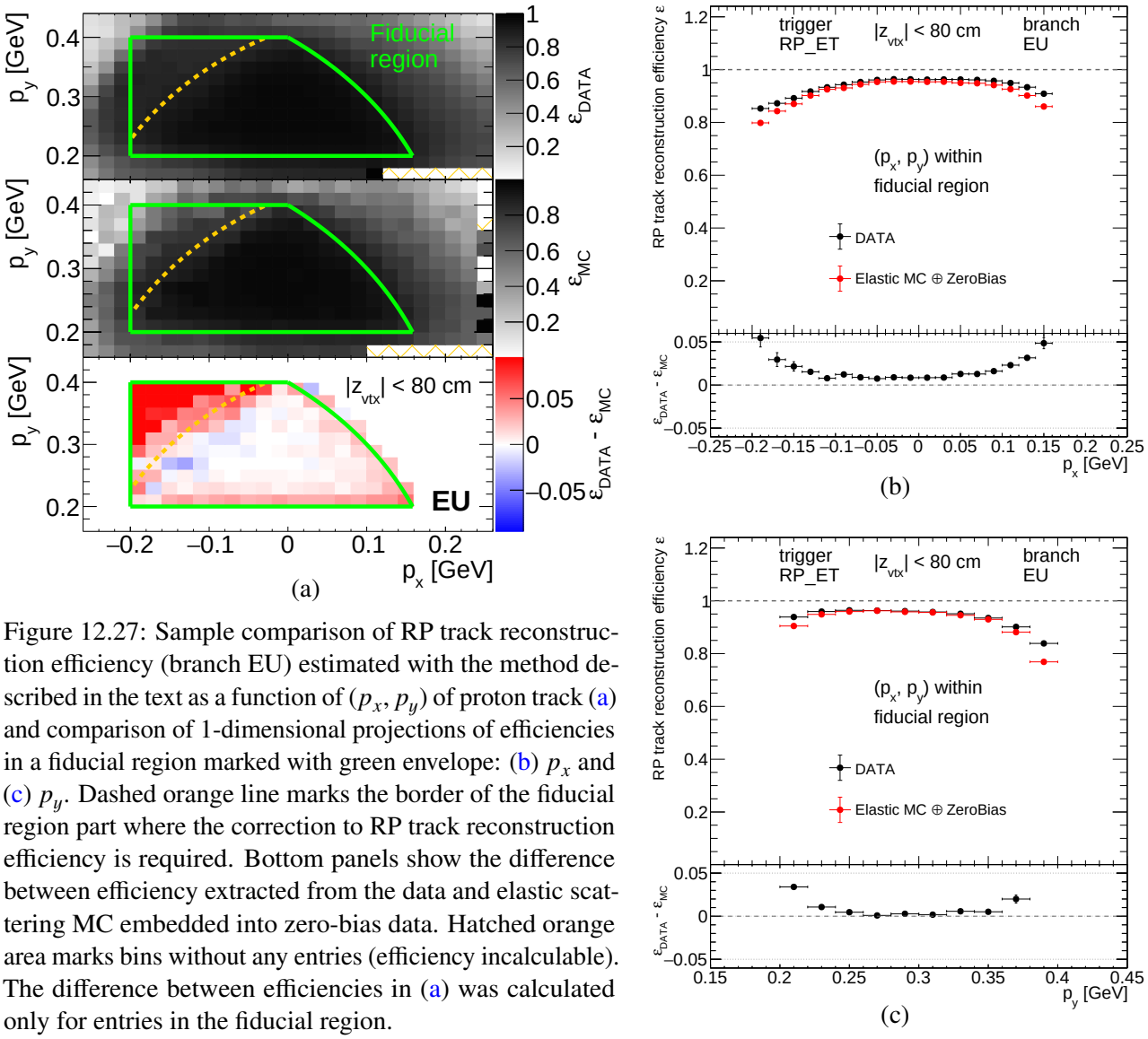

Figure 12.27: Sample comparison of RP track reconstruction efficiency (branch EU) estimated with the method described in the text as a function of (p_x, p_y) of proton track (a) and comparison of 1-dimensional projections of efficiencies in a fiducial region marked with green envelope: (b) p_x and (c) p_y. Dashed orange line marks the border of the fiducial region part where the correction to RP track reconstruction efficiency is required. Bottom panels show the difference between efficiency extracted from the data and elastic scattering MC embedded into zero-bias data. Hatched orange area marks bins without any entries (efficiency incalculable). The difference between efficiencies in (a) was calculated only for entries in the fiducial region.

The comparison between track point reconstruction efficiency in the data and simulation provides better insight to discrepancies in detector geometry and amount of material than comparison of track reconstruction efficiency, as in this case the effect of angular beam divergence is reduced by using proton track observables reconstructed on the side of studied RP detector. Relative RP efficiency is mostly sensitive to material in between the RP stations in the same branch, as the presence of elastic track reconstructed in the studied branch assures that proton survived transport from the IP to RP stations. This study provides also information about performance of the track-point reconstruction algorithm.

Unfortunately, information about the track point reconstruction efficiency is limited - there is no access to some part of the fiducial region, approximately $p_x \lesssim -0.08$ GeV. This is because the RP detectors in the 1st and the 2nd stations do not fully overlap - they are shifted with respect to each other, with the most significant offset in x direction (≈ 2 cm) due to restrictions imposed on DX-D0 chamber at the design level, mainly to accommodate ZDC detectors placed behind the 2nd RP stations.

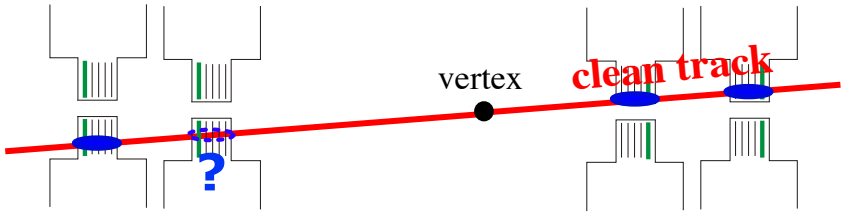

Figure 12.28: Sketch of an elastic scattering event with forward-scattered protons within the acceptance of the RP stations, illustrating the method used for estimation of the RP track point reconstruction efficiency.

In this analysis, elastic proton-proton scattering events were selected by requiring the elastic trigger (signal in PMTs in two opposite RP branches), a clean RP track with $|\xi| < 0.01$ on at least one side of the IP and a clean track point with the trigger signal in at least one RP detector (the reference RP) in the opposite branch. A track was formed from this clean track point and the two tracks were required to be collinear within 3.5 standard deviations, and in the other RP detector in the studied branch the trigger signal was also required. The probability to have exactly one track point in the studied RP with position consistent with that extrapolated from the reference RP was referred to as the track point reconstruction efficiency. The method is illustrated in Fig. 12.28. Detailed description of the algorithm is provided below, excluding steps 1–4 which are the same as in Sec. 12.4.1:

5. The RP station with a clean track point (exactly one track point in the station, reconstructed from at least three out of four SSDs) and the trigger signal in the studied branch (opposite to the tagging branch) was chosen as the reference detector. A track was formed from the track point in the reference detector. Then the collinearity between the tagging track and the track reconstructed from the clean track point in studied branch (Fig. 12.26) was calculated. If the collinearity was satisfied within 3.5 standard deviations, the reference elastic track was claimed reconstructed.

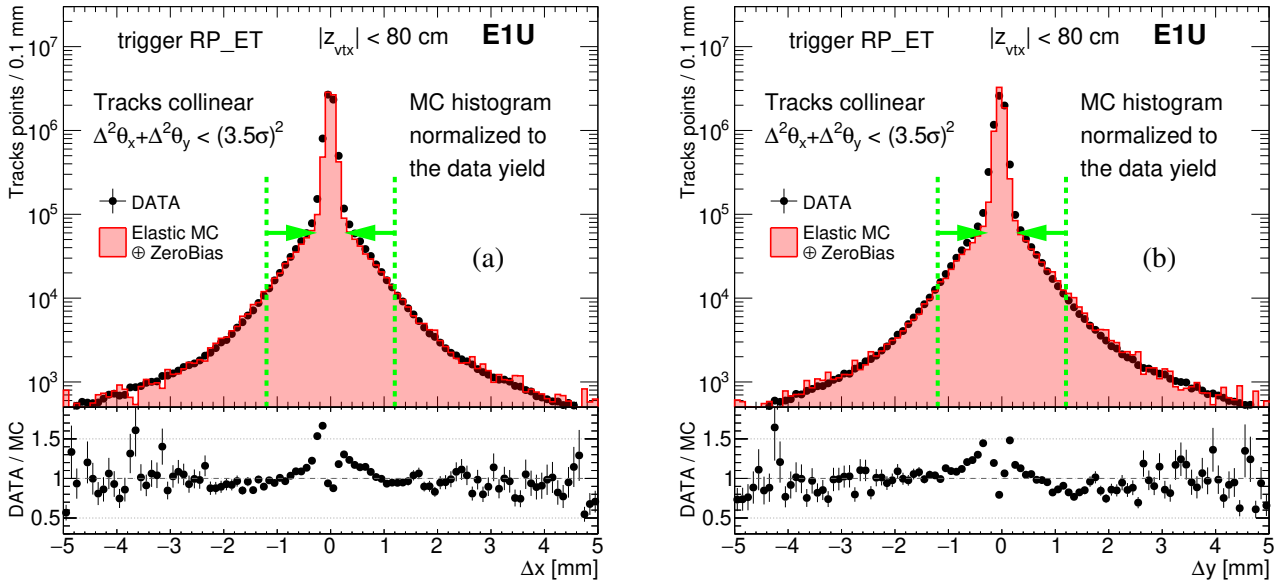

Figure 12.29: Differences between the (a) x, and (b) y positions of the track points reconstructed in E1U RP detector (if there was a trigger signal in the detector) and the expected track point position extrapolated from the reference track point reconstructed in the E2U RP detector, for elastic scattering events, assuming the collinearity with the tagging track in the opposite RP branch. A track point is claimed as reconstructed if the position difference is not larger than 1.2 mm, as marked with dashed green lines and arrows.

6. The trigger signal was required in the detector under study. The RP track point reconstruction efficiency is defined as the probability, that in the considered RP, among all reconstructed track points, exactly one track point has reconstructed (x, y) coordinates, consistent with the position $(x_{\text{extr}}, y_{\text{extr}})$ extrapolated from the reference detector within 1.2 mm (see Fig. 12.29).
7. Steps 5 and 6 were repeated for each RP station in the studied branch and also for other possible tagging track–reference track combinations.

Samples of obtained estimates of the track point reconstruction efficiencies are shown in Fig. 12.30. The efficiencies are presented two-dimensionally as functions of (p_x, p_y) and (x, y), and also as

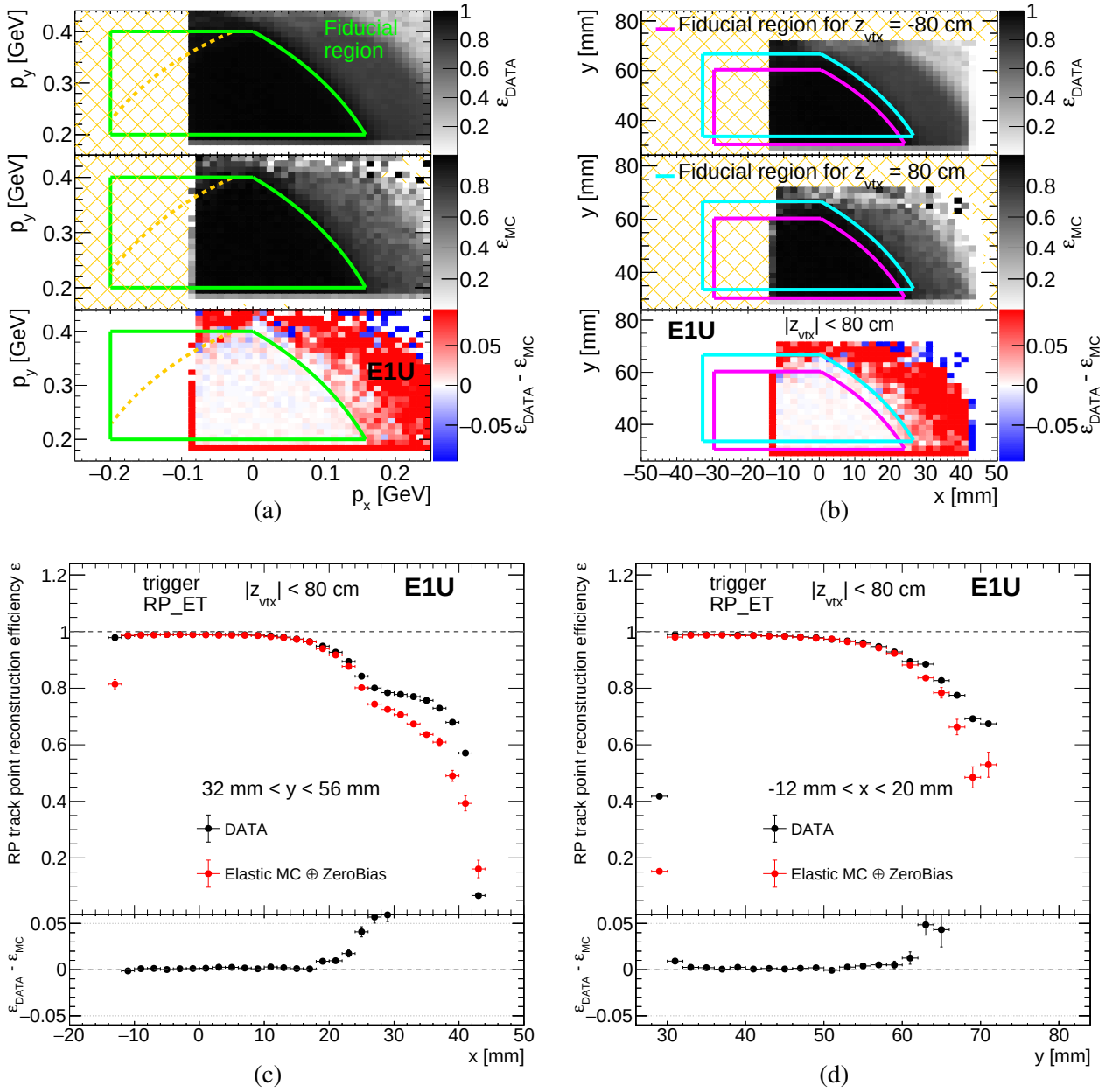

Figure 12.30: Sample distributions of RP track point reconstruction efficiency in the data and in the elastic scattering MC embedded into zero-bias data, obtained for the RP detector E1U with the method described in the text, as functions of proton's (a) momentum components (p_x, p_y), (b) position (x, y) extrapolated from the reference RP station (E2U), as well as comparison of their projections onto (c) x, and (d) y directions (within the ranges of the other coordinate stated in the plots). Bottom panels in each plot, show differences between efficiencies obtained for data and MC. Hatched orange areas mark bins with no entries. The fiducial regions in (x, y) plots are represented by the two envelopes, correspond to the extreme accepted values of z_{vtx}.

projection on the x and y axes. Within the fiducial region of the detectors used in the analysis, an excellent agreement ($< 0.5\%$) between the efficiency estimates from data and MC is found in the region with no material on the elastically-scattered protons' paths. This confirms a correct digitisation of signals from the SSDs, cluster reconstruction and matching procedures, as well as track point reconstruction and embedding. The differences between data and MC are more significant in the region of aperture shadows, e.g. DX magnet shadow, visible in Fig. 12.30c at $x \gtrsim 20$ mm (possibly too much of simulated dead material), or DX-D0 chamber entry/RF shield shadow visible in Fig. 12.30d at $y \gtrapprox 60$ mm (probably also too much simulated material).

12.4.3 RP trigger counters

Systematic uncertainty of the RP trigger counters efficiency has been estimated with a method very similar to that presented in the study of the RP track point reconstruction efficiency described in Sec. 12.4.2. In principle, methods differ only in step 6, which in the this case has the following form:

6. The clean trak point was required in the detector under study (the other detector in the same branch as a reference detector). The RP trigger counter efficiency is defined as the probability, that the counter in the considered RP station with a clean track point, gave the trigger signal.

A sample comparison of the outcome of described analysis can be found in Fig. 12.31. Similarly as in the case of relative efficiency study, the areas of the SSDs accessible is limited to the overlapping parts. One can see, that in the efficiency of the trigger counter in E1U is above 99.5%, and within the fiducial area the differences between data and MC are very small (<0.5%). Similar observation has been made for E1D, E2D, W1D, W2D and W1U. However, in the case of detectors E2U and W2U, the difference between the efficiency in the data is roughly 1% lower then in the MC. Therefore in the case of these two detectors the uncertainties of their trigger counters was assumed to be 1%.

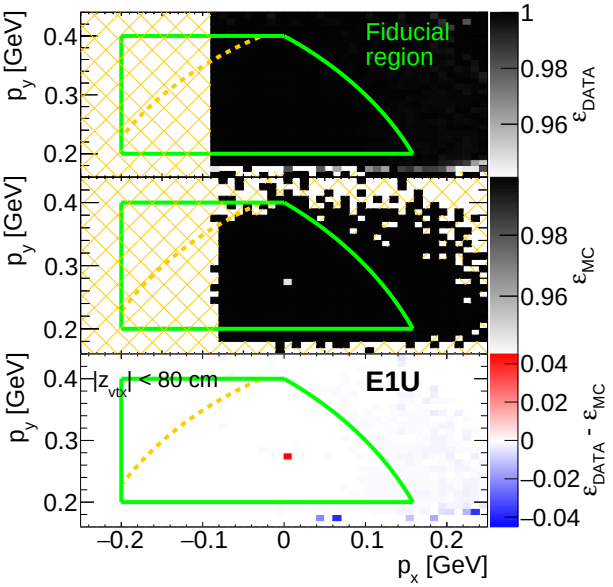

Figure 12.31: Sample comparison of RP trigger counter efficiency (detector E1U) in the data (top panel) and embedded MC (middle panel) estimated with the method described in the text as a function of (p_x, p_y) of the proton track. Bottom panel shows the difference between efficiencies extracted from the data and MC. Hatched orange area marks bins without any entries (efficiency incalculable).

12.4.4 Trigger veto effect (due to dead material)

Systematic uncertainty related to the trigger veto correction (Sec. 11.1.3) has been studied with elastic scattering events, in a way similar to analysis presented in Sec. 12.4.1.

In this study, elastic events with RP_ET trigger signals, and with additional vetoes on any activity in other STAR subdetectors (BBC, ZDC, TOF, VPD), to further reduce probability of a non-elastic pile-up interaction, were used. It has been demonstrated in Sec. 12.4.1, that once the single good quality RP track is required on one side, such sample consists only of elastic proton-proton scattering events.

Each side (branch) was analysed independently. When single, good quality RP track with $|\xi| < 0.01$ was found on the East side, the systematics for West side was investigated (and vice versa). Events selected in this way formed *set A*, and assume that their number was N_A. A subset of these events, set B, without simultaneous signals in the upper and lower RP branches on the investigated side, was then selected. Events from the *set B* were assigned weights equal to the inverses of the veto efficiencies, $1/\epsilon^{\text{side}}_{\text{DM veto}}$, obtained in Sec 11.1.3. Assuming that the sum of weights in *set B* was N_B, the ratio was constructed:

$$R_{\text{DM veto}} = \frac{N_B}{N_A}. \tag{12.4}$$

It is shown in Fig. 12.32 as a function of p_x and p_y of elastically scattered proton on studied side. If single good quality proton track was reconstructed in studied branch, parameters of that track were used. Otherwise, transverse components of momentum of unreconstructed RP track of elastic proton (e.g. due to induced shower) were estimated as $-p_x$ and $-p_y$ of RP track on the opposite side.

Results presented in Fig. 12.32 indicate imperfect description of the dead material of the elements surrounding RPs (DX-D0 chamber, RF shield), which has been also observed in studies of systematic uncertainties related to RP track reconstruction efficiency, presented in Sec. 12.4.1. Based on this study, the correction and systematic uncertainty of the dead material veto efficiency $\epsilon^{\text{side}}_{\text{DM veto}}$ were assumed to

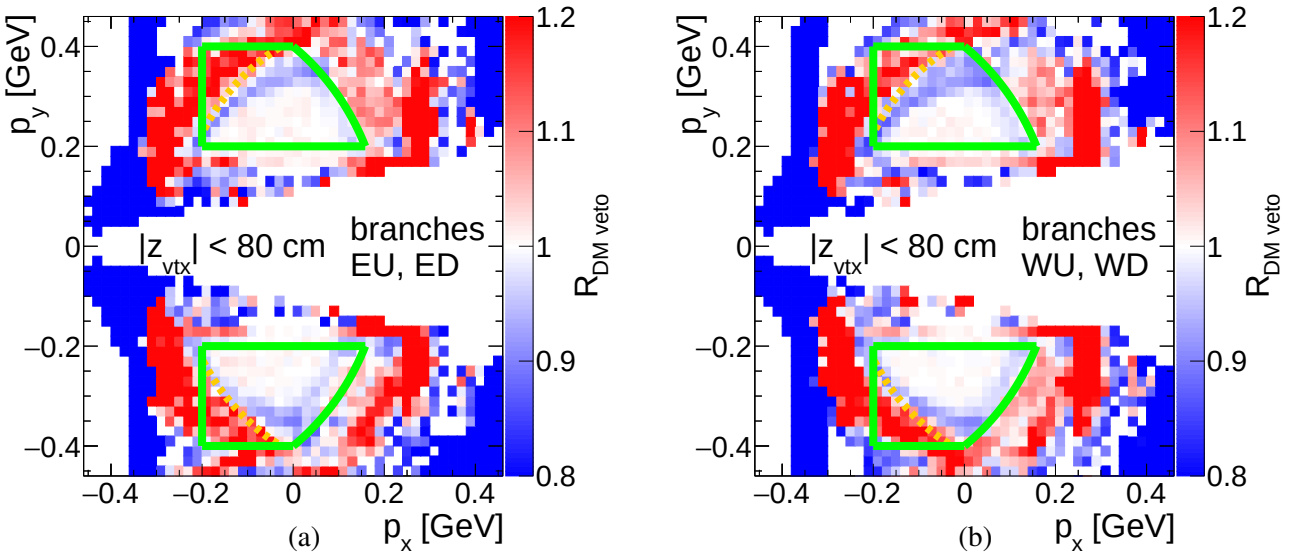

Figure 12.32: The ratio, $R_{\text{DM veto}}$, as functions of forward protons momenta components (p_x, p_y) for the (a) East and (b) West RP stations. Green envelopes mark the fiducial (p_x, p_y) region accepted in the analysis.

have the following form:

- multiplicative correction was applied to $\epsilon^{\text{side}}_{\text{DM veto}}$, equal to $1 + \frac{1}{2}(R_{\text{DM veto}} - 1)$,
- systematic uncertainty was defined by the factor equal to $\left[1 + \frac{1}{2}|R_{\text{DM veto}} - 1|\right]$, propagated on the dead material veto efficiency by multiplicative variation of the efficiency by $\left[1 \pm \frac{1}{2}|R_{\text{DM veto}} - 1|\right]$.

12.5 Summary of the systematic effects

This section summarises contributions to the overall systematic uncertainties for the cross sections measurements, which have been taken into account in the analysis. Influence of each systematic effect on measured cross sections has been tested by changing the quantity that the systematic effect refers to and comparing the result with that obtained using nominal values.

1. **Representativeness of the data sample used for MC embedding ($\Delta\varepsilon_{\text{TPC}}$ (embed. stat.)).**
   Zero-bias data available for the MC embedding was only a fraction of all zero-bias triggers. Therefore, the data used for embedding might not have been fully representative for the whole data used for determination of the TPC track reconstruction efficiency. This effect was studied by comparing estimated average levels of pile-up in the data and embedded MC. The difference was found to be of the order of 1% [33], which was used as a symmetric systematic uncertainty on the TPC track reconstruction efficiency (per track).

2. **Embedding procedure/off-time pile-up effect ($\Delta\varepsilon_{\text{TPC}}$ (pile-up)).**
   Reliability and precision of the embedding procedure and the off-time pile-up effect was verified and quantitatively estimated in the procedure described in Sec. 12.2.1. Embedded MC samples were divided into sub-samples representing different levels of off-time pile-up/density of hit points in TPC. With dedicated analysis it was possible to verify if the TPC track reconstruction efficiency is compatible between all sub-samples when the effect of pile-up (changing number of hits forming a track) is reduced. The average systematic uncertainty related to the embedding procedure was found to be $< 1\%$ (per track).

3. **Modelling of the dead material in front of the TPC ($\Delta\varepsilon_{\text{TPC}}$ (dead mat.)).**
   Not all detector elements are fully modelled in the MC simulation, quite often some simplifications are used. This leads to inaccuracies in efficiencies derived from the simulation. Systematic uncertainty related to the amount of simulated material between the primary vertex and STAR TPC was estimated to be 25%. This translates to $\approx 0.5\%$ uncertainty of the TPC track reconstruction efficiencies. See Sec. 12.2.2 for details.

4. **Modelling of TPC track quality parameters in embedded MC (N^{hits} and d_0/DCA(R)).**
   Impact of variation of the track quality cuts on the obtained cross-sections was checked. It reflects systematic uncertainty related to the quality of modelling of the quantities used to select the primary TPC tracks. The estimated uncertainty on the fiducial cross-section amounts $\pm 1.5\%$. See Sec. 12.2.3.

5. **Vertexing and longitudinal pointing resolution ($\Delta\epsilon_{\text{vtx}}$, $\Delta\epsilon_{|\Delta z_0|}$).**
   Vertexing and $|\Delta z_0|$ cut efficiency have been obtained using data-driven method presented in

Sec. 11.3.1, thus systematic uncertainty related to this efficiency has been significantly reduced. Systematic uncertainty has been estimated as a difference between efficiency with and without subtracted background (Fig. 11.17).

6. **Modelling of the TOF system and validity of derived efficiency corrections ($\Delta\varepsilon_{\mathrm{TOF}}$, $\Delta\varepsilon_{N_{\mathrm{cltrs}}^{\mathrm{TOF}}}$).**
The efficiency of matching TOF hits with the TPC tracks has been extracted from embedded MC sample. It has been confronted with TOF efficiency extracted from the data using two independent techniques: tag&probe (Sec. 11.2.2) and HFT-tagging (Sec. 12.3). Average difference between the data and MC efficiency has been used as a correction to MC efficiency, while half of the difference between the efficiencies extracted from data using the two methods has been treated as a systematic uncertainty (Fig. 12.23). This amounts 1% – 3% (per track), depending on particle species. The systematic uncertainty related to the efficiency of the cut SC7 has been evaluated based on the agreement between the distribution of $N_{\mathrm{cltrs}}^{\mathrm{TOF}}$ in the data and embedded MC (Fig. 9.16). This uncertainty amounts 1%.

7. **Modelling of the RP system and validity of derived efficiency corrections ($\Delta\varepsilon_{\mathrm{RP}}$, $\Delta\varepsilon_{\mathrm{RP}}^{\mathrm{trig.}}$ and $\Delta\varepsilon_{\mathrm{RP}}^{\mathrm{DM\ veto}}$).**
Reliability of the RP system simulation, which was used to extract the efficiency corrections for tagging of the forward-scattered protons, has been verified and quantitatively estimated in Sec. 12.4. For this purpose elastic scattering MC events embedded in the zero-bias data were used. The same analysis has been performed on embedded elastic scattering MC and the data, leading to estimates of the RP acceptance and track reconstruction efficiency. The differences between the two results has been taken as a measure of the systematic uncertainty that covers RP track reconstruction efficiency itself, detectors alignment and embedding technique. Similar studies have been performed to determine systematic uncertainty related to the trigger veto efficiency correction, as presented in Sec. 12.4.4.

8. **Pile-up veto correction ($\Delta\epsilon_{\mathrm{veto}}$).**
Luminosity-dependent correction related to veto of pile-up interactions was derived from the zero-bias data on run by run basis (Sec. 11.3.4). Residual systematic uncertainty has been estimated as a difference between the correction factor calculated for particular run, and correction factor obtained from the exponential fit to all points representing correction factors as a function of instantaneous luminosity.

9. **Longitudinal shape and position of the primary vertex distribution ($\Delta\langle z_{\mathrm{vtx}}\rangle$ and $\Delta\sigma(z_{\mathrm{vtx}})$).**
Comparison of the z_{vtx} distribution obtained from the TPC tracks and from the RP system provides conservative estimates of the systematic uncertainties on the central position and width of the vertex. They were found to be equal to 2 cm and 3 cm, respectively.

10. **Non-exclusive background estimate ($\Delta N_{\mathrm{bkgd}}^{\mathrm{non\text{-}excl}}$).**
To estimate the systematic uncertainty of the amount of the non-exclusive background, the main source of background, a variation of the method in Sec. 10.2.1 was used. Instead of the second-order polynomial fit to the $p_{\mathrm{T}}^{\mathrm{miss}}$ distribution of events with opposite-sign central tracks, the $p_{\mathrm{T}}^{\mathrm{miss}}$ template from the same-sign control channel was used, but normalised in the region of $p_{\mathrm{T}}^{\mathrm{miss}} > 0.15$ GeV, to the same events yield as in the opposite-sign data sample. The difference

between the two methods was taken as the systematic uncertainty of the amount of non-exclusive background.

11. **Luminosity determination ($\Delta\mathcal{L}$).**
    Systematic uncertainty of the integrated luminosity was estimated to be 6%, as described in Sec. 12.1.

Typical systematic uncertainties for the integrated fiducial cross sections are shown in Tab. 12.1. Relative contributions of the systematic effects discussed in Sec. 12.5 to the total systematic uncertainty on the measured differential cross section for CEP of $\pi^+\pi^-$ pairs are shown in Fig. 12.33.

$\delta_{\text{syst}}/\sigma_{\text{fid}}$ [%]

	TOF	TPC	RP	Other	Lumi.	Total
$\pi^+\pi^-$	$^{3.0}_{-2.8}$	$^{3.5}_{-3.3}$	$^{5.8}_{-5.1}$	$^{3.2}_{-3.1}$	$^{6.4}_{-5.7}$	$^{10.3}_{-9.3}$
K^+K^-	$^{9.3}_{-9.4}$	$^{5.2}_{-7.5}$	$^{4.9}_{-6.4}$	$^{4.7}_{-6.1}$	$^{6.4}_{-5.7}$	$^{14.2}_{-16.0}$
$p\bar{p}$	$^{5.8}_{-5.0}$	$^{4.1}_{-3.4}$	$^{6.5}_{-5.5}$	$^{10.2}_{-9.9}$	$^{6.4}_{-5.7}$	$^{15.4}_{-14.0}$

Table 12.1: Typical systematic uncertainties of integrated fiducial cross sections for CEP of $\pi^+\pi^-$, K^+K^- and $p\bar{p}$ pairs. Total systematic uncertainties, shown in the last column, are split into major contributions.

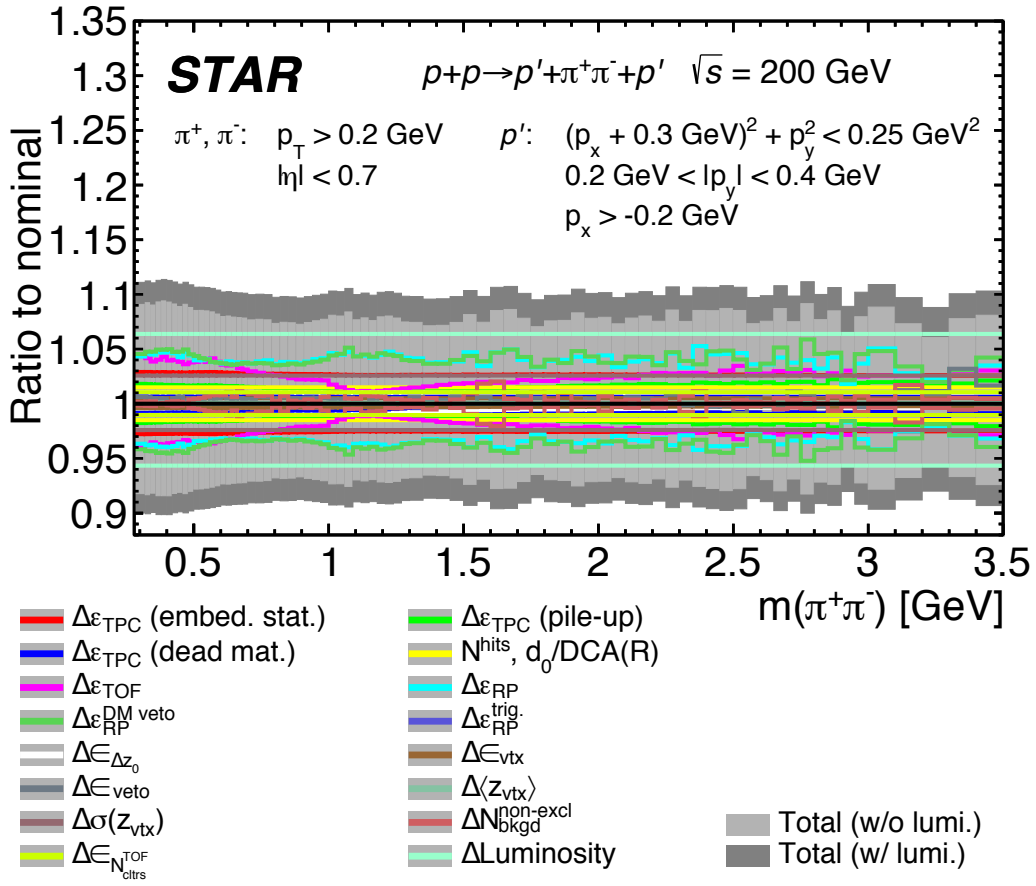

Figure 12.33: Contributions to the systematic uncertainty of the cross section measurement for CEP of $\pi^+\pi^-$ pairs in the fiducial region as a function of the pair invariant mass.

Part III

The ATLAS experiment

In this part, the ATLAS experiment at the LHC and the physics analysis of the data from proton-proton collisions at $\sqrt{s} = 13$ TeV collected by the experiment in 2015, are described. Results presented in the analysis will be published in a peer-reviewed journal in the near future.

13. Experimental setup

13.1 The Large Hadron Collider

The Large Hadron Collider (LHC, Fig. 13.1) [165] is currently the largest and most powerful circular accelerator in the world, built on the border between France and Switzerland, near Geneva. It is the main project of the European Laboratory for Particle Physics [166] (abbreviated CERN from its initial French name Conseil Européen pour la Recherche Nucléaire). The LHC has been built in the 27 km long tunnel inherited from the LEP collider. Since 2009, it provides head-on collisions of protons and heavy-ions at different centre-of-mass energies with unprecedentedly high luminosity. The highest centre-of-mass energy achieved so far in proton-proton collisions was $\sqrt{s} = 13$ TeV. The designed energy of $\sqrt{s} = 14$ is believed to be reached in Run 3.

There are four main, large experiments installed at the LHC: ALICE [167, 168], ATLAS [46, 169], CMS [170, 171] and LHCb [172, 173]. Tagging of the forward-scattered beam protons, which is essential from the point of view of this thesis, is only possible in the ATLAS and CMS/TOTEM [174] experiments. The ATLAS experiment is equipped with the ALFA spectrometer [175] and the AFP detector [176]. The CMS experiment shares the IR with the TOTEM experiment targeted to measure diffractively-scattered protons using the RP devices. The two experiments share the CT-PPS detector [177]. The AFP and CT-PPS detectors are designed to take data during normal operation of the LHC with large pile-up, while ALFA and TOTEM are capable of running only during dedicated LHC campaigns of lowered instantaneous luminosity and special beam optics.

The physics analysis presented in the following is based on the data collected by the ATLAS experiment during special runs with the ALFA detector included in operations. Descriptions of the ATLAS experiment and of the ALFA detector are presented in the next section.

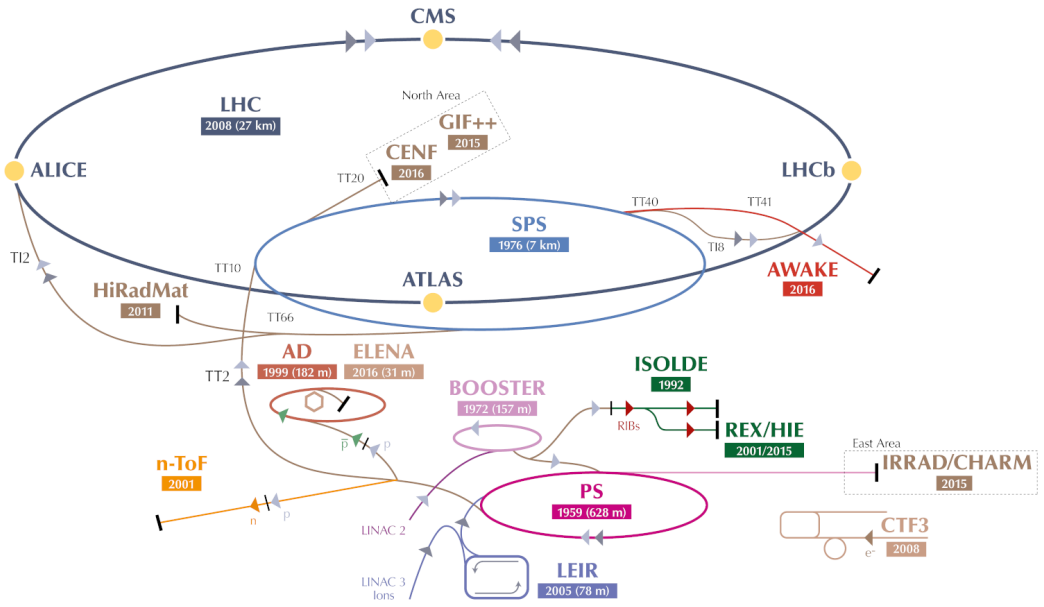

Figure 13.1: Schematic view of the accelerators infrastructure at CERN. The LHC and smaller circular and linear accelerators are shown together with locations of the current experiments. Figure adopted from [178].

13.2 The ATLAS detector

A Toroidal LHC ApparatuS (ATLAS) [46] (Fig. 13.2) is a general-purpose, forward-backward symmetric detector of almost full azimuthal coverage, located at one of four IRs of the LHC. The coordinate system adopted by ATLAS is the right-handed Cartesian system with its origin in the central point of detector, coinciding with the nominal IP. The z-axis is pointing towards the direction of the beam circulating counter-clockwise in the LHC pipeline. The x-axis is pointing radially to the centre of the LHC ring, and y-axis is directed upwards. The part of the detector installed at positive-z side is commonly called the A side, while the part at the negative-z is referred to as the C side.

ATLAS was designed to measure and determine the characteristic of the Higgs boson. For this reason the detector has extensive calorimetric system and muon spectrometry which allow reconstruction of the decay products of the Higgs particle, mainly the Z and W bosons. The calorimetry is provided by the Liquid Argon (LAr) hadronic and EM calorimeter, and the Tile calorimeters, made of steel and scintillator plates. This system covers $|\eta| < 4.9$ [46]. The muon system ($|\eta| < 2.7$) is based on several types of muon chambers (see Ref. [46] for details) contained in the toroidal magnetic field of the bending power ranging between $1 - 7.5$ T·m [46], allowing reconstruction of momenta of high-p_{T} muons.

In addition, ATLAS is equipped with a precise tracking system for charged particles, the Inner Detector (ID), designed to provide efficient reconstruction of particles with momenta $p_{\mathrm{T}} > 0.5$ GeV and within $|\eta| < 2.5$, but thanks to the special reconstruction algorithm, it is possible to extend this

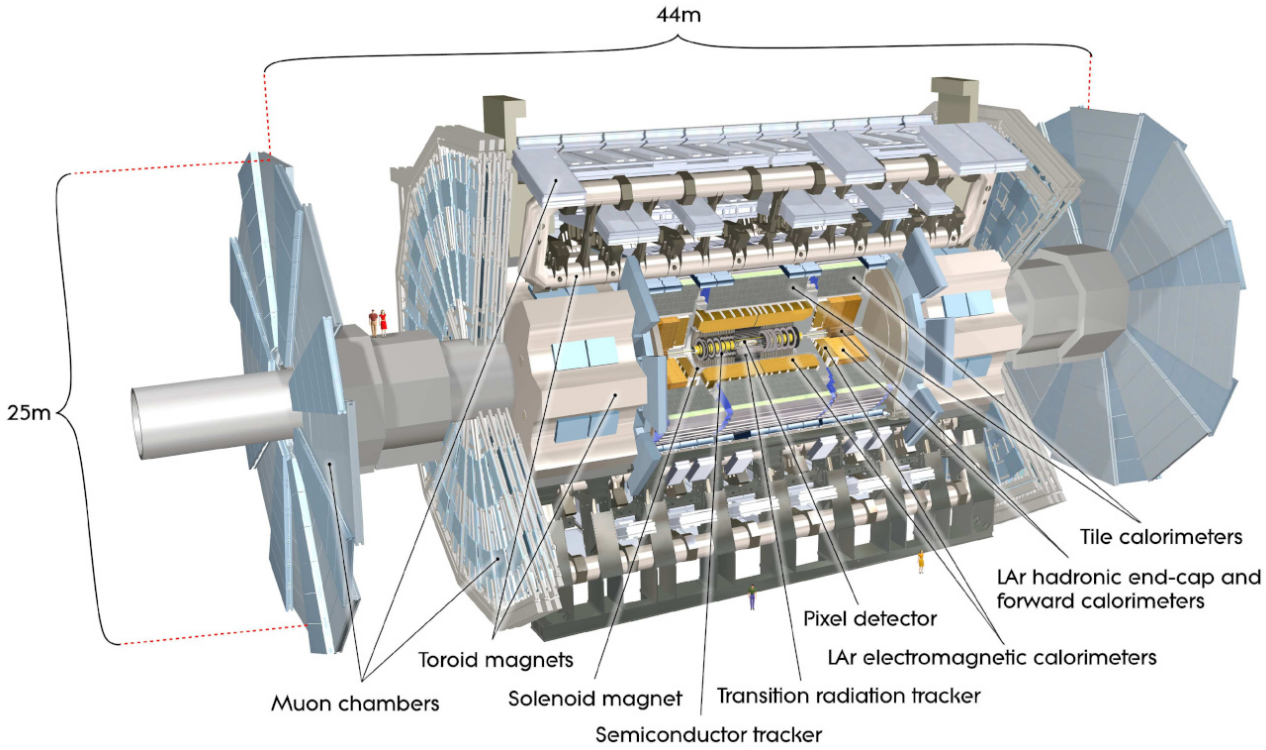

Figure 13.2: Cut-away illustration of the ATLAS detector. The detector measures 44 m in length and 25 m in diameter. It consists of several specialised subsystems, major being indicated and labelled. Figure taken from [46].

range to $p_{\mathrm{T}} > 0.1$ GeV. In the endcap regions of ID there are Minimum Bias Trigger Scintillators (MBTS) installed on either side, providing the least biased trigger for the collisions in ATLAS IP. Central part of the ATLAS detector is supplemented with subdetectors places far away from the IP, close to the beam pipe, which allow to measure beam protons scattered at very small angles. These include two RP systems: the Absolute Luminosity For ATLAS (ALFA) and the AFP.

13.2.1 Inner Detector

Charged particle tracking and vertexing in ATLAS is provided by the ID (Fig. 13.3a) immersed in 2 T solenoid field. The detector is generally divided into a barrel part and two endcaps on A and C sides, respectively. The cut-away view of the barrel part of ID is shown in Fig. 13.3b.

The closest to the IP part of the ID is the silicon Pixel detector (PXL) [179], with the innermost part upgraded in 2015 with the Insertable B-Layer (IBL) [180]. Total number of PXL layers is equal to four in the barrel, with additional three disks in each of the two endcaps. PXL provides three-dimensional space points, as well as the ADC counts transformed offline to dE/dx information for each reconstructed cluster.

Outside of the PXL, there is the Semiconductor Tracker (SCT) [181] with four cylindrical layers in the barrel and nine disks in each of the endcaps. Each layer consists of four silicon strip detectors, two on either side of the wafer, which provide binary information about the signal in each channel.

The two subsystems discussed above cover the pseudorapidity range $|\eta| < 2.5$ and operate based on the concept of silicon diodes working in a reverse-bias mode. The charge induced by a particle passing through the semiconductor material is collected on the electrodes and converted to signal.

The third, outermost part of the ID, the Transition Radiation Tracker (TRT) [182–184], significantly differs from PXL and SCT in the construction and principle of operation. The TRT covers slightly narrower pseudorapidity range compared to PXL and SCT, namely $|\eta| < 2$, of which the barrel part covers $|\eta| \lesssim 0.9$. The inner TRT radius of approximately 55.5 cm makes this subsystem useful in reconstruction of only higher-p_{T} particles with $p_{\mathrm{T}} \gtrsim 0.5$ GeV, since only those are able to reach the inner volume of detector and induce space points required in the track pattern recognition. TRT is built of thousands of drift tubes (also called straws), each 4 mm in diameter, mounted parallel to the beam axis (barrel) or radially, perpendicular to the beam (endcaps). The lengths of the straws vary from 37 cm (endcaps) to 144 cm (barrel). By design the detector is able to measure spatial coordinates perpendicular to the straws, (R, ϕ) in the barrel part, and (ϕ, z) in the case of the endcaps. Straws are filled with a xenon- or argon-based gas mixtures. They provide suitable environments for charged particles traversing the straw volume to generate free electrons by ionising the gas. Due to high voltage applied between the straw wall and the anode wire placed centrally along the straw axis, such electrons are collected at the anode, then amplified and shaped by the readout electronics. Entire space between drift tubes is filled with 19 μm diameter polypropylene fibres which serve as a the transition radiation material. Charged particles passing the borders of media having different dielectric constants emit photons which then might also ionise the gas in a straw and therefore amplify the signal. The transition radiation intensity increases significantly with growing Lorentz factor $\gamma = E/m$, therefore the signal strength is significantly larger for electrons compared to other particles. Therefore TRT provides an efficient identification of electrons in ATLAS.

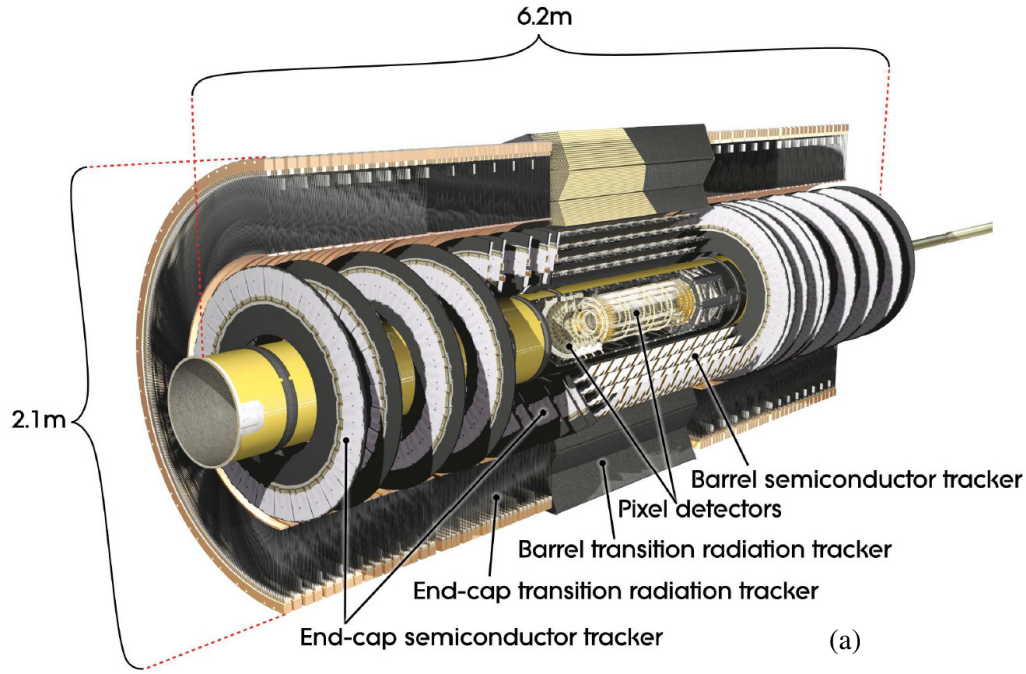

(a)

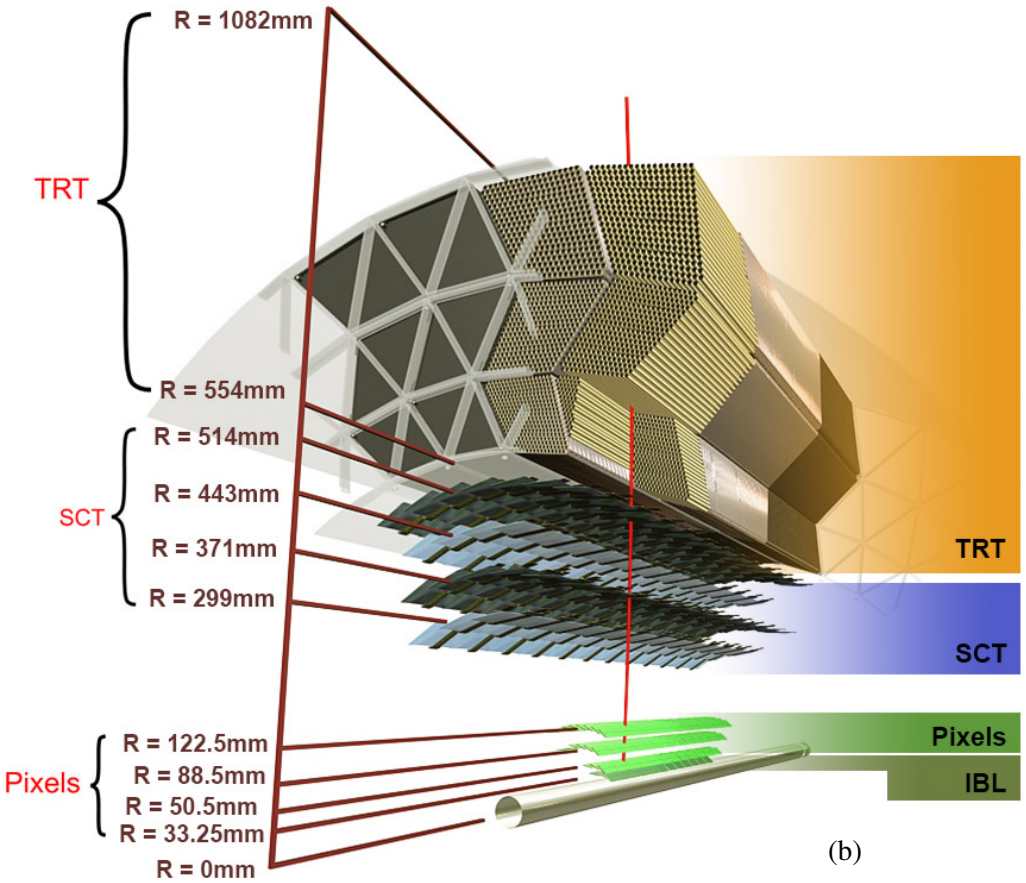

(b)

Figure 13.3: (a) Cut-away view of the ID (from [46]). (b) Illustration of the barrel section of ID decomposed to its main elements. For each component the radial distance from the beamline is provided. Starting from the beam pipe they are: PXL with the innermost IBL, SCT and TRT. Figure taken from [185].

13.2.2 Minimum Bias Trigger Scintillators

The MBTS system is formed of two disks mounted perpendicularly to the beam axis on either side of the ATLAS IP, at positions $z = \pm 3.56$ m. Inner and outer radius of a single MBTS disk is equal to approximately 14 cm and 88 cm, respectively. A layout of a single disk is shown in Fig. 13.4.

MBTS on each side is a set of 2 cm thick plastic scintillator tiles of two types. The inner part of MBTS (iMBTS) is made of eight tiles covering $2.76 < |\eta| < 3.86$. The outer part (oMBTS) consists of four tiles covering $2.07 < |\eta| < 2.76$. Scintillation light induced by charged particles passing through the active material is collected and guided with the optical Wavelength Shifter (WLS) fibres to PMTs. Light from each tile is guided to one PMT, hence there are 12 MBTS channels on each side of ATLAS.

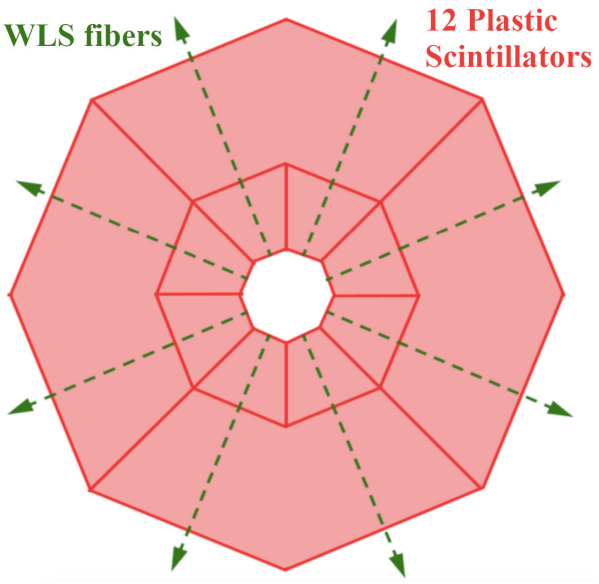

Figure 13.4: Schematic illustration of MBTS on one side of ATLAS (adopted from [186]). Single MBTS disk is divided to inner and outer part. The inner MBTS consists of eight scintillator tiles, the outer MBTS - of four scintillator tiles. The scintillation light is guided with the WLSs and read by PMTs, one PMT per tile.

13.2.3 Absolute Luminosity for ATLAS

The ALFA subsystem [175] is a crucial component for the study of CEP in ATLAS. This system of RP detectors enables triggering on and reconstruction of the forward-scattered protons. Figure 13.5 shows the layout of ALFA with a total of eight RPs deployed in four stations, two stations on either side of the ATLAS IP. A model and photograph of the single RP station is shown in Fig. 13.6. The near stations (closer to the IP) are situated at $z = \pm 237$ m, while the far stations are installed 8 m further at $z = \pm 245$ m.

Each station consists of two RPs, one above and one below the beamline. The photograph of an RP vessel is shown in Fig. 13.7a. Each RP vessel houses a detector package (Fig. 13.7b) whose main component is the Main Detector (MD), a set of ten modules with two layers of orthogonally arranged scintillating fibres (perpendicular to the beam axis). The fibres, square in cross section, are rotated by 45° with respect to global x and y axes. The local coordinates along the rotated axes are denoted with u and v. In a single layer there are 64 fibres, 0.5 mm wide each, coated with the aluminium to reduce the light crosstalk. For the ideal case of a proton track reconstructed with all ten fibre layers of the same orientation, the spatial resolution per coordinate amounts approximately $30 - 40$ μm [175].

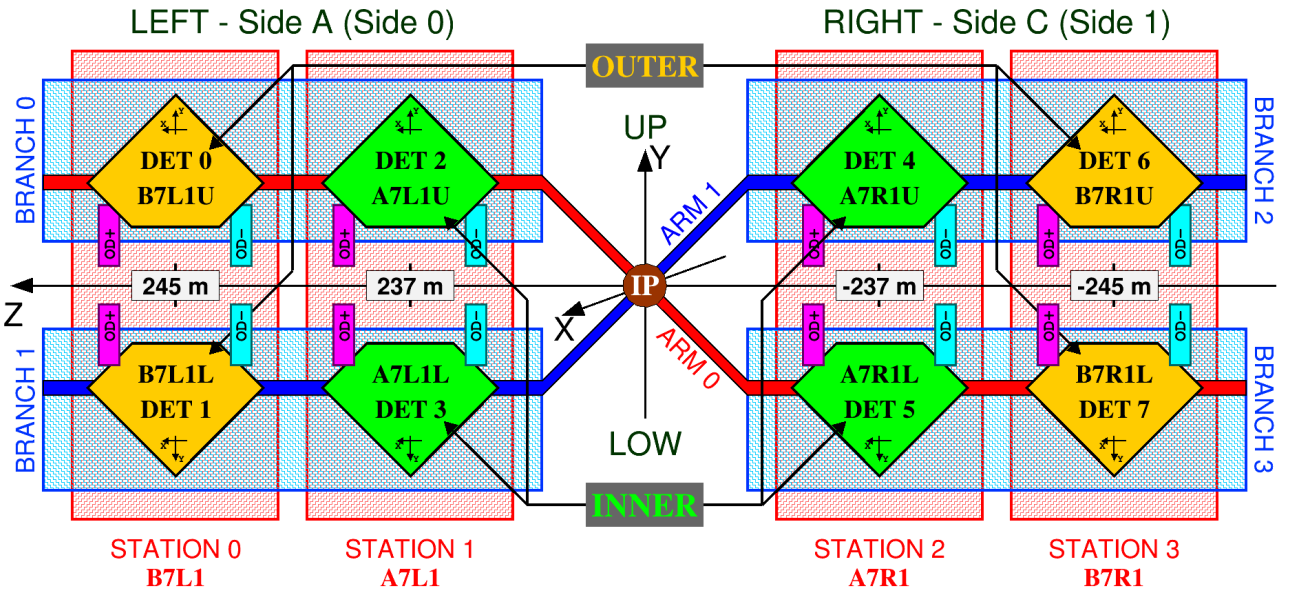

Figure 13.5: Schematic illustration of the ALFA RP detectors (from [187]). In total eight ALFA RPs are installed 237 m (near/inner stations, in green) and 245 m (far/outer stations, in orange) from the nominal IP. A pair of near and far RPs in the same yz quadrant form a branch. Combination of single branches on side A and side C form elastic (0-3 or 1-2) or anti-elastic (0-2 or 1-3) configuration reflecting various topologies of diffractive events (of the forward-scattered protons).

Scintillation light in the fibres is guided to the multi-anode PMTs (MAPMT) where it is collected and converted to electric signal, and further processed by dedicated readout electronics. Fibre bundles, starting at the edge of MD closest to the beam, connected with a support plate containing the MAPMTs, are well seen in Fig. 13.7b. In the photograph, one can also see white elements attached to the MD, which are two plastic scintillators covered with the reflecting material to increase light collection efficiency. They cover entire active area of MD and serve as trigger detectors; they are also read by MAPMTs.

There are two Overlap Detectors (ODs) in each RP which enable precise determination of the relative distance between the two RPs in the same station. Each OD is built of three layers of 30 scintillating fibres of the same kind as in the MD. In Fig. 13.7a one can see two extrusions in the top surface of RP vessel, which house ODs. Once the RPs are retracted from their home positions the ODs overlap and particle passing simultaneously through two ODs enable determination of residues of differences between active fibres in both ODs. Each OD is accompanied by a single trigger scintillator plate.

All ALFA RPs are located relatively far from the IP, downstream several dipole and quadrupole LHC magnets. This allows to take data by the ALFA detector only during appropriate beam conditions and accelerator optics. Therefore, ALFA can only take data during dedicated data-taking campaigns with lowered instantaneous luminosity, increased colliding bunch separation and lowered beam emittance. Therefore ALFA is especially suited to the measurement of elastic proton-proton scattering, which has a very large cross section. Measuring the elastic cross section and using the optical theorem, one can determine the total hadronic cross section for pp collisions.

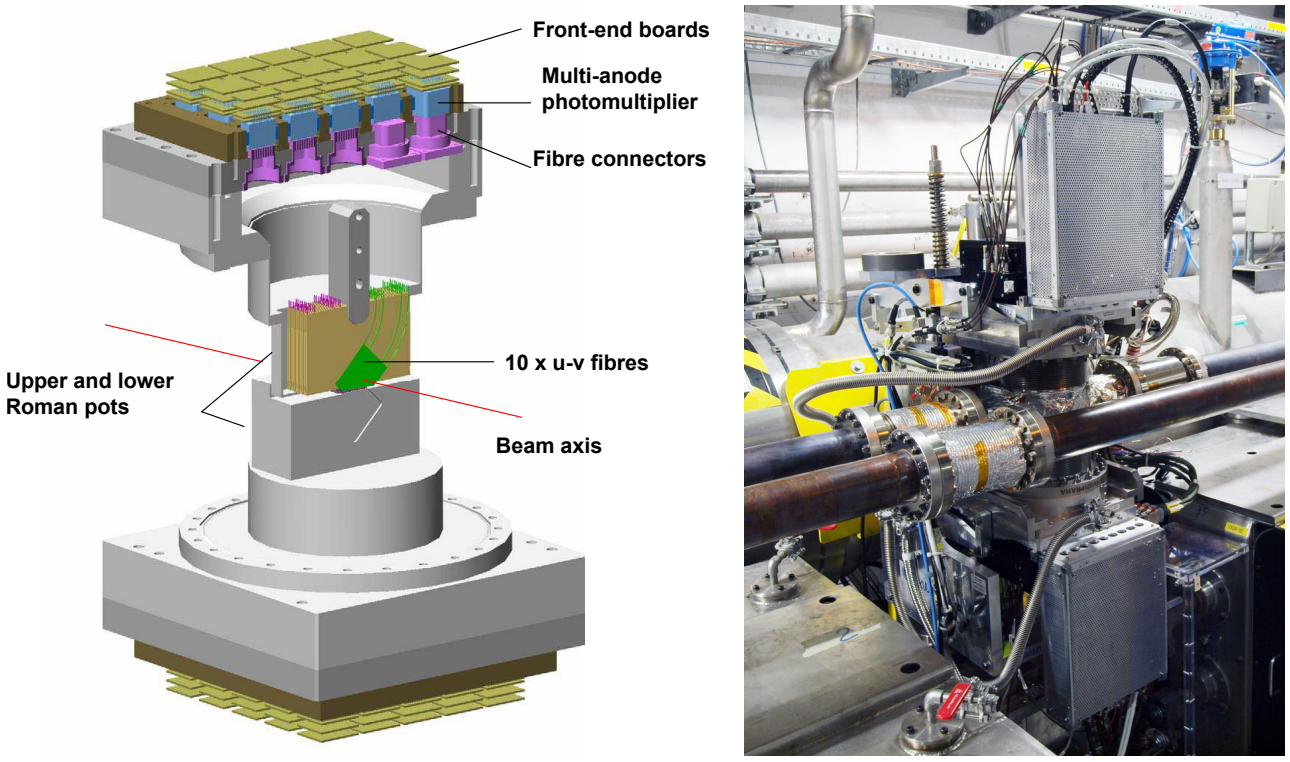

(a) (b)

Figure 13.6: (a) Schematic layout of the ALFA Roman Pot detector (from [46]). (b) Photograph of the ALFA station installed on the LHC beam pipe (from [188]).

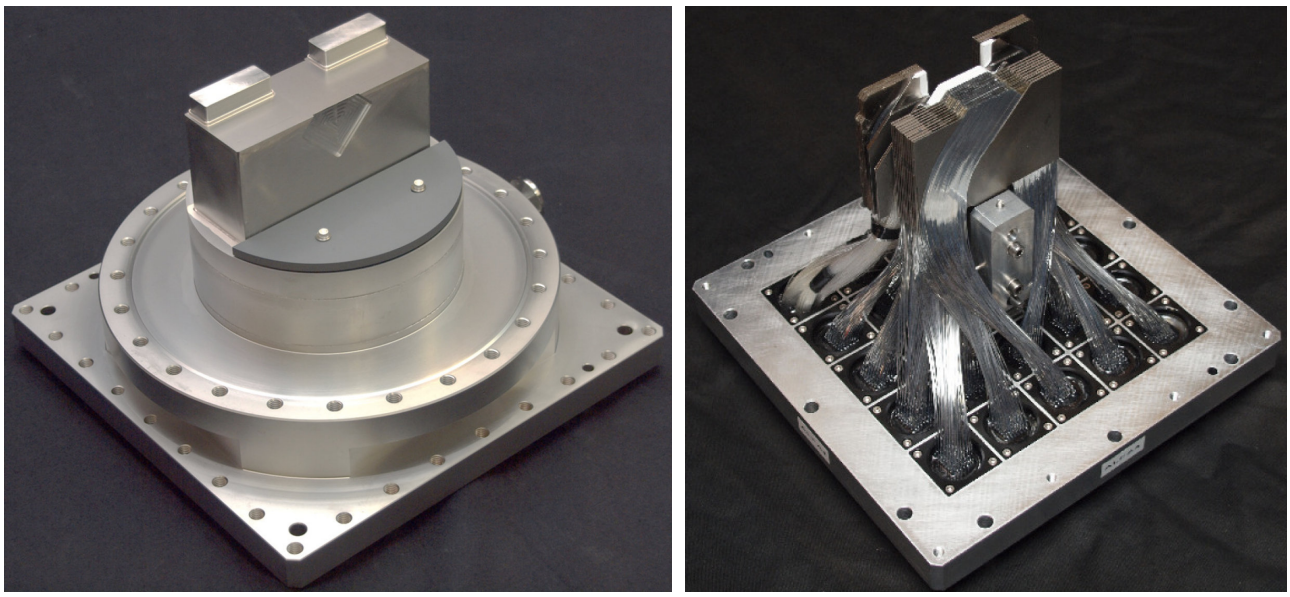

(a) (b)

Figure 13.7: Photograph of (a) Roman Pot vessel, and (b) ALFA detector package with visible scintillating fibres coated with reflective aluminium film, connected with the readout (MAPMTs). Figures taken from [175].

13.2.4 Trigger system

Trigger system in ATLAS [189, 190] operates in challenging environment with collisions taking place nominally every 25 ns, which is the design proton bunch spacing in the LHC. It is divided into three levels, L1, L2 and Event Filter (EF), the last two jointly forming the so-called High Level Trigger (HLT). One can also define the level-0 (L0), which corresponds to the hardware information about registration of a trigger signal (hit/no-hit) in a given trigger component.

The L1 trigger is hardware-based, formed of logical combinations of L0 trigger bits. It is able to analyse trigger data with a frequency of 40 MHz, which corresponds to the nominal 25 ns bunch separation. The L1 trigger information is fed to the L2 trigger and further to EF, where events ale filtered using software selections. At this trigger level, some high-level objects are reconstructed from the available, slimmed detector data (e.g. ID tracks) and are used to select events of interest. They are independent from objects reconstructed offline from all event data and using dedicated calibrations. The HLT finally reduces the rate at which data are recorded by the DAQ system [191] to 1 kHz. It is worth to note, that the analysed data were recorded with increased DAQ frequency of approximately 1.5 kHz. It was possible to achieve due to lower detector occupancy in the special ALFA runs, compared to regular high-luminosity runs.

14. Event reconstruction

14.1 Central detector data reconstruction

Reconstruction of tracks in PXL and SCT [192, 193] detectors, starts with a clustering procedure, which yields three-dimensional space points. The space points in the PXL layers are formed from clusters reconstructed as adjacent channels with signals exceeding thresholds. In the SCT, space points are formed from pairs of clusters reconstructed in the upper and bottom silicon sensors in each layer. In the next step track seeds are created from three space points in different layers of PXL and SCT. These seeds of tracks provide rough estimates of three-dimensional particle trajectory and are used in the track reconstruction algorithms based on adaptive Kalman filter that extends tracks with space points which were not used in track seeding [193]. At this stage the hits may be shared between tracks. The following step involves an algorithm based on artificial neural networks [194] dedicated to solve ambiguities in space point to track association. The algorithm scores tracks based on e.g. a number of space points shared with other tracks or a number of holes in a track (detector layers without matching space point). As the result, fake tracks are efficiently rejected as well as true tracks are reconstructed with only self-induced space points, leading to better precision of momentum reconstruction. In the next step helices of tracks reconstructed from space points in the PXL and SCT are extrapolated to the TRT. Hits in the TRT, consistent with the tracks' trajectories, are added to those tracks, leading to improvement in the momentum resolution. After the entire procedure is done, the tracks are fully defined, characterised by their momentum vector at the point of DCA to the beamline, d_0, z_0, as well as dE/dx, which is calculated from the PXL hits [195]. Only tracks with $p_{\mathrm{T}} > 0.1$ GeV are reconstructed.

From the found ID tracks, primary vertices are reconstructed. The vertexing is an iterative procedure [196, 197]. It starts with selection of ID tracks with the highest probability of representing the primary particles. The selection criteria include e.g. a cut on transverse impact parameter $|d_0| < 4$ mm, at least one space point in the IBL, at least four SCT space points, no holes in the PXL detector, and other requirements. After the tracks are selected, the vertex seeding takes place based on the local maxima in the z_0 distribution, which determine position of vertex seeds. The initial z-position of a seed is an average z_0 of potential constituent tracks, while x- and y-coordinate are given by the position of the beam spot, defined as an average transverse position of primary vertices. Next, tracks are associated with weights reflecting their compatibility with the vertex. A new vertex position is calculated accounting for the tracks' weights. These weights are updated based on refitted vertex position and its uncertainty. In each iteration, tracks significantly incompatible with the vertex are removed from the fitting of that vertex, although might be used in fitting of another one. The procedure ends if no more vertices can be formed or no more unassociated tracks are left in the event. Finally, only those primary vertices are reconstructed which have at least two ID tracks associated with them.

In the CEP analysis, also the MBTS detector is used. For each MBTS channel, information about the charge and the timing is provided. The charge is proportional to the yield of light signal received by the PMT and is obtained by integrating the signal current over time. The timing is given by the PMT signal exceeding a predefined discrimination threshold.

14.2 ALFA data reconstruction

ALFA data is first reconstructed at the level of single RP detectors. Hits are reconstructed independently in each ALFA package, separately in u and v coordinates based on positions of fibres with detected light signal (Fig. 14.1). Pairs of (u, v) hits representing transverse position of proton in RP (track points) are transformed to (x, y) coordinates with respect to the beamline. It involves usage of the LVDT readouts calibrated with the special laser survey and offline alignment of ALFA stations using the elastic scattering process [187].

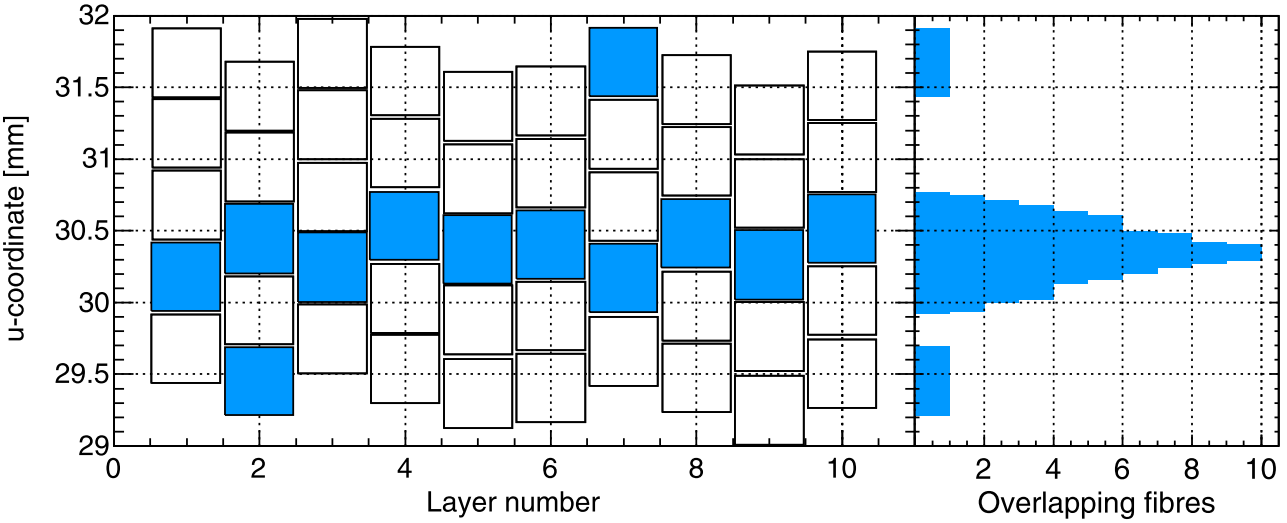

Figure 14.1: Schematic illustration of a hit reconstruction in a single transverse coordinate in ALFA (from [198]). The above example shows an event with signal detected in all ten layers measuring given spatial coordinate (fibres marked blue). The overlapping fibres are used to determine position of the proton hit.

Track points reconstructed in RP detectors in the same branch are used to reconstruct proton tracks. In the CEP analysis a method of inverse transport matrix is used to unfold the momentum of forward-scattered proton at the ATLAS IP. Protons are assumed to carry the beam momentum, which is a reasonable assumption given that the analysis focuses on measurement of low-mass central states (up to a few GeV) produced in mid-rapidity (constituent particles must fit within acceptance $|\eta| < 2.5$). It turns out from Eqs. (1.27) and (1.28), that $\xi \approx 10^{-4}$, which implies that protons scattered in the CEP process behave nearly the same, as the elastically scattered protons.

The position of vertex w ($w \in \{x, y\}$) and angle between proton momentum and z-axis in wz plane at the ATLAS IP (θ_w) can be connected with the corresponding position and angle in ALFA (superscript RP) through the linear approximation

$$\begin{bmatrix} w^{\mathrm{RP}} \\ \theta_w^{\mathrm{RP}} \end{bmatrix} = \mathbb{M}_w \begin{bmatrix} w \\ \theta_w \end{bmatrix}, \tag{14.1}$$

where $\mathbb{M}_w$ is the transport matrix (for coordinate w), whose coefficients depend also on the z-position of RP, therefore matrix is different for all four ALFA stations. The inverse relation

$$\begin{bmatrix} w \\ \theta_w \end{bmatrix} = \mathbb{M}_w^{-1} \begin{bmatrix} w^{\mathrm{RP}} \\ \theta_w^{\mathrm{RP}} \end{bmatrix} \tag{14.2}$$

is used in the reconstruction. Coefficients of the transport matrices are provided by the known values of currents in the LHC magnet lattice. Proton track is reconstructed from hits (track points) in two RP stations in a branch. The local angle, θ_w^{RP}, is calculated from the definition and used as an input to Eq. (14.2). The components of momentum of forward-scattered proton are calculated as

$$p_x = p_0 \cdot \tan\theta_x, \qquad p_y = p_0 \cdot \tan\theta_y, \qquad p_z = \sqrt{p_0^2 - p_x^2 - p_y^2}, \tag{14.3}$$

with $p_0 = 6.5$ TeV. The transverse momentum components of proton at IP are reconstructed as an average p_x and p_y from two ALFA stations, and then p_z is calculated employing those average p_x and p_y.

15. Dataset and Monte Carlo samples

15.1 Dataset

The measurement of CEP in ATLAS is performed with the data collected during dedicated data-taking campaign, that took place in October 2015. For this purpose, the intensities of the proton beams were lowered. This resulted in the lower instantaneous luminosity, $\mathcal{L}$, hence also low average number of simultaneous proton-proton interaction per bunch crossing (pile-up) with $\mu \sim 0.1$. It involved also modifications of the nominal LHC betatron function at the ATLAS IP to $\beta^* = 90$ m, and the time spacing between bunches to 100 ns. Such special conditions are suitable for the measurement of the diffractive processes and are required to operate the experiment together with the ALFA spectrometers.

The data used in this analysis were triggered at the HLT level, making use of trigger signals from ALFA, ID and MBTS. The logic of the trigger named "HLT_mb_sptrk_vetombts2in_L1ALFA_CEP" is explained below.

The HLT for CEP was seeded with the L1 trigger related to ALFA, which was designed to ensure presence of two forward-scattered protons within ALFA acceptance. At L0, the trigger signal in a given ALFA station is set, if signals in the trigger counter (two scintillator tiles read by the photo-multiplier tubes) passed predefined thresholds. At L1, the coincidence of the L0 trigger signals in ALFA branches on side A and side C is required. Trigger signal in a given branch is claimed, if at L0 the trigger signal in at least one of the two ALFA stations was present. There are four possible combinations of branches in CEP, each forming different L1 trigger, as explained in Tab. 15.1.

The part of the HLT trigger associated with the MBTS ("VetoMbts2in") is based on the topology of a CEP event, in which no particles should be present in the rapidity region between the forward and central systems. Therefore, the trigger requires a lack of signal in all but at most one of the inner MBTS tiles on either side of ATLAS IP. The signal in a single channel of the inner MBTS tiles on either side was allowed to reduce the probability of vetoing on the noise.

The remaining part of the HLT - related to ID ("SpTrk") - requires the presence of space points forming an online track. It is in accordance with an expectation of the charged particles in the final state in the mid-rapidity. The trigger requires at least three space points in the PXL, at least four space points in the SCT and at least one L2 ID track with $p_T > 0.2$ GeV.

The data collected during eight independent runs and used in the CEP analysis, contains approximately 21 M events and corresponds to the integrated luminosity of 660 nb^{-1}. In addition to this

	Branch				
L1 trigger name	0	1	2	3	Comment
L1_ALFA_ELAST15	◯			◯	Prescale ~ 2
L1_ALFA_ELAST18		◯	◯		Prescale ~ 2
L1_ALFA_SYST17	◯		◯		Unprescaled
L1_ALFA_SYST18		◯		◯	Unprescaled

Table 15.1: List of ALFA L1 trigger words and their relations to the L0 trigger signals in ALFA branches. Some of the L1 triggers were prescaled by a factor ~ 2.

dataset, the data devoted to elastic scattering process, and the control data with coincidence of ALFA signals on side A and side C, were also used for some studies. These datasets were triggered with the two first and the two last L1 triggers listed in Tab. 15.1, respectively.

15.2 Monte Carlo samples

MC sample used for comparisons of different observables with data at the detector level, and to demonstrate a proper understanding of the data in terms of signal and background contributions, was generated with Pythia 8 and consisted of CD events, which naturally include the CEP events. The Donnachie-Landshof parameterisation [70] of the IPomeron flux was used with the "A3 tune" [199] (a set of model parameters tuned to the ATLAS data). This sample was originally generated, simulated and processed in ATLAS software [200] as the sample to be used in the SD analyses (e.g. [33]), therefore its statistics is limited (CD constitutes a background to SD, and large sample was not needed for that study). Only the central ATLAS detector was simulated for this MC sample. The tracks of forward-going particles in ALFA were emulated at the stage of MC event analysis. The propagation of particles from the IP to the forward detectors was done using dedicated tool [201], based on known properties of the LHC magnet lattice and the limiting apertures between the IP and ALFA stations, and taking into account the angular divergence of the beam. For each particle successfully reaching the ALFA RP, the track was formed whose position in ALFA was smeared according to data-driven resolutions.

In addition to the Pythia CD sample, high statistics MC samples of CEP events were generated for determination of the geometrical acceptance of the ALFA stations assuming a uniform distribution for invariant mass, rapidity and forward-scattered protons' azimuthal angle and an exponential t-distribution. The momenta of forward-going protons were smeared to account for the angular beam divergence and intrinsic ALFA resolution.

The following MC samples were generated for comparisons of the measured fiducial cross sections with model predictions:

- Exclusive $\pi^+\pi^-$ from GenEx using the exponential form factor with $\Lambda^2_{\text{exp}} = 1.0\ \text{GeV}^2$.
- Exclusive $\pi^+\pi^-$ from DiMe using the exponential form factor with $\Lambda^2_{\text{exp}} = 1.0\ \text{GeV}^2$ and "model 1" of absorption effects.
- Exclusive $2\pi^+2\pi^-$ from DiMe using the exponential form factor with $\Lambda^2_{\text{exp}} = 1.0\ \text{GeV}^2$ and $\Lambda^2_{\text{exp}} = 2.2\ \text{GeV}^2$ (the latter being the default value in the generator), and "model 1" of absorption effects.
- Exclusive $n\pi^+n\pi^-$ ($n = 1, 2, 3, 4$) from Pythia 8.244 using the MBR model of the IPomeron flux, with the minimum generated mass of the central system equal to 0.5 GeV (the lowest limit allowed in Pythia).

16. Event selection

The complete list of cuts used for signal extraction is presented in Sec. 16.1. Detailed description of each cut can be found in Sec. 16.2. [Readers of the electronic version can directly jump to the description of a given cut by clicking on the bold cut number **ACX**.]

16.1 List of cuts

Some cuts (e.g. AC2) are decomposed to constituent sub-cuts. Cut is formed by the logical AND of all its sub-cuts.

AC1. At most one primary vertex reconstructed from ID tracks.

AC2. Exactly two (or four/six/eight) total-charge-zero ID tracks (AC2.1) of good quality (AC2.2) reconstructed within fiducial kinematic region of high ID and HLT acceptance (AC2.3).

AC2.1. Even number of reconstructed tracks and the total electric charge of tracks equal to zero,

AC2.2. Tracks must satisfy quality criteria:

- one hit in the IBL if the extrapolated track passes through a sensitive region of an operational module,
- at least one hit in the PXL detector,
- at least two, four or six hits in the SCT for tracks with, respectively, $p_{\mathrm{T}} < 0.3$ GeV, $0.3 < p_{\mathrm{T}} < 0.4$ GeV or $p_{\mathrm{T}} > 0.4$ GeV,
- track-fit χ^2 probability > 0.01 for tracks with $p_{\mathrm{T}} > 10$ GeV to remove mis-measured tracks with very high reconstructed transverse momentum due to issues with the detector alignment or high occupancy,
- transverse impact parameter of $|d_0| < 1.5$ mm to remove non primary tracks (e.g. from long-living particle decays),
- maximum separation of the longitudinal impact parameters of the outermost tracks $|\Delta z_0| < 20$ mm,

AC2.3. All tracks must be contained within the kinematic range: $|\eta| < 2.5$, $p_{\mathrm{T}} > 0.1$ GeV, and at least one track must have $p_{\mathrm{T}} > 0.2$ GeV: $\max(p_{\mathrm{T}}) > 0.2$ GeV.

AC3. Exactly one ALFA track of good quality (AC3.1) on each side of the ATLAS IP (AC3.2), lying within fiducial region of high geometrical acceptance (AC3.3), without significant activity in the other ALFA branches (AC3.4).

AC3.1. ALFA tracks are formed from two track-points in single ALFA stations in the same branch, with at least six (out of ten) fibre layers in both u and v coordinates used in point reconstruction,

AC3.2. Exactly one ALFA track passing cut AC3.1 on side A and side C of the interaction region,

AC3.3. Tracks passing cut AC3.2 lie within the fiducial region defined as: $0.17 < |p_y| < 0.5$ GeV,

AC3.4. Lack of simultaneous trigger signal in the near and far ALFA stations in branches other than those with forward-scattered proton tracks passing cut AC3.3.

AC4. At most one inner MBTS channel with an offline signal (on either A or C side) with $Q > Q_{\text{thr}}$ ($Q_{\text{thr}} = 0.2$ pC) and $|t| < 12$ ns.

AC5. All ID tracks consistent with the dE/dx expected for the pion, $dE/dx < 2.6$ MeV $\cdot$ cm^2/g.

AC6. Missing (total) transverse momentum $(p_x^{\text{tot}}, p_y^{\text{tot}})$ of all selected tracks consistent with zero within three detector resolutions $(\sigma_{p_x^{\text{tot}}}, \sigma_{p_y^{\text{tot}}})$.

16.2 Description of cuts

16.2.1 (AC1) Limited number of primary vertices

Selection of CEP events started with rejection of events with more than one primary vertex reconstructed from the ID tracks. As can be seen in Fig. 16.1, where the distribution of primary vertex multiplicity for all analysed events is presented, the number of events with more than one primary vertex is very low compared to zero or one primary vertex. Two or more primary vertices in an event are signature of pile-up interactions. Analysis of such events is typically more difficult and given their low contribution to the dataset they were rejected from analysis.

Figure 16.2 presents the distribution of the longitudinal position of the vertex, z_{vtx}, for events with a single reconstructed primary vertex. The normally-distributed vertex has the width of 50 mm, which is very small compared to dimensions of ATLAS and therefore no explicit limits are placed on z_{vtx}.

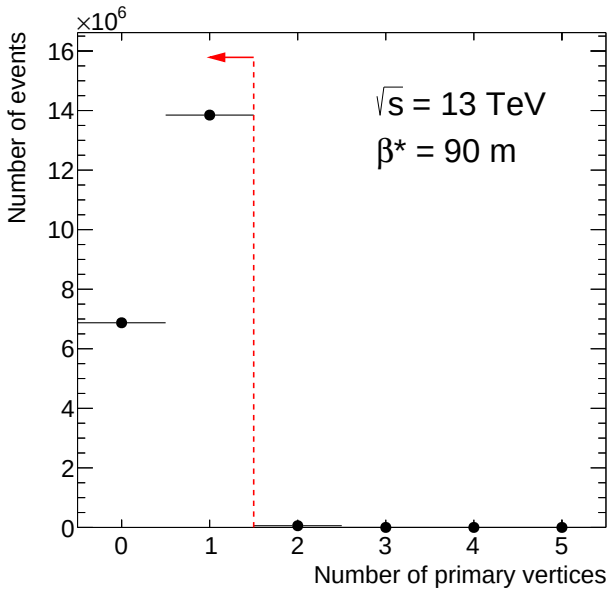

Figure 16.1: Multiplicity of primary vertices. Red dashed line and arrow marks multiplicities accepted in the analysis.

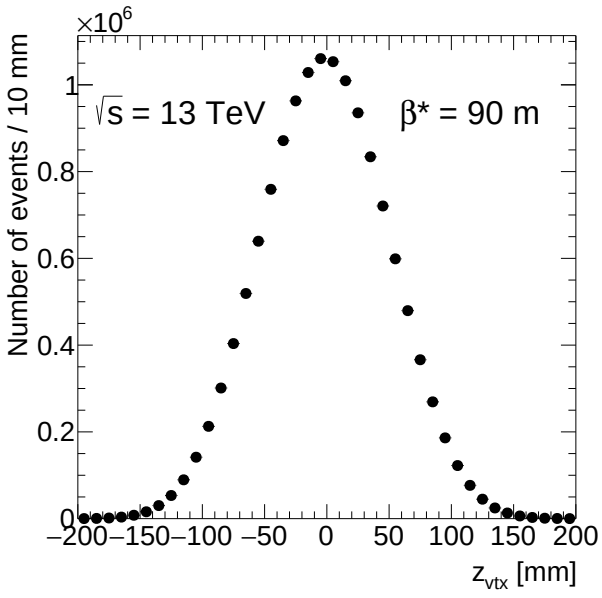

Figure 16.2: z-position of the single primary vertices.

16.2.2 (AC2) ID tracks

Selection of tracks corresponding to the centrally-produced system followed the procedure of tracks' reconstruction in the analysis of MB pp collision data at $\sqrt{s} = 13$, developed by ATLAS and outlined in Ref. [202]. The minimum p_{T} of ID tracks was allowed to be 100 MeV, instead of the typical value of 500 MeV used in standard ATLAS analyses. An even number of reconstructed ID tracks was required. Total electric charge of the tracks was required to be equal to zero[1].

All reconstructed ID tracks were required to satisfy criteria listed in AC2.2. These cuts were intended to select tracks of good quality, reconstructed within the region of high acceptance and reconstruction efficiency (first four bullets) and originating from the primary interaction vertex (last two bullets). If any of the reconstructed ID tracks did not pass the selection, event was not analysed further. Figure 16.3 shows the distribution of the transverse impact parameter d_0 (Fig. 16.3a) and the difference between longitudinal impact parameters of the most distant tracks $|\Delta z_0|$ (Fig. 16.3b), demonstrating that the tracks from the signal events fit well within the applied cuts: $|d_0| < 1.5$ mm and $|\Delta z_0| < 20$ mm. One can see in Fig. 16.3a, that MC does not entirely reproduce the shape of d_0 observed in the data. Some excess of events in data over MC predictions is observed at $|d_0| > 1$ mm which suggests slightly worse pointing resolution of the ID tracks in the data compared to MC simulation. It was found during the analysis, that the side effect of this discrepancy was a lower vertexing efficiency in

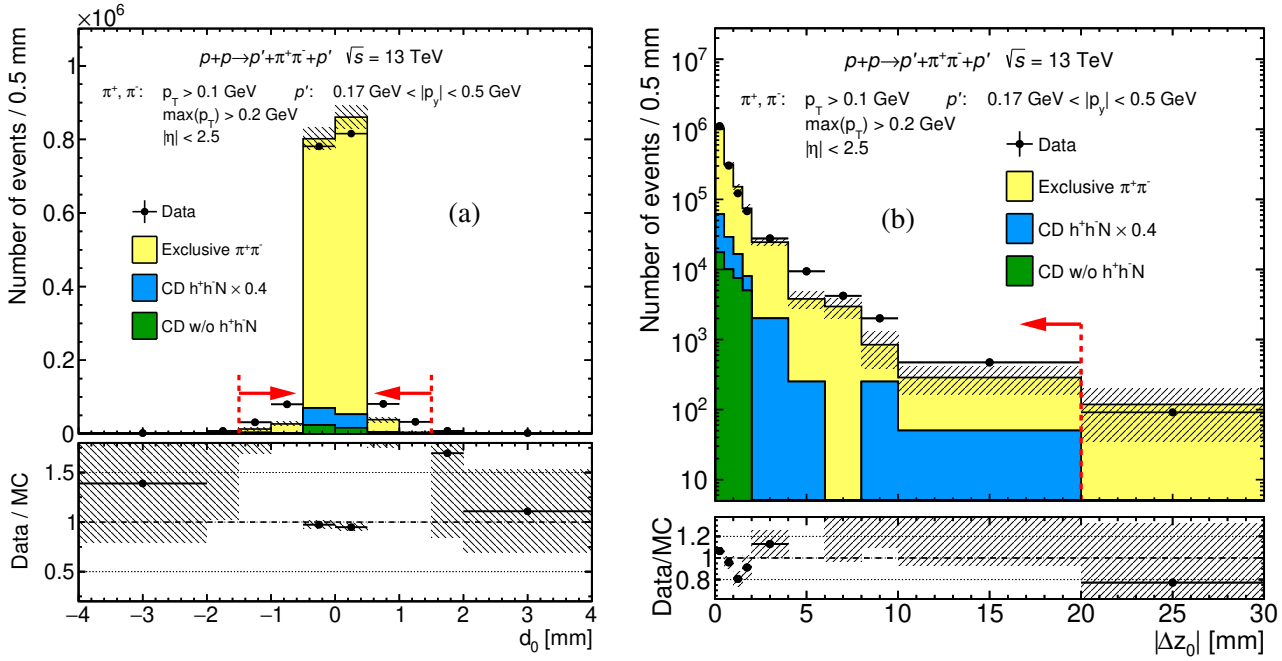

Figure 16.3: Comparison of tracks' (a) transverse impact parameter d_0, and (b) longitudinal separation of two tracks at the beamline $|\Delta z_0|$, between the data (black points) and Pythia MC predictions (stacked histograms), for CEP of $\pi^+\pi^-$ pairs. Vertical error bars represent statistical uncertainties of the data, hatched boxes represent statistical uncertainties of the MC and horizontal bars represent bin sizes. Red dashed lines and red arrows indicate the range of quantity accepted in the analysis. In the bottom panels ratios of data to MC predictions are shown.

[1] A control "same-sign" background sample was additionally formed of events with tracks whose total charge was different from zero. Those events were used e.g. in determination of systematic uncertainties related to non-exclusive background.

data compared to MC predictions. Therefore it was decided to not use the primary vertex requirement in the analysis, but rather to introduce a cut on $|\Delta z_0|$ to increase probability, that the selected tracks originate from the same primary interaction.

16.2.3 (AC3) ALFA tracks

Selection of the forward-scattered proton tracks reconstructed in ALFA RPs proceeded as follows. Branches with the trigger signal were first analysed. In all ALFA stations forming these branches, it was required to have exactly one track point with at least six (out of maximally ten) hit fibres. Requirement of at least six scintillating fibres with detected signal is more restrictive compared to the one used in the elastic-scattering analyses [203, 204], in which at least three such fibres were required. However, in those analyses the collinearity constraint was exploited to help increase the selection efficiency of a true proton tracks from many possible tracks. This is of course impossible in the CEP analysis, therefore if more than one good-quality track-point was reconstructed in single ALFA station, the event was dropped from further analysis to increase the purity of the final sample.

With two track points in the triggering branches on each side of ATLAS, a veto was imposed on simultaneous trigger signal in near and far ALFA stations in any of the two remaining branches. This way a potential backgrounds (pile-up, beam halo) with protons additional to those from CEP event, were removed.

The distribution of reconstructed transverse momentum components of the selected forward-scattered proton tracks is shown in Fig. 16.4a. The acceptance for the x-component of the transverse momentum is practically unlimited, while for the p_y a clear regions void of tracks can be observed at $|p_y| \lesssim 0.15$ GeV and $|p_y| \gtrsim 0.5$ GeV. The minimum value of $|p_y|$ corresponds to the detector's edge, which cannot approach closer to the beamline. The maximum value of $|p_y|$ is a consequence of the beam screens in front of the ALFA stations. Because of these limitations, the fiducial region for the

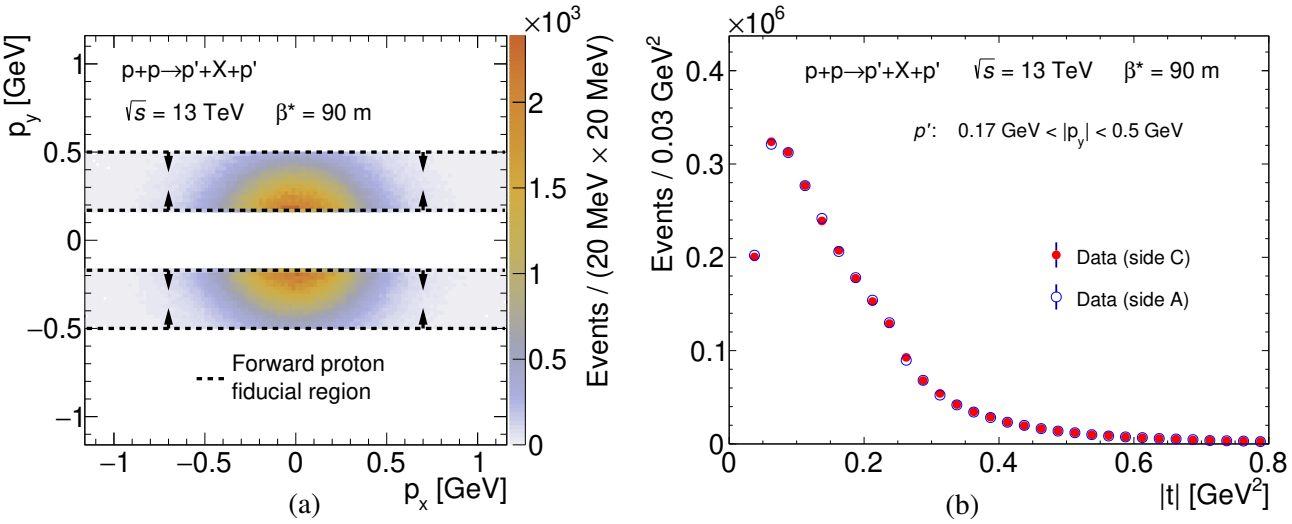

Figure 16.4: (a) Merged distributions of diffractively scattered protons momenta p_y vs. p_x in CEP events, reconstructed in the A-side and C-side ALFA stations, are shown together with the kinematic region used in the measurement marked with the black lines and arrows. (b) Distributions of measured squared four momenta transfers at the proton vertices for all selected CEP events with all particles in the fiducial phase space are shown for A- and C-side ALFA stations in blue and red colours, respectively.

forward-scattered proton tracks was defined as

$$0.17 < |p_y| < 0.5 \text{ GeV}. \tag{16.1}$$

Borders of the p_y regions from Ineq. (16.1) are drawn in Fig. 16.4a with dashed black lines. Figure 16.4b presents the distributions of the Mandelstam t for both proton vertices, obtained from the reconstructed forward-scattered protons' momenta in the fiducial region mentioned above.

The following figures show the comparisons between data and MC of the (x, y) maps of proton hits reconstructed in ALFA (Fig. 16.5), and their x- (Fig. 16.6) and y-projections (Fig. 16.7). In spite of the limited MC statistics, an acceptable agreement between data and MC is observed. Significant difference between the shape of hit distributions for the two transverse coordinates is observed, a consequence of different beam optics used along x and y.

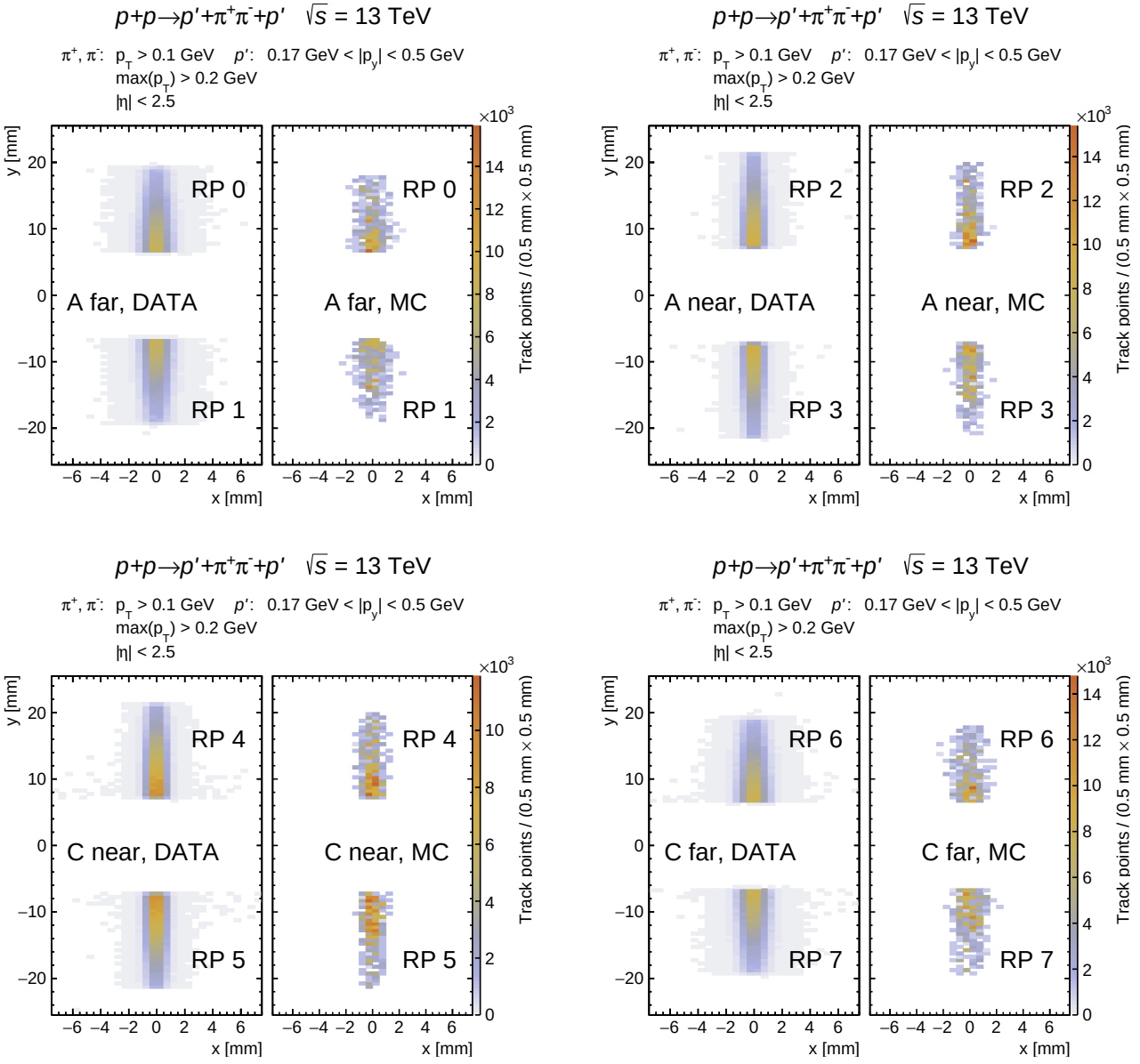

Figure 16.5: Comparison of two-dimensional track points' density maps in the data (left panels) and stacked MC (right panels). Each subfigure corresponds to a single RP station with positions of the track points measured in the upper and in the lower RP detectors, respectively.

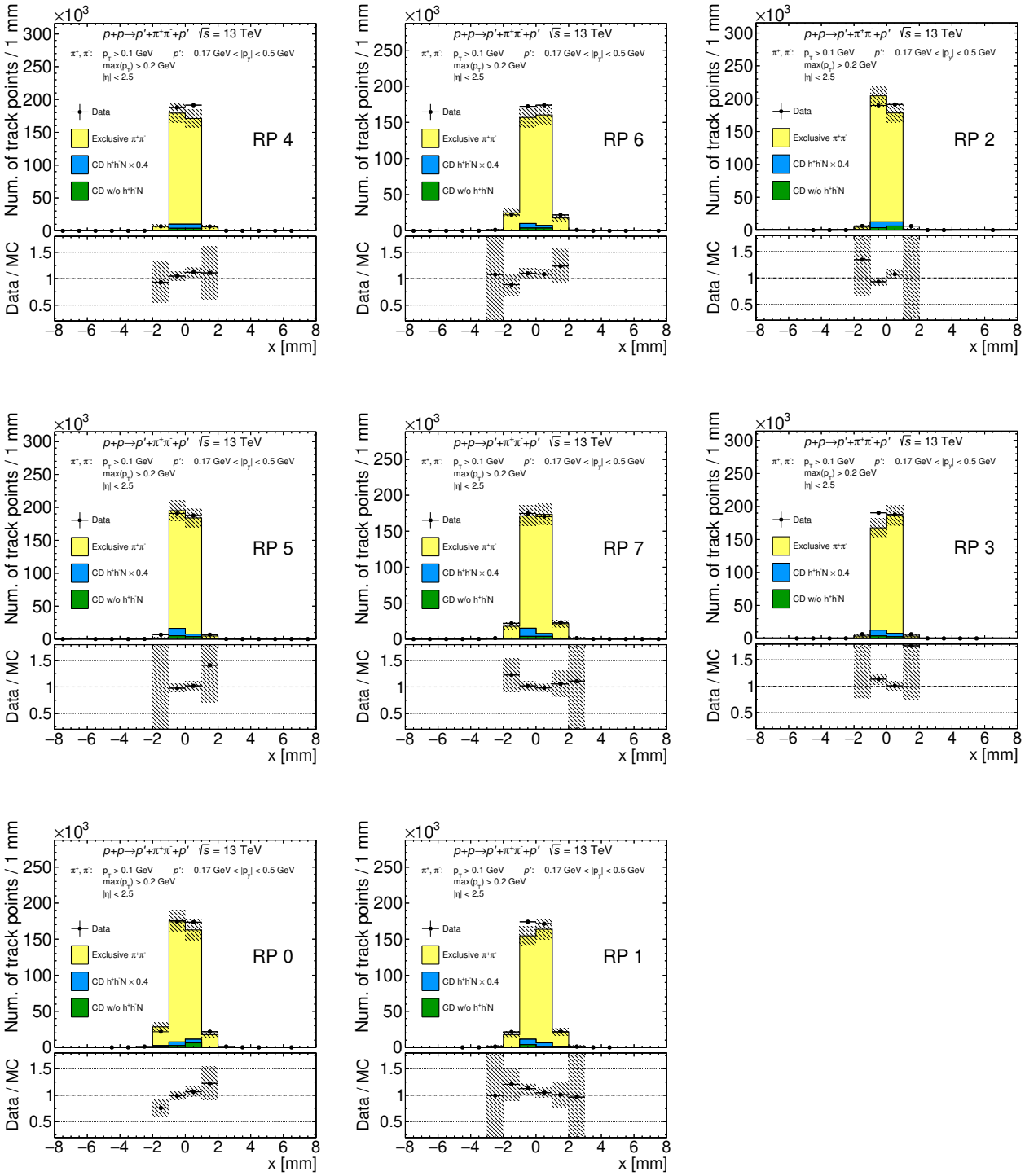

Figure 16.6: Comparison of x-position of track points between the data (black points) and MC (stacked colour histograms). Each subfigure corresponds to the single RP station, whose name is printed in the plots. Vertical error bars represent statistical uncertainties of the data, hatched boxes represent statistical uncertainties of the MC and horizontal bars represent bin sizes.

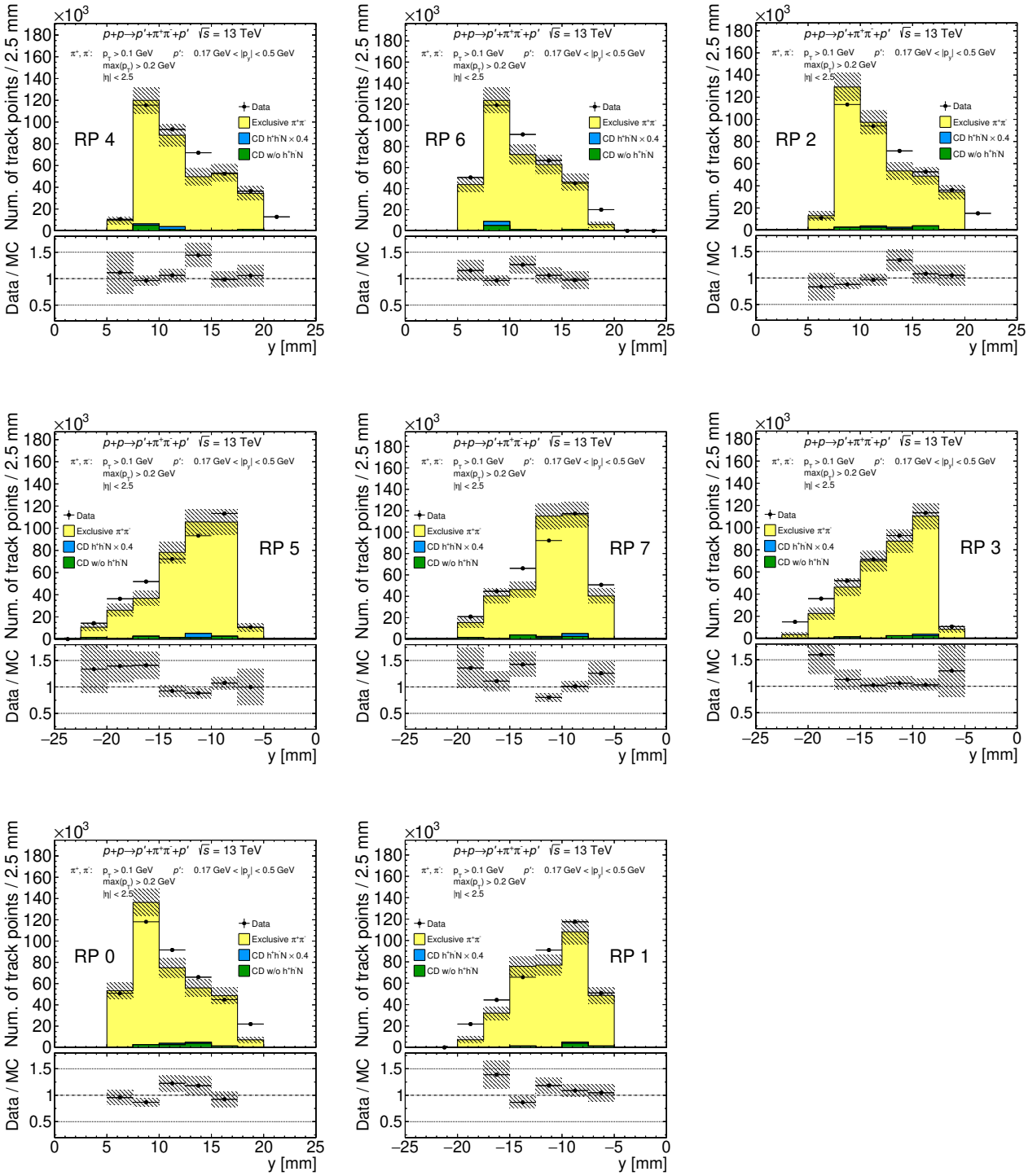

Figure 16.7: Comparison of y-position of track points between the data (black points) and MC (stacked colour histograms). Each subfigure corresponds to the single RP station, whose name is printed in the plots. Vertical error bars represent statistical uncertainties of the data, hatched boxes represent statistical uncertainties of the MC and horizontal bars represent bin sizes.

16.2.4 (AC4) Inner MBTS signal veto

CEP events, in addition to the intact beam protons detected in ALFA, are characterised by the rapidity gaps between the forward-scattered protons and the central state. This feature was used in the HLT - events with more than one online hit in the inner MBTS tiles (on A or C side) were vetoed. Nevertheless, the trigger veto was defined loosely to avoid excessive losses of signal and the room was left to improve the purity of analysed sample by tightening cut on the signal in MBTS.

Figure 16.8 shows the scatter plots with correlation between L2 (vertical axis) and offline[2] information about the collected charge (Fig. 16.8a) and time of signal detection (Fig. 16.8b) in exemplary inner MBTS channel. The majority of signals were recorded in a narrow time interval ranging between -5 ns and 5 ns, as observed in the centre of Fig. 16.8b. More inclusive requirement was imposed in the HLT, $|t| < 12$ ns, to claim presence of the signal, accompanied by the requirement of the sufficiently large collected charge $Q > 0.18$ pC.

The optimal Q value for the offline signal threshold was obtained with the help of Fig. 16.9a. The data-driven method of non-exclusive background estimation was used, which revealed that the backgrounds are low and constant (after all cuts applied except AC4) for $Q \lesssim 0.1$ pC, while at $Q \approx 0.4$ pC the level of background saturates at the maximum value of around 30%. This suggests, that in order to reduce the background contributions, the threshold should be placed somewhere within $0.1-0.4$ pC. The threshold was finally established through the data-driven study of the CEP event ($\pi^+\pi^-$ pairs) selection efficiency and fraction of non-exclusive background in sample selected using a given set of cuts. The considered cuts were the momentum balance cut, AC6, and the cut on inner MBTS signal, which included variation of the number of accepted channels with the signal, and variation of the threshold value, Q_{thr}, above which the charge collected in a given channel, i, is considered as a signal, i.e.:

$$Q_i > Q_{\text{thr}} \quad \text{and} \quad |t_i| < 12 \text{ ns}. \tag{16.2}$$

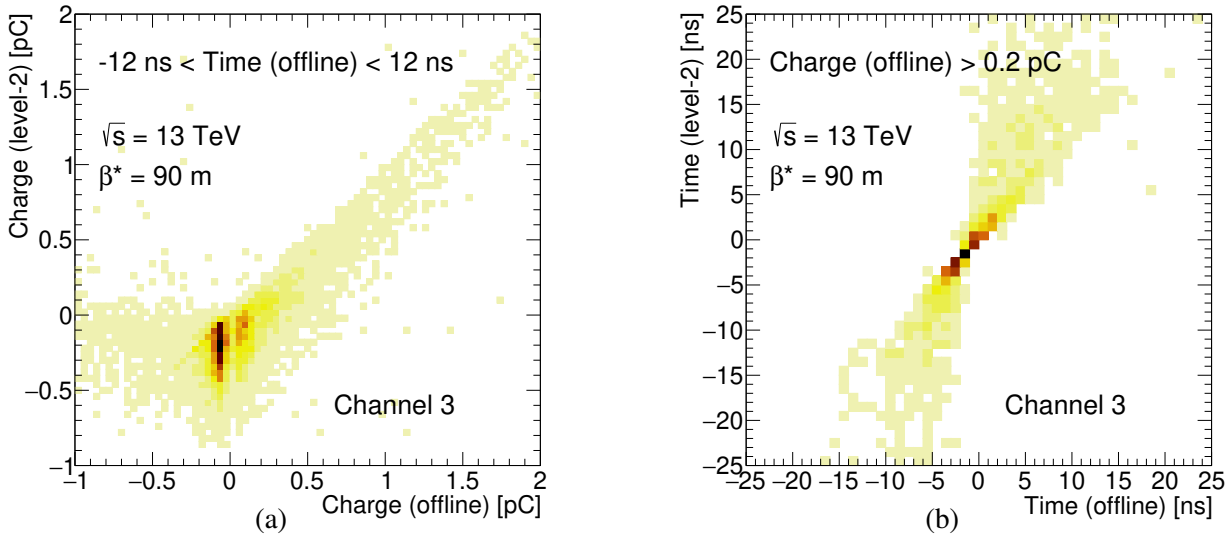

Figure 16.8: Comparison of the (vertical axis) HLT and (horizontal axis) offline (a) charge, and (b) time of signal detection, in exemplary inner MBTS channel.

[2]Offline data differs from L2 information as it includes dedicated calibrations derived after the data were processed.

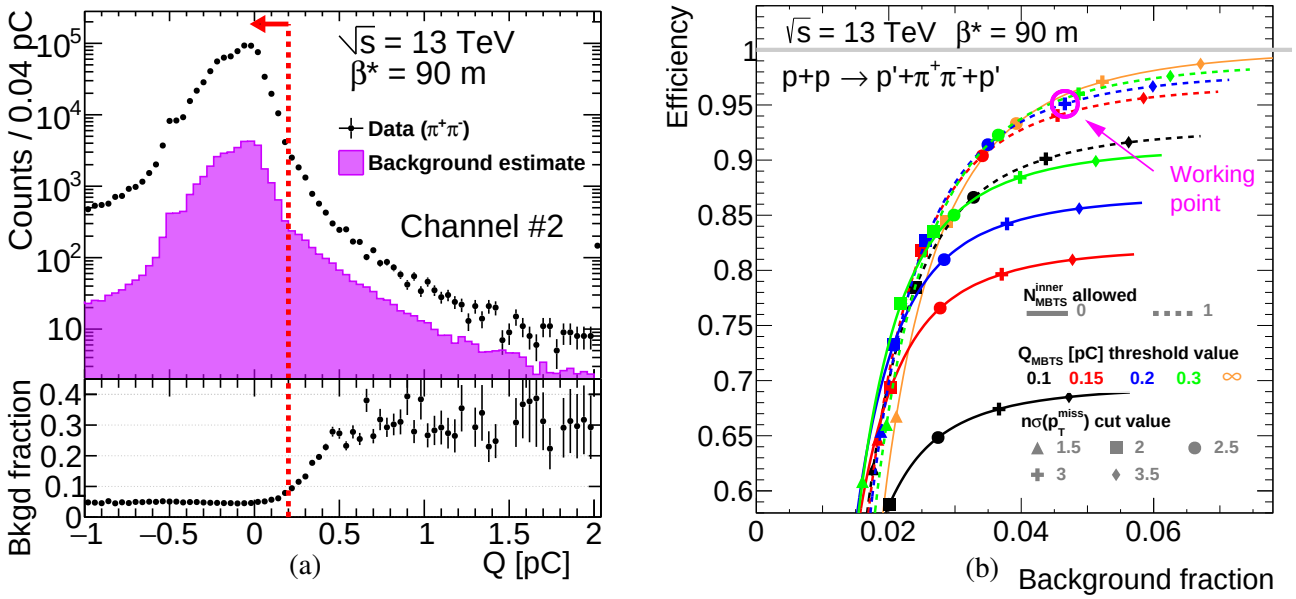

Figure 16.9: (a) Charge collected in an exemplary inner MBTS tile (channel #2). Bottom panel shows the estimated fraction of counts from events different than the CEP of $\pi^+\pi^-$. (b) Efficiency vs. purity for MBTS and exclusivity cuts.

The relation between the signal selection efficiency (vertical axis) and the background content (horizontal axis) is shown in Fig 16.9b. With a momentum balance cut fixed at a desired value (marked with crosses), it was decided to allow in analysis maximally one inner MBTS channel with a signal defined by Ineq. (16.2) using $Q_{\text{thr}} = 0.2$ pC. With such definition of the cut AC4, the resultant signal selection efficiency (with respect to sample without applied cuts AC4 and AC6) was found to be $\approx 96\%$, with acceptably low background yield of about 5.5% of the selected sample.

16.2.5 (AC5) Particle identification

Tracks of particles reconstructed in the ID contain information about the specific energy loss. This quantity is reconstructed from the energy deposit in the PXL, as explained in Sec. 13.2.1. In order to reduce contamination from processes involving particles other than pions e.g. CEP of K^+K^- pairs[3], all tracks were required to be consistent with the pion hypothesis based on dE/dx from PXL. Therefore, for all tracks the requirement

$$dE/dx < 2.6\ \text{MeV} \cdot \text{cm}^2/\text{g} \tag{16.3}$$

was imposed. This cut value is marked with dashed magenta line in Fig. 16.10, where the dE/dx distribution, as a function of the tracks' momentum, for particles of both negative and positive electric charge, is shown. It is clear from the figure that vast majority of tracks originate from charged pions, and the dE/dx cut safely removes tracks of other species of particles without notable loss of pion selection efficiency.

[3]CEP of hadronic systems other than those formed of only pions is not covered in presented analysis. However, analysis of CEP of K^+K^- and $p\bar{p}$ pairs, and potentially of $\Lambda\Lambda$ pairs and other configurations, is possible with the analysed data. Initial estimates of the numbers of CEP events in with K^+K^- and $p\bar{p}$ pairs in the analysed data are 10^4 and 300 events, respectively.

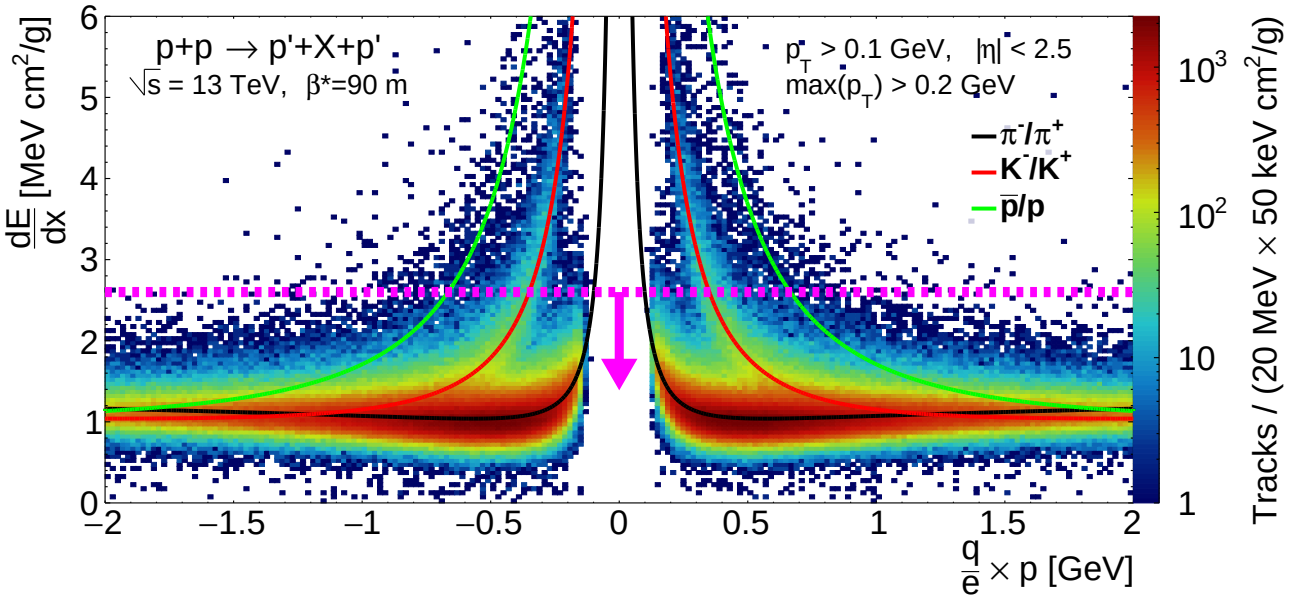

Figure 16.10: Specific energy loss of charged particle pairs in exclusive event candidates after all but the PID (AC5) cuts applied, as a function of a track momentum multiplied by the sign of track's charge. Colour lines represent MPV of dE/dx for a few particle species [33].

16.2.6 (AC6) Exclusivity cut (missing p_{T} cut)

The key selection cut, which exploits the benefit of reconstructing all final state particles, is the cut on the missing transverse momentum, $p_{\mathrm{T}}^{\mathrm{miss}}$, defined in Eq. (9.13). In case of more than two centrally-produced particles, components connected with an additional particles were added to the equation.

In Fig. 16.11, the (anti-)correlation between the components of the total momenta of the forward-scattered protons and the two/four/six pions, are presented. Similarly to Fig. 9.19, a narrow bands lying on the anti-diagonal and representing the back-to-back configuration of the forward- and central-system particles are clearly visible.

One-dimensional plots of the momentum balance for all studied central systems are shown in Figs. 16.12 and 16.13. The distributions of p_x^{miss} and p_y^{miss} were fitted with the sum of two Gaussian distributions representing, respectively, the CEP signal and the backgrounds. Results of the fit are given in each subfigure. It is clear, that widths of the signal peaks, $\sigma_{p_x^{\mathrm{miss}}}$ and $\sigma_{p_y^{\mathrm{miss}}}$, vary between the coordinates and between central states of different multiplicities. Different momentum resolutions for p_x^{miss} and p_y^{miss} are a consequence of different beam optics in the x- and y-coordinates. The differences between central systems result from the resolution worsening after adding components from the increasing number of particles. The resolutions of p_x^{miss} and p_y^{miss} being significantly different from each other require using an elliptical cut on the missing transverse momentum, that is expressed through $n\sigma(p_{\mathrm{T}}^{\mathrm{miss}})$ quantity defined based on formula from Ineq. (9.14) as

$$n\sigma(p_{\mathrm{T}}^{\mathrm{miss}}) = \sqrt{\left(\frac{p_x^{\mathrm{miss}}}{\sigma_{p_x^{\mathrm{miss}}}}\right)^2 + \left(\frac{p_y^{\mathrm{miss}}}{\sigma_{p_y^{\mathrm{miss}}}}\right)^2}. \tag{16.4}$$

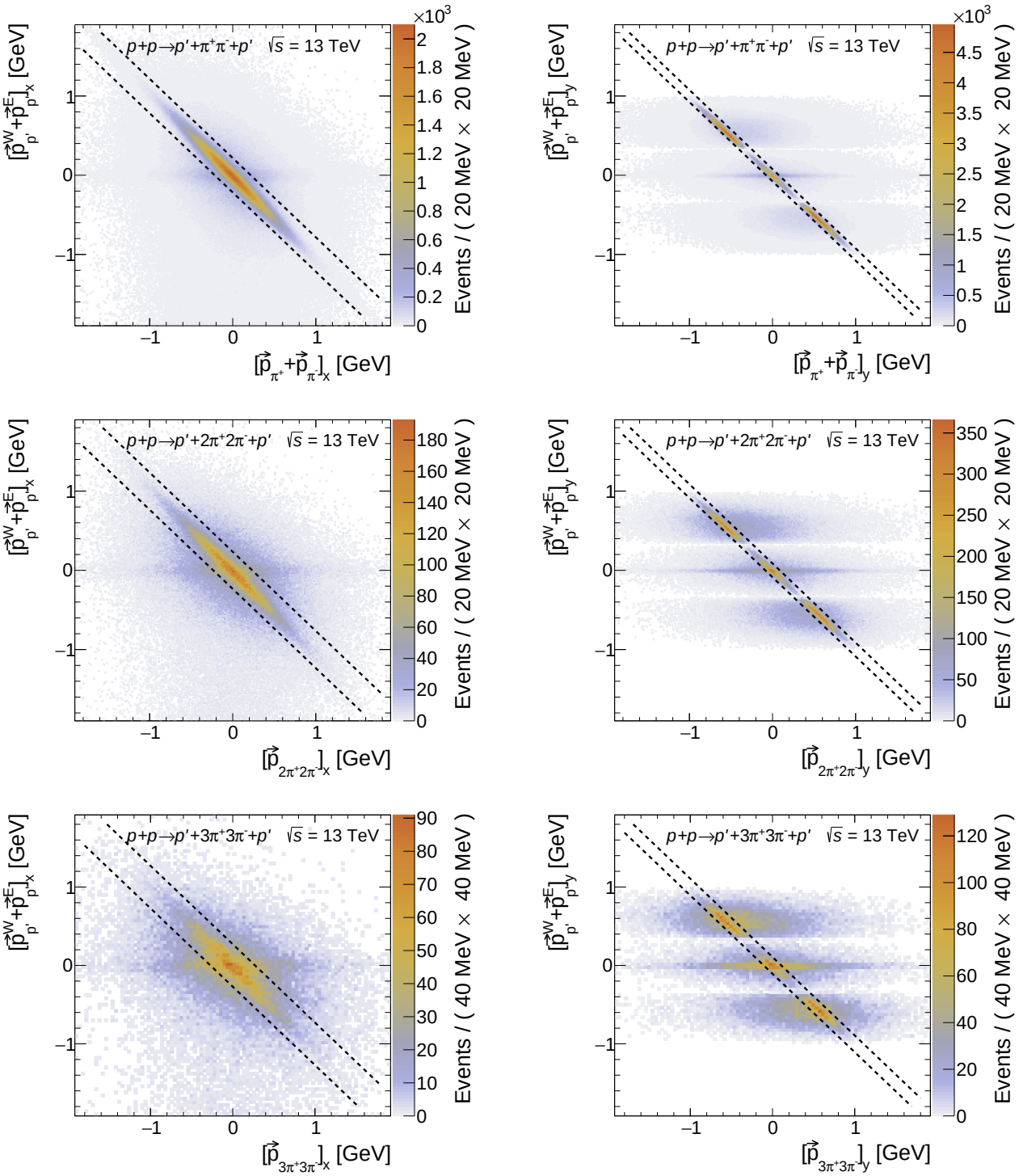

Figure 16.11: Correlation plots between the x- (left column) and y- (right column) components of the sums of forward-scattered protons momenta and the centrally produced system, for the $\pi^+\pi^-$ (top row), $2\pi^+2\pi^-$ (middle row), and $3\pi^+3\pi^-$ (bottom row) event candidates, after full event selection, except the exclusivity cut AC6. The dashed lines mark the $\pm 3\sigma$ band around the anti-diagonal representing a perfect momentum balance. The three distinct horizontal regions in plots on the right hand side correspond to different forward proton configurations: elastic-like (protons in branches 0&3 or 1&2, $\left|[\vec{p}_{p'}^{\,\mathrm{W}} + \vec{p}_{p'}^{\,\mathrm{E}}]_y\right| < 0.35$ GeV) and anti-elastic configuration (protons in branches 0&1 or 2&3, $\left|[\vec{p}_{p'}^{\,\mathrm{W}} + \vec{p}_{p'}^{\,\mathrm{E}}]_y\right| > 0.35$ GeV).

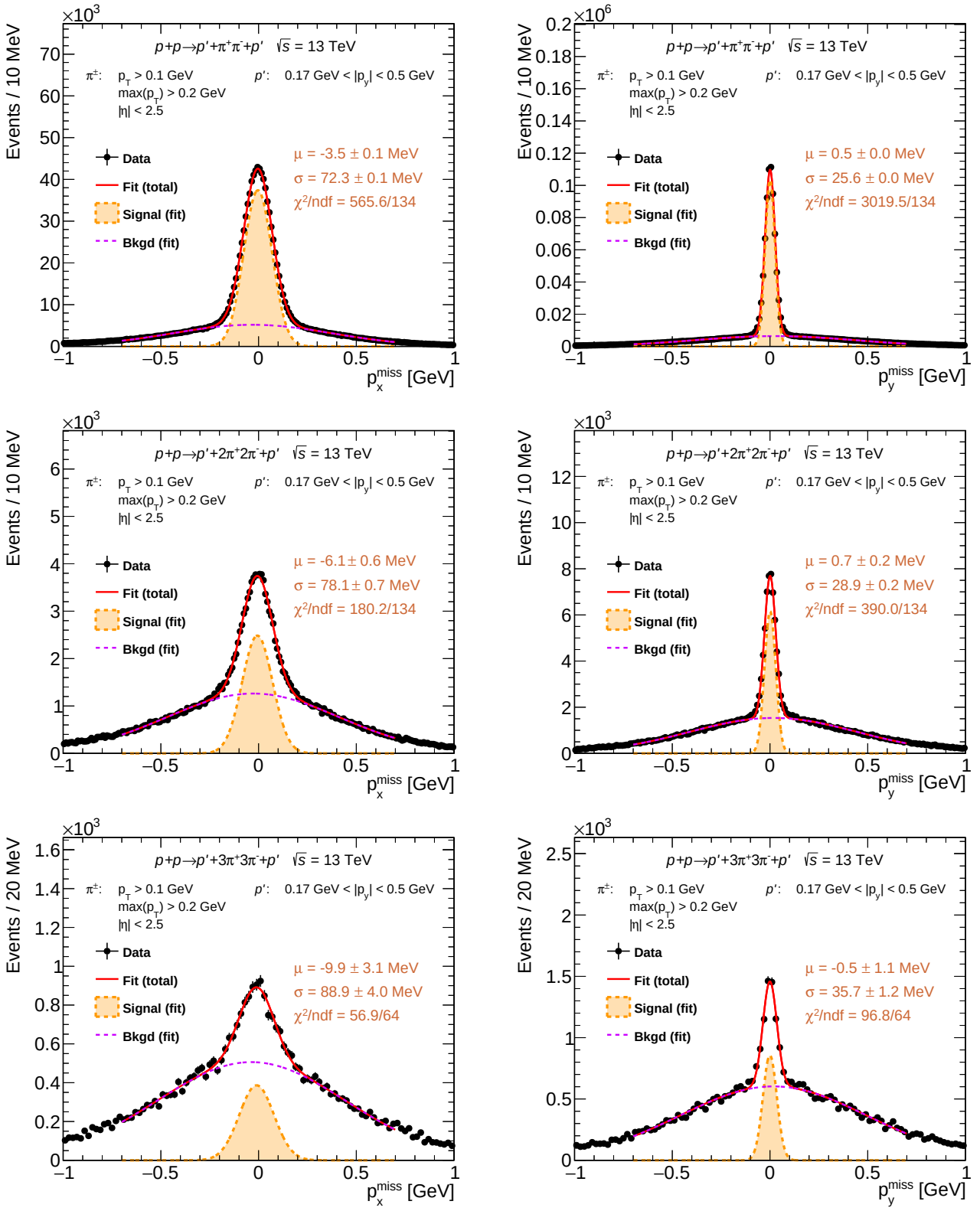

Figure 16.12: Raw distributions of p_x^{miss} (left column) and p_y^{miss} (right column) for exclusive $\pi^+\pi^-$ (top row), $2\pi^+2\pi^-$ (middle row) and $3\pi^+3\pi^-$ (bottom row) candidates after full event selection, except exclusivity cut AC6. Solid red line represents the fit of sum of two Gaussian functions representing the exclusive event signal (orange) and non-exclusive background (violet).

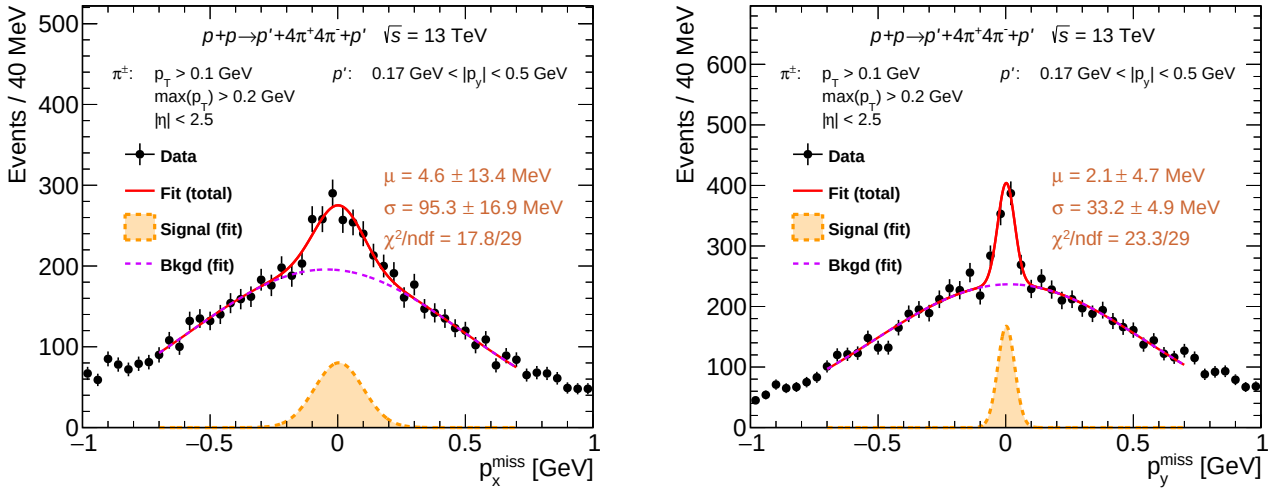

Figure 16.13: Raw distributions of p_x^{miss} (left) and p_y^{miss} (right) for exclusive $4\pi^+4\pi^-$ candidates after full event selection, except exclusivity cut AC6. Solid red line represents the fit of sum of two Gaussian functions representing the exclusive event signal (orange) and non-exclusive background (violet).

In this definition the widths $\sigma_{p_x^{\text{miss}}}$ and $\sigma_{p_y^{\text{miss}}}$ depend on a CEP channel and hence it is assured that for each channel the same fraction of signal events is selected. In the analysis the $n\sigma(p_{\text{T}}^{\text{miss}}) < 3$ is used.

17. Backgrounds

Similarly as in the case of the STAR CEP analysis, there exist two distinct classes of backgrounds in the CEP analysis of the ATLAS data. The first one, the non-exclusive background, is due to the limited detector acceptance and efficiency. Several non-CEP processes, alone or in combination with pile-up events or machine background (see discussion in Sec. 10.1.1), may resemble the topology of the CEP event. Due to the special beam conditions during the data taking by ATLAS, which provided low pile-up environment, only the possible background from the CD process is considered in the ATLAS analysis. The background was determined using the fully data-driven method described in Sec. 10.2.1, with a couple of minor changes. Instead of $p_{\mathrm{T}}^{\mathrm{miss}}$, the $n\sigma\left(p_{\mathrm{T}}^{\mathrm{miss}}\right)$ was used. The signal region was defined with help of cut AC6, while the background region, in which the polynomial fit is performed, was defined as $5 < n\sigma\left(p_{\mathrm{T}}^{\mathrm{miss}}\right) < 10$. The results of the non-exclusive background estimation for different considered central states, $n(\pi^+\pi^-)$, $n = 1, 2, 3, 4$, are shown in Fig. 17.1.

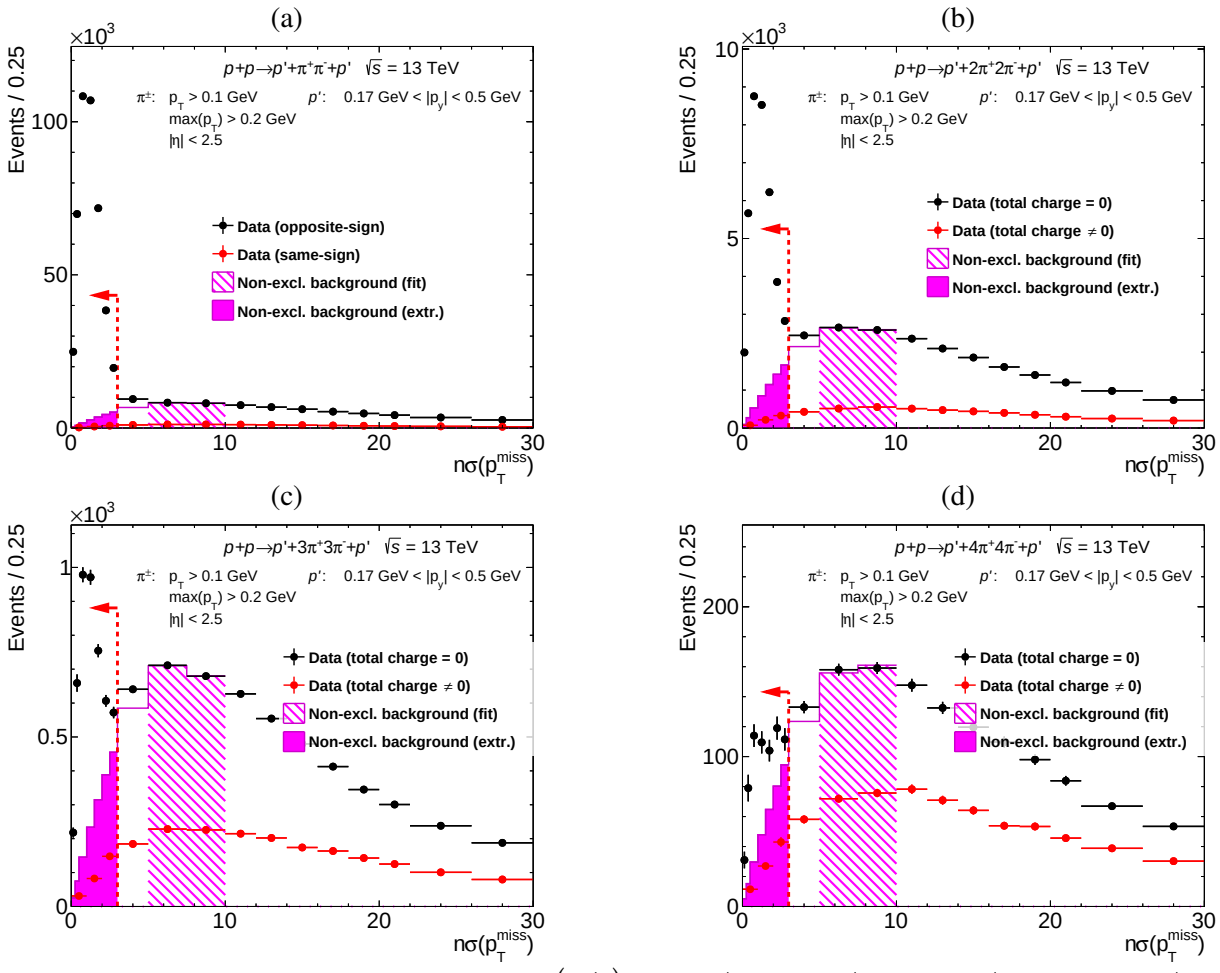

Figure 17.1: Uncorrected distributions of the $n\sigma\left(p_{\mathrm{T}}^{\mathrm{miss}}\right)$ for (a) $\pi^+\pi^-$, (b) $2\pi^+2\pi^-$, (c) $3\pi^+3\pi^-$ and (d) $4\pi^+4\pi^-$ CEP event candidates. Distributions for events with the total electric charge of the centrally-produced particles equal to zero and different from zero are shown as black and red symbols, respectively. The dashed magenta histogram, is the result of the fit in the signal-free region. Estimation of the non-exclusive background contribution in the signal region ($n\sigma\left(p_{\mathrm{T}}^{\mathrm{miss}}\right) < 3$) is shown as the full magenta histogram. The vertical error bars represent the statistical uncertainties, while the horizontal bars represent the bin sizes.

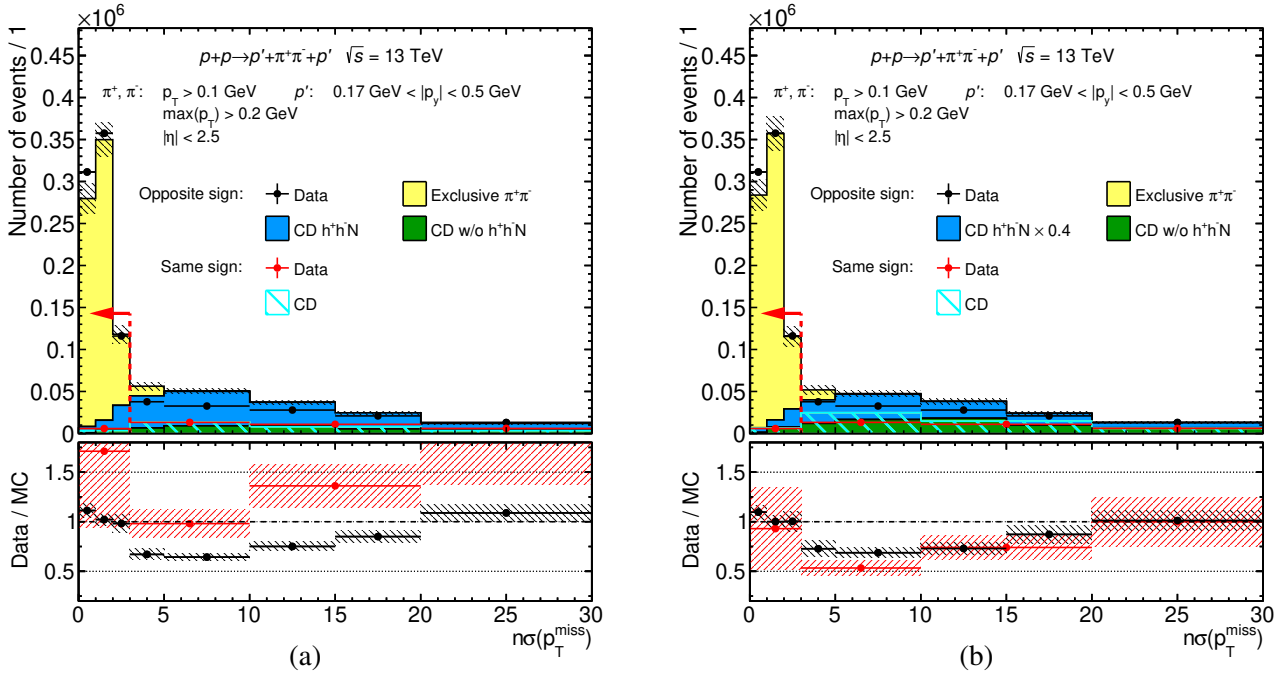

Figure 17.2: Comparison of $n\sigma\left(p_{\mathrm{T}}^{\mathrm{miss}}\right)$ for CEP $\pi^+\pi^-$ between data and MC after full selection (except cut on transverse momentum balance, AC6). Data are represented by black (opposite-sign signal channel) or red (control same-sign background channel) points, while stacked MC predictions are drawn as filled (opposite-sign) or hatched (same-sign) histograms of different colors. Histogram from each MC process has been normalised according to prescription in the text. Vertical error bars represent statistical uncertainties of the data, hatched boxes represent statistical uncertainties of the MC and horizontal bars represent bin sizes. Dashed red line and arrow represent total momentum balance cut AC6. Plots (a) and (b) differ from each other in the content of Pythia MCs; in (a) the Pythia predictions were left unchanged, while in (b) events with h^+h^-+neutrals in the central state were scaled by factor 0.3, yielding much better consistency between data and MC in the ratio of opposite-sign to same-sign events.

The second class of background, exclusive background, originates from CEP processes. Some particles in the central final state might be misidentified. For example K^+K^- pairs can be misidentified as $\pi^+\pi^-$ pairs. This kind of background was discussed in detail in Sec. 10.1.2. It was not considered provided low initial estimates of this type of background to the finally selected CEP event candidates.

The comparison of control distributions between data and MC have been performed to demonstrate good understanding of the residual backgrounds in the data. It has been tested for exclusive $\pi^+\pi^-$ channel. Only the non-exclusive backgrounds were considered here because of negligible contribution from misidentifications.

The normalisation of considered contributing processes have been determined using the opposite-sign sample. First, the non-exclusive CD MC was normalised. It was scaled to have the same integral as the data in the range $n\sigma\left(p_{\mathrm{T}}^{\mathrm{miss}}\right) > 5$, where no exclusive signal is expected. In the next step, the exclusive $\pi^+\pi^-$ MC was normalised. It was scaled to have the same integral as the data (minus non-exclusive CD background) in the range $n\sigma\left(p_{\mathrm{T}}^{\mathrm{miss}}\right) < 3$, where exclusive signal is dominant. The result of this procedure for the distribution of $n\sigma\left(p_{\mathrm{T}}^{\mathrm{miss}}\right)$ is given in Fig. 17.2. Also comparisons of separately p_x^{miss} and p_y^{miss} are shown in Figs. 17.3a and 17.3b, respectively. As can be observed, in the comparison plots, distributions representing momentum balance in the opposite-sign event sample are reasonably well described. Some mismodelling of the large-$n\sigma\left(p_{\mathrm{T}}^{\mathrm{miss}}\right)$ region may be connected

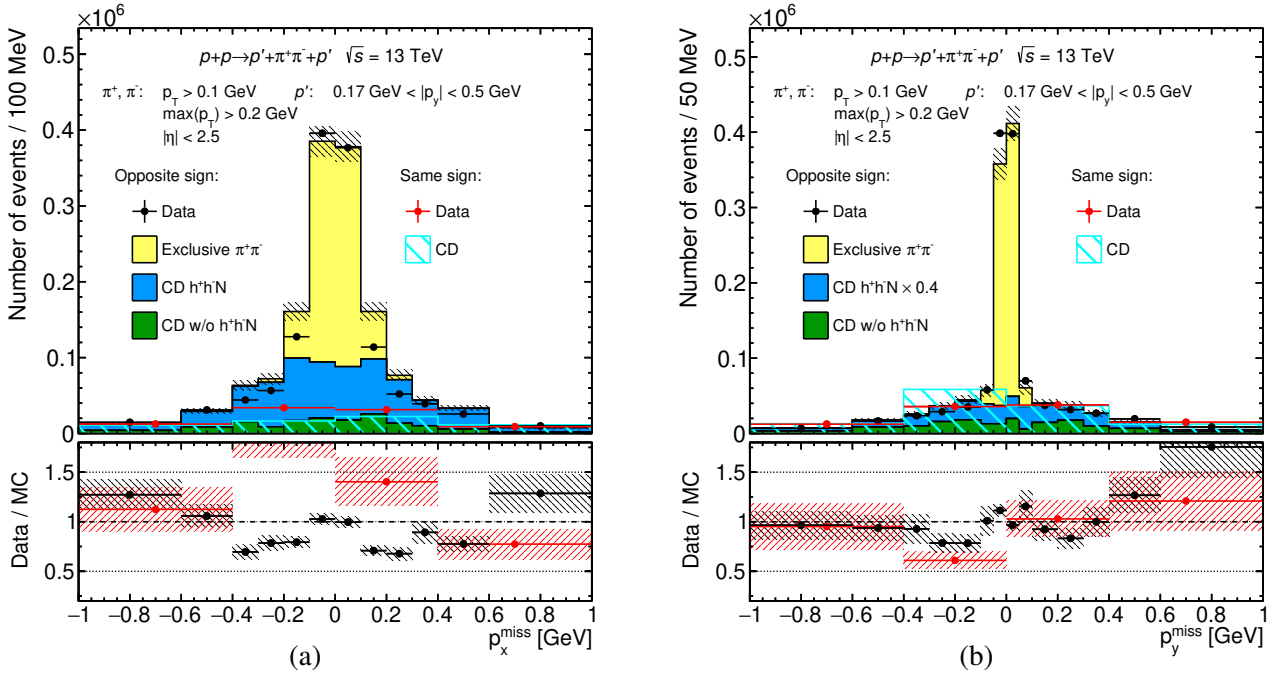

Figure 17.3: Comparison of (a) p_x^{miss} and (b) p_y^{miss} for CEP $\pi^+\pi^-$ between data and MC after full selection (except cut on transverse momentum balance, AC6). Data are represented by black (opposite-sign signal channel) or red (control same-sign background channel) points, while stacked MC predictions are drawn as filled (opposite-sign) or hatched (same-sign) histograms of different colors. Histogram from each MC process has been normalised according to prescription in the text. Vertical error bars represent statistical uncertainties of the data, hatched boxes represent statistical uncertainties of the MC and horizontal bars represent bin sizes.

with the imprecise modelling of the particle distributions in CD process in Pythia or too simplified simulation of the detector effects for the forward-scattered protons. In order to properly describe normalisations of both opposite-sign signal channel and control same-sign channel, it was necessary to reject fraction (60%) of Pythia contributions from events with the central state consisting from two opposite-sign particles and at least one neutral particle. Figure 10.12b demonstrates, that if these events are preserved, Pythia MC cannot describe data in the background-dominating region (large $n\sigma\left(p_{\text{T}}^{\text{miss}}\right)$). This observation is qualitatively consistent with a need to entirely remove contributions from $\pi^+\pi^- + N$ events (N being a set of neutral particles) in order to describe the transverse momentum balance distribution in the analysis of the STAR experiment data (Fig. 10.12).

Summary of the data-driven estimates of background contributions to the studied CEP processes is given in Tab. 17.1.

	Selected events	**Non-excl. bkgd**
$\boldsymbol{\pi^+\pi^-}$	784764	36075 (4.6%)
$\boldsymbol{2\pi^+2\pi^-}$	68013	11571 (17%)
$\boldsymbol{3\pi^+3\pi^-}$	8642	3176 (37%)
$\boldsymbol{4\pi^+4\pi^-}$	1226	655 (53%)

Table 17.1: Summary of non-exclusive background contributions to the CEP of $n\pi^+n\pi^-$ ($n = 1, 2, 3, 4$) systems. Values in brackets are fractions calculated with respect to number of selected events.

18. Corrections

In this chapter, derivation of relevant acceptances and efficiencies is described, which are later used to correct the data to the hadron-level cross sections.

18.1 Trigger efficiency

18.1.1 ALFA trigger efficiency

From the elastic scattering analyses at 7 TeV [198] and 8 TeV [204], it is known, that the efficiency of the trigger in ALFA RPs is close to 100%. It is generally preferred to determine the trigger efficiency of a subsystem using the data triggered independently from that subsystem. However, in this analysis, the efficiency was determined from the CEP events, which were triggered by ALFA. Although such method only allows to determine the relative trigger efficiency for a given ALFA station (i.e. under condition that another RP in a branch provided a trigger signal), it was used to verify the negligible ALFA trigger inefficiency and thus give an argument to skip the ALFA trigger efficiency correction in the data analysis.

The trigger efficiency in a single ALFA RP was determined from the reconstructed CEP events with the $\pi^+\pi^-$ pair in the central diffractive system. Selection of the CEP events provides a clean sample of the real forward-scattered protons traversing the active area of ALFA detectors. Although it is known from the previous chapters, that a few percent of the non-exclusive background is still present in data after the selection, the majority of the background originates from the CD process, which is also characterised by the presence of forward-scattered protons on both sides of the ATLAS IP.

Each RP detector with a reconstructed proton track was studied independently. For the ALFA station under study (i) it was required, that the other station in the branch has a valid trigger signal. Such requirement assures that the CEP HLT was satisfied by other RP detectors. Number of such events was denoted $N_{\mathrm{ALFA},i}$. Next, it was checked if there was a valid trigger signal in the ALFA station under study. If yes, such events were counted as $N^{\mathrm{trig}}_{\mathrm{ALFA},i}$. The efficiency of the trigger in the studied ALFA station was calculated as

$$\varepsilon^{\mathrm{trig}}_{\mathrm{ALFA},i} = \frac{N^{\mathrm{trig}}_{\mathrm{ALFA},i}}{N_{\mathrm{ALFA},i}}. \tag{18.1}$$

The trigger efficiencies of all ALFA stations are shown in Fig. 18.1. In the first five RPs the efficiency is literally 100%. ALFA stations 5, 6 and 7 show the efficiency of 99.4%, 91.7% and 95.7%, respectively. It was verified that the efficiency is independent of the position of the proton hit and of the number of the luminosity block (time in the run).

Stations 4 and 6, as well as 5 and 7, form common branches with the L1 trigger signal in a branch defined as the logical OR between the two stations in the branch. Therefore, assuming that the trigger signals in single stations are independent from each other, the efficiency of the trigger calculated as the probability opposite to the case with both ALFA stations being inefficient is over 99.9%.

In conclusion, the ALFA trigger can be considered 100% efficient, and no efficiency correction nor systematic uncertainty on the trigger efficiency, are needed.

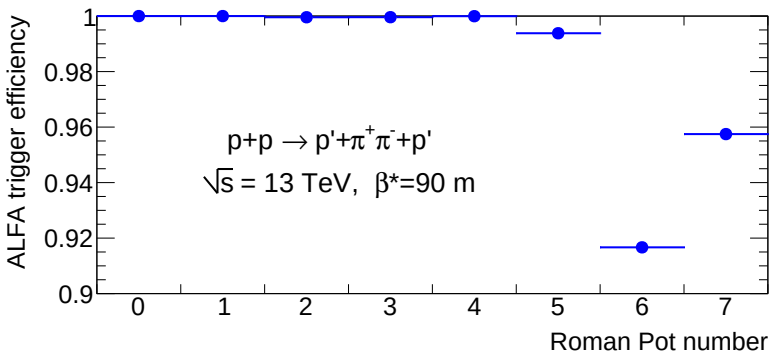

Figure 18.1: Trigger efficiencies of the individual ALFA RP stations (vessels).

18.1.2 MBTS trigger veto efficiency

Inefficiency introduced by the HLT veto, on more than one inner MBTS channel with L2 signal on either A or C side, was calculated using the elastic scattering data. An efficiency correction for a veto on the activity not originating from the studied process but presumably from a pile-up interaction, is best determined from the zero-bias data. Because of limited statistics of the zero-bias data, the elastic scattering data was used. Once the elastic scattering event was reconstructed in data from the elastic scattering trigger, all information from the central detector can be regarded as a zero-bias data (except small fraction of CD events where protons are collinear). In this way, it was possible to calculate the probability of an activity in a detector vetoing CEP events.

Elastic scattering events were selected in a similar way as in Ref. [205], but with tracks required to fulfil the same quality cuts (AC3.1) as in the CEP analysis. Single proton tracks on each side (AC3.2), in a pair of branches with the elastic scattering trigger signal (one of the two elastic ALFA arms) was required. Next, on each side, the position and angle at the far station (subscript 'far, extr') were determined from the position and angle measured in the near station (subscript 'near'), using the relation

$$\begin{bmatrix} w \\ \theta_w \end{bmatrix}_{\text{far,extr}} = \mathbb{M}_{w,\text{far}} \mathbb{M}^{-1}_{w,\text{near}} \begin{bmatrix} w^{\text{RP}} \\ \theta^{\text{RP}}_w \end{bmatrix}_{\text{near}} \tag{18.2}$$

which benefits from properties of the proton transport presented in Eqs. (14.1) and (14.2). The proton hit position measured in the far station was required to be consistent with the position in the far station extrapolated from the hit in the near station within three-and-a-half standard deviations around the average value of the difference $\mu(\Delta w) = \langle w_{\text{far}} - w_{\text{far,extr}} \rangle$, in both x- and y-coordinate:

$$\left| w_{\text{far}} - w_{\text{far,extr}} - \mu\left(\Delta w\right) \right| < 3.5 \cdot \sigma\left(w_{\text{far}} - w_{\text{far,extr}} \right). \tag{18.3}$$

Such cuts remove the proton tracks with the reconstructed momentum significantly different from the beam momentum ($\xi > 0$). Distributions of $|w_{\text{far}} - w_{\text{far,extr}}|$ are shown in Fig. 18.2. Non-zero offset $\mu(y)$ visible in the data distribution in Fig. 18.2b is a consequence of some residual misalignment, removed after the alignment optimisation.

Next, the collinearity of the above selected proton tracks was verified. Events with A- and C-side tracks, whose x-position in the near ALFA stations summed up to zero within three-and-a-half standard deviations:

$$\left| x_{\text{near},A} + x_{\text{near},C} \right| < 3.5 \cdot \sigma\left(x_{\text{near},A} + x_{\text{near},C} \right), \tag{18.4}$$

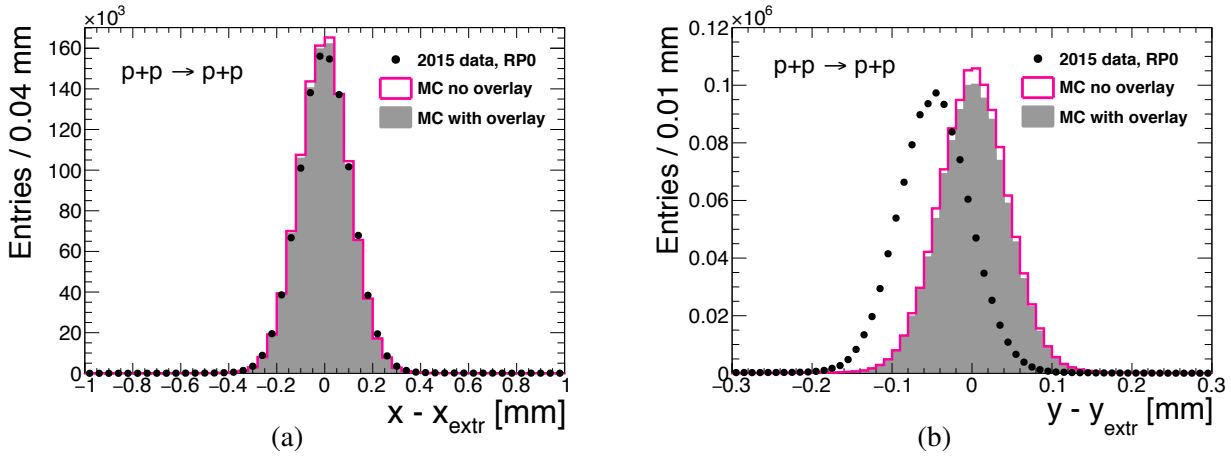

Figure 18.2: Differences between the measured and extrapolated positions of hits in the ALFA station 0, separately for (a) x- and (b) y-coordinate. Data are shown with black points, while the elastic scattering MC predictions, with and without data overlay, are shown as grey and magenta histograms, respectively. Figures courtesy of I. Lakomiec.

and whose y-position in the near ALFA stations was opposite to each other within three millimetres:

$$\left|y_{\text{near},A} + y_{\text{near},C}\right| < 3 \text{ mm}, \tag{18.5}$$

were selected. The above selection follows the elastic scattering analysis of the data collected with the ALFA detector at $\sqrt{s} = 8$ TeV [204]. Distributions of the sum of track positions in the near stations on the A and C sides are shown in Fig. 18.3.

Number of selected elastic scattering events was denoted as N_{el}. Among those, the events without the inner MBTS trigger veto were counted as $N_{\text{el}}^{\text{!veto}}$. The efficiency of the veto was calculated as

$$\varepsilon_{\text{veto}} = \frac{N_{\text{el}}^{\text{!veto}}}{N_{\text{el}}}. \tag{18.6}$$

In Fig. 18.4a, the HLT inner MBTS veto efficiency is shown as a function of the time in a run. On average the efficiency amounts approximately 92% (see also Fig. 18.4b with all runs presented).

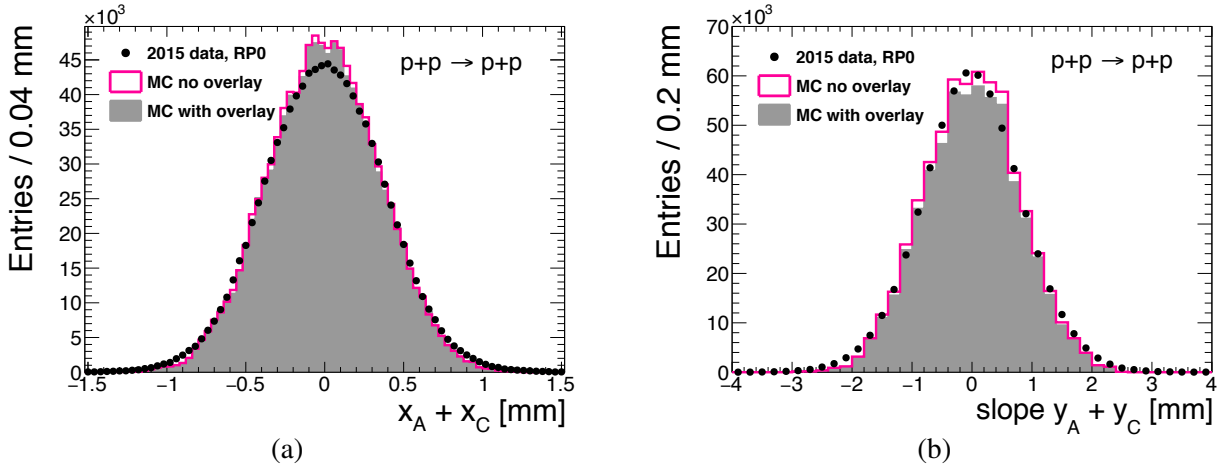

Figure 18.3: The sum of positions of the hits in the near ALFA stations on A and C side, separately for (a) x- and (b) y-coordinate. Data are shown with black points, while the elastic scattering MC predictions, with and without data overlay, are shown as grey and magenta histograms, respectively. Figures courtesy of I. Lakomiec.

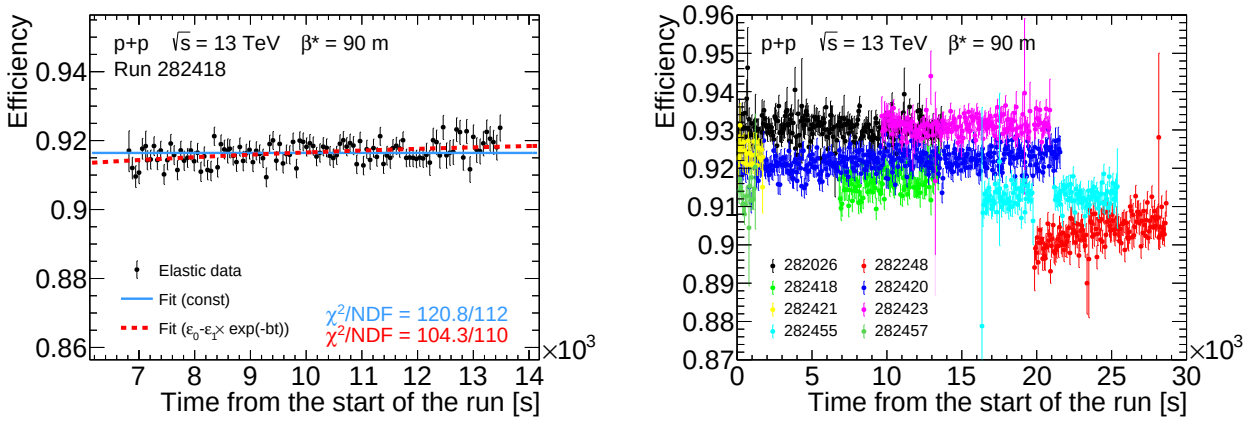

Figure 18.4: (a) MBTS trigger veto efficiency in a single run (282418) as a function of the time from the start of the run. Each point corresponds to a single luminosity block. Blue and red lines represent fits of constant and a function from Eq. (18.7), respectively. (b) MBTS trigger veto efficiency as a function of the time from the start of the run for all analysed runs.

The blue line represents a fit of the constant to the data points. The constant function does not follow the trend of data points - one can see that efficiency is increasing with time. It is the expected behaviour - the instantaneous luminosity decreases with time, which reduces probability of an inelastic proton-proton interaction potentially inducing a veto signal. The dashed red line shows a fit of the function

$$\varepsilon_{\text{veto}}(t) = \varepsilon_{\text{veto},0} - p_{\text{veto}}(t) = \varepsilon_{\text{veto},0} - p_{\text{veto},0} \cdot e^{-b_{\text{veto}} \cdot t}, \tag{18.7}$$

which takes into account the veto probability p_{veto} decreasing exponentially with time. From the χ^2/NDF provided on the plot one concludes that it is a better model for the time evolution of the MBTS veto efficiency.

Figure 18.4 shows the same efficiency for all analysed runs. Duration of the runs as well as veto efficiencies vary. The latter is due to different instantaneous luminosities in the runs. For this reason the efficiency is determined and correction is applied separately for each run, and even for each luminosity block.

18.1.3 SpTrk trigger efficiency

Efficiency of the SpTrk component of the HLT was determined using data from the elastic scattering trigger. This trigger provides large statistics of unbiased data from the perspective of the central detector part in the CEP HLT. In addition to this, the elastic trigger was a L1 seed of the CEP HLT, therefore the L2 objects e.g. space points and ID tracks were calculated for these triggers. All this makes the elastic scattering data suitable for the study of the SpTrk efficiency.

To calculate the SpTrk efficiency, events passing the HLT MBTS veto (VetoMbts2in) were selected. Exactly one reconstructed ID track was required, which in addition had to be within $|\eta| < 2.5$ and pass quality selection AC2.2. Tracks were also required to satisfy $|z_0| < 150$ mm. Number of such selected events was denoted as N^{track}. Next, the SpTrk trigger condition was verified - at least three space points in the PXL, at least four space points in the SCT and at least one L2 ID track with $p_{\text{T}} > 0.2$ GeV. Number of events with SpTrk trigger condition satisfied was denoted by $N^{\text{track}}_{\text{SpTrk}}$. Finally, the SpTrk

efficiency was calculated as the ratio

$$\varepsilon^{\text{track}}_{\text{SpTrk}} = \frac{N^{\text{track}}_{\text{SpTrk}}}{N^{\text{track}}}. \tag{18.8}$$

The result is shown in Fig. 18.5a as a function of p_{T} of the offline ID track (no significant dependence on track's η was found). Clearly, the efficiency rises rapidly around $p_{\text{T}} = 0.2$ GeV which matches the value of p_{T} required at the trigger L2. The dashed red line shows the function

$$\varepsilon^{\text{track}}_{\text{SpTrk}}(p_{\text{T}}) = \frac{1}{2} \cdot P_1 \cdot \left[\text{Erf}\left(\frac{p_{\text{T}} - P_2}{P_3}\right) + 1\right] \tag{18.9}$$

fitted to black points. This function fails to describe the p_{T}-dependence of the efficiency between $0.2 - 0.3$ GeV. Because of this, function from Eq. (18.9) was modified to the form

$$\varepsilon^{\text{track}}_{\text{SpTrk}}(p_{\text{T}}) = \frac{1}{2} \cdot P_1 \cdot \left[\text{Erf}\left(\frac{p_{\text{T}} - P_2}{P_3}\right) + 1\right] + \begin{cases} 0 & \text{for } p_{\text{T}} < 0.3 \text{ GeV} \\ P_4 & \text{for } p_{\text{T}} \geq 0.3 \text{ GeV} \end{cases}, \tag{18.10}$$

which differs from the initial form by a discontinuity at $p_{\text{T}} = 0.3$ GeV. Such value emerges from the plot and is also motivated by the correspondence to track's radius of 0.5 m, which matches the radius of the fourth SCT layer (Fig. 13.3b), hence tracks of this (and higher) radii have increased chance for inducing required number of the SCT space points. Dashed blue line in Fig. 18.5a represents a fit of the function from Eq. (18.10) to the data points. The quality of the fit shows that it is a good model for the SpTrk efficiency dependence over track's p_{T}. It is worth to mention, that the efficiency does not reach 100% and saturates at approximately 98%. It might be a result of some residual fake tracks present in a sample selected for the efficiency determination. Nevertheless, any possible bias is covered by the systematic uncertainty determined in Sec. 19.1.

In physics analysis there are at least two ID tracks, and each of them could have independently satisfied the SpTrk HLT component. For this reason, the efficiency for the entire event is calculated as

$$\varepsilon_{\text{SpTrk}}(p_{\text{T}}^{\text{max}}, p_{\text{T}}^{\text{min}}) = 1 - \underbrace{\left(1 - \varepsilon^{\text{track}}_{\text{SpTrk}}(p_{\text{T}}^{\text{max}})\right) \cdot \left(1 - \varepsilon^{\text{track}}_{\text{SpTrk}}(p_{\text{T}}^{\text{min}})\right)}_{\text{probability that neither of two tracks satisfies SpTrk}}. \tag{18.11}$$

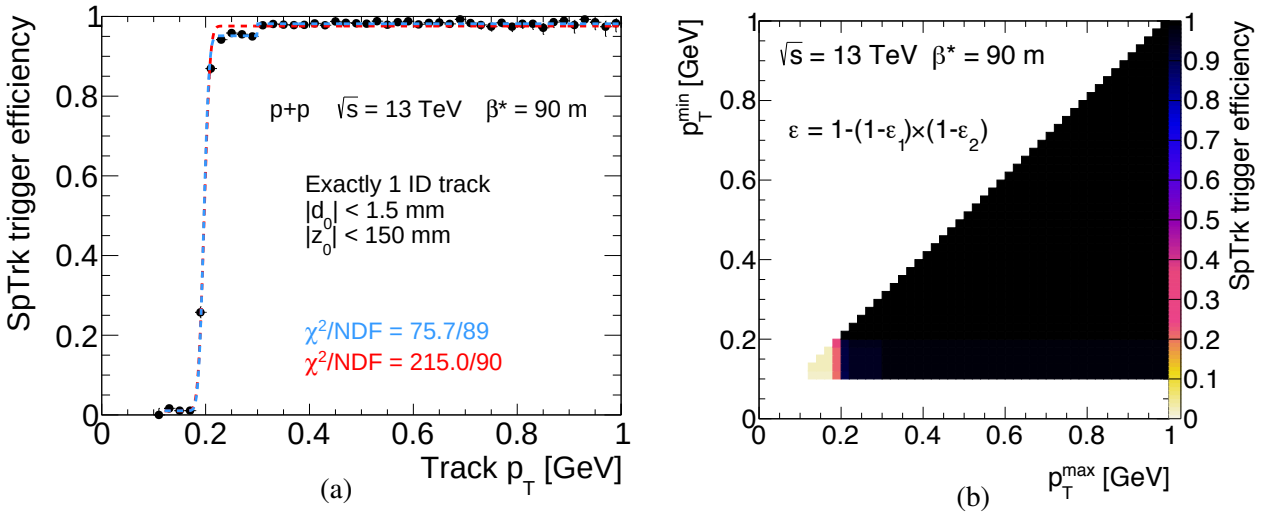

Figure 18.5: (a) Single-track SpTrk efficiency as a function of track's p_{T}, calculated with a method described in the text. Dashed red and blue lines represent functions given respectively by Eqs. (18.9) and (18.10) fitted to the data points. (b) SpTrk efficiency as a function of lower and higher p_{T} of the two tracks in an event, calculated from a single-track SpTrk efficiency.

The efficiency is plotted as a function of the higher and lower p_{T} of two tracks in Fig. 18.5b. It is evident from the plot that restriction of the fiducial region to $\max(p_{\mathrm{T}}) > 0.2$ GeV is needed to avoid correcting the data by a factor 10 or more. In analysis of the central state multiplicities greater then two, the same efficiency is used, but the two highest transverse momenta among the ID tracks are used.

18.2 Reconstruction and selection efficiencies of particle tracks

18.2.1 ID track acceptance, reconstruction and selection efficiency

Joint acceptance and efficiency of reconstruction of a track in the ID, ϵ_{ID}, was taken from the ATLAS analysis of the MB process in pp collisions at $\sqrt{s} = 13$ TeV [202]. This quantity was defined as the probability, that a particle from the primary interaction generates signal in the detector, which is reconstructed as a track that satisfies all quality criteria (AC2.2 except cut on Δz_0, whose efficiency is

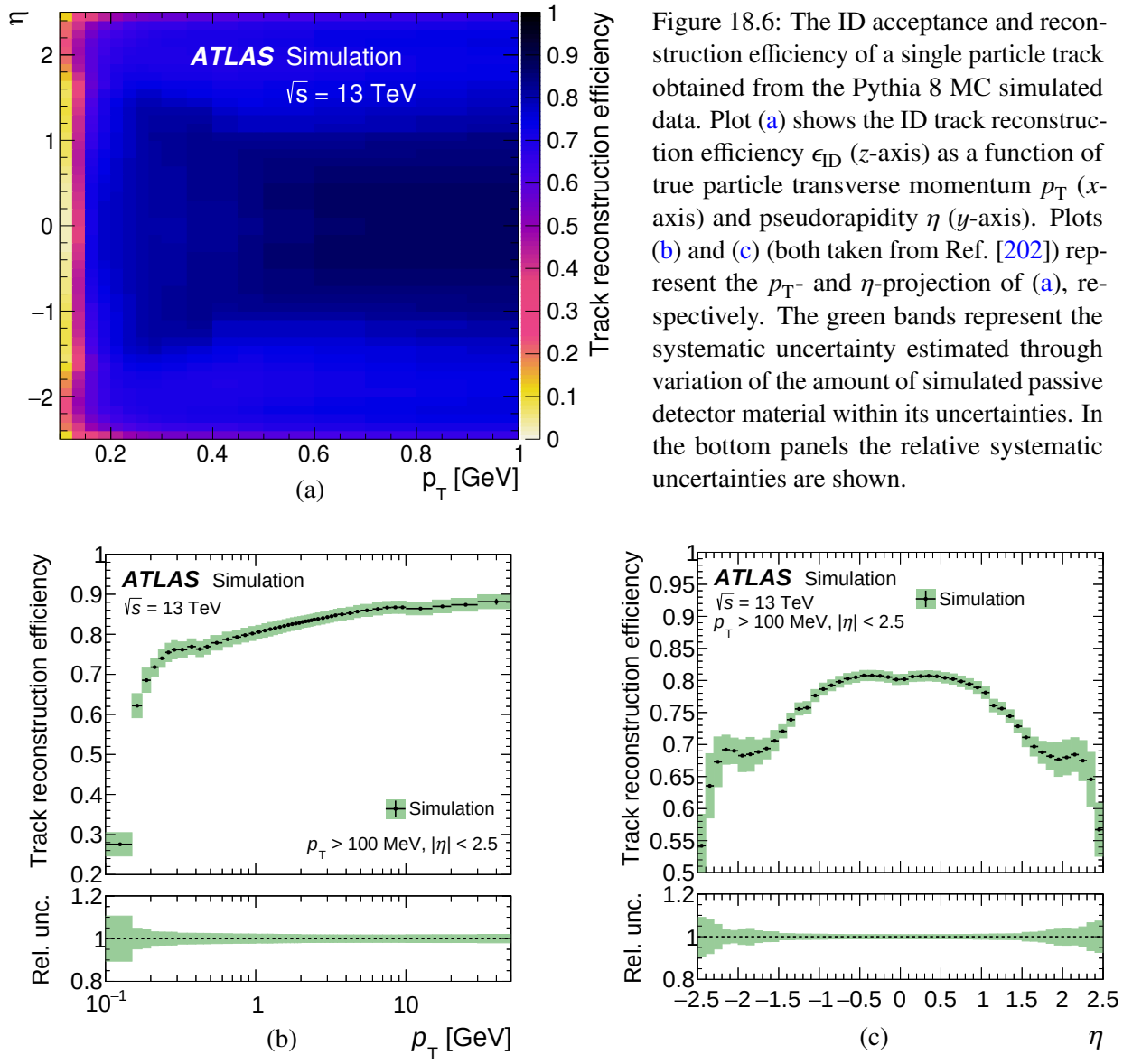

Figure 18.6: The ID acceptance and reconstruction efficiency of a single particle track obtained from the Pythia 8 MC simulated data. Plot (a) shows the ID track reconstruction efficiency ϵ_{ID} (z-axis) as a function of true particle transverse momentum p_{T} (x-axis) and pseudorapidity η (y-axis). Plots (b) and (c) (both taken from Ref. [202]) represent the p_{T}- and η-projection of (a), respectively. The green bands represent the systematic uncertainty estimated through variation of the amount of simulated passive detector material within its uncertainties. In the bottom panels the relative systematic uncertainties are shown.

presented in Sec. 18.3.2). To derive this efficiency the ND events from Pythia 8 MC generator were used. In the correction procedure the two-dimensional efficiency as a function of track's p_{T} and η is used (Fig. 18.6a). In Figs. 18.6b and 18.6c the one-dimensional ID track reconstruction efficiency projections as a function of, respectively, p_{T} and η, are shown.

18.2.2 ALFA track acceptance, reconstruction and selection efficiency

The efficiency of reconstruction and selection of the ALFA tracks using the cuts AC3 was studied in Ref. [205] with the simulation of the ALFA detector and the elastic scattering events. The efficiency of a single branch was defined as the ratio of the number of beam-momentum protons expected in a given branch (subscript 'br') based on the p_y component of the proton momentum (N_{br}) in the denominator, and the number of events with reconstructed proton track in both ALFA station in the branch and satisfying selection AC3 ($N_{\mathrm{ALFA},br}$) in the numerator:

$$\varepsilon_{\mathrm{ALFA},br} = \frac{N_{\mathrm{ALFA},br}}{N_{br}}. \tag{18.12}$$

The efficiency of the reconstruction and selection of tracks of both elastically scattered protons was defined similarly to Eq. (18.12), with the requirement of a proton track reconstructed in the single branch extended to two ALFA branches on the opposite sides of the IP (the elastic ALFA arm). Figure 18.7 shows the reconstruction and selection efficiency of two elastically-scattered protons as a function of the average absolute y-position in the near ALFA stations on side A and side C, $\bar{y} = 0.5 \cdot |y_{\mathrm{A,near}} - y_{\mathrm{C,near}}|$. The efficiency is generally constant, with slightly lower values at the edges of presented range of $\bar{y}$, which is an artefact of averaging position on A and C side. Therefore, a single efficiency value is provided in Tab. 18.1 for single ALFA branches, as well as for A- and C-side combinations of branches. In addition to efficiencies obtained directly from the simulation, i.e. for single branches and for elastic arms, there are also efficiencies for non-elastic arms provided, which were obtained from the efficiencies for the elastic arms, scaled based on efficiencies for single branches. To correct data for the inefficiency related to the reconstruction and selection of the forward-scattered

	Branch				
	0	1	2	3	Efficiency
Single branch	○				0.91
		○			0.90
			○		0.89
				○	0.91
Elastic arm	○			○	0.85
		○	○		0.82
Non-elastic arm	○		○		0.83
		○		○	0.84

Table 18.1: ALFA track reconstruction and selection efficiency for the single branch, as well as for the elastic and non-elastic arms. The values were obtained using the single track selection algorithm and the elastic scattering MC with the zero-bias data overlayed. Branches and their combinations for which the efficiencies are provided, are marked with circles. Efficiencies for non-elastic arms were determined from the efficiencies for elastic arms and single ALFA branches.

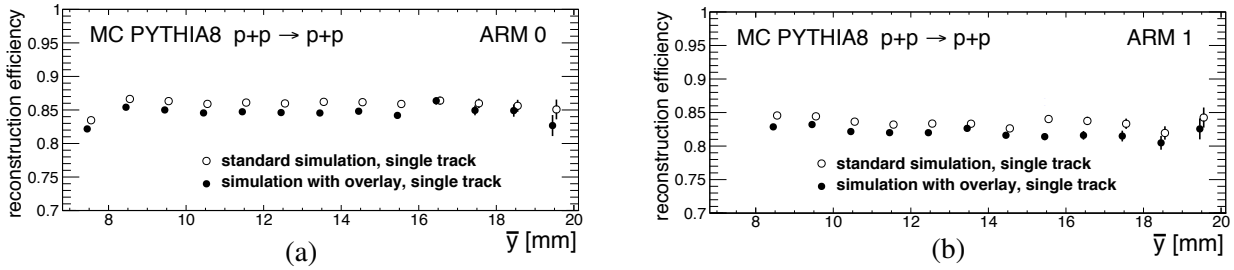

Figure 18.7: Reconstruction and selection efficiency of the two forward-scattered protons in ALFA (a) arm 0 and (b) arm 1, from the simulated elastic scattering events. Solid and open circles represent the results obtained with and without MC overlayed with the zero-bias data, respectively. Figures courtesy of I. Lakomiec.

proton tracks, one number from one of the four bottom rows in Tab. 18.1 was used, depending on the reconstructed protons' configuration.

18.3 Other reconstruction and selection efficiencies

18.3.1 Primary vertices limit (AC1), MBTS vetoes (HLT and AC4) and ALFA veto (AC3.4)

Joint efficiency of the HLT veto in the inner MBTS, offline inner MBTS veto, selection of events with maximally one primary vertex and veto on trigger signal in ALFA stations other than those with forward-scattered proton tracks, called collectively as the total veto efficiency, was calculated in a way identical to that presented in Sec. 18.1.2. Equation (18.6) was used with $N_{\mathrm{el}}^{\mathrm{!veto}}$ denoting number of selected elastic scattering events simultaneously satisfying the trigger veto in the inner MBTS, offline MBTS veto, veto on signal in ALFA stations other that those with elastically-scattered protons and requirement of no reconstructed primary vertices from the ID tracks. The efficiency is presented in Fig. 18.8a for one selected run, and in Fig. 18.8b for all analysed runs. Dashed lines represent functions

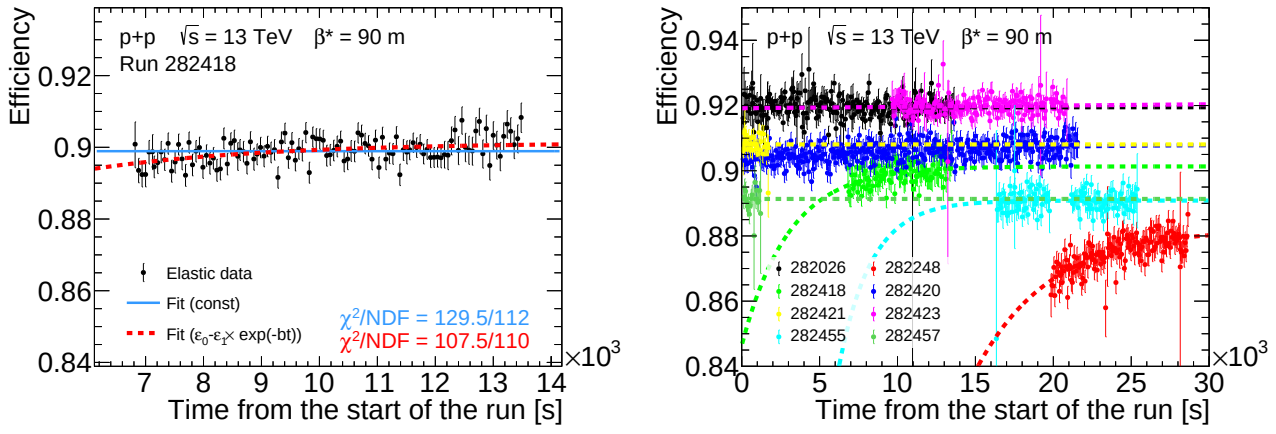

Figure 18.8: (a) Total veto efficiency in a single run (282418) as a function of the time from the start of the run. Each point correspond to a single luminosity block. Blue and red lines represent fits of a constant value and a function from Eq. (18.7), respectively. (b) Total veto efficiency as a function of the time from the start of the run for all analysed runs.

given by Eq. (18.7) fitted to data points. In the following analysis values obtained from the fit are used to correct the data for the inefficiency introduced by the related trigger components and offline selections.

This efficiency was assumed to be known accurately and therefore systematic uncertainty connected with this efficiency was assumed to be zero. It is supported by the fact that the correction was derived from the unbiased data. Additionally, the statistical uncertainty of the efficiency was found much lower compared to remaining systematic uncertainties.

18.3.2 Limited $|\Delta z_0|$ of the ID tracks (part of cut AC2.2)

Some small fraction of the CEP events was rejected with the cut $|\Delta z_0| < 20$ mm. Correction for the introduced inefficiency was calculated from the data as a function of the lower p_{T} of two outermost tracks (those which determine the $|\Delta z_0|$) - the lower the p_{T} is, the worse is the pointing resolution and thus the efficiency of the discussed cut drops. The efficiency was calculated as a ratio of the number of CEP events (after full selection and background subtraction) satisfying a limit $|\Delta z_0| < 20$ mm (denoted N_B) to number of CEP events without limited $|\Delta z_0|$ (denoted N_A):

$$\varepsilon_{|\Delta z_0|}(\min(p_{\mathrm{T}})) = \frac{N_B(\min(p_{\mathrm{T}}))}{N_A(\min(p_{\mathrm{T}}))}. \tag{18.13}$$

The efficiency is shown in Fig. 18.9, separately for the three CEP channels whose statistics was sufficient to obtain results of reasonable precision. It can be seen that the efficiency is the lowest for tracks whose $p_{\mathrm{T}} = 0.1$ GeV, however, the efficiency is very close to 100%. In general, the efficiency gets lower as the number of central state particle increases. Very small differences between the efficiencies calculated with/without subtracted non-exclusive background indicates negligible systematic uncertainty of the efficiency. Therefore, the efficiency was assumed to be known precisely. Nominally the efficiencies with subtracted background were used to correct the data.

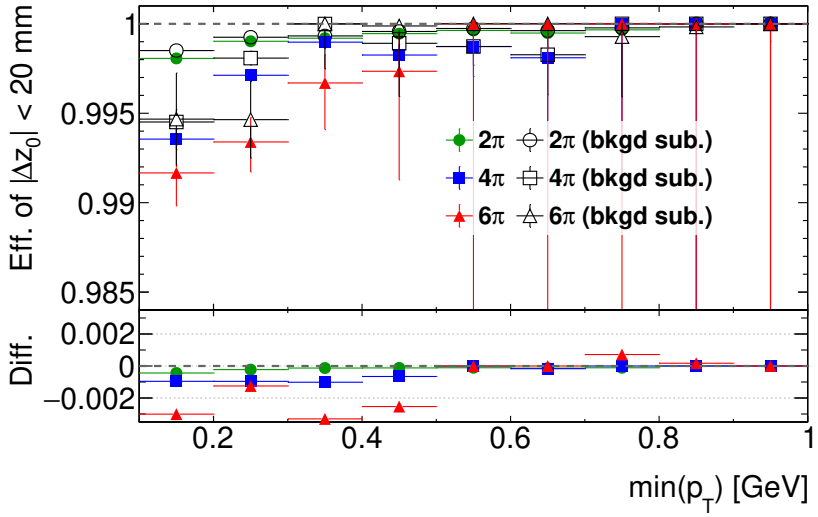

Figure 18.9: Efficiency of cut on $|\Delta z_0|$ calculated from the data for three CEP channels, separately with (open markers) and without (full markers) subtracted non-exclusive background, shown as a function of the lower p_{T} of the two outermost ID tracks. Only statistical errors are shown. In the lower panel, the differences between results without and with subtracted background are shown.

18.3.3 Particle identification (AC5)

The requirement which was imposed on each ID track to suppress contributions from particles different from pions, namely Ineq. (16.3), was chosen such that no sizeable inefficiency of pion selection was introduced (see Fig. 16.10). The pion selection efficiency was assumed 100%.

18.3.4 Exclusivity cut on $n\sigma(p_{\mathrm{T}}^{\mathrm{miss}})$ (AC6)

The cut on missing transverse momentum of all particles was defined to accept events with total p_{T} in an event balanced within three detector resolutions ($n\sigma(p_{\mathrm{T}}^{\mathrm{miss}}) < 3$). The distribution of $n\sigma(p_{\mathrm{T}}^{\mathrm{miss}})$ for the CEP events follows the Rayleigh distribution[1]. From the cumulative distribution function it is known that the probability for $n\sigma(p_{\mathrm{T}}^{\mathrm{miss}}) < 3$ is 98.9%, which is used as the efficiency of cut AC6. The efficiency of this cut was assumed to be independent from the kinematics of the event. It should not introduce considerable systematic error given very high efficiency of the cut.

18.4 Migrations into and out of the fiducial region

Corrections related to migrations of particles' tracks through boundaries of the fiducial region were calculated using definitions from Sec. 11.5. The migrations were determined using three MC samples of CEP of $\pi^+\pi^-$ pairs: GenEx, DiMe and Pythia, generated in the phase space region extended with respect to the fiducial region used in analysis. Each pion in an event was assigned with the reconstructed p_{T} and η being the true value smeared according to (η, p_{T})-dependent resolution thereof. These resolutions were determined from the full simulation of ATLAS detector response to Pythia CD events. For the forward-scattered protons, each particle was assigned with the reconstructed p_x and p_y being the true value smeared according to known angular divergence of the beam and intrinsic detector resolution.

In the analysis, the corrections related to fake tracks were not considered. The data were collected during special runs with low pile-up, therefore the number of hits in the ID, especially in the low multiplicity CEP events, was low and formation of fake tracks was extremely rare ($\lesssim 0.1\%$), as shown in the study of SD process from Ref. [33], performed using the dataset collected in the same period as the data analysed here. Regarding fake proton tracks in ALFA, the low-pile up environment and usage of single ALFA track selection algorithm was also considered to suppress fake ALFA tracks to negligible level.

The fractions of migrations into the fiducial region and outside of the fiducial region were calculated using Eq. (11.23), while the migrations correction factor was calculated using Eq. (11.24) with assumed $f_{\mathrm{fakes}} = 0$. The migrations and the correction factor for central tracks are shown in Fig. 18.10 as a function of (η, p_{T}) of the track. In the figure, the migrations obtained for DiMe MC with a p_{T} limit of 0.1 GeV are shown. Such cut is imposed on the lower momentum(a) of track(s) in an event. In the analysis, p_{T} of the track with the highest p_{T} in an event is required to be greater than 0.2 GeV,

[1] Rayleigh distribution for variable x ($x \geq 0$) has the form $f(x;\sigma) = (x/\sigma^2) \cdot \exp\left[-x^2/(2\sigma^2)\right]$. The cumulative distribution function is $F(x;\sigma) = 1 - \exp\left[-x^2/(2\sigma^2)\right]$. The distribution describes the probability of a length of a two-dimensional vector whose components follow a Gaussian distribution with mean equal zero and standard deviation equal σ. It is consistent with the definition of $n\sigma(p_{\mathrm{T}}^{\mathrm{miss}})$.

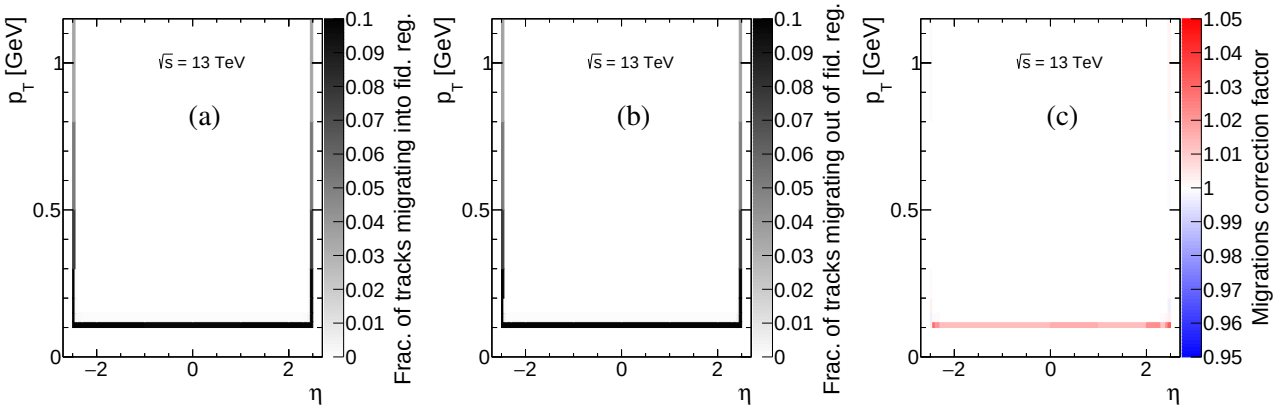

Figure 18.10: Fraction of ID tracks (a) migrating into the fiducial central tracks phase space from outside of it, (b) migrating outside the fiducial phase space from inside of it, and (c) joint correction factor for migrations through the fiducial phase space boundaries. In case of reconstructed (p_{T}, η) escaping the fiducial phase space (b) the true value of p_{T} and η is used; otherwise reconstructed values are plotted.

and analogous migrations and correction factor were also calculated but are not shown as they are very similar. The difference with respect to Fig. 18.10c is in the correction factor being significantly different from one at p_{T} slightly above 0.2 GeV, rather than above 0.1 GeV. In both cases the correction is different from one only at p_{T} up to $\sim$ 20 MeV above the threshold p_{T} and amounts ≈ 1.01.

The migrations and the correction factor for the forward-scattered protons in ALFA are shown in Fig. 18.11. They are presented as a function of $|p_y|$ of the proton because the fiducial region is restricted only by cut on this quantity (Ineq. (16.1)). There are three types of curves in Fig. 18.11 which represent results obtained for three MC generators which predict different distribution of p_y. The correction for migrations is below unity at $|p_y| < 0.23$ GeV and above unity at $|p_y| > 0.44$ GeV.

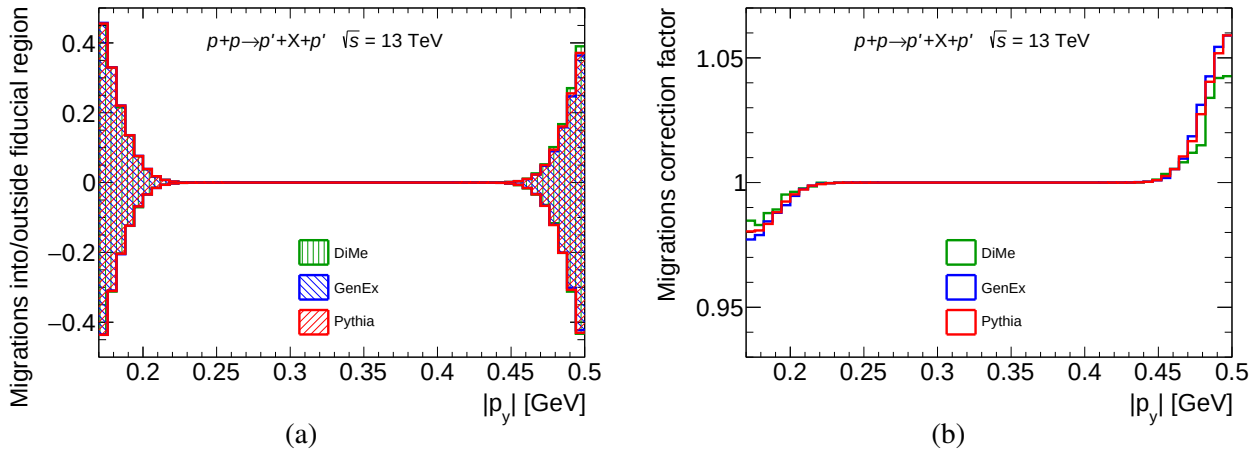

Figure 18.11: (a) Fraction of forward-scattered protons migrating into (positive values) and outside of the fiducial region (negative values) as a function of $|p_y|$. (b) Total migrations correction as a function of $|p_y|$.

18.5 Detector resolutions

The relations between the true-level and reconstructed quantities describing the centrally-produced particles were studied with the Pythia events after full simulation of the ATLAS detector. For quantities

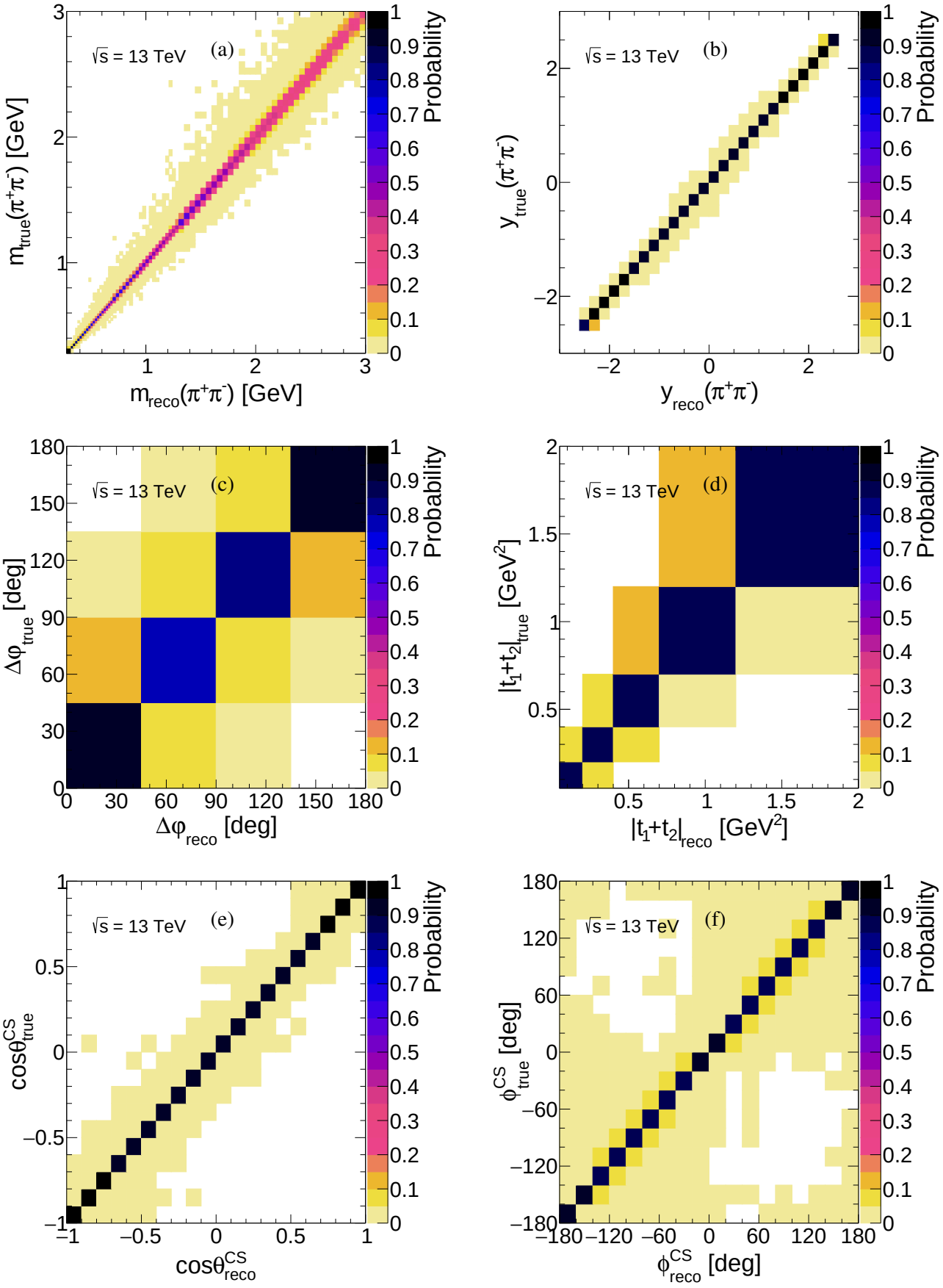

Figure 18.12: Correlations between reconstructed (x-axis) and hadron level (y-axis) observables (response matrices) of (a) $m(\pi^+\pi^-)$, (b) $y(\pi^+\pi^-)$, (c) $\Delta\varphi$, (d) $|t_1 + t_2|$, (e) $\cos\theta^{CS}$ and (f) ϕ^{CS}, from $\pi^+\pi^-$ MC. Probabilities in each bin of the true-level value were normalised to sum up to one.

related to the forward-scattered proton tracks in ALFA, the resolutions were studied with DiMe events with the smearing of forward-scattered protons' momenta according to the angular beam divergence and spatial detector resolution. In the Fig. 18.12 the response matrices are shown, connecting true-level (subscript "true") and reconstructed/smeared (subscript "reco") values of the invariant mass (Fig. 18.12a) and rapidity (Fig. 18.12b) of the $\pi^+\pi^-$ pairs, azimuthal separation of the forward-scattered protons (Fig. 18.12c), total squared four-momentum transferred in proton vertices (Fig. 18.12d), and cosine of polar angle and azimuthal angle of positive charge pion in the Collins-Soper frame [162] (Figs. 18.12e and 18.12f, respectively).

The determined resolutions were used to establish the binning of the differential cross sections. In the described analysis also CEP of exclusive $n\pi^+n\pi^-$ pairs was studied ($n = 2, 3, 4$). In those cases the binning was defined wider with respect to $\pi^+\pi^-$ channel to accommodate for worsen of resolutions related to higher particles' masses, and to reduce statistical uncertainties of data points.

18.6 Method of application of the corrections

Differential cross sections have been calculated according to Eq. (11.25). The weight assigned to each event, w, reflecting reconstruction and selection efficiency of all studied particles, was calculated as the product of inverse efficiencies of the ID, ALFA, and other correction factors and efficiencies discussed in Chap. 18. Distributions of the event weights for all studied CEP channels are shown in Fig. 18.13.

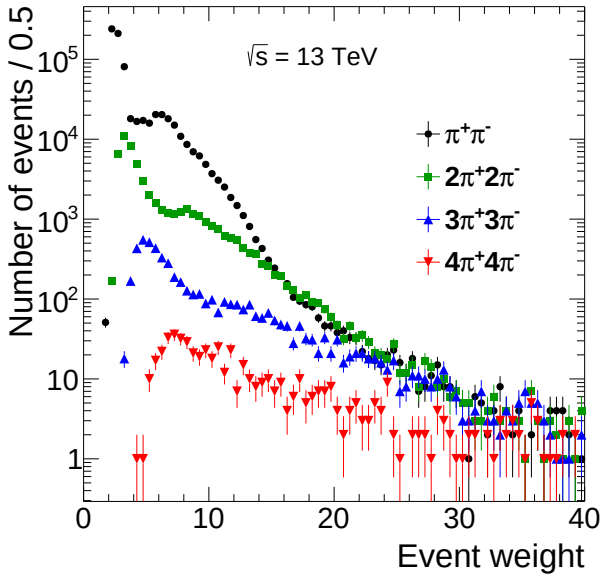

Figure 18.13: Distribution of weights assigned to selected CEP events in $\pi^+\pi^-$ (black circles), $2\pi^+2\pi^-$ (red squares), $3\pi^+3\pi^-$ (blue triangles) and $4\pi^+4\pi^-$ (red triangles) channel.

18.7 Correction for the geometrical acceptance

In order to extract the slope parameter of the exponential function $\exp[\beta(t_1 + t_2)]$ describing the double differential cross section $d^2\sigma/dt_1dt_2$, it is necessary to correct data for limited acceptance of the azimuthal angle of forward-scattered protons. Figure 18.14 shows the geometrical acceptance determined from the phase-space MC, in two ranges of $\Delta\varphi$ angle. This acceptance describes the probability that protons characterised by t_1 and t_2 and separated in azimuth by $\Delta\varphi$ lie within the fiducial

region (cut AC3.3). The obtained acceptances were used to select the t interval for the extraction of the exponential slope parameter of $d^2\sigma/dt_1dt_2$, described by $0.05\ \text{GeV}^2 \leq t_1, t_2 \leq 0.25\ \text{GeV}^2$.

Comparison with the geometrical acceptances obtained from GenEx is presented in Fig. 18.15. Geometrical acceptances obtained using alternative models (GenEx, Pythia) were used to estimate systematic (model) uncertainties of the exponential slope β. The conclusion from the ratios of acceptances is that the differences between models are low, up to approximately 3%.

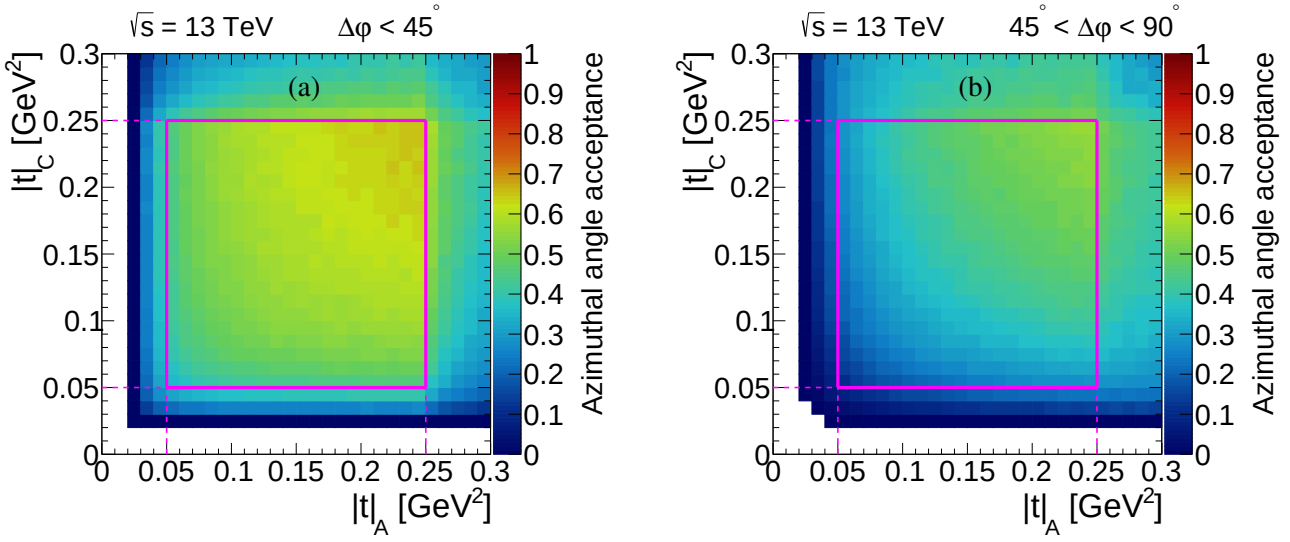

Figure 18.14: Geometrical acceptance for the forward-scattered protons being both in the ALFA fiducial region given by Eq. (16.1) if separated in azimuth by (a) $\Delta\varphi < 45^\circ$ and (b) $45^\circ < \Delta\varphi < 90^\circ$. Phase-space MC assuming flat distribution of azimuthal angle of the forward protons φ has been used for determination of this acceptance. Solid magenta lines limit the region selected for the measurement, which provides reasonably high geometrical acceptance. The acceptances for $90^\circ < \Delta\varphi < 135^\circ$ and $\Delta\varphi > 135^\circ$ were not shown as they are nearly identical as (b) and (a), respectively.

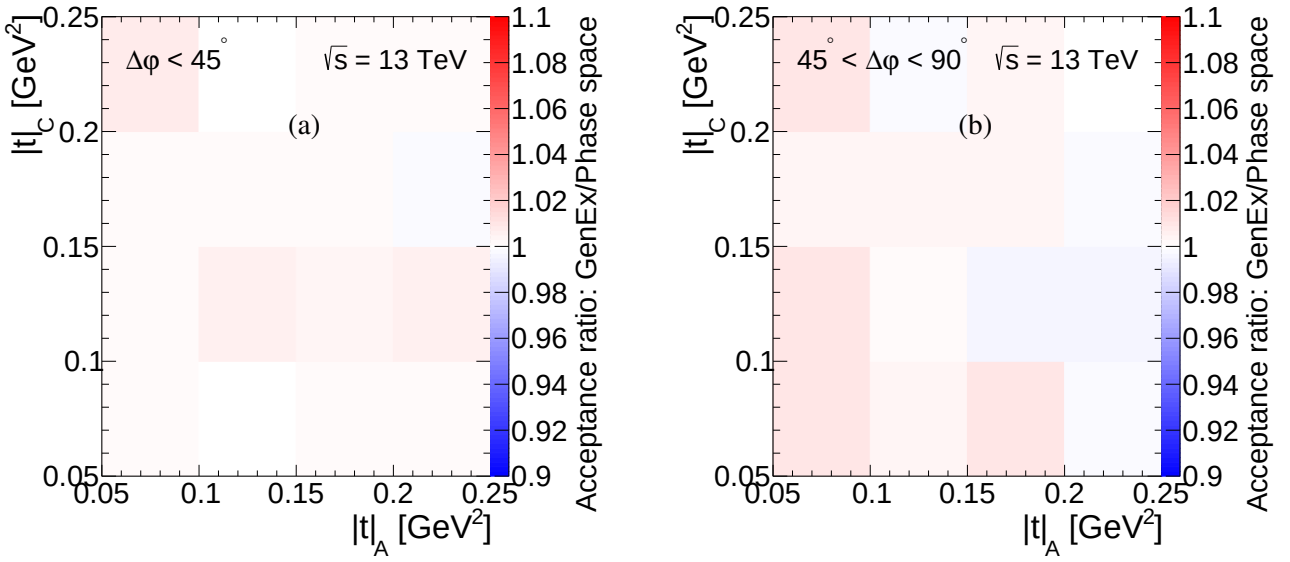

Figure 18.15: Sample ratios of geometrical acceptances determined from GenEx and phase-space MC for (a) $\Delta\varphi < 45^\circ$ and (b) $45^\circ < \Delta\varphi < 90^\circ$.

19. Systematic uncertainties

Various sources of systematic uncertainties have been considered in the analysis. Major systematic uncertainties were obtained with dedicated studies described below.

19.1 SpTrk trigger efficiency

Systematic uncertainty of the efficiency of the SpTrk component in the CEP HLT was estimated with the elastic scattering data. The SpTrk efficiency was calculated in a way similar to that described in Sec. 18.1.3, but here events with the single primary vertex and exactly two primary ID tracks were used. Tracks were required to fulfil the quality cut AC2.2, and both tracks should have $|\eta| < 2.5$. Using these events the efficiency was calculated as the ratio of the number of events with the trigger bit SpTrk set, to the number of all events. The efficiency is shown in Fig. 19.1a as a function of p_{T} of the two tracks. One can see areas in the $(p_{\mathrm{T}}^{\mathrm{max}}, p_{\mathrm{T}}^{\mathrm{min}})$ plane at high p_{T}'s without calculated efficiency, which is a result of the limited number of two-track events in the elastic scattering data. This was the reason why the efficiency obtained from two-track events was not used as the nominal one. However, it helped to estimate the systematic uncertainty of the nominal SpTrk efficiency (Fig. 18.5b) by comparing the efficiencies obtained from the two sets of events in the elastic scattering data. The difference between the efficiency in Fig. 19.1a and the nominal efficiency, $\Delta\varepsilon$, is presented in Fig. 19.1b. One can see, that the non-zero differences are found at $p_{\mathrm{T}}^{\mathrm{min}} < 0.2$ GeV, a region where mostly the track of the higher p_{T} determines the efficiency. Efficiency calculated from the two-track events is higher by approximately 0.02 (and equal to 1) then the nominal efficiency in this region. It is considered to be an effect of much higher purity of events with two primary ID tracks, so that fake tracks do not contribute and the efficiency is not underestimated. Based on the Fig. 19.1b, the systematic uncertainty assigned to the SpTrk efficiency (Fig. 18.5b) is equal to ±0.03 ($p_{\mathrm{T}}^{\mathrm{max}} > 0.3$ GeV and $p_{\mathrm{T}}^{\mathrm{min}} < 0.2$ GeV) and to ±0.05 ($p_{\mathrm{T}}^{\mathrm{max}} < 0.3$ GeV). In the region where both tracks have high p_{T}, $p_{\mathrm{T}}^{\mathrm{max}} > 0.3$ GeV and $p_{\mathrm{T}}^{\mathrm{min}} > 0.2$ GeV, the efficiency (equal to one) is assumed to be known precisely.

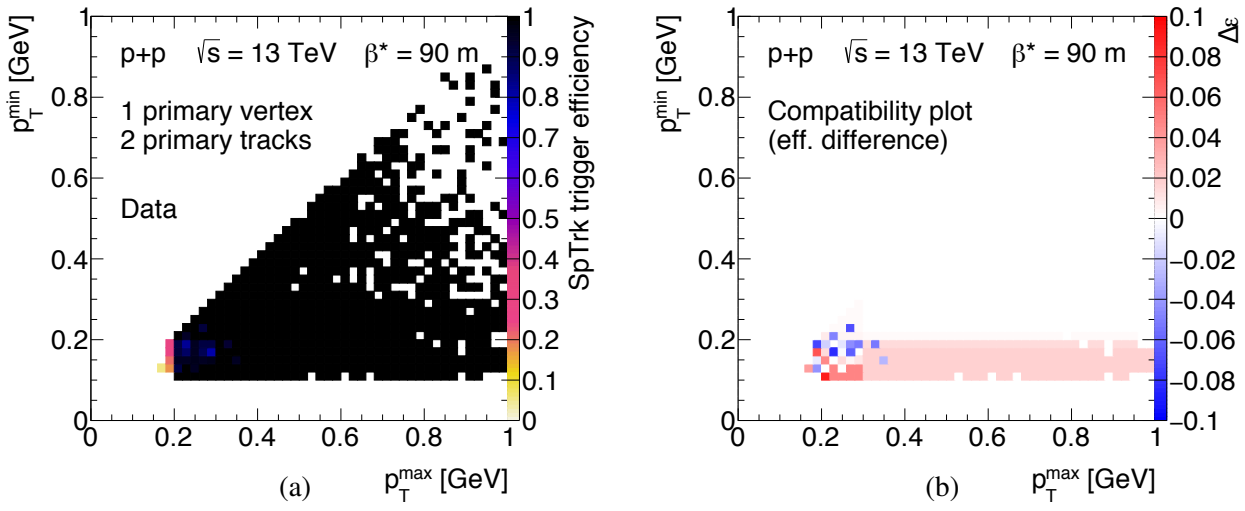

Figure 19.1: (a) SpTrk efficiency as a function of lower and higher p_{T} of two tracks in an event, calculated from the elastic scattering data with a single primary vertex and two primary ID tracks in an event. (b) Difference between the SpTrk efficiency from the plot (Fig. a) and the single-track efficiency (Fig. 18.5b).

19.2 ALFA track reconstruction efficiency

Efficiency of reconstruction and selection of the proton tracks in ALFA was determined from the MC simulation. Therefore, potential inaccuracies in the simulation propagate to the obtained results. Systematic uncertainty related to the modelling of the ALFA system in the Geant4 simulation were estimated in Ref. [205] with the elastic scattering data and simulated MC events. The same selections were applied to the present data and MC and the differences were assigned to the systematic uncertainty of the ALFA track reconstruction and selection efficiency.

Elastic scattering event selection identical to that presented in Sec. 18.2.2 was used. The number of elastic scattering events, with ALFA tracks reconstructed in all four stations in an elastic arm, were denoted $N_{4/4}$. In addition to this sample, a class of events with the elastic scattering trigger and with exactly one ALFA branch with reconstructed forward-scattered proton track was selected. In this sample, it was required that in the branch opposite to that with a track reconstructed in both ALFA stations, there were no valid ALFA tracks in neither of the two stations. Those events were denoted as $N_{2/4}$.

Figure 19.2 shows an exemplary ratio $N_{2/4}/N_{4/4}$ for one of the branches (branch 2), as a function of the y-position of the track in the near ALFA station (RP 4) on the side with the reconstructed track in the "2/4" sample. Events in the sample "2/4" correspond to a situation when one of the elastically-scattered protons is not reconstructed in ALFA, e.g. due to dissociation after inelastic interaction with the inactive material before reaching the detectors. The difference between the ratios $N_{2/4}/N_{4/4}$ in data and MC is considered as a good measure of the discrepancy of the ALFA track reconstruction efficiency in a single ALFA branch, between data and simulation. In the figure one can find that the elastic scattering MC with the zero-bias data overlay is closer to results obtained from the data, compared to MC without the zero-bias data mixed-in. Such observation demonstrates that

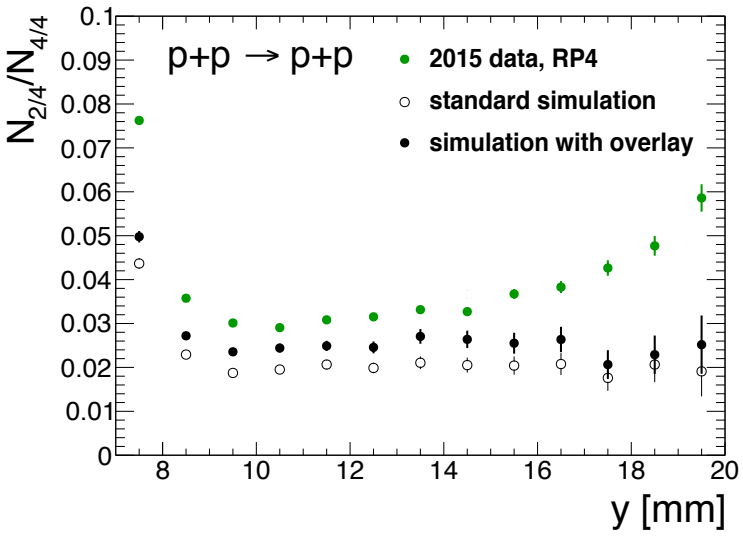

Figure 19.2: The ratio, $N_{2/4}/N_{4/4}$, as a function of the y-coordinate of the proton hit in the near ALFA station on the side with a reconstructed track in the 2/4 sample (in RP4). Green points represent data, while solid and open black circles represent the results obtained, respectively, with and without elastic scattering MC overlayed with the zero-bias data. Figure courtesy of I. Lakomiec.

the overlay technique helps to improve the agreement between MC and data. The difference between data and MC is largest at the edges of measured y range. The smallest difference, of the order of 0.01, is found in the central part of the detector. The value 0.01 was finally assigned as the systematic uncertainty of the reconstruction and selection efficiency of the proton track in a single ALFA branch. It is expected that the central part of the detector is the least sensitive to the inelastic background present in the data, which is lacking in the MC. Using the inelastic MC (mainly CD) in addition to the elastic scattering MC it will be possible to reduce further this systematic uncertainty in the future.

19.3 Summary of the systematic effects

In this section, the list of systematic effects contributing to the overall systematic uncertainties of the cross section measurements, is presented. An estimate of the contribution of each effect was obtained by varying (within its uncertainty) the quantity related to the systematic effect, and checking how this variation changes the measured cross section. The differences between the nominal and the changed cross sections were taken as the systematic uncertainties.

1. **Modelling of the dead material influencing the ID measuring capabilities ($\Delta\varepsilon_{\mathrm{ID}}$).**
   Amount of dead material, that affects ID track reconstruction efficiency is known with finite precision. The level of consistency of the amount of the material in the simulation and in the real detector was studied in Ref. [206]. In the estimation of the systematic uncertainty contributions from 5% of additional material in the entire ID, 10% of additional material in the IBL and 50% of additional material in the PXL services region at $|\eta| > 1.5$, were taken into account. The resulting uncertainty in the track reconstruction efficiency is 1% at low $|\eta|$ and high p_{T} and up to 10% for higher $|\eta|$ or for lower p_{T}.

2. **Modelling of the ALFA system ($\Delta\varepsilon_{\mathrm{ALFA}}$).**
   The efficiency corrections related to the forward-scattered proton reconstruction in ALFA were determined with simulated MC events of elastic scattering overlayed with the zero-bias data. Systematic uncertainty of the efficiency has been estimated in the procedure described in Sec. 19.2. The same analysis has been performed on elastic scattering MC and the data, leading to estimates of the ALFA track reconstruction efficiency equal to 1%.

3. **Non-exclusive background estimate ($\Delta N_{\mathrm{bkgd}}^{\mathrm{non\text{-}excl}}$).**
   The method described in Sec. 12.5 was used to estimate the systematic uncertainty of the amount of the non-exclusive background. Despite fitting the second-order polynomial to $n\sigma(p_{\mathrm{T}}^{\mathrm{miss}})$ distribution of opposite-sign events, the $n\sigma(p_{\mathrm{T}}^{\mathrm{miss}})$ template from the same-sign control channel was used, normalised to have the same event yield in the region of $n\sigma(p_{\mathrm{T}}^{\mathrm{miss}}) > 5$ as the opposite-sign events. The difference between the background yields obtained with the two methods was treated as a systematic uncertainty on the amount of non-exclusive background. This uncertainty contributes up to 2% of the systematic uncertainty of the cross sections, except for the $4\pi + 4\pi^{-}$ channel in which it is the dominant source of systematic uncertainty ($\approx 25\%$ of the cross section uncertainty).

4. **SpTrk trigger efficiency ($\Delta\varepsilon_{\mathrm{SpTrk}}$).**
   The SpTrk trigger efficiency was determined from the data with a single reconstructed ID track.

These events might have contained some small contribution from the fake tracks. Potential effect was checked with the SpTrk trigger efficiency determined from the two-track events. The difference in efficiency was found very small, at most 5% in a limited region of tracks' p_T's. See Sec. 19.1.

5. **Migrations correction for the ID tracks (ΔC_m^{π}).**
   The migrations into and out of the fiducial region obtained using (the default) DiMe MC were compared with the migrations obtained with the other available MC generators. The extreme deviations of migration correction factor with respect to nominal one were assumed to be a measure of the systematic uncertainty related to the sensitivity of migrations correction for the centrally-produced particles to the distributions of kinematic variables, which depend on the models.

6. **Migrations correction for the ALFA tracks (ΔC_m^{p}).**
   Similarly to migrations of the centrally-produced particles, the systematic uncertainty of the correction factor for migrations into and out of the fiducial region related to the forward-scattered protons was determined as an extreme deviation of the correction obtained with the DiMe MC and the remaining MC generators. This way the sensitivity of migrations correction to the model-dependent distributions of kinematic variables was taken into account.

7. **Luminosity determination ($\Delta\mathcal{L}$).**
   The uncertainty of the integrated luminosity used in the analysis equals 2.1%. It was determined with the study presented in Ref. [207], which refers to the regular LHC runs with high instantaneous luminosity. A study dedicated to the special high-β^* runs, during which the analysed data were recorded, will reduce this systematic uncertainty.

The contributions to the total systematic uncertainty, discussed above, in the case of the cross section measurement as a function of the invariant mass of the $\pi^+\pi^-$ pairs, are shown in Fig.. 12.33.

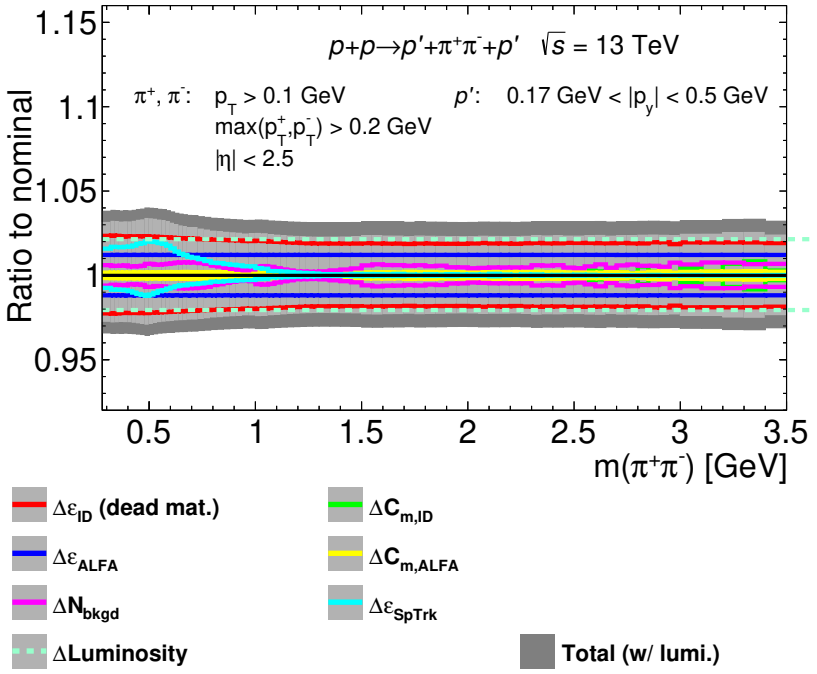

Figure 19.3: Systematic uncertainties of the differential cross sections for CEP of $\pi^+\pi^-$ pairs as a function of the invariant mass of the pair in the fiducial region explained on the plots.

Part IV

Physics results

In this part, the physics results obtained in the data analyses described in Parts II and III are presented and discussed. Common presentation of results from STAR and ATLAS provides opportunity to compare and jointly discuss corresponding observables.

20. Fiducial cross sections

In this chapter, the measured differential fiducial cross sections are presented. The presentation is divided into specific CEP channels, and the STAR and ATLAS results are shown alongside, if available. Definitions of the fiducial regions are different for the STAR and the ATLAS experiments, and are usually provided in the plots. Otherwise they can be found in Sec. 9.1 (STAR) and Sec. 16.1 (ATLAS).

20.1 Exclusive production of two-particle central systems

20.1.1 Exclusive production of $\pi^+\pi^-$ pairs

The differential fiducial cross sections for the exclusive production of $\pi^+\pi^-$ pairs, as a function of the invariant mass of the pair, are shown in Fig. 20.1. Comparison of the scales of the STAR (Fig. 20.1a) and the ATLAS (Fig. 20.1b) results, reveals a large difference of the cross sections, which mainly comes from the different geometrical acceptances (fiducial cuts) used in the two measurements. The most important contributions to this difference are more than three times wider pseudorapidity coverage in ATLAS, and lack of limitation on p_x of the forward-scattered protons in ATLAS compared to STAR.

Also, the shapes of the cross sections in the region $m(\pi^+\pi^-) < 0.7$ GeV significantly differ between STAR and ATLAS. In the case of the STAR result, the dip around 0.5 GeV is a kinematic effect related to the fiducial cuts. There is no peak in the distribution around the mass 0.8 GeV, which could be attributed to the $\rho(770)$ meson. This suggests that the contributions from photoproduction and Reggeons exchanges are insignificant. In the mass range 0.8 – 1 GeV, a peak followed by a sharp drop

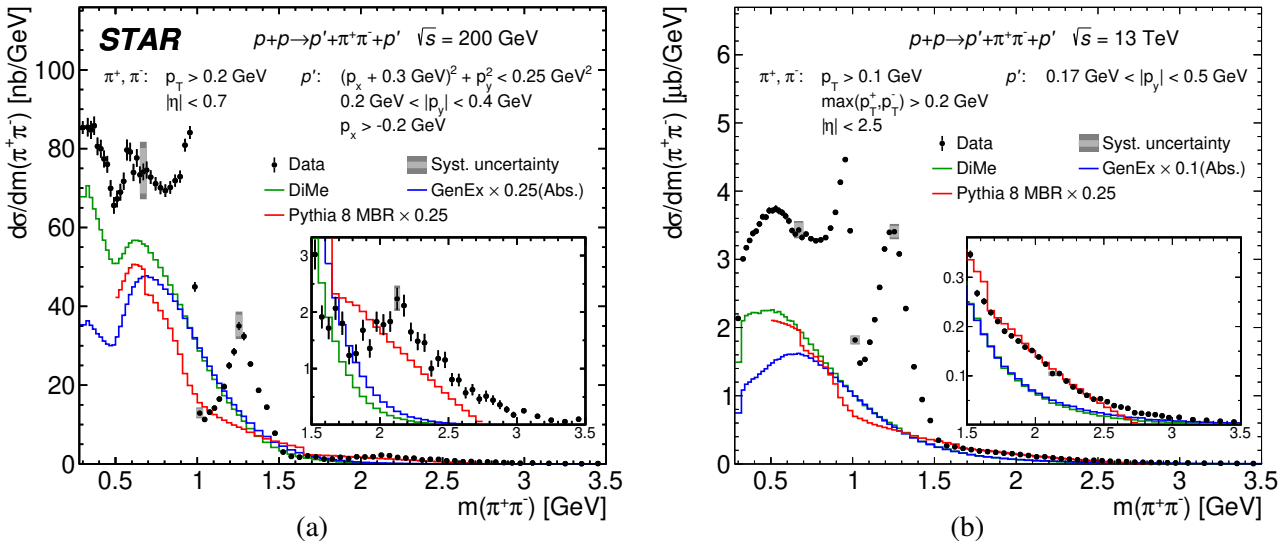

Figure 20.1: Differential cross sections for CEP of $\pi^+\pi^-$ pairs as a function of the invariant mass of the pair, in the fiducial regions explained in the plots, measured at (a) STAR, and (b) ATLAS. Data are shown as solid points with error bars representing the statistical uncertainties. The typical systematic uncertainties are shown as dark/light grey boxes (with/without luminosity uncertainty included, respectively), for only a few data points as they are almost fully correlated between neighbouring bins. Predictions from three MC models, GenEx, DiMe and MBR, are shown as histograms.

of the cross section are visible. The peak is more pronounced in the cross section measured in ATLAS, while the following drop is deeper in the STAR cross section. These structures can be attributed to $f_0(980)$ meson which interferes with the other components of the spectrum, enhancing it to the left and suppressing it to the right from the resonance mass. In the mass range $1 - 1.5$ GeV, a resonance in the STAR and ATLAS cross sections is visible, which is consistent with $f_2(1270)$. The resonance is more pronounced in the mass spectrum measured in ATLAS. The high-mass part of the peak around $1.4 - 1.5$ GeV has visible modulation of the shape, which suggests a presence of an additional state in this mass range. Above 1.5 GeV the cross section is an order of magnitude lower compared to $m(\pi^+\pi^-) \lesssim 1$ GeV, and generally decreases with increasing invariant mass. In this high-mass tail of the spectrum, there are not significant structures in the cross section from ATLAS, whereas a significant resonant peak is visible in the cross section from STAR around ~ 2.2 GeV.

The continuum predictions from DiMe, GenEx and Pythia are also shown in the plots. The GenEx predictions are scaled by 0.25 and 0.1 in the STAR and ATLAS plots, respectively. These scale factors are needed to account for the absorption effects, which are not modelled in GenEx. They were chosen to make the GenEx predictions consistent with DiMe in the region $m(\pi^+\pi^-) > 1$ GeV. The scale factor for $\sqrt{s} = 13$ TeV is lower than for 200 GeV, because the absorption effects increase with growing centre-of-mass energy. The Pythia predictions are scaled by the factor 0.25. Such scaling was introduced to simplify comparisons of the data with the Pythia predictions, which significantly overestimate the measured cross sections.

The DiMe model roughly describes both the normalisation and the shape of the continuum production under the resonances (in case of STAR only up to masses of about 1.9 GeV). The DiMe prediction notably underestimates the cross section measured in ATLAS in the low-mass region ($m \lesssim 0.7$ GeV), which indicates the presence of $f_0(500)$ resonance. Also, tuning of parameters of the pion form factor and choice of alternative absorption model can reduce the level of modelling. The GenEx model predicts lower cross section in the invariant mass region below ~0.8 GeV compared to DiMe, which makes the prediction less consistent with the data. The MBR model prediction generally follows the shape of DiMe and GenEx predictions at masses below 1 GeV, but falls less rapidly with increasing mass above 1 GeV. Notable are sharp drops of the predicted cross section at 0.7 GeV and 1.65 GeV. The former has been identified as a result of near-threshold-enhanced production of $\pi^+\pi^-$+ neutrals (mainly $\pi^0\pi^0$), which starts in Pythia 8 around 0.7 GeV. It has already been demonstrated in Sec. 10.3 and in Chap. 17 that such events are overpopulated in Pythia 8. The latter drop of the cross section at 1.65 GeV, visible mainly in the cross section from STAR, results from the fiducial cut on central particle pseudorapidities and peculiar correlation between the invariant mass and pseudorapidity of the final state particles in Pythia 8.

The differential fiducial cross sections as a function of the rapidity of the central pair are shown in Fig. 20.2. The shapes of distributions differ significantly between STAR and ATLAS. It is a consequence of the limited absolute values of pions' pseudorapidities, equal to 0.7 in STAR and 2.5 in ATLAS. In case of STAR the triangular shape is observed, while in ATLAS the shape is flat for $|y(\pi^+\pi^-)| \lesssim 1$ and drops outside this range (note the different ranges of the x-axis in Figs. 20.2a and 20.2b). Bottom panels in Fig. 20.2 show the ratio of the MC predictions (normalised to have the same integral as the data) and the data. The MC predictions generally describe the shape of the data except the Pythia prediction for the ATLAS fiducial region. Pythia predicts slightly narrower distribution than measured in ATLAS. Because all of the models are lacking the resonant component,

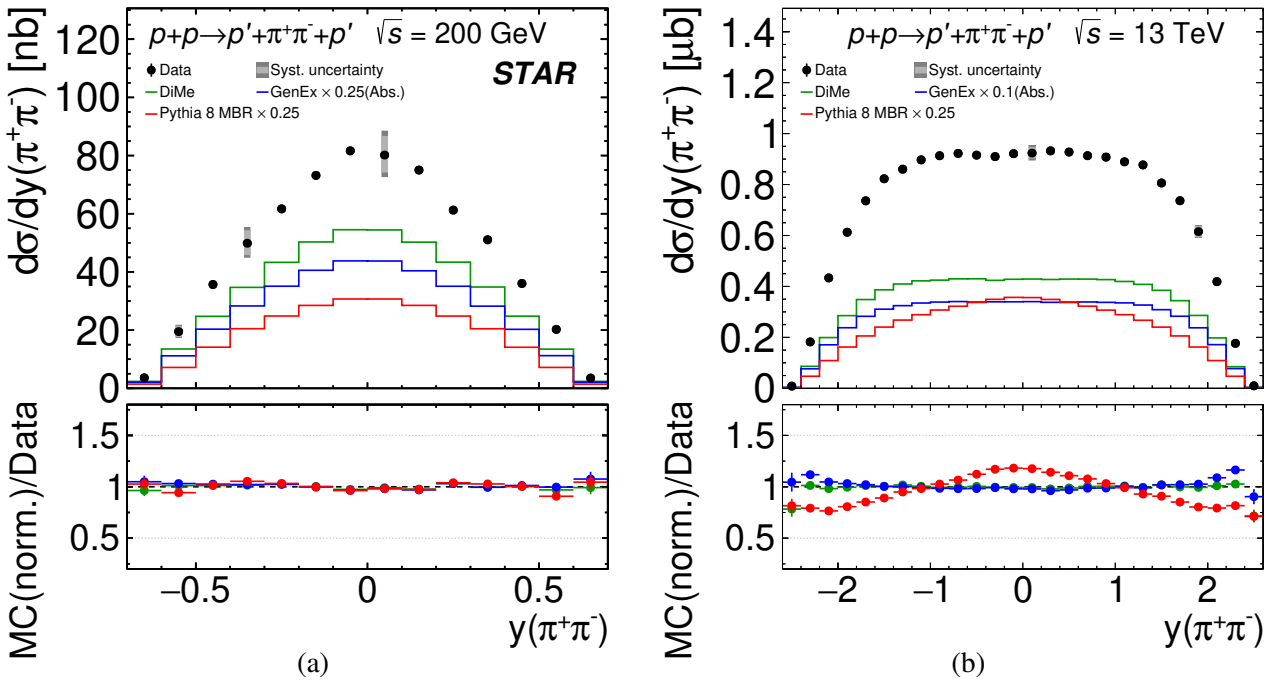

Figure 20.2: Differential cross sections for CEP of $\pi^+\pi^-$ pairs as a function of the rapidity of the pair, in the fiducial regions explained in the plots, measured at (a) STAR, and (b) ATLAS. Data are shown as solid points with error bars representing the statistical uncertainties. The typical systematic uncertainties are shown as dark/light grey boxes (with/without luminosity uncertainty included, respectively), for only a few data points as they are almost fully correlated between neighbouring bins. Predictions from three MC models, GenEx, DiMe and MBR, are shown as histograms. In the bottom panels, the ratios of the MC predictions (scaled to data) and the data, are shown.

the discussion of the absolute cross section predicted by MC is omitted. Similar discussion is also omitted for the majority of the following figures.

Figure 20.3 shows the differential cross sections as a function of the azimuthal separation of the forward-scattered protons. The binning in the cross section from ATLAS is significantly wider compared to the corresponding cross section from STAR. It is a consequence of the LHC beam optics which affects $\Delta\varphi$ resolution. The shapes of measured cross sections are strongly affected by the fiducial cuts applied to the forward-scattered protons, resulting in a low acceptance for the $\Delta\varphi \approx 90^\circ$. It is particularly important for the STAR result (Fig. 20.3a), in case of which the fiducial cross section is nearly zero at $\Delta\varphi = 90^\circ$. The data at both centre-of-mass energies exhibit significant asymmetry of the cross section between $\Delta\varphi$ lower and greater than 90°, with the cross sections higher in the former $\Delta\varphi$ range. This is also partially related to the fiducial cuts, which limit the acceptance for the invariant masses near the production threshold at $\Delta\varphi > 90^\circ$. In case of the fiducial cross section measured in the STAR experiment the shape of data is best described by DiMe predictions. GenEx and Pythia fail to describe the shape of $d\sigma/d\Delta\varphi$. The result obtained in the ATLAS experiment is not described by any of the MC predictions, with the GenEx and DiMe shapes being closest to the data.

The differential fiducial cross section $d\sigma/d|t_1 + t_2|$ is shown in Fig. 20.4. The range of $|t_1 + t_2|$ accessible in the STAR measurement (Fig. 20.4a) is significantly narrower than in the ATLAS measurement (Fig. 20.4b). It is a direct consequence of the limited p_x of the forward-scattered protons at STAR, while in ATLAS the x-components of the protons' momenta are effectively unrestricted.

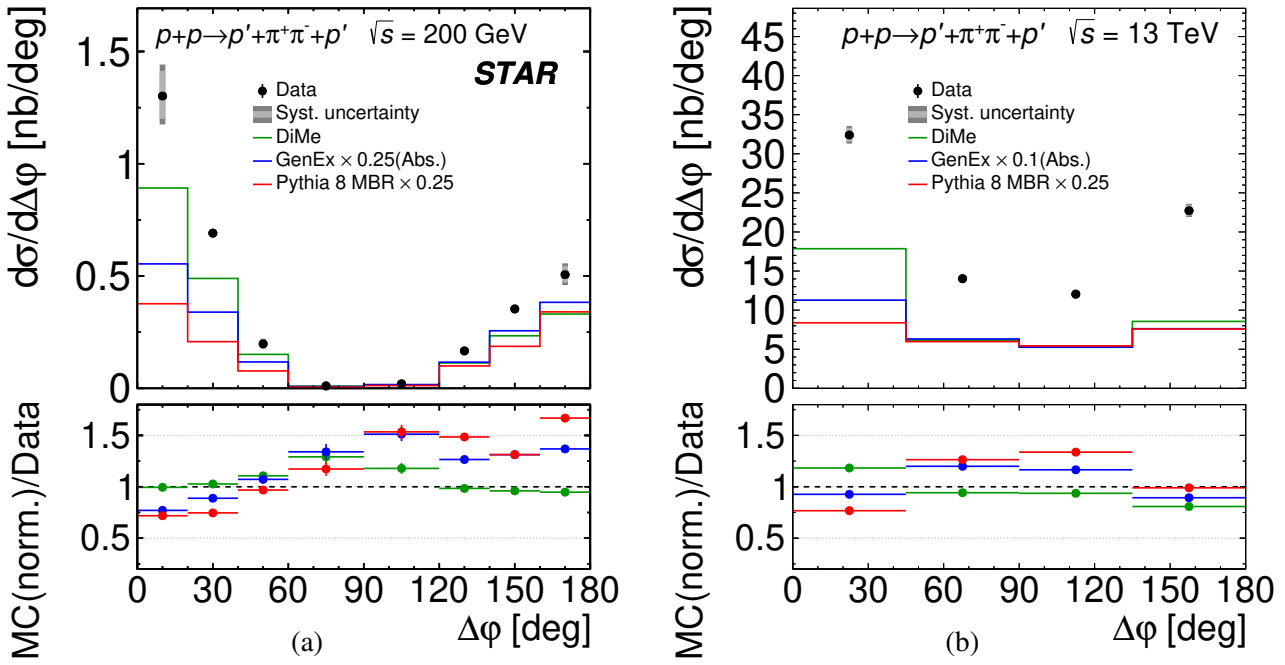

Figure 20.3: Differential cross sections for CEP of $\pi^+\pi^-$ pairs as a function of the azimuthal separation of the forward-scattered protons, in the fiducial regions explained in the plots, measured at (a) STAR, and (b) ATLAS. Data are shown as solid points with error bars representing the statistical uncertainties. The typical systematic uncertainties are shown as dark/light grey boxes (with/without luminosity uncertainty included, respectively), for only a few data points as they are almost fully correlated between neighbouring bins. Predictions from three MC models, GenEx, DiMe and MBR, are shown as histograms. In the bottom panels, the ratios of the MC predictions (scaled to data) and the data, are shown.

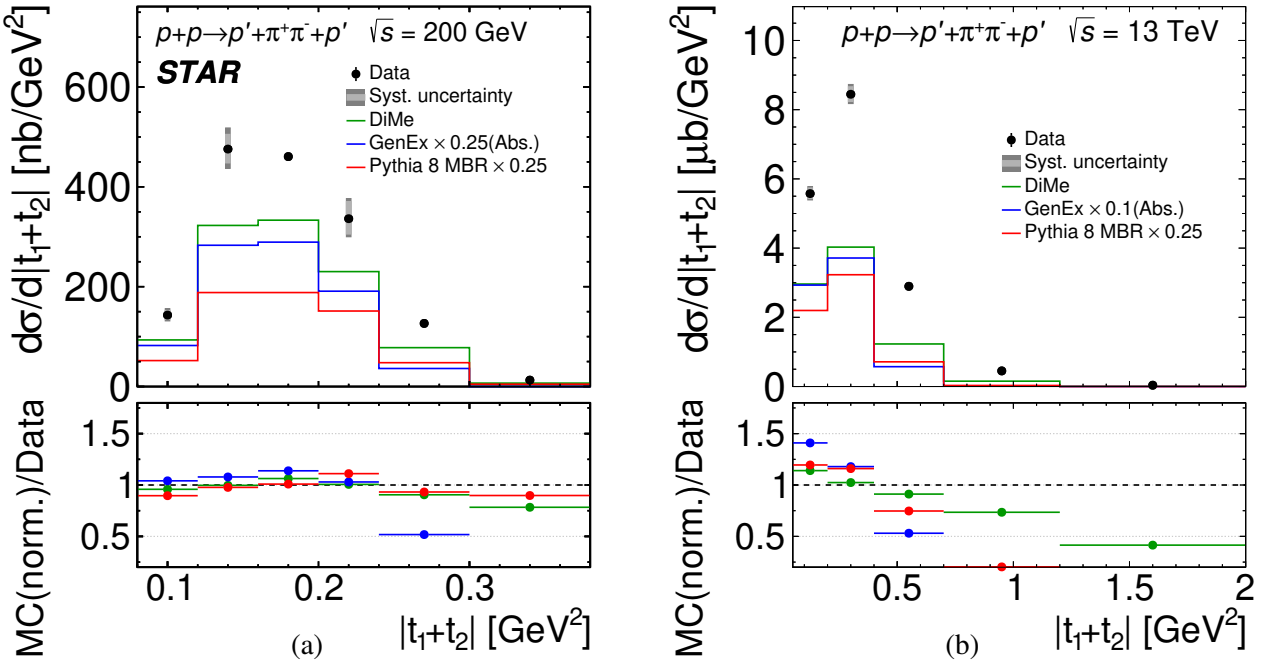

Figure 20.4: Differential cross sections for CEP of $\pi^+\pi^-$ pairs as a function of the azimuthal separation of the forward-scattered protons, in the fiducial regions explained in the plots, measured at (a) STAR, and (b) ATLAS. Data are shown as solid points with error bars representing the statistical uncertainties. The typical systematic uncertainties are shown as dark/light grey boxes (with/without luminosity uncertainty included, respectively), for only a few data points as they are almost fully correlated between neighbouring bins. Predictions from three MC models, GenEx, DiMe and MBR, are shown as histograms. In the bottom panels, the ratios of the MC predictions (scaled to data) and the data, are shown.

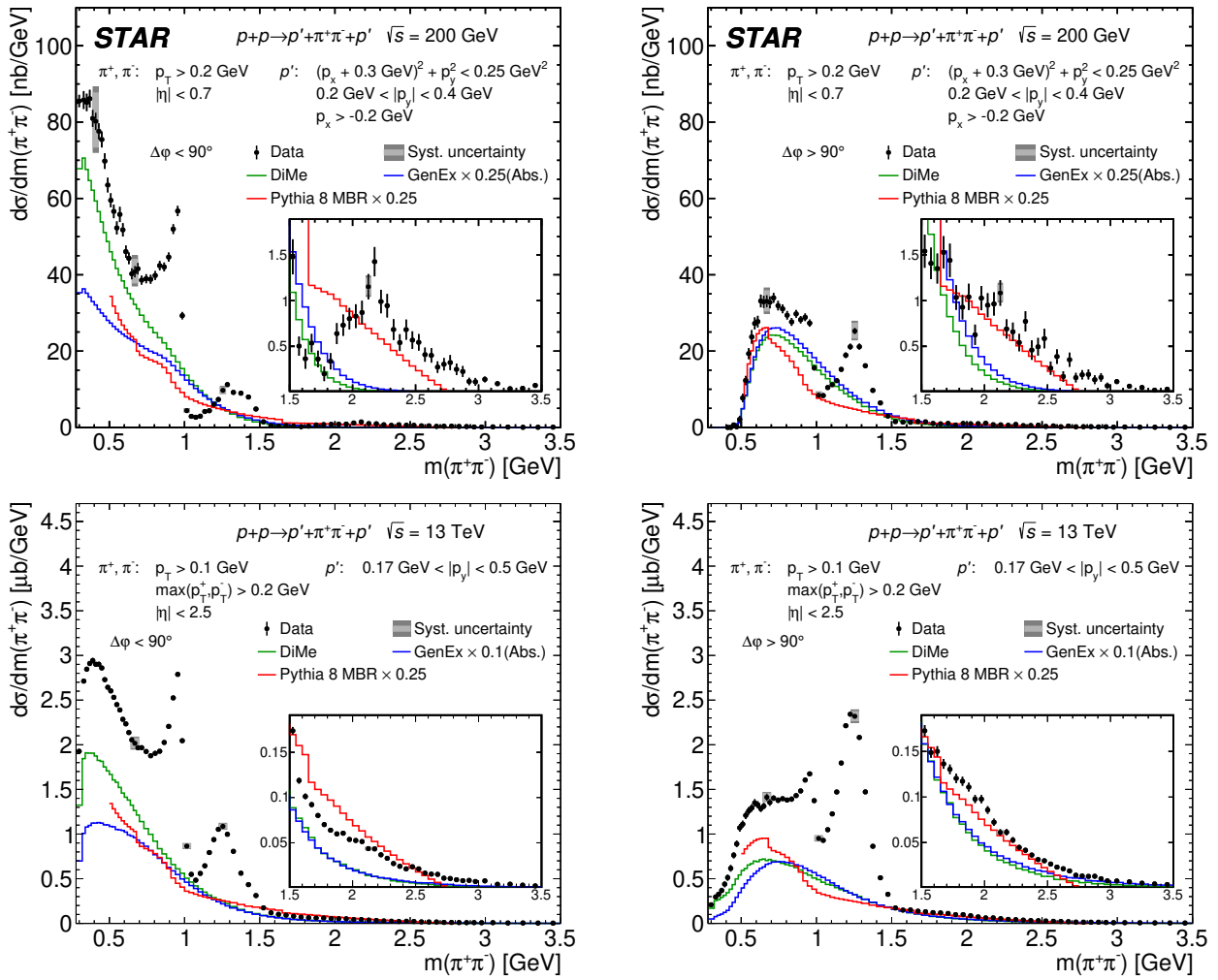

Figure 20.5: Differential cross sections for CEP of $\pi^+\pi^-$ pairs as a function of the invariant mass of the pair in two $\Delta\varphi$ regions: $\Delta\varphi < 90^\circ$ (left column) and $\Delta\varphi > 90^\circ$ (right column), measured in the STAR (top) and ATLAS (bottom) experiment in the fiducial regions explained on the plots. Data are shown as solid points with error bars representing the statistical uncertainties. The typical systematic uncertainties are shown as grey boxes for only few data points as they are almost fully correlated between neighbouring bins. Predictions from MC models GenEx, DiMe and MBR are shown as histograms.

The distributions steeply rise to reach maximum around 0.15 GeV^2 at STAR and around 0.25 GeV^2 at ATLAS, and gradually fall with increasing $|t_1 + t_2|$. The model predictions from DiMe have the shape closest to data. In the case of STAR, the DiMe shape is in good agreement with the measured $d\sigma/d|t_1 + t_2|$, whereas in ATLAS it does not describe the data but has the shape the most consistent with data among the three generators. GenEx is the least consistent with data in both cases. Pythia describes the shape of $|t_1 + t_2|$ distribution at STAR and fails to describe the shape of $|t_1 + t_2|$ distribution at ATLAS.

Figure 20.5 shows the differential cross sections for CEP of $\pi^+\pi^-$ pairs as a function of the pair invariant mass separately in two $\Delta\varphi$ regions: $\Delta\varphi < 90^\circ$ (left column) and $\Delta\varphi > 90^\circ$ (right column). The results from STAR (top row) and from ATLAS (bottom row) show similar features. In the region of low invariant masses, $m(\pi^+\pi^-) \lesssim 0.7$ GeV, the cross sections for $\Delta\varphi > 90^\circ$ are suppressed due to limited fiducial region - the same trend is demonstrated by all MC predictions. For $\Delta\varphi < 90^\circ$ a

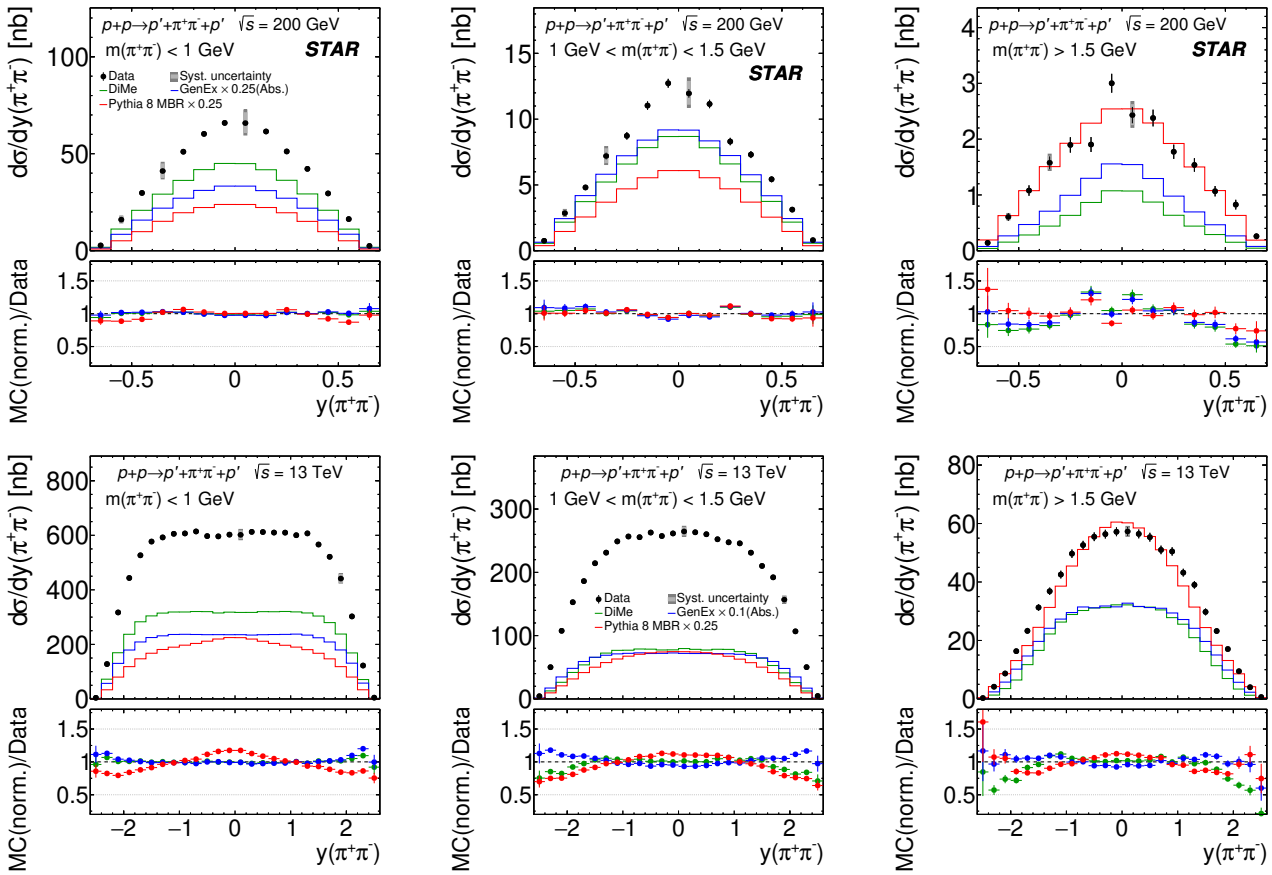

Figure 20.6: Differential cross sections for CEP of $\pi^+\pi^-$ pairs as a function of the rapidity of the pair, measured in the fiducial region explained on the plots, separately for three ranges of the $\pi^+\pi^-$ pair invariant mass: $m < 1$ GeV (left), 1 GeV $< m <$ 1.5 GeV (middle) and $m > 1.5$ GeV (right). The STAR and ATLAS results are presented in the upper and lower rows, respectively. Data are shown as solid points with error bars representing the statistical uncertainties. The typical systematic uncertainties are shown as grey boxes for only few data points as they are almost fully correlated between neighbouring bins. Predictions from MC models GenEx, DiMe and MBR are shown as histograms. In the bottom panels, the ratios of the MC predictions scaled to data and the data are shown.

possible enhancement of the cross sections might be seen below 0.5 GeV with respect to the continuum models, which might indicate presence of a resonance in this region, e.g. $f_0(500)$.

The enhancement followed by a sharp drop of the cross section around 1 GeV, that might be attributed to presence of the $f_0(980)$ meson, is much more pronounced at $\Delta\varphi < 90^\circ$, which suggests higher production cross section for this resonance in aforementioned $\Delta\varphi$ range. In contrast, a peak between 1 − 1.5 GeV expected from the $f_2(1270)$ resonance, is more pronounced for $\Delta\varphi > 90^\circ$. In addition, the $f_2(1270)$ is enhanced and more distinct in the fiducial cross section measured at ATLAS. A possible explanation for this behaviour could be, that the $f_2(1270)$ production cross section grows with increasing four-momentum transfer. Higher values of $|t_1 + t_2|$ probed at ATLAS would then result in the $f_2(1270)$ peak being more pronounced in the ATLAS cross section. An interesting feature of the discussed peak, a kind of shoulder around 1.4 GeV, is observed in STAR data for $\Delta\varphi < 90^\circ$. It indicates a possible presence of additional resonance(s) in this mass region, e.g. $f_0(1370)$, $f_0(1500)$. For the invariant masses above 1.5 GeV, tails in the cross sections can be seen. In the cross section

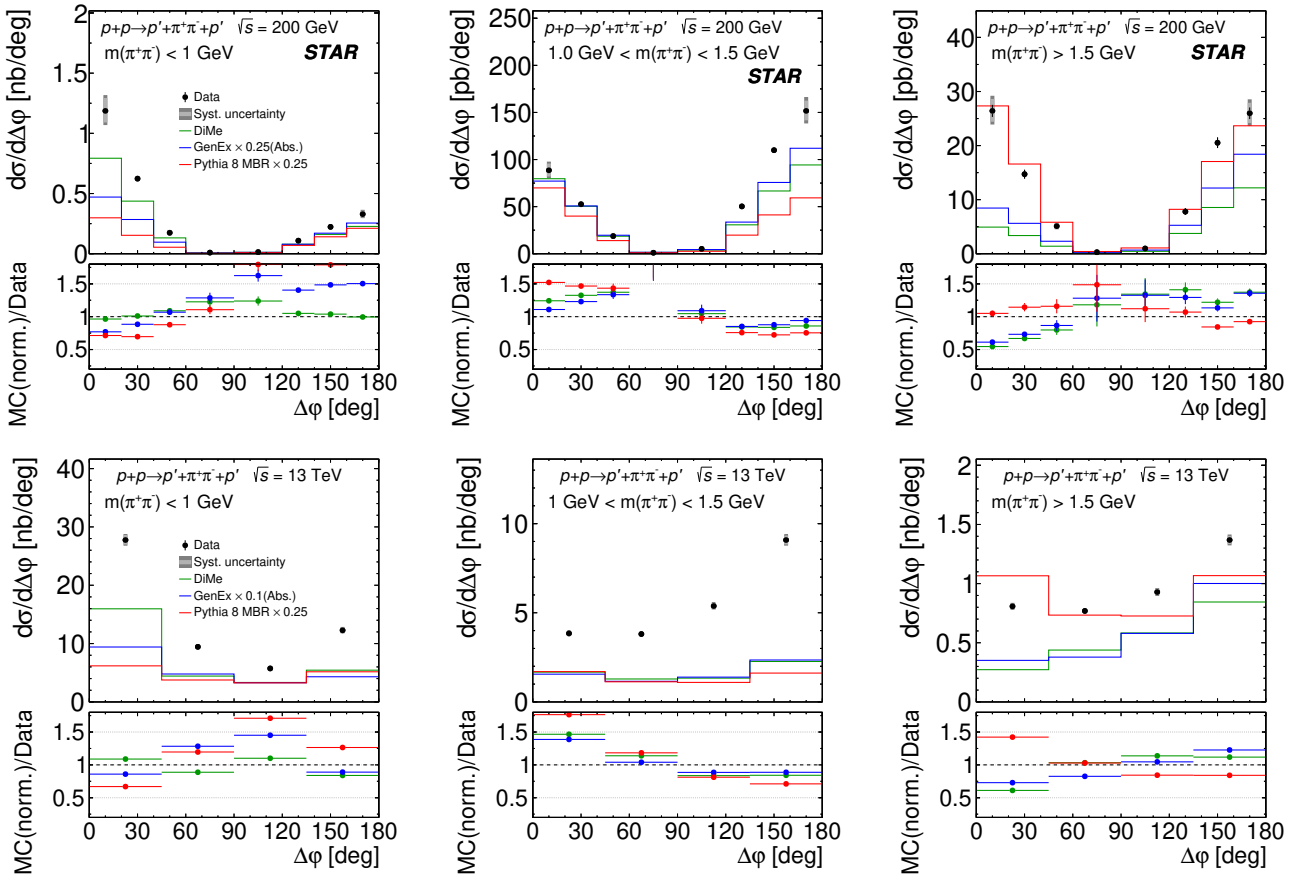

Figure 20.7: Differential cross sections for CEP of $\pi^+\pi^-$ pairs as a function of the azimuthal separation of the forward-scattered protons, measured in the fiducial region explained on the plots, separately for three ranges of the $\pi^+\pi^-$ pair invariant mass: $m < 1$ GeV (left), 1 GeV $< m <$ 1.5 GeV (middle) and $m >$ 1.5 GeV (right). The STAR and ATLAS results are presented in the upper and lower rows, respectively. Data are shown as solid points with error bars representing the statistical uncertainties. The typical systematic uncertainties are shown as grey boxes for only few data points as they are almost fully correlated between neighbouring bins. Predictions from MC models GenEx, DiMe and MBR are shown as histograms. In the bottom panels, the ratios of the MC predictions scaled to data and the data are shown.

measured at STAR for $\Delta\varphi < 90^\circ$, a significant resonance peak around 2.2 GeV is observed, better visible in the insert showing the region $1.5 < m(\pi^+\pi^-) < 3.5$ GeV in greater detail. In the cross section measured at ATLAS a small enhancement is observed around 2.2 GeV. In the case of STAR results for $\Delta\varphi < 90^\circ$, a similar but much less pronounced structure is found in this mass range. Cross section at ATLAS for $\Delta\varphi > 90^\circ$ exhibits slight enhancement around 1.8 – 2 GeV.

The correlation between resonances seen in mass spectrum and azimuthal angle between outgoing protons, which is observed in Fig. 20.5, indicates factorisation breaking between the two proton vertices.

Thanks to high statistics of the two-pion sample it is possible to study the CEP of $\pi^+\pi^-$ pairs in more detail. Figure 20.6 shows the differential cross sections for CEP of $\pi^+\pi^-$ pairs as a function of the pair rapidity in three characteristic ranges of the invariant mass of the pair: $m(\pi^+\pi^-) < 1.0$ GeV (mainly non-resonant production, left columns), $1.0 < m(\pi^+\pi^-) < 1.5$ GeV ($f_2(1270)$ mass range, middle column) and $m(\pi^+\pi^-) > 1.5$ GeV (higher invariant masses, right column). Cross sections

measured in the STAR experiment are shown in the upper row, while those measured in the ATLAS experiment are shown in the lower row. Figures 20.7 and 20.8 show the cross sections measured in the same three invariant mass intervals, but as a functions of $\Delta\varphi$ and $|t_1 + t_2|$, respectively.

In the case of the cross section $d\sigma/dy$ measured at STAR (top row in Fig. 20.6) all models agree in shape with data in all three mass ranges except for the GenEx and DiMe predictions in the highest mass range, where predictions are narrower. The shape of $d\sigma/dy$ measured in ATLAS gets narrower with increasing invariant mass, which is also qualitatively described by the MC predictions. In the region $m(\pi^+\pi^-) < 1.0$ GeV, GenEx and DiMe well describe the shape of the cross section, while Pythia predicts a different shape with visible maximum at $y = 0$. In the mass regions above 1 GeV all models fail to reproduce the shape of the data.

In Fig. 20.7, suppression of the fiducial cross section $d\sigma/d\Delta\varphi$ close to 90° (more significant at STAR) is due to the RP acceptance, while asymmetry 0° vs. 180° in the lowest mass region is due to the acceptance of the central detector (minimum p_T of central tracks). $\Delta\varphi$ distribution is sensitive

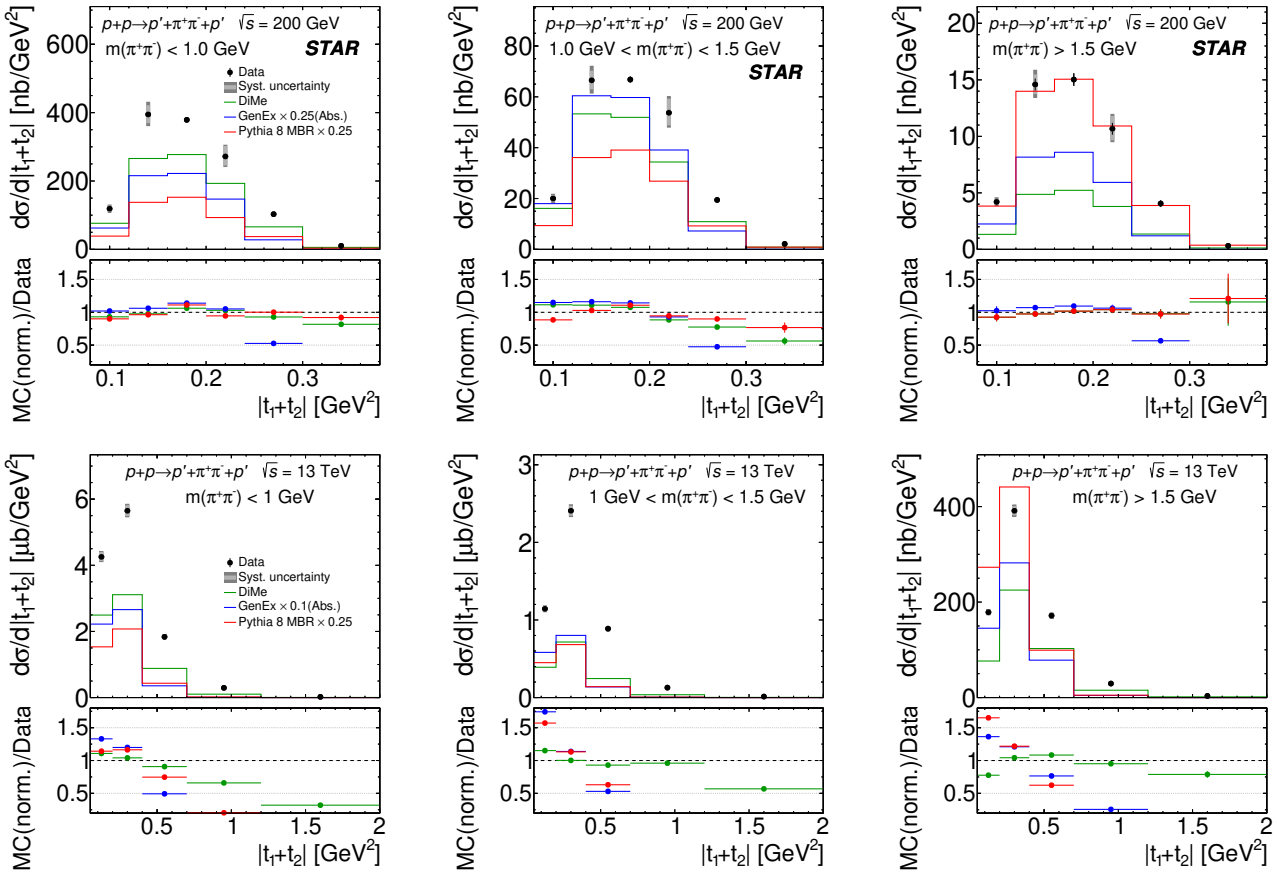

Figure 20.8: Differential cross sections for CEP of $\pi^+\pi^-$ pairs as a function of the sum of the squares of the four-momenta losses in the proton vertices, measured in the fiducial region explained on the plots, separately for three ranges of the $\pi^+\pi^-$ pair invariant mass: $m < 1$ GeV (left), 1 GeV $< m <$ 1.5 GeV (middle) and $m > 1.5$ GeV (right). The STAR and ATLAS results are presented in the upper and lower rows, respectively. Data are shown as solid points with error bars representing the statistical uncertainties. The typical systematic uncertainties are shown as grey boxes for only few data points as they are almost fully correlated between neighbouring bins. Predictions from MC models GenEx, DiMe and MBR are shown as histograms. In the bottom panels, the ratios of the MC predictions scaled to data and the data are shown.

to absorption effects which are treated fully differentially in DiMe generator and only on average in GenEx. This is consistent with generally better agreement between data and DiMe expectations except $f_2(1270)$ mass region. MBR model predicts symmetric $\Delta\varphi$ distributions in all mass ranges, which is not supported by the data.

In Fig. 20.8, the shape (slope) of the cross section as the function of $|t_1 + t_2|$ is best described by Pythia (only STAR data) and DiMe predictions (STAR and ATLAS).

A method for filtering glueballs from their $q\bar{q}$ counterparts was proposed in Ref. [208]. The gg configurations were proposed to be enhanced in the limit $|\vec{p}\,'_{1,\mathrm{T}} - \vec{p}\,'_{2,\mathrm{T}}| \to 0$. Such a configuration is already enhanced in the $\Delta\varphi < 90^\circ$ region. To further enhance a possible gg configuration, the data are studied in terms of the observable $|\vec{p}\,'_{1,\mathrm{T}} - \vec{p}\,'_{2,\mathrm{T}}|$ in the $\Delta\varphi < 90^\circ$ region. Figure 20.9 shows the differential cross sections for CEP of $\pi^+\pi^-$ as a function of the pair invariant mass, measured at STAR and at ATLAS, separately in two $|\vec{p}\,'_{1,\mathrm{T}} - \vec{p}\,'_{2,\mathrm{T}}|$ regions. They are different in the two experiments and

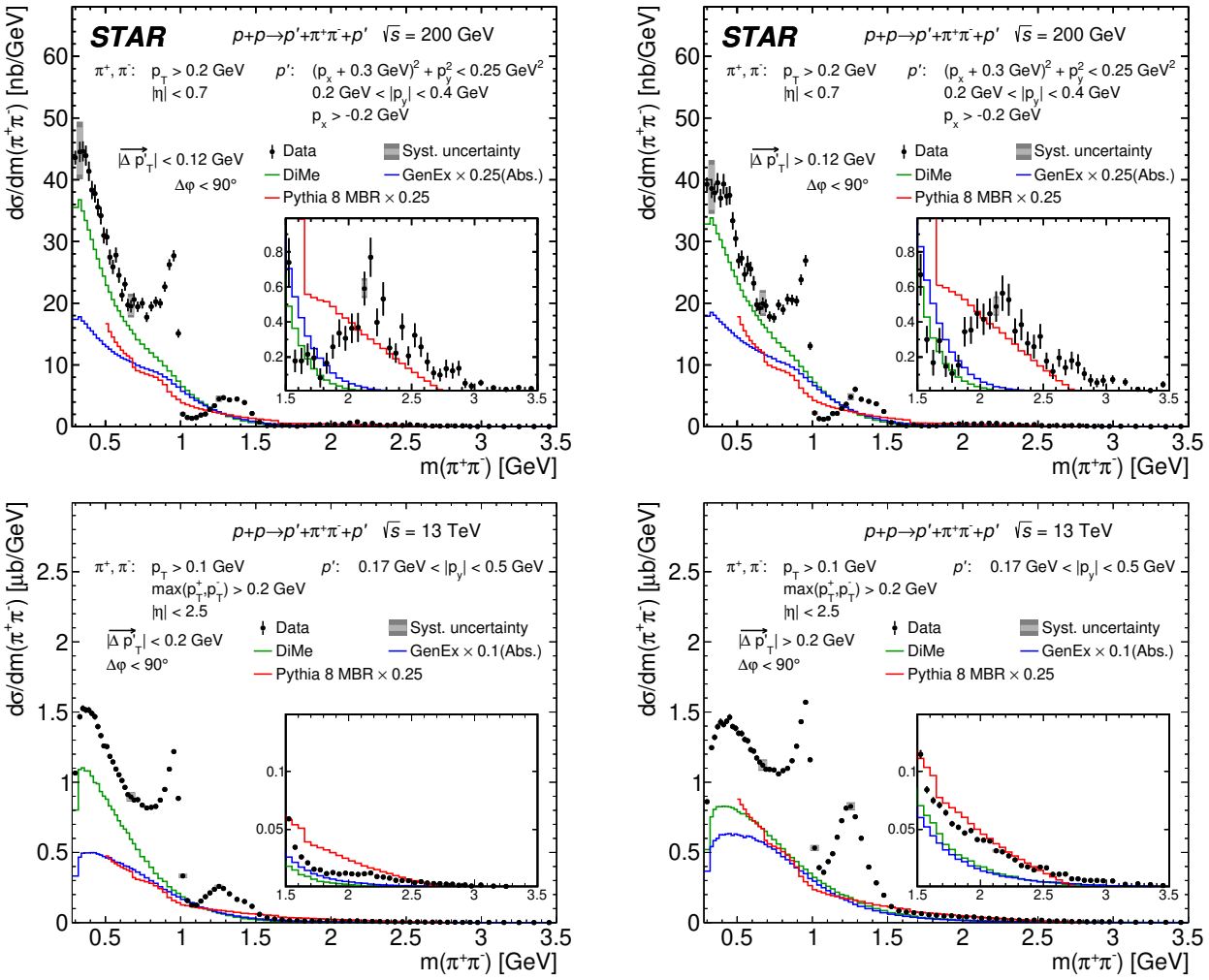

Figure 20.9: Differential cross sections $d\sigma/dm(\pi^+\pi^-)$ for CEP of $\pi^+\pi^-$ pairs in two $|\vec{p}\,'_{1,\mathrm{T}} - \vec{p}\,'_{2,\mathrm{T}}|$ regions: lower $|\vec{p}\,'_{1,\mathrm{T}} - \vec{p}\,'_{2,\mathrm{T}}|$ region (left) and higher $|\vec{p}\,'_{1,\mathrm{T}} - \vec{p}\,'_{2,\mathrm{T}}|$ region (right), in the fiducial region and for $\Delta\varphi < 90^\circ$. The STAR and ATLAS results are presented in the upper and lower rows, respectively. Data are shown as solid points with error bars representing the statistical uncertainties. The typical systematic uncertainties are shown as grey boxes for only few data points as they are almost fully correlated between neighbouring bins. Predictions from MC models GenEx, DiMe and MBR are shown as histograms.

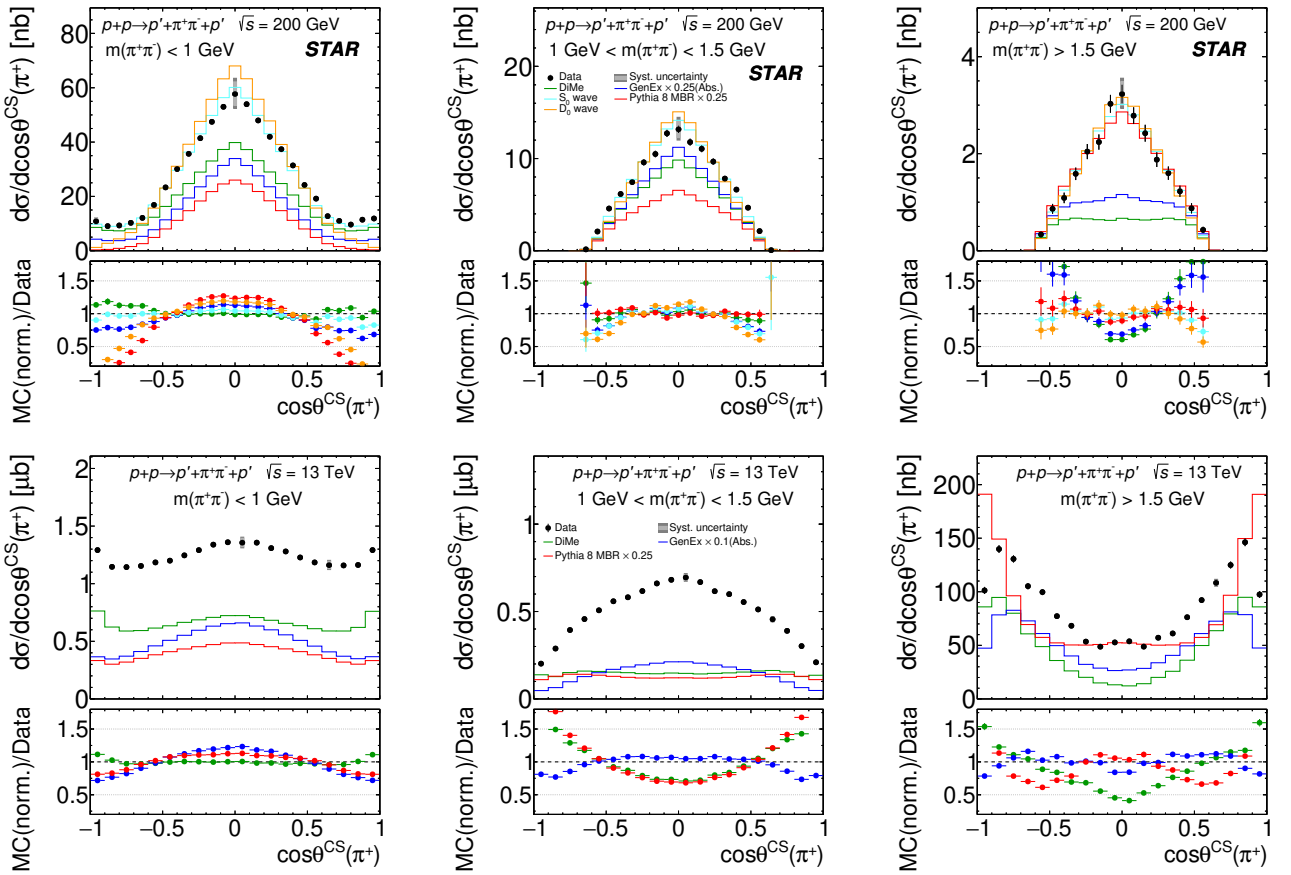

Figure 20.10: Differential cross sections for CEP of $\pi^+\pi^-$ pairs as a function of $\cos\theta^{CS}$, measured in the fiducial region explained on the plots, separately for three ranges of the $\pi^+\pi^-$ pair invariant mass: $m < 1$ GeV (left column), 1 GeV $< m <$ 1.5 GeV (middle column) and $m >$ 1.5 GeV (right column). The STAR and ATLAS results are presented in the upper and lower rows, respectively. Data are shown as solid points with error bars representing the statistical uncertainties. The typical systematic uncertainties are shown as grey boxes for only few data points as they are almost fully correlated between neighbouring bins. Predictions from MC models GenEx, DiMe and MBR are shown as histograms. In the bottom panels, the ratios of the MC predictions scaled to data and the data are shown.

were set to divide samples with $\Delta\varphi < 90^\circ$ to subsamples of similar yields. Therefore, the $|\vec{p}'_{1,T} - \vec{p}'_{2,T}|$ was required to be smaller or greater than 0.12 GeV in case of the STAR measurement, or 0.2 GeV in case of the ATLAS measurement. The STAR data do not show significant changes in the shape of the $\pi^+\pi^-$ mass spectrum for the two ranges of $|\vec{p}'_{1,T} - \vec{p}'_{2,T}|$ after filtering events with $\Delta\varphi < 90^\circ$. However, the ATLAS data show enhancement of the cross section in the $f_2(1270)$ mass region, which is consistent with the observation made in the WA102 experiment [209]. Different conclusions from the STAR and ATLAS data are potentially a result of much wider fiducial phase space region in ATLAS compared to STAR.

Also angular distributions of the charged particle pairs have been studied. This can be done in various reference frames. Here the Collins-Soper [162] reference frame was used, proposed e.g. in Ref. [210]. Figures 20.10 and 20.11 show the differential cross sections for CEP of $\pi^+\pi^-$ pairs as a function of $\cos\theta^{CS}$ and ϕ^{CS}, respectively, in three characteristic ranges of the invariant mass of the pair: $m(\pi^+\pi^-) < 1$ GeV, 1 GeV $< m(\pi^+\pi^-) <$ 1.5 GeV and $m(\pi^+\pi^-) >$ 1.5 GeV.

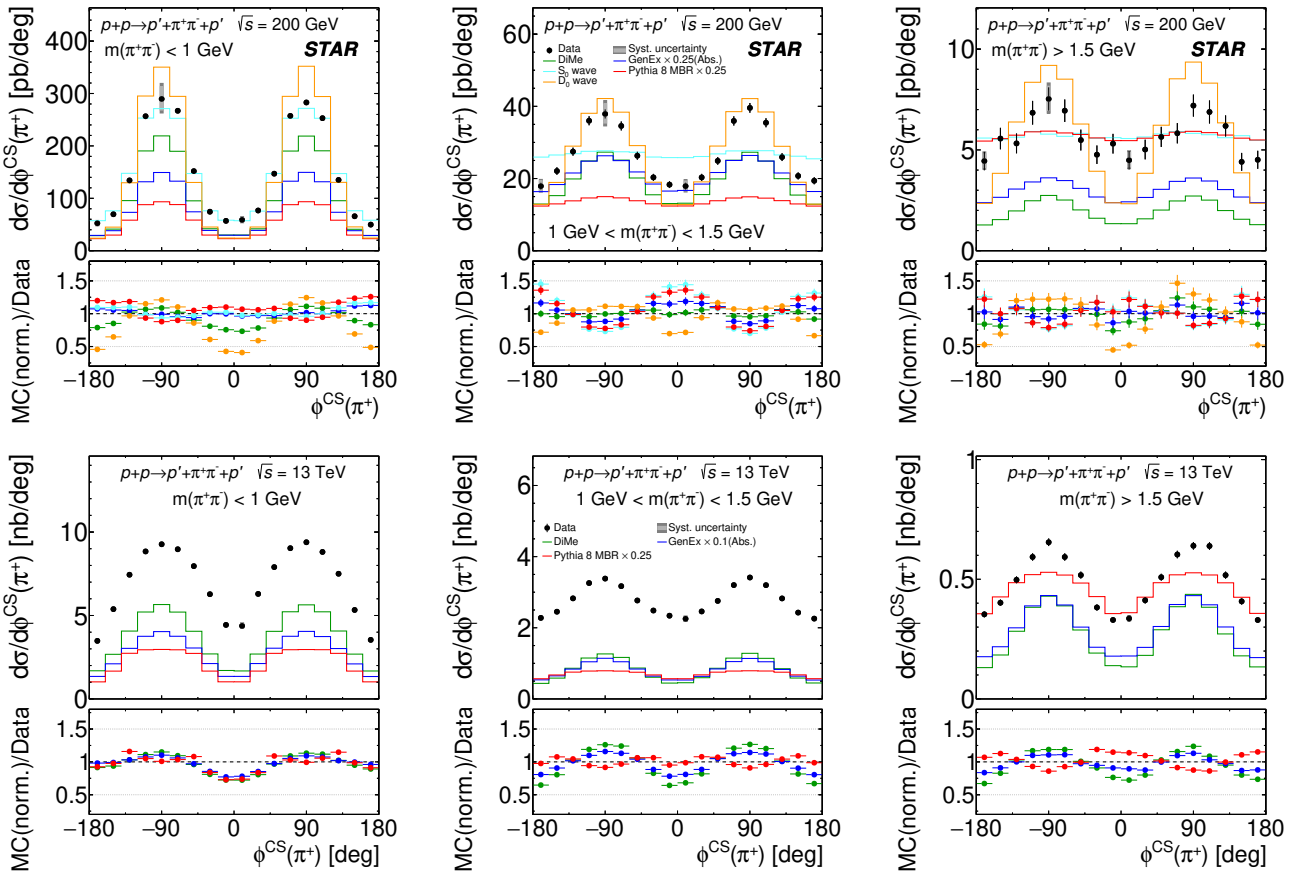

Figure 20.11: Differential cross sections for CEP of $\pi^+\pi^-$ pairs as a function of ϕ^{CS}, measured in the fiducial region explained on the plots, separately for three ranges of the $\pi^+\pi^-$ pair invariant mass: $m < 1$ GeV (left column), 1 GeV $< m <$ 1.5 GeV (middle column) and $m >$ 1.5 GeV (right column). The STAR and ATLAS results are presented in the upper and lower rows, respectively. Data are shown as solid points with error bars representing the statistical uncertainties. The typical systematic uncertainties are shown as grey boxes for only few data points as they are almost fully correlated between neighbouring bins. Predictions from MC models GenEx, DiMe and MBR are shown as histograms. In the bottom panels, the ratios of the MC predictions scaled to data and the data are shown.

To help in interpreting the data and in understanding the acceptance effects of the STAR detector, the data are compared with expectations from models with pure S_0 and D_0 waves. The S_0 wave predicts a uniform distribution of azimuthal angle ϕ, in contrast to the D_0 wave. The angular distributions are generated in the most natural Gottfried-Jackson frame [211] with the IPomeron-IPomeron direction taken as the z-axis. The transformation to the Collins-Soper frame changes the angular distributions for the D_0 wave but not for the S_0 wave. Therefore, the shape of the ϕ^{CS} distribution for S_0 wave, after applying fiducial cuts, represents also the ϕ^{CS} shape of detectors' acceptance.

The S_0 and D_0 predictions are normalised to data. The double-peak structure observed in the ϕ^{CS} distribution in the lowest mass region, where data are reasonably well described by S_0 prediction, is due to the STAR acceptance. In contrast, at higher masses, where prediction from the S_0 wave model is flat, the double-peak structure does not come from the detector acceptance. Both $\cos\theta^{CS}$ and ϕ^{CS} in the lowest mass region agree very well with the S_0 wave suggesting that this mass region is dominated by spin-0 contribution. At higher masses, pure S_0 or D_0 waves are not able to describe the data.

In the case of the differential cross section $d\sigma/d\cos\theta^{CS}$, the DiMe predictions fit the data only in the lowest mass region. In contrast, the MBR predictions fail to describe the shape of the $\cos\theta^{CS}$ distribution in this mass range only. The GenEx prediction does not describe the data in any mass range. In the case of the differential cross section $d\sigma/d\phi^{CS}$, in the lowest mass region only GenEx predicts the shape of the ϕ^{CS} distribution. The DiMe prediction fits the data well in the middle mass range. Both GenEx and DiMe predictions describe the shape of the ϕ^{CS} distribution fairly well in the highest mass region.

20.1.2 Exclusive production of K^+K^- pairs

The CEP of K^+K^- pairs has been measured in the STAR experiment. Due to limited pions and kaons separation power of the ATLAS detector, there are no cross sections provided for CEP of K^+K^- pairs at $\sqrt{s}$ = 13 TeV. Measurement of this process requires additional studies in order to obtain satisfactorily low systematic uncertainties related to PID. Such studies will be performed before the final publication of the ATLAS results.

Figure 20.12 shows the differential fiducial cross sections for CEP of K^+K^- pairs as a function of the invariant mass (20.12a) and rapidity (20.12b) of the pair, measured by the STAR experiment. The differential cross section $d\sigma/dm(K^+K^-)$ shows significant enhancement in the $f_2'(1525)$ mass region and a possible smaller resonant signal in the mass region of $f_2(1270)$. Both structures are expected to be produced in the IPomeron-IPomeron fusion process. The ratio of the STAR cross sections for $\pi^+\pi^-$ to K^+K^- production in the $f_2(1270)$ mass region is roughly 18, what is consistent with the PDG ratio of the $f_2(1270)$ branching fractions for its decays into $\pi^+\pi^-$ and K^+K^- [5], assuming similar contributions

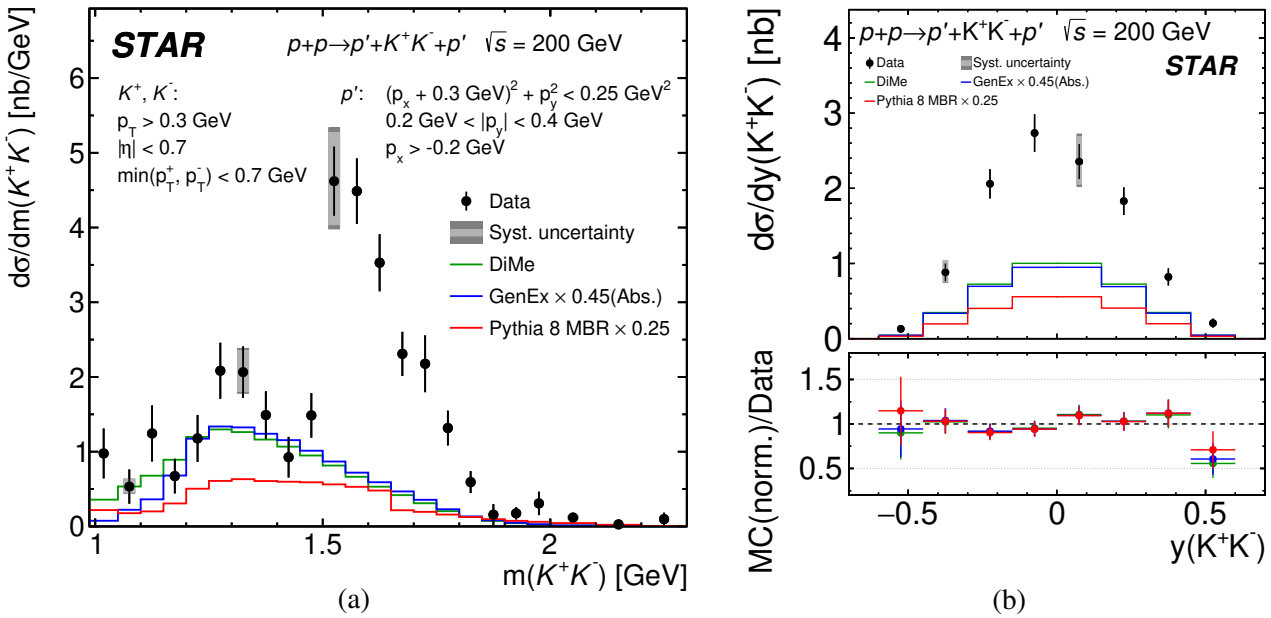

Figure 20.12: Differential cross sections for CEP of K^+K^- pairs as a function of (a) invariant mass, and (b) rapidity of the pair, in the fiducial region explained on the plots. Data are shown as solid points with error bars representing the statistical uncertainties. The typical systematic uncertainties are shown as grey boxes for only few data points as they are almost fully correlated between neighbouring bins. Predictions from MC models GenEx, DiMe and MBR are shown as histograms. In the bottom panel of (b), the ratios of the MC predictions scaled to data and the data are shown.

from non-resonant production under the $f_2(1270)$ peaks and similar STAR acceptance. The DiMe and GenEx predictions roughly describe the non-resonant contribution to the data in the resonance region. The data are also consistent with the ratio of the non-resonant exclusive production of $\pi^+\pi^-$ to K^+K^- pairs expected by GenEx and DiMe.

In case of the measured $d\sigma/dy(K^+K^-)$ (Fig. 20.12b), the shape of the distribution is generally well described by all the model predictions.

The differential fiducial cross sections for CEP of K^+K^- pairs as a function of the azimuthal angle between the forward-scattered protons and the sum of the four-momentum transfers squared in the proton vertices are shown in Fig. 20.13a and 20.13b, respectively. For the $d\sigma/d\Delta\varphi$, the shape of DiMe model prediction agrees with data. The model implemented in GenEx does not describe the shape of the data, while the MBR model implemented in Pythia 8 describes it fairly well.

For the $d\sigma/d|t_1 + t_2|$, the shape of the measured cross section is better described by the DiMe and MBR models than by the GenEx model.

Figure 20.14 shows the differential cross sections for CEP of K^+K^- pairs as a function of the pair invariant mass separately in two $\Delta\varphi$ regions: $\Delta\varphi < 90^\circ$ and $\Delta\varphi > 90^\circ$. Sharp drop in the measured cross section at $m(K^+K^-) < 1.3$ GeV for the $\Delta\varphi > 90^\circ$ range is due to the fiducial cuts applied to the forward-scattered protons. The data do not show any significant $\Delta\varphi$ asymmetry, except for a possible widening of the peak at $f_2'(1520)$ in the region $\Delta\varphi < 90^\circ$. This widening may indicate presence of additional resonances around 1.7 GeV (e.g. $f_0(1710)$) in this configuration. It is worth to remind that

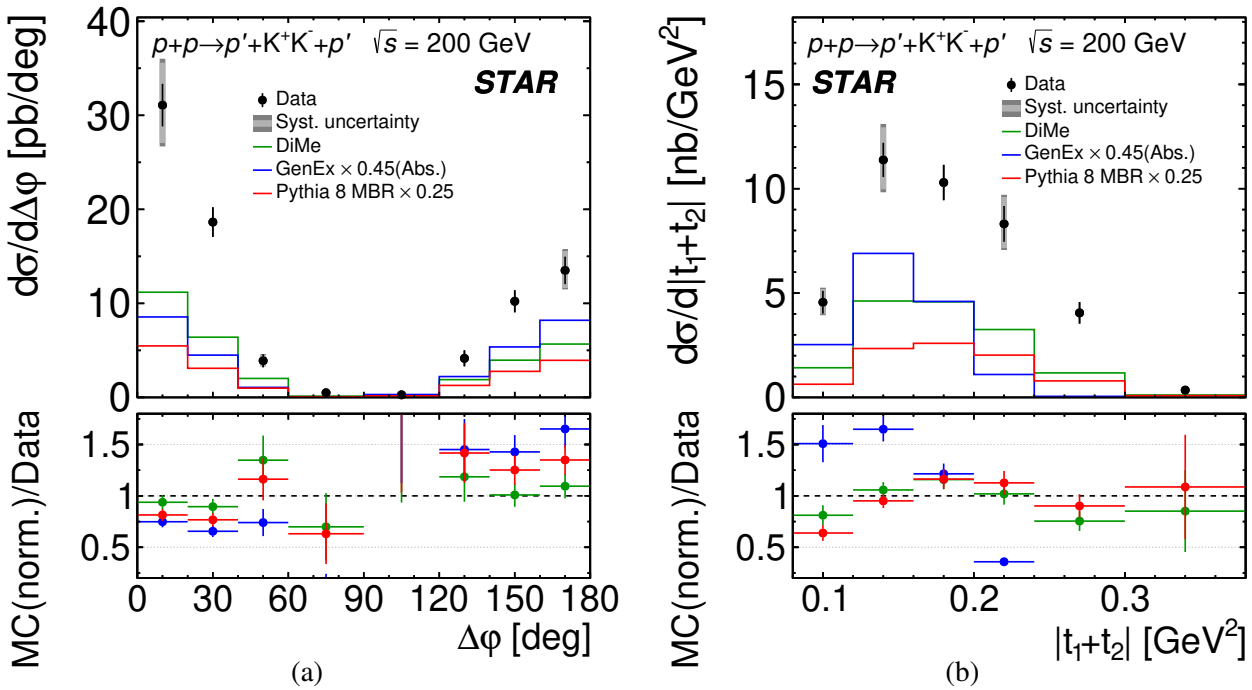

Figure 20.13: Differential cross sections for CEP of K^+K^- pairs as a function of (a) the difference of azimuthal angles of the forward-scattered protons, and (b) the sum of the squares of the four-momenta transfers in the proton vertices, measured in the fiducial region explained on the plots. Data are shown as solid points with error bars representing the statistical uncertainties. The typical systematic uncertainties are shown as grey boxes for only few data points as they are almost fully correlated between neighbouring bins. Predictions from MC models GenEx, DiMe and MBR are shown as histograms. In the bottom panels the ratios of the MC predictions scaled to data and the data are shown.

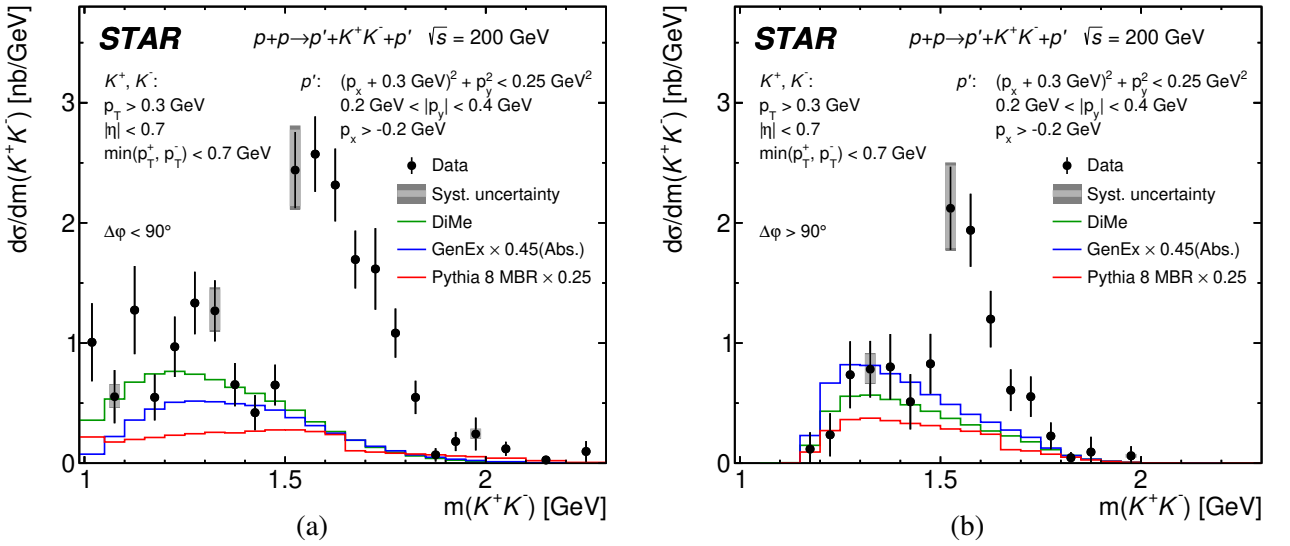

Figure 20.14: Differential cross sections for CEP of K^+K^- pairs as a function of the invariant mass of the pair in two $\Delta\varphi$ regions: (a) $\Delta\varphi < 90^\circ$ and (b) $\Delta\varphi > 90^\circ$, measured in the fiducial region explained on the plots. Data are shown as solid points with error bars representing the statistical uncertainties. The typical systematic uncertainties are shown as grey boxes for only few data points as they are almost fully correlated between neighbouring bins. Predictions from MC models GenEx, DiMe and MBR are shown as histograms.

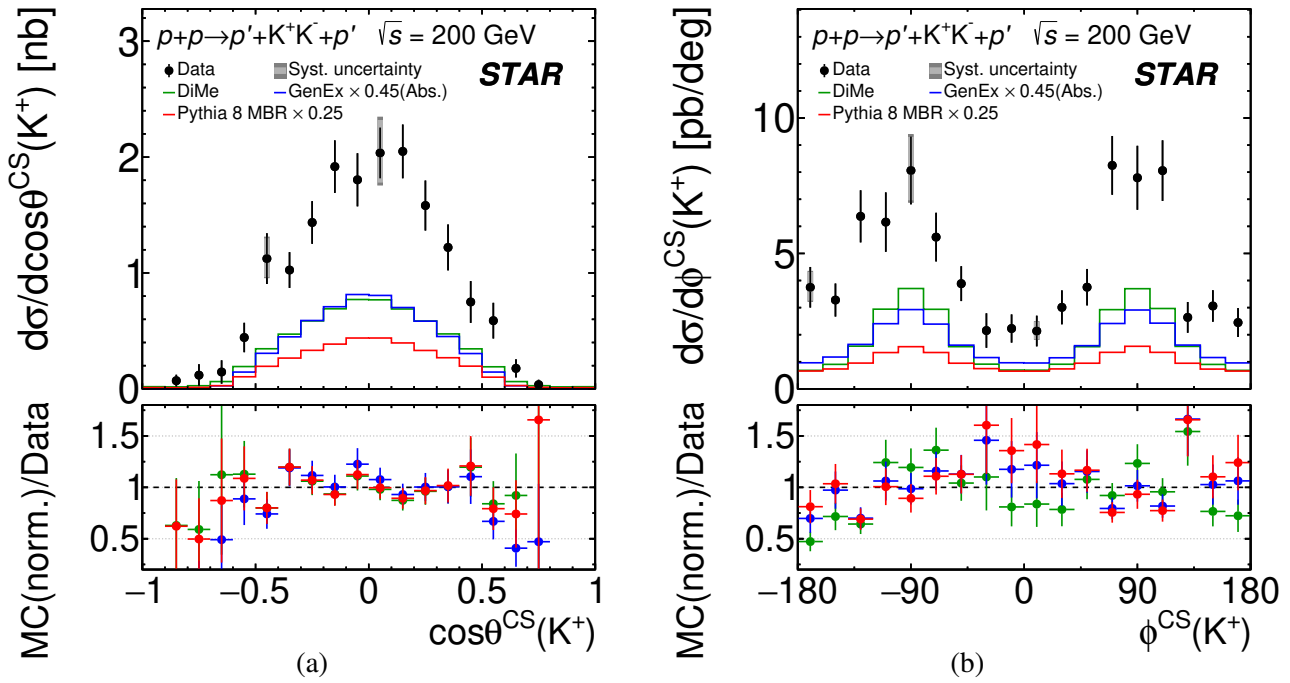

Figure 20.15: Differential cross sections for CEP of K^+K^- pairs as a function of (a) $\cos\theta^{CS}$ and (b) ϕ^{CS} of the positively charged central particle, measured in the fiducial region explained on the plots. Data are shown as solid points with error bars representing the statistical uncertainties. The typical systematic uncertainties are shown as grey boxes for only few data points as they are almost fully correlated between neighbouring bins. Predictions from MC models GenEx, DiMe and MBR are shown as histograms. In the bottom panels, the ratios of the MC predictions scaled to data and the data are shown.

$\Delta\varphi$ close to 0° corresponds to $|\vec{p}'_{1,T} - \vec{p}'_{2,T}| \to 0$, which is expected to provide an enhancement of the glueball production.

The angular distributions of positively charged kaons are shown in Fig. 20.15. The cosine of the polar angle and the azimuthal angle of K^+ in the Collins-Soper reference frame are shown in Fig. 20.15a and 20.15b, respectively. The shape of the cross section as a function of $\cos\theta^{CS}$ is generally narrower than predicted by all discussed models. Also, none of the MC predictions agrees with the shape of the differential cross section as a function of ϕ^{CS}.

20.1.3 Exclusive production of $p\bar{p}$ pairs

In the STAR experiment also exclusive production of $p\bar{p}$ pairs was studied. Differential fiducial cross section for CEP of $p\bar{p}$ pairs as a function of the invariant mass of the central pair, $d\sigma/dm(p\bar{p})$, is shown in Fig. 20.16a. For this CEP channel predictions only from the MBR model are available. As can be seen in the plot, MBR predictions overestimate the data by a factor of 8 (scaling factor 0.25 is used for the Pythia predictions to simplify comparisons). Figure 20.16b shows the differential cross section as a function of the $p\bar{p}$ pair rapidity. The shape predicted by the MBR model agrees with the data, but one should note non-negligible statistical uncertainties of the data.

The differential cross sections for CEP of $p\bar{p}$ pairs as a function of the azimuthal separation of the forward-scattered protons and the sum of Mandelstam t's in the proton vertices are shown in Figs. 20.17a and 20.17b, respectively. In Fig. 20.17a one can see, that the cross section is higher in the $\Delta\varphi > 90°$ region, while the MBR model prediction shows the opposite $\Delta\varphi$ asymmetry. In the case of the $d\sigma/d|t_1 + t_2|$, despite significant statistical uncertainties of the data points, a disagreement in slope

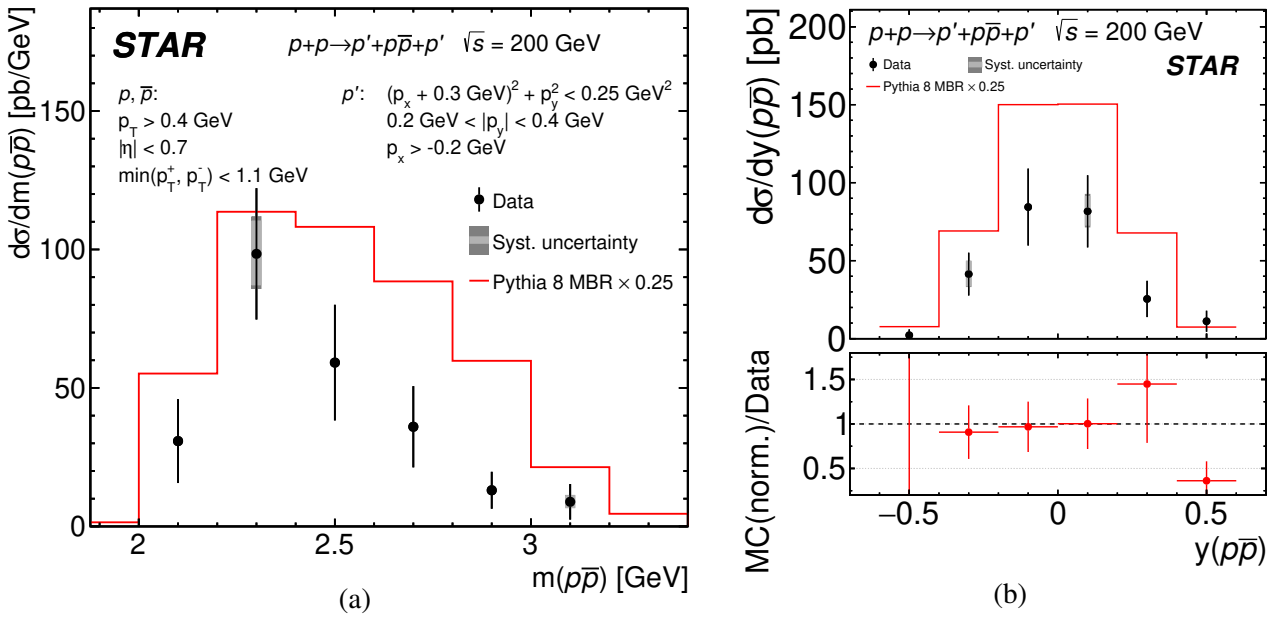

Figure 20.16: Differential cross sections for CEP of $p\bar{p}$ pairs as a function of (a) invariant mass, and (b) rapidity of the pair in the fiducial region explained on the plots. Data are shown as solid points with error bars representing the statistical uncertainties. The typical systematic uncertainties are shown as grey boxes for only few data points as they are almost fully correlated between neighbouring bins. Predictions from the MBR model implemented in Pythia are shown as histograms. In the bottom panel of (b) the ratios of the MC predictions scaled to data and the data are shown.

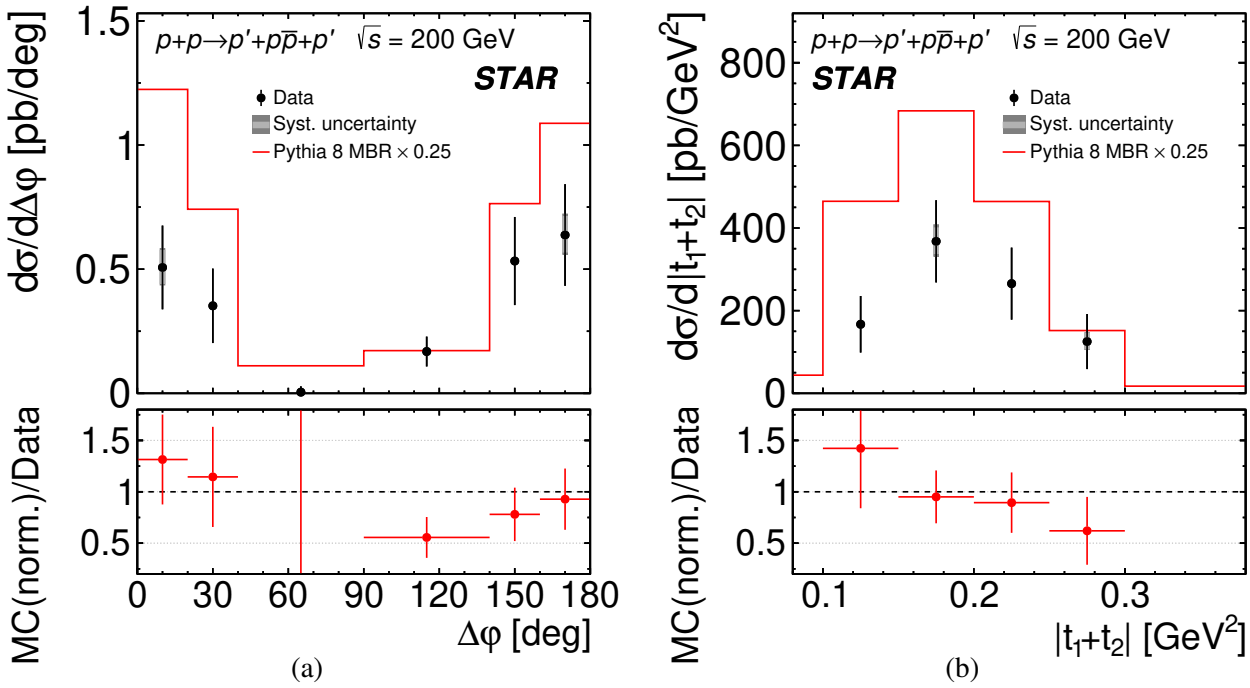

(a) (b)

Figure 20.17: Differential cross sections for CEP of $p\bar{p}$ pairs as a function of (a) the difference of azimuthal angles of the forward-scattered protons, and (b) the sum of the squares of the four-momenta transfers in the proton vertices, measured in the fiducial region explained on the plots. Data are shown as solid points with error bars representing the statistical uncertainties. The typical systematic uncertainties are shown as grey boxes for only few data points as they are almost fully correlated between neighbouring bins. Predictions from the MBR model implemented in Pythia are shown as histograms. In the bottom panels in the bottom plots the ratios of the MC predictions scaled to data and the data are shown.

of the measured distribution and the slope predicted by the model can be observed. Pythia predicts significantly larger slope of $|t_1 + t_2|$ distribution compared to the data.

Figure 20.18 shows the differential cross sections for CEP of $p\bar{p}$ pairs as a function of the pair invariant mass separately in two $\Delta\varphi$ regions: $\Delta\varphi < 90^\circ$ and $\Delta\varphi > 90^\circ$. The data do not show a significant $\Delta\varphi$ asymmetry except for a possible enhancement in the 2.2 – 2.4 GeV mass range for the $\Delta\varphi > 90^\circ$ region.

Angular distributions of the proton from the centrally-produced pair, calculated in the Collins-Soper reference frame, are shown in Fig. 20.19. In case of both $d\sigma/d\cos\theta^{CS}$ and $d\sigma/d\cos\phi^{CS}$ the statistical uncertainties make the comparisons of data with MC predictions difficult. The data demonstrate some asymmetries between positive and negative $\cos\theta^{CS}$ and ϕ^{CS}, which are not supported by the MC predictions.

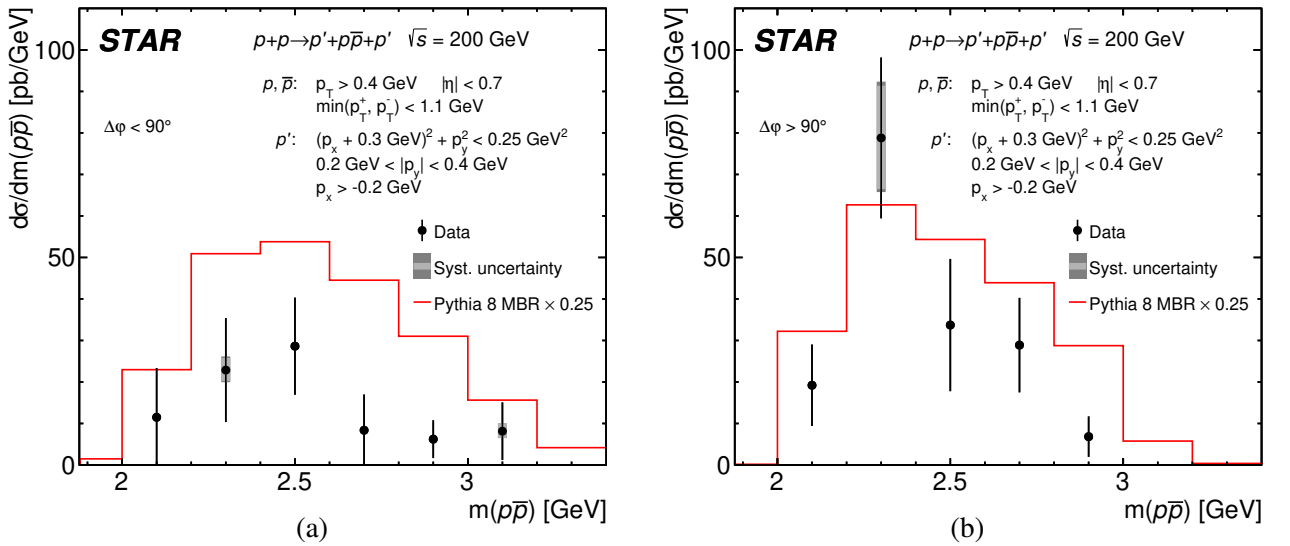

Figure 20.18: Differential cross sections for CEP of $p\bar{p}$ pairs as a function of the invariant mass of the pair in two $\Delta\varphi$ regions: (a) $\Delta\varphi < 90^{\circ}$, and (b) $\Delta\varphi > 90^{\circ}$, measured in the fiducial region explained on the plots. Data are shown as solid points with error bars representing the statistical uncertainties. The typical systematic uncertainties are shown as grey boxes for only few data points as they are almost fully correlated between neighbouring bins. Predictions from the MBR model implemented in Pythia are shown as histograms.

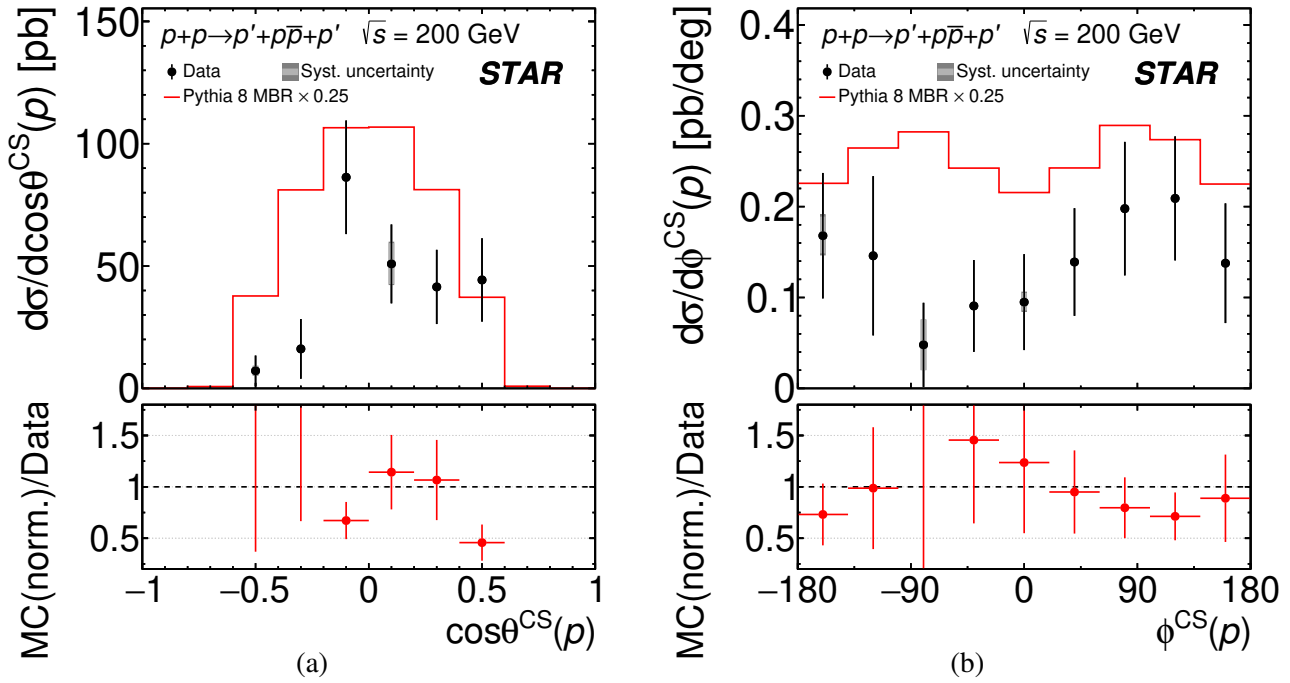

Figure 20.19: Differential cross sections for CEP of $p\bar{p}$ pairs as a function of (a) $\cos\theta^{\mathrm{CS}}$, and (b) ϕ^{CS} of the positively charged central particle, measured in the fiducial region explained on the plots. Data are shown as solid points with error bars representing the statistical uncertainties. The typical systematic uncertainties are shown as grey boxes for only few data points as they are almost fully correlated between neighbouring bins. Predictions from the MBR model implemented in Pythia are shown as histograms. In the bottom panels the ratios of the MC predictions scaled to data and the data are shown.

20.2 Exclusive production of higher-multiplicity central systems

20.2.1 Exclusive production of $2\pi^+2\pi^-$ states

Exclusively produced four charged pions, $\pi^+\pi^-\pi^+\pi^-$, were measured using data from the ATLAS experiment. Cross sections for CEP of this central system were not determined in the case of STAR due to limited event statistics. It is a consequence of relatively low efficiency of the TPC and TOF systems per single track, which also significantly increases overall systematic uncertainty.

Figure 20.20 presents the differential fiducial cross sections for the CEP of $2\pi^+2\pi^-$ states as a function of the invariant mass and rapidity of the system. The fiducial cross section is very low in the mass range starting from the production threshold up to approximately 1 GeV, which is a kinematic effect of the fiducial cuts on the forward- and central-system particles. Above 1 GeV the cross section rises rapidly, and a narrow peak is visible around 1.25 – 1.3 GeV. Small width of the peak suggests, that a narrow resonance is responsible for this structure. In this mass range, the only known narrow resonance which is quoted in PDG [5] and decays into four pions (has quantum numbers allowed in DIPE [39]) is $f_1(1285)$. Between 1.3 – 1.6 GeV another structure is visible: a peak with a maximum around 1.45 GeV, followed by a dip around 1.55 GeV. These structures can possibly be attributed to the production of the $f_0(1500)$ resonance, which has large ($\approx 50\%$ [5]) branching fraction to four pions. The enhancement and suppression of the cross section, below and above the resonance mass, respectively, might result from interference terms. Another possibility is $f_1(1420)$ resonance, albeit its

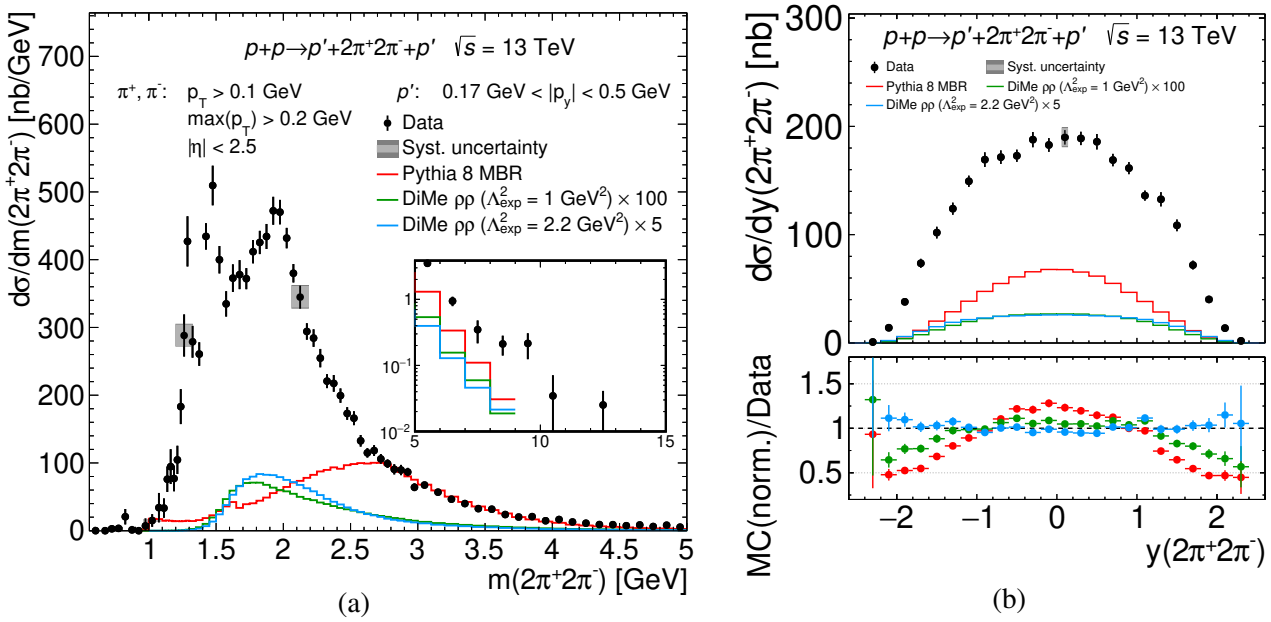

(a) (b)

Figure 20.20: Differential cross sections for CEP of $2\pi^+2\pi^-$ states as a function of the (a) invariant mass and (b) rapidity of the central state, measured at ATLAS in the fiducial region explained in the plots. Data are shown as solid points with error bars representing the statistical uncertainties. The typical systematic uncertainties are shown as dark/light grey boxes (with/without luminosity uncertainty included, respectively), for only a few data points as they are almost fully correlated between neighbouring bins. Predictions from two MC models, MBR and DiMe ($\rho\rho$), are shown as histograms. Figure (a) contains an insert with the cross section drawn for high values of invariant mass of the central state (from 5 GeV to 15 GeV). In the bottom panel of (b) the ratios between the MC predictions (scaled to data) and the data are shown.

mass is slightly lower and branching fraction to four pions is not reported in PDG [5], probably being very small. Around the mass value of 1.95 GeV another peak is visible, whose nature is not obvious. Potential resonances in this mass range, which could be produced in DPE, are $f_2(1950)$ or $f_4(2050)$. However, it is also possible that lower mass resonances (e.g. $f_0(1710)$), interfere with the four-pion continuum and other resonances, leading to the observed structure. Above 2 GeV the cross section decreases monotonically, with an interesting enhancement of the cross section around 9 – 10 GeV. The local significance of the enhancement is approximately two standard deviations. In this mass range the production of the bottomonium states is possible, i.e. $\chi_{b0}(1P)$, $\chi_{b1}(1P)$, $\chi_{b2}(1P)$ (all have $I^G = 0^+$ and PC = ++ [5]).

The data were compared with the models available in form of MC generators. The MBR model implemented in Pythia does not reproduce the shape of the data. It predicts maximum of the cross section around 2.7 GeV, while data demonstrate maximum below 2 GeV. However, MBR reasonably well predicts the normalisation of the cross section above 2.7 GeV (note that in case of $2\pi^+2\pi^-$ the MBR predictions are not scaled on the plots, as it was for two-particle central states). Predictions from DiMe generator for $\rho\rho$ production (each ρ meson decaying to $\pi^+\pi^-$) are also shown for two values of the exponential form factors of the intermediate ρ meson: $\Lambda^2_{\text{exp}} = 1$ GeV^2 (green, this value was used for $\pi^+\pi^-$ and K^+K^- predictions) and $\Lambda^2_{\text{exp}} = 2.2$ GeV^2 (blue, default generator value). Predictions for Λ^2_{exp} equal to 1 GeV^2 and 2.2 GeV^2 are scaled by 100 and 5, respectively, for better visibility. It is worth to note a significant increase of the cross section with increased value of Λ^2_{exp}. For both studied values of Λ^2_{exp} the shapes of the predictions are much closer to data compared to MBR model. The position of the maximum of the cross section shifts toward higher masses with increased Λ^2_{exp} and is more consistent with data for larger of the two values.

The differential fiducial cross section as a function of rapidity of the central system, $d\sigma/dy$ is presented in Fig. 20.20b. Its shape is similar to that for the two pion system (Fig. 20.2b), but the distribution is narrower. Only DiMe predictions for $\rho\rho$ production with $\Lambda^2_{\text{exp}} = 2.2$ GeV^2 correctly reproduce the shape of the data. DiMe with lower value of Λ^2_{exp} and MBR model predict too narrow shape.

Figure 20.21a presents differential cross section as a function of $\Delta\varphi$ for CEP of four charged pions. The cross section is suppressed around $\Delta\varphi = 90^\circ$ due to the acceptance of ALFA detector (see discussion of Fig. 20.3b). The distribution is nearly symmetric with some small enhancement of the cross section at 180° compared to 0°. The shape of distribution is quite well described by the MBR model, which predicts symmetric distribution. The DiMe $\rho\rho$ prediction has the shape significantly different from data, with larger four-pion production cross section at $\Delta\varphi < 90^\circ$ due to the absorption effects, which stronger suppress cross section at $\Delta\varphi > 90^\circ$.

The differential fiducial cross section as a function of $|t_1 + t_2|$ is shown in Fig. 20.21b. The distribution reaches the maximum value at 0.25 GeV^2 and is sightly shifted towards higher values of $|t_1 + t_2|$ compared to the case of CEP of $\pi^+\pi^-$ pairs. All considered models fail to describe the shape of the cross section, predicting in general too small slopes. Both DiMe predictions present the same level of agreement with data, which is significantly better than MBR model predictions.

Similarly to mass spectra of two-particle central states, $d\sigma/dm$ for exclusively produced $2\pi^+2\pi^-$ were studied in two ranges of the azimuthal angle between forward-scattered protons. Figures 20.22a and 20.22b show the fiducial cross sections as a function of the invariant mass of four-pion system for $\Delta\varphi < 90^\circ$ and $\Delta\varphi > 90^\circ$, respectively. The cross sections in two $\Delta\varphi$ regions differ visibly up to

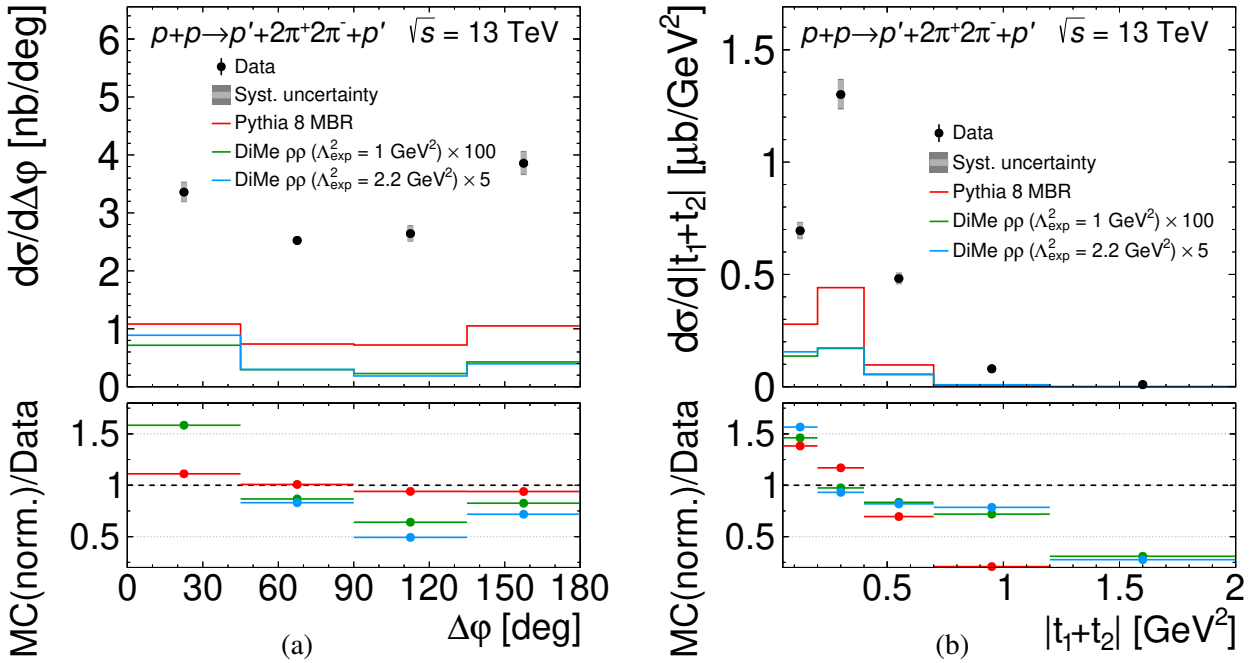

Figure 20.21: Differential cross sections for CEP of $2\pi^+2\pi^-$ states as a function of (a) $\Delta\varphi$ and (b) $|t_1 + t_2|$, measured at ATLAS in the fiducial region explained in the plots. Data are shown as solid points with error bars representing the statistical uncertainties. The typical systematic uncertainties are shown as dark/light grey boxes (with/without luminosity uncertainty included, respectively), for only a few data points as they are almost fully correlated between neighbouring bins. Predictions from two MC models, MBR and DiMe ($\rho\rho$), are shown as histograms. In the bottom panels, the ratios between the MC predictions (scaled to data) and the data are shown.

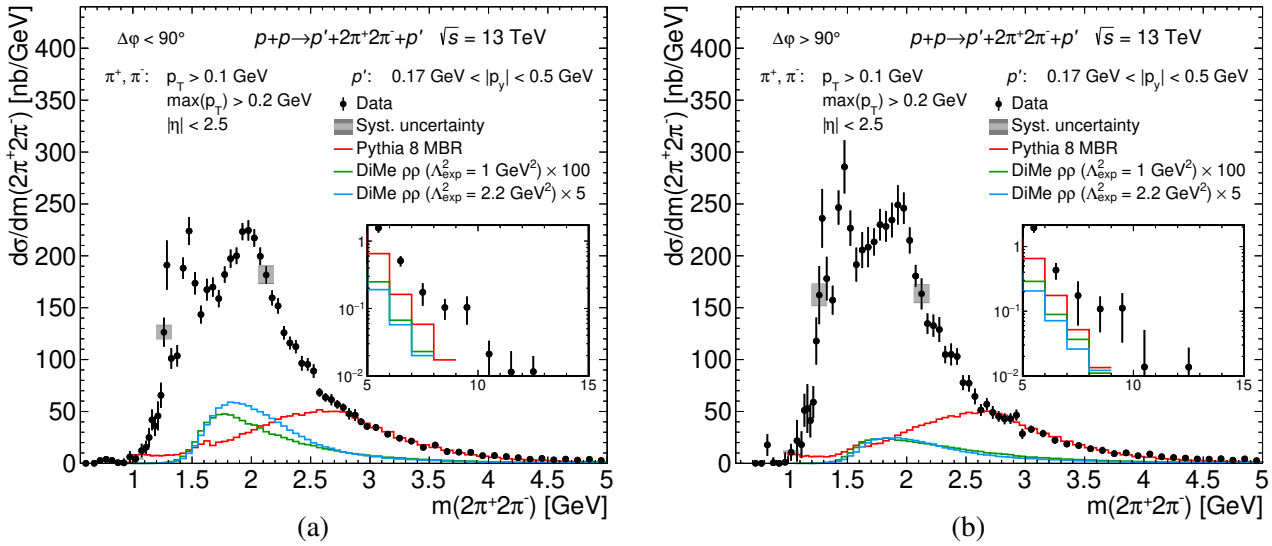

Figure 20.22: Differential cross sections for CEP of $2\pi^+2\pi^-$ states as a function of the invariant mass of the central state for two ranges of $\Delta\varphi$: (a) $\Delta\varphi < 90^\circ$ and (b) $\Delta\varphi > 90^\circ$, measured at ATLAS in the fiducial region explained in the plots. Data are shown as solid points with error bars representing the statistical uncertainties. The typical systematic uncertainties are shown as dark/light grey boxes (with/without luminosity uncertainty included, respectively), for only a few data points as they are almost fully correlated between neighbouring bins. Predictions from two MC models, MBR and DiMe ($\rho\rho$), are shown as histograms. Each plot contains an insert with the cross section drawn for high values of invariant mass of the central state (from 5 GeV to 15 GeV).

$\sim$ 2 GeV. Above 2 GeV, the distributions have similar shape and magnitude, while below this mass a few resonance structures are found. In the region of the $f_1(1285)$ resonance, the cross section is slightly larger at $\Delta\varphi > 90^\circ$, which is consistent with enhanced production of this state reported by WA102 experiment [212]. In the region of the $f_0(1500)$ resonance, the cross section and prominence of structures (peak followed by a dip) is also slightly larger for $\Delta\varphi > 90^\circ$. The maximum around 2 GeV is narrower in the $\Delta\varphi < 90^\circ$ range.

The MBR predictions fail to describe $d\sigma/dm$ in both $\Delta\varphi$ regions up to the mass of $\sim$ 2.7 GeV, but above the cross sections are reasonably well reproduced. The DiMe model of $\rho\rho$ production predicts higher cross section in the $\Delta\varphi < 90^\circ$ range, what is not supported by data. However, the shape of the tail of the spectrum in the high mass range is reasonably well described by DiMe.

Significant statistics of selected sample of exclusively produced four charged pions enabled more detailed studies. For selected observables (y, $\Delta\varphi$, $|t_1+t_2|$), the differential cross sections were calculated in three separate regions of the invariant mass of four pions: $m < 1.5$ GeV (the lowest mass range with significant resonance structures), 1.5 GeV $< m <$ 2.5 GeV (moderate masses, transition between resonance region and smooth decrease of the cross section) and $m > 2.5$ GeV (high mass region void of structures in the mass spectrum). Figure 20.23 presents the differential cross sections, $d\sigma/dy$ (left column), $d\sigma/d\Delta\varphi$ (middle column) and $d\sigma/d|t_1 + t_2|$ (right column) in the above three mass ranges.

The differential cross section as a function of rapidity of the central system demonstrates some structures in the region $|y| < 1.5$ in the lowest mass bin (Fig. 20.23, top left). It cannot be ruled out that statistical fluctuations are the source of these structures. The are no similar structures visible in the higher mass bins. In the highest mass bin, the cross section has much narrower shape compared to the lower mass bins. MC models do not predict the observed structures in the rapidity distribution in the lowest mass bin, as well as they are unable to describe the shape of rapidity-dependent cross section except the DiMe $\rho\rho$ in the mass range 1.5 GeV $< m <$ 2.5 GeV.

In case of the differential cross section as a function of $\Delta\varphi$, the data show enhanced cross section for exclusive four-pion production at $\Delta\varphi > 90^\circ$ in the lowest mass region (the same as WA102 reported for $f_1(1285)$ production [212]), nearly symmetric cross section in the moderate mass region, and slightly higher cross section at $\Delta\varphi < 90^\circ$ in the highest mass region. Model predictions generally fail to describe the shape of the cross section, except MBR model for the masses above 1.5 GeV.

The sum of squared four-momentum transfers in proton vertices has similar shape in all three mass ranges, except possible lower slope of $d\sigma/d|t_1 + t_2|$ in the lowest mass range. The DiMe MC predicts the shape most consistent with data, although still with the slope larger than observed experimentally.

CEP of four charged pions can proceed in several ways, through e.g. continuum (e.g. triple Pomeron exchange [65]), production of two resonances, each decaying to $\pi^+\pi^-$ (e.g. $\rho\rho$), or production of a single resonance that decays to $\pi^+\pi^-\pi^+\pi^-$. To help uncover the production mechanisms, two pairs of opposite-charge pions were selected from the four central-state pions. In general, two neutral pair combinations are possible. To resolve ambiguity, such combination of pion pairs was chosen, that provides the largest difference of p_T's of the two $\pi^+\pi^-$ pairs (in the laboratory frame). Figure 20.24 shows the differential cross section as a function of the lower (Fig. 20.24a) and higher (Fig. 20.24b) mass of two $\pi^+\pi^-$ pairs. The first distribution (Fig. 20.24a) starts at the two-pion production threshold with a cross section equal to its maximum value of about 1 μb/GeV, and remains constant up to 0.75 GeV. Above this mass the cross section falls rapidly, with some small enhancement of the cross section around $f_2(1270)$. The second distribution (Fig. 20.24b) starts at the two-pion production

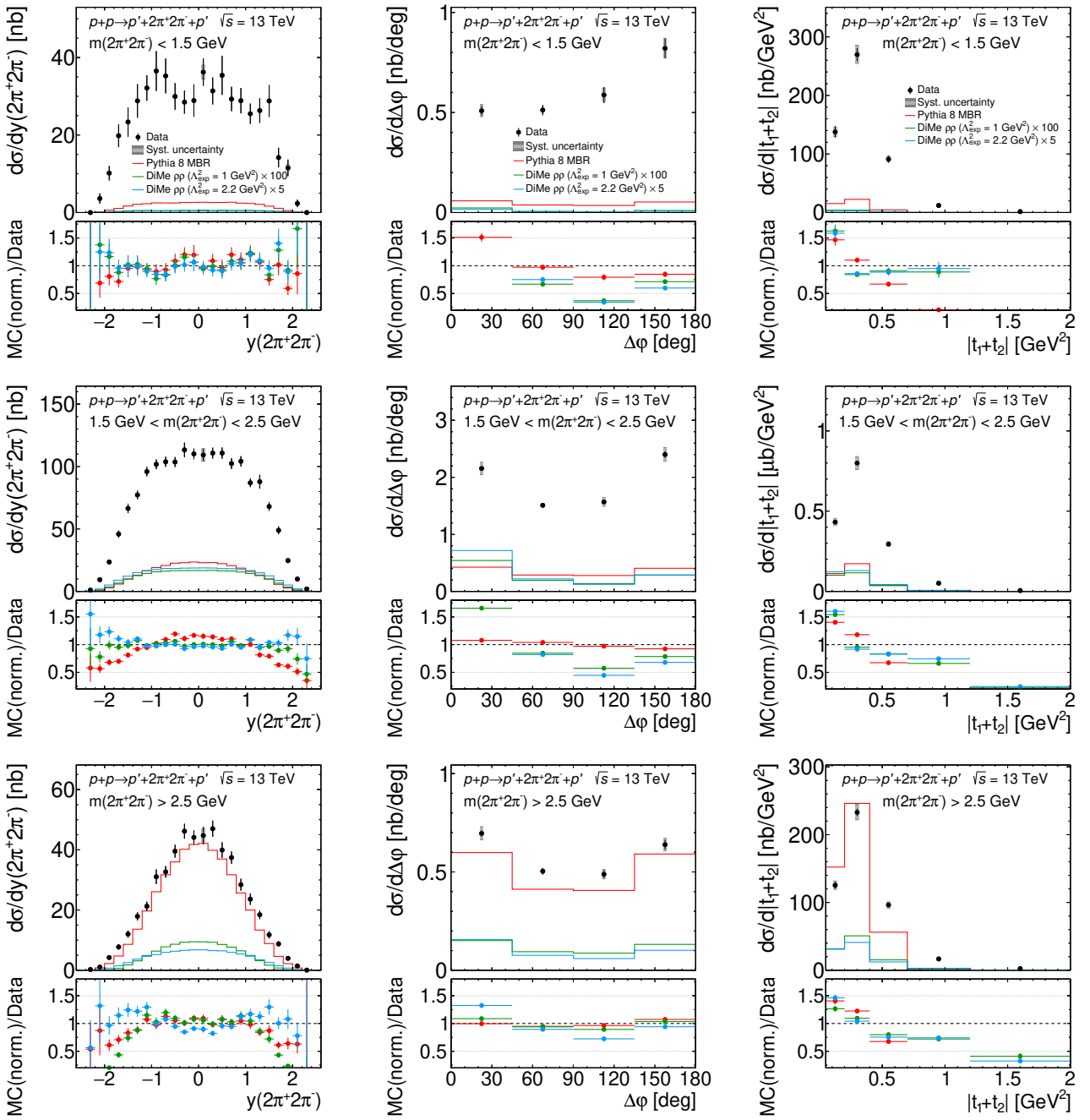

Figure 20.23: Differential cross sections for CEP of $2\pi^+2\pi^-$ states as a function of the rapidity of the central state (left column), difference of azimuthal angles of the forward-scattered protons (middle column) and of the sum of the squared four-momenta transfers in the proton vertices (right column) measured in the fiducial region explained on the plots, separately for three ranges of the central state invariant mass: $m < 1.5$ GeV (top), 1.5 GeV $< m <$ 2.5 GeV (middle) and $m >$ 2.5 GeV (bottom). Data are shown as solid points with error bars representing the statistical uncertainties. The typical systematic uncertainties are shown as grey boxes for only few data points as they are almost fully correlated between neighbouring bins. Predictions from two MC models, DiMe ($\rho\rho$) and MBR are shown as histograms. In the bottom panels, the ratios of the MC predictions (scaled to data) and the data are shown.

threshold with a cross section value being approximately one-half of the maximum value observed around 0.8 GeV. The peak position agrees with the ρ meson. Above the peak mass the distribution falls steadily, although another resonance structure is visible in the $f_2(1270)$ mass region.

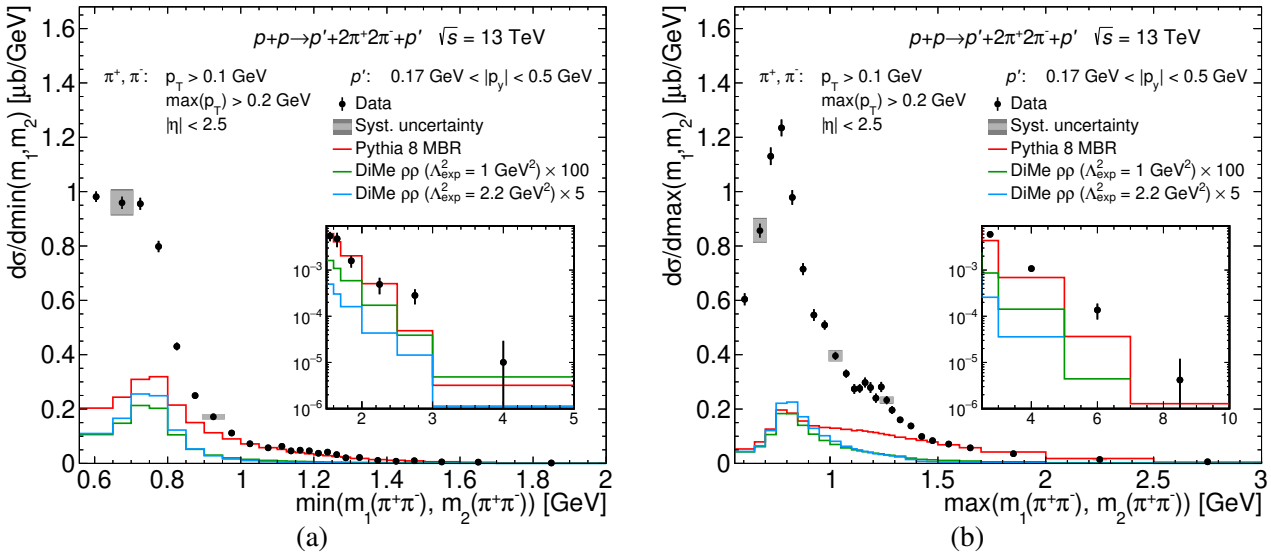

(a) (b)

Figure 20.24: Differential cross sections for CEP of $2\pi^+2\pi^-$ states as a function of the (a) lower and (b) higher invariant mass of the possible $\pi^+\pi^-$ pairs' combinations, measured at ATLAS in the fiducial region explained in the plots. Data are shown as solid points with error bars representing the statistical uncertainties. The typical systematic uncertainties are shown as dark/light grey boxes (with/without luminosity uncertainty included, respectively), for only a few data points as they are almost fully correlated between neighbouring bins. Predictions from two MC models, MBR and DiMe ($\rho\rho$), are shown as histograms. Each plot contain an insert with the cross section drawn for high values of invariant mass of $\pi^+\pi^-$.

The MBR model implemented in Pythia does not reproduce the shape of distributions described in the previous paragraph. DiMe prediction for $\rho\rho$ production also fails to describe the shape of data, although there are notable similarities between structures visible in data and MC predictions (i.e. maxima around the ρ mass). It suggests, that there is a non-negligible contribution to CEP of four charged pions from double ρ meson production. However, the maximum of the two-pion spectrum below 1 GeV is also expected in the triple Pomeron exchange mechanism [65]. All MC predictions underestimate the relative content of the cross section below the ρ meson mass, which might indicate some contribution to $2(\pi^+\pi^-)$ production from $\sigma\sigma$[1]. Studies of such production mode can be found in Ref. [69], where authors consider both $\rho\rho$ and $\sigma\sigma$ mechanism and suggest that for the fiducial region defined similarly to this analysis, cross section for $\sigma\sigma$ production is approximately two times larger than for $\rho\rho$ (neglecting absorption effects).

20.2.2 Exclusive production of $3\pi^+3\pi^-$ states

Several differential fiducial cross sections for the CEP of six charged pions ($3\pi^+3\pi^-$) have been also measured. In Fig. 20.25 the measured cross sections as functions of the invariant mass and rapidity of the central system are compared to Pythia 8 MC predictions. The cross section as a function of invariant mass starts around 2 GeV, reaches maximum around 2.5 GeV and steadily falls below 1 nb/GeV around 10 GeV. Pythia correctly predicts the integrated cross section. However, the maximum of the mass distribution in Pythia is shifted toward higher masses. In case of the $d\sigma/dy$, the distribution has no specific features and is similar to $d\sigma/dy$ for four pions (Fig. 20.20b), although notably narrower. The MBR model in Pythia does not reproduce the shape, which is significantly narrower than in the data.

[1] σ is used here as an alternative (historical) name of $f_0(500)$, like e.g. in Ref. [69].

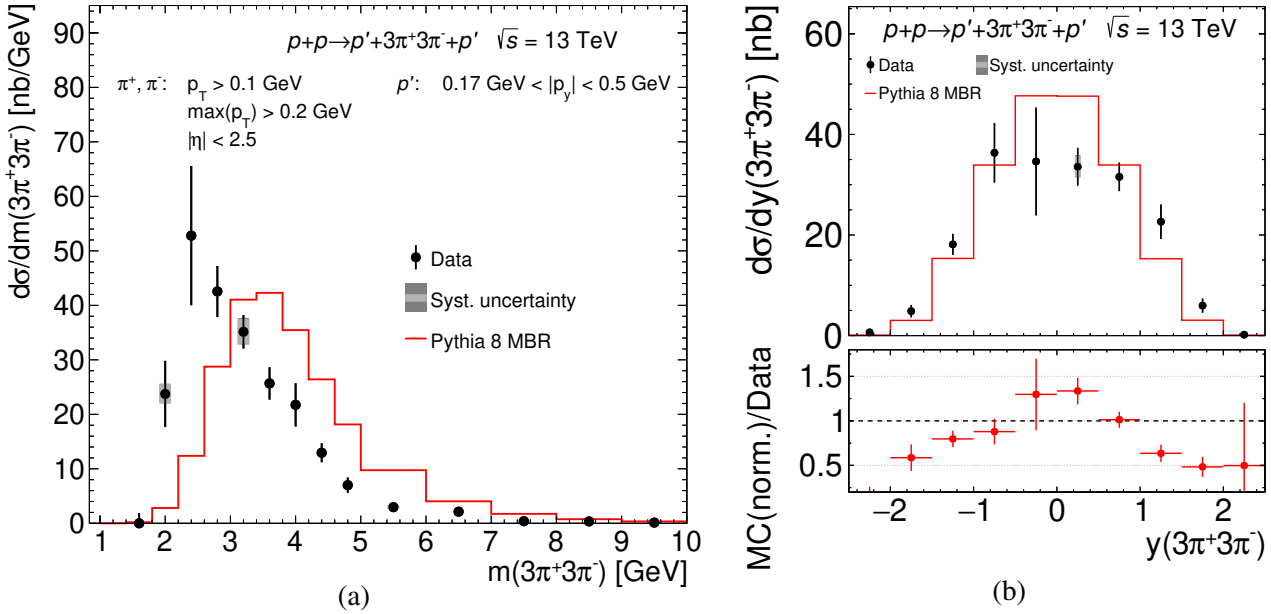

(a) (b)

Figure 20.25: Differential cross sections for CEP of $3(\pi^+\pi^-)$ as a function of the (a) invariant mass and (b) rapidity of the central state, measured at ATLAS in the fiducial region explained in the plots. Data are shown as solid points with error bars representing the statistical uncertainties. The typical systematic uncertainties are shown as dark/light grey boxes (with/without luminosity uncertainty included, respectively), for only a few data points as they are almost fully correlated between neighbouring bins. Predictions from MBR model are shown as histograms. In the bottom panel of (b) the ratio between the MC prediction (scaled to data) and the data is shown.

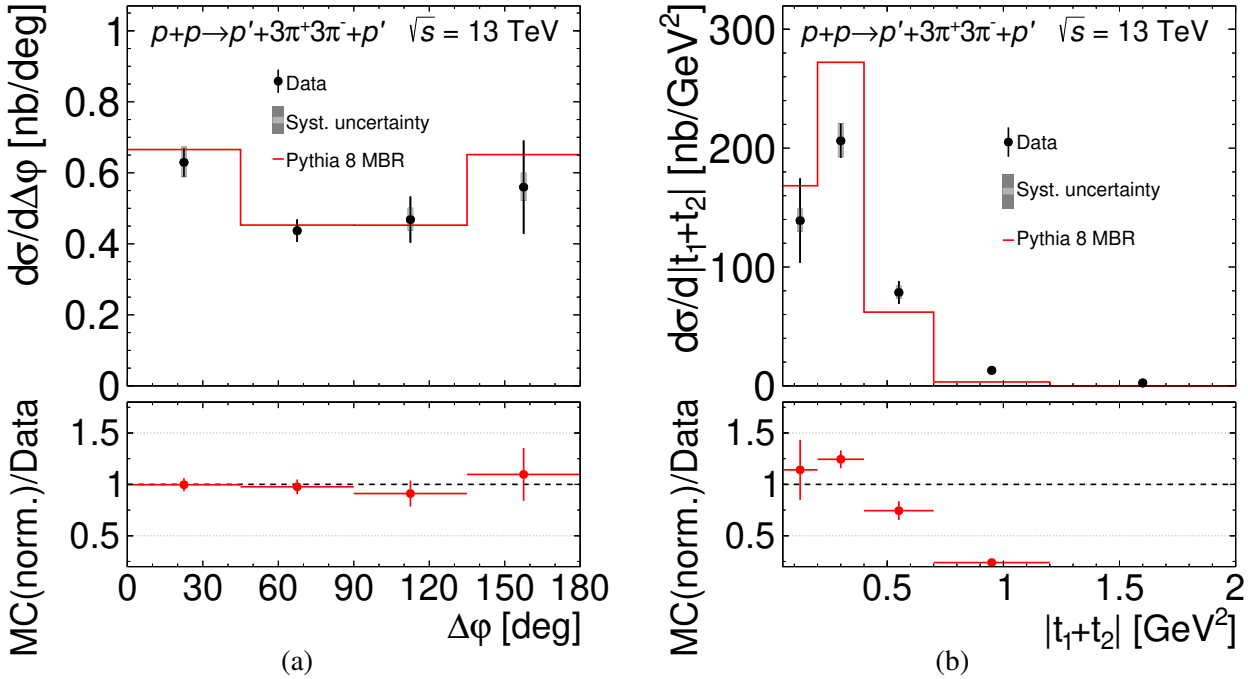

(a) (b)

Figure 20.26: Differential cross sections for CEP of $3(\pi^+\pi^-)$ as a function of (a) $\Delta\varphi$ and (b) $|t_1 + t_2|$, measured at ATLAS in the fiducial region explained in the plots. Data are shown as solid points with error bars representing the statistical uncertainties. The typical systematic uncertainties are shown as dark/light grey boxes (with/without luminosity uncertainty included, respectively), for only a few data points as they are almost fully correlated between neighbouring bins. Predictions from MBR model are shown as histograms. In the bottom panels, the ratios between the MC predictions (scaled to data) and the data are shown.

In Fig. 20.26a the differential fiducial cross section as a function of the azimuthal angle between the forward-scattered protons is shown. The measured distribution is similar to that for four pions (Fig. 20.21a), symmetric around $\Delta\varphi = 90^\circ$ and well described by Pythia.

The differential cross section as a function of the sum of the four-momenta transfers squared at proton vertices, $d\sigma/d|t_1 + t_2|$, is shown in Fig. 20.26b. The distribution is also similar to that for four pions (Fig. 20.21b), and Pythia predicts larger-than-measured slope of the distribution.

20.2.3 Exclusive production of $4\pi^+4\pi^-$ states

In this section, possibly the highest multiplicity of pion pairs, $4(\pi^+\pi^-)$, in the CEP final state, studied so far[2], is presented. Detected events may originate from the production of $f_0(1500)f_0(1500)$ central state, with both f_0s decaying to four pions. However this hypothesis needs further study. Differential fiducial cross sections for the CEP of $4\pi^+4\pi^-$ states are shown as a function of the invariant mass and rapidity of the central system in Fig. 20.27. The mass distribution peaks around 4 GeV, while predictions from Pythia, which are approximately factor of five lower than data, have maximum at 5 GeV. The rapidity distribution in the data is wider compared to Pythia predictions, similarly as for the case of CEP of $3\pi^+3\pi^-$ states.

The differential fiducial cross sections as functions of observables characterising the forward-scattered protons, $\Delta\varphi$ and $|t_1 + t_2|$, are shown in Fig. 20.28. Within the statistical uncertainties, the $\Delta\varphi$

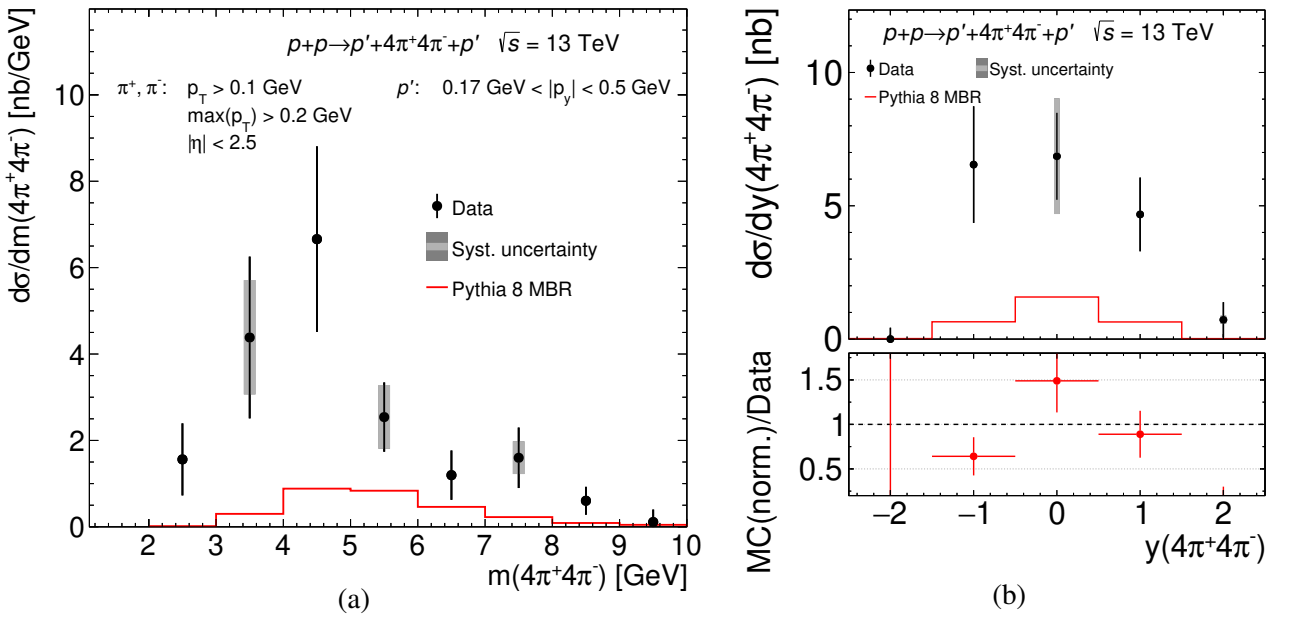

Figure 20.27: Differential cross sections for CEP of $4(\pi^+\pi^-)$ as a function of the (a) invariant mass and (b) rapidity of the central state, measured at ATLAS in the fiducial region explained in the plots. Data are shown as solid points with error bars representing the statistical uncertainties. The typical systematic uncertainties are shown as dark/light grey boxes (with/without luminosity uncertainty included, respectively), for only a few data points as they are almost fully correlated between neighbouring bins. Predictions from MBR model are shown as histograms. In the bottom panel of (b) the ratio between the MC prediction (scaled to data) and the data is shown.

[2] Author has not found in the literature any results on such high multiplicity measured in an exclusive process.

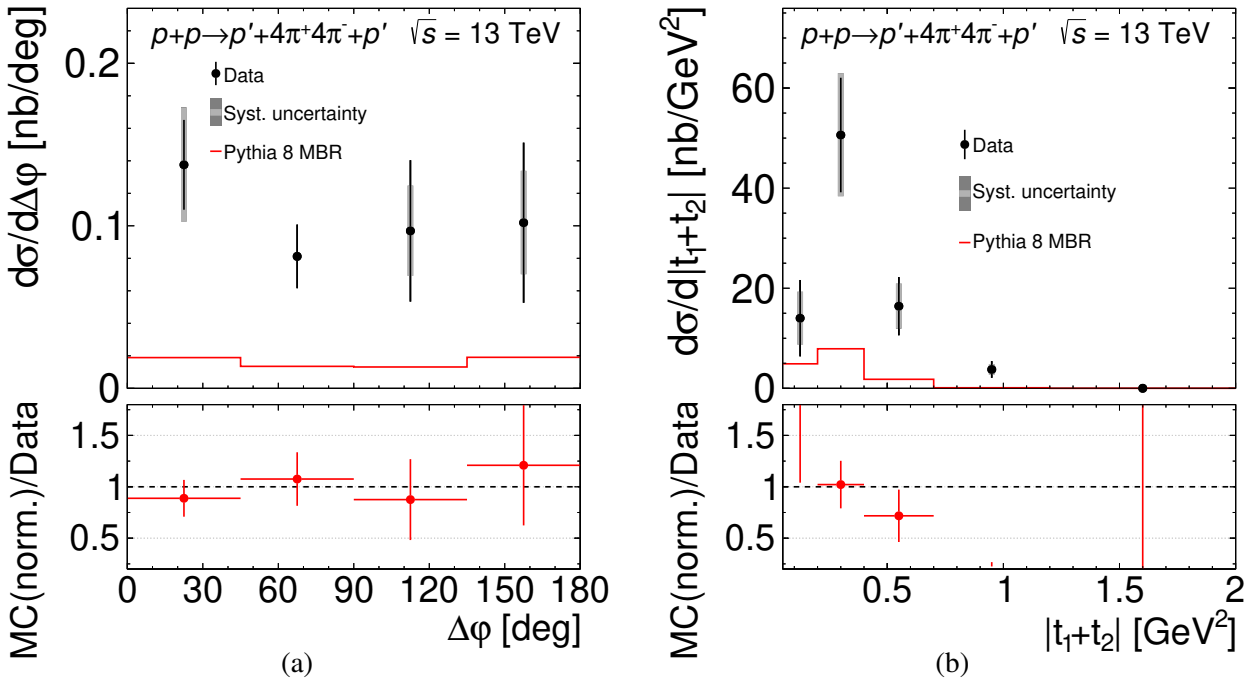

Figure 20.28: Differential cross sections for CEP of $4(\pi^+\pi^-)$ as a function of (a) $\Delta\varphi$ and (b) $|t_1 + t_2|$, measured at ATLAS in the fiducial region explained in the plots. Data are shown as solid points with error bars representing the statistical uncertainties. The typical systematic uncertainties are shown as dark/light grey boxes (with/without luminosity uncertainty included, respectively), for only a few data points as they are almost fully correlated between neighbouring bins. Predictions from MBR model are shown as histograms. In the bottom panels, the ratios between the MC predictions (scaled to data) and the data are shown.

distribution is symmetric around $\Delta\varphi = 90^\circ$ and its shape is consistent with the MBR model predictions. The $|t_1 + t_2|$ distribution is similar to that for six pions and has a slope smaller than predicted by the MBR model implemented in Pythia.

20.3 Integrated fiducial cross sections

In addition to differential fiducial cross sections presented in preceding sections, the integrated fiducial cross sections were calculated. The values were provided separately for two ranges of azimuthal angle between forward-scattered protons, $\Delta\varphi < 90^\circ$ and $\Delta\varphi > 90^\circ$, for all studied mid-rapidity systems. The results are jointly presented in Tab. 20.1.

			$\sigma_{\text{fid}} \pm \delta_{\text{stat}} \pm \delta_{\text{syst}}$	
$\sqrt{s}$	**Particle species**	**unit**	$\Delta\varphi < 90^\circ$	$\Delta\varphi > 90^\circ$
200 GeV	$\pi^+\pi^-$	**nb**	$44.1 \pm 0.2^{+4.6}_{-4.2}$	$21.1 \pm 0.2^{+2.1}_{-1.9}$
	K^+K^-	**pb**	$1087 \pm 57^{+151}_{-173}$	$568 \pm 42^{+85}_{-92}$
	$p\bar{p}$	**pb**	$17.4 \pm 4.7^{+2.9}_{-2.7}$	$31.8 \pm 6.2^{+4.7}_{-4.2}$
13 TeV	$\pi^+\pi^-$	**µb**	$2.089 \pm 0.003^{+0.071}_{-0.067}$	$1.565 \pm 0.005^{+0.055}_{-0.051}$
	$2\pi^+2\pi^-$	**nb**	$265 \pm 3^{+14}_{-13}$	$293 \pm 5^{+16}_{-15}$
	$3\pi^+3\pi^-$	**nb**	$48.0 \pm 2.3^{+3.3}_{-3.1}$	$46.3 \pm 6.5^{+3.3}_{-3.0}$
	$4\pi^+4\pi^-$	**nb**	$9.8 \pm 1.5 \pm 2.5$	$8.9 \pm 3.0 \pm 2.7$

Table 20.1: Integrated fiducial cross sections for CEP of all analysed central systems and in two ranges of azimuthal angle difference $\Delta\varphi$ between forward-scattered protons. Statistical and systematic uncertainties are provided for each cross section.

21. Modelling of the invariant mass spectrum

21.1 Exclusive production of $\pi^+\pi^-$ pairs

In this section, an attempt to fit the extrapolated differential cross section with a simplified model of the $\pi^+\pi^-$ invariant mass spectrum is presented. Details on the extrapolation of the fiducial cross section to the Lorentz invariant cross section are given in Sec. 11.9. Only the STAR data were modelled due to limited time resources, which were utilised to perform modelling of the invariant mass spectrum of exclusively produced $2\pi^+2\pi^-$ states measured in ATLAS (next section). Qualitative similarities between the fiducial cross sections for CEP of $\pi^+\pi^-$ pairs from STAR and ATLAS suggest, that conclusions from the described modelling are also applicable to ATLAS data.

The cross sections presented in this section are given in the kinematic range of $|y(\pi^+\pi^-)| < 0.4$ and $0.05\ \text{GeV}^2 < -t_1, -t_2 < 0.16\ \text{GeV}^2$ and in two intervals of $\Delta\varphi$: $\Delta\varphi < 45^\circ$ and $\Delta\varphi > 135^\circ$. The fitted invariant mass model includes contributions from the direct (non-resonant) $\pi^+\pi^-$ pair production as well as from the three resonances, $f_0(980)$, $f_2(1270)$ and $f_0(1500)$, in the mass range of 0.6 – 1.7 GeV. It is important to note, that in the fit only $f_2(1270)$ mass and width were fixed to the PDG values. For the other two resonances, the masses and widths were left free, however their fitted masses and widths turned out to be compatible with $f_0(980)$ and $f_0(1500)$ mesons, therefore such labelling is used here from the very beginning.

The total amplitude for the exclusive $\pi^+\pi^-$ production is given by:

$$\begin{aligned} A(m) = A_{\text{cont}} \times f_{\text{cont}}(m) + \\ \sqrt{\sigma_{f_0(980)}} \times \exp\left(i\phi_{f_0(980)}\right) \times \mathcal{R}_{\text{F}}\left(m; M_{f_0(980)}, \Gamma_{0,f_0(980)}\right) + \\ \sqrt{\sigma_{f_2(1270)}} \times \exp\left(i\phi_{f_2(1270)}\right) \times \mathcal{R}_{\text{BW}}\left(m; M_{f_2(1270)}, \Gamma_{0,f_2(1270)}\right) + \\ \sqrt{\sigma_{f_0(1500)}} \times \exp\left(i\phi_{f_0(1500)}\right) \times \mathcal{R}_{\text{BW}}\left(m; M_{f_0(1500)}, \Gamma_{0,f_0(1500)}\right). \end{aligned} \tag{21.1}$$

Thus all states are added coherently and could interfere with each other. The amplitude for continuum production was chosen to be real, while the amplitudes for the production cross sections for resonances in the $\pi^+\pi^-$ channel were allowed to have non-zero phase shifts, ϕ. The shape of the continuum amplitude in the fitted mass range was assumed to have the form

$$f_{\text{cont}}(m) = \sqrt{\frac{q}{m}} \times \exp\left[-\frac{B}{2} \cdot q\right], \tag{21.2}$$

with the break-up momentum $q(m) = \frac{1}{2}\sqrt{m^2 - 4m_\pi^2}$. This continuum effectively includes the production of other wide resonant states, e.g. $f_0(500)$, with a phase of amplitude slowly varying within the fit range, as described below in the discussion of the fit result. For the $f_2(1270)$ and $f_0(1500)$ resonances, the relativistic Breit-Wigner form of the production amplitude with mass-dependent width was used:

$$\mathcal{R}_{\text{BW}}(m; M, \Gamma_0) = \frac{1}{\sqrt{\mathcal{I}}} \times \frac{M\sqrt{\Gamma_0}\sqrt{\Gamma(m)}}{M^2 - m^2 - iM\Gamma(m)}, \qquad \Gamma(m) = \Gamma_0 \frac{q}{m}\frac{M}{q_0}\left(\frac{B_J(q^2R^2)}{B_J(q_0^2R^2)}\right)^2. \tag{21.3}$$

A factor $\mathcal{I}$ was introduced to provide proper normalisation, $\int_{2m_\pi}^{+\infty} dm\,|\mathcal{R}_{\text{BW}}|^2 = 1$. As a result, the total cross sections, $\sigma_{f_0(980)}$, $\sigma_{f_2(1270)}$ and $\sigma_{f_0(1500)}$, for resonance production (in the $\pi^+\pi^-$ channel) were

directly obtained from the fit. The centrifugal effects were accounted for in Eq. (21.3) through the Blatt-Weisskopf barrier factors, B_J [213, 214], with the empirical interaction radius, R, set to 1 fm and $q_0 = q(M)$. $J = 2$ and $J = 0$ were used for $f_2(1270)$ and $f_0(1500)$, respectively.

The $f_0(980)$ meson requires a different treatment due to the large branching ratio to the $K\bar{K}$ channel, which opens in the vicinity of the mass peak. This changes the resonance shape and was accounted for in the parameterisation of the amplitude via the Flatté formula [215]:

$$\mathcal{R}_{\mathrm{F}}(m; M, \Gamma_0) = \frac{1}{\sqrt{\mathcal{I}}} \times \frac{M\sqrt{\Gamma_0}\sqrt{\Gamma_\pi(m)}}{M^2 - m^2 - iM\left(\Gamma_\pi(m) + \Gamma_K(m)\right)}. \tag{21.4}$$

The partial widths, Γ_j ($j = \pi, K$), are described by the product of the coupling parameter g_j and the break-up momentum q_j for particle j:

$$\Gamma_j(m) = g_j q_j(m) = \frac{g_j}{2}\sqrt{m^2 - 4m_j^2}. \tag{21.5}$$

$\Gamma_0 \equiv \Gamma_\pi(M)$ is the partial width in the $\pi^+\pi^-$ channel at the resonance mass. In the fit, the ratio g_K/g_π was fixed to 4.21, the value well-constrained experimentally through the measurement of J/ψ decays into ϕ mesons and $\pi^+\pi^-/K^+K^-$ pairs [216].

To fit model parameters to the data, the binning in the invariant mass distribution required adjustment to the expected structures in the cross section. Therefore, a narrower binning than for the measurement of the fiducial cross section was introduced, and the impact of detector resolution was taken into account in the fit. The squared amplitude from Eq. (21.1), $|A|^2$, was convoluted for the purpose of the fit with the normal distribution, $\mathcal{N}(0, \sigma_{\mathrm{res}})$, representing the finite measurement resolution of the invariant mass of the pion pair. The resolution parameter, $\sigma_{\mathrm{res}}(m)$, was provided to the fitting algorithm; it was set to grow linearly with increasing invariant mass according to MC simulation of the STAR TPC detector. The $m(\pi^+\pi^-)$ resolution at the lower and upper limit of the fit range is equal to 4 MeV and 13 MeV, respectively (see Fig. 11.32a). The final form of the function fitted to the extrapolated $d\sigma/dm(\pi^+\pi^-)$ distribution was given by the convolution of the total amplitude squared with the normal distribution:

$$\mathcal{F}(m) = \left(|A|^2 \otimes \mathcal{N}\left(0, \sigma_{\mathrm{res}}\right)\right)(m) = \int_{2m_\pi}^{+\infty} dm'\, \mathcal{N}\left(m' - m; 0, \sigma_{\mathrm{res}}(m')\right) |A(m')|^2. \tag{21.6}$$

The fitting was performed using the Minuit2 toolkit [217] within the ROOT analysis software [218]. The standardly-defined χ^2 was minimised simultaneously in two $\Delta\varphi$ ranges. For each of the two f_0 resonances the fitted values of mass and width in the two $\Delta\varphi$ subsets were forced to be equal, while the phases and absolute values of amplitudes of all resonances were left independent. The mass and width of the $f_2(1270)$ resonance was fixed to the well-known Particle Data Group values [5].

The experimental systematic uncertainties of the model parameters were estimated through the independent fits to the extrapolated $d\sigma/dm(\pi^+\pi^-)$ distributions with each of the systematic variations described in Chap. 12 applied. In addition to this, the sensitivity of the fit result to the modelling of the extrapolation to the full kinematic region was taken into consideration. The effect of the extrapolation to the full solid angle in the $\pi^+\pi^-$ rest frame was checked, assuming a smooth transition from the angular distributions for pure S_0-wave (up to 1 GeV) to the angular distributions for pure D_0-wave

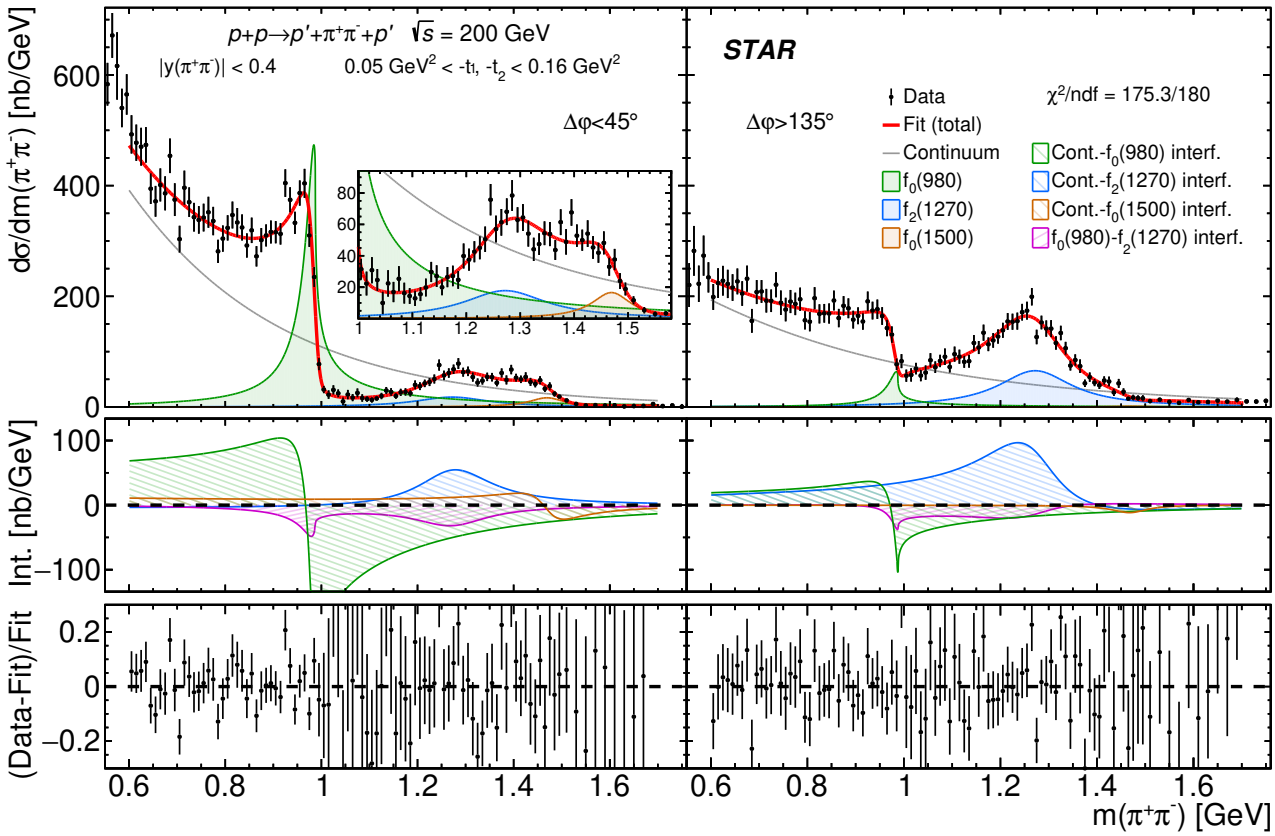

Figure 21.1: Differential cross section $d\sigma/dm(\pi^+\pi^-)$ extrapolated from the fiducial region to the Lorentz-invariant phase space given by the central-state rapidity, $|y(\pi^+\pi^-)| < 0.4$, and squared four-momentum transferred in forward proton vertices, $0.05\,\mathrm{GeV}^2 < -t_1, -t_2 < 0.16\,\mathrm{GeV}^2$. The left and right columns show the cross sections for $\Delta\varphi < 45^\circ$ and $\Delta\varphi > 135^\circ$, respectively. The data are shown as black points with error bars representing statistical uncertainties. The result of the fit, $\mathcal{F}(m)$, is drawn with a solid red line. The squared amplitudes for the continuum and resonance production are drawn with lines of different colours, as explained in the legend. The most significant interference terms are plotted in the middle panels, while the relative differences between each data point and the fitted model is shown in the bottom panels.

(starting at 1.2 GeV). The effect of using the extrapolation calculated with predictions from the DiMe and GenEx generators was also checked, both for the central state and for the forward-scattered protons. The result of the fit with the ratio g_K/g_π varied within its uncertainties was also checked. The systematic uncertainty on a parameter was separated into two parts. The first one is related to the experimental uncertainties and was calculated as the quadratic sum of the differences between the nominal fit result and the result of the fit to $d\sigma/dm(\pi^+\pi^-)$ with each systematic effect. The second part is related to the extrapolation and is quoted as the largest deviation from the nominal result.

The extrapolated cross sections are shown in Fig. 21.1, together with the result of the fit described above. The model parameters providing the minimum χ^2 are listed in Tab. 21.1. The fit, with a total of 20 free parameters, gives $\chi^2/\mathrm{ndf} = 175/180$ which shows that the data and the model are in excellent agreement in the fit region. Fits to $d\sigma/dm(\pi^+\pi^-)$ extrapolated using alternative geometrical acceptance corrections (see Sec. 11.9) show a similar quality, although some parameters change significantly as can be noted from the model-related uncertainties in Tab. 21.1[1]. The fitted model shows a small deviation

[1] A remark should be made, that authors of analysis from Ref. [107] did not correct the cross section for limited

		unit	$\Delta\varphi < 45^\circ$				$\Delta\varphi > 135^\circ$			
Continuum	A	$(\text{nb/GeV})^{\frac{1}{2}}$	69	± 5	± 4	$^{+1}_{-12}$	39	± 3	± 3	$^{+2}_{-10}$
	B	GeV^{-1}	6.4	± 0.4	± 0.1	$^{+0.1}_{-0.9}$	4.7	± 0.3	± 0.2	$^{+0.2}_{-1.1}$
$f_0(980)$	σ	nb	43.3	± 4.7	$^{+4.6}_{-4.1}$	$^{+2.7}_{-4.4}$	5.8	± 1.0	$^{+0.6}_{-0.5}$	$^{+0.3}_{-1.7}$
	ϕ	rad	0.66	± 0.08	$^{+0.01}_{-0.02}$	$^{+0.02}_{-0.06}$	0.56	± 0.10	± 0.01	$^{+0.01}_{-0.09}$
	M	MeV	$956 \pm 7 \pm 1\ ^{+4}_{-6}$							
	Γ_0	MeV	$163 \pm 26 \pm 3\ ^{+17}_{-20}$							
$f_2(1270)$	σ	nb	4.9	± 1.1	$^{+0.6}_{-0.5}$	$^{+0.3}_{-2.0}$	17.9	± 1.6	$^{+1.9}_{-1.7}$	$^{+0.2}_{-5.2}$
	ϕ	rad	-1.83	± 0.12	± 0.01	$^{+0.03}_{-0.12}$	-0.92	± 0.05	± 0.03	$^{+0.06}_{-0.23}$
$f_0(1500)$	σ	nb	2.3	± 0.5	± 0.2	$^{+1.1}_{-0.7}$	0.2	± 0.1	± 0.0	$^{+0.1}_{-0.0}$
	ϕ	rad	0.16	± 0.17	$^{+0.04}_{-0.03}$	$^{+0.04}_{-0.15}$	1.59	± 0.31	± 0.04	$^{+0.04}_{-0.07}$
	M	MeV	$1469 \pm 9 \pm 1 \pm 2$							
	Γ_0	MeV	$89 \pm 14 \pm 2\ ^{+4}_{-3}$							

Table 21.1: Results of the fit described in the text and visualised in Fig. 21.1, in two ranges of azimuthal angle difference $\Delta\varphi$ between forward-scattered protons. Statistical, systematic and model uncertainties are provided for each parameter.

from the extrapolated data around 1.37 GeV. This might result from the presence of the $f_0(1370)$, however the inclusion of the $f_0(1370)$ is not necessary to describe the data. The cross section for $f_0(1500)$ production differs from zero by 5 and 2 standard deviations in the $\Delta\varphi < 45^\circ$ and $\Delta\varphi > 135^\circ$ regions, respectively. Removing the $f_0(1500)$ from the fit makes the χ^2/ndf change to 352/186, a 7.0 standard-deviation effect (Fig. 21.2). From this, one infers that the shape of $d\sigma/dm(\pi^+\pi^-)$ around 1.4 – 1.6 GeV, the high-mass part of the $f_2(1270)$ region, is primarily determined by the $f_0(1500)$ interfering with $\pi^+\pi^-$ continuum.

Since the masses and widths of the $f_0(980)$ and the $f_0(1500)$ are free parameters, one can compare their fitted values with the PDG data [5]. In the case of the $f_0(980)$, the mass and width are found to be $M_{f_0(980)} = 956 \pm 7(\text{stat.}) \pm 1(\text{syst.})\ ^{+4}_{-6}(\text{mod.})$ MeV and $\Gamma_{0,f_0(980)} = 163 \pm 26(\text{stat.}) \pm 3(\text{syst.})\ ^{+17}_{-20}(\text{mod.})$ MeV, respectively. These values differ from the PDG estimates of mass (990 ± 20 MeV) and width (from 10 MeV to 100 MeV). However, the PDG emphasises a strong dependence of the resonance parameters on the model of the amplitude. Some measurements listed in Ref. [5] are in reasonable agreement with our measured numbers. In addition to this, the mass and width of the $f_0(980)$ resulting from the fit with the Breit-Wigner form (instead of the Flatté form) of the amplitude (Fig. 21.3) gives $M_{f_0(980)} = 974 \pm 1(\text{stat.}) \pm 1(\text{syst.})$ MeV and $\Gamma_{0,f_0(980)} = 65 \pm 3(\text{stat.}) \pm 1(\text{syst.})$ MeV (albeit with a notably worse χ^2/ndf of 226/180 providing evidence for a significant branching fraction for the decay into $K\bar{K}$, which needs to be accounted for in the resonance parameterisation). These values are in excellent agreement with PDG estimates and $f_0(980)$ parameters from other measurements that assume

geometrical acceptance (limited p_T and η) before fitting the mass spectrum in a broad range of invariant masses, which is incorrect and introduces systematic error to results of the fit. In particular, the cross sections are underestimated.

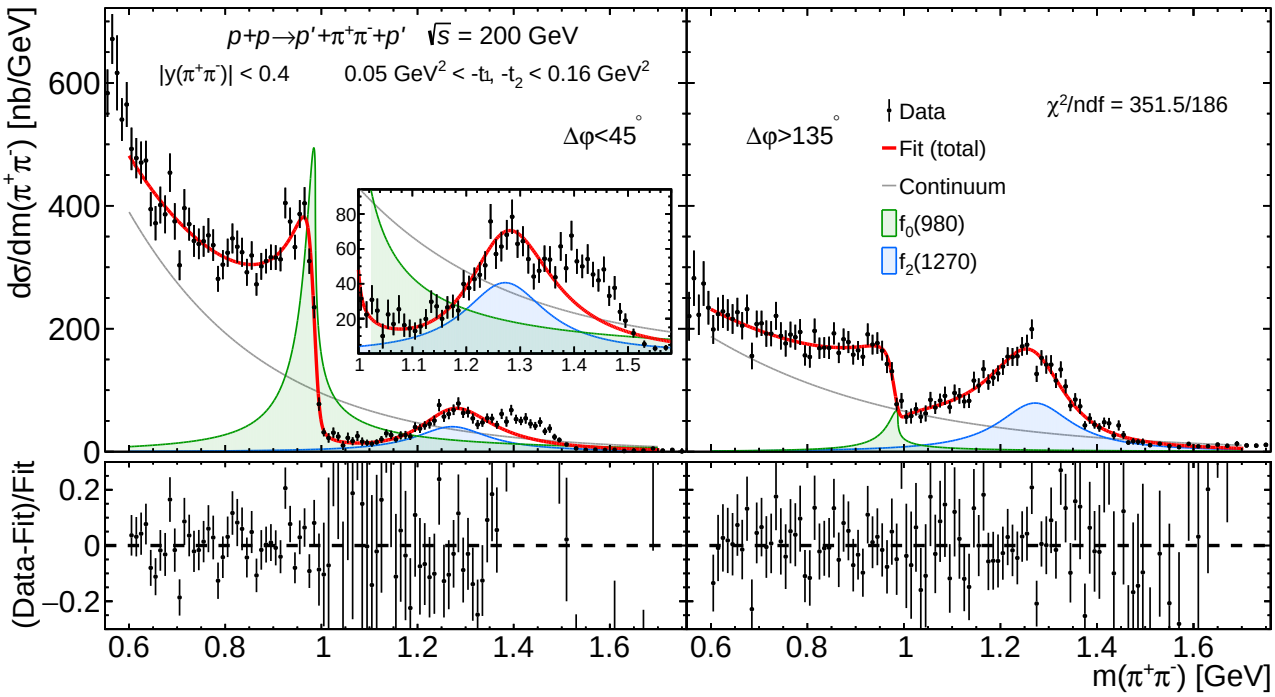

Figure 21.2: Results of the fit to the extrapolated differential cross section $d\sigma/dm(\pi^+\pi^-)$ without the $f_0(1500)$ component.

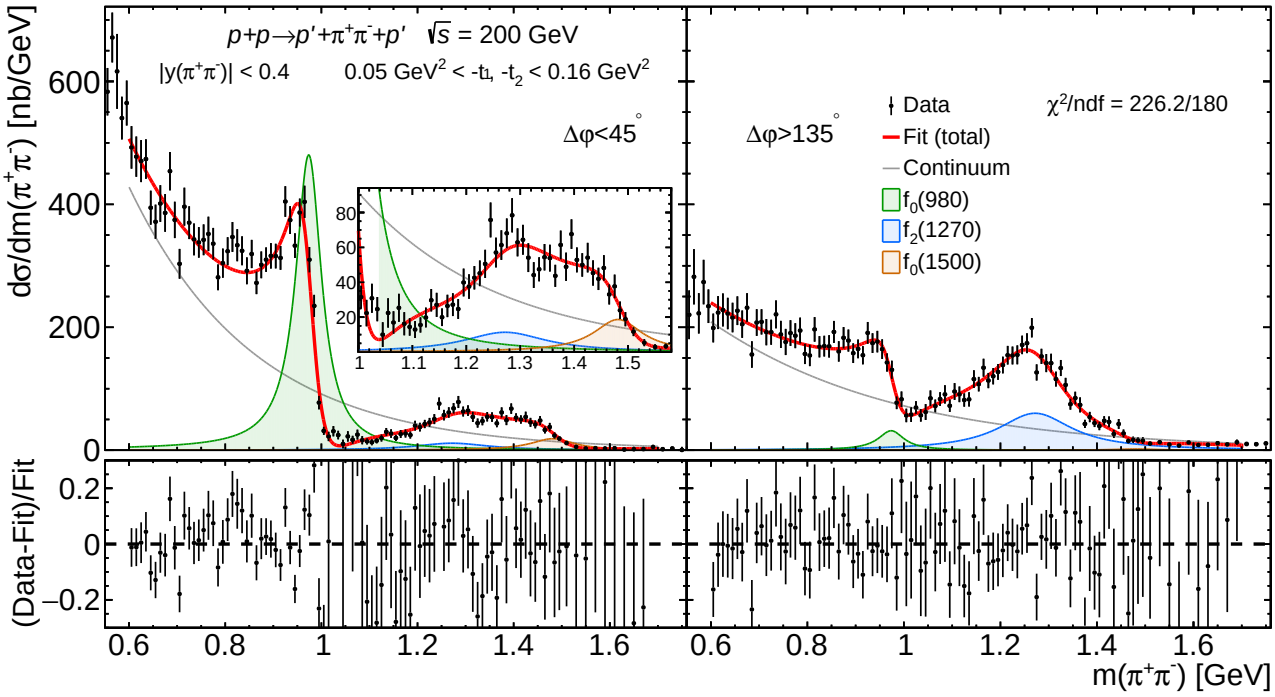

Figure 21.3: Results of the fit to the extrapolated differential cross section $d\sigma/dm(\pi^+\pi^-)$ assuming Breit-Wigner amplitude for $f_0(980)$.

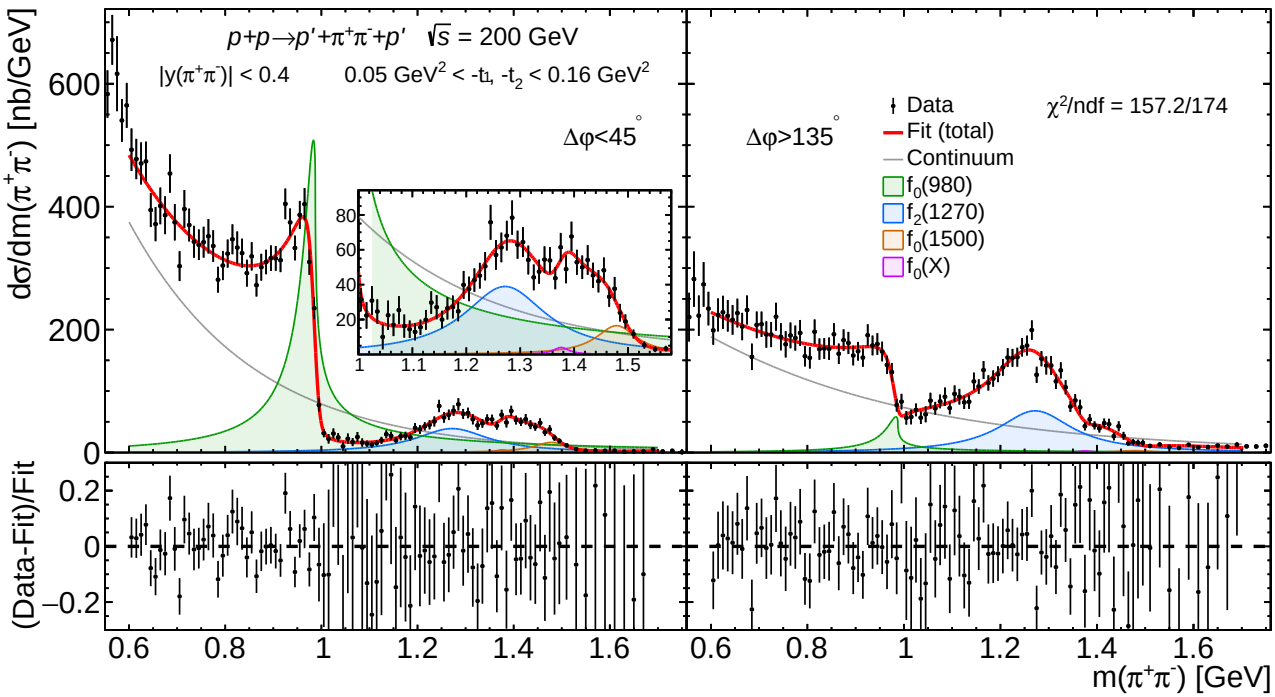

Figure 21.4: Results of the fit to the extrapolated differential cross section $d\sigma/dm(\pi^+\pi^-)$ with the fit allowing for an additional $f_0(X)$ component.

a Breit-Wigner resonance shape [5].

For the $f_0(1500)$, one obtains from the fit $M_{f_0(1500)} = 1469 \pm 9(\text{stat.}) \pm 1(\text{syst.}) \pm 2(\text{mod.})$ MeV and $\Gamma_{0,f_0(1500)} = 89 \pm 14(\text{stat.}) \pm 2(\text{syst.}) {}^{+4}_{-3}(\text{mod.})$ MeV. These values also deviate from the PDG averages 1505 ± 6 MeV for the mass and 109 ± 7 MeV for the width. However, numerous measurements on $f_0(1500)$ referenced in the PDG (and not used for the average calculation) report masses below 1500 MeV and widths below 100 MeV that are consistent with presented result.

The possibility of the existence of an additional resonance produced in the mass range 1.2 – 1.5 GeV was tested (Fig. 21.4). With an f_0-like component added to the model in Eq. (21.1), the best fit is achieved for $M_{f_0} = 1372 \pm 13(\text{stat.})$ MeV and $\Gamma_{0,f_0} = 44 \pm 24(\text{stat.})$ MeV. In that case, the χ^2/ndf is equal to 157/174 (p-value: 0.8), compared to the nominal value 175/180 (p-value: 0.6). The cross section $d\sigma/dm(\pi^+\pi^-)$ around 1.37 GeV for $\Delta\varphi < 45^\circ$ is better described than with the nominal fit. Other parameters in the fit change slightly but remain compatible with their original values. The fitted cross section of the additional f_0 resonance is several times lower than the extracted yield of $f_0(1500)$ for $\Delta\varphi < 45^\circ$, while for $\Delta\varphi > 135^\circ$ it is consistent with 0. The value of the mass agrees with that of the $f_0(1370)$ resonance, however the measured width is much narrower than PDG estimates of about 200 – 500 MeV.

The ratios of the total cross sections $\sigma_{f_0(980)}/\sigma_{f_2(1270)}$ and $\sigma_{f_0(1500)}/\sigma_{f_2(1270)}$ in two $\Delta\varphi$ regions were also calculated, as well as the ratio $\sigma(\Delta\varphi < 45^\circ)/\sigma(\Delta\varphi > 135^\circ)$ for all resonances, as listed in Tab. 21.2. In the ratios, many of the systematic uncertainties cancelled out. A significant dependence of the resonance production cross sections on the azimuthal separation of the forward-scattered protons is observed. The two scalar mesons, $f_0(980)$ and $f_0(1500)$, are produced predominantly at $\Delta\varphi < 45^\circ$, whereas the tensor meson $f_2(1270)$ is produced predominantly at $\Delta\varphi > 135^\circ$. This $\Delta\varphi$ dependence is consistent with the measurement performed by the WA102 Collaboration [22].

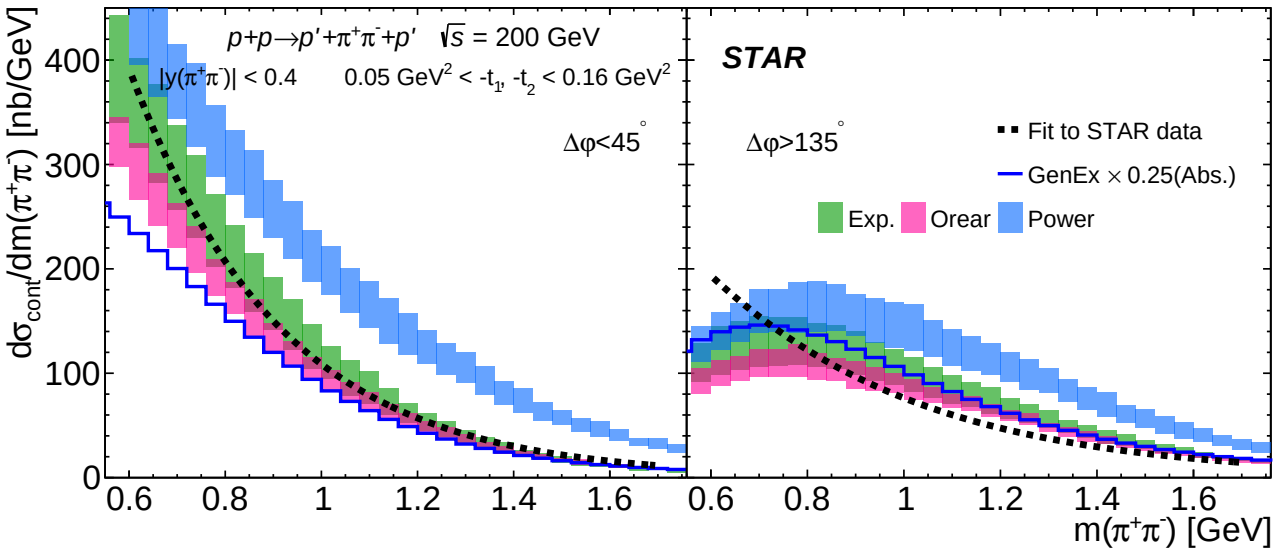

Figure 21.5: Comparison of the continuum production cross section obtained from the fit to the extrapolated $d\sigma/dm(\pi^+\pi^-)$ (dotted black line) with predictions from the continuum models. Scaled GenEx predictions are shown with the blue histogram. Three predictions from DiMe representing different meson form factors are shown as coloured bands, each spanning between minimum and maximum predicted cross sections from four available absorption models. Left and right panels show cross sections for $\Delta\varphi < 45^\circ$ and $\Delta\varphi > 135^\circ$, respectively.

The differential cross section for the $\pi^+\pi^-$ continuum production, $d\sigma_{\text{cont}}/dm(\pi^+\pi^-) = A^2_{\text{cont}} f^2_{\text{cont}}(m)$, was extracted from the fit to the extrapolated $d\sigma/dm(\pi^+\pi^-)$ distribution. It was then compared with expectations from GenEx and DiMe models using all three forms of meson form factors ($\Lambda^2_{\text{exp}} = 1.0$ GeV^2, $b = 2$ GeV^{-1} and $a^2 = 0.5$ GeV^2, and $a_0 = 1.0$ GeV^2) and four models of absorption [47]. All models predict a shape for $d\sigma_{\text{cont}}/dm(\pi^+\pi^-)$ that is different from the assumed form, f^2_{cont}, as shown in Fig. 21.5. The shape of the continuum predicted by the models can be achieved by changing the factor $\sqrt{q/m}$ in Eq. (21.2) to $(\sqrt{q/m})^P$, with the parameter P taking values between 2 and 10. Using such a modified continuum amplitude in the fit one obtains a P parameter consistent with 1 in both $\Delta\varphi$ ranges, and the remaining parameters are consistent with the results of the nominal fit. The deviation of the fitted $d\sigma_{\text{cont}}/dm(\pi^+\pi^-)$ from all the model predictions is most evident at the lower edge of the fit range. A possible explanation of this observation is the presence of the $f_0(500)$ state, expected in DPE, and the photo-produced ρ^0 vector meson, generally suppressed within the kinematic region of this

	$\sigma/\sigma_{f_2(1270)}$								$\frac{\sigma(\Delta\varphi < 45^\circ)}{\sigma(\Delta\varphi > 135^\circ)}$			
	$\Delta\varphi < 45^\circ$				$\Delta\varphi > 135^\circ$							
$f_0(980)$	8.9	± 2.3	$^{+0.4}_{-0.5}$	$^{+7.2}_{-0.3}$	0.33	± 0.06	± 0.01	$^{+0.13}_{-0.08}$	7.4	± 1.6	± 0.2	$^{+2.4}_{-0.2}$
$f_2(1270)$	1				1				0.27	± 0.07	± 0.01	$^{+0.02}_{-0.05}$
$f_0(1500)$	0.47	± 0.15	± 0.03	$^{+0.24}_{-0.05}$	0.01	± 0.01	± 0.00	± 0.00	12.3	± 8.6	$^{+0.7}_{-0.8}$	$^{+2.3}_{-3.6}$

Table 21.2: Ratios of integrated cross sections of resonance production. For each ratio statistical, systematic and model uncertainties are provided, in that order.

measurement. One should therefore treat the continuum obtained from the fit as an effective description of the coherent sum of the continuum and other states not explicitly included in the Eq. (21.1).

21.2 Exclusive production of $2\pi^+2\pi^-$ states

In the distribution of invariant mass of the centrally-produced $2\pi^+2\pi^-$ system, a few resonant structures at masses below $\sim$ 2 GeV are observed. In this mass region production of an axial-vector resonance $f_1(1285)$, decaying to four charged pions, is expected [219]. In order to extract the cross section for production of $f_1(1285)$ meson, the fit to differential cross section $d\sigma/dm(2\pi^+2\pi^-)$ was performed in a manner similar to that used for the invariant mass spectrum of exclusive $\pi^+\pi^-$ pairs. Here the differential fiducial cross section was not extrapolated to an unmeasured phase space region, therefore the fit provides information about the fiducial cross section for the $f_1(1285)$ production in the $2\pi^+2\pi^-$ channel. Cuts placed on p_T and η of single pions generally modify the line shape of the resonance (the acceptance varies with mass), but given very small width of the resonance under study (23 MeV according to PDG [5]) it was found a justified solution, which in addition helps to avoid modelling uncertainties.

The total amplitude for the exclusive $2\pi^+2\pi^-$ production is given by:

$$A(m) = A_{\text{other}} \times f_{\text{other}}(m) + \sqrt{\sigma_{f_1}} \times \exp\left(i\phi_{f_1}\right) \times \mathcal{R}_{\text{BW}}\left(m; M_{f_1}, \Gamma_{0,f_1}\right). \tag{21.7}$$

The main focus of the fit is put on the f_1 resonance, therefore no other states were explicitly specified. The form of component describing production of all states other than $f_1(1285)$ was chosen to provide good description of the cross section within the fitted mass range, and was assumed to be given by:

$$f_{\text{other}}(m) = \sqrt{m^C} \times \exp\left[-\frac{B}{2} \cdot m\right]. \tag{21.8}$$

For the purpose of the fit, the differential fiducial cross section was calculated using a bin width of 10 MeV to enable modelling of narrow structures caused by the $f_1(1285)$ resonance. The fit of function from Eq. (21.6), with the total amplitude A given by Eq. (21.7), was done in the mass range 1.15 GeV $< m <$ 1.45 GeV, simultaneously in two bins of $\Delta\varphi$: $\Delta\varphi < 90^\circ$ and $\Delta\varphi > 90^\circ$. The invariant mass resolution, σ_{res}, was taken into account in the fit and assumed to grow linearly within the fitted mass range, $\sigma_{\text{res}} = 1.7\% \cdot m$, as provided by the ATLAS simulation of $2\pi^+2\pi^-$ central systems from the Pythia CD sample. In order to estimate systematic uncertainties of the parameters of $f_1(1285)$ resonance, the fit was repeated with each of the systematic variations described in Sec. 19.3 applied, and all changes of parameters' values with respect to the nominal fit were added in quadrature. In addition to this, the sensitivity of the fit result on the assumed mass resolution was added to the overall systematic uncertainty. The mass resolution accuracy was conservatively estimated to ±25%.

The differential fiducial cross section for exclusive production of the $2\pi^+2\pi^-$ system, together with the result of the fit described above, are shown in Fig. 21.6. The parameters obtained from the fit are listed in Tab. 21.3. The fitted function well describes the differential cross section within the fitted mass range, yielding χ^2/ndf equal to 49.3/48. The mass and width of the $f_1(1285)$ resonance, which were free parameters in the fit, were found to be $M_{f_1(1285)} = 1294^{+5}_{-4}$ MeV and $\Gamma_{0,f_1(1285)} = 15^{+16}_{-2}$ MeV, respectively. The width is compatible with the PDG value of 22.7 ± 1.1 MeV within the systematic uncertainties, which dominate overall uncertainty. However, the obtained mass is higher by three

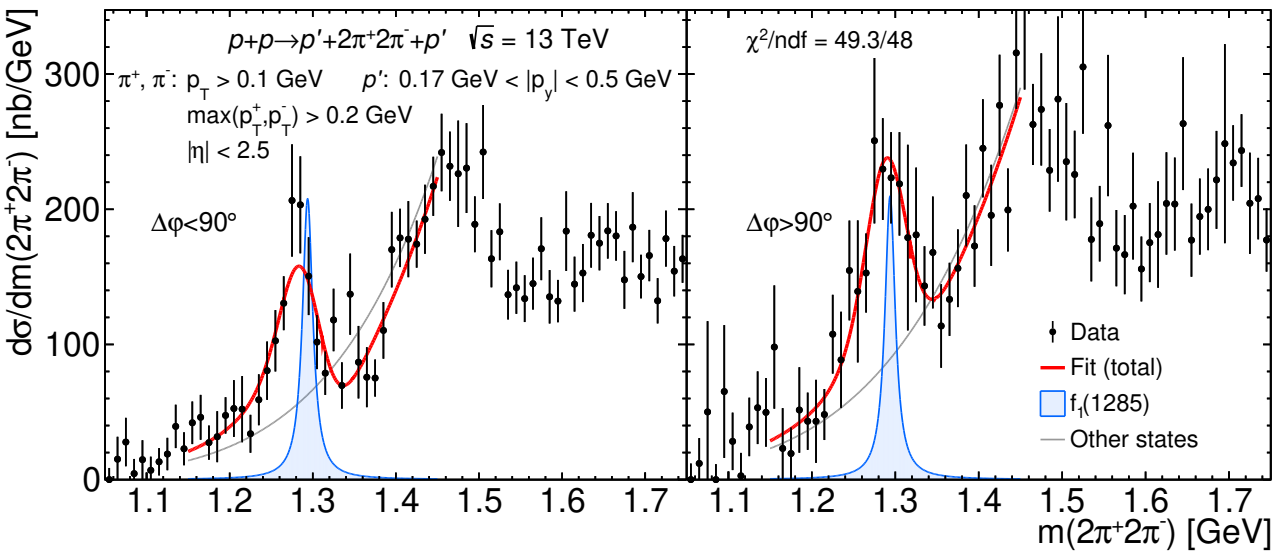

Figure 21.6: Differential fiducial cross section $d\sigma/dm(2\pi^+2\pi^-)$ measured in the ATLAS experiment with a fit of $f_1(1285)$ resonance. The left and right columns show the cross sections for $\Delta\varphi < 90^\circ$ and $\Delta\varphi > 90^\circ$, respectively. The data are shown as black points with error bars representing statistical uncertainties. The result of the fit, $\mathcal{F}(m)$, is drawn with a solid red line. The squared amplitudes for the production of $f_1(1285)$ and the coherent sum of the remaining states, are drawn with lines of different colours, as explained in the legend.

standard deviations than the PDG estimate of 1281.9 ± 0.5 MeV. This difference might have its origin in the simplified model used in the fit, which neglects presence of $f_2(1270)$ resonance (branching ratio to $2\pi^+2\pi^-$ of approximately 3%) in the vicinity of $f_1(1285)$ peak. The integrated cross sections for production of $f_1(1285)$ resonance and decay to $2\pi^+2\pi^-$, with the statistical uncertainties being dominant, are found compatible between $\Delta\varphi < 90^\circ$ and $\Delta\varphi > 90^\circ$ regions (Tab. 21.3). The ratio of the cross sections is equal to

$$\frac{\sigma_{f_1}(\Delta\varphi < 90^\circ)}{\sigma_{f_1}(\Delta\varphi > 90^\circ)} = 0.99 \pm 0.24^{+0.05}_{-0.07}. \tag{21.9}$$

The above results are potentially valuable to help constraining the $\mathbb{P}\mathbb{P}f_1$ couplings, as described in Ref. [219].

		unit	$\Delta\varphi < 90^\circ$	$\Delta\varphi > 90^\circ$
$f_1(1285)$	σ	nb	$4.9 \pm 0.9^{+2.0}_{-1.0}$	$4.9 \pm 0.8^{+1.7}_{-0.8}$
	ϕ	rad	$-0.25 \pm 0.20^{+0.36}_{-0.31}$	$-1.00 \pm 0.18^{+0.20}_{-0.13}$
	M	MeV	$1293.8 \pm 2.6^{+3.9}_{-2.2}$	
	Γ_0	MeV	$15.1 \pm 1.7^{+16}_{-0.2}$	

Table 21.3: Results of the fit described in the text and visualised in Fig. 21.6, in two ranges of azimuthal angle difference $\Delta\varphi$ between forward-scattered protons. Statistical and systematic uncertainties are provided for each parameter.

22. Extraction of exponential slope parameter of $d^2\sigma/dt_1dt_2$

Apart from the extrapolation and modelling of the $\pi^+\pi^-$ and $2\pi^+2\pi^-$ cross sections as functions of the invariant mass, geometrical acceptance corrections to the $d^2\sigma/dt_1dt_2$ distributions were applied.

They are required to extract the slope parameter, β, describing exponential dependence of the double differential cross section:

$$d^2\sigma/dt_1dt_2 \propto \exp[\beta t_1] \cdot \exp[\beta t_2]. \tag{22.1}$$

Variation of the slope with the invariant mass, m, of the central system, and the azimuthal angle between forward-scattered protons, $\Delta\varphi$, can provide important constraints for model developers. For example, it was pointed out in Ref. [24] that the $f_2(1270)$ cross section may show an enhancement when $t_1 \to 0$ and $t_2 \to 0$ for some $I\!P I\!P f_2$ couplings, while for others a suppression is expected. This enhancement or suppression results in a larger or smaller value of β, respectively.

The measurement of the parameter β in the STAR experiment was performed in the same Lorentz-invariant phase space as the modelling of the exclusive $\pi^+\pi^-$ invariant mass spectrum, given by $|y(\pi^+\pi^-)| < 0.4$ and $0.05 \leq -t_1, -t_2 \leq 0.16$ GeV^2, and in two $\Delta\varphi$ ranges ($\Delta\varphi < 45^\circ$ and $\Delta\varphi > 135^\circ$). In the case of the ATLAS experiment, the measurement was performed within the fiducial region characterising the centrally-produced particles ($\pi^+\pi^-$ pairs and $2\pi^+2\pi^-$ systems), but after extrapolation to the phase-space describing the forward-scattered protons given by 0.05 GeV$^2 \leq -t_1, -t_2 \leq 0.25$ GeV^2. Also, it was performed in four ($\pi^+\pi^-$ pairs) and two ($2\pi^+2\pi^-$ central states) equal-width bins of $\Delta\varphi$.

These cross sections were fitted in two dimensions with an exponential function from Eq. (22.1). The fits were performed separately in three ranges of $m(\pi^+\pi^-)$: 0.6 GeV $\leq m \leq 1.0$ GeV, 1 GeV $< m \leq 1.5$ GeV, $m > 1.5$ GeV, and three ranges of $m(2\pi^+2\pi^-)$: 1.1 GeV $\leq m \leq 1.5$ GeV, 1.5 GeV $< m \leq 2$ GeV, $m > 2$ GeV. An exemplary fits to the STAR and ATLAS data are shown in Fig. 22.1. The values of β obtained from the fits are displayed in Figs. 22.2 and 22.3. For these values, modelling uncertainties were not separated since they are generally much smaller than experimental uncertainties. This is a consequence of the uniform φ distribution in all the models and the rather weak dependence of the cross section on $\Delta\varphi$ within the measured ranges. Such approximations are well-founded and in good agreement with the data.

The results for exclusive $\pi^+\pi^-$ production (Fig. 22.2) show, that in the range $\Delta\varphi < 45^\circ$ the slope β is similar for all ranges of the invariant mass of the central system and for both centre-of-mass energies. In the lowest mass range (0.6 GeV $\leq m \leq 1$ GeV) the value of slope increases with $\Delta\varphi$, while for the higher mass bins it decreases with $\Delta\varphi$. The results from STAR and ATLAS are in most cases compatible with each other. In the case of the ATLAS measurement in the mass range 0.6 GeV $\leq m \leq 1$ GeV and $\Delta\varphi$ range $135^\circ < \Delta\varphi < 180^\circ$, the exponential function does not describe the shape of $d^2\sigma/dt_1dt_2$ in the entire studied t range. The distribution appears to have two distinctive parts, the high slope part in the region of lower four-momentum transfers, and very low slope part in the region of higher four-momentum transfers. Therefore, in this particular m and $\Delta\varphi$ region, the fit to ATLAS data was performed in the narrower t range, 0.05 GeV$^2 \leq -t_1, -t_2 \leq 0.13$ GeV^2,

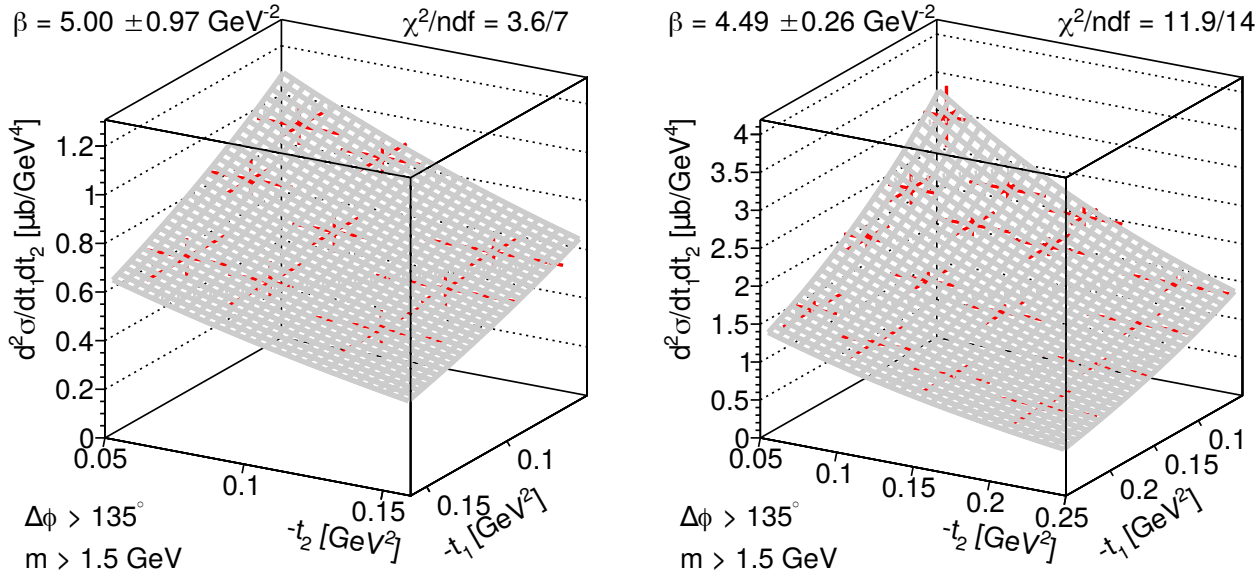

(a) (b)

Figure 22.1: Sample double differential cross sections $d^2\sigma/dt_1dt_2$ for CEP of $\pi^+\pi^-$ pairs in the mass range $m(\pi^+\pi^-) > 1.5$ GeV and for azimuthal angles between forward-scattered protons $\Delta\varphi > 135^\circ$, measured in (a) the STAR experiment, and (b) the ATLAS experiment. The grey surfaces represent exponential fits to $d^2\sigma/dt_1dt_2$. Values of slopes and χ^2/ndf are provided on the plots.

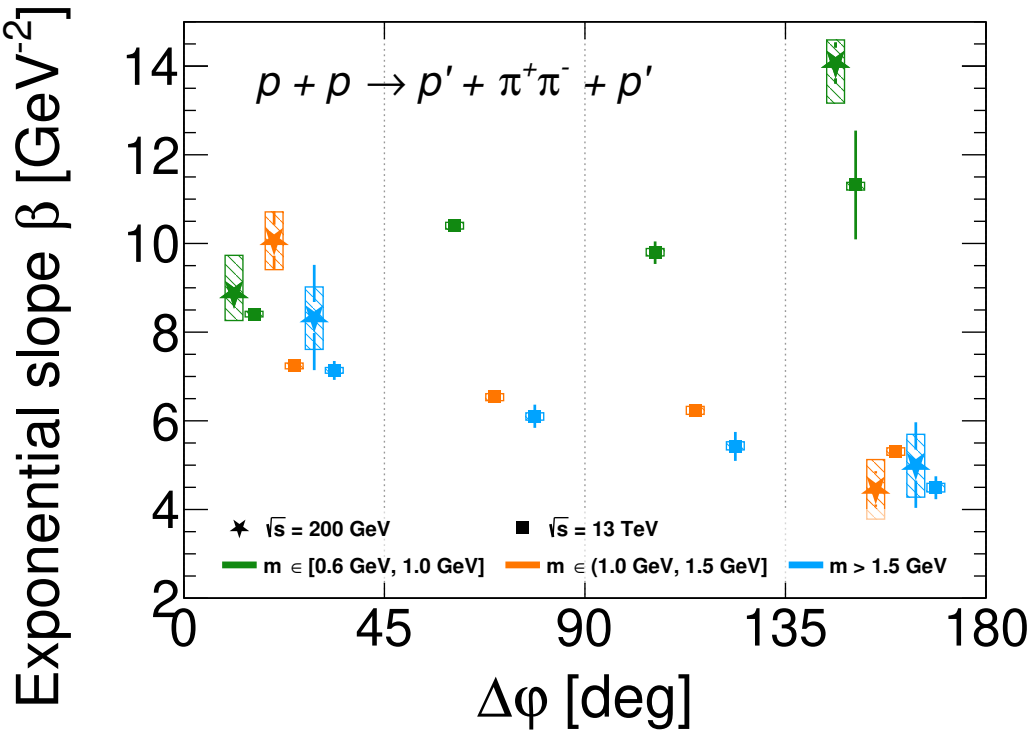

Figure 22.2: Exponential slope parameter, β, of the cross section for CEP of $\pi^+\pi^-$ pairs measured at $\sqrt{s}$ = 200 GeV (STAR) and $\sqrt{s}$ = 13 TeV (ATLAS) in three ranges of the invariant mass of the pair. Statistical and systematic uncertainties are shown with vertical bars and rectangles, respectively. The results are shown in two (STAR) and four (ATLAS) intervals of $\Delta\varphi$ marked with vertical dotted lines. The data points are spread within the $\Delta\varphi$ intervals for better visibility, and the actual positions of the points within a bin do not have any meaning.

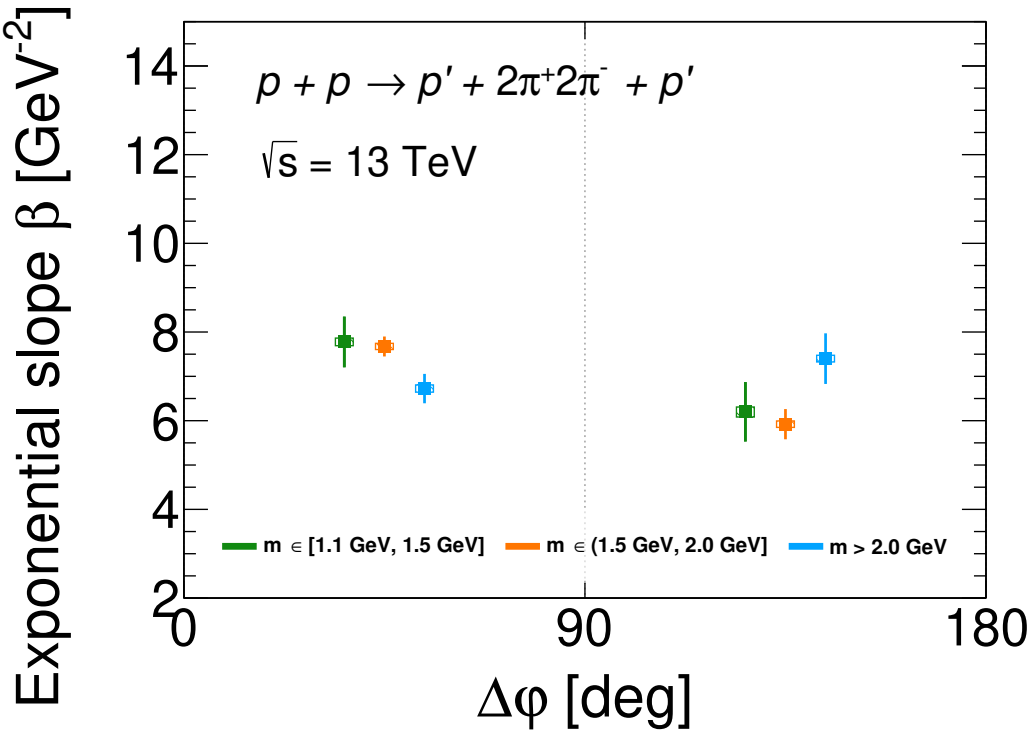

Figure 22.3: Exponential slope parameter, β, of the cross section for CEP of $2\pi^+2\pi^-$ states measured at $\sqrt{s}$ = 13 TeV (ATLAS) in three ranges of the invariant mass of the pair. Statistical and systematic uncertainties are shown with vertical bars and rectangles, respectively. The results are shown in two intervals of $\Delta\varphi$ marked with a vertical dotted line. The data points are spread within the $\Delta\varphi$ intervals for better visibility, and the actual positions of the points within a bin do not have any meaning.

which almost entirely overlaps with the t range in STAR. In this limited t range, the $d^2\sigma/dt_1dt_2$ was successfully fitted with the exponential function. Both STAR and ATLAS results show that the slope parameter is the highest in this kinematic region. The described peculiar behaviour of the $d^2\sigma/dt_1dt_2$ for 0.6 GeV $\leq m \leq$ 1 GeV and $135^\circ < \Delta\varphi < 180^\circ$ might be a signature of significant absorption effects which distort the cross sections in (t_1, t_2) plane.

In case of the exclusive production of $2\pi^+2\pi^-$ systems (Fig. 22.3), the variations of slope β with mass and azimuthal angle between protons are much smaller compared to production of $\pi^+\pi^-$ pairs, with the slope values ranging between 6 GeV^{-2} – 8 GeV^{-2}. Such behaviour may be connected with lower contributions to production of $2\pi^+2\pi^-$ systems through the production of single resonances, which have been found significant in the $\pi^+\pi^-$ channel. Some evidence for decreasing value of the slope with increasing $\Delta\varphi$ is observed for masses below 2 GeV, and very small evidence for increasing value of the slope for the higher invariant masses.

Summary

In this dissertation, the measurements of the CEP processes in the STAR experiment at RHIC ($\sqrt{s}$ = 200 GeV) and in the ATLAS experiment at LHC ($\sqrt{s}$ = 13 TeV), were presented. These are the highest centre-of-mass energies, at which these kind of processes have been measured with a detection of the forward-scattered protons. The analysed data were collected in regular runs with nominal beam optics at STAR, and in special runs with dedicated beam optics at ATLAS, and correspond to integrated luminosities of 14.2 pb^{-1} and 0.66 pb^{-1}, respectively.

Capability of detecting intact beam protons enabled verification of event exclusivity, using the transverse momentum balance of all detected particles, as well as select the DPE mechanism as dominant (suppressed photo-production events). Event selection, with a key component being the momentum balance constraint, led to reduction of non-exclusive backgrounds down to several percent level in most of the analysed reaction channels.

To make the measurement possible, dedicated tools and techniques were developed for the purpose of efficiency calculation and estimation of systematics uncertainties. These were, e.g., Geant4 simulation of the RP detectors at STAR. Studies of the non-exclusive backgrounds, which were well understood and controlled in both analyses, revealed imperfect description of the Central Diffraction process in Pythia MC event generator in terms of contributions from $\pi^+\pi^-$+neutrals production.

The main results of the analyses were measurements of differential cross sections of exclusively produced $\pi^+\pi^-$ pairs (STAR and ATLAS), K^+K^- and $p\bar{p}$ pairs (STAR), $2\pi^+2\pi^-$, $3\pi^+3\pi^-$ and $4\pi^+4\pi^-$ central systems (ATLAS), in fiducial regions corresponding to the acceptances of the STAR and ATLAS detectors. High statistics of $\pi^+\pi^-$ samples and the $2\pi^+2\pi^-$ sample allowed studies of several observables with respect to the azimuthal separation of the forward-scattered protons and invariant mass of the centrally-produced states. The systematic precision of the measurements is several times better compared to previous results obtained with tagged intact beam particles. CEP of eight pions with two intact protons detected in ATLAS-ALFA is potentially the highest particle multiplicity ever measured in the exclusive process.

Structures observed in the invariant mass spectra of exclusively produced $\pi^+\pi^-$ pairs are consistent with production of the $f_0(980)$ and $f_2(1270)$ resonances expected in DPE, in addition to the continuum. Also, a resonance around the invariant mass of 2.2 GeV was observed. No signatures of vector mesons such as $\rho(770)$ or J/ψ were found, which indicates low contributions from Pomeron-photon and sub-leading Reggeon exchanges. In the invariant mass spectrum of the exclusively produced K^+K^- pairs, the resonance structures were found suggesting production of $f_2(1270)$, $f_2'(1525)$ and $f_0(1710)$. In the invariant mass spectrum of $2\pi^+2\pi^-$, the structures consistent with the axial vector meson $f_1(1285)$ were observed, as well as peaks and dips in the higher-mass part of the spectrum originating from additional resonances. In the case of $3\pi^+3\pi^-$ and $4\pi^+4\pi^-$ channels, invariant mass spectra did not exhibit significant structures.

A strong dependence of the magnitude of the structures in the invariant mass spectra on the angle between the forward-scattered protons, was also observed. It indicates the factorisation breaking between the two proton vertices.

The differential fiducial cross sections were compared with available models of the CEP process implemented in form of MC generators: GenEx, DiMe and Pythia (MBR model). Models currently

implemented in MC generators provide only predictions for the continuum production, therefore comparisons were mostly qualitative. In the case of angular distributions for $\pi + \pi^-$ pairs, comparisons with predictions for pure S_0 and D_0 waves suggest dominance of the spin-0 states production at invariant masses below 1 GeV.

The differential fiducial $\pi^+\pi^-$ cross section as a function of the invariant mass of the pair measured at STAR was extrapolated to the Lorentz-invariant phase space given by $0.05\,\mathrm{GeV}^2 < -t_1, -t_2 < 0.16\,\mathrm{GeV}^2$ and $|y(\pi^+\pi^-)| < 0.4$ in two ranges of $\Delta\varphi < 45^\circ$ and $\Delta\varphi > 135^\circ$. This allowed to fit the extrapolated differential cross section with a minimal model of the $\pi^+\pi^-$ invariant mass spectrum consisting of $f_0(980)$, $f_2(1270)$ and $f_0(1500)$ resonances and direct non-resonant $\pi^+\pi^-$ production. The masses and widths of the $f_0(980)$ and $f_0(1500)$ resonances obtained from the fit were found to be in good agreement with the PDG values. The two scalar mesons, $f_0(980)$ and $f_0(1500)$, were predominantly produced at $\Delta\varphi < 45^\circ$, whereas the tensor meson $f_2(1270)$ was predominantly produced at $\Delta\varphi > 135^\circ$.

A weak evidence for an additional resonant state with a mass of 1372 ± 13(stat.) MeV and a width of 44 ± 24(stat.) MeV was observed. The extrapolated cross sections of continuum production within the mass range $0.6\,\mathrm{GeV} < m < 1.7\,\mathrm{GeV}$ showed an expected $\Delta\varphi$ asymmetry caused by absorption.

The differential fiducial $2\pi^+2\pi^-$ cross section as a function of the invariant mass of the centrally-produced system measured at ATLAS was fitted with a minimal model including $f_1(1285)$ resonance and the sum of remaining states. Extracted parameters of $f_1(1285)$ meson were found roughly consistent with the PDG data. Information about the fiducial cross sections for exclusive $f_1(1285)$ production in two mass regions, $\Delta\varphi < 90^\circ$ and $\Delta\varphi > 90^\circ$, should help constraining values and forms of IPomeron-IPomeron-f_1 couplings.

Fits to an exponential function of the form $\propto \exp[\beta t_1]\exp[\beta t_2]$ were performed to the differential cross sections $d^2\sigma/dt_1dt_2$ in the $\pi^+\pi^-$ and $2\pi^+2\pi^-$ channels, to extract the slope of the $-t$ distributions. Variations in the slope with m and $\Delta\varphi$ can give important constraints for construction of phenomenological models of CEP, including couplings of the IPomerons to f-mesons.

Bibliography

[1] STAR Collaboration, J. Adam et al., *Measurement of the central exclusive production of charged particle pairs in proton-proton collisions at* $\sqrt{s} = 200$ *GeV with the STAR detector at RHIC*, JHEP **07** (2020) 178, arXiv: 2004.11078 [hep-ex]. (Cit. on pp. xvi, 27.).

[2] STAR Collaboration, J. Adam et al., *Results on Total and Elastic Cross Sections in Proton-Proton Collisions at* $\sqrt{s} = 200$ *GeV*, Phys. Lett. B **808** (2020) 135663, arXiv: 2003.12136 [hep-ex]. (Cit. on pp. xvi, 9, 38, 39, 43, 145.).

[3] ATLAS Collaboration, G. Aad et al., *Observation of a new particle in the search for the Standard Model Higgs boson with the ATLAS detector at the LHC*, Phys. Lett. B **716** (2012) 1, arXiv: 1207.7214 [hep-ex]. (Cit. on p. 3.).

[4] CMS Collaboration, S. Chatrchyan et al., *Observation of a New Boson at a Mass of 125 GeV with the CMS Experiment at the LHC*, Phys. Lett. B **716** (2012) 30, arXiv: 1207.7235 [hep-ex]. (Cit. on p. 3.).

[5] Particle Data Group Collaboration, M. Tanabashi et al., *Review of Particle Physics*, Phys. Rev. D **98** (2018) 030001. (Cit. on pp. 3, 5, 17, 220, 226, 227, 237, 239, 241, 243.).

[6] ALEPH Collaboration, D. Decamp et al., *Determination of the Number of Light Neutrino Species*, Phys. Lett. B **231** (1989) 519. (Cit. on p. 3.).

[7] ALEPH, DELPHI, L3, OPAL, SLD, LEP Electroweak Working Group, SLD Electroweak Group, SLD Heavy Flavour Group Collaboration, S. Schael et al., *Precision electroweak measurements on the Z resonance*, Phys. Rept. **427** (2006) 257, arXiv: hep-ex/0509008. (Cit. on p. 3.).

[8] Y. Sumino, *QCD potential as a 'Coulomb plus linear' potential*, Phys. Lett. B **571** (2003) 173, arXiv: hep-ph/0303120. (Cit. on p. 4.).

[9] V. Barone and E. Predazzi, *High-Energy Particle Diffraction*, vol. v.565, Texts and Monographs in Physics, Springer-Verlag, 2002, ISBN: 3540421076. (Cit. on pp. 6–10.).

[10] S. Donnachie, H.G. Dosch, O. Nachtmann, and P. Landshoff, *Pomeron physics and QCD*, vol. 19, Cambridge University Press, 2004, ISBN: 978-0-511-06050-2. (Cit. on pp. 6–10.).

[11] G.F. Chew and S.C. Frautschi, *Regge Trajectories and the Principle of Maximum Strength for Strong Interactions*, Phys. Rev. Lett. **8** (1962) 41. (Cit. on p. 7.).

[12] U. Amaldi, M. Jacob, and G. Matthiae, *Diffraction of Hadronic Waves*, Ann. Rev. Nucl. Part. Sci. **26** (1976) 385. (Cit. on pp. 7, 8.).

[13] STAR Collaboration, L. Adamczyk et al., *Coherent diffractive photoproduction of ρ0 mesons on gold nuclei at 200 GeV/nucleon-pair at the Relativistic Heavy Ion Collider*, Phys. Rev. C **96** (2017) 054904, arXiv: 1702.07705 [nucl-ex]. (Cit. on p. 8.).

[14] G.F. Chew and S.C. Frautschi, *Principle of Equivalence for All Strongly Interacting Particles Within the S Matrix Framework*, Phys. Rev. Lett. **7** (1961) 394. (Cit. on p. 8.).

[15] V.N. Gribov, *Possible Asymptotic Behavior of Elastic Scattering*, JETP Lett. **41** (1961) 667. (Cit. on p. 8.).

[16] A. Donnachie and P.V. Landshoff, *Total cross-sections*, Phys. Lett. B **296** (1992) 227, arXiv: hep-ph/9209205. (Cit. on p. 9.).

[17] STAR Collaboration, L. Adamczyk et al., *Single Spin Asymmetry A_N in Polarized Proton-Proton Elastic Scattering at $\sqrt{s} = 200$ GeV*, Phys.Lett. **B719** (2013) 62, arXiv: 1206.1928 [nucl-ex]. (Cit. on pp. 9, 29, 34.).

[18] C. Ewerz, P. Lebiedowicz, O. Nachtmann, and A. Szczurek, *Helicity in proton–proton elastic scattering and the spin structure of the pomeron*, Phys. Lett. B **763** (2016) 382, arXiv: 1606.08067 [hep-ph]. (Cit. on p. 9.).

[19] A. Donnachie and P.V. Landshoff, *p p and anti-p p Elastic Scattering*, Nucl. Phys. B **231** (1984) 189. (Cit. on p. 9.).

[20] A. Donnachie and P.V. Landshoff, *Dynamics of Elastic Scattering*, Nucl. Phys. B **267** (1986) 690. (Cit. on p. 9.).

[21] A. Donnachie and P.V. Landshoff, *Hard Diffraction: Production of High p(T) Jets, W or Z, and Drell-Yan Pairs*, Nucl. Phys. B **303** (1988) 634. (Cit. on p. 9.).

[22] WA102 Collaboration, D Barberis et al., *Experimental evidence for a vector like behavior of Pomeron exchange*, Phys. Lett. B **467** (1999) 165, arXiv: hep-ex/9909013. (Cit. on pp. 9, 23, 241.).

[23] C. Ewerz, M. Maniatis, and O. Nachtmann, *A Model for Soft High-Energy Scattering: Tensor Pomeron and Vector Odderon*, Annals Phys. **342** (2014) 31, arXiv: 1309.3478 [hep-ph]. (Cit. on p. 9.).

[24] P. Lebiedowicz, O. Nachtmann, and A. Szczurek, *Central exclusive diffractive production of $\pi^+\pi^-$ continuum, scalar and tensor resonances in pp and $p\bar{p}$ scattering within tensor pomeron approach*, Phys. Rev. **D93** (2016) 054015, arXiv: 1601.04537 [hep-ph]. (Cit. on pp. 9, 19, 20, 245.).

[25] ZEUS Collaboration, M. Derrick et al., *Observation of events with a large rapidity gap in deep inelastic scattering at HERA*, Phys. Lett. B **315** (1993) 481. (Cit. on p. 10.).

[26] H1 Collaboration, C. Adloff et al., *Inclusive measurement of diffractive deep inelastic ep scattering*, Z. Phys. C **76** (1997) 613, arXiv: hep-ex/9708016. (Cit. on p. 10.).

[27] H1 Collaboration, A. Aktas et al., *Measurement and QCD analysis of the diffractive deep-inelastic scattering cross-section at HERA*, Eur. Phys. J. C **48** (2006) 715, arXiv: hep-ex/0606004. (Cit. on p. 10.).

[28] V.S. Fadin, E.A. Kuraev, and L.N. Lipatov, *On the Pomeranchuk Singularity in Asymptotically Free Theories*, Phys. Lett. B **60** (1975) 50. (Cit. on p. 10.).

[29] I.I. Balitsky and L.N. Lipatov, *The Pomeranchuk Singularity in Quantum Chromodynamics*, Sov. J. Nucl. Phys. **28** (1978) 822. (Cit. on p. 10.).

[30] A. Breakstone et al., *A Measurement of $\bar{p}p$ and pp Elastic Scattering in the Dip Region at $\sqrt{s} = 53$-GeV*, Phys. Rev. Lett. **54** (1985) 2180. (Cit. on p. 10.).

[31] H1 Collaboration, C. Adloff et al., *Search for odderon induced contributions to exclusive pi0 photoproduction at HERA*, Phys. Lett. B **544** (2002) 35, arXiv: hep-ex/0206073. (Cit. on p. 10.).

[32] TOTEM Collaboration, G. Antchev et al., *First determination of the ρ parameter at $\sqrt{s} = 13$ TeV: probing the existence of a colourless C-odd three-gluon compound state*, Eur. Phys. J. C **79** (2019) 785, arXiv: 1812.04732 [hep-ex]. (Cit. on p. 10.).

[33] L. Fulek, "Charged particle production in diffractive proton-proton scattering at the RHIC and LHC energies", PhD thesis: AGH University of Science and Technology, 2020. (Cit. on pp. 12, 43, 96, 97, 115, 116, 129, 130, 132, 141, 153, 171, 181, 197.).

[34] R. Shankar, *Can and does the pomeron occur more than once in a single process?*, Nucl. Phys. B **70** (1974) 168. (Cit. on p. 12.).

[35] D.M. Chew and G.F. Chew, *Prediction of Double-Pomeron Cross-Sections from Single-Diffraction Measurements*, Phys. Lett. B **53** (1974) 191. (Cit. on p. 12.).

[36] D.M. Chew, *Double-Pomeron Prediction for Colliding Beam Experiments*, Phys. Lett. B **65** (1976) 367. (Cit. on p. 12.).

[37] J. Pumplin and F. Henyey, *Double Pomeron Exchange in the Reaction p p –> p p pi+ pi-*, Nucl. Phys. B **117** (1976) 377. (Cit. on p. 12.).

[38] B.R. Desai, B.C. Shen, and M. Jacob, *Double Pomeron Exchange in High-energy pp Collisions*, Nucl. Phys. B **142** (1978) 258. (Cit. on p. 12.).

[39] P. Lebiedowicz, O. Nachtmann, and A. Szczurek, *Exclusive central diffractive production of scalar and pseudoscalar mesons tensorial vs. vectorial pomeron*, Annals Phys. **344** (2014) 301, arXiv: 1309.3913 [hep-ph]. (Cit. on pp. 12, 15, 19, 226.).

[40] S.U. Chung, *Techniques of amplitude analysis for two pseudoscalar systems*, Phys. Rev. D **56** (1997) 7299. (Cit. on p. 12.).

[41] L.A. Harland-Lang, V.A. Khoze, M.G. Ryskin, and W.J. Stirling, *The Phenomenology of Central Exclusive Production at Hadron Colliders*, Eur. Phys. J. C **72** (2012) 2110, arXiv: 1204.4803 [hep-ph]. (Cit. on pp. 13, 19, 20.).

[42] CDF Collaboration, T. Aaltonen et al., *Observation of Exclusive Gamma Gamma Production in $p\bar{p}$ Collisions at $\sqrt{s} = 1.96$ TeV*, Phys. Rev. Lett. **108** (2012) 081801, arXiv: 1112.0858 [hep-ex]. (Cit. on pp. 13, 23.).

[43] CDF Collaboration, T. Affolder et al., *Dijet production by double pomeron exchange at the Fermilab Tevatron*, Phys. Rev. Lett. **85** (2000) 4215. (Cit. on pp. 13, 23.).

[44] CDF Collaboration, T. Aaltonen et al., *Observation of exclusive charmonium production and $\gamma + \gamma$ to $\mu^+\mu^-$ in $p\bar{p}$ collisions at $\sqrt{s} = 1.96$ TeV*, Phys. Rev. Lett. **102** (2009) 242001, arXiv: 0902.1271 [hep-ex]. (Cit. on pp. 13, 23.).

[45] A. Bialas and P.V. Landshoff, *Higgs production in p p collisions by double pomeron exchange*, Phys. Lett. B **256** (1991) 540. (Cit. on p. 13.).

[46] ATLAS Collaboration, G. Aad et al., *The ATLAS Experiment at the CERN Large Hadron Collider*, JINST **3** (2008) S08003. (Cit. on pp. 14, 159, 160, 162, 165.).

[47] L. A. Harland-Lang, V. A. Khoze, and M. G. Ryskin, *Modelling exclusive meson pair production at hadron colliders*, Eur. Phys. J. **C74** (2014) 2848, arXiv: 1312.4553 [hep-ph]. (Cit. on pp. 15, 19, 20, 242.).

[48] OPAL Collaboration, G. Abbiendi et al., *Tests of models of color reconnection and a search for glueballs using gluon jets with a rapidity gap*, Eur. Phys. J. C **35** (2004) 293, arXiv: hep-ex/0306021. (Cit. on p. 16.).

[49] ALEPH Collaboration, S. Schael et al., *Test of Colour Reconnection Models using Three-Jet Events in Hadronic Z Decays*, Eur. Phys. J. C **48** (2006) 685, arXiv: hep-ex/0604042. (Cit. on p. 16.).

[50] DELPHI Collaboration, J. Abdallah et al., *Study of Leading Hadrons in Gluon and Quark Fragmentation*, Phys. Lett. B **643** (2006) 147, arXiv: hep-ex/0610031. (Cit. on p. 16.).

[51] Axial Field Spectrometer Collaboration, T. Akesson et al., *A Search for Glueballs and a Study of Double Pomeron Exchange at the CERN Interacting Storage Rings*, Nucl. Phys. B **264** (1986) 154. (Cit. on pp. 16, 22.).

[52] Ames-Bologna-CERN-Dortmund-Heidelberg-Warsaw Collaboration, A. Breakstone et al., *The Reaction pomeron-pomeron —> pi+ pi- and an unusual production mechanism for the f2 (1270)*, Z. Phys. C **48** (1990) 569. (Cit. on pp. 16, 22.).

[53] A. Kirk, *A review of central production experiments at the CERN Omega spectrometer*, Int. J. Mod. Phys. A **29** (2014) 1446001, arXiv: 1408.1196 [hep-ex]. (Cit. on p. 16.).

[54] Y. Chen et al., *Glueball spectrum and matrix elements on anisotropic lattices*, Phys. Rev. D **73** (2006) 014516, arXiv: hep-lat/0510074. (Cit. on p. 16.).

[55] R.C. Brower, S.D. Mathur, and C.-I Tan, *Glueball spectrum for QCD from AdS supergravity duality*, Nucl. Phys. B **587** (2000) 249, arXiv: hep-th/0003115. (Cit. on p. 16.).

[56] T. Gutsche, *Exotic mesons*, Prog. Part. Nucl. Phys. **67** (2012) 380, ed. by A. Faessler and V. Rodin. (Cit. on p. 17.).

[57] W. Ochs, *The Status of Glueballs*, J. Phys. G **40** (2013) 043001, arXiv: 1301.5183 [hep-ph]. (Cit. on p. 17.).

[58] H.B. Meyer and M.J. Teper, *Glueball Regge trajectories and the pomeron: A Lattice study*, Phys. Lett. B **605** (2005) 344, arXiv: hep-ph/0409183. (Cit. on p. 17.).

[59] H.B. Meyer, "Glueball regge trajectories", PhD thesis: University of Oxford, 2004, arXiv: hep-lat/0508002. (Cit. on p. 17.).

[60] P. Lebiedowicz and A. Szczurek, *Exclusive $pp \to pp\pi^+\pi^-$ reaction: From the threshold to LHC*, Phys. Rev. **D81** (2010) 036003, arXiv: 0912.0190 [hep-ph]. (Cit. on pp. 19, 20.).

[61] R.A. Ryutin, *Central exclusive diffractive production of two-pion continuum at hadron colliders*, Eur. Phys. J. C **79** (2019) 981, arXiv: 1910.06683 [hep-ph]. (Cit. on p. 19.).

[62] R. Fiore, L. Jenkovszky, and R. Schicker, *Resonance production in Pomeron–Pomeron collisions at the LHC*, Eur. Phys. J. **C76** (2016) 38, arXiv: 1512.04977 [hep-ph]. (Cit. on p. 19.).

[63] P. Lebiedowicz, O. Nachtmann, and A. Szczurek, *Towards a complete study of central exclusive production of K^+K^- pairs in proton-proton collisions within the tensor Pomeron approach*, Phys. Rev. D **98** (2018) 014001, arXiv: 1804.04706 [hep-ph]. (Cit. on p. 19.).

[64] P. Lebiedowicz and A. Szczurek, *$pp \to ppK^+K^-$ reaction at high energies*, Phys. Rev. D **85** (2012) 014026, arXiv: 1110.4787 [hep-ph]. (Cit. on pp. 19, 20.).

[65] R. Kycia, P. Lebiedowicz, A. Szczurek, and J. Turnau, *Triple Regge exchange mechanisms of four-pion continuum production in the $pp \to pp\pi^+\pi^-\pi^+\pi^-$ reaction*, Phys. Rev. D **95** (2017) 094020, arXiv: 1702.07572 [hep-ph]. (Cit. on pp. 19, 229, 231.).

[66] P. Lebiedowicz and A. Szczurek, *Revised model of absorption corrections for the $pp \to pp\pi^+\pi^-$ process*, Phys. Rev. D **92** (2015) 054001, arXiv: 1504.07560 [hep-ph]. (Cit. on p. 19.).

[67] P. Lebiedowicz, O. Nachtmann, and A. Szczurek, *ρ^0 and Drell-Söding contributions to central exclusive production of $\pi^+\pi^-$ pairs in proton-proton collisions at high energies*, Phys. Rev. D **91** (2015) 074023, arXiv: 1412.3677 [hep-ph]. (Cit. on p. 19.).

[68] A. Bolz et al., *Photoproduction of π^+ π^- pairs in a model with tensor-pomeron and vector-odderon exchange*, JHEP **01** (2015) 151, arXiv: 1409.8483 [hep-ph]. (Cit. on p. 19.).

[69] P. Lebiedowicz, O. Nachtmann, and A. Szczurek, *Exclusive diffractive production of $\pi^+\pi^-\pi^+\pi^-$ via the intermediate $\sigma\sigma$ and $\rho\rho$ states in proton-proton collisions within tensor pomeron approach*, Phys. Rev. D **94** (2016) 034017, arXiv: 1606.05126 [hep-ph]. (Cit. on pp. 19, 231.).

[70] A. Donnachie and P.V. Landshoff, *Total cross-sections*, Phys.Lett. **B296** (1992) 227, arXiv: hep-ph/9209205 [hep-ph]. (Cit. on pp. 20, 171.).

[71] R. A. Kycia, J. Chwastowski, R. Staszewski, and J. Turnau, *GenEx: A simple generator structure for exclusive processes in high energy collisions*, Commun. Comput. Phys. **24** (2018) 860, arXiv: 1411.6035 [hep-ph]. (Cit. on p. 20.).

[72] M. Trzebinski, "GenEx - Exclusive Meson Generator", *17th conference on Elastic and Diffractive Scattering*, 2017, arXiv: 1711.03797 [hep-ph]. (Cit. on p. 20.).

[73] T. Sjöstrand et al., *An Introduction to PYTHIA 8.2*, Comput. Phys. Commun. **191** (2015) 159, arXiv: 1410.3012 [hep-ph]. (Cit. on p. 20.).

[74] R. Ciesielski and K. Goulianos, *MBR Monte Carlo Simulation in PYTHIA8*, PoS **ICHEP2012** (2013) 301, ed. by A. Limosani, arXiv: 1205.1446 [hep-ph]. (Cit. on p. 21.).

[75] CDF Collaboration, D. Acosta et al., *Inclusive double pomeron exchange at the Fermilab Tevatron $\bar{p}p$ collider*, Phys. Rev. Lett. **93** (2004) 141601, arXiv: hep-ex/0311023. (Cit. on p. 21.).

[76] L.A. Harland-Lang, V.A. Khoze, and M.G. Ryskin, *Exclusive LHC physics with heavy ions: SuperChic 3*, Eur. Phys. J. C **79** (2019) 39, arXiv: 1810.06567 [hep-ph]. (Cit. on p. 21.).

[77] S.R. Klein, J. Nystrand, J. Seger, Y. Gorbunov, and J. Butterworth, *STARlight: A Monte Carlo simulation program for ultra-peripheral collisions of relativistic ions*, Comput. Phys. Commun. **212** (2017) 258, arXiv: 1607.03838 [hep-ph]. (Cit. on p. 21.).

[78] T. Pierog, Iu. Karpenko, J.M. Katzy, E. Yatsenko, and K. Werner, *EPOS LHC: Test of collective hadronization with data measured at the CERN Large Hadron Collider*, Phys. Rev. C **92** (2015) 034906, arXiv: 1306.0121 [hep-ph]. (Cit. on p. 21.).

[79] T. Pierog, Private communication, September 2019. (Cit. on p. 21.).

[80] T. Pierog et al., *EPOS 3 and Air Showers*, EPJ Web Conf. **210** (2019) 02008, ed. by I. Lhenry-Yvon, J. Biteau, O. Biteau, and P. Ghia. (Cit. on p. 21.).

[81] M. Mieskolainen, *GRANIITTI: A Monte Carlo Event Generator for High Energy Diffraction*, (2019), arXiv: 1910.06300 [hep-ph]. (Cit. on p. 21.).

[82] M. Derrick, B. Musgrave, P. Schreiner, and H. Yuta, *THE REACTION P P —> P P PI+ PI- AT 205-GEV/C.*, Phys. Rev. D **9** (1974) 1215. (Cit. on p. 22.).

[83] Bonn-Hamburg-Muenchen Collaboration, V. Blobel et al., *Investigation of the reactions $pp \to pp$ meson resonance at 12 and 24 GeV/c.*, Nucl. Phys. B **69** (1974) 237. (Cit. on p. 22.).

[84] France-Soviet Union Collaboration, D. Denegri et al., *Double Pomeron Exchange and Diffractive Dissociation in the Reaction p p –> p p pi+ pi- at 69-GeV/c*, Nucl. Phys. B **98** (1975) 189. (Cit. on p. 22.).

[85] CERN-Holland-Manchester Collaboration, J.C.M. Armitage et al., *A study of the reaction $pp \to ppX$ at ISR energies*, Phys. Lett. B **82** (1979) 149. (Cit. on p. 22.).

[86] CERN-PARIS-HEIDELBERG-KARLSRUHE Collaboration, M. Della Negra et al., *Study of Double Pomeron Exchange in p p Collisions at s**(1/2) = 31-GeV*, Phys. Lett. B **65** (1976) 394. (Cit. on p. 22.).

[87] Axial Field Spectrometer Collaboration, T. Akesson et al., *A Study of Exclusive Central Hadron Production at the ISR as a Search for Gluonium States*, Phys. Lett. B **133** (1983) 268. (Cit. on p. 22.).

[88] WA102 Collaboration, D. Barberis et al., *A Partial wave analysis of the centrally produced pi+ pi- system in p p interactions at 450-GeV/c*, Phys. Lett. B **453** (1999) 316, arXiv: hep-ex/9903043. (Cit. on pp. 22, 23.).

[89] Ames-Bologna-CERN-Dortmund-Heidelberg-Warsaw Collaboration, A. Breakstone et al., *Production of the F0 Meson in the Double Pomeron Exchange Reaction $pp \to pp\pi^+\pi^-$ at $\sqrt{s}$ = 62-GeV*, Z. Phys. C **31** (1986) 185. (Cit. on p. 22.).

[90] Ames-Bologna-CERN-Dortmund-Heidelberg-Warsaw Collaboration, A. Breakstone et al., *Inclusive Pomeron-pomeron Interactions at the CERN ISR*, Z. Phys. C **42** (1989) 387, [Erratum: Z.Phys.C 43, 522 (1989)]. (Cit. on p. 22.).

[91] Ames-Bologna-CERN-Dortmund-Heidelberg-Warsaw Collaboration, A. Breakstone et al., *Evidence for f2 (1720) production in the reaction pomeron-pomeron —> pi+ pi- pi+ pi-*, Z. Phys. C **58** (1993) 251. (Cit. on p. 22.).

[92] WA102 Collaboration, D. Barberis et al., *A Coupled channel analysis of the centrally produced K+ K- and pi+ pi- final states in p p interactions at 450-GeV/c*, Phys. Lett. B **462** (1999) 462, arXiv: hep-ex/9907055. (Cit. on p. 23.).

[93] WA102 Collaboration, D. Barberis et al., *A Partial wave analysis of the centrally produced K+ K- and K0(S) K0(S) systems in p p interactions at 450-GeV/c and new information on the spin of the f(J)(1710)*, Phys. Lett. B **453** (1999) 305, arXiv: hep-ex/9903042. (Cit. on p. 23.).

[94] WA102 Collaboration, D Barberis et al., *A Spin analysis of the 4 pi channels produced in central p p interactions at 450-GeV/c*, Phys. Lett. B **471** (2000) 440, arXiv: hep-ex/9912005. (Cit. on p. 23.).

[95] WA102 Collaboration, D. Barberis et al., *A Study of the centrally produced pi+ pi- pi+ pi- channel in p p interactions at 450-GeV/c*, Phys. Lett. B **413** (1997) 217, arXiv: hep-ex/9707021. (Cit. on p. 23.).

[96] WA102 Collaboration, D. Barberis et al., *A Measurement of the branching fractions of the f(1)(1285) and f(1)(1420) produced in central p p interactions at 450-GeV/c*, Phys. Lett. B **440** (1998) 225, arXiv: hep-ex/9810003. (Cit. on p. 23.).

[97] WA102 Collaboration, D Barberis et al., *A Study of the f(0)(1370), f(0)(1500), f(0)(2000) and f(2)(1950) observed in the centrally produced 4 pi final states*, Phys. Lett. B **474** (2000) 423, arXiv: hep-ex/0001017. (Cit. on p. 23.).

[98] WA102 Collaboration, D. Barberis et al., *A Partial wave analysis of the centrally produced pi0 pi0 system in p p interactions at 450-GeV/c*, Phys. Lett. B **453** (1999) 325, arXiv: hep-ex/9903044. (Cit. on p. 23.).

[99] WA102 Collaboration, D. Barberis et al., *A Study of pseudoscalar states produced centrally in p p interactions at 450-GeV/c*, Phys. Lett. B **427** (1998) 398, arXiv: hep-ex/9803029. (Cit. on p. 23.).

[100] WA102 Collaboration, D Barberis et al., *A Study of the centrally produced phi phi system in p p interactions at 450-GeV/c*, Phys. Lett. B **432** (1998) 436, arXiv: hep-ex/9805018. (Cit. on p. 23.).

[101] CDF Collaboration, T. Aaltonen et al., *Measurement of central exclusive $\pi^+\pi^-$ production in $p\bar{p}$ collisions at $\sqrt{s} = 0.9$ and 1.96 TeV at CDF*, Phys. Rev. D **91** (2015) 091101, arXiv: 1502.01391 [hep-ex]. (Cit. on pp. 23, 24.).

[102] L. Adamczyk, W. Guryn, and J. Turnau, *Central exclusive production at RHIC*, Int. J. Mod. Phys. A **29** (2014) 1446010, arXiv: 1410.5752 [hep-ex]. (Cit. on pp. 23, 24.).

[103] COMPASS Collaboration, A. Austregesilo, *Light Scalar Mesons in Central Production at COMPASS*, AIP Conf. Proc. **1735** (2016) 030012, ed. by M.R. Pennington, arXiv: 1602.03991 [hep-ex]. (Cit. on p. 23.).

[104] ALICE Collaboration, R. Schicker, "Central Meson Production in ALICE", *14th International Conference on Hadron Spectroscopy*, 2011, arXiv: 1110.3693 [hep-ex]. (Cit. on pp. 23, 24.).

[105] ALICE Collaboration, R. Schicker, "Central exclusive meson production in proton-proton collisions in ALICE at the LHC", *18th International Conference on Hadron Spectroscopy and Structure*, 2019, arXiv: 1912.00611 [hep-ph]. (Cit. on p. 23.).

[106] CMS Collaboration, V. Khachatryan et al., *Exclusive and semi-exclusive pi+pi- production in proton-proton collisions at sqrt(s) = 7 TeV*, (2017), arXiv: 1706.08310 [hep-ex]. (Cit. on p. 23.).

[107] CMS Collaboration, A.M. Sirunyan et al., *Study of central exclusive $\pi^+\pi^-$ production in proton-proton collisions at $\sqrt{s} = 5.02$ and 13 TeV*, Eur. Phys. J. C **80** (2020) 718, arXiv: 2003.02811 [hep-ex]. (Cit. on pp. 23, 24, 238.).

[108] CMS and TOTEM Collaboration, *Background rejection technique for central exclusive production of low-mass resonances with joint CMS-TOTEM high-β^* 2015 pp data*, CMS-DP-2017-008 (2017). (Cit. on p. 23.).

[109] LHCb Collaboration, R. McNulty, "Central Exclusive Production at LHCb", *17th conference on Elastic and Diffractive Scattering*, 2017, arXiv: 1711.06668 [hep-ex]. (Cit. on p. 23.).

[110] *STAR graphics repository (courtesy of T. Sakuma)*, https://drupal.star.bnl.gov/STAR/public/img/SketchUpSTAR. (Cit. on pp. 29–31.).

[111] *RHIC accelerator website*, https://www.bnl.gov/RHIC/. (Cit. on p. 29.).

[112] *Brookhaven National Laboratory website*, http://www.bnl.gov. (Cit. on p. 29.).

[113] I. Alekseev et al., *Polarized proton collider at RHIC*, Nucl. Instrum. Meth. A **499** (2003) 392. (Cit. on p. 29.).

[114] A. Zelenski et al., *Optically-pumped Polarized H^- and $3HE^{++}$ ion Sources Development at RHIC*, PoS **SPIN2018** (2018) 100, ed. by P. Lenisa, G. Ciullo, M. Contalbrigo, and L. Pappalardo. (Cit. on p. 29.).

[115] *PHOBOS experiment website*, https://www.bnl.gov/phobos/. (Cit. on p. 29.).

[116] PHOBOS Collaboration, B.B Back et al., *The PHOBOS detector at RHIC*, Nucl. Instrum. Meth. A **499** (2003) 603. (Cit. on p. 29.).

[117] *BRAHMS experiment website*, http://www4.rcf.bnl.gov/brahms/WWW/brahms.html. (Cit. on p. 29.).

[118] BRAHMS Collaboration, M Adamczyk et al., *The BRAHMS experiment at RHIC*, Nucl. Instrum. Meth. A **499** (2003) 437. (Cit. on p. 29.).

[119] *PHENIX experiment website*, https://www.phenix.bnl.gov/. (Cit. on p. 29.).

[120] PHENIX Collaboration, K. Adcox et al., *PHENIX detector overview*, Nucl. Instrum. Meth. A **499** (2003) 469. (Cit. on p. 29.).

[121] *STAR experiment website*, https://www.star.bnl.gov. (Cit. on p. 29.).

[122] STAR Collaboration, K.H. Ackermann et al., *STAR detector overview*, Nucl.Instrum.Meth. **A499** (2003) 624. (Cit. on pp. 29, 30.).

[123] *PP2PP experiment website*, https://www.racf.bnl.gov/Facility/pp2pp/. (Cit. on p. 29.).

[124] S. Bultmann et al., *The PP2PP experiment at RHIC: Silicon detectors installed in Roman Pots for forward proton detection close to the beam*, Nucl. Instrum. Meth. A **535** (2004) 415, ed. by M. Jeitler, M. Krammer, M. Regler, and G. Badurek. (Cit. on p. 29.).

[125] STAR Collaboration, J. Adams et al., *Experimental and theoretical challenges in the search for the quark gluon plasma: The STAR Collaboration's critical assessment of the evidence from RHIC collisions*, Nucl. Phys. A **757** (2005) 102, arXiv: nucl-ex/0501009. (Cit. on p. 30.).

[126] STAR Collaboration, K.C. Meehan, *Fixed Target Collisions at STAR*, Nucl. Phys. A **956** (2016) 878, ed. by Y. Akiba et al. (Cit. on p. 30.).

[127] *Brookhaven National Laboratory flickr album*, https://www.flickr.com/photos/brookhavenlab/sets/72157613690851651/. (Cit. on p. 30.).

[128] M. Anderson et al., *The Star time projection chamber: A Unique tool for studying high multiplicity events at RHIC*, Nucl. Instrum. Meth. A **499** (2003) 659, arXiv: nucl-ex/0301015. (Cit. on pp. 30, 31.).

[129] STAR Collaboration, M. Beddo et al., *The STAR barrel electromagnetic calorimeter*, Nucl. Instrum. Meth. A **499** (2003) 725. (Cit. on p. 30.).

[130] STAR Collaboration, C.E. Allgower et al., *The STAR endcap electromagnetic calorimeter*, Nucl. Instrum. Meth. A **499** (2003) 740. (Cit. on p. 30.).

[131] J. Wu et al., *The performance of the TOFr tray in STAR*, Nucl. Instrum. Meth. A **538** (2005) 243. (Cit. on pp. 30, 33.).

[132] STAR Collaboration, C.A. Whitten, *The beam-beam counter: A local polarimeter at STAR*, AIP Conf.Proc. **980** (2008) 390. (Cit. on p. 30.).

[133] C. Adler, A. Denisov, E. Garcia, M.J. Murray, and Sebastian N. Strobele H.and White, *The RHIC zero degree calorimeter*, Nucl. Instrum. Meth. A **470** (2001) 488, arXiv: nucl-ex/0008005. (Cit. on pp. 30, 32.).

[134] STAR Collaboration, Giacomo Contin, *The STAR Heavy Flavor Tracker and Upgrade Plan*, Nucl. Phys. A **956** (2016) 858, ed. by Y. Akiba et al. (Cit. on pp. 30, 33.).

[135] STAR Collaboration, L. Kotchenda et al., *STAR TPC gas system*, Nucl. Instrum. Meth. A **499** (2003) 703. (Cit. on p. 31.).

[136] STAR Collaboration, J. Kiryluk, *Relative luminosity measurement in STAR and implications for spin asymmetry determinations*, AIP Conf. Proc. **675** (2003) 424, ed. by Y.I. Makdisi, A.U. Luccio, and W.W. MacKay. (Cit. on p. 32.).

[137] *BBC group at STAR*, https://www.star.bnl.gov/public/bbc/index.html. (Cit. on pp. 32, 33.).

[138] C. Adler et al., *The RHIC zero-degree calorimeters*, Nucl. Instrum. Meth. A **499** (2003) 433. (Cit. on p. 32.).

[139] Y.-F. Xu et al., *Physics performance of the STAR zero degree calorimeter at relativistic heavy ion collider*, Nucl. Sci. Tech. **27** (2016) 126. (Cit. on p. 32.).

[140] W.J. Llope et al., *The TOFp / pVPD time-of-flight system for STAR*, Nucl. Instrum. Meth. A **522** (2004) 252, arXiv: nucl-ex/0308022. (Cit. on p. 33.).

[141] M. Shao et al., *Extensive particle identification with TPC and TOF at the STAR experiment*, Nucl. Instrum. Meth. A **558** (2006) 419, arXiv: nucl-ex/0505026. (Cit. on p. 33.).

[142] STAR Collaboration, W.J. Llope, *The large-area time-of-flight (TOF) upgrade for the STAR detector*, AIP Conf. Proc. **1099** (2009) 778, ed. by F. McDaniel and B.L. Doyle. (Cit. on p. 33.).

[143] *Nuclear Science and Technology website*, https://nsww.org/projects/bnl/star/subsystems.php. (Cit. on p. 33.).

[144] *Brookhaven National Laboratory Media and Communications Office*, https://www.bnl.gov/newsroom/news.php?a=112222. (Cit. on p. 33.).

[145] J. Schambach et al., "The STAR Heavy Flavor Tracker (HFT)", *20th International Conference on Particles and Nuclei*, 2014 659. (Cit. on p. 33.).

[146] R. Sikora, "Study of elastic proton-proton scattering with the STAR detector at RHIC", MSc Thesis: AGH-UST, Krakow, 2014. (Cit. on pp. 34, 38, 43, 68, 94.).

[147] E.G. Judd et al., *The evolution of the STAR Trigger System*, Nucl. Instrum. Meth. A **902** (2018) 228. (Cit. on p. 36.).

[148] STAR Collaboration, A. Rose, *STAR integrated tracker*, (2003), arXiv: nucl-ex/0307015. (Cit. on p. 37.).

[149] P. Astier et al., *Kalman filter track fits and track break point analysis*, Nucl. Instrum. Meth. A **450** (2000) 138, arXiv: physics/9912034. (Cit. on p. 37.).

[150] R. Reed et al., *Vertex finding in pile-up rich events for p+p and d+Au collisions at STAR*, J. Phys. Conf. Ser. **219** (2010) 032020, ed. by J. Gruntorad and M. Lokajicek. (Cit. on p. 37.).

[151] D. Smirnov, J. Lauret, V. Perevoztchikov, G. Van Buren, and J. Webb, *Vertex Reconstruction at STAR: Overview and Performance Evaluation*, J. Phys. Conf. Ser. **898** (2017) 042058, ed. by Richard Mount and Craig Tull. (Cit. on pp. 37, 103.).

[152] H. Bichsel, *A method to improve tracking and particle identification in TPCs and silicon detectors*, Nucl. Instrum. Meth. **A562** (2006) 154. (Cit. on p. 38.).

[153] R. Sikora, *Study of elastic proton-proton scattering with the STAR detector at RHIC*, Proc. SPIE Int. Soc. Opt. Eng. **9662** (2015) 96622F, ed. by R.S. Romaniuk. (Cit. on p. 38.).

[154] V. Schoefer et al., "RHIC Polarized Proton-Proton Operation at 100 GeV in Run 15", *6th International Particle Accelerator Conference*, 2015 TUPWI060. (Cit. on p. 41.).

[155] R. Brun et al., *GEANT Detector Description and Simulation Tool*, CERN-W-5013 (1994). (Cit. on p. 43.).

[156] R. Sikora, "Elastic proton-proton scattering in the STAR experiment at RHIC", BSc Thesis: AGH-UST, Krakow, 2013. (Cit. on p. 43.).

[157] L. Fulek, "Transport of particles through the RHIC accelerator magnet system", Polish edition, BSc Thesis: AGH-UST, Krakow, 2013. (Cit. on p. 43.).

[158] L. Fulek, "Study of single diffractive dissociation in proton-proton scattering with STAR detector at RHIC", Polish edition, MSc Thesis: AGH-UST, Krakow, 2014. (Cit. on p. 43.).

[159] GEANT4 Collaboration, S. Agostinelli et al., *GEANT4: A Simulation toolkit*, Nucl. Instrum. Meth. A **506** (2003) 250. (Cit. on p. 43.).

[160] S. Das, *A simple alternative to the Crystal Ball function*, (2016), arXiv: 1603.08591 [hep-ex]. (Cit. on p. 50.).

[161] *RHIC Run 15 Overview*, http://www.agsrhichome.bnl.gov/RHIC/Runs/index.html#Run-15. (Cit. on p. 114.).

[162] J. C. Collins and D. E. Soper, *Angular Distribution of Dileptons in High-Energy Hadron Collisions*, Phys. Rev. D **16** (1977) 2219. (Cit. on pp. 119, 200, 218.).

[163] S. van der Meer, *Calibration of the Effective Beam Height in the ISR*, CERN-ISR-PO-68-31 (1968). (Cit. on p. 128.).

[164] A. Drees, *Effective ZDC cross section measurement during a dedicated STAR elastic scattering physics store in Run15*, BNL-212462-2019-TECH (2019). (Cit. on p. 128.).

[165] *LHC accelerator website*, https://home.cern/science/accelerators/large-hadron-collider. (Cit. on p. 159.).

[166] *CERN website*, https://home.cern. (Cit. on p. 159.).

[167] ALICE Collaboration, K. Aamodt et al., *The ALICE experiment at the CERN LHC*, JINST **3** (2008) S08002. (Cit. on p. 159.).

[168] *ALICE experiment website*, http://alice.web.cern.ch. (Cit. on p. 159.).

[169] *ATLAS experiment website*, https://atlas.cern. (Cit. on p. 159.).

[170] CMS Collaboration, S. Chatrchyan et al., *The CMS Experiment at the CERN LHC*, JINST **3** (2008) S08004. (Cit. on p. 159.).

[171] *CMS experiment website*, https://cms.cern. (Cit. on p. 159.).

[172] LHCb Collaboration, Jr. Alves A.Augusto et al., *The LHCb Detector at the LHC*, JINST **3** (2008) S08005. (Cit. on p. 159.).

[173] *LHCb experiment website*, http://lhcb.web.cern.ch. (Cit. on p. 159.).

[174] TOTEM Collaboration, G. Anelli et al., *The TOTEM experiment at the CERN Large Hadron Collider*, JINST **3** (2008) S08007. (Cit. on p. 159.).

[175] S. Abdel Khalek et al., *The ALFA Roman Pot Detectors of ATLAS*, JINST **11** (2016) P11013, arXiv: 1609.00249 [physics.ins-det]. (Cit. on pp. 159, 163, 165.).

[176] ATLAS Collaboration, L. Adamczyk et al., *Technical Design Report for the ATLAS Forward Proton Detector*, CERN-LHCC-2015-009 (2015). (Cit. on p. 159.).

[177] CMS and TOTEM Collaboration, M. Albrow et al., *CMS-TOTEM Precision Proton Spectrometer*, CERN-LHCC-2014-021 (2014). (Cit. on p. 159.).

[178] E. Mobs, *The CERN accelerator complex. Complexe des accélérateurs du CERN*, (2016), General Photo, URL: https://cds.cern.ch/record/2197559. (Cit. on p. 159.).

[179] G. Aad et al., *ATLAS pixel detector electronics and sensors*, JINST **3** (2008) P07007. (Cit. on p. 161.).

[180] ATLAS Collaboration, M. Capeans et al., *ATLAS Insertable B-Layer Technical Design Report*, CERN-LHCC-2010-013 (2010). (Cit. on p. 161.).

[181] ATLAS Collaboration, G. Aad et al., *Operation and performance of the ATLAS semiconductor tracker*, JINST **9** (2014) P08009, arXiv: 1404.7473 [hep-ex]. (Cit. on p. 161.).

[182] ATLAS TRT Collaboration, E. Abat et al., *The ATLAS Transition Radiation Tracker (TRT) proportional drift tube: Design and performance*, JINST **3** (2008) P02013. (Cit. on p. 161.).

[183] ATLAS TRT Collaboration, E. Abat et al., *The ATLAS TRT barrel detector*, JINST **3** (2008) P02014. (Cit. on p. 161.).

[184] E. Abat et al., *The ATLAS TRT end-cap detectors*, JINST **3** (2008) P10003. (Cit. on p. 161.).

[185] K. Potamianos, *The upgraded Pixel detector and the commissioning of the Inner Detector tracking of the ATLAS experiment for Run-2 at the Large Hadron Collider*, (2015), arXiv: 1608.07850 [physics.ins-det]. (Cit. on p. 162.).

[186] ATLAS Collaboration, *Performance of the Minimum Bias Trigger in p-p Collisions at Sqrt(s) = 900 GeV*, ATLAS-CONF-2010-025 (2010). (Cit. on p. 163.).

[187] ATLAS Collaboration, K.W. Janas, *The track-based alignment of the ALFA Roman Pot detectors of the ATLAS experiment*, tech. rep. ATL-FWD-PROC-2019-003, CERN, 2019. (Cit. on pp. 164, 168.).

[188] CERN Bulletin, *ATLAS gets its own luminosity detector. ATLAS est doté de son propre détecteur de luminosité*, (2011) 6, URL: https://cds.cern.ch/record/1338531. (Cit. on p. 165.).

[189] S. Ask et al., *The ATLAS central level-1 trigger logic and TTC system*, JINST **3** (2008) P08002. (Cit. on p. 166.).

[190] ATLAS TDAQ Collaboration, M. Abolins et al., *The ATLAS Data Acquisition and High Level Trigger system*, JINST **11** (2016) P06008. (Cit. on p. 166.).

[191] ATLAS Collaboration, *ATLAS high-level trigger, data acquisition and controls: Technical design report*, ATLAS-TRD-016 (2003). (Cit. on p. 166.).

[192] ATLAS Collaboration, M. Aaboud et al., *Performance of the ATLAS Track Reconstruction Algorithms in Dense Environments in LHC Run 2*, Eur. Phys. J. C **77** (2017) 673, arXiv: 1704.07983 [hep-ex]. (Cit. on p. 167.).

[193] T. Cornelissen et al., *The new ATLAS track reconstruction (NEWT)*, J. Phys. Conf. Ser. **119** (2008) 032014, ed. by R. Sobie R.and Tafirout and J. Thomson. (Cit. on p. 167.).

[194] ATLAS Collaboration, G. Aad et al., *A neural network clustering algorithm for the ATLAS silicon pixel detector*, JINST **9** (2014) P09009, arXiv: 1406.7690 [hep-ex]. (Cit. on p. 167.).

[195] ATLAS Collaboration, *dE/dx measurement in the ATLAS Pixel Detector and its use for particle identification*, ATLAS-CONF-2011-016 (2011). (Cit. on p. 167.).

[196] ATLAS Collaboration, S. Boutle et al., *Primary vertex reconstruction at the ATLAS experiment*, J. Phys. Conf. Ser. **898** (2017) 042056, ed. by Richard Mount and Craig Tull. (Cit. on p. 167.).

[197] ATLAS Collaboration, M. Aaboud et al., *Reconstruction of primary vertices at the ATLAS experiment in Run 1 proton–proton collisions at the LHC*, Eur. Phys. J. C **77** (2017) 332, arXiv: 1611.10235 [physics.ins-det]. (Cit. on p. 167.).

[198] ATLAS Collaboration, G. Aad et al., *Measurement of the total cross section from elastic scattering in pp collisions at* $\sqrt{s} = 7$ *TeV with the ATLAS detector*, Nucl. Phys. B **889** (2014) 486, arXiv: 1408.5778 [hep-ex]. (Cit. on pp. 168, 188.).

[199] ATLAS Collaboration, *The Pythia 8 A3 tune description of ATLAS minimum bias and inelastic measurements incorporating the Donnachie-Landshoff diffractive model*, ATL-PHYS-PUB-2016-017 (2016). (Cit. on p. 171.).

[200] ATLAS Collaboration, G. Aad et al., *The ATLAS Simulation Infrastructure*, Eur. Phys. J. C **70** (2010) 823, arXiv: 1005.4568 [physics.ins-det]. (Cit. on p. 171.).

[201] P. Bussey, *FPTrack Programme*, http://www.ppe.gla.ac.uk/~bussey/FPTRACK, 2008. (Cit. on p. 171.).

[202] ATLAS Collaboration, M. Aaboud et al., *Charged-particle distributions at low transverse momentum in* $\sqrt{s} = 13$ *TeV pp interactions measured with the ATLAS detector at the LHC*, Eur. Phys. J. C **76** (2016) 502, arXiv: 1606.01133 [hep-ex]. (Cit. on pp. 174, 193.).

[203] ATLAS Collaboration, G. Aad et al., *Measurement of the total cross section from elastic scattering in pp collisions at* $\sqrt{s} = 7$ *TeV with the ATLAS detector*, Nucl. Phys. B **889** (2014) 486, arXiv: 1408.5778 [hep-ex]. (Cit. on p. 175.).

[204] ATLAS Collaboration, M. Aaboud et al., *Measurement of the total cross section from elastic scattering in pp collisions at* $\sqrt{s} = 8$ *TeV with the ATLAS detector*, Phys. Lett. B **761** (2016) 158, arXiv: 1607.06605 [hep-ex]. (Cit. on pp. 175, 188, 190.).

[205] ATLAS Collaboration, L. Adamczyk and I. Lakomiec, *Study of the proton reconstruction efficiency with the ALFA detector using an overlay technique of Monte Carlo signal events with zero-bias collider data*, Internal documentation (2020). (Cit. on pp. 189, 194, 203.).

[206] ATLAS Collaboration, *Studies of the ATLAS Inner Detector material using* $\sqrt{s}$ *=13 TeV pp collision data*, ATL-PHYS-PUB-2015-050 (2015). (Cit. on p. 204.).

[207] ATLAS Collaboration, *Luminosity determination in pp collisions at* $\sqrt{s} = 13$ *TeV using the ATLAS detector at the LHC*, ATLAS-CONF-2019-021 (2019). (Cit. on p. 205.).

[208] F. E. Close and A. Kirk, *A Glueball - q anti-q filter in central hadron production*, Phys. Lett. **B397** (1997) 333, arXiv: hep-ph/9701222 [hep-ph]. (Cit. on p. 217.).

[209] WA102 Collaboration, D. Barberis et al., *A Kinematical selection of glueball candidates in central production*, Phys. Lett. B **397** (1997) 339, [Erratum: Phys.Lett.B 410, 353–353 (1997)]. (Cit. on p. 218.).

[210] P. Lebiedowicz, O. Nachtmann, and A. Szczurek, *Extracting the pomeron-pomeron-*$f_2(1270)$ *coupling in the* $pp \to pp\pi^+\pi^-$ *reaction through angular distributions of the pions*, Phys. Rev. D **101** (2020) 034008, arXiv: 1901.07788 [hep-ph]. (Cit. on p. 218.).

[211] K. Gottfried and J. D. Jackson, *On the Connection between production mechanism and decay of resonances at high-energies*, Nuovo Cim. **33** (1964) 309. (Cit. on p. 219.).

[212] WA102 Collaboration, D. Barberis et al., *A Measurement of the branching fractions of the f(1)(1285) and f(1)(1420) produced in central p p interactions at 450-GeV/c*, Phys. Lett. B **440** (1998) 225, arXiv: hep-ex/9810003. (Cit. on p. 229.).

[213] J.M. Blatt and V.F. Weisskopf, *Theoretical nuclear physics*, John Wiley & Sons, 1952. (Cit. on p. 237.).

[214] F. Von Hippel and C. Quigg, *Centrifugal-barrier effects in resonance partial decay widths, shapes, and production amplitudes*, Phys. Rev. D **5** (1972) 624. (Cit. on p. 237.).

[215] S.M. Flatte, *Coupled - Channel Analysis of the pi eta and K anti-K Systems Near K anti-K Threshold*, Phys. Lett. B **63** (1976) 224. (Cit. on p. 237.).

[216] BES Collaboration, M. Ablikim et al., *Resonances in J / psi —> phi pi+ pi- and phi K+ K-*, Phys. Lett. B **607** (2005) 243, arXiv: hep-ex/0411001. (Cit. on p. 237.).

[217] M. Hatlo et al., *Developments of mathematical software libraries for the LHC experiments*, IEEE Trans. Nucl. Sci. **52** (2005) 2818. (Cit. on p. 237.).

[218] R. Brun and F. Rademakers, *ROOT: An object oriented data analysis framework*, Nucl. Instrum. Meth. A **389** (1997) 81, ed. by M. Werlen and D. Perret-Gallix. (Cit. on p. 237.).

[219] P. Lebiedowicz, J. Leutgeb, O. Nachtmann, A. Rebhan, and A. Szczurek, *Central exclusive diffractive production of axial-vector $f_1(1285)$ and $f_1(1420)$ mesons in proton-proton collisions*, (2020), arXiv: 2008.07452 [hep-ph]. (Cit. on pp. 243, 244.).

[220] S.G. Peggs, "Beam-beam collisions and crossing angles in RHIC", *Workshop on Beam-Beam Effects in Large Hadron Colliders*, 1999 70. (Cit. on p. 268.).

Appendices

A. Acronyms

A.1 General

ADC	Analogue-to-Digital Converter
BNL	Brookhaven National Laboratory
CERN	European Laboratory for Particle Physics
CD	Central Diffraction
CEP	Central Exclusive Production
DD	Double Diffraction
DPE	Double Pomeron Exchange
EM	Electromagnetic
HLT	High Level Trigger
IP	Interaction Point
IR	Interaction Region
L0	Level 0
L1	Level 1
L2	Level 2
LEP	Large Electron Positron Collider
LHC	Large Hadron Collider
LVDT	Linear Variable Differential Transformer
MB	Minimum Bias
MBR	Minimum Bias Rockefeller
MPV	Most Probable Value
MC	Monte Carlo
ND	Non-Diffraction
PDG	Particle Data Group
PID	Particle Identification
PWA	Partial Wave Analysis
PXL	Pixel detector
QCD	Quantum Chromodynamics
QED	Quantum Electrodynamics
QGP	Quark Gluon Plasma
RHIC	Relativistic Heavy Ion Collider
RP	Roman Pot
SD	Single Diffraction
SM	Standard Model
TAC	Time-to-Amplitude Converter
TDC	Time-to-Digital Converter
WLS	Wavelength Shifter

A.2 The ATLAS experiment

AC	ATLAS Cut
AFP	ATLAS Forward Proton
ALFA	Absolute Luminosity For ATLAS
ATLAS	A Toroidal LHC Apparatus
EF	Event Filter
IBL	Insertable B-Layer
ID	Inner Detector
LAr	liquid argon
MBTS	Minimum Bias Trigger Scintillators
MD	Main Detector
OD	Overlap Detector
SCT	Semiconductor Tracker
SPS	Super Proton Synchrotron
SpTrk	space points and a track requirement (component of the HLT)
TDAQ	Trigger and Data Acquisition
TRT	Transition Radiation Tracker
VetoMbts2in	inner MBTS veto (component of the HLT)

A.3 The STAR experiment

AGS	Alternating Gradient Synchrotron
BBC	Beam Beam Counter
BEMC	Barrel Electromagnetic Calorimeter
DAQ	Data Acquisition
HFT	Heavy Flavor Tracker
IST	Inner Silicon Tracker
MRPC	Multi-gap Resistive Plate Chamber
MWPC	Multi Wire Proportional Chamber
RF	Radio Frequency
SC	STAR Cut
SSD	Silicon Strip Detector
SST	Silicon Strip Tracker
STAR	Solenoidal Tracker at RHIC
TOF	Time of Flight
TPC	Time Projection Chamber
VPD	Vertex Position Detector
ZDC	Zero-Degree Calorimeter

B. Momentum reconstruction using STAR RP system

A method for momentum reconstruction of protons tagged by the RP detectors is presented below. A geometrical approach is used with an assumption of a constant and uniform magnetic field inside the DX magnet.

The RP subsystem (Fig. 5.8), with two vertical RP stations on each side of the STAR IP, allows to measure positions of scattered proton at two locations, 15.8 m and 17.6 m from the IP. From the measured coordinates (x_1, y_1) and (x_2, y_2) one can reconstruct local angles, θ_x^{RP} and θ_y^{RP}, using simple relations:

$$\tan\theta_x^{\mathrm{RP}} = \frac{x_2 - x_1}{d_{\mathrm{RP}}}, \qquad \tan\theta_y^{\mathrm{RP}} = \frac{y_2 - y_1}{d_{\mathrm{RP}}}, \tag{B.1}$$

where d_{RP} is the distance between the RP stations in the same branch.

Assuming that there is a constant and uniform magnetic field inside the DX magnet, $\vec{B} = (0, -B, 0)$, the y-component of the scattered proton's momentum remains unchanged on its way from the IP to the RP stations, hence the y-component of the scattered proton's polar angle at the IP, $\theta_y = \theta_y^{\mathrm{RP}}$ (Fig. B.2).

However, the trajectory of the proton in the xz plane is curved when traversing the DX magnet due to the Lorentz force (Figs. B.1 and B.3). The radius of the circular path is given by:

$$R = \frac{p_{xz}}{eB}, \tag{B.2}$$

where p_{xz} is the momentum component in the xz plane, related to the total momentum, p, by

$$\frac{p_{xz}}{p} = \cos\theta_y. \tag{B.3}$$

Introducing the fractional momentum loss of of the scattered proton, $\xi = (p_0 - p)/p_0$, where p_0 is the beam proton momentum, one can express the radius of curvature as:

$$R = \underbrace{\frac{p_0}{eB}}_{R_0} \cdot \cos\theta_y \cdot (1 - \xi), \tag{B.4}$$

where R_0 is the radius of curvature of the beam trajectory inside the DX dipole. Since maximum θ_y contained within RP acceptance is expected to be of the order of 5 mrad, factor $\cos\theta_y$ changes R by 0.001%, hence it can be neglected in further calculations. The B-field for $p = 100$ GeV is nominally equal to 1.7 T, which yields $R_0 = 196.2$ m.

In order to find the relation between local angle θ_x^{RP} and corresponding angle θ_x at IP let us use the STAR coordinate system. We assume ideal alignment of the DX magnet with respect to the beam (beam perpendicular to DX at the entrance). Let us write an equation describing the circle with centre at $S = (d_1 - \Delta z, x_{\mathrm{IP}} + x_{in} - \Delta x + R)$, whose part is the trajectory of proton inside DX magnet:

$$(z - d_1 + \Delta z)^2 + (x - x_{\mathrm{IP}} - x_{in} + \Delta x - R)^2 = R^2. \tag{B.5}$$

Symbols used in Eq. (B.5) are explained in Figs. B.1 and B.3. From above one can find, that for proton

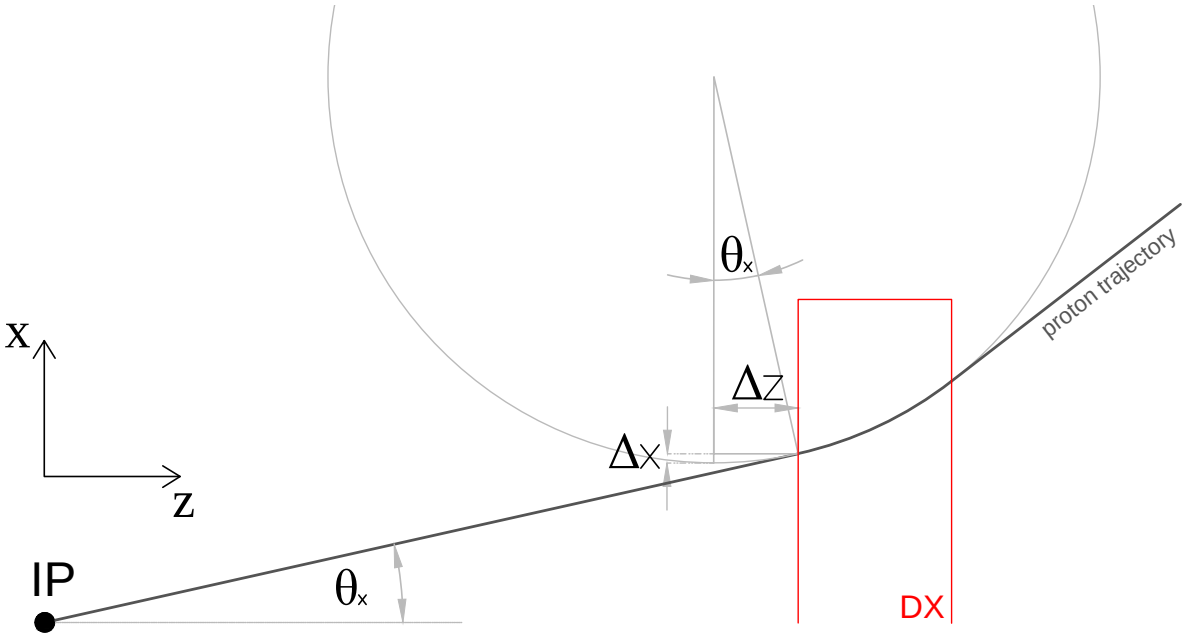

Figure B.1: Scheme of proton trajectory. Proportions of elements are not preserved.

in DX magnet

$$x(z) = x_{\mathrm{IP}} + x_{in} - \Delta x + R - R\sqrt{1 - \left(\frac{z - d_1 + \Delta z}{R}\right)^2}. \tag{B.6}$$

From the derivative of Eq. (B.6),

$$\frac{dx}{dz} = \frac{z - d_1 + \Delta z}{R} \Bigg/ \sqrt{1 - \left(\frac{z - d_1 + \Delta z}{R}\right)^2}, \tag{B.7}$$

one can easily find the angle, at which proton leaves the field of magnet DX:

$$\left.\frac{dx}{dz}\right|_{z=d_1+l_{\mathrm{DX}}} = \tan\alpha_p = \frac{l_{\mathrm{DX}} + \Delta z}{R} \Bigg/ \sqrt{1 - \left(\frac{l_{\mathrm{DX}} + \Delta z}{R}\right)^2}. \tag{B.8}$$

From Figs. B.1 and B.3 one can find the following relations:

$$\Delta z = R\sin\theta_x, \qquad \Delta x = R(1 - \cos\theta_x), \qquad x_{in} = (d_1 - z_{\mathrm{IP}})\tan\theta_x. \tag{B.9}$$

Inserting formulas for Δx and R to Eq. (B.8) one obtains:

$$\tan\alpha_p = \left(\frac{l_{\mathrm{DX}}}{R_0(1-\xi)} + \sin\theta_x\right) \Bigg/ \sqrt{1 - \left(\frac{l_{\mathrm{DX}}}{R_0(1-\xi)} + \sin\theta_x\right)^2}. \tag{B.10}$$

Then, for beam protons (no scattering i.e. $\theta_x = 0$, $\xi = 0$, $\alpha_p = \alpha_0$) one obtains

$$\tan\alpha_0 = \frac{l_{\mathrm{DX}}}{R_0} \Bigg/ \sqrt{1 - \left(\frac{l_{\mathrm{DX}}}{R_0}\right)^2} \quad \Rightarrow \quad \alpha_0\big|_{p=100\ \mathrm{GeV}} = 18.86\ \mathrm{mrad}. \tag{B.11}$$

The above value is in perfect agreement with declared value of the bending angle of DX magnet [220].

Since $l_{\mathrm{DX}} \ll R_0$ and α_0 is small,

$$\alpha_0 \approx \frac{l_{\mathrm{DX}}}{R_0}. \tag{B.12}$$

The local angle measured in Roman Pots is related to the bending angle of the trajectory of scattered proton by

$$\alpha_p = \alpha_0 + \theta_x^{\mathrm{RP}} \tag{B.13}$$

(see Fig. B.3). Simple transformation of Eq. (B.10) and insertion of (B.13) gives formula for θ_x:

$$\sin\theta_x = \frac{\tan\left(\alpha_0 + \theta_x^{\mathrm{RP}}\right)}{\sqrt{1+\tan^2\left(\alpha_0 + \theta_x^{\mathrm{RP}}\right)}} - \frac{l_{\mathrm{DX}}}{R_0(1-\xi)}. \tag{B.14}$$

For small angles, which are considered here, one can approximate Eq. (B.14) by

$$\theta_x \approx \theta_x^{\mathrm{RP}} - \alpha_0 \frac{\xi}{1-\xi}. \tag{B.15}$$

As one can notice, for the elastic scattering ($\xi = 0$), the angle measured in RP system and the initial angle at the vertex, are equal.

To reconstruct θ_x and ξ, one has to use the position of proton at the face of detector. Using Fig. B.3, one can find the following relations:

$$x_1 = \widetilde{x} + \left(d_2 - \widetilde{d}\right)\tan\theta_x^{\mathrm{RP}}, \qquad \frac{\widetilde{x}}{\delta x} = \cos\alpha_0, \qquad \frac{\widetilde{d}}{\delta x} = \sin\alpha_0. \tag{B.16}$$

Combining the above leads to

$$x_1 = \delta x\left(\cos\alpha_0 - \sin\alpha_0\tan\theta_x^{\mathrm{RP}}\right) + d_2\tan\theta_x^{\mathrm{RP}}. \tag{B.17}$$

The difference, δx, between the x-positions of the scattered and beam protons, at the exit of DX magnet, can be written as

$$\delta x = x(d_1 + l_{\mathrm{DX}}; \theta_x, \xi) - x_0, \tag{B.18}$$

where

$$x_0 = x(d_1 + l_{\mathrm{DX}}; 0, 0) = R_0\left[1 - \sqrt{1 - \left(\frac{l_{\mathrm{DX}}}{R_0}\right)^2}\right] \approx \frac{l_{\mathrm{DX}}^2}{2R_0} \approx 3.49\ \mathrm{cm}. \tag{B.19}$$

Merging Eq. (B.18) with (B.6) and (B.19) results in

$$\delta x = x_{\mathrm{IP}} + (d_1 - z_{\mathrm{IP}})\tan\theta_x + R_0(1-\xi)\left[\cos\theta_x - \sqrt{1 - \left(\frac{l_{\mathrm{DX}}}{R_0(1-\xi)} + \sin\theta_x\right)^2}\right] - R_0\left[1 - \sqrt{1 - \left(\frac{l_{\mathrm{DX}}}{R_0}\right)^2}\right]. \tag{B.20}$$

All the components of Eq. (B.17) are now represented in the form dependent on θ_x or θ_x^{RP}, hence one can easily derive dependencies between position of scattered proton in the detector x_1 and the scattering angle at the vertex, θ_x, fractional momentum loss, ξ, or the angle in the RP system, θ_x^{RP}:

$$x_1 = x_{\mathrm{IP}} + (d_1 + l_{\mathrm{DX}} - z_{\mathrm{IP}})\,\theta_x + d_2\theta_x^{\mathrm{RP}} + \frac{l_{\mathrm{DX}}^2}{2R_0}\cdot\frac{\xi}{1-\xi}, \tag{B.21}$$

$$\theta_x = \frac{x_1 - x_{\mathrm{IP}} - \left(d_2 + \frac{1}{2}l_{\mathrm{DX}}\right)\theta_x^{\mathrm{RP}}}{d_1 - z_{\mathrm{IP}} + \frac{1}{2}l_{\mathrm{DX}}}, \qquad \xi = \left(1 + \frac{\alpha_0\left(d_1 + \frac{1}{2}l_{\mathrm{DX}} - z_{\mathrm{IP}}\right)}{\theta_x^{\mathrm{RP}}\left(d_1 + l_{\mathrm{DX}} + d_2 - z_{\mathrm{IP}}\right) - x_1 + x_{\mathrm{IP}}}\right)^{-1}. \tag{B.22}$$

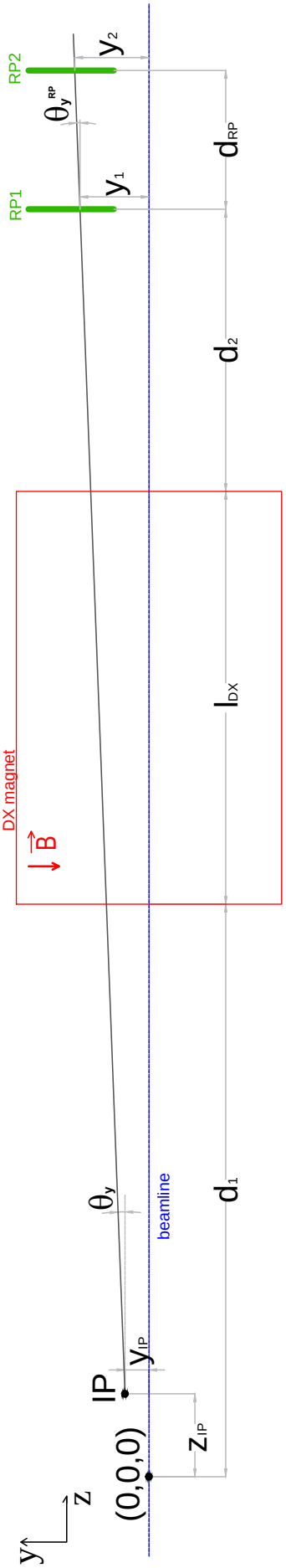

Figure B.2: Schematic view of the projection of the beam line and the scattered proton trajectory on the yz plane (side view). Proportions of the elements are not preserved.

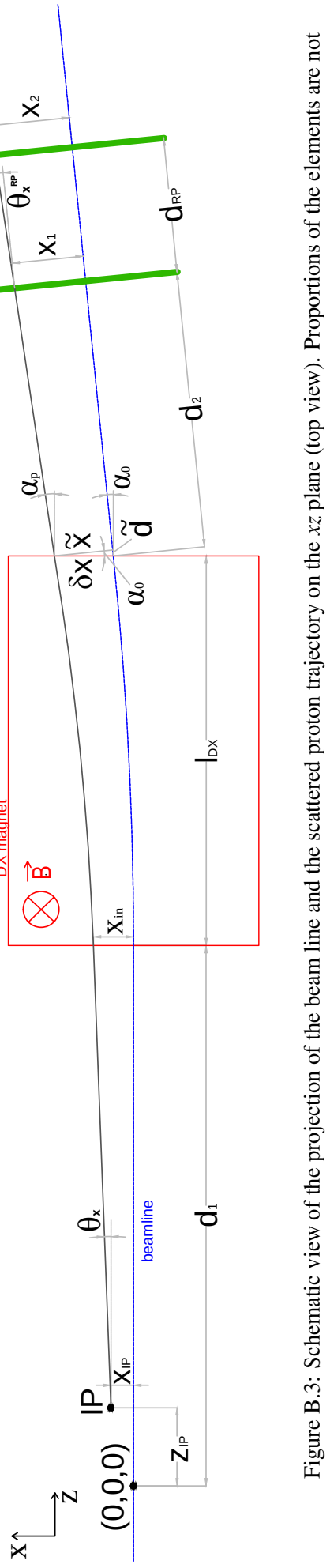

Figure B.3: Schematic view of the projection of the beam line and the scattered proton trajectory on the xz plane (top view). Proportions of the elements are not preserved.

C. Reconstruction of m^2_{TOF}

Definitions:

t_0 - time of the primary pp interaction,
t_i - time of detection of the hit in TOF by particle $i = 1, 2$,
L_i - helical path of the particle $i = 1, 2$ from the interaction vertex to the TOF cell with reconstructed hit,
p_i - magnitude of the momentum of particle $i = 1, 2$,
m_i - mass of particle $i = 1, 2$.

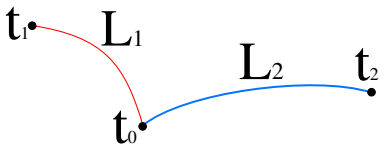

Figure C.1: Sketch of two central tracks of lengths L_1 and L_2, produced in a common vertex at t_0, hitting TOF detector at times t_1 and t_2.

We consider two particles, which produce two helical tracks in the TPC and produce hits in the TOF detector, see Fig. C.1. The time difference, Δt, of their arrivals to the TOF is equal to:

$$\begin{cases} t_1 - t_0 = L_1 \sqrt{1 + \frac{m_1^2}{p_1^2}}, \\ t_2 - t_0 = L_2 \sqrt{1 + \frac{m_2^2}{p_2^2}}. \end{cases} \quad \Rightarrow \quad \Delta t = t_1 - t_2 = L_1 \sqrt{1 + \frac{m_1^2}{p_1^2}} - L_2 \sqrt{1 + \frac{m_2^2}{p_2^2}}. \tag{C.1}$$

Assuming that the particles come from the process of CEP of h^+h^- pairs, i.e. they have the same masses, $m_1 = m_2 = m_{\mathrm{TOF}}$, one gets from Eq. (C.1):

$$\mathcal{A} \times \left(m^2_{\mathrm{TOF}}\right)^2 + \mathcal{B} \times m^2_{\mathrm{TOF}} + C = 0. \tag{C.2}$$

where

$$\mathcal{A} = -2\frac{L_1^2 L_2^2}{p_1^2 p_2^2} + \frac{L_1^4}{p_1^4} + \frac{L_2^4}{p_2^4}, \tag{C.3}$$

$$\mathcal{B} = -2L_1^2 L_2^2 \left(\frac{1}{p_1^2} + \frac{1}{p_2^2}\right) + \frac{2L_1^4}{p_1^2} + \frac{2L_2^4}{p_2^2} - 2\left(\Delta t\right)^2 \left(\frac{L_1^2}{p_1^2} + \frac{L_2^2}{p_2^2}\right), \tag{C.4}$$

$$C = \left(\Delta t\right)^4 - 2\left(\Delta t\right)^2 \left(L_1^2 + L_2^2\right) + L_1^4 + L_2^4 - 2L_1^2 L_2^2. \tag{C.5}$$

Finally[1]:

$$m^2_{\mathrm{TOF}} = \frac{-\mathcal{B} + \sqrt{\mathcal{B}^2 - 4\mathcal{A}C}}{2\mathcal{A}}. \tag{C.6}$$

[1] Only one root of Eq. (C.2) is physically meaningful (the one which yields positive m^2_{TOF}).

D. Total RP efficiency

Definitions:

RP^{E}	- single good quality track (satisfying cuts SC4.1-SC4.2) on the East side,
RP^{W}	- single good quality track (satisfying cuts SC4.1-SC4.2) on the West side,
TR^{E}	- trigger signal in the RP branch with the single good track on the East side,
$\mathrm{TR}^{\mathrm{E}}_{\mathrm{other}}$	- trigger signal in the RP branch other than the branch with the single good track on the East side,
TR^{W}	- trigger signal in the RP branch with the single good track on the West side,
$\mathrm{TR}^{\mathrm{W}}_{\mathrm{other}}$	- trigger signal in the RP branch other than the branch with the single good track on the West side,
Veto	- trigger veto on the simultaneous trigger signal in Upper and Lower RP detectors,
$\mathrm{Veto}^{\mathrm{PU}}$	- trigger veto on ET&IT (Veto) due to pile-up interactions,
$\mathrm{Veto}^{\mathrm{DM}}$	- trigger veto on ET&IT (Veto) due to forward proton interaction with dead material.

The total trigger and reconstruction efficiency for tagging of the forward-scattered protons in the CEP events in both the East and the West RP stations can be written as:

$$\begin{aligned}\varepsilon\left(\mathrm{RP}^{\mathrm{E}} \wedge \mathrm{RP}^{\mathrm{W}} \wedge \mathrm{TR}^{\mathrm{E}} \wedge \mathrm{TR}^{\mathrm{W}} \wedge \ !\mathrm{Veto}\right) = \\ = \varepsilon\left(\mathrm{RP}^{\mathrm{E}} \wedge \mathrm{RP}^{\mathrm{W}} \,\middle|\, \mathrm{TR}^{\mathrm{E}} \wedge \mathrm{TR}^{\mathrm{W}} \wedge \ !\mathrm{Veto}\right) \cdot \varepsilon\left(\mathrm{TR}^{\mathrm{E}} \wedge \mathrm{TR}^{\mathrm{W}} \wedge \ !\mathrm{Veto}\right),\end{aligned} \tag{D.1}$$

where the factorisation on r.h.s. follows from the definition of conditional probability. Note, that the first term on the r.h.s. represents the reconstruction efficiency of the forward-scattered protons under the condition that the event is triggered, and the second term is just the trigger efficiency.

This first term on the r.h.s. of Eq. (D.1), can be represented as a product of single-proton reconstruction and selection efficiencies described in Sec. 11.2.3 and an additional component, that accounts for the correlation between the East and the West RP's efficiencies. This correlation is defined as:

$$\rho_{\mathrm{EW}} = \frac{\varepsilon_{\mathrm{EW}} - \varepsilon_{\mathrm{E}} \cdot \varepsilon_{\mathrm{W}}}{\sqrt{\varepsilon_{\mathrm{E}} \cdot (1-\varepsilon_{\mathrm{E}}) \cdot \varepsilon_{\mathrm{W}} \cdot (1-\varepsilon_{\mathrm{W}})}}, \tag{D.2}$$

where

$$\varepsilon_{\mathrm{E}} = \varepsilon\left(\mathrm{RP}^{\mathrm{E}} \,\middle|\, \mathrm{TR}^{\mathrm{E}} \wedge \ !\mathrm{TR}^{\mathrm{E}}_{\mathrm{other}}\right), \qquad \varepsilon_{\mathrm{W}} = \varepsilon\left(\mathrm{RP}^{\mathrm{W}} \,\middle|\, \mathrm{TR}^{\mathrm{W}} \wedge \ !\mathrm{TR}^{\mathrm{W}}_{\mathrm{other}}\right),$$
$$\varepsilon_{\mathrm{EW}} = \varepsilon\left(\mathrm{RP}^{\mathrm{E}} \wedge \mathrm{RP}^{\mathrm{W}} \,\middle|\, \mathrm{TR}^{\mathrm{E}} \wedge \mathrm{TR}^{\mathrm{W}} \wedge \ !\mathrm{Veto}\right).$$

From the above we get

$$\varepsilon\left(\mathrm{RP}^{\mathrm{E}} \wedge \mathrm{RP}^{\mathrm{W}} \,\middle|\, \mathrm{TR}^{\mathrm{E}} \wedge \mathrm{TR}^{\mathrm{W}} \wedge \ !\mathrm{Veto}\right) = \varepsilon_{\mathrm{E}} \cdot \varepsilon_{\mathrm{W}} + \rho_{\mathrm{EW}} \cdot \sqrt{\varepsilon_{\mathrm{E}} \cdot (1-\varepsilon_{\mathrm{E}}) \cdot \varepsilon_{\mathrm{W}} \cdot (1-\varepsilon_{\mathrm{W}})}. \tag{D.3}$$

The correlation coefficient, ρ_{EW}, provides information on simultaneous (un)successful reconstruction/selection of RP track on the East and the West side in the same event. Simultaneous unsuccessful reconstruction of the two forward-scattered protons can be a result of e.g. a pile-up interaction, typically of elastic proton-proton scattering, producing additional tracks/showers simultaneously in the East and the West RPs and thus introducing simultaneous East and West RP inefficiency. With the above

correlation taken into account, one is able to properly reconstruct yield of true-level observables and shape of their distributions, as shown in the closure test in Sec. 11.8.2.

In the component of RP efficiency related to the trigger we can use again the conditional probability and factorise it to the part connected with the trigger veto and the efficiency of detecting signals for both forward-scattered protons by the trigger system:

$$\varepsilon\left(\mathrm{TR}^{\mathrm{E}} \wedge \mathrm{TR}^{\mathrm{W}} \wedge \ !\mathrm{Veto}\right) = \varepsilon\left(!\mathrm{Veto} \,\middle|\, \mathrm{TR}^{\mathrm{E}} \wedge \mathrm{TR}^{\mathrm{W}}\right) \cdot \varepsilon\left(\mathrm{TR}^{\mathrm{E}} \wedge \mathrm{TR}^{\mathrm{W}}\right). \tag{D.4}$$

The triggering efficiency, $\varepsilon\left(\mathrm{TR}^{\mathrm{E}} \wedge \mathrm{TR}^{\mathrm{W}}\right)$, is better than 99% (see Sec. 12.4.3). Efficiency of the (lack of) veto under the condition that the forward-scattered protons were triggered in the East and the West RPs, can be decomposed into an efficiency of the veto induced by a pile-up interaction in the same bunch crossing ($\mathrm{Veto}^{\mathrm{PU}}$) and an efficiency of the veto induced by the interaction of the forward-scattered protons with the dead material ($\mathrm{Veto}^{\mathrm{DM}}$):

$$\begin{aligned}\varepsilon\left(!\mathrm{Veto} \,\middle|\, \mathrm{TR}^{\mathrm{E}} \wedge \mathrm{TR}^{\mathrm{W}}\right) = \left|\mathrm{Veto} = \mathrm{Veto}^{\mathrm{PU}} \vee \mathrm{Veto}^{\mathrm{DM}}\right| = \varepsilon\left(!\mathrm{Veto}^{\mathrm{PU}} \wedge \ !\mathrm{Veto}^{\mathrm{DM}} \,\middle|\, \mathrm{TR}^{\mathrm{E}} \wedge \mathrm{TR}^{\mathrm{W}}\right) = \\ = \varepsilon\left(!\mathrm{Veto}^{\mathrm{DM}} \,\middle|\, !\mathrm{Veto}^{\mathrm{PU}} \wedge \mathrm{TR}^{\mathrm{E}} \wedge \mathrm{TR}^{\mathrm{W}}\right) \cdot \varepsilon\left(!\mathrm{Veto}^{\mathrm{PU}} \,\middle|\, \mathrm{TR}^{\mathrm{E}} \wedge \mathrm{TR}^{\mathrm{W}}\right).\end{aligned} \tag{D.5}$$

The first conditional efficiency in the second line of Eq. (D.5) has been already discussed in Sec. 11.1.3 and is equal to the complementary probability to that provided in Eq. (11.3). It can be further factorised into separate efficiencies corresponding to the East and the West RPs, as the probabilities for the forward-scattered protons to induce RP trigger vetoes on the East and one the West sides are independent:

$$\begin{aligned}\varepsilon\left(!\mathrm{Veto}^{\mathrm{DM}} \,\middle|\, !\mathrm{Veto}^{\mathrm{PU}} \wedge \mathrm{TR}^{\mathrm{E}} \wedge \mathrm{TR}^{\mathrm{W}}\right) = \\ = \varepsilon^{\mathrm{E}}\left(!\mathrm{Veto}^{\mathrm{DM}} \,\middle|\, !\mathrm{Veto}^{\mathrm{PU}} \wedge \mathrm{TR}^{\mathrm{E}} \wedge \mathrm{TR}^{\mathrm{W}}\right) \cdot \varepsilon^{\mathrm{W}}\left(!\mathrm{Veto}^{\mathrm{DM}} \,\middle|\, !\mathrm{Veto}^{\mathrm{PU}} \wedge \mathrm{TR}^{\mathrm{E}} \wedge \mathrm{TR}^{\mathrm{W}}\right)\end{aligned} \tag{D.6}$$

The second conditional efficiency in the second line of Eq. (D.5) related with the pile-up is incorporated to overall efficiency of online and offline vetoes described in Sec. 11.3.4 - this is required by the correlation of vetoes, the possibility that vetoes in independent subdetectors take place in the same bunch crossing. This could happen if e.g. single diffraction event occurs on top of the CEP event, yielding a BBC signal and RP signal, both vetoing RP_CPT2 trigger.